Structural and metamorphic evolution of the Zanskar Himalaya, Suru Valley region, NW India



Ian Peter Cawood

University of Oxford

A thesis submitted for the degree of
Doctor of Philosophy

Worcester College June 2024

Acknowledgements

A lengthy thesis necessitates a lengthy list of thank-yous. First and foremost, I would like to thank my all star team of supervisors: Mike Searle, Owen Weller, Marc St-Onge, Nick Roberts, and Dave Waters. I'm thankful to each and every individual for their patience with the unending levels of pestering they were subjected to. Mike 'just map from Leh to Padum' Searle, I'm extremely grateful to have been introduced to such an incredible and unique field area and for the opportunity to share in Mike's unending knowledge of the Himalayas. It should also go without saying that the beer garden pints were always a welcome treat. There's been a legacy of talented hard rock wallahs under Mike, I'm convinced it must be something in all those chapattis. Owen 'Chapter 3 was a waste of time' Weller, providing both the necessary questioning, and the space and support when I inevitably decided to carve my own path. I've learnt an incredible amount from Owen and had immense fun doing it along the way. Marc '1013 comments' St-Onge, possessing an incredible eye for maps, minerals, grammar, and of course a 'nice cold one'. There was never any fear of getting an early night or becoming 'dehydrated' around Marc. Thanks to the 'Beer Ledger Boiz' for providing one of the best fieldwork experiences to date. Nick 'let's just blast everything' Roberts, for allowing me to work through a gargantuan number of samples and nearly as many accessory phases. Every lab trip was equal parts hectic and fun, of course excluding the one session I'd sooner forget... jokes about broken thin sections will always be treated as "too soon". Dave 'I've got a spreadsheet for that' Waters, Chapters 3 and 4 would have been quicker, shorter, and worse of for it. There's more knowledge available then any one individual should be able to house, I'm convinced that the flat cap must provide extra storage.

I'd also like to say thanks to a few extra people without which this project wouldn't have been possible. Talat Ahmad, for providing invaluable support during several seasons of fieldwork and his input on the regional geology. To Nabiley and his family at Sia-La for their kindness and assistance with fieldwork logistics in Leh. Hamish Stirling and Jordy De Vries for being A^+ field assistants.

Whether teetering off the edge of a ridgeline, sliding down landslides, or wading through glacial rivers, I couldn't have asked for better set of rock mules. To the various drivers from Kargil, most notably Mohammed Ali, who very much seemed the most popular man in all of Jammu & Kashmir, taking more phone calls during our trips than most individuals receive in one life time. Tsering and Gailpo, for providing delicious meals, endless chapattis, good humour and a friendly face at whatever hour of the day it was required. Highlights include: pakhora, milky tea, matar paneer, and the seemingly magical ability to conjur up cake on the camp stove. I would also like to thank the people of the Suru Valley region for welcoming me with such warmth throughout my trips. This included providing free rides in the back of trucks, stopping to give us juice drinks on the side of the road, offering yak-butter tea (which was of course declined) or milky tea (which was of course chugged by the litre), and to the seemingly constant interest from any local kid who wanted to join us around the outcrops. Particular thanks to the porters during our treks down Chellong nala, Shanshin nala, and Lalung valley, not only providing incredible agility and strength despite some individuals being more than double my age, but for also being so good-humoured and teaching us the ropes of treacherous river crossings. Despite not acting as a formal supervisor, Richard Palin deserves significant thanks for his incredible willingness and generosity with his time. John Wells, for making all those thin sections; and Andrew Matzen and Jon Wade, for helping me carve through more samples on the probe then most students should be allowed to.

Whilst few in number, the hard rock geologists at Oxford provided much needed sanity during the final stages of the PhD. Tobermory Mackay-Champion deserves a medal for putting up with my incessant nattering and pedantic behaviour on all things P-T, it's been a lot of fun working together and I look forward to future collaborations. Of course, not forgetting our many tennis and squash matches, though generally I like to remember the latter and forget the former. Lot Koopmans, also for our squash sessions, and for showing that someone else in the department understands the importance of a good rock collection. I would also like to thank all the other wonderful members of the department, Bei Bei Morrison Evans, Nikki Sridhar, for consistent snacks and laughter over our fieldtrip demonstrating, and to the excellent office mates of 30.18 during the early PhD years. Never has one person been so incessantly bullied for spending all their time "colouring in".

I was lucky enough to start my PhD with an incredible cohort of other PhD students. Special shoutout to the numerous potlucks with the Abbey-

Addison-Forker gang; bike rides and pottery sessions with Benedict; and tennis procrastination with Felix. I was also fortunate enough to be subjected to living with some of this cohort during our very extended PhD soiree. Matthew, David, Ben and Nacho, there are too many memories and 'supplementary beverages' to count, but I couldn't have asked for a more supportive, board-game-obsessed, bunch of nutters. I think we all managed to keep ourselves sane by going slightly insane together.

Despite not being subjected to the day to day insanity of PhD lives together, the St Andrews crew have also been an excellent source of good humour over the last few years. Thanks for the pestering to get it done, and providing housing during my many Scotland hiking trips.

To Claire, for her unending support and patience throughout it all, and for constantly dragging me out of whatever rabbit hole I'd managed to descend into. I look forward to future adventures together, this time without a PhD-laden boyfriend.

Last but not least, my heartfelt thanks goes to my family. Despite several years hiding at the back of lectures pretending to be unrelated to the short-short strutting, loud-mouthed, Professor Peter Fucking Cawood, I think it's all been worth it in the end. Thanks for being a sounding board for anything and everything rock-related, and for the encouragement along the way. To Emma, for her reassurance and advice (especially when the advice came in the form of booze). To mum and dad, for their endless love and support, and for keeping me fed during the final months.

Abstract

The Suru Valley, NW India, is unique in the Himalayan mountain belt in preserving a widespread pressure-temperature-time-deformation (*P*-*T*-*t*-D) record of the early part of the collisional orogenic cycle, characterised by pervasive crustal thickening and Barrovian metamorphism. In addition, widespread magmatism and metamorphism (*ca.* 505–453 Ma) occurred on the Indian margin during the Bhimphedian orogeny and subsequent localised magmatism during the Permian (*ca.* 282-268 Ma). These records are deciphered by integrating petrographic and structural analysis, phase equilibrium modelling, and U-(Th)-Pb geochronology. During the India-Asia collision, the Indian margin experienced SW-vergent thrusting and folding (D_1 and D_2) with greenschist- to amphibolite-facies metamorphism. Mineral isograd patterns and the relationship between porphyroblast growth and fabric development suggest the thermal peak of metamorphism outlasted deformation within the Himalayan metamorphic core (HMC). Deformation and metamorphism propagated SW-wards with decreasing structural level and increasing metamorphic grade. Prograde conditions, syn-D_2, are dominantly attained between *ca.* 38–30 Ma. Peak M_1 conditions are recorded syn- to post-D_2 between *ca.* 37–27 Ma. Average metamorphic field gradients are 36 °C kbar^{-1} during the early stages of metamorphism, with progressive M_1 peak attained at 47 °C kbar^{-1}. In the deepest structural levels of the HMC, decompression initiates after *ca.* 28 Ma on a near-isothermal path towards sillimanite-grade conditions and peak M_2 is recorded across grades between *ca.* 25–21 Ma, coincident with extension on the Zanskar Shear Zone (ZSZ, local equivalent of the South Tibetan Detachment) at around *ca.* 23 Ma. These temporal constraints and limited recorded displacement along the ZSZ suggest unroofing through erosion may first drive metamorphic decompression, prior to main phase of movement on the ZSZ. Consistent passive margin-stratigraphy, an inter-tectonic thermal peak, thick and melt-poor GHS, and minor D_3 development and ZSZ displacement are not supported by a channel flow model for exhumation of the HMC.

Table of contents

List of figures **xv**

List of tables **xxi**

1 Introduction and Regional Geology **1**

1.1 Introduction 2
1.2 Regional Geology of the Himalaya 3
1.3 South Tibetan Detachment System (STDS) 6
1.4 Greater Himalayan Sequence (GHS) 6
1.5 Main Central Thrust (MCT) zone 7
1.5.1 Geological subdivision of the Himalaya 7
1.6 Models for exhumation of the HMC 8
1.7 Aims and thesis structure 10

2 Structural and Metamorphic Architecture **11**

2.1 Introduction 12
2.2 Geological Overview and Previous Work 14
2.2.1 Geological setting of the Zanskar Himalaya 14
2.2.1.1 Indus Suture Zone (ISZ) 14
2.2.1.2 Tethyan Himalayan Sequence (THS) 16
2.2.1.3 Greater Himalayan Sequence (GHS) 17
2.2.2 Regional geology of the Suru Valley area 17
2.2.3 Previous metamorphic constraints and geochronology of NW India 20
2.3 Methods 21
2.4 Lithostratigraphic architecture and geological map 24
2.5 Lithostratigraphy 28
2.5.1 Indus Suture Zone 28
2.5.1.1 Dras Volcanics 28
2.5.1.2 Lamayuru Complex - Metasedimentary units . . 29
2.5.1.3 Lamayuru Complex - Metavolcanic rocks 30

2.5.2 GHS–THS . . . 30
2.5.2.1 Metasedimentary units . . . 30
2.5.2.2 Metavolcanic and subvolcanic rocks . . . 31
2.5.2.3 Metamorphosed granites . . . 32
2.5.2.4 Migmatite . . . 33
2.6 Structural architecture . . . 34
2.6.1 $S_0/S_1/L_1$ . . . 35
2.6.2 $S_2/L_2/F_2$ . . . 39
2.6.3 $S_3/L_3/F_3$ . . . 42
2.6.4 F_4 . . . 44
2.6.5 F_5 . . . 45
2.6.6 Structural zones . . . 45
2.7 Metamorphic architecture . . . 48
2.7.1 Pelite index minerals . . . 48
2.7.2 Metabasite index minerals . . . 54
2.7.3 Other minerals . . . 57
2.7.4 Relationship of peak metamorphic minerals to penetrative fabrics . . . 57
2.7.5 Isograds . . . 58
2.8 Discussion and Tectonic Implications . . . 61
2.8.1 Mechanisms of crustal thickening and burial during orogenesis 63
2.8.2 Relationship between lithostratigraphy, fabric development, macroscale deformation and metamorphism in the HMC . 65
2.8.3 Crustal scale folding and domal culminations . . . 66
2.8.4 Implications for Himalayan tectonics and orogenic processes 68
2.9 Conclusions . . . 71

3 Petrography and Mineral Chemistry 77
3.1 Petrographic descriptions . . . 78
3.1.1 ISZ . . . 78
3.1.1.1 Dras Volcanics . . . 78
3.1.1.2 Metasedimentary rocks . . . 79
3.1.1.3 Metavolcanic rocks . . . 83
3.1.2 GHS–THS . . . 85
3.1.2.1 Metasedimentary rocks . . . 85
3.1.2.2 Metavolcanic rocks . . . 93
3.1.2.3 Metagranites . . . 96
3.1.2.4 Migmatite . . . 100

3.2 Mineral chemistry . . . 103
3.2.1 Methods . . . 103
3.2.2 Pelitic units . . . 104
3.2.2.1 Garnet . . . 104
3.2.2.2 Staurolite . . . 108
3.2.2.3 Plagioclase & K-feldspar . . . 109
3.2.2.4 Chlorite . . . 110
3.2.2.5 Biotite . . . 111
3.2.2.6 Muscovite . . . 114
3.2.3 Metabasic units . . . 117
3.2.3.1 Amphibole . . . 117
3.2.3.2 Garnet . . . 119
3.2.3.3 Plagioclase . . . 120
3.2.3.4 Chlorite . . . 122
3.2.3.5 Biotite . . . 123
3.2.3.6 Epidote . . . 126
3.3 Comparison of pelitic and metabasic mineral chemistry and textures 126

4 Phase Equilibrium Modelling 135
4.1 Principles of thermobarometry . . . 136
4.1.1 Equilibrium . . . 136
4.1.2 Thermodynamics . . . 137
4.1.2.1 Gibbs free energy . . . 138
4.1.2.2 Activity . . . 139
4.1.2.3 Fundamental equations . . . 140
4.1.3 Geothermometry . . . 142
4.1.3.1 Geobarometry . . . 143
4.1.3.2 Single phase concentration thermobarometry . . . 144
4.1.3.3 Multi-equilibrium thermobarometry . . . 145
4.1.3.4 Elastic Thermobarometry . . . 147
4.1.4 Phase equilibrium modelling . . . 148
4.1.4.1 Gibbs Phase Rule . . . 149
4.1.4.2 Duhem's theorem . . . 150
4.1.4.3 Types of phase diagrams . . . 151
4.1.5 Limitations and uncertainties . . . 152
4.1.5.1 Geological error . . . 153
4.1.5.2 Analytical error . . . 155
4.1.5.3 Parameter error . . . 155

4.1.5.4 Model error . . . 157
4.2 Thermobarometry methods . . . 158
4.2.1 Pseudosection setup . . . 158
4.2.2 Thermometry . . . 160
4.2.2.1 Zr-in-rutile . . . 162
4.2.2.2 Hornblende-plagioclase and Ti-in-Ca-amphibole . 162
4.2.2.3 Zr-in-titanite . . . 163
4.2.2.4 Ti-in-biotite . . . 163
4.2.3 Constraining $a\mathrm{H_2O}$ and pseudosection construction . . . 164
4.2.4 Grid-search non-linear inversion . . . 166
4.2.5 X-ray fluorescence . . . 168
4.3 Sample descriptions . . . 168
4.3.1 Pelite . . . 169
4.3.1.1 Garnet zone: ICSV86, ICSV38, ICSV130 . . . 169
4.3.1.2 Staurolite zone: ICSV109, ICSV113, ICSV30 . . 175
4.3.1.3 Kyanite zone: ICSV13, ICSV12 . . . 179
4.3.1.4 Sillimanite zone: ICSV91, ICSV81 . . . 183
4.3.1.5 Sillimanite+K-feldspar zone: ICSV145, ICSV150 186
4.3.2 Metabasite . . . 190
4.3.2.1 Hornblende zone: ICSV50, ICSV2 . . . 190
4.3.2.2 Oligoclase zone: ICSV92 . . . 194
4.3.2.3 Garnet+plagioclase zone . . . 196
4.4 *P-T* results . . . 201
4.4.1 Single phase concentration and mineral pair thermometry . 201
4.4.1.1 Zr-in-rutile . . . 202
4.4.1.2 Hornblende-plagioclase and Ti-in-Ca-amphibole . 203
4.4.1.3 Zr-in-titanite . . . 204
4.4.1.4 Ti-in-biotite . . . 204
4.4.1.5 Multiphase thermometry summary and limitations 206
4.4.2 Multi-equilibrium barometry . . . 209
4.4.3 Impact of $a\mathrm{H_2O}$ . . . 211
4.4.3.1 ICSV86 (garnet zone) and ICSV13 (kyanite zone) 212
4.4.4 Pelite . . . 218
4.4.4.1 Garnet zone . . . 219
4.4.4.2 Staurolite zone . . . 223
4.4.4.3 Kyanite zone . . . 227
4.4.4.4 Sillimanite zone . . . 232
4.4.4.5 Sillimanite+K-feldspar zone . . . 234

4.4.5 Metabasite . . . 239
4.4.5.1 Hornblende zone . . . 240
4.4.5.2 Oligoclase zone . . . 244
4.4.5.3 Garnet+plagioclase zone . . . 246
4.4.6 Comparison of pelitic and metabasic *P-T* results . . . 253
4.4.7 *P-T* record of the Suru Valley region and implications for GHS . . . 259
4.4.8 Implications of reduced aH_2O . . . 263
4.4.9 Uncertainty on *P-T* measurements . . . 265
4.5 Conclusion . . . 266

5 Multiphase U-(Th)-Pb geochronology 269
5.1 Principles of radioisotopic dating . . . 270
5.1.1 Equations of decay . . . 270
5.1.2 U-Th-Pb systematics . . . 271
5.1.3 Interpretation and visualisation of U-(Th)-Pb data . . . 274
5.2 Analytical approach . . . 275
5.2.1 Sample selection and preparation . . . 275
5.2.2 Mass spectrometry . . . 276
5.2.3 Data reduction . . . 277
5.2.4 Data quality control . . . 279
5.2.5 Nu-Attom and Agilent (LASS) . . . 280
5.3 Titanite . . . 281
5.3.1 Results . . . 281
5.3.1.1 Group 1: low-grade porphyropblastic titanite (*ca.* 38–30 Ma) . . . 281
5.3.1.2 Group 2: porphyroblast hosted titanite(*ca.* 46–37 Ma) . . . 284
5.3.1.3 Group 3: high-grade coarse titanite (*ca.* 22–21 Ma) 287
5.3.1.4 Group 4: polycrystalline matrix titanite (*ca.* 21 Ma) . . . 288
5.3.1.5 Group 5: coarse matrix and porphyroblast hosted titanite (17-16 Ma)) . . . 288
5.3.1.6 Other . . . 290
5.3.1.7 Zr-in-titanite and trace element discrimination . . 291
5.3.2 Interpretation . . . 296
5.3.2.1 Pre-Himalayan metamorphism and magmatism . 296
5.3.2.2 Prograde–peak . . . 297

5.3.2.3 Decompression . . . 298
5.3.2.4 Recrystallisation and cooling . . . 299
5.4 Allanite . . . 299
5.4.1 Results . . . 299
5.4.1.1 Biotite- & garnet-zone pelite: porphyroblastic allanite . . . 299
5.4.1.2 Garnet- & kyanite-zone graphite-rich pelite: porphyroblast- or coarse matrix-hosted . . . 303
5.4.2 Interpretation . . . 304
5.4.2.1 Timing of fabric development . . . 304
5.4.2.2 Timing of porphyroblast growth . . . 305
5.5 Monazite . . . 306
5.5.1 Results . . . 306
5.5.1.1 Garnet zone . . . 307
5.5.1.2 Staurolite zone . . . 307
5.5.1.3 Kyanite zone . . . 308
5.5.1.4 Sillimanite zone . . . 312
5.5.1.5 Sillimanite+K-feldspar zone . . . 313
5.5.1.6 LASS . . . 315
5.5.1.7 Microstructure-age relationship . . . 317
5.5.1.8 Laser Ablation Split-Stream (LASS) petrochronology . . . 319
5.5.2 Interpretation . . . 323
5.5.2.1 Pre-Himalayan metamorphism . . . 323
5.5.2.2 Prograde–peak . . . 324
5.5.2.3 Decompression . . . 328
5.6 Zircon . . . 328
5.6.1 Results . . . 328
5.6.2 Psammite . . . 328
5.6.3 Metavolcanic rock . . . 329
5.6.4 Metamorphosed granite & leucogranite . . . 331
5.6.5 Interpretation . . . 332
5.6.5.1 Detrital record . . . 332
5.6.5.2 Igneous activity . . . 332
5.7 Rutile . . . 334
5.7.1 Results . . . 334
5.7.1.1 Metacarbonate . . . 334
5.7.1.2 Pelite . . . 334

5.7.1.3 Metabasite 336
5.7.2 Interpretation 336
5.8 Apatite 337
5.8.1 Results 337
5.8.1.1 Group B volcanic rock 337
5.8.2 Interpretation 338
5.9 Summary of multiphase geochronology 338
5.9.1 Pre-Himalayan magmatism and metamorphism 340
5.9.2 Constraints on burial, fabric development and metamorphism 343
5.9.3 Comparison to timing of events in NW Indian Himalaya . 349
5.9.3.1 Burial and prograde–peak metamorphism 350
5.9.3.2 Decompression, Zanskar Shear Zone movement and leucogranite crystallisation 352
5.9.4 Controlling factors on distribution of isotopic ages 355
5.9.4.1 Titanite 356
5.9.4.2 Allanite 357
5.9.4.3 Monazite 357
5.10 Conclusions 364

6 Synthesis and Tectonic Implications 367
6.1 Integrated *P-T-t-D* evolution of the Suru Valley region 368
6.1.1 Pre-collisional history 368
6.1.2 Crustal thickening and M_1 (> *ca.* 38–28 Ma) 370
6.1.3 Decompression, M_2 and D_3 exhumation (*ca.* 28–20 Ma) . . 374
6.1.4 Continued exhumation, backthrusting and $D_{4–5}$ ()< *ca.* 20 Ma) 375
6.2 Implications for the metamorphic evolution of the Himalaya . . . 376
6.3 Future work 381

References 385

Appendix A Structure 429

List of figures

1.1 Simplified geological map of the Himalaya 5

2.1 Simplified geological map of NW India 15
2.2 Published P-T data for HMC rocks in NW India 19
2.3 Published geochronology data for HMC rocks in NW India 22
2.4 1:50,000-scale geological map of the Suru Valley region 25
2.5 Vertical cross-sections of the Suru Valley region 25
2.6 Lithostratigraphy of the Suru Valley region 27
2.7 Form-line map with planar structural elements 36
2.8 Form-line map with linear structural elements 37
2.9 Meso-scale field photos of planar and linear features formed during D_1–D_3 38
2.10 Annotated panoramic field photographs of macro-scale folds 40
2.11 Simplified geological map of the Suru Valley region with D_1–D_3 stereonet data 46
2.12 Mineral growth–deformation relationship photomicrographs 49
2.13 Meso-scale field photos of mineral growth relative to $D_{2–3}$ fabric development 51
2.14 Inferred mimetic and epitaxial growth of peak porphyroblast phases 52
2.15 Form-line map with metasedimentary rock mineral assemblages . . 53
2.16 Simplified geological map with metabasite metamorphic mineral assemblages 55
2.17 Summary of fabric development vs. mineral growth 58
2.18 Mid-crustal block diagrams summarising the tectonic evolution of the Suru Valley region 62
2.19 Schematic summary of the macro- to micro-scale relationship between deformation and metamorphism at thermal peak 69

3.1 Photomicrographs of the Dras Volcanics 79
3.2 Photomicrographs of the Lamayuru Complex 80
3.3 Photomicrographs of the group B metavolcanic rock samples 84

3.4 Photomicrographs of pelite; mixed psammite, pelite, and semipelite; and psammite units 86
3.5 Photomicrographs of metacarbonate; and mixed semipelite, metacarbonate, and pelite units 91
3.6 Photomicrographs of group A metavolcanic rock samples 94
3.7 Photomicrographs of metamorphosed granites 97
3.8 Photomicrographs of migmatite lithology 101
3.9 Photomicrographs of representative garnets hosted in migmatite . . 102
3.10 Garnet compositional profiles from the garnet and staurolite zones . 105
3.11 Garnet compositional profiles from the kyanite to sillimanite+K-feldspar zone 106
3.12 Pelitic garnet core and rim values against metamorphic grade . . . 107
3.13 Staurolite composition plots 109
3.14 Pelitic feldspar composition variation by metamorphic grade 110
3.15 Pelitic chlorite composition plots 111
3.16 Major biotite substitutions grouped by metamorphic grade 112
3.17 Pelitic biotite and muscovite compositional variation vs metamorphic grade 113
3.18 Major muscovite substitutions grouped by metamorphic grade . . . 116
3.19 Amphibole compositional plots 119
3.20 Garnet compositional profiles for hornblende and garnet+plagioclase zones 120
3.21 Metabasite garnet core and rim values vs metamorphic grade 121
3.22 Metabasite feldspar composition varying by metamorphic grade . . 122
3.23 Metabasite chlorite compositional variation plots 123
3.24 Major biotite substitutions in metabasite grouped by metamorphic grade 124
3.25 Biotite compositions in metabasite vs metamorphic grade 125
3.26 Epidote substitutions vs metamorphic grade 126
3.27 Pelite and metabasite mineral compositional variation vs metamorphic grade 128
3.28 Pelite and metabasite feldspar compositional variation vs metamorphic grade 130
3.29 Pelite and metabasite biotite compositions vs metamorphic grade . 131

4.1 Distribution coefficient and equilibrium constant contoured P-T space for example thermobarometers 144
4.2 Example AvP calculations constraining $X\mathrm{CO}_2$ 147

4.3 Graphical schematic of bulk composition nomenclature 153
4.4 Schematic of geological uncertainty propagation 154
4.5 Grid-search non-linear inversion workflow 166
4.6 Form-line map with *P-T* sample locations 170
4.7 Petrographic images of garnet- and staurolite-zone samples 171
4.8 Garnet BSE images and X-ray compositional maps for garnet-zone samples 172
4.9 Garnet BSE images and X-ray compositional maps for staurolite- and kyanite-zone samples 176
4.10 Petrographic images of kyanite-, sillimanite-, and sillimanite+K-feldspar-zone samples 180
4.11 Garnet BSE images and X-ray compositional maps for kyanite-, sillimanite-, and sillimanite+K-feldspar-zone samples 182
4.12 Petrographic images of hornblende-, oligoclase-, and garnet+plagioclase-zone samples 191
4.13 Garnet BSE images and X-ray compositional maps for hornlende-zone and garnet+plagioclase-zone samples 192
4.14 Petrographic images of garnet+plagioclase-zone samples 200
4.15 Thermometry results for Zr-in-rutile, hornblende-plagioclase and Zr-in-titanite 203
4.16 Ti-in-biotite thermometry results between varying calibrations and rock compositions 205
4.17 Comparison of multiphase thermometry results across metamorphic grade and rock type 207
4.18 AvP results across metamorphic grade at selected thermometer value 211
4.19 Example $a\mathrm{H_2O}$ constraints through AvP and Ti-in-biotite in ICSV86 213
4.20 Example $a\mathrm{H_2O}$ constraints through AvP and Ti-in-biotite in ICSV13 214
4.21 Peak assemblage and mineral stability changes through varying $a\mathrm{H_2O}$ in ICSV86 216
4.22 Peak assemblage and mineral stability changes through varying $a\mathrm{H_2O}$ in ICSV13 217
4.23 Garnet zone: ICSV86 pseudosection and bootstrapped best-fit *P-T* result 220
4.24 Garnet zone: ICSV130 pseudosection and bootstrapped best-fit *P-T* result 222
4.25 Staurolite zone: ICSV109 pseudosection and bootstrapped best-fit *P-T* result 225

4.26 Staurolite zone: ICSV113 pseudosection and bootstrapped best-fit *P-T* result . . . 226
4.27 Kyanite zone: ICSV13 pseudosection and bootstrapped best-fit *P-T* result . . . 229
4.28 Kyanite zone: ICSV12 pseudosection and bootstrapped best-fit *P-T* result . . . 231
4.29 Sillimanite zone: ICSV91 pseudosection and bootstrapped best-fit *P-T* result . . . 233
4.30 Sillimanite zone: ICSV81 pseudosection and bootstrapped best-fit *P-T* result . . . 235
4.31 Sillimanite+K-feldspar zone: ICSV145 pseudosection and *P-T* constraints . . . 237
4.32 Sillimanite+K-feldspar zone: ICSV150 pseudosection and *P-T* constraints . . . 238
4.33 Hornblende zone: ICSV50 pseudosection and bootstrapped best-fit *P-T* result . . . 241
4.34 Hornblende zone: ICSV2 pseudosection and bootstrapped best-fit *P-T* result . . . 243
4.35 Oligoclase zone: ICSV92 pseudosection and bootstrapped best-fit *P-T* result . . . 245
4.36 Garnet+plagioclase zone: ICSV138 pseudosection and bootstrapped best-fit *P-T* result . . . 248
4.37 Garnet+plagioclase zone: ICSV117 pseudosection and bootstrapped best-fit *P-T* result . . . 249
4.38 Garnet+plagioclase zone: ICSV5 pseudosection and bootstrapped best-fit *P-T* result . . . 251
4.39 Garnet+plagioclase zone: ICSV144 pseudosection and bootstrapped best-fit *P-T* result . . . 252
4.40 Form-line map with *P-T* results from pelitic and metabasic rocks . 256
4.41 Comparison of *P-T* results from pelitic and metabasic assemblages . 257
4.42 Schematic of *P-T* paths during crustal thickening accounting for variation in P_{max} and T_{max} . . . 260
4.43 Schematic *P-T* path for evolution of the Suru-Valley region . . . 263

5.1 Closure temperatures for commonly used thermochronometers . . . 272
5.2 LASS setup . . . 280
5.3 Form-line map with petrochronology sample locations . . . 282

5.4 BSE images of titanite microstructure and fabric and/or mineral relationships . . . 283
5.5 X-ray compositional zoning maps of titanite part 1 . . . 285
5.6 X-ray compositional zoning maps of titanite part 2 . . . 286
5.7 Tera-Wasserburg U-Th-Pb titanite plots part 1 . . . 289
5.8 Tera-Wasserburg U-Th-Pb titanite plots part 2 . . . 290
5.9 Titanite trace element plots . . . 292
5.10 BSE images of allanite porphyroblast and fabric relationship and X-ray compositional zoning maps . . . 300
5.11 X-ray compositional zoning maps of allanite grains . . . 301
5.12 U-Pb Tera-Wasserburg plots of allanite samples . . . 302
5.13 BSE images of monazite microstructural context . . . 306
5.14 BSE images and X-ray compositional maps for monazite from garnet to sillimanite zones . . . 308
5.15 BSE images and X-ray compositional maps for monazite from the sillimanite zone and sillimanite+K-feldspar zone . . . 309
5.16 U-(Th)-Pb results of monazite in garnet- to kyanite-zone samples . 310
5.17 U-(Th)-Pb results of monazite in kyanite-zone samples . . . 311
5.18 U-(Th)-Pb results of monazite in kyanite-zone and sillimanite-zone samples . . . 312
5.19 U-(Th)-Pb results of monazite in sillimanite+K-feldspar-zone samples . . . 314
5.20 U-(Th)-Pb results of monazite separates kyanite- and sillimanite+K-feldspar-zone samples analysed with LASS setup . . . 315
5.21 Age ranked and KDE Th-Pb monazite results separated by varying microstructural context . . . 318
5.22 Monazite trace element discrimination ratios and concetrations vs. Th-Pb ages . . . 321
5.23 Age ranked monazite Th-Pb analyses coloured by trace element discrimination ratios . . . 322
5.24 KDE plots for monazite partitioned by metamorphic grade . . . 325
5.25 Collated Th-Pb monazite analyses . . . 326
5.26 CL images of representative zircon grains . . . 329
5.27 U-Pb zircon concordia, lower intercept and KDE plots . . . 330
5.28 U-Pb results from rutile on Tera-Wasserburg plots part 1 . . . 335
5.29 U-Pb results from rutile on Tera-Wasserburg plots part 2 . . . 335
5.30 U-Pb results of apatite from ICSV225 on a Tera-Wasserburg plot . 338
5.31 Form-line map with summary of multiphase petrochronology results 339

5.32 Summary of multiphase U-(Th)-Pb geochronology results for Cambro-Ordovician age populations. 341
5.33 Summary of multiphase U-(Th)-Pb petrochronology results for Himalayan age populations 344
5.34 Variation of recovered monazite ages from kyanite-zone samples . . 362

6.1 Schematic summary of *P-T-t-D* conditions of the Suru Valley region 372
6.2 Mid-crustal block diagrams summarising *P-T-t-D* evolution of the Suru Valley regions 373

List of tables

2.1 Main deformation fabrics observed in Suru Valley area, Zanskar Himalaya. 34

2.2 Micro-, meso-, and macro-scale relationship between deformation and metamorphism in pelitic and metabasic rocks of the Suru Valley region. 64

4.1 Paired thermometry and AvP results 210

4.2 Best=fit P-T results from the MATLAB bootstrapping routine . . . 255

5.1 Petrochronological constraints on development of metamorphic fabrics and M_1 345

5.2 Petrochronological constraints on development of metamorphic fabrics and M_2 347

A.1 Structure of digital appendices and location and contents of all files 430

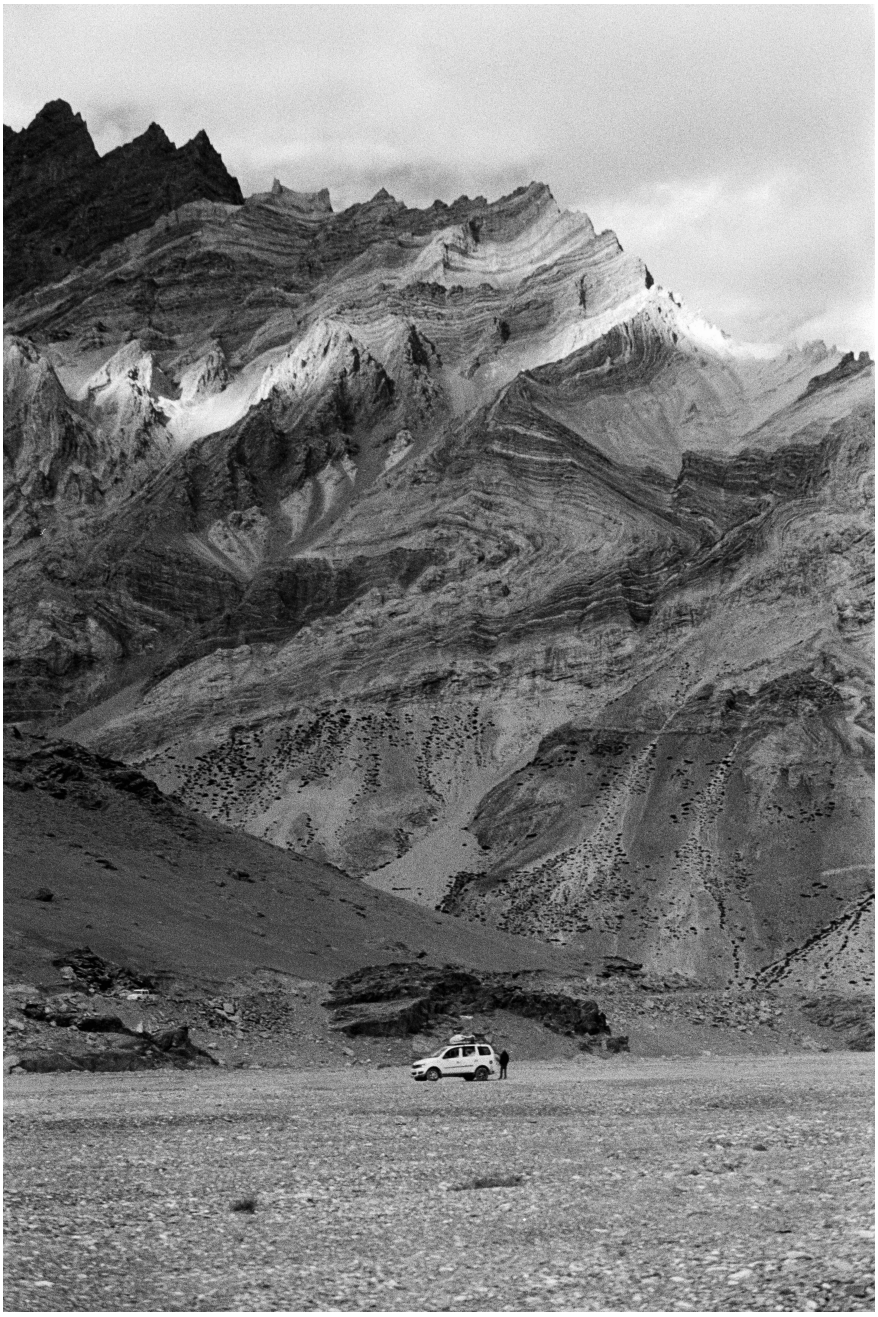
Abbreviations and symbols

Notation	Description
D	Deformation
G	Gibbs free energy
P	Pressure
S	Entropy
T	Temperature
V	Volume
X	Composition
X_{Alm}	Fe^{2+} / (Fe^{2+} + Mg + Ca + Mn); almandine content of garnet
X_{Cel}	Mg apfu; celadonite content in white mica
X_{Fe}	Fe^{3+} / (Al + Fe^{3+}); pistacite content of epidote
X_{Grs}	Ca / (Fe^{2+} + Mg + Ca + Mn); grossular content of garnet
X_{Jd}	Al^{VI} / (Na + Ca); jadeite content of clinopyroxene
X_{K}	K/(Na + Ca + K); potassium content of K-feldspar
X_{Mg}	Mg/(Mg + Fe^{2+}); the proportion of Mg in ferromagnesian minerals
X_{Na}	Na/(Na + Ca + K); albite content of plagioclase
X_{Pa}	Na/(Na + Ca + K); paragonite content of white mica
X_{Prp}	Mg / (Fe^{2+} + Mg + Ca + Mn); pyrope content of garnet
X_{Sps}	Mn / (Fe^{2+} + Mg + Ca + Mn); spessartine content of garnet
$X_{\mathrm{Fe^{3+}}}$	Fe^{3+}/(Fe^{2+} + Fe^{3+}); ferric iron ratio
μ	Chemical potential
$a\mathrm{H_2O}$	Activity of water
n	Number of moles
t	Time
apfu	Atoms per formula unit
AvP	Average pressure calculation within THERMOCALC
BGS	British Geological Survey
BSE	Backscattered electron
CL	Cathodoluminescence
EPMA	Electron microprobe analyser
GHS	Greater Himalayan Sequence
HMC	Himalayan metamorphic core

Notation	**Description**
IQR	Interquartile range
LASS	Laser ablation split-stream
LHS	Lesser Himalayan Sequence
MBT	Main Boundary Thrust
MCT	Main Central Thrust
MSWD	Mean squared weighted deviation
RM	Reference material
SD	Standard deviation
STD	South Tibetan Detachment
STDS	South Tibetan Detachment System
THS	Tethyan Himalayan Sequence
ZSZ	Zanskar Shear Zone

Chapter 1

Introduction and Regional Geology



Folded Tethyan shelf at Rangdum

1.1 Introduction

Mountain belts create the most extreme and rugged zones of topography on Earth. They have significant influence over weather and seismic hazard, host unique ecosystems and resources, modulate the global carbon cycle, and form geopolitical boundaries. Mountain belts have formed throughout much of Earth's 4.5 billion year history, the plate margins at which they form foster the continuous creation of new crust and simultaneous deformation and destruction of old crust. The stabilisation of this crust in mountain belts represent the interaction between surficial and deep Earth processes. Thus, modern and ancient mountain belts are the main source of information on the long-term evolution of our planet.

Continental crust within mountain belts is stabilised through crustal thickening and then dissipation of the resultant potential energy via erosion, extensional faulting, or a combination of both. The first-order nature of these processes has been known for many years, but the relative temporal and spatial relationships, and quantitative rates at which such processes propagate through the crust remain poorly constrained. The crustal record in continental collision zones may be effectively studied in metamorphic rocks that are buried to great depths and capture fragments of evolving pressure-temperature-time-deformation (P-T-t-D) conditions (e.g., Weller *et al.*, 2021). Significant advancements have been made in techniques, including phase equilibrium modelling (e.g., Powell & Holland, 2008; Holland & Powell, 2011; Green *et al.*, 2016; Lanari *et al.*, 2019) and geochronology (e.g., Kylander-Clark *et al.*, 2013; Engi, 2017) that can place precise constraints on the rate, depth and timing under which these conditions occur at various points of the evolving metamorphic path. Determining these conditions and their integration with rigorous classical field geology and petrology enables a clearer understanding of crustal record and the processes defining its characteristics.

The Himalayan mountain belt represents a key analogue for modern and ancient continent-continent collisional mountain belts, preserving a unique, exceptionally well-exposed and actively forming assemblage of rock units within a rigorously studied kinematic framework. Notably, it contains the thickest continental crust on Earth at ~70–80 km thick (Huang *et al.*, 2009; Mitra *et al.*, 2023). The strength of the Himalayas as a natural laboratory relies on three key features: 1) the area of exposure (in excess of 100,000 km^2) and length of the belt (~2500 km), 2) a significant range of metamorphic conditions up to partial melting, and 3) extreme relief and moderate dip of the metamorphic sequence providing significant crustal exposure. The mountain represents an excellent

location upon which to effectively integrate the outlined techniques to further our understanding of Earth's crustal record.

Although the Himalayas represents one of the most studies orogenic sequences on Earth (Yin, 2006; Kohn, 2014a; Goscombe *et al.*, 2018), relatively few areas in the mountain range have a pervasive structural and metamorphic record of the early crustal response to collision. In contrast, the metamorphic record of the orogen is dominated by lower-pressure assemblages and metamorphic fabrics that developed during later exhumation of the orogenic core. Although the early P-T, t and/or D record of the Himalaya has been locally investigated (e.g., Aikman *et al.*, 2008; Stübner *et al.*, 2014; Larson & Cottle, 2015; Khanal *et al.*, 2021), rarely are all features well preserved, documented over a range of metamorphic grades and structural levels, and/or studied in tandem. This fragmentary record of the early portion of the orogenic cycle hinders our understanding of: 1) the mechanisms, rates, and spatial distribution by which crustal thickening and heat propagates through the crust; 2) the relationship of crustal thickening, heat, and rheology influence the subsequent dissipation of the potential energy during exhumation; and 3) whether along-strike homogeneity reflects a consistent response to initial collision and/or subsequent exhumation. This has led to numerous models attempting to understand the mechanism by which exhumation occurs and by which the current architecture of the Himalayan metamorphic belt can be explained without the detailed constraints provided by early tectonometamorphic record of the mountain belt. The early tectonometamorphic response to initial collision between India and Asia is well preserved across significant structural thickness and across a range of metamorphic grades in the Zanskar Himalaya of NW India. This study documents P-T-t-D conditions from the onset of crustal thickening through to exhumation of the metamorphic core of the orogen in order to better understand the early rheological behaviour of the continental crust during the orogenic cycle.

1.2 Regional Geology of the Himalaya

The Himalayan-Karakoram-Tibet orogen is the largest orogen on Earth and is particularly well exposed along the frontal Himalayan ranges and therefore provide a window into how continental crust accommodates deformation during continental collision. The orogen formed following the collision of Indian and Asian plates in the early Cenozoic, with the suggested timing of collision varying depending on the criterion applied. Ages include: *ca.* 61 Ma, based on the

stratigraphically defined provenance reversal of sediments on the Indian passive margin (An *et al.*, 2021); *ca.* 59 Ma, from the oldest Tethys strata containing zircons of Asian affinity (DeCelles *et al.*, 2014; Hu *et al.*, 2015; Metcalf & Kapp, 2017); > *ca.* 51 Ma, reflecting a pulse of upper plate magmatic activity correlated to decrease in rate of convergence (Zhu *et al.*, 2015, 2019); *ca.* 51 Ma, determined from the youngest marine sedimentary strata in suture zone (Green *et al.*, 2008); or > *ca.* 47 Ma, defined by the oldest post-collisional molasse sedimentation in the suture zone (St-Onge *et al.*, 2010). The collision formed an orogenic belt that spans 2,500 km across Pakistan, India, Nepal, Bhutan and Tibet. A tripartite lithotectonic subdivision of the Indian margin has been distinguished: Tethyan, Greater and Lesser Himalayan Sequences (THS, GHS and LHS respectively; Fig. 1.1), the zones bounded by major faults. This division can be traced back to Heim & Gansser (1939) with recent reviews by Yin (2006); Kohn (2014a); Searle (2015). The THS is mainly a late Proterozoic to Eocene (meta)sedimentary sequence bounded by the Great Counterthrust (or Zanskar backthrust) along the north and by the South Tibetan Detachment System (STDS) or South Tibetan Detachment (STD), a long-angle normal fault, in the south. The THS shows a minor increase in metamorphic grade from unmetamorphosed at upper structural units to lower-greenschist or amphibolite facies at the STDS. The GHS is a late Proterozoic to Mesozoic metasedimentary sequence typically of middle amphibolite (kyanite zone) to lower-granulite facies. From the upper contact of the STDS the metamorphic grade increases downwards to middle crust where partial melts are more common, followed by a relative decrease in metamorphic grade towards the lower bounding Main Central Thrust (MCT). The LHS is mainly composed of Proterozoic basement and dominated by medium- to low-grade units bound to the north by the MCT and to the south by the Main Boundary Thrust (MBT). Metamorphic grade decreases in structural grade moving from mid-amphibolite facies (staurolite and kyanite zone) at the MCT to greenschist facies (chlorite zone) at the MBT where it is emplaced over the Siwalik Group or Subhimalayan Zone (unmetamorphosed Eocene to present day foreland sediments). This distribution of metamorphic units create a metamorphic "sandwich" of lower grade THS and LHS rocks with intervening higher grade GHS rocks.

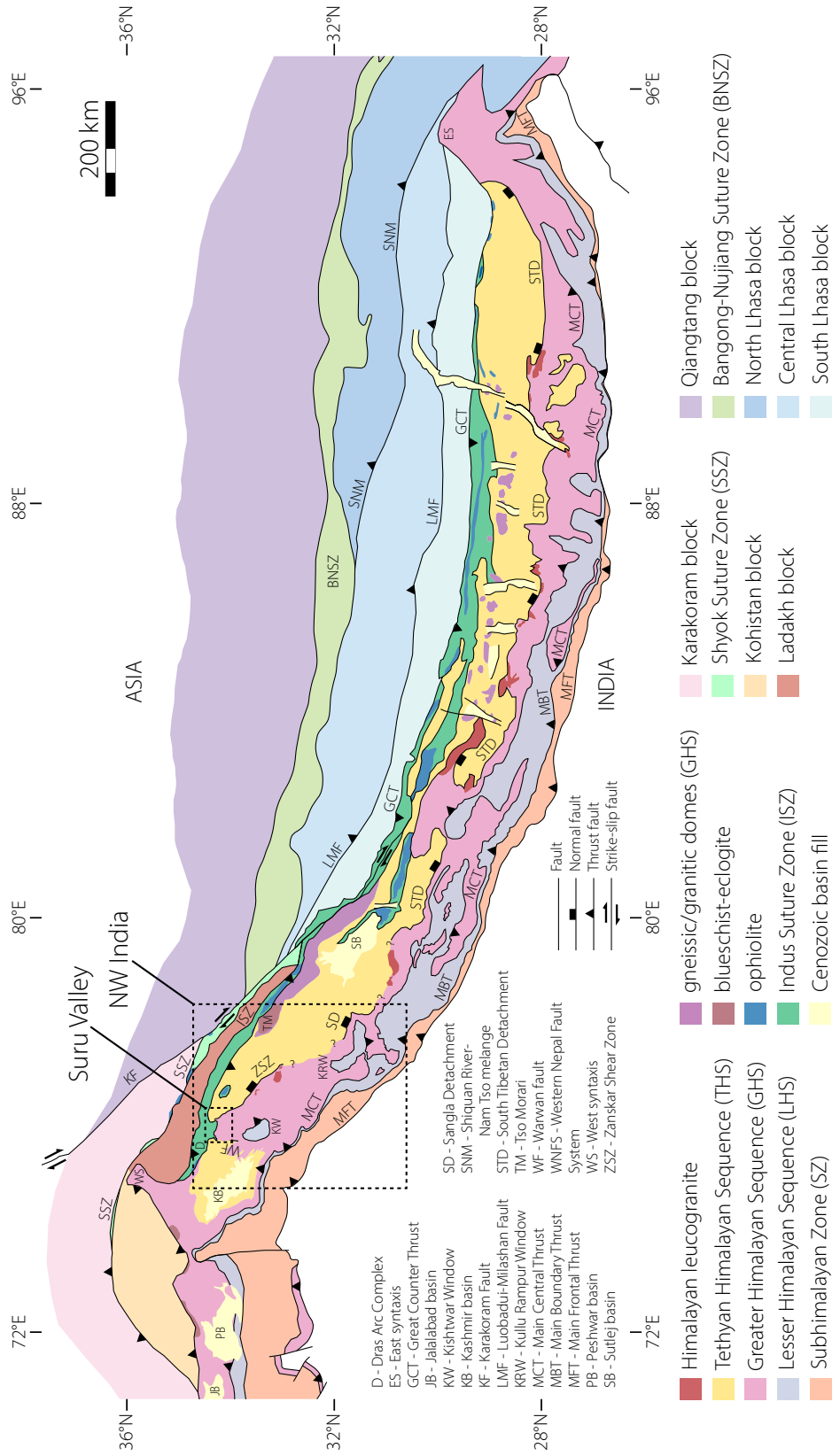


Fig. 1.1 Simplified geological map of the Himalaya with location of the Suru Valley field area, modified from Parsons *et al.* (2020), with NW India India constraints placed on the summary map by Steck (2003).

1.3 South Tibetan Detachment System (STDS)

A paradoxical feature that develops during orogenic processes is formation of major extensional structures within overall compressive systems. In inactive mountain belts such as the Variscan belt of Europe (Malavieille, 1993) or the Norwegian Caledonides (Norton, 1986; Wilks & Cuthbert, 1994), extensional features are interpreted to develop only once shortening processes have nearly ceased. In active mountain belts like the Alps (Ratschbacher *et al.*, 1989; Steck & Hunziker, 1994), the Andes (Dalmayrac & Molnar, 1981) or the Himalaya (Burchfiel *et al.*, 1992; Burchfiel & Royden, 1985; Herren, 1987; Hodges *et al.*, 1992; Searle & Fryer, 1986; Kellett *et al.*, 2019), evidence shows crustal thickening and shortening to be contemporaneous with development of major extensional structures. One of the most remarkable examples of synorogenic extension is the Himlayan STDS. This structure is a low-angle, north-dipping normal-sense fault defined by a series of comprising both ductile shear zones and brittle or brittle-ductile detachment faults extending for some 2000 km between Zanskar to Bhutan-SE Tibet in the east (Burchfiel *et al.*, 1992; Kellett *et al.*, 2019). The STDS is proposed to either shallow northwards, forming backthrusts (Yin, 2006) or merge with the Main Himalayan Thrust (MHT) at depth (Burchfiel & Royden, 1985).

1.4 Greater Himalayan Sequence (GHS)

The medium to high-grade GHS rocks generally form a continuous belt along the length of the Himalayan range. Along the belt the structural thickness of the GHS is variable, reaching minimum value of 2–3 km in western Nepal (e.g., Carosi *et al.*, 2007) up to 30 km in Eastern Nepal and Bhutan (e.g., Daniel *et al.*, 2003). The lower GHS is characterised by an inverted metamorphic field gradient, with highest metamorphic grade above lowest metamorphic grade (Gansser, 1964; Searle & Rex, 1989), and a right-way-up metamorphic field gradient in the upper GHS. In the well-documented central portion of the orogen the GHS, the upper GHS records long-lived metamorphism extending between at least *ca.* 38–28 Ma and recording shallow $\delta P/\delta T$ burial-heating, decompression-heating trajectories, isothermal decompression through the peak of metamorphism, and finally post-peak isobaric cooling (Goscombe *et al.*, 2018). The lower GHS records burial between *ca.* 33–27 Ma with subsequent later stages of pulsed burial between *ca.* 26–14 Ma. Prograde metamorphism followed moderately steep $\delta P/\delta T$ burial-

heating trajectories with peak metamorphism coincident with maximum pressures, and metamorphism was terminated by near isothermal decompression (Goscombe *et al.*, 2018).

1.5 Main Central Thrust (MCT) zone

The MCT zone displays an inverted metamorphic sequence progressing from sillimanite grade downwards into garnet grade where the ductile shear zone and brittle thrust occur. Various definitions have been proposed for the MCT defined on differing criteria (see summaries in Searle *et al.*, 2008; Martin, 2016). This study follows the definition of Searle *et al.* (2008) that requires the southwest-vergent thrust to be defined on strain criteria.

1.5.1 Geological subdivision of the Himalaya

The separation of the Himalaya into a series of geological and/or geographic units may be traced back to the preliminary work of Heim & Gansser (1939). Since then, the use of geographically, structurally, stratigraphically defined zones have been used interchangeably (see discussion in Yin, 2006). Attempts to standardise the use of this terminology (e.g., Yin, 2006; Martin, 2017) are inconsistently applied in the literature, and the terms THS, GHS, and LHS are most commonly used to describe fault-bounded lithotectonic assemblages (e.g., Kohn, 2014a; Cottle *et al.*, 2015; Carosi *et al.*, 2018). The use of lithotectonic units has proved key to emphasising the apparent along strike consistency of the geological record along the orogen and are most appropriate when applied at broad length-scales. Nevertheless, several issues impede the consistent application of lithotectonic units in all regions and at all scales: the debated location of bounding faults (Goscombe *et al.*, 2006; Searle *et al.*, 2008; Larson & Godin, 2009; Webb *et al.*, 2011; Stübner *et al.*, 2014; Martin, 2016; Hughes *et al.*, 2019); undefined and/or depositional continuity between the domains (e.g., Honegger, 1983; Vannay & Steck, 1995; Long & Mcquarrie, 2010); and/or most problematically, the discontinuous or segmented nature of the fault systems (e.g., Vannay & Steck, 1995; Epard & Steck, 2004; Kellett & Grujic, 2012; Stübner *et al.*, 2014; Kellett *et al.*, 2019). These problems have resulted in rock packages variably ascribed to different lithotectonic units and resulting in contrasting tectonic models. As such, recent studies have favoured terms that refer to broad metamorphic domains (e.g., Himalayan Metamorphic Front or HMC; Goscombe *et al.*, 2006; Cottle *et al.*,

2015). Without a continuous bounding structure between lithotectonic domains, the classic terminology may not be uniformly applied, as such where possible this study favours the term HMC, following Cottle *et al.* (2015).

1.6 Models for exhumation of the HMC

Various end-member models have been proposed for the development and exhumation of the HMC (see summaries in Yin, 2006; Webb *et al.*, 2011; Montomoli *et al.*, 2013; Kohn, 2014a; Cottle *et al.*, 2015; He *et al.*, 2015; Waters, 2019). Some models, such as the continental subduction model of Chemenda *et al.* (1995, 2000) or the proposal that the MCT represents an early Paleozoic suture (subsequently reactivated) and the HMC displays high-grade Cambro-Ordovician metamorphism (DeCelles *et al.*, 2000; Gehrels *et al.*, 2003) are not explored further as the are generally thought to be incompatible with current observations for the Himalayan orogen (e.g. Vannay & Grasemann, 2001; Yin, 2006). Currently supported models for the exhumation of the HMC are summarised as follows:

1. Channel Flow model (Beaumont *et al.*, 2001; Godin *et al.*, 2006): Heat and mass are advected by protracted flow of a weak, viscous fluid-filled channel between rigid yet deformable sheets. The mid-crustal channel flows laterally southwards (relative to upper and lower crustal units) due to pressure gradient from hinterland to foreland, underthrusting, and focused erosion. Flow is greatest where the rocks are weakest (i.e. at the base of the channel). The folded metamorphic isograd model of Searle & Rex (1989) and ductile wedge models of Grujic *et al.* (1996); Grasemann *et al.* (1999); Vannay & Grasemann (2001) are best expressed as early variants of the Channel Flow model.

2. Critical Taper model (Kohn, 2008): Based on mechanical models assuming a wedge of rock is everywhere at a condition of critical failure (Dahlen, 1990). The wedge maintains its size typically through in-sequence thrusting, erosion at its upper surface is balanced by underplating of new material at the base or grows by accretion of material to its base. The wedge maintains a regular, material-specific geometry by extension if the wedge is over thickened, internal shortening (out-of-sequence thrusting) if the wedge is thinned, and/or continued accretion at the base of the wedge.

3. Tectonic wedging/Wedge insertion model (Yin, 2006; Webb *et al.*, 2007, 2011; He *et al.*, 2015): This model accounts for the leading edge geometry of the GHS where the STDS and MCT are interpreted to converge at the Kathmandu Nappe. Thus, the GHS has a southward-tapering geometry with the STDS acting largely as a subhorizontal backthrust off of the MCT, with top-to-the-north shear surfacing as the Great Counter thrust system (Webb *et al.*, 2007). Duplexing may promote exhumation of the GHS (e.g., He *et al.*, 2015) and duplex culmination in the LHS results in warping of the STD, MCT and rocks of the GHS. Characteristics of this end-member may also be viewed in the context of a composite model (e.g., He *et al.*, 2015).

4. Duplexing/In-sequence shearing (Carosi *et al.*, 2010; Montomoli *et al.*, 2013; Carosi *et al.*, 2018): Exhumation is driven by the progressive activation of contractional top-to-the-S/SW ductile shear zones. This begins in the upper HMC and progressively moves to the lower parts of the HMC. This process has been active since the middle-late Eocene (Mottram *et al.*, 2014a).

Recent studies also acknowledge that many of the processes operating in such models are not mutually exclusive (e.g. Cottle *et al.*, 2015; Jamieson & Beaumont, 2013; Parsons *et al.*, 2016b; Chambers *et al.*, 2011; Larson *et al.*, 2010; Mukherjee, 2013; Waters, 2019). It may be possible to transition or alternate between end-member processes over time and/or such processes may operate simultaneously or in progression within different structural levels of the orogen. Multiple different variations of these composite systems are present in the literature. The composite models outlined in Cottle *et al.* (2015); Parsons *et al.* (2016b) suggest that mid-crustal material extruded laterally from deep hinterland towards the foreland via channel flow. Subsequent intrusion into the foreland resulted in cooling of the material, which became more rigid and deformation initiated as part of a tectonic wedge with or without an underplating mechanism.

The Himalaya shows both temporal and spatial orogen-parallel variations, suggesting that exhumation of the HMC may have been a complex and heterogeneous process (e.g., Kohn, 2014a; Parsons *et al.*, 2016a; Kellett *et al.*, 2019; Mottram *et al.*, 2019), which effects the relevance or applicability of different models. Although the region of this study is less dominated by the latter metamorphic record of the orogen, it may provide further insight into the pre-requisite architecture and conditions under which decompression and exhumation initiate.

1.7 Aims and thesis structure

The aim of this thesis is to decipher the tectonometamorphic response of the Zanskar HMC following continent-continent collision through to exhumation using information within greenschist- to amphibolite-facies metamorphic rock samples. This is firstly achieved through the presentation of a detailed geological map from which field and petrographic observations may be referenced (Chapters 2 & 3). This is then integrated with modern techniques of phase equilibrium modelling (Chapter 4) and petrochronology (Chapter 5) to constrain the *P-T-t-D* conditions of the metamorphic cycle (Chapter 6). This dataset constrains the tectonometamorphic architecture of the HMC; and relative and quantitative constraints on the distribution of deformation and metamorphism across a range of structural levels and metamorphic grades. These constraints inform the conditions under which competing models for the evolution of the Zanskar HMC must adhere.

The general layout of this thesis is summarised below:

Chapter 2 presents a geological map and cross-sections of the Suru Valley region, and discusses the lithotectonic and metamorphic architecture from micro- to macro-scale.

Chapter 3 provides detailed petrographic descriptions of lithological units and mineral chemistry trends between pelitic and metabasic lithologies.

Chapter 4 quantifies the *P-T* conditions of metamorphism during prograde–peak evolution within both pelitic and metabasic rock units.

Chapter 5 uses U-Th-Pb dating on a variety of accessory phases, to place temporal constraints on the timing of metamorphism and magmatism within the context of sequences of deformation constrained through petrological analysis.

Chapter 6 provides an integrated synthesis of the *P-T-t-D* evolution of the Suru Valley region and test the relative applicability of the region to models of exhumation.

Chapter 2

Structural and Metamorphic Architecture



Nun (7,135 m) and Parkachik glacier

2.1 Introduction

Mountain building (orogenesis) leads to a complex evolution in the pressure-temperature (P-T) structure of the lithosphere with time (t). Given the broad length-scales (up to 1000s of km) and timescales (up to 100s Myr) that can characterise orogens, decoding their history is challenging and typically requires integrating observations over a range of structural levels (England & Jackson, 1989; Weller *et al.*, 2021). A critical step in this process is the identification of lithostratigraphic units and tectonothermal events, which can be achieved by integrating a range of datasets including macro-scale geological field mapping and micro-scale petrographic analysis to provide a reference frame to understand the tectonic evolution of a region.

Following initial collision of India and Asia, significant crustal shortening, thickening, and Barrovian metamorphism occurred within and on the margin of the Indian continental crust. The highest-grade metamorphic rocks of the Himalaya are found within the Himalayan Metamorphic Core (HMC), which refers to a package of pervasively deformed mid-crustal rocks recording Cenozoic metamorphism, deformation, and cooling (Cottle *et al.*, 2015). Numerous studies have documented that the metamorphic evolution of the HMC is characterised by two main events: an earlier (Eocene–Oligocene) higher-pressure phase dominated by kyanite-bearing assemblages, and a later (Oligocene–Miocene) lower-pressure phase associated with sillimanite-bearing assemblages (e.g., Kundig, 1989; Stäubli, 1989; Searle *et al.*, 1992, 1999b; Stephenson *et al.*, 2000, 2001; Walker *et al.*, 2001). Most regions of the HMC have equilibrated under the latter sillimanite-grade conditions and thus are dominated by Oligocene to Miocene metamorphic ages (*ca.* 30–15 Ma; Kohn, 2014a; Wang *et al.*, 2016; Goscombe *et al.*, 2018; Waters, 2019). The earlier Eocene–Oligocene metamorphic record is typically best preserved in the cores of larger grains of dateable phases (e.g., monazite) in assemblages that are otherwise relatively overprinted during latter stages of the metamorphic cycle (e.g., monazite; Cottle *et al.*, 2009b; Larson *et al.*, 2010; Kellett *et al.*, 2014; Stübner *et al.*, 2014; Ambrose *et al.*, 2015; Iaccarino *et al.*, 2015; Khanal *et al.*, 2021). Therefore, the early tectonometamorphic architecture prior to sillimanite-grade metamorphism remains poorly preserved and constrained. In the Zanskar Himalaya of NW India, extensive kyanite-grade mineral assemblages prevail (Figs. 1.1 & 2.1; Honegger *et al.*, 1982; Searle & Fryer, 1986; Searle *et al.*, 1999b; Walker *et al.*, 2001). In particular, the Suru Valley region, the focus of this study, documents on average higher pressures (approximately +2 kbar) than those

recorded in the rest of the Zanskar Himalaya (Fig. 2.2) and significant SW-vergent folding and thrusting along NE-dipping shear zones (e.g., Searle *et al.*, 1992). The abundance of higher-pressure assemblages and SW-vergent structures recorded in the Zanskar Himalaya are interpreted to result from substantial crustal thickening and burial following the onset of collision, thereby making it a choice location to study the early tectonometamorphic architecture of the HMC (e.g., Searle *et al.*, 1992; Walker *et al.*, 2001). The Suru Valley region also features aspects that are relatively unique to the Himalaya, including the map-scale closure of mineral isograds (Searle & Rex, 1989); greenschist-facies metamorphosed assemblages of the ISZ (Honegger, 1983); amphibolite-facies strata of the Neotethyan shelf within the HMC (Honegger *et al.*, 1982; Searle *et al.*, 2007), low modal abundance of migmatite (Honegger, 1983); and variation in localisation of deformation and offset along the South Tibetan Detachment (STD) system (Inger, 1998). Therefore, detailed study of the relationship between deformation and metamorphism in the region is required to deconvolve whether specific features of the Suru Valley area pertain to the exposure of different structural levels and/or an earlier phase of metamorphism than the bulk of the orogen, or whether the region is truly heterogenous, with implications for the applicability of tectonic models and our understanding of orogenic processes.

Herein, we present the results of detailed field mapping and a three-dimensional (3D) structural study of the HMC as exposed within the Suru Valley region of the Zanskar Himalaya. Notably, this region preserves a complete chlorite- to sillimanite+K-feldspar-grade Barrovian sequence completed by metabasic assemblages (e.g., Honegger *et al.*, 1982; Honegger, 1983; Walker *et al.*, 2001), albeit sillimanite-grade conditions and above comprise a smaller domain than other areas of the HMC. The aim of this study is to understand the structural and metamorphic architecture of the Suru Valley area and in particular: 1) how crustal-thickening is accommodated following initial continent-continent collision, 2) how peak metamorphic assemblages relate to deformation from the macro- to micro-scale, 3) how the tectonometamorphic architecture of the HMC documented in the Suru Valley region compares along strike across the orogen, and 4) to discuss the wider implications for our understanding of orogenic processes. We start by presenting an outline of the geology of the Zanskar Himalaya, then document the relationships between lithostratigraphy, folds, thrusts, deformation fabrics, metamorphic isograds, and porphyroblast growth in the Suru Valley area to determine the sequence of deformation events and the spatial and relative temporal evolution of thickened Himalayan crust.

2.2 Geological Overview and Previous Work

2.2.1 Geological setting of the Zanskar Himalaya

The Zanskar Himalaya exposes rocks of the India-Asia suture zone and the north Indian passive continental margin (Searle *et al.*, 1988; Steck, 2003; Searle *et al.*, 2007). Lithostratigraphic units can be grouped into the following three divisions from NE–SW: the Indus Suture Zone (ISZ), the Tethyan Himalayan Sequence (THS), and the Greater Himalayan Sequence (GHS). As locally documented in this study, in the surrounding Lahaul and Spiti regions the boundary between the THS and the underlying GHS remains poorly defined (Fig. 2.1), lacking evidence for a significant tectonic/structural contact (Vannay & Steck, 1995; Stübner *et al.*, 2014) and/or characterised by ongoing debate on the location of the boundary (Searle *et al.*, 1988; Thakur, 1998; Jain *et al.*, 1999; Webb *et al.*, 2011). Consistent with the scale, the Himalayan map shown in Figure 1.1 shows the classic lithotectonic subdivisions of the Himalaya, with all other maps (Figs. 2.1 & 2.4) grouping the THS and GHS together with map units separated by lithostratigraphic and/or chronostratigraphic criteria.

2.2.1.1 Indus Suture Zone (ISZ)

The ISZ in the Zanskar and Ladakh ranges is bounded to the north by the Ladakh batholith and to the south by a series of back-thrusts that place folded THS rocks over the ISZ (Fig. 1.1 & 2.1). The following units are included in the ISZ:

1. Permian–Mesozoic slope-facies and proximal-basin deep-water marine sedimentary rocks (Lamayuru Complex), and Mesozoic deep-water sedimentary and basic volcanogenic rocks (Karamba Complex) that are distal equivalents of the Indian rift–passive shelf–slope succession (Thakur, 1981; Searle *et al.*, 1988; Gaetani & Garzanti, 1991; Robertson & Degnan, 1993; Robertson & Sharp, 1998).

2. Permian and Triassic exotic carbonate platform blocks (e.g., 'Mulbeck exotics'), which may represent platform edge extensional fault blocks or olistoliths of oceanic island carbonate associated with alkaline within-plate volcanic rock (Searle, 1983; Searle *et al.*, 1988; Robertson & Degnan, 1993; Sinha & Upadhyay, 1993; Robertson, 1998; Bhat *et al.*, 2023).

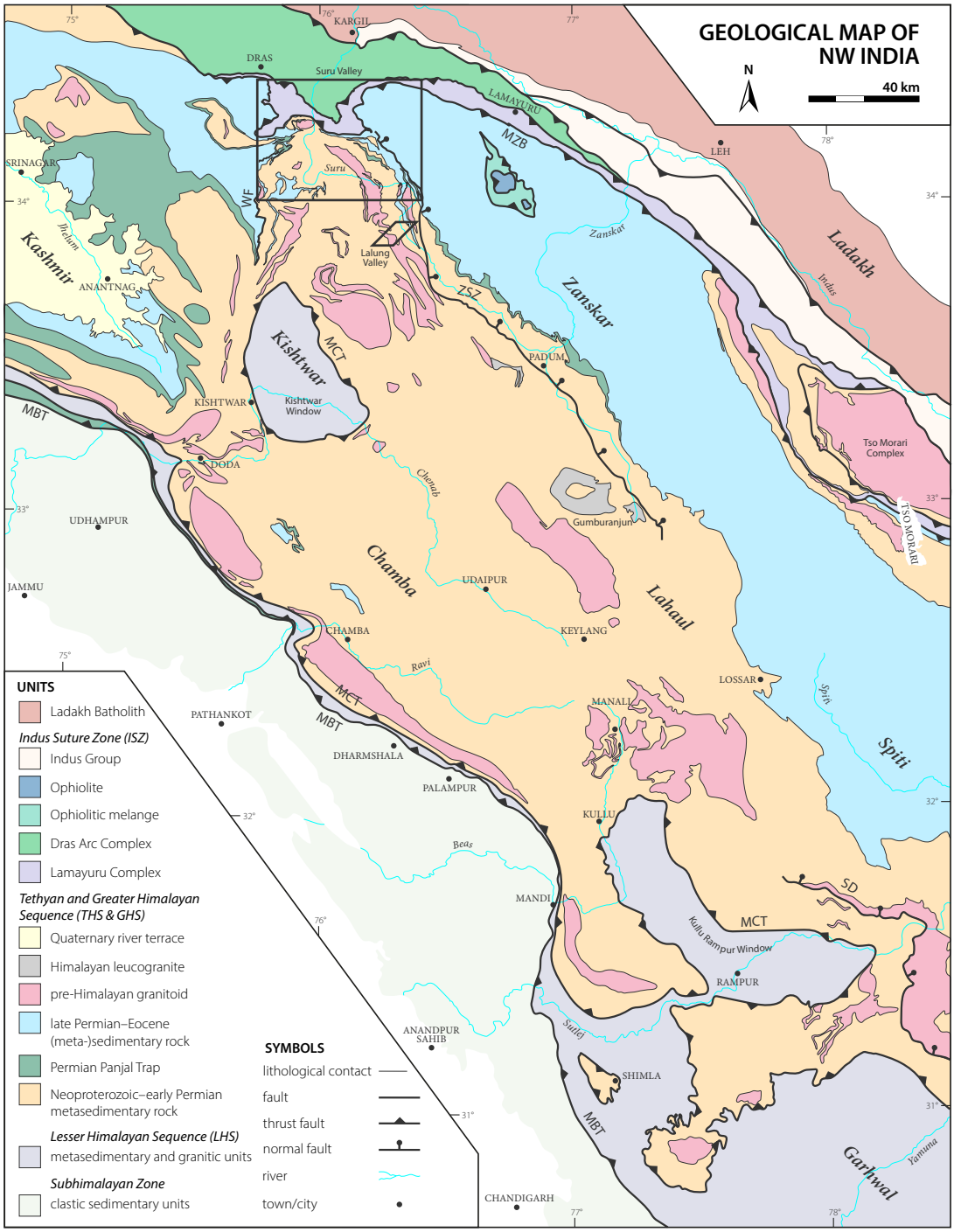


Fig. 2.1 Simplified geological map of NW India modified from Steck (2003), with adjustments to Suru Valley region (rectangular box) based on Figure 2.4. Completed transect through the Lalung Valley is shown by the small rhomboid box. MZB = Main Zanskar Backthrust, WF = Warwan fault, SD = Sangla Detachment, MCT = Main Central Thrust, MBT = Main Bounary Thrust.

3. Upper Jurassic–Cretaceous intra-oceanic island arc sequence (Dras Arc Complex or Dras-Nindam terrane) dominated by andesite, basaltic andesite, dacite and rhyolite (Dras Volcanics) as well as forearc volcaniclastic sedi-

mentary rocks (Nindam Formation; Raz & Honegger, 1989; Reuber *et al.*, 1989; Robertson & Degnan, 1994; Clift *et al.*, 2000; Bhat *et al.*, 2019a). The Dras Arc Complex is a continuation of the lower crustal Chilas Complex of the Kohistan Arc to the west in Pakistan (e.g., Khan *et al.*, 1989).

4. Mélanges (locally ophiolitic) characterised by thrust imbricates, or broken formations, that include distal passive margin volcanic-sedimentary rocks (Lamayuru Complex and Karamba Complex), arc-type volcanic and volcaniclastic sedimentary rocks (Dras Arc Complex), sheared serpentinite, and rare glaucophane-bearing blueschist with a dominantly sedimentary mudstone matrix (Honegger *et al.*, 1989; Robertson, 2000; Bhat *et al.*, 2019b).

5. Post-collisional fluvio-alluvial conglomerate, shale, siltstone and sandstone (Indus Group molasse) deposited in an intermontane basin along the ISZ, with debris derived mainly from the Ladakh batholith to the north, units within the ISZ, and less commonly from the THS to the south (Garzanti & Van Haver, 1988; Searle *et al.*, 1988, 1990; Sinclair & Jaffey, 2001; Clift *et al.*, 2002; Wu *et al.*, 2007; St-Onge *et al.*, 2010).

2.2.1.2 Tethyan Himalayan Sequence (THS)

The THS is a Neoproterozoic to early Eocene sequence of siliciclastic and carbonate sedimentary rocks interstratified with Permian Panjal Traps (Fuchs, 1982; Searle, 1983; Gaetani *et al.*, 1986; Searle *et al.*, 1988). The Panjal Traps mark the opening of the Neotethys ocean and deposition of the early Permian–early Eocene Neotethyan sedimentary sequence on the Indian margin (Fig 2.1; Gaetani *et al.*, 1986; Shellnutt, 2018). The THS ranges from unmetamorphosed to lower amphibolite-facies. Following the initial collision of India and Asia, the THS is estimated from balanced and restored cross-sections to have experienced at least 85 km of NE–SW shortening (Corfield & Searle, 2000). In the Zanskar Himalaya the base of the THS (immediate hanging wall of the ZSZ) comprises the Haimanta Group, a thick succession of sedimentary and metasedimentary rocks, which extends from the Chamba Formation at the base, through the Manjir, Phe, Parahio, Karsha, and Kurgiakh formations (Hughes *et al.*, 2018). Only the Cambrian rocks of the latter four formations are well exposed, with the Kurgiakh Formation ending at the regional Cambrian–Ordovician unconformity (Nanda & Singh, 1976; Gaetani *et al.*, 1986; Myrow *et al.*, 2006). The Haimanta Group is unconformably overlain by a sequence of Ordovician–early Eocene sedimentary

rocks (Thaple–Chulung La formations; Fuchs, 1982; Baud *et al.*, 1984; Gaetani *et al.*, 1986; Garzanti *et al.*, 1987; Gaetani & Garzanti, 1991; Searle *et al.*, 2007). The THS is bounded to the north by the ISZ and to the south, where present, by the Zanskar Shear Zone (ZSZ), a north- to northeast-dipping normal-sense shear zone (Figs. 1.1 & 2.1). The ZSZ is interpreted as the western strand of the STD system (e.g., Dèzes *et al.*, 1999), which is defined by a series of extensional shear structures that can be near continuously traced for ~2000 km along the Himalayan orogen (Fig. 1.1; Burchfiel *et al.*, 1992; Yin, 2006; Kellett *et al.*, 2019).

2.2.1.3 Greater Himalayan Sequence (GHS)

The GHS in the Zanskar Himalaya is a 50–55 km-thick (ZSZ to MCT at the Kishtwar Window, plan-view; Fig. 2.1) Neoproterozoic to Mesozoic metasedimentary sequence of greenschist- to upper amphibolite-facies schist, gneiss, migmatite and leucogranite. The metasedimentary rocks of the GHS are inferred to represent metamorphosed Haimanta Group, though also include younger Mesozoic formations of the Neotethyan shelf (Fig. 2.1; Honegger *et al.*, 1982; Searle *et al.*, 2007). The GHS was metamorphosed during the late Eocene to Miocene (e.g., Searle *et al.*, 1999b; Vance & Harris, 1999; Walker *et al.*, 1999; Robyr & Lanari, 2020; Štípská *et al.*, 2020). The sequence is bounded to the southwest by a major south-vergent high-strain shear zone, the Main Central Thrust (MCT), which places the GHS over the low-grade to unmetamorphosed Proterozoic sedimentary strata of the Lesser Himalayan Sequence (LHS; Fig. 1.1 & 2.1). Where exposed in the Kishtwar Window (Fig. 2.1) it is expressed as a condensed inverted metamorphic sequence (amphibolite- to greenschist-facies) coincident with a ductile high-strain zone (1.5 to 3 km-wide) showing SW-vergent kinematic indicators (Stephenson *et al.*, 2000, 2001).

2.2.2 Regional geology of the Suru Valley area

The northern part of the Suru Valley area contains the metamorphosed equivalents of the Permian–Mesozoic Lamayuru Complex of the ISZ (Honegger *et al.*, 1982), including graphite-rich and/or carbonate-bearing metasedimentary rocks, and metavolcanic rocks. To the south of the ISZ, the region contains pelitic to psammitic rocks that are correlated with the Neoproterozoic Haimanta series; as well as metamorphosed carbonate-rich rock and associated metamorphosed volcanic rocks, which are respectively correlated with Mesozoic carbonate and

volcanic units of the Permian Panjal Traps (Honegger *et al.*, 1982; Walker, 1999; Searle *et al.*, 2007). A variety of pre-collisional granitoid bodies, subsequently metamorphosed during Himalayan metamorphism, and post-collisional plutonic units formed during Himalayan metamorphism are present in the Suru Valley region. The oldest granitoids, recognised across Zanskar, comprise a series of prominent K-feldspar augen gneisses with Cambro-Ordovician magmatic ages (e.g., Pognante *et al.*, 1990). Similar ages are purported for the Suru Valley region, most notably including the Rangdum granite (e.g., Honegger *et al.*, 1982; Noble *et al.*, 2001). Permian granitoid bodies occur at Sankoo, Tongul, Parkachik, and Shafat (*ca.* 284–268 Ma; U-Pb zircon; Noble *et al.*, 2001; Horton & Leech, 2013). Leucogranite formed during Himalayan metamorphism with Miocene ages of crustal melting (20.8 ± 0.3 Ma, U-Pb monazite; Noble & Searle, 1995) is documented around Shafat.

Initial geological mapping of the Suru Valley was carried out by Honegger *et al.* (1982); Honegger (1983); Searle (1983); Searle & Fryer (1986); Gilbert (1986); Fuchs (1987); Searle *et al.* (1988) and Walker *et al.* (2001) with constraints from further east along the Zanskar Valley by Herren (1987); Kundig (1989); Stäubli (1989) and Dèzes *et al.* (1999). The maps of Honegger *et al.* (1982); Honegger (1983); Gilbert (1986); Searle & Fryer (1986); Searle & Rex (1989); Gapais *et al.* (1992); Searle *et al.* (1992) and Walker *et al.* (2001) display a series of km-scale SW-verging recumbent folds in the HMC underlain by a younger lower domal structure. Honegger *et al.* (1982) documented complex folding of Tethyan Mesozoic carbonate and volcanic units of the Permian Panjal Traps into the sequence. Searle *et al.* (1992, 1999a) and Walker *et al.* (2001) determined that these structures were bound to the NE of the GHS by the ZSZ. Honegger (1983) mapped a series of discontinuous detachments (equivalent to the ZSZ) between the GHS and the THS, and a fault (termed the 'Zanskar-Sanku-Pindras Thrust') between the GHS–THS and ISZ dominantly defined by back-thrusting. The ZSZ was first described and traced from the Zanskar valley, NW to the Suru Valley, by Gapais *et al.* (1984); Gilbert (1986); Searle & Fryer (1986) and Herren (1987). To the southwest of the Suru Valley, low-grade sedimentary rocks are juxtaposed above the GHS by either a detachment fault (Honegger, 1983) or a steep, late-stage NE-vergent back-thrust (Warwan back-thrust; Searle *et al.*, 1992). This structure is herein referred to as the Warwan fault, and is reportedly exposed at the SW periphery of the mapped region (Fig. 2.1). The low-grade to unmetamorphosed (meta-)sedimentary rocks in the hanging wall of the fault have been correlated with Mesozoic platform sedimentary rocks (Honegger *et al.*,

1982), Kashmir Tethyan basin strata (Singh *et al.*, 2000), or Proterozoic–Mesozoic Kashmir sedimentary units (Searle *et al.*, 1992, 1999b). The hanging wall units of the Warwan fault can therefore be viewed as belonging to the THS, a correlation that is supported by remote-sensed mapping in this study. The MCT is not exposed in the mapped area, but is exposed to the south of the Suru Valley region around the Kishtwar Window (Fig. 2.1). The trace of isograd surfaces from the Suru Valley region to the Kishtwar window produce a map scale closure between a right-way-up and inverted metamorphic sequence (Honegger, 1983; Searle & Fryer, 1986).

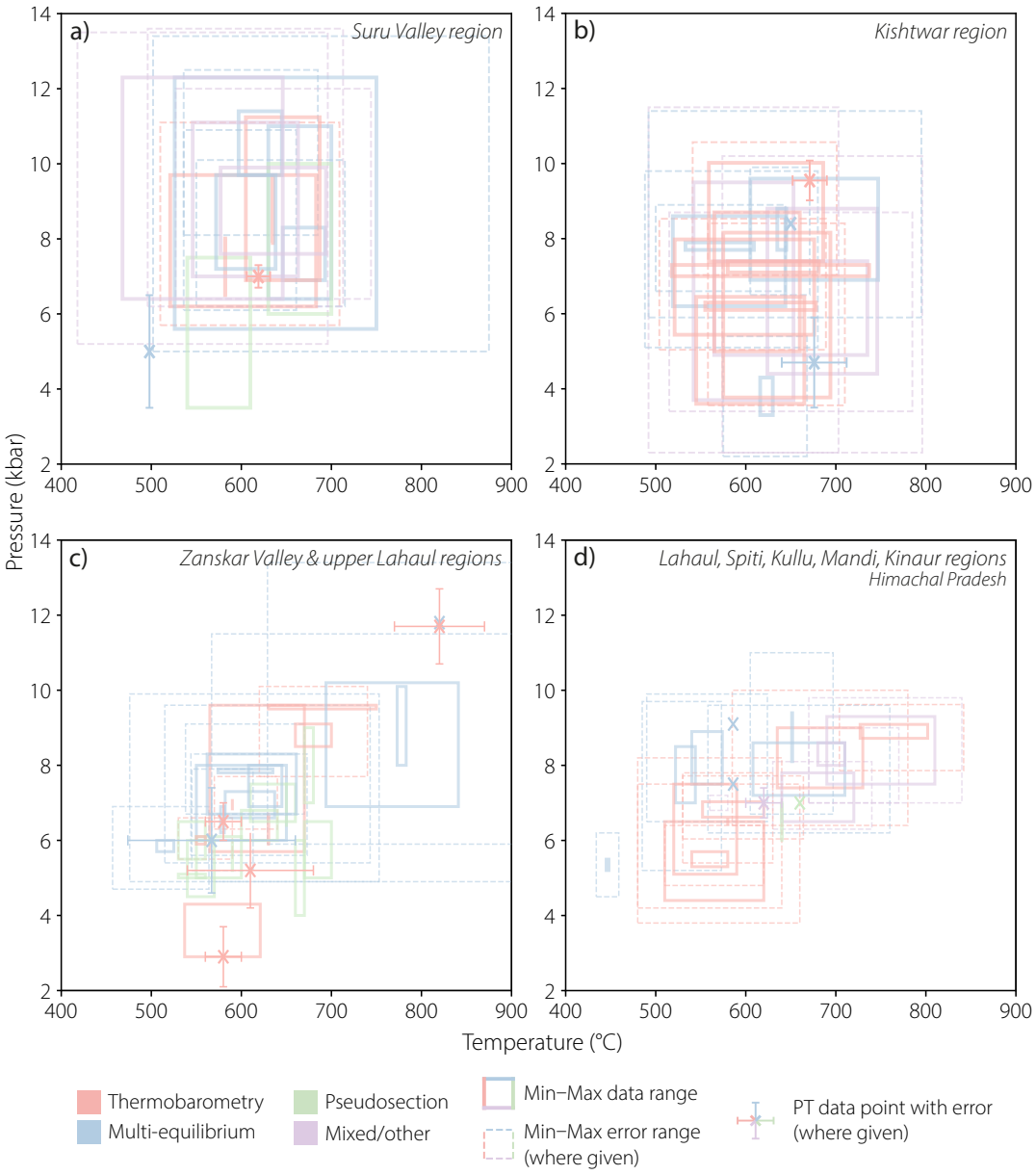


Fig. 2.2 (Caption on the following page.)

Fig. 2.2 Summary of published *P-T* data for the HMC of the a) Suru Valley region, b) Kishtwar region, c) Zanskar Valley and upper Lahaul regions, and d) Lahaul, Spiti, Kullu, Mandi, Kinaur regions in Himachal Pradesh (see Fig. 2.1). Due to debated trend of the South Tibetan Detachment System and correlation of units in the Himachal Pradesh (e.g., Stübner *et al.*, 2014), *P-T* data includes areas above and below the South Tibetan Detachment where defined, thereby locally comprising units assigned to greenschist- to amphibolite-facies units of the THS (e.g., Chambers *et al.*, 2009). Core compositions used in thermobarometry are generally excluded with the exception of results from Stephenson (1997); Stephenson *et al.* (2000) or where inferred to correlate to peak. Suru Valley region *P-T* data: Gilbert (1986); Searle *et al.* (1992); Vance & Mahar (1998); Walker (1999); Searle *et al.* (1999b); Walker *et al.* (2001); Kishtwar region *P-T* data: Stäubli (1988, 1989); Guntli (1993); Jain & Manickavasagam (1993); Stephenson (1997); Manickavasagam *et al.* (1999); Searle *et al.* (1999b); Stephenson *et al.* (2000); Zanskar Valley and upper Lahaul regions: Jain & Manickavasagam (1993); Dransfield (1994); Pognante & Lombardo (1989); Pognante *et al.* (1990); Pognante (1992); Dèzes *et al.* (1999); Manickavasagam *et al.* (1999); Walker *et al.* (1999); Robyr (2002); Finch *et al.* (2014); Štípská *et al.* (2020); Lahaul, Spiti, Kullu, Mandi, Kinnaur regions (Himachal Pradesh): Stephenson (1997); Vannay & Grasemann (1998); Manickavasagam *et al.* (1999); Vannay *et al.* (1999); Wyss (2000); Thakur & Tripathi (2008); Chambers *et al.* (2009); Leger *et al.* (2013).

2.2.3 Previous metamorphic constraints and geochronology of NW India

Peak metamorphic pressures from the HMC in the Suru Valley area (6–12 kbar; Fig. 2.2a) are on average higher than those recorded in other regions of NW India, including: Kishtwar at 4–10 kbar (Fig. 2.2b), Zanskar Valley and Upper Lahaul at 5–10 kbar (Fig. 2.2c), and in Lahaul and Himachal Pradesh at 5–9 kbar (Fig. 2.2d; see locations on Fig. 2.1). A migmatitic sample from the Gumuranjun dome is an exception with a high pressure of 11.7 ± 1.0 and 11.8 kbar (no reported error; Dèzes *et al.*, 1999; Robyr, 2002, Fig. 2.2c). Peak metamorphic temperatures in the Suru Valley area (500–700 °C; Fig. 2.2a), represent on average a decreased temperature range when compared to all other regions (500–800 °C; Fig. 2.2b–d). All *P-T* conditions are constrained through conventional thermobarometry, multi-equilibrium thermobarometry, and/or phase equilibrium modelling (Fig. 2.2). Differences in the *P-T* conditions of the Suru Valley area are in agreement with observations reporting a dominance of higher-pressure kyanite-bearing assemblages (e.g., Searle *et al.*, 1992; Walker *et al.*, 2001) in comparison to other regions that are more dominated by lower-pressure sillimanite-bearing and migmatitic assemblages (e.g., Vannay & Grasemann, 1998; Manickavasagam

et al., 1999; Searle *et al.*, 1999a; Stephenson *et al.*, 2000; Robyr, 2002; Finch *et al.*, 2014). The HMC in NW India consistently preserves a record of mid-Eocene to Oligocene prograde–peak metamorphic ages ranging from *ca.* 44–27 Ma (Fig. 2.3; U-(Th)-Pb zircon, monazite, xenotime, uraninite; Sm-Nd garnet; Vance & Harris, 1999; Walker *et al.*, 1999; Chambers *et al.*, 2009; Thöni *et al.*, 2012; Horton & Leech, 2013; Stübner *et al.*, 2014; Robyr & Lanari, 2020; Štípská *et al.*, 2020). Few data points from previous studies are available from the Suru Valley region, however Sm-Nd core–rim garnet ages from kyanite-grade samples give lower Oligocene ages (*ca.* 33–28 Ma) consistent with prograde–peak metamorphism within deeper structural levels of the Suru Valley region (Vance & Harris, 1999).

2.3 Methods

The Zanskar Himalaya lies along the NW limit of the Indian monsoon system, resulting in reduced vegetation cover when compared to the central and eastern Himalaya. In addition, river gorges are deeply incised and provide up to *ca.* 3500 m of topographic relief between valley floor and surrounding peaks. Consequently, the study area is exceptionally well exposed.

Geological mapping was completed on 1:50,000 Sentinel-2 aerial imagery (Sentinel-2 L1C; September 2017, and August 2018) from Copernicus Open Access Hub (https://scihub.copernicus.eu/dhus/) and 100 m contours were produced in ArcMap (ArcGIS versions 10.5 to 10.7) using SRTM digital elevation data (SRTM 1-Arc second: September 2014) from USGS (https://earthexplorer.usgs.gov/). The basemap was produced using the WGS84 UTM zone 43N coordinate system. A GPS was used to reference the position (WGS84-UTM) of all outcrops, samples and measured structures in the field. Collected data and scanned field maps were georeferenced in ArcMap under the same coordinate system. The final geological map (Fig. 2.4) was compiled at 1:50,000 scale in Adobe Illustrator using a Sentinel-2 aerial imagery underlay (Sentinel-2 L1C; September 2021) from Copernicus Open Access Hub that was desaturated and exported from ArcMap to use as a universal basemap for all layers. All georeferenced data, maps and 200 m contours were exported from ArcMap and aligned to the aerial imagery underlay.

The geological map is constrained by field mapping (1,500 km^2) and remote-sensed mapping (900 km^2). The limit of field mapping is shown by the white

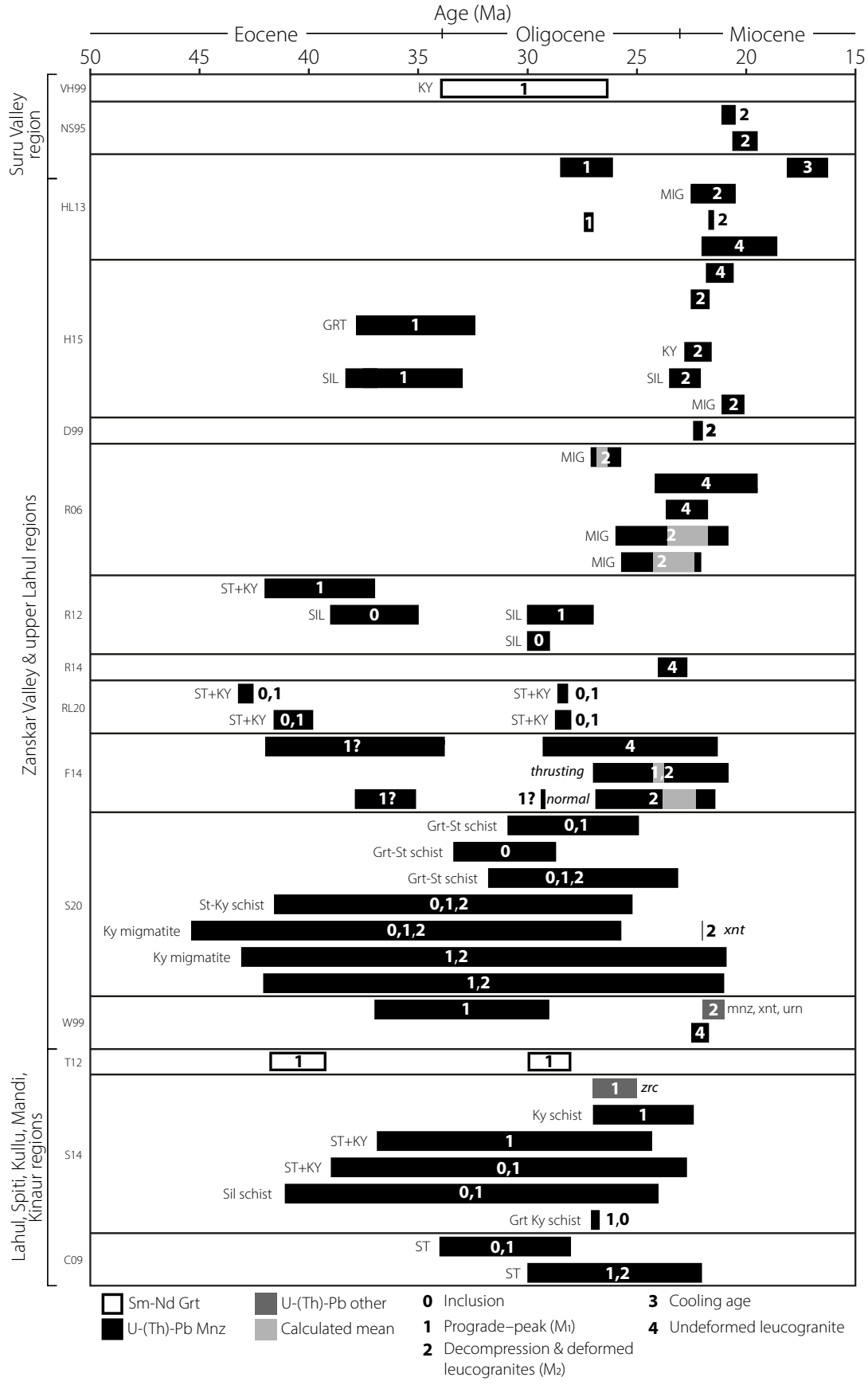


Fig. 2.3 (Caption on the following page.)

Fig. 2.3 Summary of published geochronological data for HMC rocks of the Suru Valley, Zanskar Valley, and Himachal Pradesh. Ranges include reported error. VH99 — Vance & Harris (1999), NS95 — Noble & Searle (1995), HL13 — Horton & Leech (2013), H15 — Horton *et al.* (2015), D99 — Dèzes *et al.* (1999), R06 — Robyr *et al.* (2006), R12 — Robyr *et al.* (2012), R14 — Robyr *et al.* (2014), RL20 — Robyr & Lanari (2020), F14 — Finch *et al.* (2014), S20 — Štípská *et al.* (2020), W99 — Walker *et al.* (1999), T12 — Thöni *et al.* (2012), S14 — Stübner *et al.* (2014), C09 — Chambers *et al.* (2009).

dashed line in Figure 2.4. Remote-sensed mapping, outside this boundary was completed using data sources from Google Earth (version 7.3.4.8642; July 2013, October 2017, October 2019) and Copernicus Sentinel Hub (Sentinel-2 L1C; bands 4,3,2 and 12,4,2; September 2019, September 2021; https://apps.sentinel-hub.com/sentinel-playground/). No fold structures or isograds were extended through these regions. The remote-sensed data was also used in the field area to aid mapping or extend lithostratigraphic contacts, as well as structural features between traverses. Due to the range of elevation in the Suru Valley region, which varies from *ca.* 2,900 m around Sankoo to 7,135 m at the highest point at Nun, some fold structures in the field mapped area are inferred from exposures across mountain sides and from aerial imagery sources where the geology was inaccessible. These folds are annotated with an asterisk on Figure 2.4.

Primary bedding (S_0) was identified in rocks at low metamorphic grade (based on compositional layering) and subsequent deformation fabrics were characterised with respect to episodes of folding, shearing and/or transposition of the compositional anisotropy in sedimentary rocks. Porphyroblast growth-fabric development relationships, fabric defining metamorphic mineral assemblages, and shear sense were also used to distinguish differing fabrics. Index minerals in pelitic bulk compositions were used to map out the position of Barrovian metamorphic isograds, defined by chlorite- to sillimanite+K-feldspar-zone assemblages. Assemblages were also documented in metabasic units yielding a complementary sequence in actinolite (± tremolite) to hornblende+garnet zones. Where pelitic bulk compositions were absent in the metasedimentary rock sequence, assemblages from metavolcanic rocks were used to help constrain the equivalent metamorphic grades in pelitic compositions, with consequent uncertainties displayed on relevant sections of the isograd linework of Figure 2.4.

Four cross sections (A-A', B-B', C-C', and D-D'; Fig. 2.5) were constructed to provide 3D constraints on the distribution of lithostratigraphic units and principal deformation features at depth and section lines were oriented sub-perpendicular

to the orientation of the dominant regional fabric. In sections A-A' and D-D', the line of section is segmented to remain sub-perpendicular to major units and optimise proximity to field structural measurements. Apparent dips were calculated from structural measurements that were within approximately 3 km of a line of section and shown directly below topography on the associated cross section. Lithological contacts, isograds, and major faults and folds are extended 1,500 m above and below topography on the cross sections to better correlate between sections and deconvolve complicated regional structures. Across large portions of the map and cross sections folded strata are distinguished, rather than thrust imbricated sequences, based on consistent preservation of fold closures at mesoscale and macroscale; and evident lack of developed ductile mylonitic fabrics or brittle faults within the rock sequence (outside those marked on Figs 2.4 and 2.5).

Representative rock samples were collected at all metamorphic grades, and where possible were oriented relative to linear structural features in the field. When relevant, thin sections were cut parallel to the mineral stretching lineation and perpendicular to compositional layering to characterise shear sense.

Stereonets were generated for six different map transects (Fig. 2.11) using OpenStereo software (v2.0b Grohmann & Campanha, 2010). Contouring was applied in areas of sufficient data for stretching lineations or poles of foliation. A 1% area method for contours was applied using the estimation method of Robin & Jowett (1986). The Bingham method (Bingham, 1974) was used for mean vectors, mean planes, and mean fold axes as appropriate.

2.4 Lithostratigraphic architecture and geological map

The Suru Valley region exposes a volcanic and siliciclastic dominated lithostratigraphic succession comprising seventeen map units. Map units dip gently to the north and north-east and original stratigraphic contacts are structurally transposed. Figure 2.4 shows a geological map of the region and Figure 2.5 displays associated cross-sections (1:50,000 scale-figures included at the end of this chapter); lithological units are referenced from these figures. Seven units are assigned to the Indus Suture Zone - which is further subdivided into the Indus Group, the Dras Volcanics, and the Lamayuru Complex - with the remaining units belonging to the THS and GHS. No subdivision between the THS and GHS is shown on figures 2.1–2.5 owing to the lack of a continuous tectonic boundary

between these sequences and correlative metamorphosed sedimentary or volcanic lithological units within both sequences (e.g., group A metavolcanic rock; mixed semipelite, metacarbonate, and pelite; and metacarbonate; Figs. 2.4 and 2.5; Searle *et al.*, 2007). Representative field photographs of map units are given in Figure 2.6. Detailed descriptions of all map units are provided, with the exception of the Indus Group molasse which is the highest-structural unit and lies outside the field mapped area (dashed white box of Fig. 2.4).

The Dras Volcanics (Fig. 2.6a–b) dominantly comprise extrusive volcanic rocks (basalt and basaltic-andesite), with subordinate epiclastic breccia. They form part of an interpreted island arc terrane known as the Dras Arc Complex (after Robertson & Degnan, 1994; Bhat *et al.*, 2019a) or Dras-Nindam terrane (after Walsh *et al.*, 2021). Locally these units are cut by the gabbroic to granodioritic Kargil Intrusives (Honegger *et al.*, 1982; Dietrich *et al.*, 1983; Bhat *et al.*, 2019a; Walsh *et al.*, 2021). The metasedimentary rocks of the Lamayuru Complex (Fig. 2.6c–e) from deeper to shallower lithostratigraphic levels include: 1) graphitic pelite, 2) mixed pelite, psammite, and semipelite, and 3) mixed graphitic pelite, semipelite, and metacarbonate. This sequence is intercalated with metavolcanic rocks (group B metavolcanic rock; Fig. 2.6f).

The metasedimentary rocks of the GHS–THS (Fig. 2.6g–k) from lithostratigraphically deeper to shallower levels include: 1) pelite, 2) a mixed package of psammite, pelite, and semipelite, 3) psammite, locally with preserved cross-stratification, 4) thick-bedded metacarbonate, and 5) a mixed package of semipelite, metacarbonate, and pelite. Like the Lamayuru Complex, the GHS–THS is also intercalated with metavolcanic rocks (group A metavolcanic rock; Fig. 2.6l). The metamorphosed volcanic rocks present in the Lamayuru Complex

Fig. 2.4 1:50,000-scale geological map of the HMC of the Suru Valley region, displaying the southern extent of the ISZ and and THS, and upper portion of the GHS. The white dashed line represents the limit of field mapping with regions outside this area constrained by remote-sensed mapping.

Fig. 2.5 Vertical cross-sections of the Suru Valley region. Lines of section are shown on Fig. 2.4. Sections display lithological contacts, mineral isograds, and major faults and folds 1.5 km above and below topography to better represent the complicated structure of the region. Lighter shading represents rocks that have passed above the erosion surface. Cross-sections A-A' B-B' and C-C' are aligned to cross over points as viewed on geological map, D-D' does not cross over with other sections.

and the GHS–THS are separated into two groups based on structural position, lithological correlation, and overall lithostratigraphic setting. Both groups are characterised by a fine- to medium-grained silica-poor and ferromagnesian-rich mineral assemblage that include a combination of actinolite, tremolite, hornblende, albite/plagioclase, chlorite, biotite, epidote, and muscovite. This mineral assemblage is consistent with a volcanic and/or subvolcanic rock protolith. The volcano-siliciclastic sequence of the GHS–THS is variably associated with pre-Himalayan age m- to km-scale granitoids that are metamorphosed to biotite muscovite syenogranite and garnet biotite muscovite granite assemblages (Fig. 2.6m–n), and intruded by Himalayan age cm- to m-scale lenses of garnet tourmaline leucogranite (Fig. 2.6o). Leucogranite occurs as localised < 40 m thick bodies in the area; migmatite (*sensu stricto*) does not occur in the main study area. *in situ* migmatisation (Fig. 2.6p) occurs ~20 km SSW of Rangdum, outside the study area shown on Figure 2.4; detailed field and petrographic observations of a traverse through this zone (Lalung Valley; Fig. 2.1) are incorporated into the study to ensure that all metamorphic zones regionally are documented.

The progressive change documented from deeper to shallower lithostratigraphic levels in the HMC are interpreted to represent laterally continuous regional lithostratigraphic packages. These packages comprise: 1) graphitic pelite, 2) mixed pelite, psammite, and semipelite, and 3) mixed graphitic pelite, semipelite, and metacarbonate of the Lamayuru Complex (Fig. 2.6c–e); or 1) pelite, 2) mixed psammite, pelite, and semipelite, 3) psammite, 4) metacarbonate, and 5) mixed semipelite, metacarbonate, and pelite of the GHS–THS (Fig. 2.6g–k). Regional metamorphism and polyphase deformation have reworked the original stratigraphic sequence. Nevertheless, the sequence remains readily discernable for the following reasons. Firstly, folding transposed but did not disaggregate the original lithostratigraphic units and associated sedimentary structures (e.g., Fig. 2.6h, i). Second, in the absence of large quantities of fluid during regional metamorphism, compositional mass transfer is restricted to the grain and micro-domain scale (Walther & Orville, 1982). Consequently, compositionally defined sedimentary features, such as cross-stratification, graded bedding and changes of mudstone content in a turbidite succession, remain identifiable following regional metamorphism (e.g., Myers, 2001; Dyck *et al.*, 2019). Such features are readily observed in the Suru Valley area (Fig. 2.6i).

The macro-scale architecture of the study area, shown on figures 2.4 and 2.5, is that of a tightly folded package of metasedimentary and metavolcanic rocks with the deepest lithostratigraphic units exposed in the centre of the map area



Fig. 2.6 Field photographs of the Dras Volcanics, ISZ and THS-GHS lithological units. c–e and g–k = deeper to shallower levels variably intruded by f, l–o. *in situ* partial melting of pelitic layers in h forms p.

between Panikhar and Tongul due to late open folding. Higher structural levels of the GHS are exposed towards the edge of the mapped area as are clearly recorded by the increased abundance of a) mixed semipelite, metacarbonate, and pelite (pale blue) and b) group A metavolcanic rocks (dark green). These units correlate to the shallowest lithostratigraphic levels yet are also consistently folded as thinner discontinuous horizons into the deepest structural levels. The eastern and western portions of the map show the transition from the GHS to the THS, across the ZSZ and the possible Warwan fault. The northern portion of the map area is underlain by the unmetamorphosed to metamorphosed units of the ISZ,

which are tectonically juxtaposed against the GHS–THS (no tectonic boundary) and are similarly deformed by late open folds. Pre-Himalayan granites outcrop at a range of structural levels, from deeper structural levels in the southeast at Shafat, to shallower levels in the north at Karpokhar.

2.5 Lithostratigraphy

2.5.1 Indus Suture Zone

2.5.1.1 Dras Volcanics

The southern extent of the Dras Arc Complex is exposed in the Suru Valley. In the mapped region, the Dras Arc Complex outcrops as the Dras Volcanics, composing extrusive volcanic rocks (basalt and basaltic andesite) and epiclastic breccia. As only a minor component of the Dras Arc Complex is contained in the mapped region, additional details from previous studies in the region are brought in where relevant to lithological descriptions.

Extrusive volcanic rocks occur as dark green to pale green, locally layered, porphyritic to locally aphanitic lava flows (Fig. 2.6a). Porphyritic lava is dominated by clinopyroxene, hornblende and occasionally plagioclase-phyric basalt and basaltic andesite. Most clinopyroxene and hornblende range from mm-scale to ≤ 2 cm in length. Extrusive volcanic rocks are intercalated with subordinate volcaniclastic sandstone. Flows are several metres in thickness. Other studies from the region report the following: clinopyroxene is up to 10 cm in length (Searle, 1983); flows may range up to tens of metres in thickness (Honegger *et al.*, 1982; Robertson & Degnan, 1994); pillow lavas are reported in certain layers at the base of the Dras Arc Complex (Juteau & Reibel, 1981; Searle, 1983; Robertson & Degnan, 1994). Further to the north the Dras Volcanics also include minor andesite and dacite (Fuchs, 1982; Honegger *et al.*, 1982; Searle, 1983).

Epiclastic breccia outcrops as massive, poorly sorted and weakly stratified bodies that are light grey to pale brown in coour and locally light green to maroon (Fig. 2.6b). It is composed of heterogenous mm- to 10s of cm-scale sub-angular to sub-rounded clasts of volcanic extrusive units, dolerite, gabbro, red radiolarian chert and carbonates within a volcaniclastic to tuffaceous matrix. This unit is best exposed S of Dras at the contact to the underlying Lamayuru Complex. Up to metre-sized clasts are reported from other studies in the region and the

thickness of these successions range up to hundreds of metres thick and occur interlayered with lavas (Searle, 1983; Robertson & Degnan, 1994).

Detailed descriptions of the Dras Volcanics and the greater Dras Arc Complex, including the lithologies found outside the mapped region are given in Honegger *et al.* (1982); Searle (1983); Robertson & Degnan (1994); Reuber *et al.* (1989); Bhat *et al.* (2019a); Walsh *et al.* (2019). Metamorphism of the Dras Volcanics ranges from zeolite to lower greenschist facies. Ages of the Dras Arc range from 160 ± 3 Ma to 80 ± 1 Ma in Walsh *et al.* (U-Pb zircon; 2019), with the younger pulse also reported by older studies at *ca.* 82–70 Ma ($^{40}Ar/^{39}Ar$ Hornblende, K-Ar white mica and biotite; Brookfield & Reynolds, 1981; Honegger *et al.*, 1982).

2.5.1.2 Lamayuru Complex - Metasedimentary units

Graphitic pelite is dark grey to black, fine-grained and finely laminated with a prominent cleavage (Fig. 2.6c). The unit weathers easily and defines most of the scree slopes within the zones west and east from Sankoo. The unit has a structural thickness of ∼ 2–4 km. Locally, thin 1-10 cm thick horizons of metamarl or metacarbonate are interlayered with the graphitic pelite. The unit is dominated by graphitic phyllite, with zones locally containing mm-scale biotite and albite porphyroblasts at the relevant metamorphic grade.

The graphitic pelite grades into a mixed pelite, psammite, and semipelite. It is light grey to pale green, fine- to medium-grained and appears layered to finely laminated (Fig. 2.6d). The transition zone shows thicker mm- to cm-scale graphite-rich layers of psammite or semipelite with thin mm-scale laminae of pelite and fining upwards grading. The unit is best characterised by alternating layers of approximately equal thickness of pelite with psammite and or semipelite. This lowermost structural zone contains mm-scale porphyroblastic titanite in pelite layers, and/or ankerite or calcite in psammite layers. This unit has a maximum structural thickness of ∼ 1.5 km and is dominated by chlorite biotite schist.

The lithostratigraphically highest unit of the Lamayuru Complex as exposed in the Suru Valley area is a mixed graphitic pelite, semipelite and metacarbonate. The contact from the underlying mixed pelite, psammite, and semipelite is gradational. The mixed graphitic pelite, semipelite, and metacarbonate is dark grey, fine-grained, and finely laminated (Fig. 2.6e). Cm-scale horizons of metamarl and metacarbonate are repeated throughout. The unit has a maximum structural

thickness of approximately 200 m and comprises graphitic calc-phyllite and calc-schist.

2.5.1.3 Lamayuru Complex - Metavolcanic rocks

Group B metavolcanic rocks are light to dark green, fine-grained and have a layered appearance when metamorphosed to greenschist facies and massive, blocky appearance with mm-scale quartz veins where in the sub-greenschist facies N of Umba (Fig. 2.4, 2.6f). The quartz veins have a lenticular shape in outcrop and/or occur as discontinuous layers within the graphitic pelite. Green to dark grey graphitic phyllites and locally cm-thick metacarbonates (within the graphitic pelite unit) are often intercalated with the group B metavolcanic rocks at cm- to m-scale. These rocks comprise actinolite schist, and meta-alkali basalt or meta-alkali andesite.

2.5.2 GHS–THS

2.5.2.1 Metasedimentary units

The lithostratigraphically (and structurally) lowest level of the GHS–THS is dark-colored, medium-grained, and finely laminated pelite (Figure 2.6g). The true structural thickness of the pelite unit is unknown thought displays a maximum across strike extent of $\sim$ 4 km. The unit is dominated by kyanite-staurolite schist with a porphyroblastic texture.

The pelite unit grades upwards into a mixed package of psammite, pelite and semipelite. Psammite is the most abundant component and appears relatively homogenous to thickly layered in outcrop. It is light grey, fine- to medium-grained and displays fining upwards grading (Figure 2.6h). Pelite and semipelite layers are dark colored, medium-grained, locally graphite- and carbonate mineral-rich and are characterised by thin laminae capping the psammite or as individual layers. The mixed psammite, pelite and semipelite has the largest structural thickness in the study area (km-scale) and is present at all metamorphic grades. In outcrop, the unit can be described as a schist or gneiss with associated porphyroblasts of the relevant metamorphic grade.

At or near the top of the mixed pelite, semipelite and psammite sequence, is a locally developed light grey, fine-grained and equigranular psammite (Fig. 2.6i). The unit appears homogenous to layered in outcrop. The thickness of the unit

is generally < 100 m. Composition ranges from arkosic to quartzitic. 1–2 mm garnets are often present, but index minerals of higher metamorphic grades are not.

Metacarbonate outcrops within 1 km of the equigranular psammite and locally overlies the unit. It is cream to light grey and fine- to medium-grained with a granoblastic texture (Figure 2.6j). In outcrop it is layered to homogenous and varies from thinly to thickly bedded (m-scale to 200 m) and is as a marble.

The uppermost lithostratigraphic unit of the GHS–THS in the Suru Valley comprises a mixed package of semipelite, metacarbonate, and pelite. The semipelite and pelite are dark grey to black and are fine- to medium-grained (Figure 2.6k). They are finely laminated to layered and locally show a dominant graphitic and carbonaceous component. The metacarbonate is light grey with characteristic orange weathering and fine-grained with a granoblastic texture. Metacarbonate often alternates and/or is folded into the semipelite and pelite such that it alternates at cm-scale and locally at 10–100 m-scales. The mixed semipelite, metacarbonate and pelite dominantly outcrops at the edges of the mapped area (Fig. 2.4) and is occasionally folded into the mixed psammite, pelite, and semipelite. The mixed semipelite, metacarbonate and pelite shows variation in mineral assemblage, grain size and coour across the mapped area though generally is as a calc-schist.

2.5.2.2 Metavolcanic and subvolcanic rocks

Group A comprises dark green, fine- to medium-grained metamorphosed subvolcanic and volcanic rocks and are layered at mm- to cm-scale (Figure 2.6l). The group generally occurs as discontinuous sheets within the mixed semipelite, metacarbonate and pelite, and/or defining the contact between this mixed unit and the mixed psammite, pelite, and semipelite (Fig. 2.4). In outcrop, group A metamorphosed volcanic rocks vary in unit thickness from cm-scale to 250 m). These rocks are amphibolite. Geochemical studies (Sr-Nd isotopes; whole rock major and trace elements) suggest these units are the metamorphosed equivalents of the lower Pemian Panjal Trap volcanics (Honegger *et al.*, 1982; Shellnutt, 2018). The Panjal Trap volcanics (Lydekker, 1883; Wadia, 1961) are known to be aphyric tholeiitic to mildly alkalic in composition (Shellnutt, 2018). They represent basalt flow covering an area of approximately 12,000 km^2 that mark the end of volcanic activity that began in the late Carboniferous and record the break-up of Gondwana (Pareek, 1976; Honegger *et al.*, 1982; Shellnutt, 2018).

2.5.2.3 Metamorphosed granites

Three types of metamorphosed granite occur in the Suru Valley, which from oldest to youngest are biotite-muscovite syenogranite, garnet-biotite-muscovite granite and garnet tourmaline leucogranite (Fig. 2.6m–o). The garnet tourmaline leucogranite is present as < 40 m bodies within the mapped area, therefore are only locally recorded on Figures 2.4 and 2.5. The leucogranites become more extensive S of the Suru Valley region (Fig. 2.1), and are associated with the sillimanite-grade migmatites in the highest-grade zone of the HMC (Searle, 1986).

The biotite-muscovite syenogranite is light grey to cream, coarse-grained and frequently porphyritic, containing coarse poikiloblastic K-feldspar phenocrysts (1–10 cm; Fig. 2.6m). In regions of lower strain, the granite possesses a coarse equigranular texture. In proximity to shear zones, the granite displays increased evidence of deformation and shows an augen gneiss texture (comprising K-feldspar) with a prominent C-S-C' fabric. At the regional scale, syenogranite form km-scale bodies that are sub-parallel to the regional tectonic foliation.

The garnet-biotite-muscovite granite is light grey to cream, medium- to coarse-grained and outcrops as homogeneous sill-like bodies parallel or sub-parallel to the regional tectonic fabric (Figs. 2.4 and 2.6n). These bodies vary from monzogranite (e.g., S of Sankoo; Fig. 2.6n) to syenogranite (e.g., Shafat) in composition, the latter are frequently porphyritic, containing coarse poikiloblastic K-feldspar phenocrysts (0.5–6 cm). A medium-grained more leucocratic phase of the granite is commonly emplaced subparallel to the fabric in the granite. The leucocratic phase of the granite exhibits more mafic-rich rims in contact to the adjacent units. Fine-grained, and pegmatitic leucocratic phases were also identified. Field relations do not infer consistent crosscutting relationships and therefore differing ages between the different phases (though the fine-grained, and pegmatitic leucocratic phases generally crosscut the fabric in the granite). As such, the different phases and compositions (monzogranite, syenogranite, minor leucocratic phases) are interpreted to represent intrusive components of a single granitic complex. In outcrop, large bodies of granite are associated with group A metavolcanic rocks. The group A metavolcanic rocks (generally $\leq$1.5 m thickness) appear to have intruded as sills into the granite as observed at the Sankoo granite (Fig. 2.4), as has been previously suggested (Walker, 1999; Noble *et al.*, 2001). However, field relations also indicate that the group A metavolcanic rocks may also appear as xenoliths within the granite. At the regional scale, the granite forms km-scale bodies or layers that are parallel to the regional tectonic foliation,

though some discordance between intrusive contacts and deformation fabrics in the host rocks is visible in outcrop (e.g., Shafat). Dating of the garnet-biotite-muscovite granite at Sankoo has yielded a Permian age of 268 ± 5 Ma, and discordant results at Parkachik suggests an age of *ca.* 270 Ma (U-Pb zircon; Noble *et al.*, 2001). Another outcrop of the granite at Tongul has also been dated at 284 ± 4.4 Ma (U-Pb zircon Horton & Leech, 2013).

The garnet tourmaline leucogranite is white to cream colored, fine- to coarse-grained leucogranite with an irregular to lenticular shape in outcrop (Fig. 2.6o). Layers of garnet tourmaline leucogranite define a stromatitic layering in the metasedimentary sequence, both subparallel and discordant to the regional fabric. Coarse cm-scale tourmaline is present locally. Where leucogranite is coarse grained it occurs as pegmatite. Pegmatite forms tabular to lenticular bodies and may crosscut or lie parallel to dominant regional foliation. U-Pb monazite dating of leucogranites from Zanskar give an age of *ca.* 20.8–19.5 Ma for crustal melting, with those dated at Shafat producing a measured age of 20.8 ± 0.3 Ma (Noble & Searle, 1995).

2.5.2.4 Migmatite

Although migmatite is not shown on the geological map in Figure 2.4, it is present just SSW of Rangdum in the Lalung valley (Fig. 2.1). Migmatite is characterised by white–cream, medium-grained, wavy to lenticular leucosome (Fig. 2.6p). The leucosome occurs as cm to 10s of cm long discontinous lenses that lie sub-parallel and/or crosscut the dominant regional foliation. Boundaries between the leucosome and the neosome are curvilinear to interlobate and are often defined by increased mica and aluminosilicate content (interpreted as residuum). The mixed psammite, pelite, and semipelite unit is inferred to comprise the paleosome, with most of the melting occurring in the fertile pelitic layers. These textures are consistent with *in situ* migmatisation and are absent within leucogranite which is therefore interpreted to represent structurally higher coalesced products of *in situ* partial melting. This is supported by the U-Pb monazite ages of leucogranite from Noble & Searle (1995) which overlap with ages for migmatites (Figure 2.3).

2.6 Structural architecture

Five generations of planar and/or linear structural features are identified in the study region. Three penetrative fabrics (S_1, S_2, and S_3); three linear elements (L_1, L_2, and L_3); and four macro-scale fold generations (F_2, F_3, F_4, F_5) are documented and then discussed in the context of five interpreted deformation events ($D_{1–5}$). A summary of the structural features defining these deformation events are presented in Table 2.1 and Figures 2.7 and 2.8 show the spatial distribution of recorded planar and linear structural elements across the mapped region. Field photographs documenting examples of planar and linear fabrics are shown in Figure 2.9, and macro-scale fold interference patterns in Figure 2.10. Finally, a simplified geological map of the region separated into 6 zones with associated stereonet data for $D_{1–3}$ planar and linear structural elements is shown in Figure 2.11.

Table 2.1 Main deformation fabrics observed in Suru Valley area, Zanskar Himalaya.

Planar and linear structural features	**Expression**	**Data**
S_1/L_1	S_1: NE- dipping schistosity parallel or sub-parallel to S_0. L_1: W- to E- plunging mineral stretching lineation (NE-directed where least reworked).	L_1: 19 → 090
$S_2/L_2/F_2$	S_2: NW- to NE-dipping fabric displaying crenulation cleavage, schistosity and C-S structures. L_2: SW- to NE-plunging mineral stretching lineation associated with thrust sense shearing. F_2: Folding of S_1 fabric. S_2 is axial planar to F_2.	L_2: 16 → 079 F_2: 17 → 082
$S_3/L_3/F_3$	S_3: NE-dipping composite fabric comprising mylonitic C-S-C' planar elements, schistosity, and a crenulation cleavage. Coaxial with S_2. L_3: NE-plunging mineral stretching lineation associated with normal sense shearing. Coaxial with L_2. F_3: Folding of S_2 (and locally S_1) fabric. S_3 is axial planar to F_3.	L_3: 38 → 071 F_3: 10 → 092
F_4	Open km-scale cross-folds with NE- and SW-plunging fold axes and SE- or NW-dipping axial surfaces. No penetrative fabric developed.	F_4: 07 → 056
F_5	Open km-scale folds with NW- and SE-plunging fold axes and sub-vertical axial surface. No penetrative fabric developed.	
N.b., F_3 measurements include both meso-scale F_3 and micro-scale crenulation measurements, i.e., $L_3(c)$		

The nomenclature used to record planar and/or linear structural elements and their associated deformation events keeps track of superposed fabrics and mineral assemblage relationships by locality. These fabrics and associated assemblages represent markers within the context of progressive regional metamorphism and deformation. They most likely developed at different structural levels at different times and do not imply discrete temporal events.

Deformation fabrics ($S_{1–3}$) in the Suru Valley region are identified in metasedimentary rocks by the alignment of phyllosilicate minerals and flattening of quartz and feldspar. In metavolcanic rocks they are defined by the preferred orientation of chlorite, biotite and locally by amphibole mats and plagioclase-quartz aggregate laminations. Fabrics are associated with well-developed lineations ($L_{1–3}$) defined in metasedimentary rocks by elongate rods of quartz and feldspar and aspect ratio of phyllosilicate minerals. In metavolcanic rocks, the lineation is defined by the orientation of actinolite, tremolite, and hornblende, and aspect ratio of chlorite and biotite. Detailed descriptions of fabric-defining metamorphic mineral assemblages for each deformation event are included in the Appendix (A.1).

2.6.1 $S_0/S_1/L_1$

The oldest deformation fabric (S_1) identified in the study area is manifest as a schistosity. S_1 lies parallel or sub-parallel to the bedding plane (S_0) locally preserved in metasedimentary rocks (Fig. 2.9a). S_1 is associated with a well-developed stretching lineation (L_1). Where minimally disturbed, S_1 dips moderately to the NE and L_1 plunges to the E. However, S_1 is dominantly re-oriented by later sequences of deformation, thus a clear original orientation of early planar elements is rarely preserved (Fig. 2.7). L_1 is dominantly co-axial to the most penetrative later sequences of deformation ($D_{2–3}$), thus is likely less re-oriented (Fig. 2.8).

S_1 is documented in all units except the pelite unit (where a pervasive S_2 is the earliest planar fabric recognised) and the Dras Volcanics, and is best preserved in psammite-rich zones of the mixed psammite, pelite, and semipelite (Fig. 2.9a). D_1 represents the first expressed phase, which is poorly constrained to have had a NE–SW orientation.

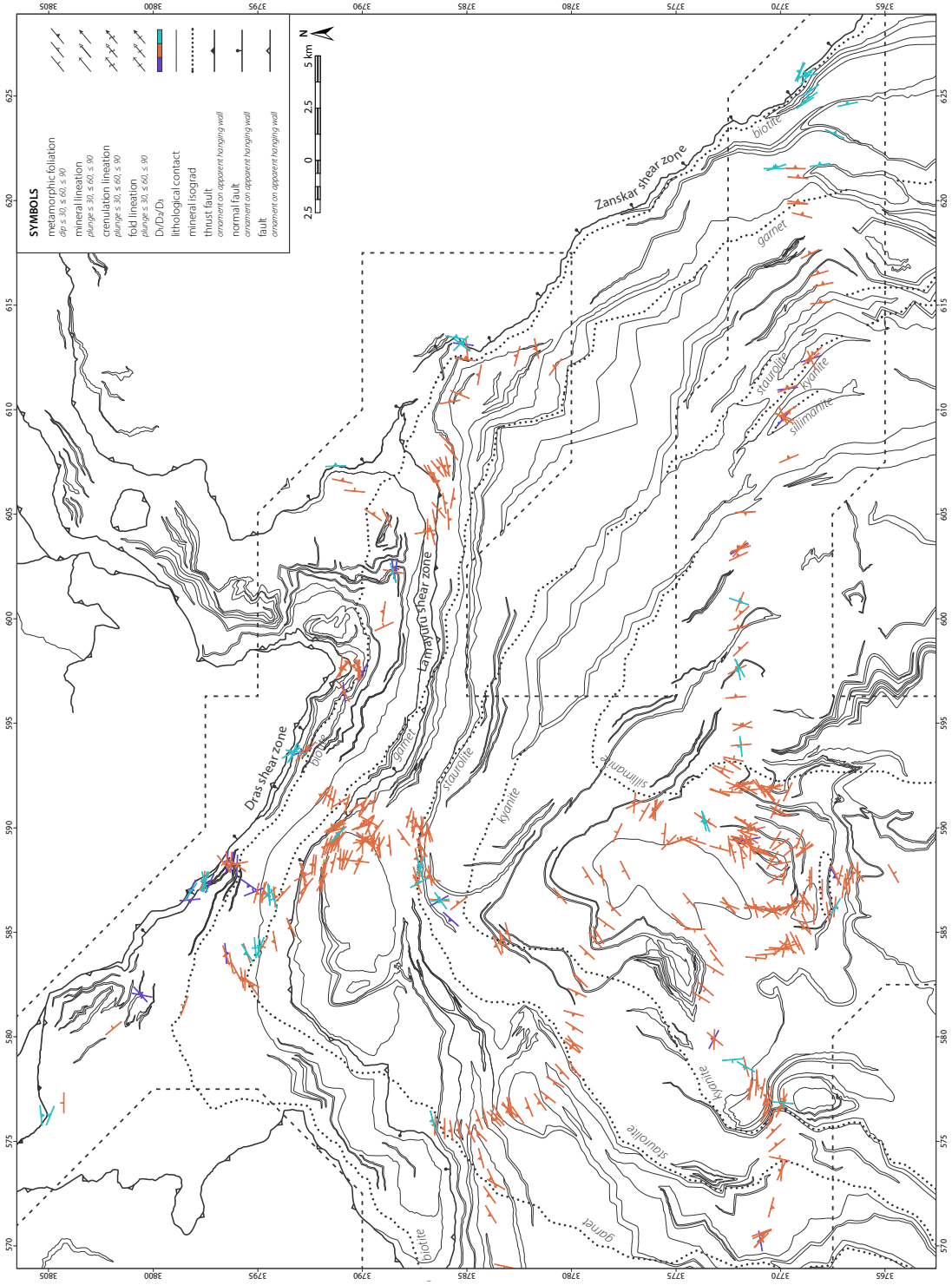


Fig. 2.7 Form-line map of major lithological, tectonic and metamorphic features of the Suru Valley area with planar structural elements colored by associated deformation event. Grid references are truncated, with final three zeros omitted.

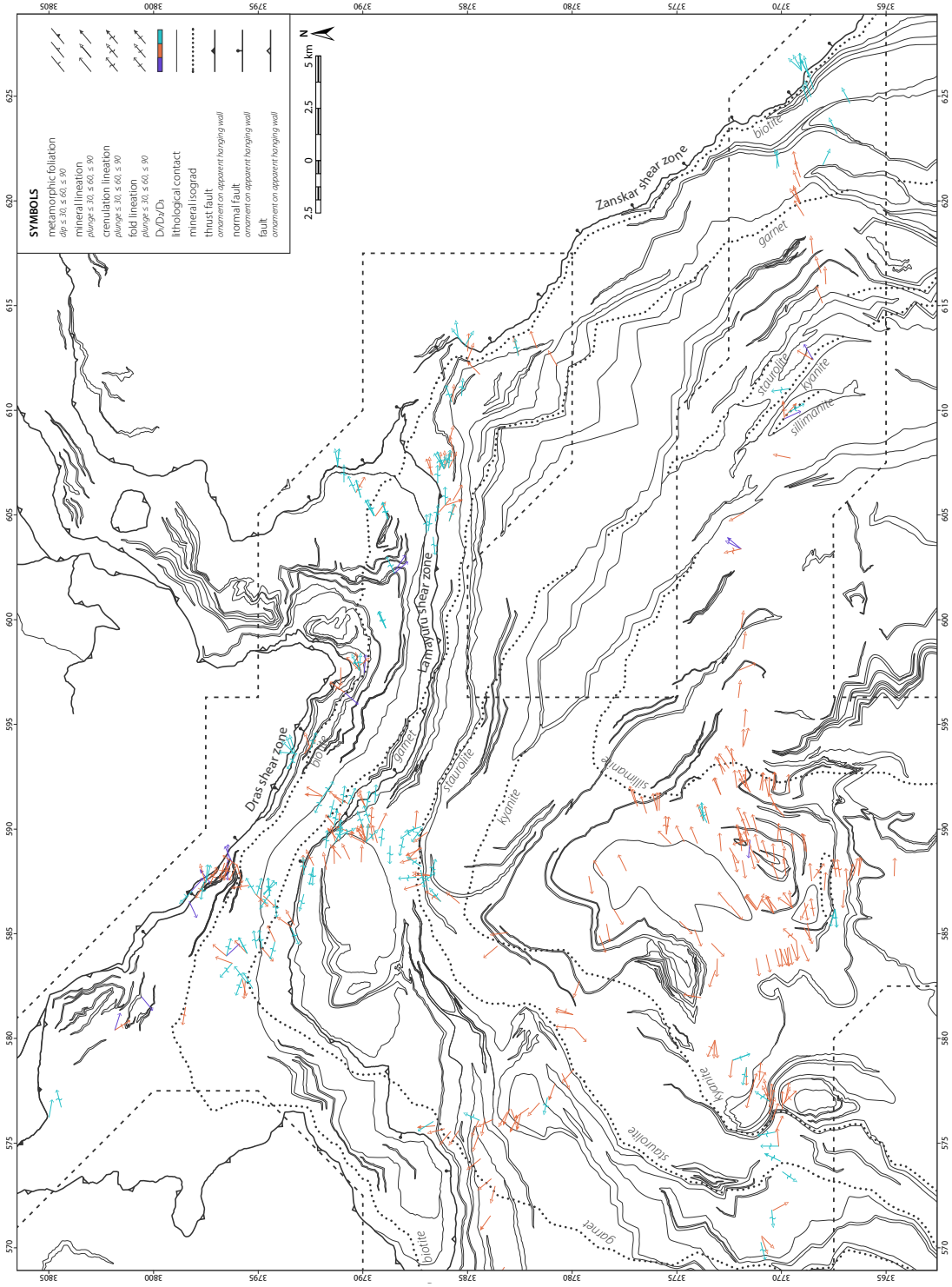


Fig. 2.8 Form-line map of major lithological, tectonic and metamorphic features of the Suru Valley area with linear structural elements colored by associated deformation event. Grid references are truncated, with final three zeros omitted.

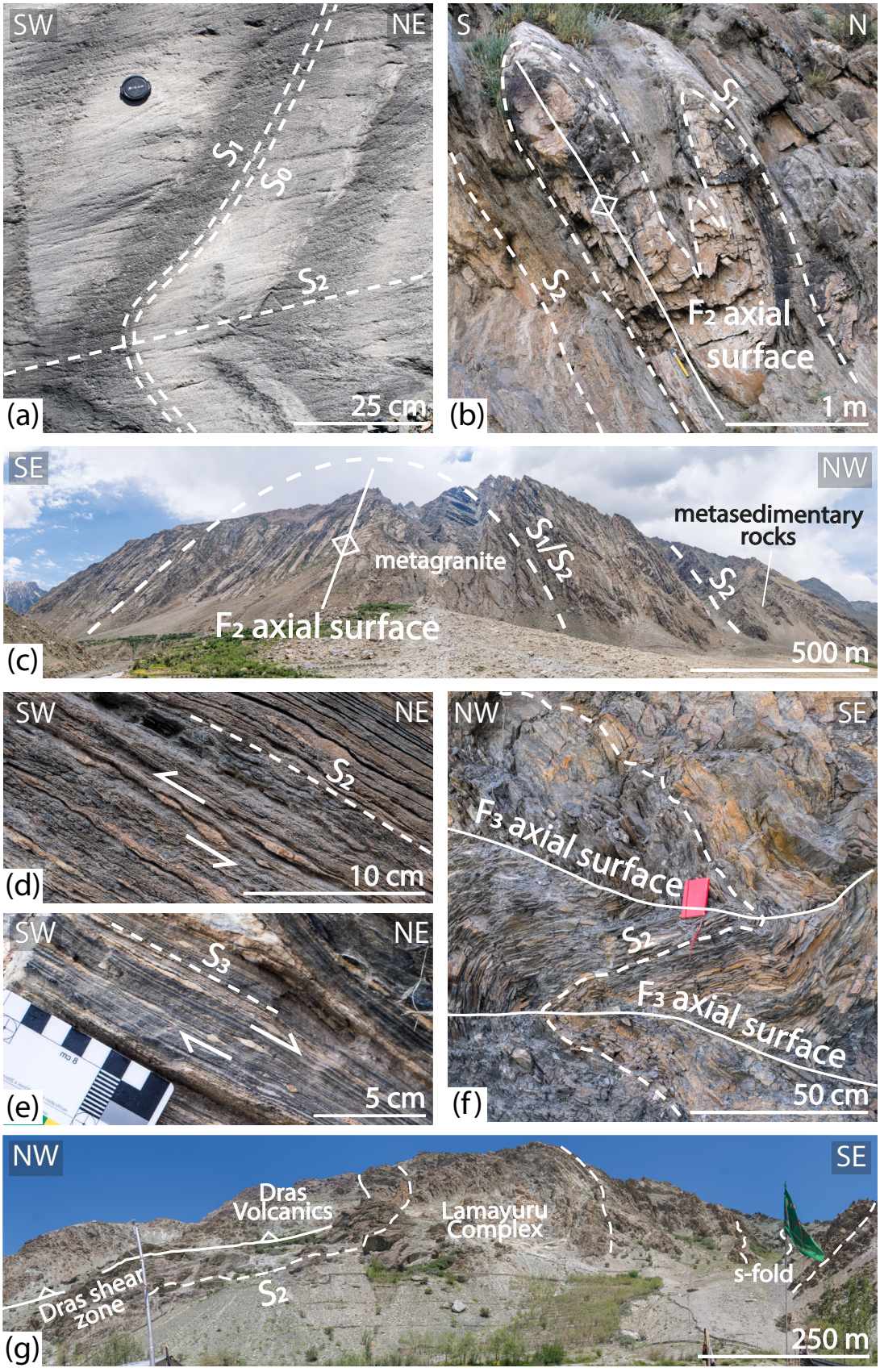


Fig. 2.9 (Caption on the following page.)

Fig. 2.9 Meso-scale field photos of planar and linear features formed during D_1–D_3. a) cm-scale S_1 fabric deformed by D_2 to form an axial planar S_2; b) m-scale isoclinal folding of transposed S_1 fabric by F_2 to develop axial planar S_2; c) km-scale folding of S_1 fabrics by Karpokhar antiform F_2 fold, subsequent fabric development produces penetrative S_2 fabric on fold limbs; d) thrust-sense augen and mylonitic S_2 fabric formed during D_2; e) normal-sense augen and mylonitic S_3 fabric, through reactivation of S_2 during D_3; f) cm- to m-scale F_3 folds with sharp hinge zones deforming S_2 fabric; and g) km-scale panorama of Barsoo antiformal backfold, a SE-plunging F_3 structure (fold hinge further to the N), (apparent) normal movement is inferred on the lower limb, as documented on the Dras shear zone, that becomes overturned and transitions to a NE-directed back-thrust.

2.6.2 $S_2/L_2/F_2$

S_2 comprises a crenulation cleavage, axial planar to crenulations of S_1 (Fig. 2.9a, b), that dominantly develops into a penetrative schistosity (Fig. 2.9a). S_2 dips gently to moderately to the NW to NE (locally to the SW and SE, Figs. 2.9c & 2.7). The associated well-developed L_2 plunges to the NW to NE (Fig. 2.8). Dominantly thrust-sense shearing can be observed in augen and/or locally developed C-S fabrics (Fig. 2.9d).

S_2 is axial planar to associated folds (F_2; Fig. 2.9b). F_2 are generally type 2 (occasionally type 3 or 1c; Ramsay, 1967), tight to isoclinal (rarely close), inclined, overturned, or recumbent, m- to km-scale folds of the S_1 fabric (Fig. 2.10). Drag folds and secondary folds are associated with development of larger folds. Limb thickness, as measured perpendicular to the dip of the axial surface, varies from cm-scale to ~3 km across the mapped area. The inter-limb angle of macro-scale folds, defined here as those that can be distinguished at map-scale (i.e., approximate wavelength greater than 200 m), is tight–isoclinal at higher structural levels and decreases to dominantly isoclinal at deeper structural levels, where evidence of S_1 is poorly preserved. S_2 and L_2 are coaxial with S_1 and L_1. Shearing and folding of S_1 is interpreted as resulting in S_2. Folding brings S_1 compositional layering progressively into alignment with S_2 (e.g., Fig. 2.9a).

The best developed km-scale F_2 folds are observed at Karpokhar, Donara, and Tongul (Fig. 2.4; A-A' and C-C' of Fig. 2.5). Characteristic examples for F_2 folds are shown in figures 2.9a, b, c & 2.10. The Karpokhar antiform is located directly south of Sankoo at Karpokhar village (Fig. 2.4); the antiform is an overturned northeast-plunging open fold of garnet biotite muscovite granite and mixed psammite, pelite, and semipelite (A-A' of Fig. 2.5 and Fig. 2.9c). Linked

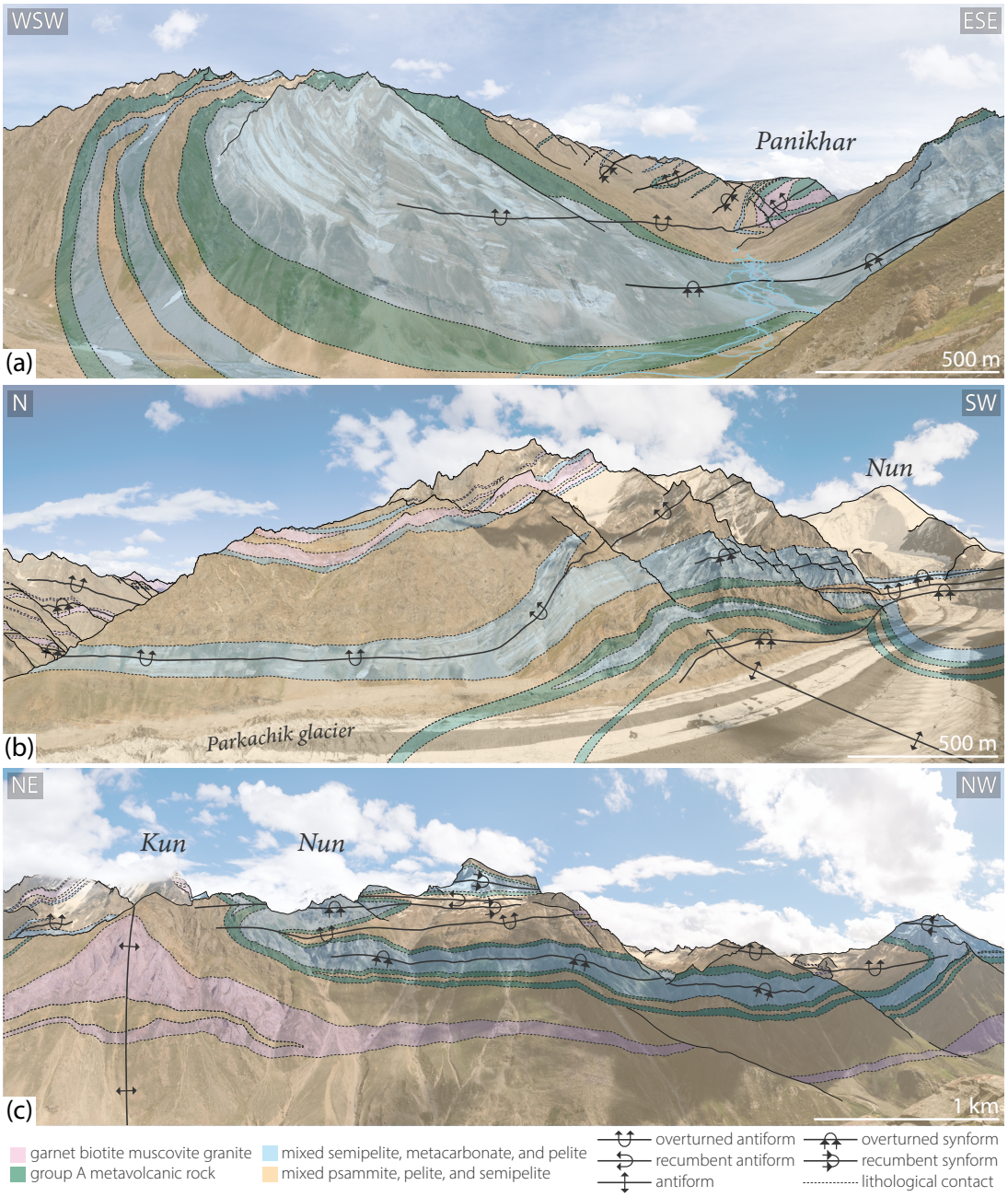


Fig. 2.10 Annotated panoramic field photographs of macro-scale folds. Lithological colors match those in the legend of Figure 2.4 and 2.5. a) Oblique perspective of the Donara antiform at the river confluence along Chellong Nala, view to the N. b) Intersecting F_2 and F_4 folds above Parkachik glacier, view to the SEE. Geometry and lithology of rocks below glacier inferred from observed structures and rock units bounding the glacier. c) View above Tongul over to Parkachik metagranite and intersecting F_2 and F_4 folds, the Tongul antiform extends from the SE peaks to underlying Nun in the centre of the panorama, view to the S. Original panoramic photographs with no annotation are included in the Appendix (A.1).

cm- to m-scale asymmetric parasitic F_2 folds are found on both fold limbs, and isoclinal F_2 synforms are developed on the N- and S- side of the antiform (Fig. 2.4 and A-A' of Fig. 2.5). A significant competency contrast is inferred between the granite and metasedimentary rocks, with the interpreted higher competency granite causing the fold hinge to be significantly more open than other F_2 folds (Fig. 2.9c). Despite the open fold hinge, these lithological units have a dominant S_2 (and/or subparallel S_1) fabric that is best developed in the metasedimentary rocks. The southern side of the Karpokhar antiform locally records a moderately to steeply S-dipping S_2 fabric (Fig. 2.4 and A-A' of Fig. 2.5), and is interpreted to be characterised by a minor N-dipping blind thrust to accommodate competency variation between the granite and metasedimentary rocks (A-A' of Fig. 2.5).

The Donara antiform is located directly N of the Donara campsite along Chellong Nala (Fig. 2.4). It is a km-scale open southwest plunging overturned antiform that folds the mixed semipelite, metacarbonate, and pelite; mixed psammite, pelite, and semipelite; interlayered garnet biotite muscovite granite and metavolcanic rock group A (A-A' of Fig. 2.5 and Fig. 2.10a). A km-scale isoclinal F_2 synform extending from Tanak peak SE of Tongul occurs near the hinge of the Donara antiform (Fig. 2.4). The axial traces of these folds start to converge in this area due to later stage warping or folding interpreted to relate to movement on the Warwan fault located further to the SW (A-A' of Fig. 2.5 and Fig. 2.10a).

The Tongul antiform, located just south of Tongul (Fig. 2.4), is a km-scale overturned to recumbent isoclinal northeast plunging antiform developed within the mixed psammite, pelite, and semipelite; mixed semipelite, metacarbonate, and pelite; and group A metavolcanic rock (Fig. 2.10c). Late open folding (F_4) re-orients the Tongul antiform from early SW-vergence (B-B' and C-C' of Fig. 2.5 and Fig. 2.10c).

S_2 is the most penetrative structural fabric in the Zanskar Himalaya and it is recognisable at all structural levels and in all lithologies. Large (up to km-scale) F_2 folds are best preserved in the mixed semipelite, metacarbonate, and pelite and/or pure metacarbonate, which deformed in a ductile manner and as such highlight the folding of D_1 fabrics and any sub-parallel S_0 (e.g., Fig. 2.10a–c). Due to the intensity of S_2 fabric development, preservation of folding at smaller scales (m-scale) and evidence of crenulation cleavage is best observed in the psammite of the mixed psammite, pelite, and semipelite (e.g. Fig. 2.9a). S_2, L_2 and F_2 represent the effects of continued NE-SW oriented deformation. D_2

fabrics and structures have accommodated significant thickening of the HMC through isoclinal folding from micro- to macro-scale. Thrust fabrics show that significant shearing occurred during D_2.

2.6.3 $S_3/L_3/F_3$

S_3 comprises a mylonitic fabric (locally displaying C-S or composite C-S-C'), or crenulation cleavage that is axial planar to crenulations of S_1 and S_2. L_3 is associated with a normal sense of shear as identified by C-S-C' fabrics, rotated porphyroblasts and/or augen (Fig. 2.9e). An oblique orientation of L_3 to dip direction and evidence of extensional boudins perpendicular to stretching lineations are visible in outcrop, representing non-coaxial simple shear. S_3 dips gently to moderately to the N to ENE (locally to the NW and SE; Fig. 2.7) and L_3 plunges towards the ENE (Fig. 2.8). S_3 and L_3 are broadly coplanar or coaxial with S_2 and L_2. Shearing and/or folding of S_2 are interpreted to result in development of S_3.

S_3 is axial planar to associated folds (F_3). F_3 are dominantly restricted to the northern area of the map (Figs. 2.4 and 2.8). These folds are type 1c (occasionally type 1b or 2; Ramsay, 1967), open to close (variation from gentle to isoclinal as a function of position with respect to the shear zone), inclined, or overturned, or recumbent, m-scale (rarely km-scale) folds of S_2 and/or S_1 fabric (Fig. 2.9f). F_3 folds generally show normal-vergence. A km-scale F_3 antiformal backfold (Barsoo antiform) east of Sankoo, which folds the Dras Volcanics and the underlying Lamayuru Complex, is defined by inclined to open limbs and a SEE-plunging fold axis (B-B' of Fig. 2.5 and Fig. 2.9g). Secondary folds are associated with development of this F_3 (Fig. 2.9g). Another km-scale F_3 antiformal backfold is interpreted from remote sensed mapping north of Tapshah and southwest from Sankoo (Fig. 2.4, and C-C' of Fig. 2.5). Limb thickness of F_3 structures, as measured perpendicular to the dip of the axial surface, varies from cm- to m-scale (generally < 5 m), though the Barsoo antiform has a thickness of 2 km.

Three dominant shear zones are documented in the area: 1) ZSZ, 2) Dras shear zone (juxtaposing the Dras Volcanics in the NE and Lamayuru Complex in the SW), and 3) Lamayuru shear zone (juxtaposing the Lamayuru complex in the NE with the units of the Indian slope–shelf on the SW). Shear zones are defined based on footwall-hanging wall relations (lithostratigraphy and metamorphic grade) and ductile and brittle fabric development. These structures are displayed in Figure 2.4 and across the lines of section in Figure 2.5. The term ZSZ solely refers to the

later intense normal-sense shearing that occurred during exhumation (e.g., Patel *et al.*, 1993), and excludes previous thrust fabrics that likely developed during the early stages of crustal thickening where the GHS was underthrust below the THS (e.g., Patel *et al.*, 1993; Dèzes *et al.*, 1999; Robyr, 2002; Finch *et al.*, 2014). The Dras and Lamayuru shear zones record a heterogeneously distributed zone of polyphase normal-thrust movements that is herein termed the Sankoo fault zone. These polyphase movements initiated prior to the India-Asia collision (e.g., Robertson, 2000). Given the complicated polyphase history across all these three shear zones, this study focuses on later (dominantly normal-sense) movements occurring during D_3.

At the highest structural levels of the GHS, in the southeastern portion of the map, S_3 and L_3 are pervasive within a ~3–4 km-thick mylonitic fault zone within the footwall of the ZSZ (Figs. 2.7 & 2.8), which is dominated by metacarbonate, group A metavolcanic rock, and mixed semipelite, metacarbonate, and pelite. Toward the NE extent of the ZSZ, S_3 and L_3 occur within a ~100 m-thick zone. In these areas, adjacent to the ZSZ, S_3 is dominantly mylonitic in nature, and displays a transition from ductile to brittle structures as observed by tension gashes crosscutting the shear fabric. In the northern portion of the map, S_3 and F_3 have developed a broad zone of crenulated fabric in the metasedimentary and metavolcanic rock units of the Lamayuru Complex, with a penetrative mylonitic fabric (S_3 and L_3) developed locally (50–250 m thickness) along the footwall contact of shear zones (Figs. 2.7 & 2.8). Away from these shear zones, S_3 and associated crenulation lineations are also commonly observed in the pelite layers of the mixed psammite, pelite, and semipelite. The S_3 fabric is best displayed in pelitic tops of this package as the less competent mica-rich compositions allow for crenulations to develop more so than in the more competent psammitic intervals. At deep structural levels S_3 displays a strong crenulation cleavage that is locally developed as a penetrative schistosity.

Normal shearing and movement on the ZSZ and late movement on the Sankoo fault zone in the northern part of the map is interpreted as D_3. Due to the growth of retrograde mineral phases during D_3 (e.g., chlorite and biotite growth along shear bands), D_3 is interpreted as a post-metamorphic peak event. The transition from thrust-sense fabrics in D_2 to normal-sense shear fabrics in D_3 and the co-axial nature of the respective structures can be used as evidence to suggest that D_3 largely involved the reactivation of D_2 structures, with consistent orientation of the major stress direction (overall compressional regime; e.g., Kellett *et al.*, 2019). Observed extensional boudins imply that there may be both a flattening

and an extensional vector, or strike-slip component, resulting in non-ideal simple shearing during development of the ZSZ fabrics, as has been previously suggested (see Walker, 1998; Walker *et al.*, 2001). In contrast, the northern portion of the mapped area displays a wide zone of distributed shearing and folding across the Lamayuru Complex. Late-stage open folding (F_3 backfolds) in this region appears to overturn faults (e.g., Lamayuru shear zone) and produce apparent normal-sense or thrust-sense movement. Although in parts of the northern area it is possible to deconvolve the origin of these movements from early pre-collisional thrusting and subsequent late warping during D_3, often it is difficult. We infer the zone to be characterised by both normal-sense and back-thrust movement (thrusting to the NE). D_3 can therefore be described as a protracted phase of deformation initially propagating from NE to SW, characterised by normal-sense movement, and later progressing into NE-directed back-thrusting.

2.6.4 F_4

F_4 are type 3 (Ramsay, 1967), open symmetric, km-scale cross-folds. Fold axes plunge gently towards the north-east (e.g., between Panikhar and Parkachik on Fig. 2.4 or zone B of Fig. 2.11) and south-west with axial surfaces dipping steeply towards the north-west or south-east. No meso- or micro-scale fabrics are directly associated with F_4, though F_4 structures warp $D_{1–3}$ structures. Older mineral stretching lineations ($L_{1–3}$) are minimally affected by the F_4 structures as fold axes are subparallel to the pre-existing lineations (see Table 2.1 and 2.8). L_3 fabric crenulations are often developed near F_4 structures (Fig. 2.4), therefore, it is possible that F_4 may be associated with a late D_3 event. Alternatively, D_3 structural elements may represent sites of crustal weakness where further buckling during D_4 is focused. F_4 km-scale open cross-folds of previous fabrics are best observed between Panikhar, Tongul, and Parkachik (Fig. 2.4 and B-B', C-C' of Fig. 2.5).

The southern limbs of F_4 folds are often defined by transposed earlier fold generations that are now NE-verging structures. This may be observed south of Tongul where multiple fabric generations are all S-dipping, defining the lower limb of an overturned N-verging F_2 fold (B-B' and C-C' of Fig. 2.5). Mineral growth-fabric relations indicate these fabrics are consistent with N- to NE-dipping fabrics found elsewhere in the mapped area. These fabrics are assigned as S_1 and S_2 and emphasises that F_4 structures refold previous linear and planar structures and are the direct result of NE-vergent F_2 structures. Importantly, NE-vergent folds in

the Suru Valley region do not represent a prolongation of early NE-directed folds and thrusts that pre-date SW-directed folding and thrusting (c.f. Steck, 2003).

2.6.5 F_5

F_5 are late km-scale folds that are open and symmetric with upright/steeply dipping axial surfaces that trend to the NW or SE. No meso- or micro-scale fabrics are associated with F_5, and F_5 structures appear to fold $D_{1–3}$ structures. F_5 folds are best observed in the region between Sangrah and Parkachik (Fig. 2.4). The S_2 fabrics dip away from the intersection of $D_{4–5}$ folds (Fig. 2.7) and L_2 are perpendicular to the axial surface of F_5 folds (Fig. 2.8). This results in a crustal doming pattern. D_3 crenulations and planar S_3 observed on the hill between Panikhar and Parkachik are perpendicular to the axis of F_5 and crenulations display normal-sense vergence (i.e., cascading folds); this implies such generations are likely distinct. Fold axes are not displayed on areas outside the main mapping area, however, remote-sensed mapping indicates that at the NE and NW portion of the map (Fig. 2.4), the THS, Lamayuru Complex and intervening Lamayuru shear zone are folded around the axis of large NW-SE oriented km-scale open synforms. These synformal structures are inferred to be coincident with the D_5 event on the basis of their scale, orientation, symmetrical nature, and inferred timing (post-dating all phases of movement on the Lamayuru shear zone).

2.6.6 Structural zones

The mapped region is separated into six structural zones with stereonet data displaying planar and linear structural elements from D_1–D_3 (Fig. 2.11). Zones were selected based on completed transects along valleys and the overall structural architecture. Subscript "s" and "c" refer to mineral stretching and crenulation lineations respectively. Zones are presented and discussed in clockwise order: easternmost zone A displays $D_{1–3}$ fabrics; central zone B preserves D_2 fabrics warped by late $D_{4–5}$ folding; westernmost zones C and D document D_2 and D_3 fabrics; and zones E and F located in the north of the mapped area record D_1 and D_2 fabrics subsequently reoriented by D_3 crenulations and folding. The following observations are summarised with reference to Figure 2.11:

1. Zone A: Linear and structural planar elements in this zone are co-planar across D_1–D_3. Foliation dips to the NE and stretching lineations plunge

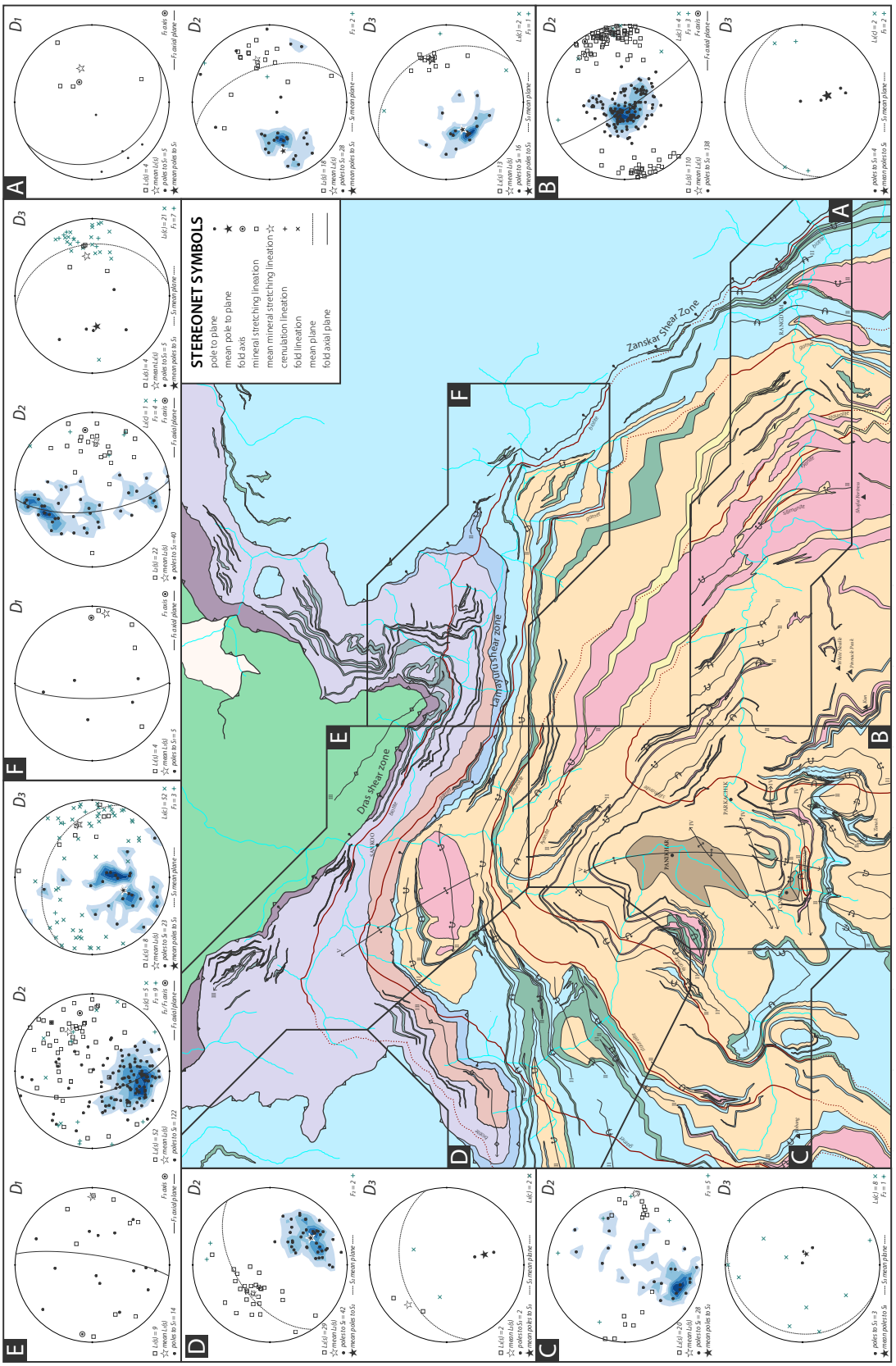


Fig. 2.11 Simplified geological map of the Suru Valley area, with D_1–D_3 planar and linear structural data separated into 6 zones with stereonets. Insufficient D_1 linear and planar elements were recorded in Zones B, C, and D ($n = \leq 3$) to warrant structural interpretations from corresponding stereonets. For lithostratigraphy and symbols refer to Figure 2.4.

to the ENE. No late folds are present in this zone as is supported by the consistent orientation of structures and map units.

2. Zone B: Poles to S_2 define a centred cluster representing a gently dipping S_2 in all directions. $L_2(s)$, $L_2(c)$ and meso-scale F_2 record a strongly bipolar ENE-WSW distribution. These observations are also broadly consistent for the recorded structural and planar elements of D_3. F_4 only weakly reorients the linear elements due to the co-axial orientation of the fold hinge and linear structural elements. The NNW–SSE trending F_5 domal culmination results in the warping and bipolar distribution of the linear structural elements of both D_2 and D_3.

3. Zone C: Poles to S_2 record a distributed girdle. This is not indicative of a fold axis as the local foliation changes from moderately NE-dipping, to steeply dipping, to overturned and SW-dipping (see SW end of A-A' on Fig. 2.5). Rather the distribution of S_2 is inferred to result from the development of the Warwan fault, which produced progressive steepening and overturning of pre-existing planar and linear structural elements. The Warwan fault might transect the SW extent of section A-A' or within 7 km SW of A' (Honegger, 1983; Searle *et al.*, 1992). $L_2(s)$ displays a bipolar E–W plunge. S_3 is characterised in this region by a NW-dipping foliation and $L_3(c)$ varies from W- to N-plunging.

4. Zone D: Poles to S_2 and S_3 define a mean NW-dipping foliation with NW-plunging $L_2(s)$, $L_3(s)$ and $L_3(c)$.

5. Zone E: Poles to S_1 record a weakly distributed girdle defining a W-E oriented F_3 axial plane. An E-plunging $L_1(s)$ is only weakly disturbed by F_3. Poles to S_2 define a distributed girdle that represents an ENE plunging F_2 that is later disturbed by F_3. F_2 is locally recorded here as a distributed girdle due to a strong competency contrast between the rigid metamorphosed granite south of Sankoo and the surrounding metasedimentary rocks yielding a fold (Karpokhar antiform) that is both open and overturned (see A-A' on Fig. 2.5). Subsequent meso-scale F_3 folds and $L_3(c)$ are documented, with fold axes subparallel to F_2. Due to the co-axial nature, this is represented as a combined F_2/F_3 pole to the girdle plane. A NE-plunging $L_2(s)$, $L_2(c)$ and meso-scale F_2 are weakly reoriented by F_3. D_3 planar and linear structural elements define a NE-dipping S_3 with an ENE plunging $L_3(s)$ and bipolar E–W distribution of $L_3(c)$ and F_3. D_3 planar and linear structural elements are locally warped around late F_5.

6. Zone F: Poles to S_1 and S_2 record a distributed girdle defining a W-E oriented F_3 axial plane. A ESE-plunging $L_1(s)$ and E-plunging $L_2(s)$ are only weakly reoriented by F_3. D_3 is characterised in this zone by an E-dipping S_3 and ENE-plunging $L_3(s)$, $L_3(c)$ and F_3. S_3 appears consistent around the hinge and limbs of the antiform indicating the fabric is either synchronous or post-dates D_3 (Fig. 2.7). The axial plane of the antiform is co-axial with meso-scale F_3 supporting a km-scale F_3 (backfold) interpretation.

2.7 Metamorphic architecture

Given the widespread distribution of both pelite and metabasite in the study area, the relationship of progressive fabric development (as outlined above) with respect to the prograde growth of metamorphic index minerals can be constrained using both rock types. It is recognised that that bulk composition will control the timing of porphyroblast growth in any one rock type and, therefore, observations are restricted to rock types of similar bulk composition (e.g., pelite and semipelite rather than psammite). The objective is to constrain the relative timing of mineral growth during metamorphic peak with respect to the penetrative deformation events outlined above and illustrated by photomicrographs in Figure 2.12, and then summarised in Figure 2.17. These observations are then compared to relationships between the trace of metamorphic mineral isograds and meso- to macro-scale lithotectonic features as documented in figures 2.4, 2.5, 2.15 and 2.16. Index minerals can be associated with varying assemblages during a prograde–retrograde metamorphic cycle, which further enables the recognition of differing generations of mineral growth (i.e. I, II, III).

2.7.1 Pelite index minerals

The pelitic component of the HMC displays a complete Barrovian metamorphic sequence from chlorite zone (greenschist-facies) to sillimanite-K-feldspar zone (upper amphibolite-facies; Fig. 2.15). An increase in grade is observed moving structurally down-section from the ZSZ to the migmatitic zone exposed in the Lalung Valley 20 km SSW of Rangdum (Fig. 2.1 & 2.4), followed by a decrease in grade moving further south and/or west towards the Warwan fault (Honegger, 1983; Searle *et al.*, 1992) or MCT zone (Stephenson *et al.*, 2000, 2001).



Fig. 2.12 Mineral growth–deformation relationships. (a) Biotite porphyroblast overgrowing S_2 fabric outlined by matrix parallel graphite inclusions. (b) Garnet porphyroblasts recording syn- to post-D_2 growth as documented by graphite and ilmenite inclusion trails. (c) Staurolite overgrowing S_2 fabric. (d) Kyanite porphyroblast documenting post-D_2 growth, crosscutting the S_2 foliation. (e) Fibrolitic and prismatic sillimanite overgrowing S_2. (f) Actinolite defining and overgrowing S_2 fabric, indicating syn- to post-D_2 growth. (g) Hornblende both aligned and overgrowing the S_2 fabric, indicating syn- to post-D_2 growth. (h) Hornblende porphyroblast in volcano-sedimentary rock overgrowing S_2 fabric. (i) Garnet porphyroblast overgrowing S_2 fabric. (j) Kyanite porphyroblast overgrowing the S_2 fabric. Bt = biotite, Grt = garnet, Ms = muscovite, St = staurolite, Ky = kyanite, Sil = sillimanite, Act = actinolite, Rt = rutile, Hbl = hornblende after Whitney & Evans (2010).

Chlorite is the first Barrovian index mineral observed in the pelitic component of the Suru Valley region. Chlorite locally occurs as small (sub-mm) porphyroblasts in the sheared rocks belonging to the ZSZ and associated normal-sense shear zones. Where present in the low-grade rocks near Sankoo and Rangdum (Fig. 2.4), tabular chlorite defines S_1 and is reoriented parallel to S_2 (chlorite I). Chlorite porphyroblasts are wrapped by S_3 and preserve cleavage domains perpendicular to the mylonitic fabric and are interpreted as having been originally aligned with S_1 or S_2. Taken as a set, these observations suggest that chlorite grew syn-D_1 and growth continued during the early stages of D_2. Retrogressive chlorite (chlorite II) is also associated with C-S-C' fabrics developed along S_3 shear bands.

The biotite-in isograd is marked by the incoming of sub-mm to mm-scale poikiloblasts of biotite in graphitic pelite (Lamayuru Complex) near the Dras shear zone and in the mixed metacarbonate, semipelite, and pelite (GHS–THS) near the ZSZ. Dominantly tabular subhedral to euhedral biotite grains are aligned with S_2 (biotite I). At higher grades biotite poikiloblasts overgrow the S_2 fabric and preserve matrix-concordant inclusion trails (biotite II, Figure 2.12a). These observations suggest biotite commenced growth syn-D_2 and growth and recrystallisation continued post-D_2. Retrogressive biotite growth was coincident with garnet breakdown and is locally also associated with S_3 C'-fabrics (biotite III).

Garnet occurs as subhedral to euhedral poikiloblasts that occasionally overgrow isoclinal F_2 microfolds. Garnet cores typically display spiral or concordant inclusion trails with respect to the main S_2 fabric (garnet I, Figs. 2.12b and 2.13a). Generally, inclusion-poor rims that overgrow the S_2 fabric are also present at staurolite-grade and above (garnet II). Where the S_2 fabric is crenulated by D_3, inclusions in the garnet porphyroblasts appear discordant to the developing S_3 fabric (Fig. 2.13b). In localities where S_3 has become dominant, S_3 wraps both phases of garnet growth and inclusion trails are discordant to the main fabric. These observations suggest that most garnet growth occurred syn- to post-D_2 and prior to D_3.

Staurolite occurs as subhedral to euhedral tabular to rounded grains. It is found near the garnet rims (garnet I & II locally resorbed) or as matrix poikiloblasts. In high-Al pelite (generally found adjacent to mixed semipelite, metacarbonate, and pelite), matrix staurolite locally displays a shape preferred orientation parallel to S_2 aligned micas, likely nucleating mimetically on such phyllosilicate minerals (Fig. 2.14a; e.g., Patrick & Lieberman, 1988; Gibson, 1993).

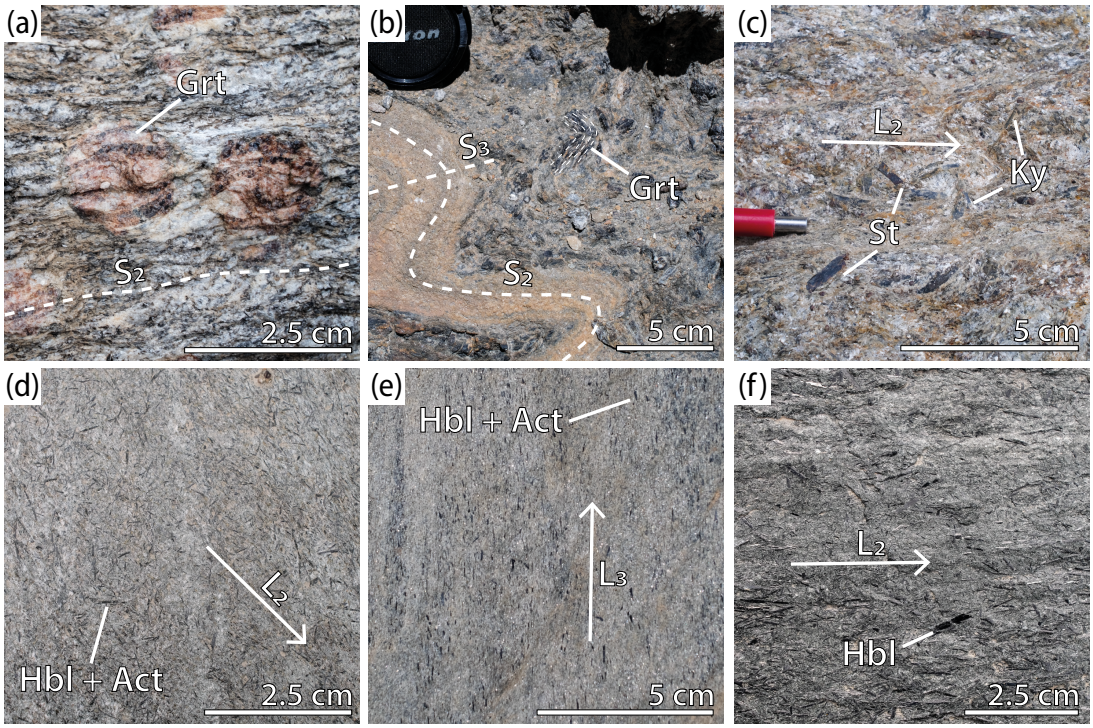


Fig. 2.13 Mesoscale field photos of mineral growth relative to fabric development during $D_{2–3}$. a) Garnet porphyroblast overgrowing S_2 fabric, and in the core showing clockwise rotation synchronous with S_2. b) Mesoscale F_3 folds developing a crenulation cleavage of S_2, garnet shows inclusion trails suggesting growth after D_2 but prior to F_3 folding. c) Pelite with staurolite and kyanite porphyroblasts crosscutting the L_2 mineral stretching lineation. d) Group A metavolcanic rock showing actinolite and hornblende needles crosscutting L_2. e) Group A metavolcanic rock with actinolite and hornblende needles reoriented parallel to L_3. f) Group A metavolcanic rock showing tabular hornblende crystals both crosscutting and aligned relative to L_2.

In such samples staurolite dominantly extinguishes along the long axis, thereby parallel to phyllosilicate grain extinction, implying possible structural control from earlier mica. S_2 aligned staurolite commonly displays matrix-concordant graphitic inclusion trails, with no evidence for rotation of prismatic staurolite after growth. In all other pelitic samples, staurolite crosscuts the S_2 fabric and preserves S_2 concordant inclusion trails (Figure 2.12c). No distinct alignment of the long axis of staurolite with respect to L_2 is visible in outcrop (Fig. 2.13c). S_3 wraps around staurolite porphyroblasts and is associated with post-peak mineral assemblages. These observations suggest that staurolite growth dominantly occurred post-D_2 with localised syn-D_2 and/or post-tectonic mimetic growth occurring in high-Al pelite.

Kyanite poikiloblasts occasionally show examples of growth coincident with staurolite breakdown, however staurolite remains present in many kyanite-bearing

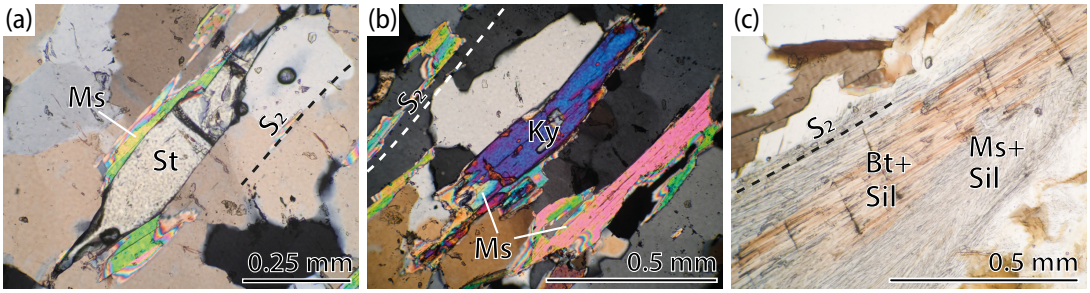


Fig. 2.14 Shape preferred orientation of a) staurolite, and b) kyanite parallel to S_2 aligned micas, possibly nucleating mimetically on and overgrowing such phyllosilicates (dominantly muscovite). Epitaxial growth of c) fibrolitic sillimanite on biotite and muscovite. These observations suggest that all peak mineral growth at these grades demonstrably occured after the development of the S_2 fabric. Alternatively, staurolite and kyanite growth may have begun in select compositions during D_2.

samples (e.g., Pattison & Spear, 2018). Kyanite is observed adjacent to garnet rims (garnet I & II locally resorbed) or as discrete matrix phases. Kyanite locally lies within the S_2 fabric (Fig. 2.14b) and crosscuts the S_2 fabric in all other samples (kyanite I, Fig. 2.12d). Where it lies within the fabric, as observed in high-Al pelite layers, kyanite appears to preferentially overgrow white mica and thus may represent mimetic growth (Fig. 2.14b; e.g., Spry, 1963; Harte & Johnson, 1969). When present, S_3 fabrics wrap around kyanite porphyroblasts (kyanite I). No distinct alignment of the long axis of kyanite with respect to L_2 is visible in outcrop (Fig. 2.13c). A later stage of kyanite growth (kyanite II) is also preserved, coincident with garnet breakdown in certain sillimanite-zone samples. Locally, larger kyanite crystals are aligned to S_3 whilst smaller skeletal grains appear to crosscut the fabric. This suggests initial decompression and breakdown of garnet after post-D_2 garnet rim growth (garnet II), prior to and/or during D_3. These observations suggest that kyanite growth dominantly occurred post-D_2 and pre-D_3 (kyanite I) with secondary/late growth occurring coincident with garnet breakdown (inferred as broadly concurrent with D_3, kyanite II). Localised syn-D_2 and/or post-tectonic mimetic growth is also recorded in high-Al pelite.

Where kyanite and sillimanite coexist, sillimanite typically appears to nucleate on biotite and muscovite as fibrous mats (fibrolite) or is found within garnet corona associated with biotite (biotite III) and plagioclase. With increasing grade, sillimanite becomes prismatic and lies both within and crosscuts S_2 (Figure 2.12e). Locally, alignment of the long axis of sillimanite with the principal mineral stretching directions is visible in outcrop, though generally sillimanite shows a random distribution with respect to L_2. Biotite and muscovite at these grades

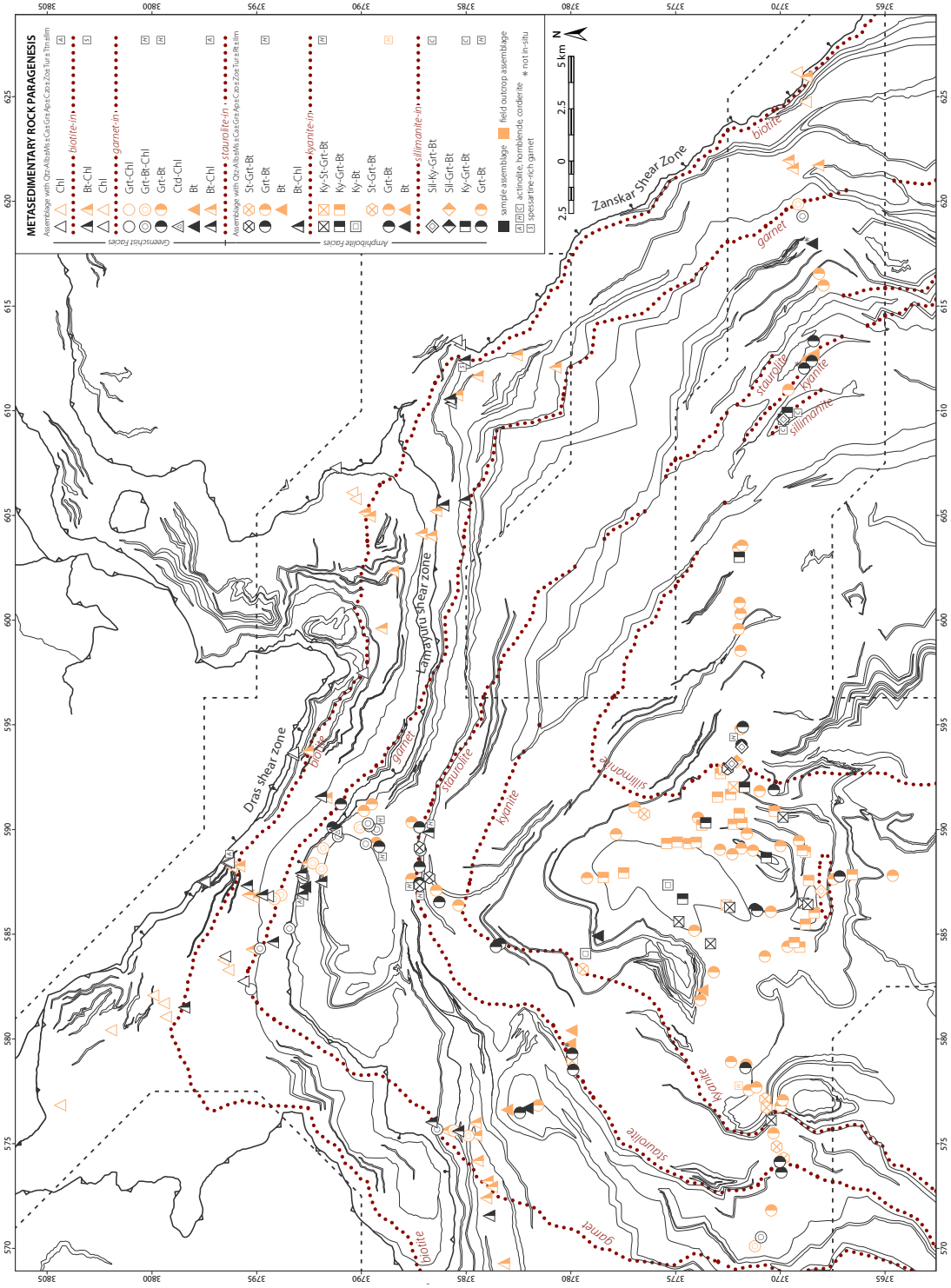


Fig. 2.15 Form-line map of major lithological, tectonic and metamorphic features of the Suru Valley area overlain with distribution of metasedimentary rock mineral assemblages as constrained through both petrographic and hand lens observations across samples and field outcrops. Retrogressive mineral phases are excluded. Grid references are truncated, with final three zeros omitted.

dominantly lie within S_2 and are aligned to L_2, thereby likely that alignment of sillimanite to S_2 and L_2 represents epitaxial nucleation (Fig. 2.14c; e.g., Chinner, 1961; Carmichael, 1969; Yardley, 1977). Sillimanite growth therefore initiated post-D_2 or syn-D_3. The dominant phase of growth is inferred to develop during decompression when the ZSZ was active (Searle *et al.*, 1992), consistent with syn-D_3 growth of kyanite II or sillimanite following garnet breakdown.

The highest-grade index mineral in metasedimentary rocks is K-feldspar stable with sillimanite. The crystallisation of K-feldspar appears coincident with *in situ* small-scale (cm to 10s of cm) partial melting. Leucosomes appear either concordant with the S_2 fabric or crosscut the fabric as part of a stockwork. Leucosomes are characterised by the mineral assemblage quartz-K-feldspar-plagioclase-sillimanite-garnet-biotite. Sillimanite is dominantly prismatic and shows similar relationships to S_2 as described for the sillimanite zone. Garnet in these rocks is found in both the paleosome and the leucosome, with the mineral core often defined by an inclusion-poor earlier growth phase (consistent with microstructural characteristics of lower-grade garnet). The rim is rich in inclusions of sillimanite displaying no consistent orientation (garnet III) and wraps resorbed previous phases of growth. Leucosomes are also host to larger (~1–5 mm) garnet grains (garnet III) that preserve coarse-grained quartz in lobate embayments and inclusions that are inferred to develop during dehydration melting (Waters, 2001).

Mineral growth in the higher temperature range of the Barrovian sequence (staurolite to sillimanite+K-feldspar) shows relationships to the main regional fabric (S_2) that implies dominantly post-D_2 growth, whereas mineral growth at lower grades shows mineral-fabric relationships supporting growth syn- to post-D_2. Taken as a set, these observations document that peak temperature mineral growth outlasted development of the dominant (S_2) regional fabrics.

2.7.2 Metabasite index minerals

Mineral assemblages in metabasite also show a systematic change with increasing metamorphic grade (e.g., Bégin, 1992; Starr *et al.*, 2020). The following prograde sequence is observed: actinolite-albite-chlorite-epidote (± tremolite), hornblende-actinolite-albite-epidote (± chlorite), hornblende-actinolite-plagioclase-epidote, hornblende-plagioclase (± epidote), garnet-hornblende-plagioclase, clinopyroxene-hornblende-plagioclase (± K-feldspar). Broadly these changes define actinolite-, hornblende-, oligoclase-, and garnet+plagioclase-zones (Fig. 2.16).

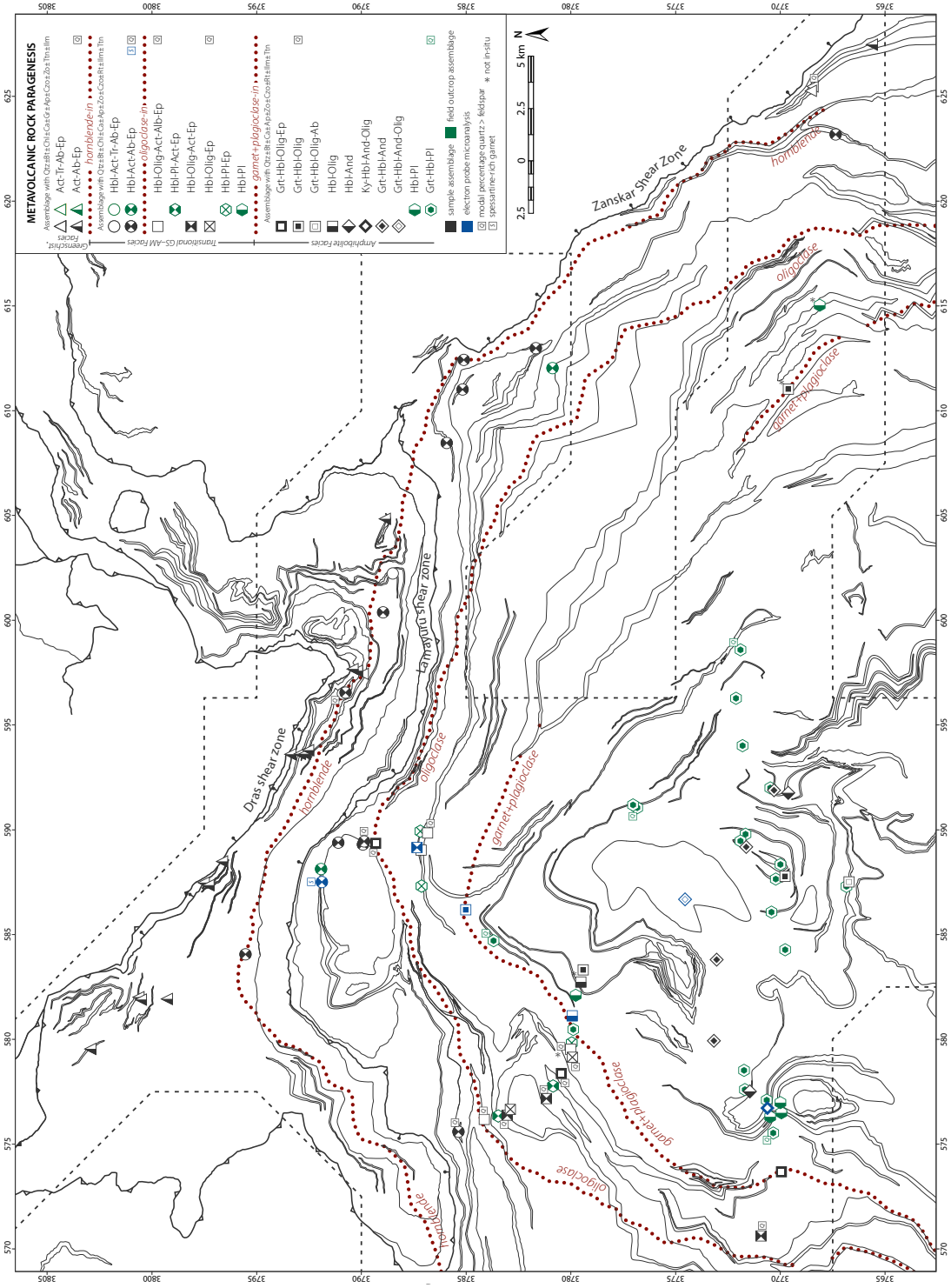


Fig. 2.16 Form-line map of major lithological, tectonic, and metamorphic features of the Suru Valley area showing metavolcanic rock mineral assemblages as constrained through both petrographic and hand lens observations across samples and field outcrops. Retrogressive mineral phases are excluded. Optical methods were used to determine plagioclase composition. In outcrop a composition of albite is assumed at sub-amphibolite-facies, and > 10% anorthite (plagioclase) at amphibolite facies. Samples with more quartz than Na-feldspar are not used to define isograd surfaces. Grid references are truncated, with the final three zeros omitted.

Actinolite nucleates as acicular grains at the lowest grade observed. At lower greenschist-facies mats of actinolite define a weak S_1 as well as a weak L_1. Where D_2 crenulates S_1, actinolite grains largely crosscut or show a very weak alignment with the stretching lineation (L_2; Fig. 2.13d). Similarly, at lower greenschist-facies S_2 is weakly defined by mats of actinolite and plagioclase-quartz aggregate laminations. Once transitional greenschist–amphibolite-facies conditions are reached (as defined by Starr *et al.*, 2020), actinolite defines L_2 and S_2, although there are multiple occurrences where the amphibole crystals crosscut the dominant planar and linear structural elements. Where S_3 fabrics are present, actinolite grains are always folded and reoriented by D_3 to define S_3 and L_3 (Fig. 2.13e). All mineral growth-fabric relationships outlined for actinolite also apply to tremolite, where present. These observations suggest that actinolite and tremolite growth is syn-D_1, syn- to post-tectonic with respect to $D_{1–2}$ (Figure 2.12f) and pre-D_3.

The first appearance of hornblende in metabasic rocks occurs between the biotite and garnet isograds constrained in adjacent metasedimentary rock units, though the volumetrically-dominant amphibole at these grades remains actinolite (Figs. 2.15, 2.16). Actinolite in metabasic rocks largely disappears after the staurolite-in isograd in adjacent metasedimentary rock units (Figs. 2.15, 2.16). Hornblende and plagioclase are the dominant minerals in metabasic rocks at amphibolite-facies. Hornblende first occurs as elongate needles on the S_2 foliation plane and is dominantly misoriented with respect to L_2, especially in the transitional greenschist–amphibolite-facies (Fig. 2.13d). As grade increases into the amphibolite-facies domain, hornblende shows increasing alignment with L_2 (Fig. 2.13f). Ultimately hornblende both lies in the S_2 fabric and overgrows it (Figure 2.12g). Where S_3 is developed, matrix hornblende appears folded by F_3 microfolds and S_3 wraps around hornblende porphyroblasts. Matrix hornblende is reoriented parallel to L_3 (Fig. 2.13e). Porphyroblastic hornblende also occurs within supracrustal volcano-sedimentary layers associated with metabasite flows. In these layers, hornblende overgrows the S_2 fabric (Figure 2.12h). These observations suggest that hornblende growth is syn- to post-D_2 and reoriented during D_3.

At middle amphibolite grade, garnet porphyroblasts appear in metabasic rocks of the HMC associated with hornblende and plagioclase. This occurs between the staurolite- and kyanite-in isograds in the metasedimentary rock sequence (Figs. 2.15, 2.16). Garnet grows across the hornblende-defined S_2 fabric (Figure 2.12i) or appears to be wrapped by hornblende, developing strain caps and strain shadows around the porphyroblast. S_3 is deflected around garnet porphyroblasts.

Garnet in the metabasite sequence is interpreted to have grown syn- to post-D_2 and prior to D_3.

Rare examples of kyanite in metabasic rock occurs as part of the assemblage hornblende-plagioclase-kyanite. Kyanite appears to overgrow S_2 (Figure 2.12j), however, no examples of an S_3 fabric are documented with such assemblages. Kyanite in the metabasite sequence is interpreted to have grown post-D_2.

The highest-grade zone of the HMC shows bulk composition variation within metabasite, locally including clinopyroxene with hornblende corona. No clear fabric-mineral growth relationships are observed. Clinopyroxene-hornblende (-garnet) assemblages are also noted by Honegger (1983) and Pognante & Lombardo (1989).

2.7.3 Other minerals

Biotite within metavolcanic rocks appears aligned with S_2, although biotite porphyroblasts also show evidence of overgrowing the same fabric. This suggests syn- to post-D_2 growth of biotite as reported for the metasedimentary rocks.

Ilmenite and rutile within the metasedimentary and metavolcanic sequence often appears aligned with S_2. Examples of rutile overgrowing the S_2 fabric are documented within the metasedimentary rock sequence. Where ilmenite is present as S_2 inclusions in garnet it is disjunctive with the matrix S_3 fabric. These observations imply syn-D_2 and pre-D_3 growth of ilmenite and syn- to post-D_2 growth of rutile.

Titanite within the graphitic mixed semipelite, psammite, and pelite overgrows the S_2 fabric and is aligned to crenulations formed by D_3. This suggests post-D_2 growth of titanite within this sequence.

2.7.4 Relationship of peak metamorphic minerals to penetrative fabrics

Figure 2.17 summarises the relationship of metamorphic mineral growth relative to penetrative fabric development in the Suru Valley region. The principal observations are that: 1) the lower grade minerals (chlorite–garnet) consistently show evidence of syn-D_2 growth, 2) all metamorphic minerals bar chlorite (i.e., biotite to sillimanite+K-feldspar) document post-D_2 growth, 3) amphibolite-grade pelitic minerals (i.e., staurolite–sillimanite) initiated growth post-D_2, and 4) all

metamorphic minerals, excluding sillimanite and K-feldspar, and late growth of chlorite, biotite, and kyanite, terminated growth prior to D_3 fabric development. It should be noted that where present, apparent alignment of staurolite and kyanite relative to the S_2 fabric could represent mimetic nucleation on fabric-defining phyllosilicate minerals (Fig. 2.14a, b; e.g., Spry, 1963; Harte & Johnson, 1969; Patrick & Lieberman, 1988; Gibson, 1993). S_2- and L_2-aligned fibrolitic and prismatic sillimanite, where present, is interpreted as epitaxial nucleation on fabric-defining micas (Fig. 2.14c; e.g., Chinner, 1961; Carmichael, 1969; Yardley, 1977).

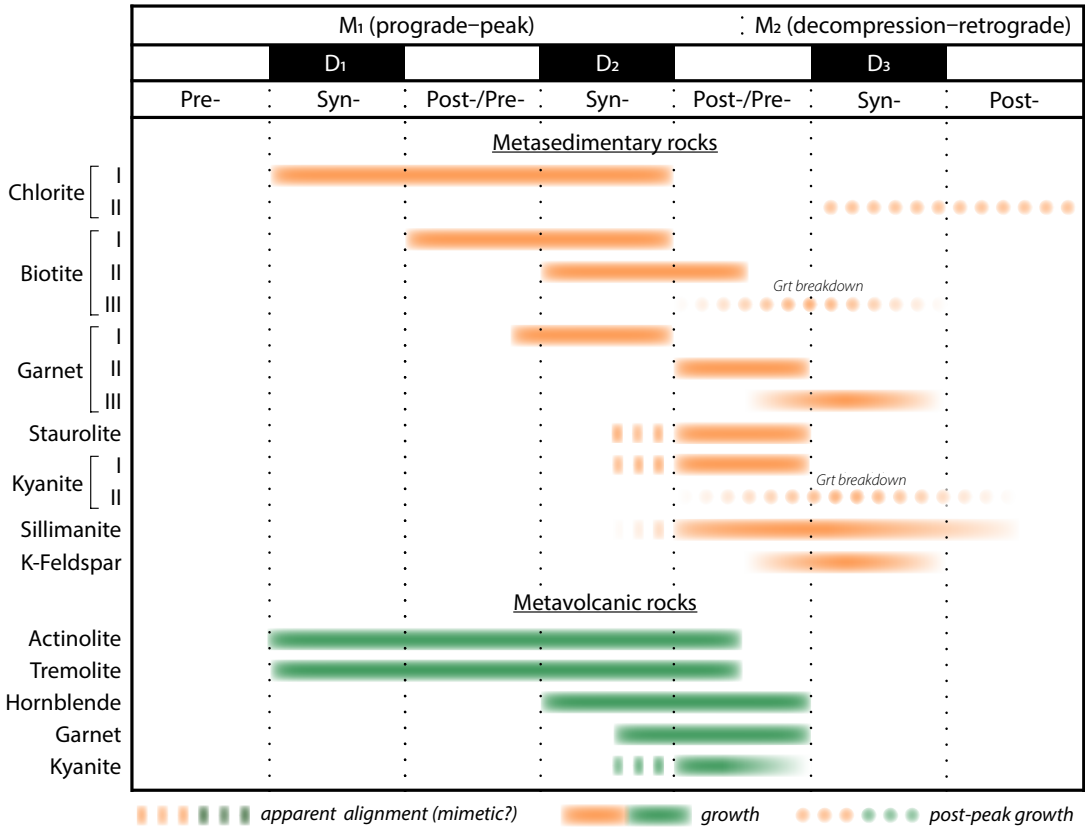


Fig. 2.17 Summary of fabric development vs. mineral growth in the Suru Valley area for metasedimentary and metavolcanic rocks. Faded edges on left and/or right side of bars indicate initiation and/or termination of growth are undefined with respect to preceding and subsequent deformation phases.

2.7.5 Isograds

The relationships between the trace of metamorphic mineral isograds and meso- to macro-scale lithotectonic features also informs a discussion of prograde mineral growth and regional deformation. The relationship of the trace of isograds to D_1

structures is not directly considered as linear and planar features are generally only preserved at micro- and meso-scale. However, as S_1 is sub-parallel to original bedding (S_0), the subsequently deformed lithostratigraphic sequence (a feature that can be readily viewed at map scale) is interpreted to be representative of transposed D_1 architecture. Figures 2.4, 2.5, and 2.15 show the trace of the pelitic isograds in both map and cross-section view. Figure 2.16 shows the interpreted trace of the metavolcanic isograds in map view. Using this 3D perspective of the metamorphic culmination within the study area, the following observations can be made:

1. The trace of the biotite-in isograd is sub-parallel to lithostratigraphy, S_2, axial surfaces of F_2 folds, and D_3 features (Fig. 2.4 and A-A', B-B' and D-D' of Fig. 2.5). Specifically, the biotite isograd is aligned with D_3 shear zones, and where D_3 structural elements are not pervasive the biotite isograd is parallel to major lithostratigraphic contacts, S_2, and the axial surface of F_2 (though the isograd is not folded around these folds). The garnet isograd is broadly parallel to D_2 structural elements when in proximity to the ZSZ or normal-sense structures of the Sankoo fault zone (Fig. 2.4 and all sections of Fig. 2.5). Away from these normal-sense shear zones the garnet isograd varies from sub-parallel to strongly discordant to lithostratigraphic contacts, S_2, and the axial surfaces of F_2 folds. The crosscutting nature of the garnet isograd is best observed in the western section of the map along Shanshin Nala (Fig. 2.4). These observations suggest that at biotite-grade there is concurrent development of the peak metamorphic assemblages and D_2 planar structural features. In contrast, at garnet-grade, the peak metamorphic assemblages appear locally concurrent with regional D_2 structural elements in some regions, yet clearly post-date D_2 elsewhere (Fig. 2.15), with the establishment of the garnet isograd reached after the development of F_2. These inferences match micro-scale observations: both syn- and post-tectonic growth of garnet is observed in microstructures (Fig. 2.12b) and garnet grains are documented overgrowing isoclinal microfolding of S_1 fabrics. It is interpreted that the trace of the garnet isograd is parallel to both the ZSZ and associated D_3 movement on shear zones of the Sankoo fault zone due to reactivation and/or refolding of D_2 structures during D_3.

2. The discordance between the thermal peak of metamorphism and the structural architecture of the HMC is best observed at higher metamorphic grades with the trace of the kyanite and sillimanite isograds on figures 2.4 and 2.15. In the western section of the map, just west of Panikhar, between

Shanshin Nala and Chellong Nala the kyanite isograd cuts up-section, across F_2 structures and lithostratigraphic contacts. The trace of the sillimanite isograd shows a large discordance to the axial surface of F_2 structures and lithostratigraphic contacts. This is particularly obvious north of Parkachik on Figure 2.4. In Figure 2.5 (cross-sections B-B' and C-C'), the sillimanite isograd truncates at high angles the axial surface of F_2 structures and lithostratigraphic units near Tongul and Panikhar. These observations strongly suggest development of peak metamorphic assemblage at kyanite- and sillimanite-grade and the establishment of the related isograds after D_2.

3. The relative structural spacing between isograds is generally independent of whether the isograds are aligned or crosscutting lithostratigraphy and D_2 planar features. However, across the mapped region the distance between isograds is notably more condensed in the eastern section between Parkachik to Rangdum, defined by D_3 reactivation of D_2 structural features, in comparison to the northern and northwestern portions of the map, defined by D_3 crenulation, folding and local reactivation of $D_{1\text{-}2}$ structural features (Figs. 2.4, 2.15, 2.7, and 2.8). These observations suggest prominent tectonic thinning adjacent to zones defined by D_3 reactivation of earlier structural features (i.e., near the ZSZ).

4. Isograds of all grades (including peak kyanite and sillimanite fabrics) are folded around the axis of late open folds. This includes the F_4 folds and the axis of large NNW-SSE trending open folds (F_5), thus outlining a broad $D_{4\text{-}5}$ domal culmination (Fig. 2.4, and B-B' and C-C' of Fig. 2.5).

5. In the metavolcanic rock sequence, the hornblende and oligoclase isograds are notably discordant to transposed lithostratigraphy in the western section of the mapped area (Fig. 2.16). However, like the garnet isograd in the metasedimentary sequence, the trace of the hornblende and oligoclase isograds are parallel with the plane of the ZSZ and associated normal-sense shear zones of the Sankoo fault zone. Integrating the observations made for equivalent greenschist- and greenschist–amphibolite-facies isograds in the metasedimentary sequence, the syn- to post-D_2 development of hornblende in outcrop and thin-section (Figs. 2.12g,h and 2.13d–f), and the observations based on the metabasic isograds, suggests that the latter isograds were established syn- to post-D_2 and prior to D_3.

6. In the metabasic isograd sequence, hornblende-in occurs between biotite- and garnet-in isograds, oligoclase-in between the garnet- and staurolite-

in isograds, and garnet+plagioclase-in isograd occurs at or between the staurolite-in and kyanite-in isograds (Figs. 2.15 & 2.16).

Combined, these observations document the final establishment of the metamorphic isograds (and thus the thermal culmination) in the later stages of shortening, transposition and thickening of the lithostratigraphic sequence, concurrent with the development of D_2 structures at lower grades and following formation of D_2 structures at higher grades. The biotite and garnet isograds from the metasedimentary rock sequence and the hornblende and oligoclase isograds from the metavolcanic rock sequence are sub-parallel with the plane of the ZSZ (where adjacent to this structure), implying that at least these grades pre-date the development of features associated with D_3. $D_{4–5}$ structures are observed to modify all regionally mapped metamorphic isograds, thereby documenting that all mineral isograds in the map area were established prior to $D_{4–5}$. Outside the map area, in the Lalung valley, SSW of Rangdum (Fig. 2.1), only one transect was undertaken into the sillimanite+K-feldspar-zone, therefore relevant observations of the trace of this isograd relative to $D_{2–5}$ structures are not available. However, the mapped trace of the sillimanite+K-feldspar isograd reported in Honegger (1983) suggests that this isograd is also discordant to transposed lithostratigraphy and thereby D_1–D_2 structures.

2.8 Discussion and Tectonic Implications

The extensive higher-pressure, and likely older, assemblages developed in the Suru Valley area, make it an advantageous location to study the early tectonometamorphic architecture of the predominantly sillimanite-grade HMC (e.g., Searle *et al.*, 1992; Walker *et al.*, 2001). Results presented here highlight how field geological maps, structural cross-sections, and detailed observations of fabric development and metamorphic mineral growth can be used to constrain the sequence of crustal thickening, metamorphism and exhumation in a collisional mountain belt. Specifically, four aspects of HMC evolution are considered below: 1) how folding and thereby crustal-thickening is accommodated in the crust during the early stages of orogenesis; 2) how the growth of peak metamorphic assemblages relates to deformation at macro-, meso-, and micro-scale; 3) how the tectonometamorphic architecture of the HMC documented along the Suru Valley area compares along strike; and 4) the broader implications for our understanding of orogenic processes.

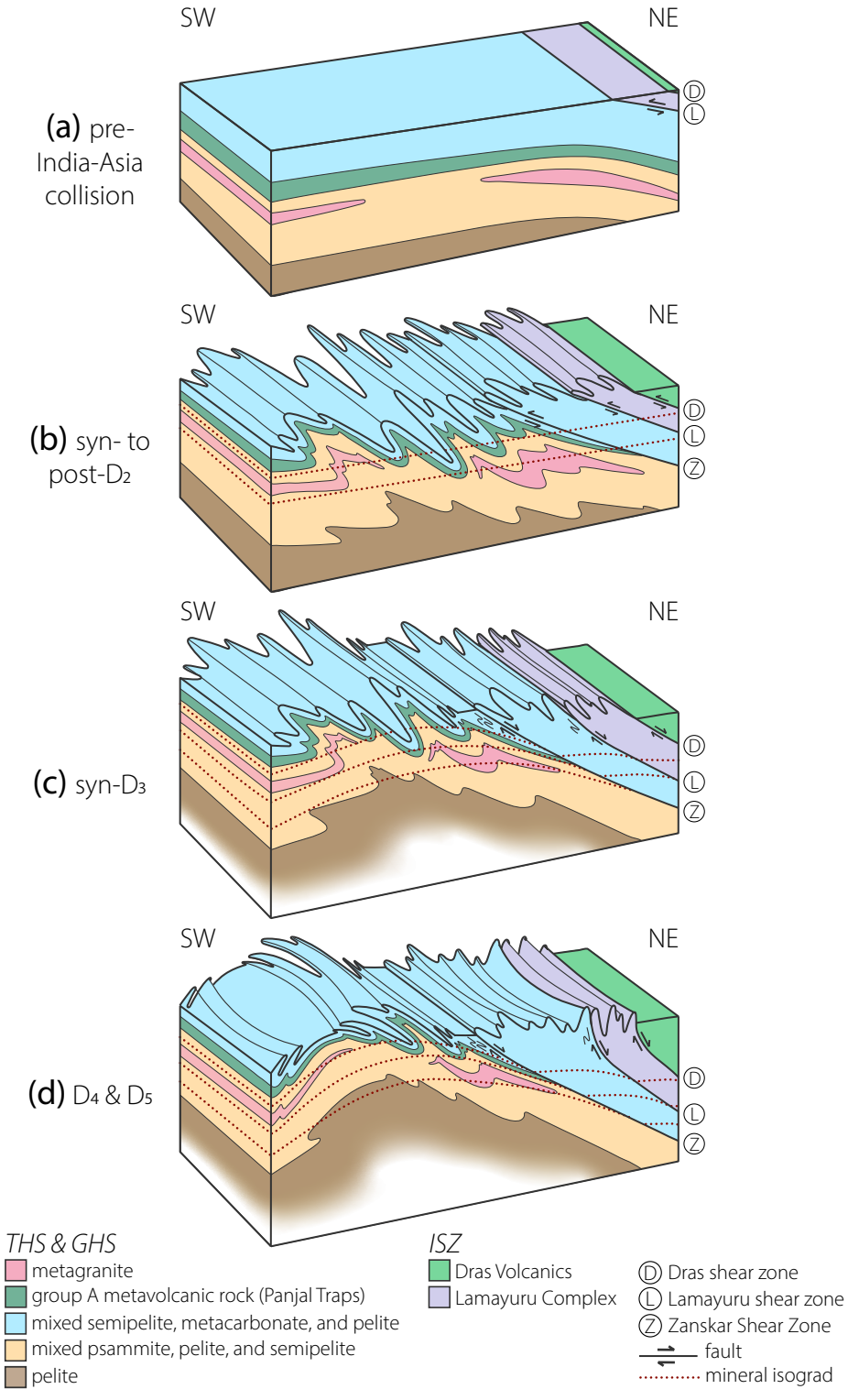


Fig. 2.18 Schematic mid-crustal block diagrams summarising the tectonic evolution of the Suru Valley region: a) prior to initiation of India-Asia collision, b) thermal equilibration following progression of D_2 from high to low structural levels, c) D_3 reactivation and exhumation of the sequence, coincident with sillimanite-grade metamorphism. d) $D_{4–5}$ km-scale open warping of the earlier established lithological, tectonic and metamorphic architecture. Effects of late D_3 backthrusting are preserved along the Dras, Lamayuru and Zanskar shear zones.

2.8.1 Mechanisms of crustal thickening and burial during orogenesis

Thickening of crust on the Indian margin following collision of India and Asia is dominantly accommodated by SW-vergent folding and thrusting along NE-dipping shear and thrust zones (Fig. 2.18a, b; Honegger *et al.*, 1982; Honegger, 1983; Searle, 1983; Gilbert, 1986; Searle & Fryer, 1986; Searle & Rex, 1989; Gapais *et al.*, 1992; Searle *et al.*, 1992, 1999b; Hodges, 2000; Stephenson *et al.*, 2000, 2001; Walker *et al.*, 1999; Wyss *et al.*, 1999; Walker *et al.*, 2001; Wiesmayr & Grasemann, 2002). SW-vergent deformation is expressed in the Suru Valley region as planar and/or linear structural features associated with D_1 and D_2. Pervasive folding and thrusting, and thereby thickening of the HMC, characterises the D_2 event (Fig. 2.18b). The following features of F_2 structures can be emphasised: they are tight to isoclinal and involve different lithological units of varying competencies; the folds are perpendicular in attitude to the shortening direction (where not disrupted by later refolding); and are documented from micro- to macro-scale. Furthermore, the folds display significant amplitude, folding the shallowest lithostratigraphic levels into the lowest structural levels. These characteristics imply that the confining stresses exerted by plate convergence during orogenesis were both pervasive and penetrative across the region at all scales. Although F_2 structures are observed in most units, strain is preferentially distributed into less competent lithologies that undergo enhanced ductile deformation. Less competent units (e.g., pelite) dominantly preserve micro-scale F_2 whereas more competent mixed units (e.g., mixed semipelite, metacarbonate, and pelite) preserve folds at all scales. Sub-parallel planar and linear structural elements from D_1 through to D_3 imply a continuous sequence of deformation with a consistent orientation of the major stress direction from early- to late-structures (Table 2.1). The oblique orientation of mineral stretching lineations to the dip direction during these deformation phases imply there was non-coaxial ductile deformation, as inferred across other areas of NW India (e.g., Patel *et al.*, 1993; Walker *et al.*, 1999; Wyss *et al.*, 1999; Stephenson *et al.*, 2000; Vannay *et al.*, 2004; Wiesmayr & Grasemann, 2002). Thickening of the crust occurred principally during D_2 and created the dominant regional deformation fabric. Although some thickening of the crust was accommodated by F_4 and F_5 structures, these are discrete open features that clearly post-date the main prograde–peak regional metamorphism of the Suru Valley area.

Table 2.2 Micro-, meso-, and macro-scale relationship between deformation and metamorphism in pelitic and metabasic rocks of the Suru Valley region.

Indicator mineral	**Macroscale**	**Mesoscale**	**Microscale**
		Pelitic sequence	
Biotite	Biotite isograd sub-parallel to D_2 and early–mid D_3 structures, weakly folded by mid–late D_3 backfolds.	Defines S_2 and aligned to L_2.	Low grade: Syn-D_2 and re-oriented by D_3. Mod–high grade: Syn- to post-D_2 and re-oriented by D_3. Recrystallisation and retrograde growth continues post-D_2 and syn-D_3.
Garnet	Garnet isograd sub-parallel to crosscutting D_2 structures and sub-parallel to early–mid D_3 structures, weakly folded by mid–late D_3 backfolds.	Garnet shows spiral inclusion trails or overgrow S_2 fabric, where wrapped by S_3 internal S_2 is disjunctive.	Low grade: Syn- to post D_2 growth. Mod–high grade: Syn-D_2 core with post-D_2 rim.
Staurolite	Staurolite isograd sub-parallel to D_2 structures.	Staurolite overgrows S_2 and is not aligned with L_2.	Dominantly post-D_2 with S_2 concordant inclusion trails, wrapped by S_3 where present.
Kyanite-grade	Kyanite isograd sub-parallel to crosscutting D_2 structures.	Kyanite overgrows S_2 and is not aligned with L_2.	Dominantly post-D_2 and wrapped by S_3 where present. Late growth (garnet breakdown) syn-D_3.
Sillimanite-grade	Sillimanite isograd sub-parallel to crosscutting D_2 structures.	Sillimanite overgrows S_2 and is oriented with (mimetic?) or crosscutting L_2.	Post-D_2.
Sillimanite+ K-feldspar-grade	No macro-scale observations.	Leucosome sub-parallel to crosscuting S_2. Sillimanite aligned to crosscutting L_2.	Sillimanite post-D_2. Garnet growth with sillimanite inclusions encloses previous garnet phases, and garnet growth in leucosome form during dehydration melting.

Table 2.2 - continued

Indicator mineral	Macroscale	Mesoscale	Microscale
		Metabasic sequence	
Actinolite	N/A	Greenschist facies: mats define a weak S_1 and S_2, grains aligned to L_1, and weakly aligned or crosscut L_2. Greenschist–amphibolite facies: strongly aligned to L_2 and defines S_2. All: reoriented by S_3 and L_3.	Syn-D_1 and syn-D_2 growth. Where present, reoriented by D_3.
Hornblende	Hornblende isograd subparallel to crosscutting D_2 structures. Subparallel to early–mid D_3 structures and weakly folded by mid–late D_3 backfolds.	Weakly aligned to misoriented to L_2 and S_2. Folded and reoriented by F_3 and S_3.	Syn- to post-D_2. Wrapped by S_3 where present.
Oligoclase	Oligoclase isograd subparallel to crosscutting D_2 structures.	N/A	N/A
Garnet+ plagioclase	Garnet+plagioclase isograd subparallel to crosscutting D_2 structures.	Overgrows and/or wrapped by hornblende defined S_2, wrapped by S_3.	Syn- to post-D_2. Locally kyanite occurs and is post-D_2.

2.8.2 Relationship between lithostratigraphy, fabric development, macroscale deformation and metamorphism in the HMC

The observations presented in this study indicate that final establishment of peak metamorphic mineral assemblages and conditions occurred after extensive penetrative deformation of the lithostratigraphic sequence during D_1 and D_2 and prior to D_3 (summarised in Table 2.2). Isograds are generally sub-parallel to transposed lithostratigraphy at lower grades where brought into alignment along D_3 structures (Fig. 2.18c). In the Suru Valley area, isograds are discordant across lithostratigraphic contacts and early folds (Fig. 2.19a), particularly in the western

section of the map (Fig. 2.4), as also noted by Honegger *et al.* (1982). The same broad structure of isograds can be observed in both the pelitic (Fig. 2.15) and metabasic (Fig. 2.16) rock sequences. As with any isograd mapping, subtle changes in bulk chemistry (e.g., variation in $X_{\mathrm{Mg}} = \frac{Mg}{Mg+Fe^{2+}}$ or Al-content) could also exert a control on isograd spacing. Given the relative structural spacing of the isograds is consistent, regardless of whether they are parallel to or crosscut lithostratigraphic contacts, the trace of the isograds would appear to be controlled by the overall thermal structure rather than the effects of bulk rock chemistry. Tectonic thinning during D_3, and crustal scale folding during $D_{4–5}$ disturbed the overall pattern (Fig. 2.18c, d), however due to the localised and/or open nature of these later deformation phases, any discordance between the isograds and transposed lithostratigraphic contacts must be early.

Given the lack of substantial plutonic bodies of Cenozoic age in the study area, tectonic thickening of the crust during $D_{1–2}$, accommodated through folding and thrusting (Fig. 2.18b), and the increase in radiogenic heat available from thickened crust, is interpreted as having been the dominant cause of metamorphism within the orogenic pile. Peak metamorphism in the Suru Valley area is constrained to being synchronous to post-dating the development of regional fabrics associated with crustal thickening during D_2, as documented from macro- to micro-scale (Fig. 2.19). The documentation of post-tectonic metamorphic assemblages throughout the study area imply that crustal thickening in the Zanskar Himalaya principally occurred early in the orogenic cycle.

2.8.3 Crustal scale folding and domal culminations

The final stage of deformation in the Suru Valley region is expressed as crustal scale folding (i.e. D_4 and D_5), producing dome and basin culminations of the pre-existing structural and metamorphic architecture (Fig. 2.18d). In particular, domal structures may have played a significant role in the exhumation of high-grade rocks of the HMC. A variety of emplacement mechanisms have been suggested for domal culminations in the Himalaya including diapirism, structural interference patterns, isostatic uplift in the footwall of an extensional detachment, compressional core complexes, thrust duplex formation, and/or surficial erosion (see discussion in Kundig, 1989; Searle *et al.*, 1992; Robyr *et al.*, 2006; Horton *et al.*, 2015; Searle & Lamont, 2019). Domal structures across Zanskar appear to be coincident with crustal exhumation along the STD system and MCT and/or postdate such events (e.g., Kundig, 1989; Stephenson *et al.*, 2001; Robyr *et al.*,

2006). Kundig (1989) suggested that domes originate from local syn-metamorphic movement relating to tectonic uplift from the MCT and ZSZ. Similarly, Searle *et al.* (1992) suggested domes could be thrust-related culminations, splaying off the MCT (e.g., Burg *et al.*, 1984). Although such interpretations may be relevant elsewhere, they seem unlikely to apply in the Suru Valley area where the domal culminations have a symmetrical structure and the final structures appear to post-date shear zone movement. The bipolar NE-SW distribution of L_2 in the Suru domal culmination (Fig. 2.8) can only be reasonably explained by a km-scale open F_5 with F_4 only minimally reorienting L_2 given its co-axial orientation (Table 2.1). We propose that domal culminations in the Suru Valley area dominantly result from structural interference patterns of high-angle fold axial traces (F_4 and F_5; Ramsay, 1962, 1967). Consequently, the D_2 fabrics that best outline the domal culmination, pre-date the formation of the dome itself, rather than being linked to its formation (cf. Gilbert, 1986; Gapais *et al.*, 1992; Searle *et al.*, 1992). Similar observations are also documented with the cross-folding of the Sankoo granite (F_2, Karpokhar antiform, and F_5) that resulted in a domal culmination with a type 1 interference pattern (Ramsay, 1967) as outlined by the metamorphic foliations and stretching lineations and isograds in this area (Figs. 2.4, 2.5, 2.7, and 2.8). These observations for the Sankoo granite were also reported by Gilbert (1986).

Given that the western Himalaya is dominated by NE–SW directed compressional tectonics, a high-angle (NW–SE) phase of shortening is required to produce a superposition of folds resulting in a domal interference pattern (Robyr *et al.*, 2006). It is possible that following accommodation of a consistent major stress direction during exhumation of the HMC, accumulation of subsequent strain to the polydeformed terrain may have locally necessitated alternate vectors and/or variations in strain to be exerted orthogonal to the regional strike of the mountain belt (e.g., formation of map-scale F_4 cross folds). Reports of deformation orthogonal to the principal stress axes (i.e., NW-SE to N-S oriented deformation) and cross-folding of earlier fold generations are reported in Himachal Pradesh (Pandey *et al.*, 2003).

The axes of D_5 folds are perpendicular to the primary stress axes of the mountain belt and are best observed trending between Stakpa and Tongul in the main mapped region (Fig. 2.4). Remote-sensed mapping also highlights inferred F_5 folds at the NE and NW of the mapped region where the contacts between the THS, Lamayuru Complex, and Dras Volcanics, as well as the trace of faults along the Lamayuru and Dras shear zones, appear folded around the

axis of large NW-SE km-scale open synforms (fold axes not shown on Fig. 2.4). Late NW-SE folds are similarly proposed across NW India by Thakur (1981). Steck (2003) inferred the Suru dome to have formed during the late Pliocene to Holocene. Domal culmination in the Kishtwar Window to the southwest is also proposed to have resulted from a late km-scale N-S oriented antiform that produced a symmetrical pattern and post-dated movement on the MCT zone (Stephenson *et al.*, 2001). It is therefore reasonable to infer that late NW–SE oriented folding of the Suru Valley area and Kishtwar Window relate to the same event, as suggested by Honegger (1983).

The cooling history of rocks from the Shafat region was calculated by Searle *et al.* (1999b) and shows rapid cooling between 21 and 18.5 Ma (exhumation rates of 6–10 mm a^{-1}). This is calculated by fitting a cooling curve to K-Ar and $^{40}Ar/^{39}Ar$ ages from hornblende, biotite and muscovite; and a leucogranite U-Pb monazite age from Noble & Searle (1995). This model assumes leucogranite crystallisation coincides with sillimanite-grade (M_2) metamorphic peak (~650 °C) through to the closure temperature for muscovite and biotite in the Ar system down to 300 °C (Searle *et al.*, 1999b). This age range overlaps with postulated timing for normal-sense shearing on the ZSZ (Finch *et al.*, 2014; Dèzes *et al.*, 1999). Kumar *et al.* (1995) also documents uplift at slower rates from apatite fission-track ages between 5–1 Ma in samples from the Suru domal culmination (exhumation rates of $\leq$ 0.33 mm a^{-1}) and Kishtwar Window ($\leq$ 3.6 mm a^{-1}) (Kumar *et al.*, 1995). Late uplift along a N-S oriented domal axis has a significant impact on the current architecture of the Suru Valley and Kisthwar regions. It might therefore be reasonable to suggest the domal structures initiated during uplift along the ZSZ, and were accentuated subsequently by late F_5 folding.

2.8.4 Implications for Himalayan tectonics and orogenic processes

The Zanskar Himalaya preserves early fabrics and structures formed at mm- to km-scales ($D_{1–2}$; Fig. 2.19) by significant SW-directed crustal thickening following initial collision of India and Asia. Relationships between prograde–peak metamorphic growth and these early fabrics show that thickening of the crust, through folding and thrusting, followed by thermal relaxation (Fig. 2.18b, 2.19a) caused thermal peak in peak-pressure assemblages across the HMC in Zanskar prior to development of STD-related exhumation fabrics (Fig. 2.17, 2.18c). Later assemblages (i.e. sillimanite and post-peak kyanite II) formed during

decompression from peak pressures and are associated with the development of these exhumation fabrics.

The preserved architecture of the Suru Valley region is typical of regional metamorphic systems where burial and crustal thickening occurs faster than thermal equilibration yielding clockwise *P-T* paths (England & Thompson, 1984; Weller *et al.*, 2013), as reflected by predominant late- to post-tectonic mineral

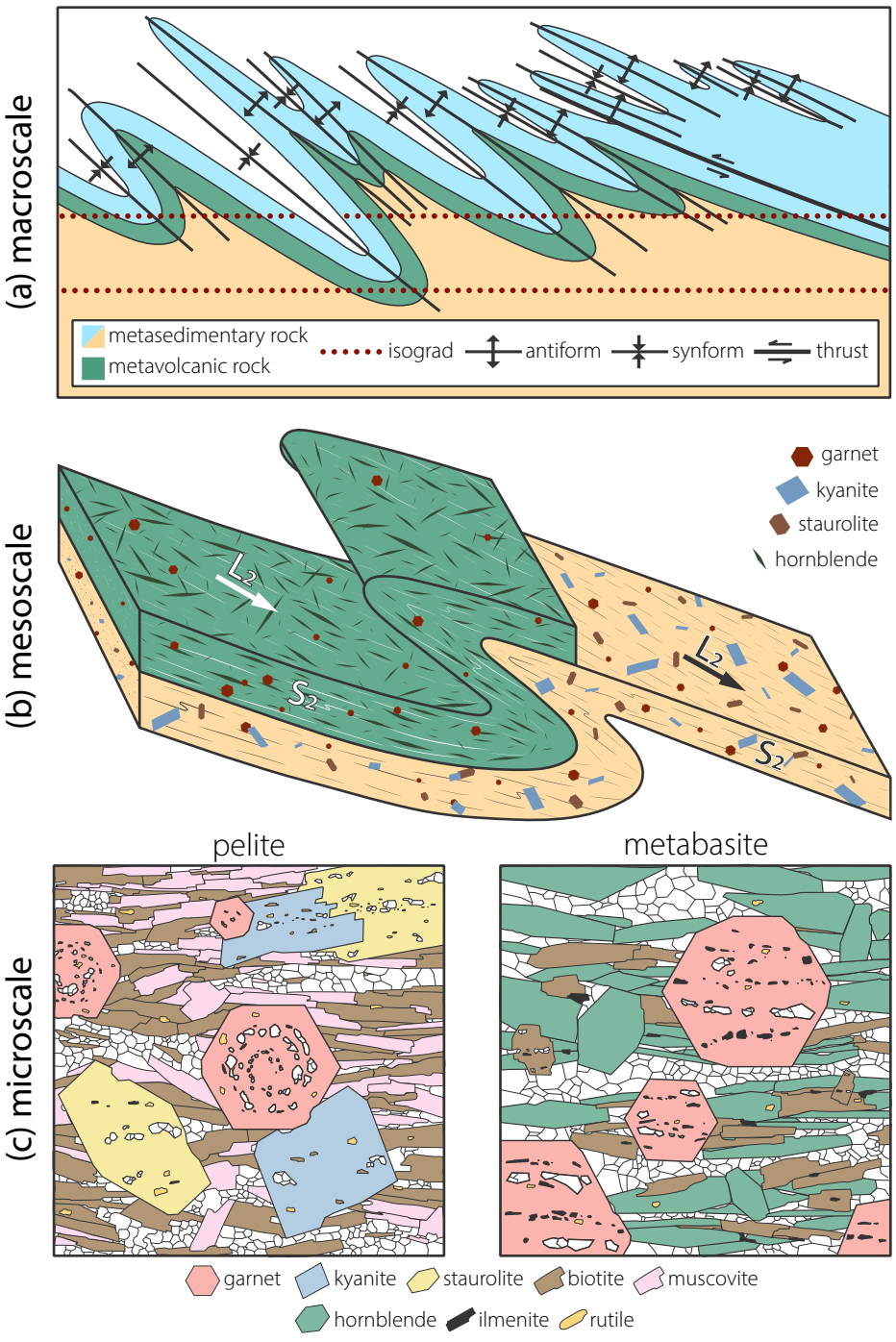


Fig. 2.19 (Caption on the following page.)

Fig. 2.19 Schematic summary of the macroscale to microscale relationship between deformation and metamorphism in pelitic and metabasic rocks at thermal peak (post-D_2). a) Macroscale mid-crustal schematic cross-section displaying thermal equilibration after isoclinal F_2 of metasedimentary and metavolcanic rock layers. b) Mesoscale isoclinal F_2 fold of garnet amphibolite (metabasite) and kyanite-staurolite schist (pelite) showing crenulation cleavage defined by S_2. The long axis of hornblende, kyanite, and staurolite show no consistent orientation with respect to the L_2 stretching lineation. c) Characteristic microscale relations between peak porphyroblast phases and S_2 fabric. In pelite, garnet documents a syn-D_2 core, defined by quartz and Ti-oxides, and post-D_2 rim crosscutting the S_2 micaceous fabric. Kyanite and staurolite overgrow S_2, defined by matrix concordant inclusion trails and no warping of external matrix fabric. For metabasite, aligned biotite, laminated hornblende, and quartzo-feldspathic layers produce the dominant S_2 fabric, locally with cross-cutting hornblende and biotite. Garnet overgrows S_2.

growth (Brodie & Rutter, 1985; Stüwe, 2007; Brown, 2009). Consistent with the interpretation of this study, these characteristics reflect a thermal response to rapid thickening rather than rapid exhumation (Brown, 2009). The Suru Valley region also documents other classical examples of collisional orogenesis, including polyphase deformation; non-coaxial plane strain (Dewey *et al.*, 1998); late-orogenic, long-wavelength folding (Lucas, 1989; Lucas & Byrne, 1992); and a complete Barrovian metamorphic isograd sequence. The occurrence of metabasic isograds interspersed with or alternating with the pelitic isograd sequence yields a finer documentation of the metamorphic architecture and evolution of greenschist- to amphibolite-facies assemblages. Furthermore, the consistency in the spacing and map pattern of the isograd sequence in each rock type (Figs. 2.15 & 2.16) emphasise a thermal architecture that is relevant to tectonothermal processes at the region scale rather than one controlled by local variations in bulk composition.

The Himalayas is frequently suggested to exhibit significant along-strike homogeneity, as inferred from the impressive continuity of structures along the ~2500 km length. However, in detail the Himalayan orogen features variations in the nature of the dominant regional fabric and diachroneity in the timing of metamorphism relative to regional deformation. Therefore, understanding the specific nature of fabrics and their associated tectonostructural context, as done in this study, is key to constraining the resulting metamorphic architecture of the HMC. In contrast to the Suru Valley region, numerous studies of the HMC in other parts of the orogen record a dominance of pre and/or syn-tectonic growth of peak-pressure and peak-temperature metamorphic assemblages relative to the main regional fabric: Western Himalaya (Kundig, 1989; Pognante *et al.*, 1993;

Stephenson *et al.*, 2000; Finch *et al.*, 2014; Phukon *et al.*, 2019); Central Himalaya (Cottle *et al.*, 2007; Jessup *et al.*, 2008; Larson *et al.*, 2010; Yakymchuk & Godin, 2012; Montomoli *et al.*, 2015; Thakur *et al.*, 2015; Braden *et al.*, 2017; Iaccarino *et al.*, 2017a,b; Soucy La Roche *et al.*, 2018; Carosi *et al.*, 2019; Montemagni *et al.*, 2019; Soucy La Roche *et al.*, 2019; Dyck *et al.*, 2020); and Eastern Himalaya (Goswami *et al.*, 2009; Groppo *et al.*, 2012; Kellett *et al.*, 2013; Smit *et al.*, 2014; Chakraborty *et al.*, 2016; Zhang *et al.*, 2018; Kalita *et al.*, 2022). Whilst the dominant regional fabric in each locality is not directly correlative with those observed in this study, most areas of the HMC preserve metamorphic conditions and associated tectonostructural relationships indicative of processes associated with decompression and exhumation (e.g., Goscombe *et al.*, 2018). Therefore, the observed orogen-parallel heterogeneity in the preserved timing of peak assemblages relative to regional deformation possibly reflects differences in the timing, rates, and spatial distribution of exhuming fault systems. Notably the Suru Valley region exhibits less metamorphism associated with exhumation driven fabrics and the cessation of a near continuous detachment system. Along-strike variation may also result from differences in rates of thickening and radiogenic heating, which are also crucial parameters in determining *P-T* history, or from the structure of the bounding plates, such as passive margin stratigraphy. Such complexity is the hallmark of continental tectonics, which departs significantly from the simple kinematics of plate tectonics (Copley & Weller, 2024). In this sense, it is the apparent continuity of structures along-strike that is perhaps the most remarkable aspect of Himalayan tectonics.

2.9 Conclusions

A comprehensive analysis of the relationship between lithostratigraphic units, folds, faults, deformation fabrics, metamorphic isograds, and the relative timing of porphyroblast growth within the Suru Valley area of the Zanskar Himalaya, NW India enables a thorough documentation of the tectonometamorphic evolution of the HMC. Deciphering the 3D geology of the region is based on a new 1:50,000 scale geological map of the Suru Valley area, associated structural cross-sections, field observations at mm- to km-scale, and petrographic analysis. Findings presented here highlight five main phases of deformation with all but one deformation phase oriented parallel to the strike of the mountain chain in NW India.

The oldest deformation phase, D_1, manifests as a relic greenschist-facies fabric subparallel to S_0. It records incipient NE–SW directed deformation linked with

the early stage of collision between India and Asia. D_2 formed by penetrative crenulation of pre-existing D_1 fabrics and resulted in formation of the dominant regional fabric, defined by greenschist to amphibolite-facies mineral assemblages. D_2 lineations record associated SW-vergent thrust-sense deformation. During D_3, earlier fabrics were reactivated during exhumation of the GHS in the footwall of the ZSZ, an along-strike equivalent structure to the STD. D_3 fabrics associated with the ZSZ are mylonitic and lineations record normal-sense shearing. In the northern part of the mapped area, the GHS and THS are juxtaposed against the ISZ by a set of long-lived fault structures that record polyphase deformation. Normal-sense D_3 fabrics are also developed in this region, yet are defined by a crenulation cleavage (locally penetrative) and meso- to macro-scale folding. The variation in the nature of D_3 is interpreted to represent a transition from exhumation along the ZSZ to backfolding and back-thrusting towards the NE. Lastly, D_4 and D_5 are characterised by open km-scale folding of planar and some linear features associated with previous deformation events.

The relationship of mineral isograd surfaces and metamorphic porphyroblast growth relative to the suite of deformation fabrics constrains the metamorphic evolution of this region. Isograd surfaces exhibit varying relationships to D_2 planar structural elements, ranging from sub-parallel to crosscutting. Peak metamorphic phases, ranging from greenschist to upper amphibolite-facies in both pelitic and metabasic lithologies, are synchronous with or post-date D_2 fabrics. Tectonic thinning adjacent to D_3 normal faults telescopes the isograds and reorients isogradic surfaces into parallelism with the faults. D_3 fabrics are documented as post-dating prograde–peak garnet, staurolite, kyanite, and hornblende porphyroblasts and are observed to realign actinolite and hornblende parallel to linear structural elements. Finally, $D_{4–5}$ structures are observed to modify all regionally mapped mineral isograds. These observations indicate that thermal peak metamorphism was reached after the dominant phase of deformation (D_2) and that peak pressure kyanite-grade conditions preceded movement on the ZSZ (D_3).

As a whole, the new dataset highlights that peak metamorphic conditions in the Zanskar Himalaya are primarily attained following crustal thickening of the Indian margin, rather than predominantly influenced by processes occurring during decompression and exhumation of the HMC, as is documented for other areas along strike. Variable levels of crustal exposure, as a result of the discontinuous nature and/or reduced expression of exhuming fault systems may account for the preservation of this unique record. These results are consistent with classical

characteristics of collisional orogenesis including implied clockwise P-T paths, polyphase deformation, and a complete Barrovian metamorphic isograd sequence supplemented by complementary metabasic isograds. Commensurate with the intricate spatial and temporal distribution of deformation and metamorphism during continental tectonics, datasets over a range of structural levels and large length-scales are necessary to decipher their inherent complexity.

GEOLOGICAL MAP OF THE SURU VALLEY REGION, ZANSKAR HIMALAYA, NW INDIA

Scale 1 : 50 000

2.5 0 2.5 5 km

N

LITHOSTRATIGRAPHY

Indus Suture Zone (ISZ)

- **molasse**
  Fluvio-alluvial conglomeratic, shale, siltstone and sandstone (Eocene–Miocene).
- **volcanics (undifferentiated)**
  Undifferentiated andesites, basalts, and epiclastic breccia of the Dras Volcanics, and minor Kargil Intrusives (Jurassic–Cretaceous).
- **tectonised intercalation**
  Tectonised intercalation of Dras volcanics (undifferentiated), radiolarian chert, graphitic pelite, and group B metavolcanic rocks contacts between blocks or lenses defined by faults/shear zones.
- **group B metavolcanic rock**
  Actinolite schists and amphibolites (Triassic–Jurassic).
- **mixed graphitic semipelite, metacarbonate, and pelite**
  Metamorphosed graphite-rich siltstone and shale; metacarbonate; intercalated metamorphosed calcareous siltstone and shale. Includes minor metacarbonate and metavolcanic rocks.
- **mixed pelite, psammite, and semipelite**
  Alternating layers of pelite, psammite, and semipelite. Locally carbonate bearing.
- **graphitic pelite**
  Metamorphosed graphite-rich siltstone and shale.

Tethyan and Greater Himalayan Sequence (THS & GHS)

- **granite (undifferentiated)**
- **garnet tourmaline leucogranite**
  In situ products of metamorphosed sedimentary rocks. Includes minor mixed psammite, pelite, and semipelite (Miocene).
- **garnet biotite muscovite granite**
  Varying composition from monzo- to syenogranite (Permian); includes xenoliths of group A metavolcanic rock and minor discontinuous layers of leucogranite.
- **biotite muscovite syenogranite**
  Megacrystic K-feldspar syenogranite (Cambro-Ordovician).
- **group A metavolcanic rock (Panjal Traps)**
  Actinolite schists and amphibolites of the Panjal Traps (Permian).
- **mixed semipelite, metacarbonate, and pelite**
  Metamorphosed siltstone and shale; metacarbonate; intercalated metamorphosed calcareous siltstone and shale. Includes minor metacarbonate and metavolcanic rocks.
- **metacarbonate**
  Layers of metacarbonate with little or no clastic metasedimentary rock.
- **psammite**
  Varying composition of psammite from arkosic to quartzitic locally characterized by hummocky cross stratification.
- **mixed psammite, pelite, and semipelite**
  Pelitic and semipelitic tops present as thin layers over psammite. Locally graphite-rich.
- **pelite**
  Includes minor semipelite and psammite.

MINERALS

biotite	Bt	K-feldspar	Kfs
garnet	Grt	chloritoid	Ctd
staurolite	St	tremolite	Tr
kyanite	Ky	actinolite	Act
sillimanite	Si	hornblende	Hbl

SYMBOLS

- **metamorphic foliation**
  roman numeral indicates generation (I/II/III = 1°/2°/3°)
- **mineral lineation**
  roman numeral indicates generation (I/II/III = 1°/2°/3°)
- **crenulation lineation**
  roman numeral indicates generation (II/III = 2°/3°)
- **lithological contact**
  defined, approximate, inferred
- **mineral isograd**
  defined, approximate, inferred, unknown (mineral listed on high temperature side)
- **thrust fault**
  defined, approximate, inferred (ornament on apparent hanging-wall)
- **normal fault**
  defined, approximate, inferred (ornament on apparent hanging-wall)
- **fault**
  thrust or normal; defined, approximate, inferred (ornament on apparent hanging-wall)
- **antiform axial trace**
  defined, approximate, inferred; roman numeral = generation (I/II/III = 2°/4°/7°)
- **synform axial trace**
  defined, approximate, inferred; roman numeral = generation (I/II/III = 2°/5°)
- **backfold antiform axial trace**
  defined, approximate, inferred; roman numeral = generation (III = 3°)
- **overturned antiform axial trace**
  defined, approximate, inferred; roman numeral = generation (II = 2°)
- **overturned synform axial trace**
  defined, approximate, inferred; roman numeral = generation (II = 2°)
- **recumbent antiform axial trace**
  defined, approximate, inferred; roman numeral = generation (II = 2°)
- **recumbent synform axial trace**
  defined, approximate, inferred; roman numeral = generation (II = 2°)
- **aerial imagery source**
  fold structure inferred from aerial imagery
- **topographic contour**
  200 m interval
- **river**
- **town**
- **camp**
- **peak**
- **pass**

REFERENCES

aerial imagery basemap
Copernicus Sentinel-2 (L1C, September 2021, processed by ESA.

digital elevation data
SRTM 1-Arc second; September 2014, processed by USGS. https://earthexplorer.usgs.gov/.

remote sensed mapping sources
Sentinel Playground, Sentinel-2 L1C, Bands 4,3,2 & 12,4,2; September 2019, September 2021. https://apps.sentinel-hub.com/sentinel-playground, Sinergise Ltd.
Copernicus Sentinel data 2017-2022, processed by ESA.
Google Earth, Google Earth V 7.3.4.8642. (July 2013, October 2017, October 2019). Landsat/Copernicus, CNES/Airbus 2023, Maxar Technologies 2023.

LITHOSTRATIGRAPHY

Indus Suture Zone (ISZ)

Dras volcanics

- volcanics (undifferentiated)
  Undifferentiated andesites, basalts, and epiclastic breccia of the Dras Volcanics, and minor Kargil Intrusives (Jurassic–Cretaceous)

Lamayuru Complex

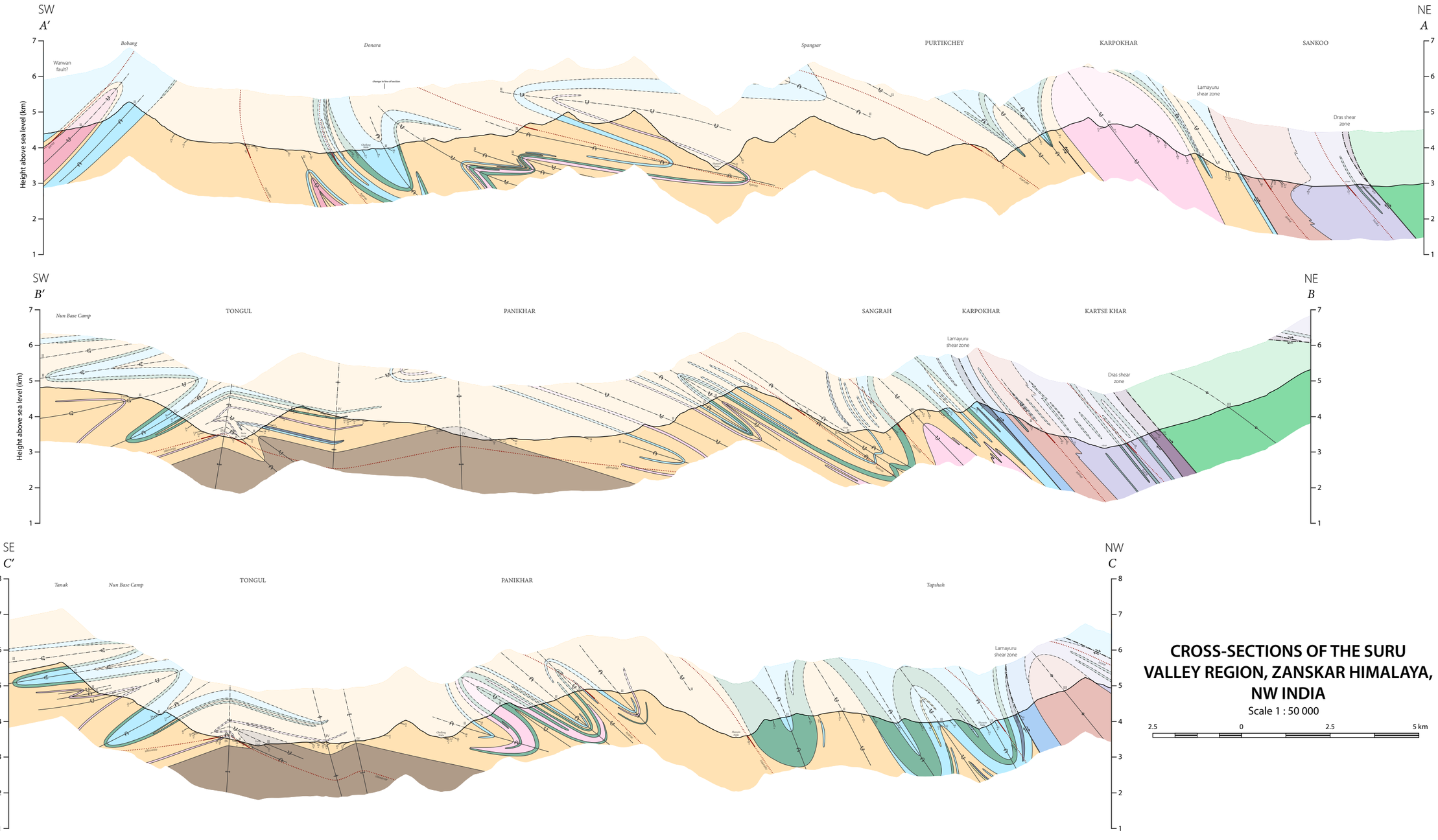
- tectonised intercalation
  Tectonised intercalation of Dras volcanics (undifferentiated), radiolarian chert, graphitic pelite, and group B metavolcanic rocks contacts between blocks or lenses defined by faults/shear zones
- group B metavolcanic rock
  Actinolite schists and amphibolites (Triassic–Jurassic)
- mixed graphitic semipelite, metacarbonate, and pelite
  Metamorphosed graphite rich siltstone and shale; metacarbonate; intercalated metamorphosed calcareous siltstone and shale. Includes minor metacarbonate and metavolcanic rocks
- mixed pelite, psammite, and semipelite
  Alternating layers of pelite and psammite or semipelite horizons
- graphitic pelite
  Metamorphosed graphite-rich silstone and shale

Tethyan and Greater Himalayan Sequence (THS & GHS)

- granite (undifferentiated)
- garnet tourmaline leucogranite
  Ex-situ products of metamorphosed sedimentary rocks. Includes minor mixed psammite, pelite, and semipelite (Miocene)
- garnet biotite muscovite granite
  Varying composition from monzo- to syenogranite (Permian), includes xenoliths of group A metavolcanic rock and minor discontinuous layers of leucogranite
- biotite muscovite syenogranite
  Megacrystic K-feldspar syenogranite (Cambro-Ordovician)
- group A metavolcanic rock (Panjal Traps)
  Actinolite schists and amphibolites of the Panjal Traps (Permian)
- mixed semipelite, metacarbonate, and pelite
  Metamorphosed siltstone and shale; metacarbonate; intercalated metamorphosed calcareous siltstone and shale. Includes minor metacarbonate and metavolcanic rocks
- metacarbonate
  Layers of metacarbonate with little or no clastic metasedimentary rock
- psammite
  Varying composition of psammite from arkosic to quartzitic locally characterized by hummocky cross stratification
- mixed psammite, pelite, and semipelite
  Pelitic and semipelitic tops present as thin layers over psammite. Locally graphite rich
- pelite
  Includes minor semipelite and psammite

SYMBOLS

- apparent dip
  roman numeral indicates generation (I/II/III= 1st/2nd/3rd)
- geological contact
  below topography, aerial
- mineral isograd
  below topography, aerial; mineral listed on high temperature side
- fault
  below topography, aerial; arrows indicate normal or thrust-sense throw
- antiform axial trace
  defined, approximate, inferred; roman numeral = generation (I/II/IV = 2nd/4th/5th)
- synform axial trace
  defined, approximate, inferred; roman numeral = generation (II/IV = 2nd/4th)
- backfold antiform axial trace
  defined, approximate, inferred; roman numeral = generation (III = 3rd)
- overturned antiform axial trace
  defined, approximate, inferred; roman numeral = generation (II = 2nd)
- overturned synform axial trace
  defined, approximate, inferred; roman numeral = generation (II = 2nd)
- recumbent antiform axial trace
  defined, approximate, inferred; roman numeral = generation (II = 2nd)
- recumbent synform axial trace
  defined, approximate, inferred; roman numeral = generation (II = 2nd)



CROSS-SECTIONS OF THE SURU VALLEY REGION, ZANSKAR HIMALAYA, NW INDIA

Scale 1 : 50 000

2.5 0 2.5 5 km

NOTES

A-A′ notes:

- *Small scale folding in Lamayuru Group lithologies represent minor F_3 folds as described in text. The change in S_2 from NE-dipping to SW-dipping reflects F_3 fold structures, with developing S_4 consistently shallowly NE dipping.*
- *Warwan fault located at A′ as suggested by Honegger (1983) or anywhere from this point to 7 km SW as may be inferred from remote sensed mapping.*

B-B′ notes:

- *Small scale folding in Lamayuru Group lithologies represent minor F_3 folds as described in text.*
- *The large overturned F_3 fold and localised inversion of the sequence to place Lamayuru complex above the Dras Volcanics is inferred from the trend of the Dras shear zone N of Shispur and remote sensed mapping. It is supported by the sections of Gilbert (1986), Honegger (1983), and Steck (2003). This is likely a larger equivalent of the minor F_3 folds displayed in A-A′. Normal sense movement on the shear zone is warped by the backfold into alligirment with NE-directed backthrusting.*

C-C′ notes:

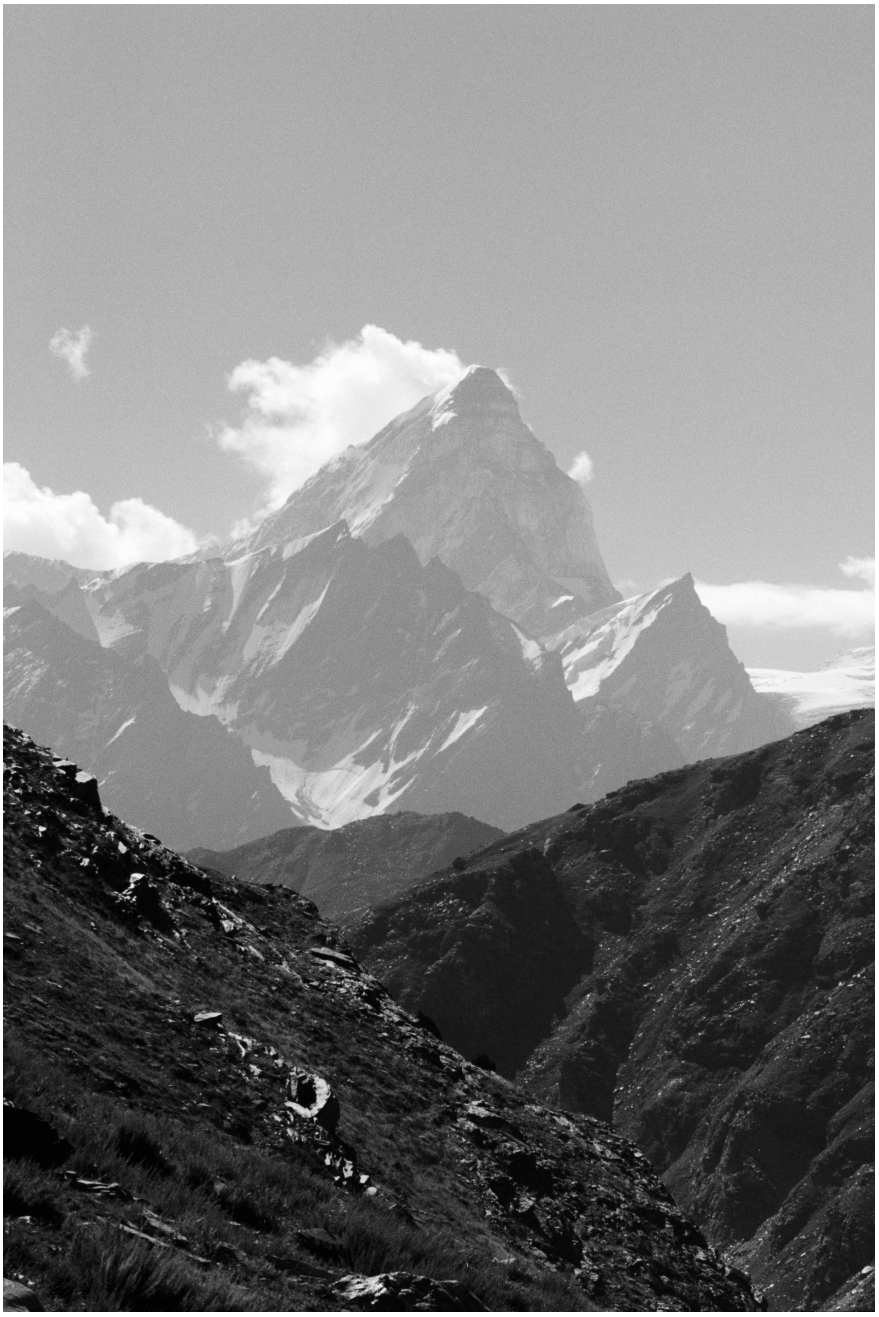
- *The faults on the NW side of the section display composite normal- and thrust-sense movement, these structures originated as thrust faults, therefore although the structures are folded, the zones reactivated by normal-sense movement post-date the F_2 folding.*
- *The folding of the Lamayuru fault is constrained by remote sensed mapping and interpretations of Honegger (1983).*

D-D′ notes:

- *Subsurface leucogranite is constrained by dominance of cm-scale intrusions of leucogranite in host mixed psammite, pelite, and semipelite at surface localities.*

Chapter 3

Petrography and Mineral Chemistry



The towering peak of Kun (7,077 m)

This chapter summarises the petrographic observations of representative samples from each lithology and the mineral compositional data of select samples from pelitic and metabasic assemblages. From these datasets, the prominent textural changes and chemical trends over varying metamorphic grade are outlined for pelitic and metabasic lithologies. The dependence of these changes on varying bulk composition is assessed. For petrographic descriptions, information on porphyroblastic minerals and key indicator minerals is presented first followed by documentation of the matrix phases. Accessory minerals are not discussed unless deemed relevant.

3.1 Petrographic descriptions

3.1.1 ISZ

3.1.1.1 Dras Volcanics

The extrusive units of the Dras Volcanics contain the primary volcanic mineral assemblage Ca-rich plagioclase (dominantly replaced), clinopyroxene and hornblende. Accessories include quartz (often present as amygdales) and Fe-Ti-oxides. Regional metamorphism and alteration results in variable amounts of actinolite, albite, chlorite, calcite, epidote, clinozoisite saussirite (after plagioclase), titanite, and serpentine minerals. Honegger *et al.* (1982) also recorded prehnite and pumpellyite, but these minerals were not observed in the sample set of this study.

Clinopyroxene occurs as xenomorphic to idiomorphic oikocrysts (~0.5–4 mm). The c-axis of clinopyroxene is replaced by fine to medium-grained acicular actinolite, with minor clinopyroxene. Inclusions of calcite (secondary?) are common and locally ragged chadacrysts of hornblende are preserved. Widespread serpentinisation and epidote growth are common.

Hornblende appears as two phases, as hypidiomorphic prismatic grains (~0.25–2.0 mm) in the matrix and as ragged < 0.1 to ~0.25 mm chadacrysts within the clinopyroxene.

Pseudomorphs after plagioclase appear as xenomorphic to hypidiomorphic oval grains of variable size (~1.0–5.0 mm). Plagioclase is completely saussuritised with little preserved of the original grain. Epidote and actinolite form the dominant minerals within saussurite and are widespread (Fig. 3.1a). Albite is also present.

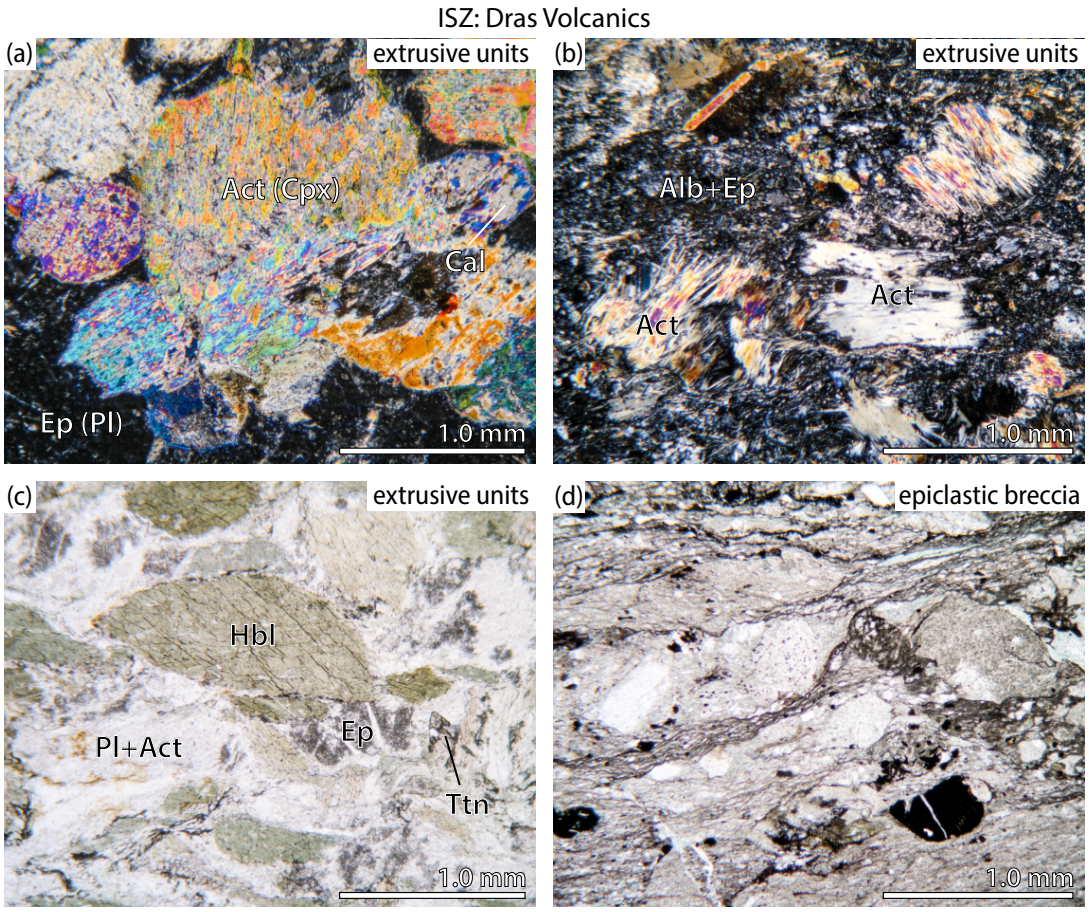


Fig. 3.1 Photomicrographs of representative samples from the Dras Volcanics including both a–c) extrusive units and d) epiclastic breccia.

Saussuritisation and epidotisation result in pronounced embayment of primary pyroxene and hornblende.

Fe-Ti oxides occur as medium-grained euhedral prisms up to 1 mm in length. These are rimmed by corona of polycrystalline titanite (~0.1–0.4 mm in thickness).

A sample of epiclastic breccia displays sub-angular to sub-rounded clasts within a volcaniclastic to tuffaceous matrix (Fig. 3.1d). For a more detailed description of this unit see Robertson & Degnan (1994).

3.1.1.2 Metasedimentary rocks

Graphitic pelite

Graphitic pelite contains graphite, quartz, albite, muscovite, chlorite, calcite, and minor ankerite. Biotite is present depending on grade and bulk composition. Accessories include Fe-Ti oxides and epidote. Texturally the lithology is generally

fine-grained, equigranular, moderately to strongly deformed with a penetrative foliation defined by mica, flattening of calcite, quartz, albite, and alignment of graphite (Fig. 3.2a, b). Small porphyroblasts of chlorite or plagioclase and quartz lenses are wrapped by the fabric.

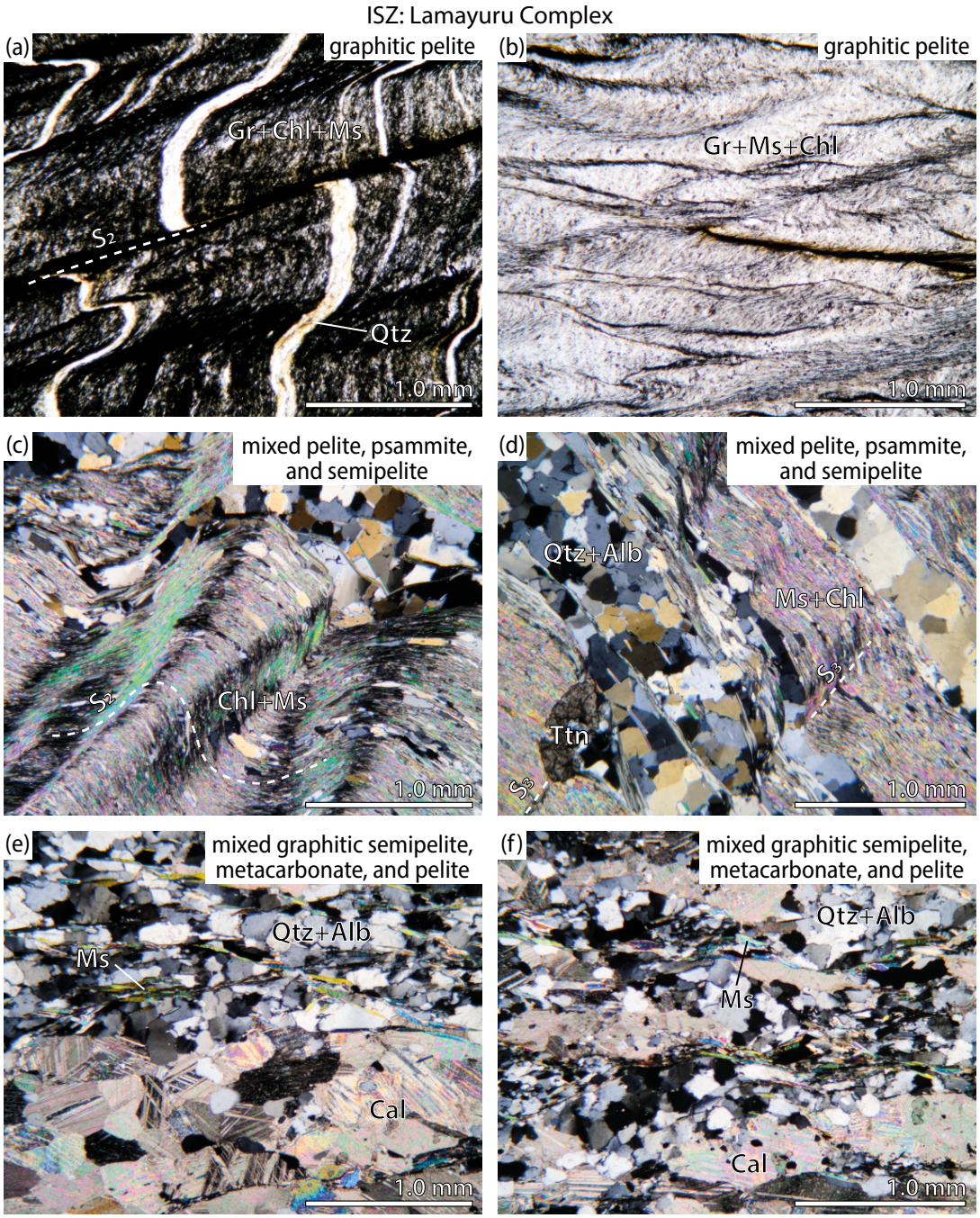


Fig. 3.2 Photomicrographs of representative deformed samples from the Lamayuru Complex including a, b) graphitic pelite, c, d) mixed pelite, psammite, and semipelite; and e, f) mixed graphitic semipelite, metacarbonate, and pelite.

Graphite occurs as polycrystalline layers within the rock, and rarely display distinguishable crystals. The development of shear bands and/or crenulations concentrate the graphite into opaque layers separated locally by more quartzo-feldspathic lenses (Fig. 3.2a, b).

Chlorite occurs as subhedral porphyroblastic augen (~≤ 0.1–1.0 mm). Cleavage varies from oblique to aligned with the S_2 fabric and is notably discordant to the S_3 fabric. Biotite occurs as small (~≤ 0.1 mm) tabular euhedral grains nucleated along the cleavage planes of chlorite. Locally chlorite is fully replaced. Muscovite occurs as elongate tabular subhedral to euhedral grains up to 1.5 mm in length. Muscovite is found both defining the main matrix foliation and aligned along chlorite cleavage planes. Common deformation textures in the micas are kinking, folding and undulose extinction.

Quartz is present with albite as polycrystalline flattened lenses that are up to cm-scale in length. The long axis of flattened quartzo-feldspathic lenses defines the fabric. Lenses are locally isoclinally folded (Fig. 3.2a). Quartz displays sub-grain rotation, characteristic of regime 2 of Hirth & Tullis (1992). Where graphite is less abundant and shearing less prominent, quartz is present as an equigranular matrix phase and displays undulose extension and bulging at grain boundaries characteristic of regime 1 of Hirth & Tullis (1992).

Albite is present as to rounded subhedral grains (~≤ 0.6 mm) defining porphyroblastic augen. Undulose extinction and deformed twins are observed in some grains.

Calcite and ankerite occur as anhedral to subhedral rounded grains of variable size (~0.1–1.0 mm). The carbonate minerals occur as polycrystalline lenses or interstitially between quartz and feldspars. Deformed twins, undulose extinction and flattening of grains are observed.

Mixed pelite, psammite, and semipelite

The mineral assemblage in samples from the mixed pelite, psammite and semipelite comprises quartz, albite/plagioclase, muscovite, chlorite, biotite, and/or titanite. Garnet occurs depending on grade and bulk composition. Accessories include calcite, epidote, graphite, apatite, and Fe-Ti oxides. Compositional variation between psammite, pelite, and semipelite occurs at cm-scale (Fig. 3.2c, d). In the pelitic layers a penetrative foliation is defined by the alignment of mica. Generally graphite is less abundant or absent compared to graphitic pelite. Texturally pelitic layers are inequigranular to seriate, fine- to medium-grained and

moderately deformed with sub-mm-scale poikiloblasts. Semipelitic and psammitic layers are equigranular, medium-grained and are weakly deformed, and can be carbonate rich. Index minerals are generally developed in the pelitic layers.

Porphyroblasts of garnet occur as small rounded grains (up to 1.0 mm) and their first occurrence defines the garnet isograd in pelitic compositions.

Muscovite and chlorite occurs as small subhedral to euhedral tabular grains (~0.1–2.0 mm), though muscovite locally grows up to 5.0 mm in length. The two micas are often intergrown and define the dominant penetrative S_2 foliation, though only muscovite grows along the crenulation cleavage associated with S_3 fabric (Fig. 3.2c, d). Locally late chlorite displays strong berlin blue interference colours suggesting a Fe-rich composition, inferred to have grown on the retrograde path. Biotite occurs as small (~$\leq$ 0.1–1.0 mm) tabular euhedral grains localised in the cleavage domains of chlorite. Common deformation textures in the micas include folding, kinking and undulose extinction.

Albite is present as small (~0.1–0.5 mm) subhedral rounded matrix grains. Round inclusions of quartz are common. Locally polysynthetic twins are developed and are often deformed, though strain is dominantly accommodated in surrounding quartz.

Quartz is present as subhedral grains (~$\leq$ 0.1–1.0 mm) and forms rounded grains concentrated in the polycrystalline quartzo-feldspathic domains. Boundaries between quartz grains are curvilinear whilst they are sharp where in contact with micas. Recovery in quartz grains is dominantly accommodated via patchy undulose extinction. Recrystallisation is most often displayed by bulging at grain boundaries, though locally examples of sub-grain rotation are present. Where the sample is strongly crenulated sub-grain rotation develops parallel to fold axes of micro-crenulations, and perpendicular to the quartzo-feldspathic ribbons which do not display the developed crenulations. These microstructures are dominantly in regime 1, though extend up to regime 2 of Hirth & Tullis (1992).

Titanite porphyroblasts occur as euhedral to subhedral prismatic to oval grains (~$\leq$ 0.1–1.0 mm). Porphyroblasts are concentrated within pelitic layers and are generally reoriented parallel to D_3 crenulations. Cores of grains are fluid-inclusion rich whilst the rims are inclusion poor.

Mixed graphitic semipelite, metacarbonate, and pelite

The mineral assemblage of samples from within the mixed graphitic semipelite,

metacarbonate, and pelite unit comprise quartz, calcite/ankerite, graphite, muscovite, biotite, and/or albite/plagioclase. Accessories include titanite, clinozoisite, apatite, and Fe-Ti oxides. Garnet is present depending on grade and bulk composition. Texturally the units are generally equigranular and fine- to medium-grained (Fig. 3.2e, f).

Garnet is rare, though where present occurs as skeletal rounded poikiloblasts (up to 0.5 mm in size). Largely garnet is replaced by Fe-rich chlorite, biotite, and small amounts of muscovite. Inclusions of quartz are common and show minimal evidence of deformation.

Muscovite and primary chlorite occur as small subhedral to euhedral tabular grains (~0.1–2.0 mm). The two micas are often intergrown with graphite and biotite to define the dominant penetrative S_2 foliation. Locally retrograde chlorite displays an Fe-rich composition. Biotite occurs as small-medium (~$\leq$ 0.25–2.0 mm) tabular euhedral grains localised along cleavage planes of chlorite. Common deformation textures in the micas include folding, kinking and undulose extinction. All micas contain graphite inclusions.

Albite is present as small (~0.1–1.0 mm) subhedral oval to prismatic matrix grains and locally as porphyroblastic augen that overgrow the main fabric and are deformed by subsequently developed crenulation and shear bands. Locally polysynthetic twins are developed and graphite inclusions trails are abundant.

Calcite and ankerite crystals are rounded to ovoid, subhedral to anhedral grains (~0.5–2.0 mm). The long axis of crystals weakly defines a fabric (Fig. 3.2e, f). Grains are often interstitial between quartz. Deformed twins, undulose extinction and flattening of grains are observed.

3.1.1.3 Metavolcanic rocks

Group B metavolcanic rock

Group B metavolcanic rock contains the assemblage chlorite, actinolite, quartz, albite, with grade and bulk dependent hornblende, tremolite, biotite, calcite, and/or stilpnomelane. Accessories include epidote, and titanite. The unit is typically equigranular, though porphyritic, amygdaloidal, and/or tuffaceous textures can be preserved (Fig. 3.3a–d). Amygdales are filled by quartz, and/or calcite. Relict porphyritic textures results in flattened and sheared lenses of varying compositions, dominated by: a) actinolite; b) fine-grained albite; and c) chlorite, clinozoisite, titanite, and albite (Fig. 3.3d).

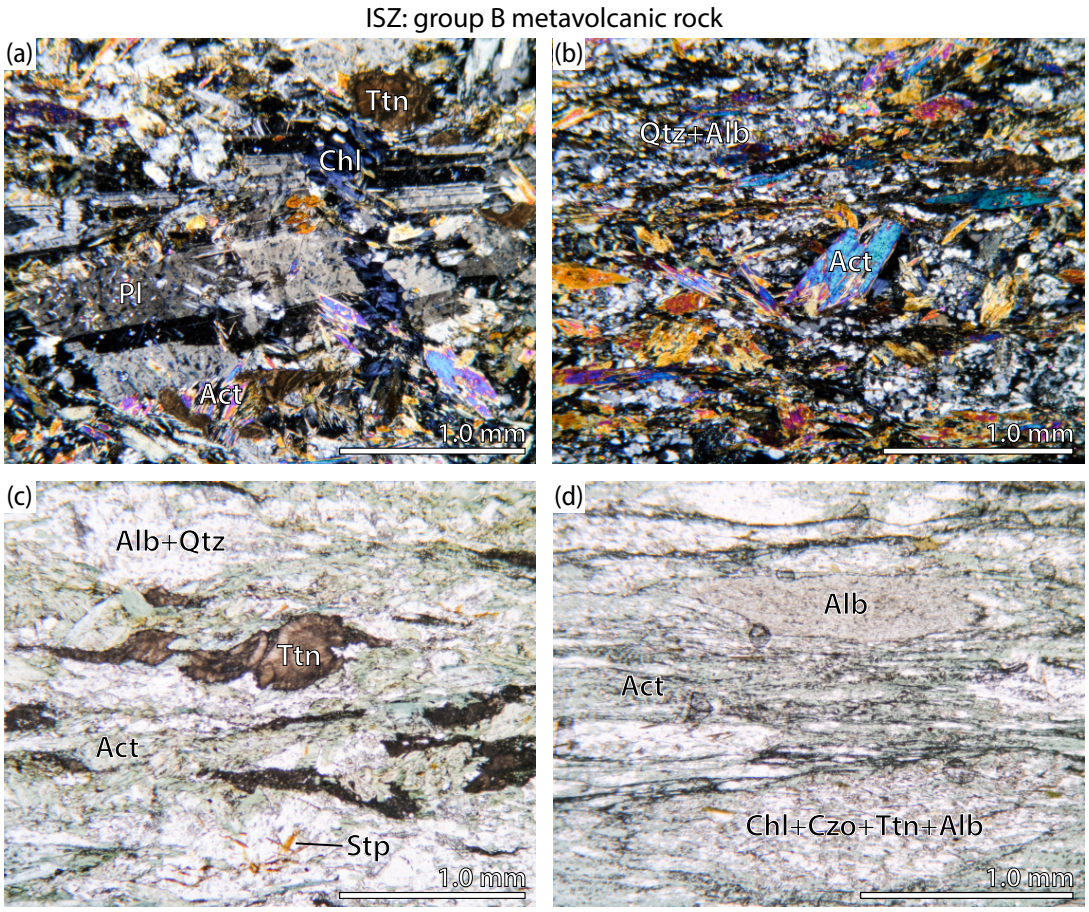


Fig. 3.3 Photomicrographs of representative samples from group B metavolcanic rocks.

Actinolite is present as euhedral acicular to prismatic grains (~≤ 0.1–0.8 mm). When aligned, the actinolite defines S_2 whilst remaining weakly aligned to S_1 (with some grains cross-cutting this fabric). Crenulation of D_1 fabric results in fracturing and kinking of the acicular grains parallel to the plane of the newly developing fabric. Tremolite locally occurs as fine euhedral acicular grains.

Hornblende occurs as euhedral prismatic grains (~≤ 0.3–1.0 mm in length). At the hornblende isograd actinolite locally shows strong compositional zoning and dark green rims may represent newly-formed hornblende rims.

Chlorite occurs as interlocking tabular subhedral to euhedral grains (~≤ 0.1–0.4 mm). Chlorite-rich domains and quartzo-feldspathic domains alternate at mm-scale and the compositional fabric is interpreted to represent original S_0 compositional variation, now transposed into the S_1 fabric. Chlorite (and biotite) are aligned with S_2 where it crenulates S_1 or is dominant. Late biotite replaces chlorite.

Albite occurs as prismatic subhedral to euhedral grains (~< 0.1–1.5 mm). Deformed twins and kinking of grains parallel to the axis of cleavage development is common. Grains may have epidote inclusions.

Quartz is present as rounded to flattened subhedral to anhedral grains (~≤ 0.1). Quartz generally displays undulose extinction and sub-grain rotation, characteristic of regime 2 of Hirth & Tullis (1992).

Calcite occurs as rounded to ovoid subhedral grains (~0.1–0.4 mm). Calcite normally occurs in lenses or in an amygdaloidal texture with the long axis of lenses aligned to S_1.

Stilpnomelane locally occurs as euhedral prismatic grains (~0.1–0.5 mm) often in radiating bow-tie clusters. It is weakly to moderately aligned with the S_2 fabric or as clusters within amygdales (Fig. 3.3c). Colour ranges between samples from classic deep-orange to brown-green suggesting compositional variation. Stilpnomelane was previously documented in the Suru Valley (Honegger, 1983) and in other metabasic sequences at greenschist-grade and more rarely at the greenschist–amphibolite-facies transition zone (e.g., Starr *et al.*, 2020).

Although an accessory, titanite is described here given its relevance to transitioning metamorphic grade. Titanite typically occurs as polycrystalline clusters surrounding other Fe-Ti oxides, similar to its occurrence in the Dras Volcanics (Fig. 3.3a, c). The Fe-Ti oxides are interpreted to be primary in origin whilst the titanite is either primary or metamorphic. Moving up grade, the titanite rims coarsen.

3.1.2 GHS–THS

3.1.2.1 Metasedimentary rocks

Pelite

Samples from the pelite unit include muscovite, biotite, quartz, plagioclase, and/or garnet with variable amounts of staurolite and kyanite. Accessory phases include zoisite, clinozoisite, apatite, tourmaline, rutile, ilmenite, monazite, and/or zircon. Texturally the rocks are generally seriate, medium- to coarse-grained and moderately deformed (Fig. 3.4a, b). A strong penetrative foliation is defined by mica and flattening of quartz with coarse poikiloblasts either wrapped and/or cross-cutting the fabric. Coarse- to very coarse-grained quartz lenses with minor feldspar are common.

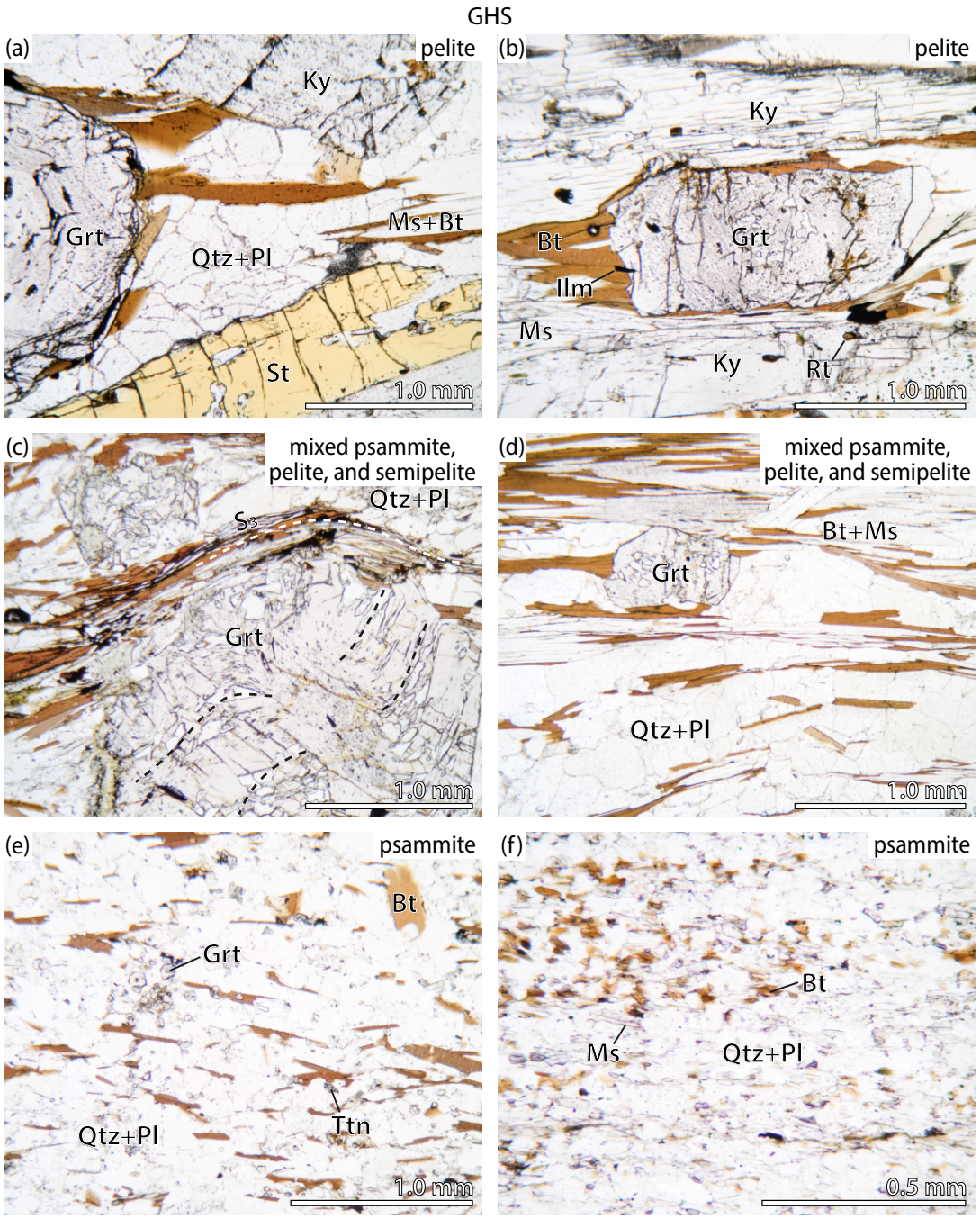


Fig. 3.4 Photomicrographs of representative samples of the GHS–THS including a, b) pelite; c, d) mixed psammite, pelite, and semipelite; and e, f) and psammite.

Poikiloblastic garnet occurs as subhedral to euhedral grains of variable size (~0.1–10.0 mm) hosting inclusions of quartz, biotite, ilmenite, and rutile. Inclusions are concentrated in the core of garnet, whereas the rim is predominantly clear or contains fine sub-mm inclusions, interpreted to reflect two phases of growth. The garnet core (garnet I) is typically wrapped by the S_2 fabric whilst the garnet rim (garnet II) overgrows the S_2 fabric. Embayed garnets show textures

associated with breakdown, usually to Pl + Ms ± Bt. Chlorite growth is also recorded at garnet rims and in brittle fractures, associated with retrogression.

Staurolite and kyanite occur as a function of bulk composition and metamorphic grade, with both index minerals absent from Al-poor metasedimentary strata. Staurolite occurs as euhedral porphyroblasts (~0.5–15 mm) often with fine inclusions of ilmenite, apatite, quartz, tourmaline and/or rutile. Brittle fracturing of the grains sub-perpendicular to the foliation is common (Fig. 3.4a). Kyanite is present as euhedral prismatic poikiloblasts (~0.5–20 mm), with undulose extinction and deformed twins locally observed. Kyanite can be found as matrix porphyroblasts and/or in contact with staurolite rims. Garnet, quartz, rutile, apatite, and/or tourmaline often occur as inclusions in kyanite. Kyanite partly breaks down to fine-grained polymineralic aggregates of muscovite + plagioclase. Symplectites of kyanite and quartz are also often present. Staurolite and kyanite overgrow the main S_2 fabric. Kyanite occasionally shows some alignment with the fabric, possibly related to biotite replacement (Fig. 3.4b).

Biotite and muscovite occur as subhedral to euhedral tabular grains (~0.5–3.0 mm). These two micas are often intergrown and define the dominant penetrative S_2 foliation. Minor kinking of cleavage is common and locally folding of grains is present. Monazite and zircon are common as inclusions within biotite. Muscovite is commonly found as foliation parallel ragged inclusions in poikiloblastic plagioclase, interpreted to represent muscovite breakdown.

Plagioclase occurs as prismatic to oval subhedral grains (~0.5–3.0 mm) generally aligned with the fabric. Plagioclase twins are often deformed to wedges or are kinked. Some crystal plasticity in the feldspars is displayed through moderate sweeping undulose extinction and brittle deformation is shown through fracturing, infilled by mica growth. Fracturing does not appear to disrupt extinction continuity thus likely post-dates any plastic deformation. Locally interlobate–amoeboid grains are present representing migration of grain boundaries (examples of bulging and grain boundary migration are observed).

Quartz is present as subhedral grains (~0.1–2 mm). It typically forms flattened grains and polycrystalline lenses, boundaries between quartz grains are curvilinear to euhedral whereas are sharp with surrounding minerals. Recovery in quartz grains is dominantly accommodated via patchy undulose extinction and recrystallisation is displayed by bulging at grain boundaries. These microstructures are similar to those of regime 1 described by Hirth & Tullis (1992) in experimentally deformed quartzites.

Mixed package of psammite, pelite, and semipelite

The mineral assemblage in the samples from the mixed package of psammite, pelite, and semipelite comprises quartz, albite/plagioclase, biotite, and muscovite, with varying amounts of garnet, staurolite, kyanite, and/or sillimanite depending on metamorphic grade. Accessories include chlorite, zoisite, clinozoisite, chloritoid, apatite, ilmenite, rutile, titanite, zircon, and/or monazite. Compositional variation between psammite, pelite, and semipelite is locally visible at cm-scale. A penetrative foliation (strongly defined in the pelitic and semipelitic layers) is characterised by mica and quartz flattening with poikiloblasts either wrapped or overgrowing the fabric. Texturally pelitic and semipelitic layers are inequigranular to seriate, medium- to coarse-grained and moderately deformed. These layers contain mm- to cm-scale poikiloblasts (Fig. 3.4c, d). Psammitic layers are equigranular, medium-grained and weakly to moderately deformed with mm-scale poikiloblasts. Coarse- to very coarse-grained quartz lenses with minor feldspar are locally present, mostly in the pelitic and semipelitic layers. Psammitic layers rarely display index minerals higher than garnet and staurolite irrelevant of metamorphic grade.

Poikiloblastic garnet occurs as anhedral to euhedral grains of variable size (~0.1–50.0 mm) containing inclusions of quartz, biotite, graphite, zoisite/clinozoisite, ilmenite, and/or rutile. Garnet growth generally displays two phases with syn-tectonic inclusion-rich cores (Garnet I) and post-tectonic inclusion-poor rims (Garnet II). Chlorite growth is present along garnet rims and in fractures, associated with retrogression (Fig. 3.4c). Near Parkachik and Shafat, garnet has locally reacted to biotite-kyanite-plagioclase. At Shafat, this has occurred in a static environment whilst at Parkachik, kyanite is domminantly alligned to the S_3 fabric.

Staurolite occurs as rounded subhedral to euhedral prismatic grains of variable size (~0.25–3.0 mm) containing inclusions of ilmenite and rutile. Brittle fracturing of the grain sub-perpendicular to the S_2 foliation is common. The mineral is found in two textural settings, both as matrix porphyroblasts and along garnet rims. Staurolite porphyroblasts appear to have grown post-D_2 as defined by ilmenite and rutile inclusions that are aligned with the matrix S_2 foliation.

Porphyroblastic kyanite occurs as subhedral to euhedral prismatic grains of variable size (<0.1 to ~7.0 mm) containing inclusions of ilmenite, rutile and/or tourmaline. Undulose extinction and deformed twins are present in some grains. Locally kyanite partly or totally retrogresses to fine-grained polymineralic ag-

gregates of muscovite and plagioclase. Kyanite is post-tectonic with respect to D_2.

Sillimanite occurs as euhedral fibrous to acicular to prismatic grains. Fibrolite is present as fine sub-mm knots or matted needles, prismatic sillimanite is up to ~1.0 mm in length. Both are commonly intergrown with biotite and muscovite. Prismatic sillimanite is often fractured perpendicular to the length of the mineral. Fibrolite is commonly aligned parallel to the regional fabric (S_2) as needles overgrowing biotite and/or muscovite (epitaxial growth). Prismatic sillimanite is occasionally aligned with the fabric, and often appears to have no distinct orientation.

In the high-grade zone south of Rangdum, K-feldspar becomes a principal phase of the metamorphic mineral assemblage. It forms large (~0.5–4.0 mm) anhedral to subhedral grains. K-feldspar grains can include minor fibrolite and be decorated by numerous fine to coarse perthitic exsolutions. Deformation microstructures include: brittle fracturing (infilled by mica), sweeping undulose extinction, flame shaped perthite at grain boundaries, and/or myrmekite growth along foliation parallel crystal faces. Interfaces to matrix quartz are often serrated.

Plagioclase is the dominant feldspar in all other samples. Plagioclase forms smaller (~0.1–1.5 mm) rounded subhedral to prismatic grains. At low-grades it may also be present as a porphyroblast. Locally grains show compositional zonation and/or partial retrogression to sericite. Deformation twins, undulose extinction, and bulging recrystallisation with core and mantle structures are present.

Biotite and muscovite occur as subhedral to euhedral tabular grains (~0.1–10.0 mm). These two minerals are often intergrown to define the dominant penetrative S_2 foliation, with biotite locally present as a porphyroblast phase. Monazite and zircon are common as inclusions within biotite. Biotite and muscovite both appear to have two growth generations. Biotite I and muscovite I define the S_2 foliation. Biotite II is generally coarser and often occurs as a porphyroblast phase, syn- to post-tectonic to the S_2 fabric. Biotite II and staurolite could form concurrently through the following reaction:

$$\mathrm{Grt + Ms + Chl = St + Bt + Qtz + H_2O}$$

Biotite often shows brittle deformation features and kinking of cleavage. Additional biotite may recrystallise or grow within these brittle fracture domains. Muscovite shows folding, kinking and locally forms mica fish. Muscovite similarly

often shows a second growth phase, muscovite II being dominantly post-D_2 and not appearing to define an obvious foliation. A higher abundance of interlayed quartzo-feldspathic layers results in higher rock rigidity, as such crenulation cleavage often has larger angles and is therefore well preserved in this unit.

Zoisite is locally abundant in this unit, appearing as subhedral to euhedral prismatic grains (~0.5–3.0 mm). It occurs dominantly in pelitic rich layers and displays brittle fracturing perpendicular to the long-axis of the grain. Zoisite occurs parallel to S_2 foliation or where present as a porphyroblast phase, cross cutting this fabric. Growth is interpreted to be syn- to post-D2. At the edges of lenticular domains, zoisite breaks down to plagioclase. Quartz and zoisite symplectites are locally present.

Quartz is present as subhedral grains (~0.1–2 mm). Quartz forms rounded grains distributed throughout the matrix though in polycrystalline quartzo-feldspathic lenses it can occur as flattened grains. Boundaries between quartz grains are curvilinear but sharp with surrounding minerals. Recovery in quartz grains is accommodated via patchy undulose extinction which locally displays chessboard extinction textures. Recrystallisation is most often displayed by bulging at grain boundaries, though locally examples of sub-grain rotation and grain boundary migration are present. These microstructures are dominantly in regime 1, though extend up to lower regime 3 of Hirth & Tullis (1992).

Psammite

The psammite unit is defined by the presence of quartz, plagioclase, biotite, muscovite ±garnet. Accessory minerals include tourmaline, calcite, apatite, titanite, and/or ilmenite. Flattening of quartz, opaques and minor mica define a weak foliation with an equigranular and granoblastic matrix (Fig. 3.4e, f). Poikiloblasts of garnet are present. The unit is fine grained, and weakly deformed owing to the high content of quartz and feldspar.

Biotite and muscovite occur as isolated tabular to acicular anhedral to euhedral flakes seldom exceeding 1.0 mm in length. These minerals define a weak penetrative fabric.

Plagioclase and quartz are the dominant constituents of the granoblastic matrix. They both occur as rounded grains ($<$ 0.5 mm). Quartz displays brittle fracturing, patchy undulose extinction, and bulging at grain boundaries, characteristic of regime 1 of Hirth & Tullis (1992).

Garnet occurs as subhedral to euhedral matrix grains (< 0.1 mm). These largely cross cut the S_2 fabric.

The rock is generally poor in opaques and small (< 0.1 mm) grains of ilmenite lie subparallel to the weak foliation.

Metacarbonate The metacarbonate unit is characterised by varying proportions of calcite and dolomite with minor quartz and plagioclase. Accessories include muscovite, rutile, scapolite and/or apatite. Biotite and chlorite were identified in the field. Texturally the unit is fine- to medium-grained, equigranular, moderately to strongly deformed with a weak foliation displayed by flattening of calcite, dolomite and locally quartz (Fig. 3.5a, b). Where present, micas also define the foliation.

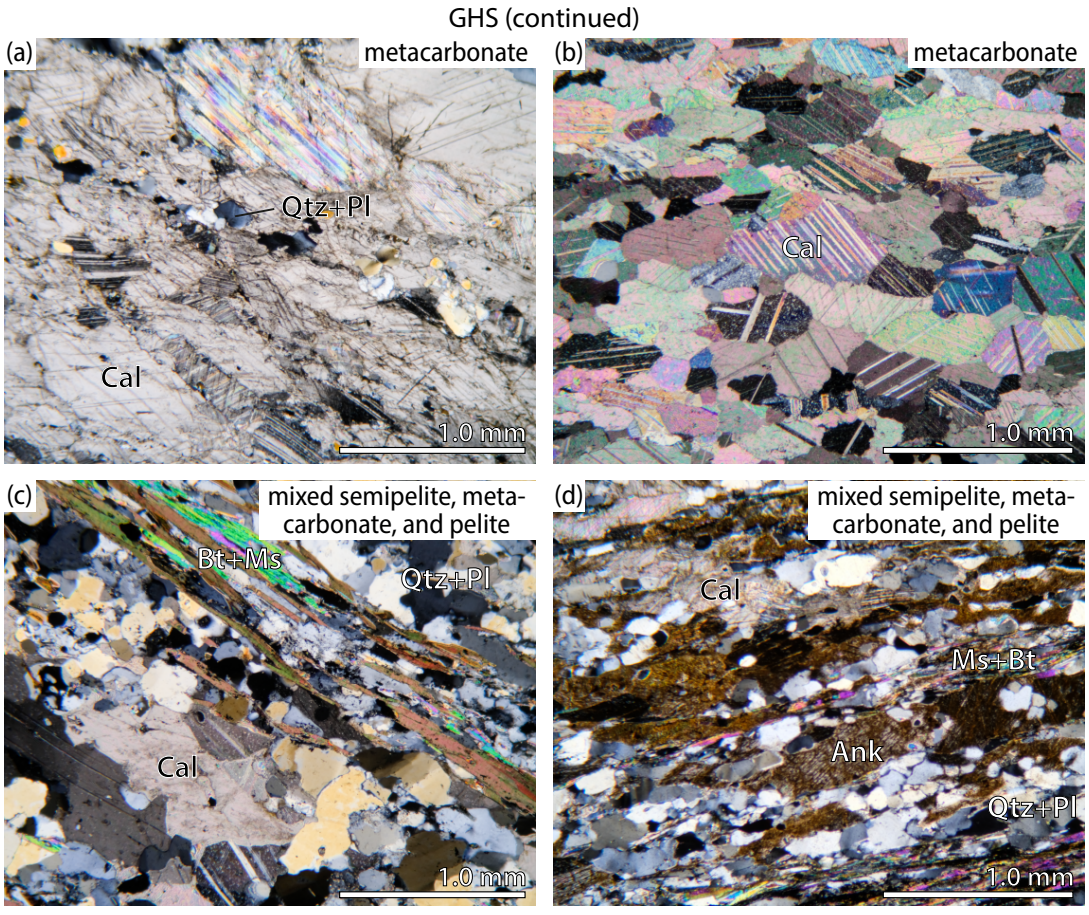


Fig. 3.5 Photomicrographs of representative samples of a, b) metacarbonate; and c, d) mixed semipelite, metacarbonate, and pelite of the GHS–THS.

Calcite and dolomite crystals are rounded to ovoid subhedral grains (~≤ 0.5 mm) and define the dominant constituents of the metacarbonate unit. The long axis of crystals appear weakly aligned to create a fabric (Fig. 3.5a, b). The

minerals appear heavily recrystallised due to tapered twins near grain boundaries and old large grains fringed by smaller ones. Other deformation textures include, kinked and wedged twins, kinking of grains, and sweeping undulose extinction.

Muscovite occurs as tabular subhedral flakes rarely exceeding ~0.5 mm in length and define the S_2 or S_3 fabric where present. Kinking of cleavage and fish structures are observed.

Plagioclase is present as prismatic subhedral grains (~$\leq$ 0.2 mm). Quartz is present as rounded to flattened anhedral to subhedral grains (~0.2–2.0 mm). The long axis of flattened quartz defines the fabric. Flattening of quartz increases moving from deeper structural levels towards the ZSZ. Near the ZSZ, long elongate quartz ribbons up to 5 cm in length are observed, with individual grains on the cm-scale. The quartz ribbons show deformation twins and brittle fracturing due to inactivation of slip systems at low temperatures. Quartz generally displays minor bulging at grain boundaries, characteristic of regime 1 of Hirth & Tullis (1992), though in the ZSZ can display sub-grain rotation and/or grain boundary migration, characteristic of up to regime 3 of Hirth & Tullis (1992).

Scapolite forms rounded to ovoid (~$\leq$ 0.2 mm) subhedral to anhedral grains. The long axis lies parallel to the foliation.

Mixed package of semipelite, metacarbonate, and pelite

The mixed semipelite, metacarbonate, and pelite contains quartz, plagioclase, muscovite, biotite, calcite with minor ankerite, actinolite, and hornblende. Inconstant proportions of chlorite, garnet, staurolite, and/or kyanite are included depending on grade and bulk composition. Accessories include graphite, tourmaline, apatite, ilmenite, titanite, rutile, and magnetite. Texturally the rocks are generally seriate, medium-grained and moderately deformed (Fig. 3.5c, d). A strong penetrative foliation is defined by mica and flattening of quartz with coarse poikiloblasts being wrapped or cross-cutting the fabric.

Poikiloblastic garnet occurs as subhedral to euhedral grains of variable size (~1.0–5.0 mm) with inclusions of quartz, calcite, and/or graphite.

Staurolite occurs as anhedral to subhedral prismatic to rounded grains of variable size (~0.1–10.0 mm). Brittle fracturing of the grains sub-perpendicular to the foliation is common.

Kyanite is present as subhedral prismatic grains generally $\leq$ 2.0 mm. Locally kyanite partly or totally breaks down to fine-grained polymineralic aggregates of muscovite + plagioclase. Undulose extinction is observed.

In a few localities hornblende is visible as subhedral to euhedral porphyroblasts (~0.25–5.0 mm). The long axis lies parallel to or at an angle to the foliation. Locally rims are defined by a yellow pale alteration. Grains are often fractured perpendicular to the long axis.

Muscovite and biotite are tabular subhedral to euhedral flakes rarely exceeding ~1.0 mm in length. The micas are sparse where the carbonate component is more dominant. Where they are present in higher abundances, they often define the foliation (S_1, S_2, or S_3 depending on structural position). Monazite and zircon can be present as inclusions within biotite. In lower grade samples, tabular euhedral primary chlorite is also present, generally $\leq$ 0.5 mm in length. Common deformation textures in the micas are kinking, folding and undulose extinction.

Quartz is present as rounded to flattened subhedral grains (~0.1–0.5 mm). The long axis of flattened quartz defines the fabric. Flattening of quartz increases moving from deeper structural levels towards the ZSZ. Quartz generally displays minor bulging at grain boundaries, characteristic of regime 1 of Hirth & Tullis (1992), though near the ZSZ or associated shear zones sub-grain rotation is the dominant form of dynamic recrystallisation.

Plagioclase is present as small prismatic to rounded subhedral matrix grains (~0.1–0.5 mm). Where they occur as porphyroblasts, the rounded grains may be as large as 1.75 mm. Graphite and epidote occur as inclusions within the porphyroblasts. Deformed twins and undulose extinction are observed in some grains.

Ankerite and calcite occur as anhedral to subhedral rounded grains of variable size (~0.5–2.0 mm). They occur as either matrix or porphyroblastic phases. Matrix phases are often interstitial between quartz and feldspars. Deformed twins, undulose extinction and flattening of grains are observed.

3.1.2.2 Metavolcanic rocks

Group A metavolcanic rock

Group A metavolcanic rock contains albite/plagioclase and quartz with variable amounts of biotite, actinolite, tremolite, hornblende, garnet, staurolite and/or

kyanite are present depending on grade and bulk composition. Quartz content decreases and plagioclase content increases with grade (with variation as a function of bulk composition). Texturally the rocks vary with increasing grade from equigranular and fine grained to inequigranular and medium- to coarse-grained (Fig. 3.6a–f). Accessories include epidote, rutile, titanite, ilmenite, magnetite, zoisite, ankerite, calcite and/or apatite.

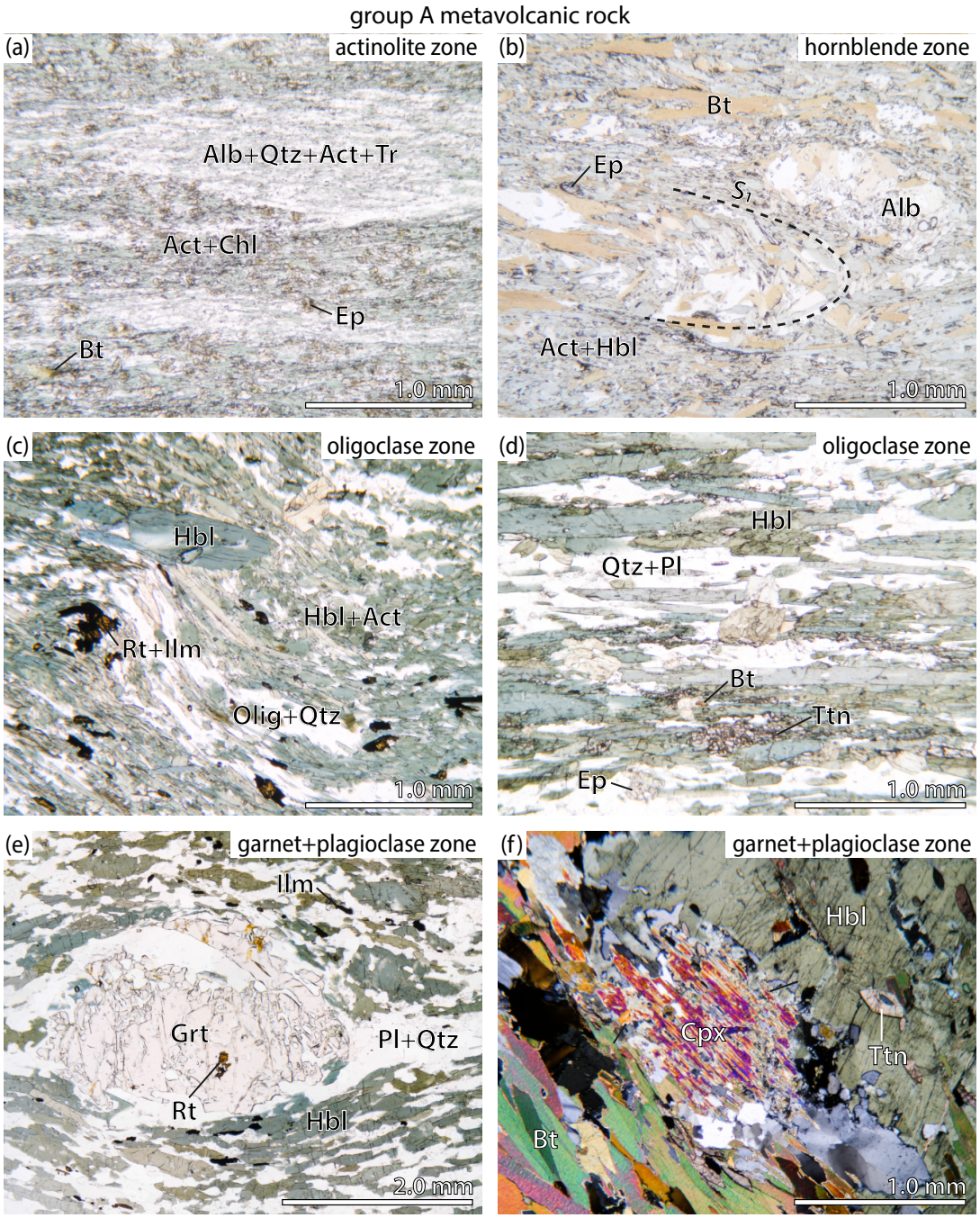


Fig. 3.6 Photomicrographs of representative samples from group A metavolcanic rocks ordered in the figure by relative increase in metamorphic grade: a) actinolite zone; b) hornblende zone; c, d) oligoclase zone; and e, f) garnet+plagioclase zone.

Poikiloblastic garnet occurs as subhedral to euhedral grains of variable size (~≤ 0.1–6.0 mm) with inclusions of quartz, calcite, zoisite, ilmenite, and/or rutile (Fig. 3.6e). Where fractured, late biotite and chlorite growth is common.

Poikiloblastic kyanite occurs as anhedral to subhedral prismatic grains with a skeletal texture. Grains are of variable size (~0.5–2.0 mm) and can contain hornblende inclusions. Kyanite overgrows S_2.

Plagioclase is present in the matrix as small prismatic to rounded subhedral grains (~0.1–0.8 mm). Flattening of grains is common where the long axis is aligned to S_2. Where they occur as porphyroblasts, plagioclase are rounded and approximately 0.5 mm in size. Epidote, clinozoisite, and/or titanite occur as inclusions.

Biotite is present in the matrix as subhedral to euhedral tabular grains (~0.1–4.0 mm). It can also occur as a coarser (~3.0–6.0 mm) porphyroblastic phase. Porphyroblastic biotite is syn- to post-tectonic to the S_2 fabric. It can comprise a second generation of biotite growth. Biotite, often associated with plagioclase, is also concentrated at the rim of garnet where it occurs with a ragged shape. These biotite grains are interpreted to have grown during garnet breakdown occurring post-D_2. Fine-grained ragged crystals are also present in the matrix in garnet+plagioclase-zone samples, locally associated with chlorite.

Tremolite is characterised by euhedral acicular grains (~≤ 0.1–1.0 mm). It is weakly aligned or overgrows S_1 and strongly realigned with S_3. These fabrics characterise the lowest-grade samples where tremolite is present.

Actinolite occurs in most greenschist facies metavolcanic rocks. It is characterised by euhedral acicular to prismatic grains (~≤ 0.1–2.0 mm) that weakly define S_1 and dominantly define S_2 (with some grains cross-cutting S_2; Fig. 3.6b).

Hornblende characterises higher grade rocks of the metabasic sequence and grains coarsen upwards with grade (Fig. 3.6b–f). It is characterised by subhedral to euhedral prismatic to acicular grains (~0.2–6.0 mm) that dominantly define S_2. Some grains, commonly more porphyroblastic ones, cross-cut the main fabric. Inclusions of plagioclase, epidote, titanite, rutile, and/or ilmenite are common.

Quartz is present as rounded to flattened subhedral grains (~0.1–0.5 mm). The long axis of flattened quartz defines the fabric. Quartz generally displays minor patchy undulose extinction and minor bulging at grain boundaries, characteristic of regime 1 of Hirth & Tullis (1992). Evidence of static recrystallisation resulting in a granoblastic texture is present in some samples.

3.1.2.3 Metagranites

Biotite muscovite syenogranite

The biotite muscovite syenogranite is a coarse-grained, inequigranular and frequently porphyritic rock defined by the presence of quartz, K-feldspar, plagioclase, biotite, and muscovite (Fig. 3.7a, b). Accessory minerals include garnet, apatite, epidote, clinozoisite, and/or zircon.

K-feldspar occurs as prismatic to oval subhedral porphyroclasts (~1.0–20.0 mm). K-Feldspar in the field ranges up to 10 cm in length. A prominent perthitic texture is present and inclusions of muscovite, quartz, are clinozoisite are common (Fig. 3.7b). Grains boundaries are locally embayed the growth of myrmekite.

Plagioclase is characterised by prismatic to oval anhedral to subhedral porphyroclasts (~0.5–5.0 mm), though may also be present as a matrix phase. Deformation to twins, undulose extinction and oscillatory zoning are common. Grains may contain inclusions of quartz, muscovite, biotite and/or zircon. Both feldspars can display weak sericitisation.

Gefüllte (= stuffed) microstructure containing abundant inclusions of muscovite or epidote/clinozoisite is locally present in K-feldspar (and exsolved perthitic plagioclase), and abundant in plagioclase porphyroblasts. This texture is commonly developed in Alpine metadiorites and metatonalites (e.g., Ackermand & Karl, 1972). The texture is interpreted to form through an originally moderately An-rich plagioclase reacting with K-feldspar and H_2O to form a more Ab-rich plagioclase with abundant inclusions of clinozoisite, muscovite, and quartz. This occurs during greenschist–amphibolite facies metamorphism where Al is released from anorthite to form white mica or clinozoisite (Barker, 1998) and has been previously identified in the Suru Valley region (Burton, 1995).

Biotite is present as tabular subhedral grains (~0.25–3.0 mm) that define the S_2 fabric. Biotite form augen with associated feldspars. Inclusions of zircon in biotite are common. Muscovite occurs as tabular subhedral grains and is locally porphyroblastic (~0.1–3.0 mm). Growth of muscovite is concentrated along plagioclase grain boundaries or between fractures. Growth also appear at K-feldspar grain boundaries.

Quartz occurs as rounded to oval anhedral grains (~0.25–3.0 mm). Flattening is present with the long-axis aligned to S_2. Boundaries between quartz grains are curvilinear and are sharp to other surrounding minerals. Recovery in quartz grains is dominantly accommodated via patchy undulose extinction which locally

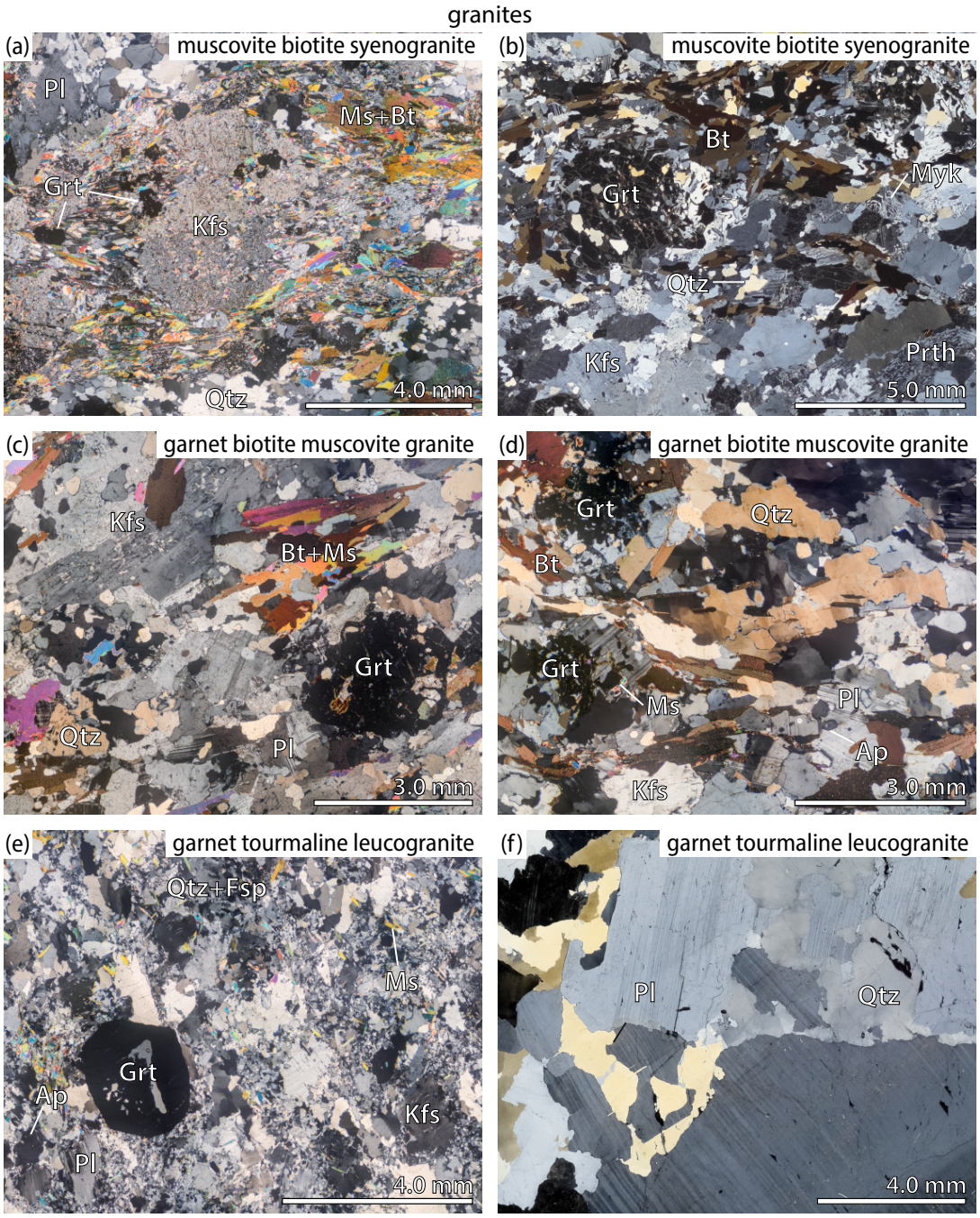


Fig. 3.7 Photomicrographs of representative samples from the metamorphic granites of the GHS–THS, including a, b) biotite muscovite syenogranite; c, d) garnet biotite muscovite granite; and e, f) garnet tourmaline leucogranite.

displays chessboard extinction textures. Recrystallisation is most often displayed by grain boundary migration, though locally examples of sub-grain rotation and bulging are present. Sub-grain rotation occurs in strain shadows to garnet porphyroblasts. These microstructures are characteristic of lower regime 3 of Hirth & Tullis (1992).

Garnet occurs as skeletal rounded subhedral porphyroblasts (~0.25–3.0 mm) wrapped by the micaceous S_2 fabric. Cores are obviously more skeletal than rims and locally atoll structures are developed.

Biotite muscovite garnet granite

The biotite muscovite garnet granite is equigranular to inequigranular medium- to coarse-grained and defined by the presence of quartz, K-feldspar, plagioclase, muscovite, biotite, and garnet (Fig. 3.7c, d). Diopside is present at higher grade. Accessory minerals include epidote, apatite, titanite, chlorite (secondary), allanite, calcite and/or zircon. The granite varies from monzogranite to syenogranite in composition.

Garnet occurs as skeletal rounded subhedral poikiloblasts (~0.5–4.0 mm) that can be wrapped by micaceous S_2 fabric (Fig. 3.7d). Inclusions of epidote and quartz are common.

K-feldspar occurs as subhedral prismatic to rounded porphyroclasts (~0.5–8.0 mm), though can also form part of the matrix. K-Feldspars in the field range up to 10 cm in length. Perthitic exsolution (inherited) is common with some grains displaying lamellae visible in section (sub-mm scale). Undulose extinction is also common, and grain boundaries of both feldspars are often embayed by growth of myrmekite. Inclusions present include muscovite, quartz, biotite, and/or zircon. Late-sericitisation is also present.

Plagioclase is characterised by prismatic to rounded subhedral to anhedral porphyroclasts (~0.5–2.5 mm), and can also form part of the matrix. Antiperthite (inherited), undulose extinction, oscillatory zoning and deformed twins are present in some grains. Grains can contain inclusions of biotite, muscovite, zircon, epidote/clinozoisite and/or quartz, late-sericitisation is also present. Plagioclase occurs as rounded porphyroblasts or form augen in select samples. Gefüllte crystals containing inclusions or muscovite or epidote/clinozoisite are locally developed. This suggests metamorphism of pre-existing granitoids at a temperature lower than igneous crystallisation(Burton, 1995).

Diopside occurs at higher grades as anhedral to subhedral rounded grains (~0.25–1.0 mm).

Biotite (sometimes green) is present as tabular subhedral to euhedral grains (~0.5–4.0 mm) and comprises the main mica in the metagranites. Biotite defines

the S_2 fabric in the rock and can outline the shear fabric of associated feldspar pophyroclasts. Inclusions of zircon in biotite are common.

Muscovite occurs as tabular to acicular subhedral to euhedral grains (~0.25–1.0 mm). Growth of muscovite is concentrated along biotite grain boundaries and cleavage domains. Growth is also common along K-feldspar grain boundaries with a noticeably more ragged crystal habit. Where muscovite has replaced biotite, minute flakes of biotite are often present inside the grain aligned to cleavage.

Quartz occurs as rounded to oval anhedral grains (~0.15–3.0 mm). Flattening is present with the long-axis aligned to S_2. Boundaries between quartz grains are curvilinear and sharp with surrounding minerals. Quartzo-feldspathic lenses are common throughout the metagranites. They are fringed by mica with quartz largely present in the strain shadow of augen. Recovery in quartz grains is dominantly accommodated via patchy undulose extinction that locally displays chessboard extinction textures. Recrystallisation is most often displayed by grain boundary migration, though locally examples of sub-grain rotation and bulging are present. Sub-grain rotation occurs in strain shadows to garnet porphyroblasts. These microstructures are characteristic of regime 1 and lower regime 3 of Hirth & Tullis (1992).

More leucocratic phases are also associated with the biotite muscovite garnet granite unit. Field relations support classification under the same intrusive complex. Grain size varies from more fine grained, coarser grained, and pegmatitic in comparison to the dominant metagranite. Garnet and micas are less abundant, whilst quartzo-feldspathic components are more abundant.

Garnet tourmaline leucogranite

The garnet tourmaline leucogranite comprises quartz, plagioclase, K-feldspar, muscovite, garnet, and/or tourmaline. It varies from fine–medium grained, pegmatitic, or coarse-grained and equigranular(Fig. 3.7e, f). Accessory minerals include tourmaline, biotite, and/or zircon.

Garnet is present as rounded euhedral porphyroblasts (~0.5–2.0 mm). Grains can contain inclusions of quartz, muscovite and/or zircon.

K-feldspar occurs as rounded subhedral porphyroblasts (~1.0–4.0 mm) with inclusions of muscovite and zircon. Plagioclase occurs as rounded anhedral to subhedral porphyroblasts (~1.0–2.5 mm) with inclusions of muscovite, quartz

and/or zircon. Plagioclase shows evidence of crystal-plastic deformation with deformed twins (wedging and kinking) and undulose extinction (Fig. 3.7f).

Muscovite occurs as subhedral to euhedral mica-fish and tabular flakes (~0.5–3.0 mm). Minor kinking of cleavage is common. Where present as inclusions, it occurs as smaller tabular–acicular grains that are not aligned to the fabric (~0.1–0.2 mm). Minor late-stage overgrowth of muscovite is also present.

Quartz falls into two petrographic groups. Group 1 occurs as anhedral to subhedral tabular grains (~0.2–0.2.5 mm) that form cm-scale polycrystalline elongate ribbons. Sweeping–patchy undulose extinction is common. Group 2 quartz occurs as anhedral rounded matrix grains (~0.1–0.3 mm) that show evidence of post-peak static recrystallisation producing a weak granoblastic texture in some domains. Group 2 is interpreted to have formed originally via sub-grain rotation. The boundary between group 1 and group 2 quartz is sharp, and parallel to the long-axis of the ribbon.

3.1.2.4 Migmatite

Migmatite forms within the mixed psammite, pelite, and semipelite. For the mineral assemblage of the paleosome refer to Section 3.1.2.1. The leucosome contains the following mineral assemblage: quartz, K-feldspar, plagioclase, biotite, muscovite and sillimanite. Accessories include garnet, monazite, apatite, and/or ilmenite. The mineral assemblage of the darker residuum (melanosome) comprises: biotite, muscovite, sillimanite, quartz, plagioclase, and locally containing variable amounts of garnet and (pseudomorphed) cordierite. Accessories include monazite, ilmenite, and/or apatite. Minerals from both components of the migmatite (the neosome) are described together and any differences in habit, composition, microstructure and texture highlighted as required.

Several phases of garnet are identified (Fig. 3.9). Garnet I/II displays the same characteristics as described in Section 3.1.2.1. Garnet I/II occurs as subhedral rounded poikiloblasts (~0.75–3.0 mm). Dominant inclusions in garnet I/II are quartz, biotite, and/or ilmenite. Although not abundant, the inclusions appear consistent with the matrix S_2 suggesting growth post-D_2. Garnet III occurs as inclusion-rich subhedral rounded poikiloblasts (~0.1–1.5 mm). Dominant inclusions are sillimanite and biotite. Inclusions are generally misaligned or weakly aligned to S_2. Where weakly aligned, the internal fabric and matrix fabric are either continuous or display minor rotation of the poikiloblast. Garnet III

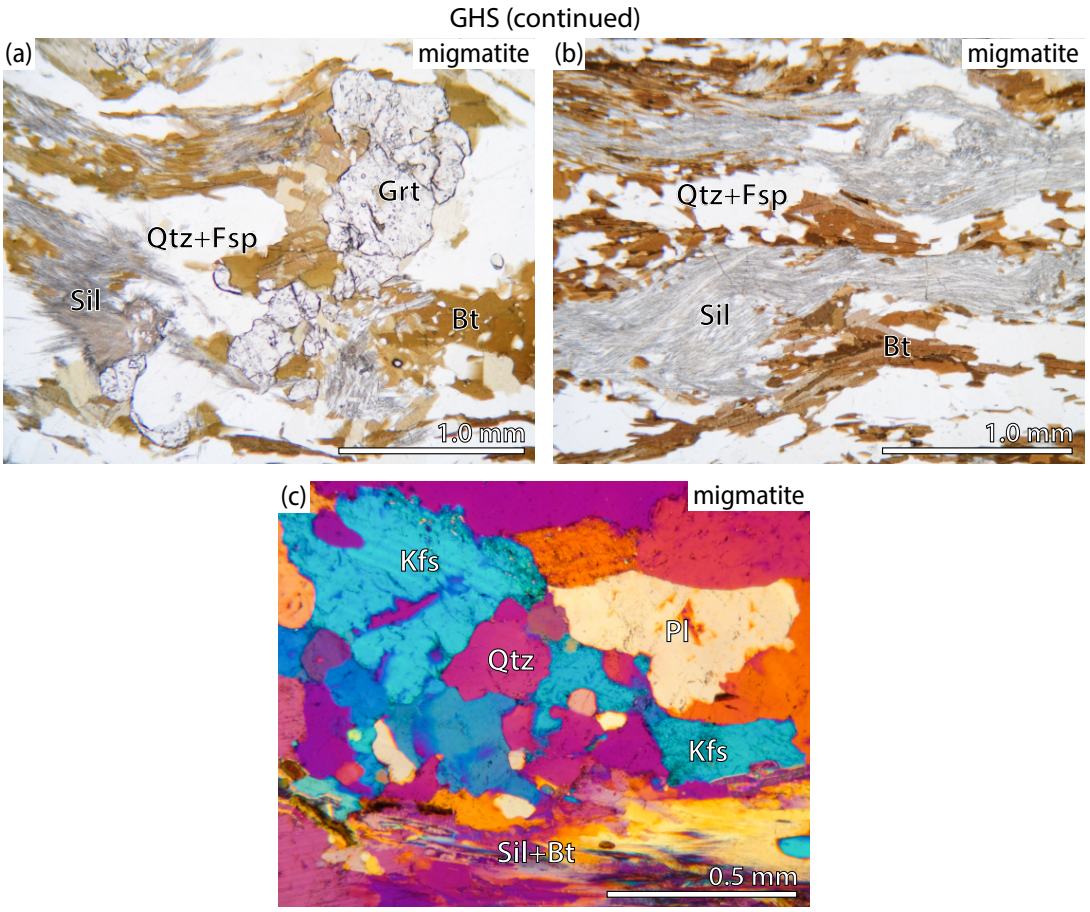


Fig. 3.8 a-b) Photomicrographs of representative samples from the migmatite lithology of the GHS–THS, and c) sensitive tint plate of cuspate K-feldspar grains.

grows around and sometimes entraps or embays previous garnet phases (Fig. 3.9a). Garnet I/II displays breakdown textures, interpreted to have occurred prior to Garnet III growth. These phases of garnet occur in both the leucosome and the melanosome, however, the leucosome is also host to a larger (~0.1–1.5 mm) phase of skeletal garnet. These grains are subhedral and rounded with coarse-grained quartz in lobate embayments and inclusions (Fig. 3.9b). These textures suggest growth during dehydration melting (Waters, 2001).

Sillimanite is present as euhedral fibrous to prismatic grains. Fibrolite occurs as fine sub-mm needles or polycrystalline knots and prismatic sillimanite is up to ~1.5 mm in length. Both are commonly intergrown with biotite and muscovite. Fibrolite mostly grows sub-parallel to the regional fabric (S_2) where present as needles, larger knots may be misaligned. Prismatic sillimanite occasionally appears to be aligned to S_2, though often has no distinct orientation. The apparent alignment of these minerals is interpreted to result from precipitation of the mineral on previously aligned mica. Fibrolite is commonly concentrated

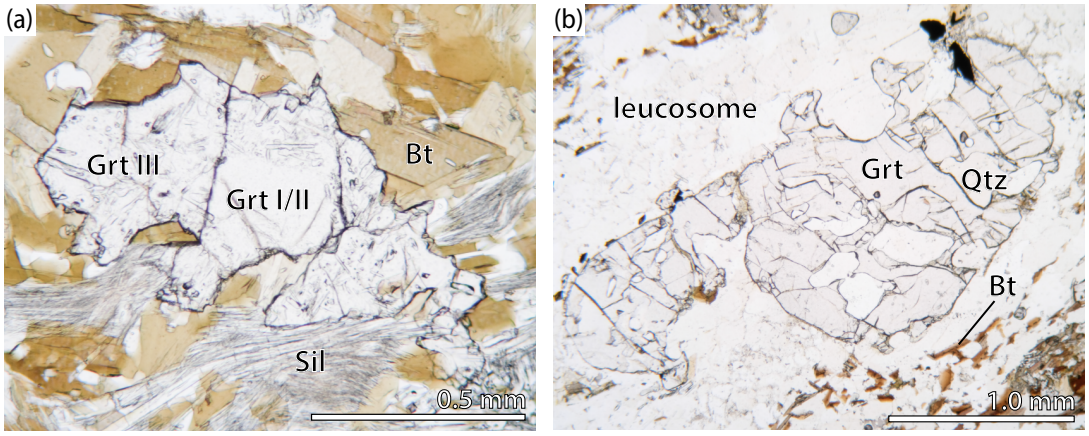


Fig. 3.9 Photomicrographs of representative garnets in migmatite of the Suru Valley region, a) phases of garnet growth in the palaeosome and b) peritectic growth of garnet in the leucosome with lobate boundaries and curvilinear quartz inclusions.

in the melanosome with mica though it is present throughout the rest of the neosome. Prismatic sillimanite is generally only found in the melanosome.

K-feldspar forms large (~0.5–10.0 mm) anhedral to subhedral grains in both the leucosome and melanosome, though it is dominantly present in the leucosome. Grains may include minor fibrolite and are often decorated with fine to coarse perthitic exsolution. Inclusions of muscovite and quartz are common. Interfaces with matrix quartz are often serrated. K-feldspar can be embayed along rims by formation of myrmekite. K-feldspar grains are highly cuspate in the leucosome (Fig. 3.8c). Locally K-feldspar is weakly sericitised. Plagioclase forms (~0.1–2.0 mm) subhedral rounded to prismatic grains in the rock matrix. Inclusions of muscovite and sillimanite are common and plagioclase locally display intergrowths with quartz to form myrmekite. Select grains of plagioclase are partially retrogressed to sericite. Both feldspars are noticeably more subhedral to euhedral in the leucosome.

Biotite and muscovite occur as subhedral to euhedral tabular grains (~0.1–3.5 mm). These two minerals are often intergrown to define the penetrative S_2 foliation. Fibrolite is largely associated with biotite and muscovite grains. Biotite is the dominant mica with muscovite present in variable amounts (some samples contain no muscovite). Sillimanite, monazite, and/or zircon are common as inclusions within biotite. Muscovite often has inclusions of sillimanite. Garnet breakdown is associated with patchy biotite growth.

In the leucosome, quartz occurs as coarse anhedral grains with interlobate boundaries (~0.2–4.0 mm). Flattening of grains is common and recovery in

quartz is accommodated via patchy undulose extinction that locally displays chessboard extinction textures. Recrystallisation is most often recorded by bulging at grain boundaries, though locally examples of grain boundary migration are present. Static recrystallisation is also observed. Late brittle fracturing of larger grains is common, representing inactivation of slip systems at lower T. These microstructures are dominantly in regime 1, though extend up to lower regime 3 of Hirth & Tullis (1992).

In the melanosome quartz is present as anhedral to subhedral rounded grains (~0.1–1.5 mm). Recovery is accommodated by sweeping undulose extinction and in select grains by weak patchy extinction and bulging recrystallisation. These microstructures are dominantly in regime 1 of Hirth & Tullis (1992).

3.2 Mineral chemistry

3.2.1 Methods

Mineral compositional analysis and element-distribution maps were completed on a Cameca SX5-Fe electron microprobe with a tungsten tipped field emission gun at the Department of Earth Sciences, University of Oxford. Analyses were conducted on carbon coated, polished thin sections, ~30 µm thick. Full spectrometer setup and operating parameters are included in the appendix.

Between 2 (low modal abundance) and 34 (porphyroblastic phases) wavelength dispersive spectrometer spot analyses were collected for each mineral in each thin section. Line profiles were used for porphyroblastic phases and individual spots were randomly selected for different textural positions of the matrix phases. A population average and 2 standard deviation was calculated for analyses from each matrix mineral phase (representative spot analyses were used for AvP in Chapter 4). Element-distribution maps (see Chapter 4) were produced using wavelength dispersive spectrometer stage scans on 2-3 representative garnet porphyroblasts in each section.

Raw microprobe-derived mineral analyses (oxide weight%) were recalculated using the program AX to a standard number of oxygens per formula unit for each mineral: garnet (12), staurolite (46), plagioclase (3), K-feldspar (8), biotite (11), muscovite (11), chlorite (14), ilmenite-hematite (3), amphibole (23), epidote (12.5), clinopyroxene (6). The proportion of Fe_3+/Fe_{total} and activities of mineral end-members was calculated using AX.

3.2.2 Pelitic units

3.2.2.1 Garnet

Garnet zoning profiles were produced using compositional data attained from microprobe traverses. Illustrative zoning profiles are presented in Figures 3.10 and 3.11. A comparison of core and rim values, separated by metamorphic grade, is documented on Figure 3.12. The prefix "ICSV" has been removed from sample numbers on figures throughout this chapter, so they appear as plain numbers. Core values were taken from the point were X_{Sps} was greatest and rim values were taken in garnet zone to sillimanite zone samples at a location prior to an upward inflection in Mn. If there was no upward inflection, the lowest Mn value was selected. In the sillimanite+K-feldspar zone, rim values were taken at the furthest point from the core. Compositional traverses and maps record dominantly unzoned and normal growth zoned garnets, with local reverse zoning. Normal growth zoning is recorded by Mn- and Ca-rich cores, and Fe- and Mg-rich rims, which are typical for prograde garnet growth (e.g., Woodsworth, 1977). Compositional profiles for all divalent cations and results from X-ray mapping confirm that the zoning of Mn, Mg, Fe, and Ca is approximately radially symmetric with respect to the crystal centre. Profiles may appear asymmetric or incomplete where garnets are partly resorbed and replaced by mica and plagioclase, or where a second phase of garnet growth has not grown symmetrically around the core.

The change in the nature of compositional zoning is recorded from low- to high-grade (Fig. 3.12). At low-grade (garnet isograd) garnet is dominantly unzoned or shows weak normal zoning patterns with relatively flat compositional traverses. At higher-grade, compositional zoning becomes progressively more pronounced where the greatest core-rim differential is observed for X_{Grs} in the staurolite zone and X_{Alm}, X_{Sps}, and X_{Prp} in the kyanite zone (Fig. 3.12). Flattening of compositional profiles is observed in the sillimanite zone, which is interpreted to reflect increasing homogenisation by cation diffusion (Tracy, 1982). As such, core compositions up to the kyanite zone are considered primary and a reflection of prograde garnet growth. Prominent reverse zoning is recorded in garnet in the sillimanite+K-feldspar zone. Re-incorporation of Mn in the rim suggests resorption of a high-temperature garnet, and the consistent profile of X_{Grs} is consistent with decompression at high-temperatures. Alternatively if the garnet is pre-himalayan (e.g. Lihter *et al.*, 2022) then such a signature could represent a Himalayan overprint. Due to the possible interpretation of significant resorption in the sillimanite+K-feldspar zone, the core composition is interpreted as representative of metamorphic "peak".

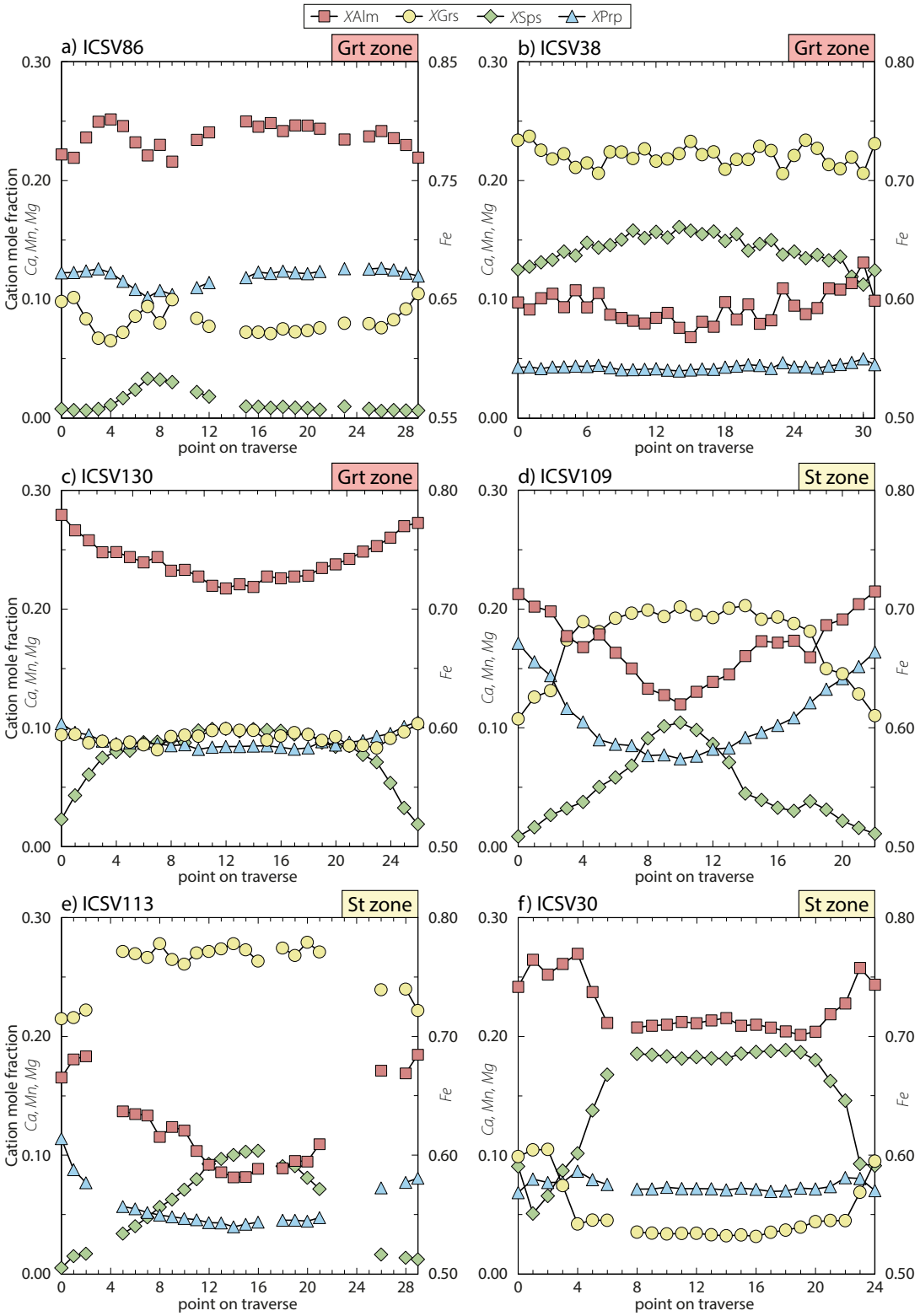


Fig. 3.10 Representative garnet compositional profiles for a–c) garnet-zone, and d–f) staurolite-zone samples. Line profiles are non-continuous due to traverses crossing over inclusions and fractures, such points are excluded from the profiles.

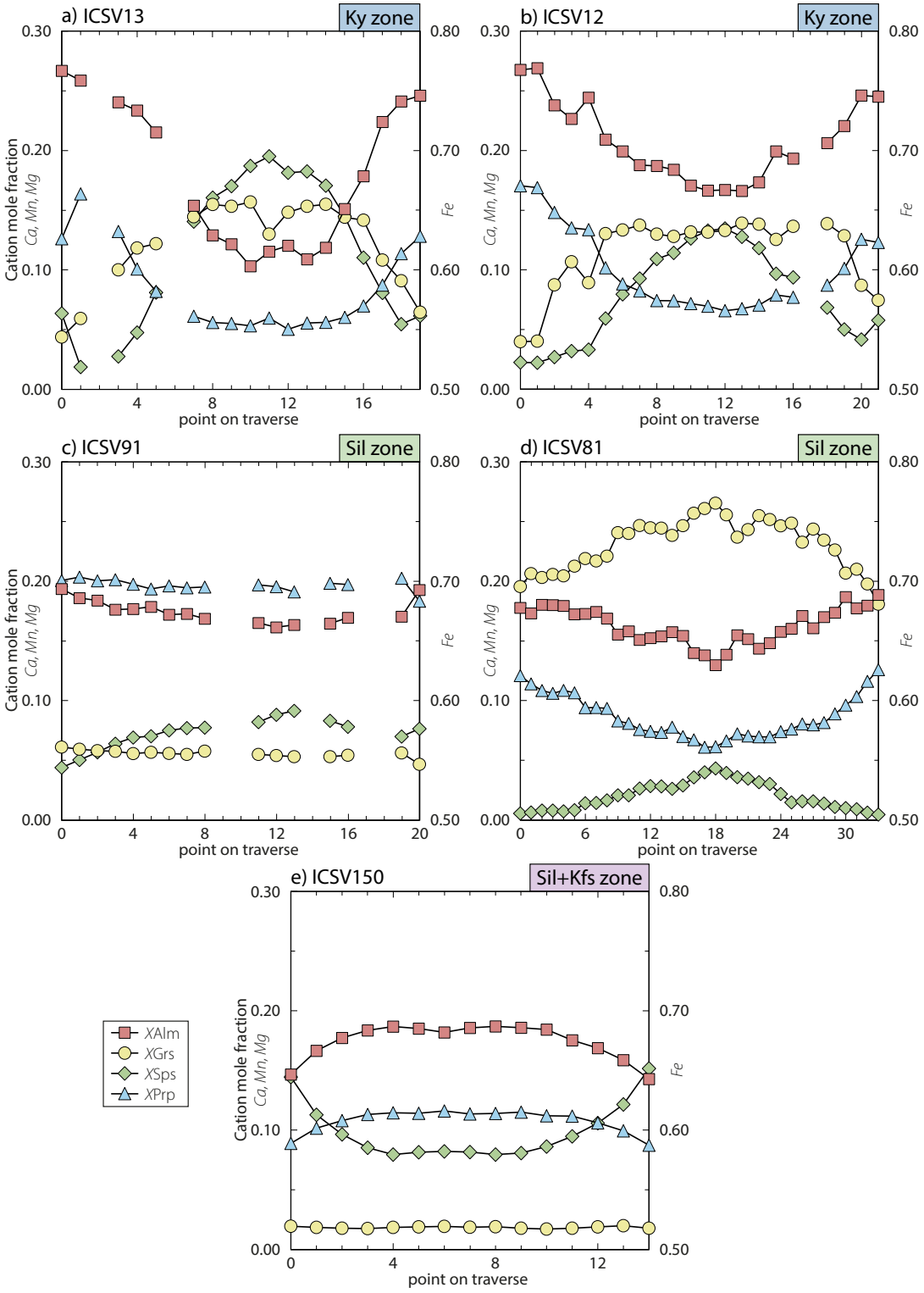


Fig. 3.11 Representative garnet compositional profiles for a, b) kyanite-zone; c, d) sillimanite-zone; and e) sillimanite+K-feldspar-zone samples. Line profiles are non-continuous due to traverses crossing over inclusions and fractures, such points are excluded from the profiles.

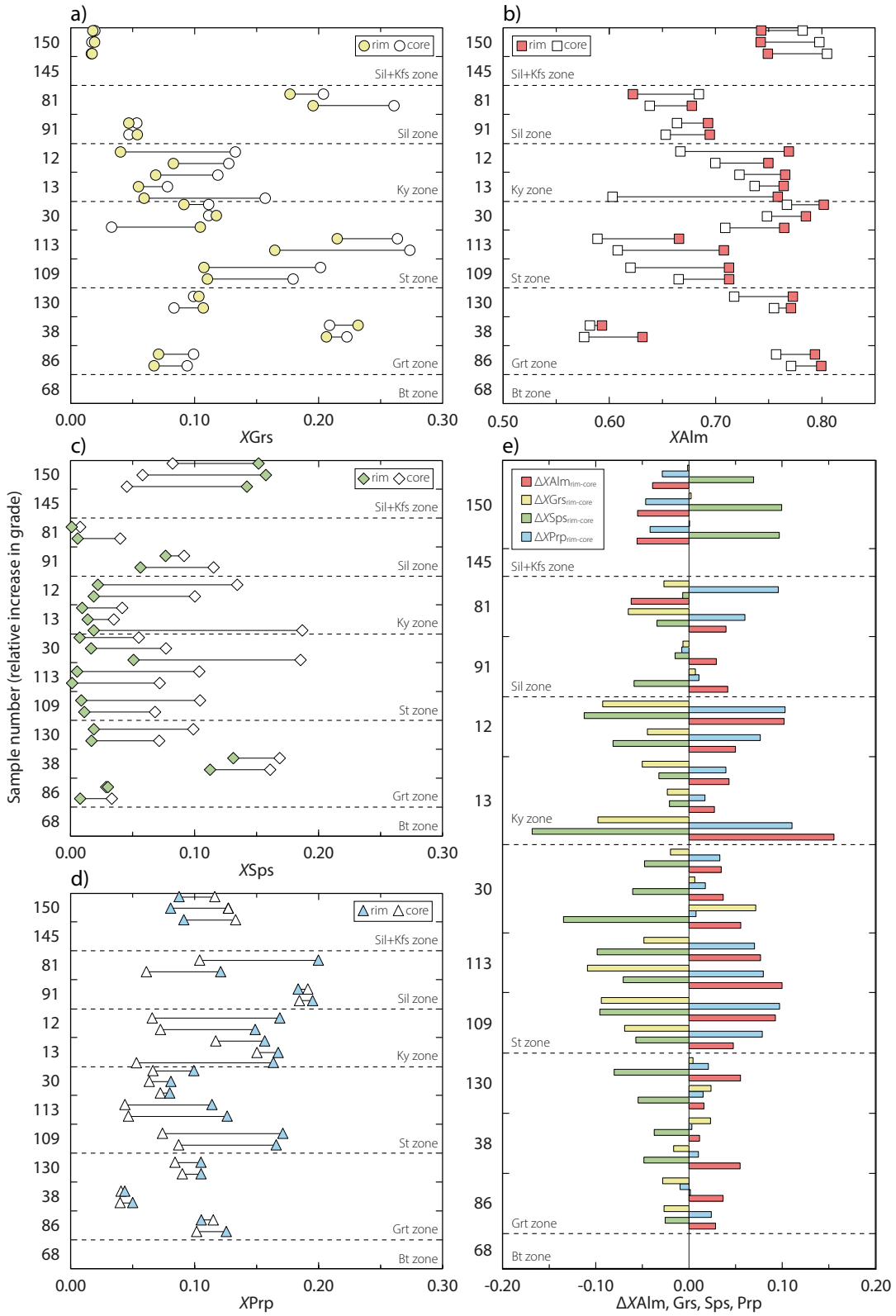


Fig. 3.12 Garnet core-rim values for a) X_{Grs}, b) X_{Alm}, c) X_{Sps}, and d) X_{Prp} plotted for increasing grade with relative grade denoted by dashed line between samples. e) The $\Delta_{\mathrm{rim-core}}$ for each end-member. Normal zoning in both plots is observed from garnet-zone to sillimanite-zone samples, with reverse zoning patterns observed in sillimanite-zone samples.

No significant trends are recorded from absolute values of X_{Alm}, X_{Grs}, X_{Sps}, and X_{Prp}. Both core and rim values of X_{Alm} show a slight decrease from the garnet zone to the sillimante zone. Similar observations apply to X_{Grs}, which also decreases in the sillimanite+K-feldspar zone. X_{Sps} and X_{Prp} are fairly consistent across grade and show minimal variation, with an increase in compositional zoning in X_{Sps} between the staurolite and kyanite zones and in X_{Prp} between the staurolite and sillimanite zones. It is important to emphasise that almandine is generally the largest mole fraction in pelitic systems such that in a constant-sum composition the absolute value is most dependent on the variation of the other phase components (Waters, 2019).

Garnet from the western portion of the map (ICSV109, ICSV130), collected down Chellong Nala and Shanshin Nala (Fig. 2.4) is essentially unmodified by diffusion and late resorption. Garnet from the main valley traverse (Sankoo-Parkachik-Rangdum; Fig. 2.4) commonly shows an upward Mn inflection in the rim which correlates to minor resorption (e.g., ICSV30 & ICSV13; Figs. 3.10 & 3.11). There is microstructural evidence for garnet resorption and breakdown to muscovite + biotite + plagioclase (and locally chlorite) at the rim (Fig. 3.4c), which corroborates modification of the zoning profiles. Local downward inflection and Mn sequestration is associated with garnet growth (e.g., George & Gaidies, 2017; Kohn & Spear, 2000). In some samples that show prominent microstructural evidence for two-stage garnet growth, a significant decrease of Mn occurs at the core to rim boundary (e.g., ICSV30; Fig. 3.10), whilst others display no downward inflection (e.g., ICSV81, Fig. 3.11).

3.2.2.2 Staurolite

Staurolite only sporadically occurs in the staurolite zone likely owing to the impact of varying bulk-composition (often semipelite or psammite) and/or the impact of sluggish reaction kinetics (e.g., Rubie, 1998; Pattison *et al.*, 2011). It is most common in high-Al pelites of the kyanite zone where it co-exists with kyanite and garnet. Analysed staurolite records tightly clustered values of Fe (3.00–3.14 apfu), Al (17.17–17.26 apfu) and X_{Mg} (0.20–0.26), with slight variation of Mg (0.80–1.05 apfu). These values are well within the range of collected data from the L400 series of Searle *et al.* (1992) displayed in Figure 3.13. Though the L400 series shows larger variation of Al contents reflecting variation of bulk composition and/or weak dependence on grade, most samples from this series are similarly collected from the kyanite zone.

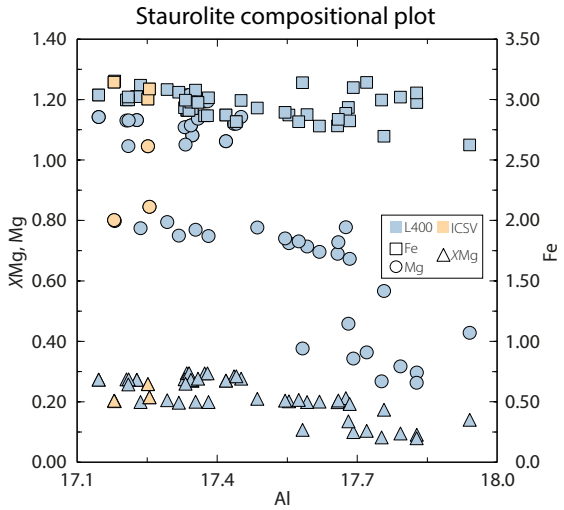


Fig. 3.13 Compositional plots (Al apfu vs X_{Mg}, Mg apfu, and Fe apfu) for staurolite in both samples from this study and a larger sample set from the L400 series of Searle *et al.* (1992).

3.2.2.3 Plagioclase & K-feldspar

Feldspar composition in metamorphic rocks is a function of metamorphic grade as well as variations in bulk composition (Deer *et al.*, 2013). Composition varies according to the coupled substitution NaSi $\rightleftharpoons$ CaAl. Feldspar composition variation with grade is plotted in Figure 3.14. With increasing grade, plagioclase becomes more CaAl rich such that Na and Si decrease accordingly. Plagioclase in the biotite and garnet zones are albite to oligioclase in composition ($Ab_{99–87}$). Compositions become more calcic moving into the staurolite zone where it varies from oligoclase–andesine in composition ($Ab_{88–65}$), however, in the kyanite zone the composition is tightly clustered at the albite to oligoclase boundary ($Ab_{88–90}$). ICSV91 from the sillimanite zone displays albitic plagioclase at Ab_{93}, in co-existence with a grossular content of approximately 5 % (Fig. 3.12) which would support high P equilibrium conditions in the GASP barometry system (e.g., Holdaway, 2001). ICSV81 is dominated by andesine (Ab_{66}). X_{Na} increases in plagioclase in the sillimanite+K-feldspar zone with the precipitation of K-feldspar in the system. At the sillimanite+K-feldspar isograd, plagioclase is Ab_{73} and moving further up-grade Ab_{88} coincident with decreasing volume of plagioclase and increasing K-feldspar volume. X_{K} in K-feldspar composition is $Or_{81–87}$ though shows a large variation between grains (2 SD = 0.08–0.12).

The range of plagioclase feldspar compositions corroborates that reported in previous studies, although generally less calcic than reported here. For example, Searle *et al.* (1992) documented plagioclase compositions from $Ab_{90–60}$ in the

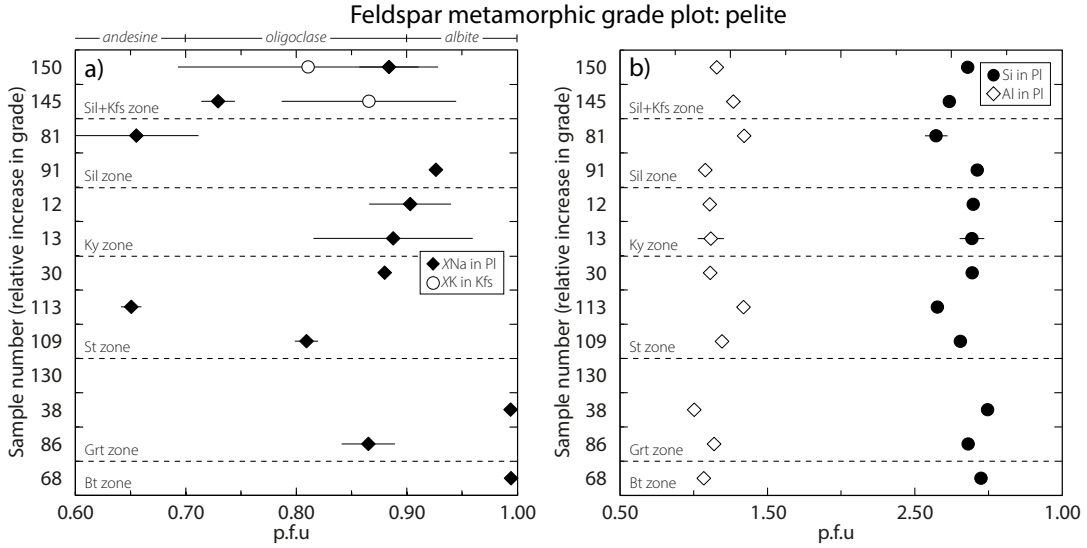


Fig. 3.14 Variation in feldspar composition relative to increasing metamorphic grade. a) X_{Na} and X_{K} for plagioclase and K-feldspar respectively and b) Si and Al apfu.

Suru Valley region and Stäubli (1989) published ranges of $\mathrm{Ab}_{89–58}$ from the Kishtwar window area. It should be noted that previous studies did not document plagioclase compositions from lower metamorphic grades as documented here.

3.2.2.4 Chlorite

Prograde and retrograde chlorite compositions are plotted in Figure 3.15, along with data from the L400 series of Searle *et al.* (1992) and ZD series of Dransfield (1994). Si in prograde grains vary from 2.4–2.7 apfu and retrograde from 2.4–2.7 apfu. Octahedral Al varies from 0.6–1.4 apfu, whilst retrograde is clustered around 1.4. For comparison to L400 and ZD which assume all Fe as Fe^{3+}, Fe_{total} in the samples from the present study is 2.2–2.7 apfu in prograde grains and a greater distribution of 1.8–2.6 apfu in retrograde grains. Ti varies from 0.003–0.007 apfu in prograde samples with a broader distribution from 0.002–0.011 apfu in retrograde grains, appearing to show a slight positive correlation with Si. Finally, X_{Mg} (assuming total Fe) varies from 0.4–0.6 in both prograde and retrograde grains. Results of all compositional parameters are well clustered with those of previous studies, though this study shows a wider range of Si cations, as similarly shown in Walker (1999), though most results cluster at 2.6–2.7 apfu. Compositionally both prograde and retrograde chlorite are ripidolite, in the classification scheme of Hey (1954).

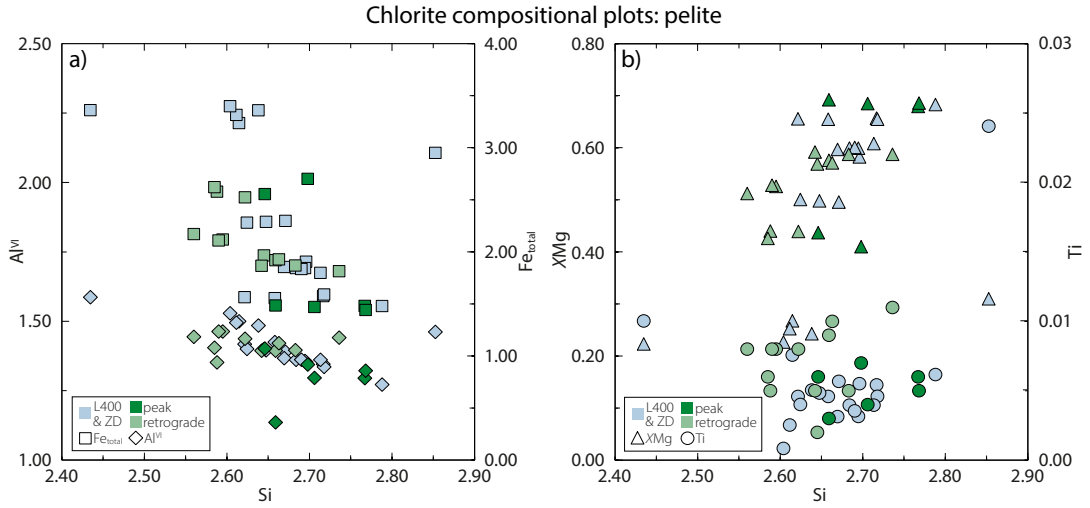


Fig. 3.15 Compositional plots for prograde and retrograde chlorite from this study and a larger sample set from the L400 series of Searle *et al.* (1992) and ZD series of Dransfield (1994). a) Al_{VI} or Fe_{total} vs Si apfu and b) X_{Mg} or Ti vs Si apfu. Samples from other studies are not separated between prograde and retrograde.

3.2.2.5 Biotite

Biotite was studied by plotting major cation substitutions in biotite crystal chemistry. Bioitite has the following major end-members for which there are thermodynamic data:

$KMg_3\,[AlSi_3]\,O_{10}(OH)_2$: phlogopite

$KFe_3\,[AlSi_3]\,O_{10}(OH)_2$: annite

$K\,[Mg_2Al]\,[Al_2Si_2]\,O_{10}(OH)_2$: eastonite

$NaMg_3\,[AlSi_3]\,O_{10}(OH)_2$: Na-phlogopite

A variety of substitutions take place between these end-members as well as other variations with grade and/or bulk composition:

1. Phlogopite to annite involves Fe-Mg substitutions in octahedral sites. With an increase in grade biotite becomes more Mg-rich and Fe-poor resulting in decreasing X_{Mg} (Fig. 3.16 & 3.17a). X_{Mg} varies from sample means of 0.67–0.41 in the biotite and garnet zones, 0.59–0.34 in the staurolite and kyanite zones, and 0.59–0.35 in the sillimanite and sillimanite+K-feldspar zones. A notable drop in X_{Mg} occurs at the garnet isograd where garnet sequesters Fe as it grows (Fig. 3.17a).

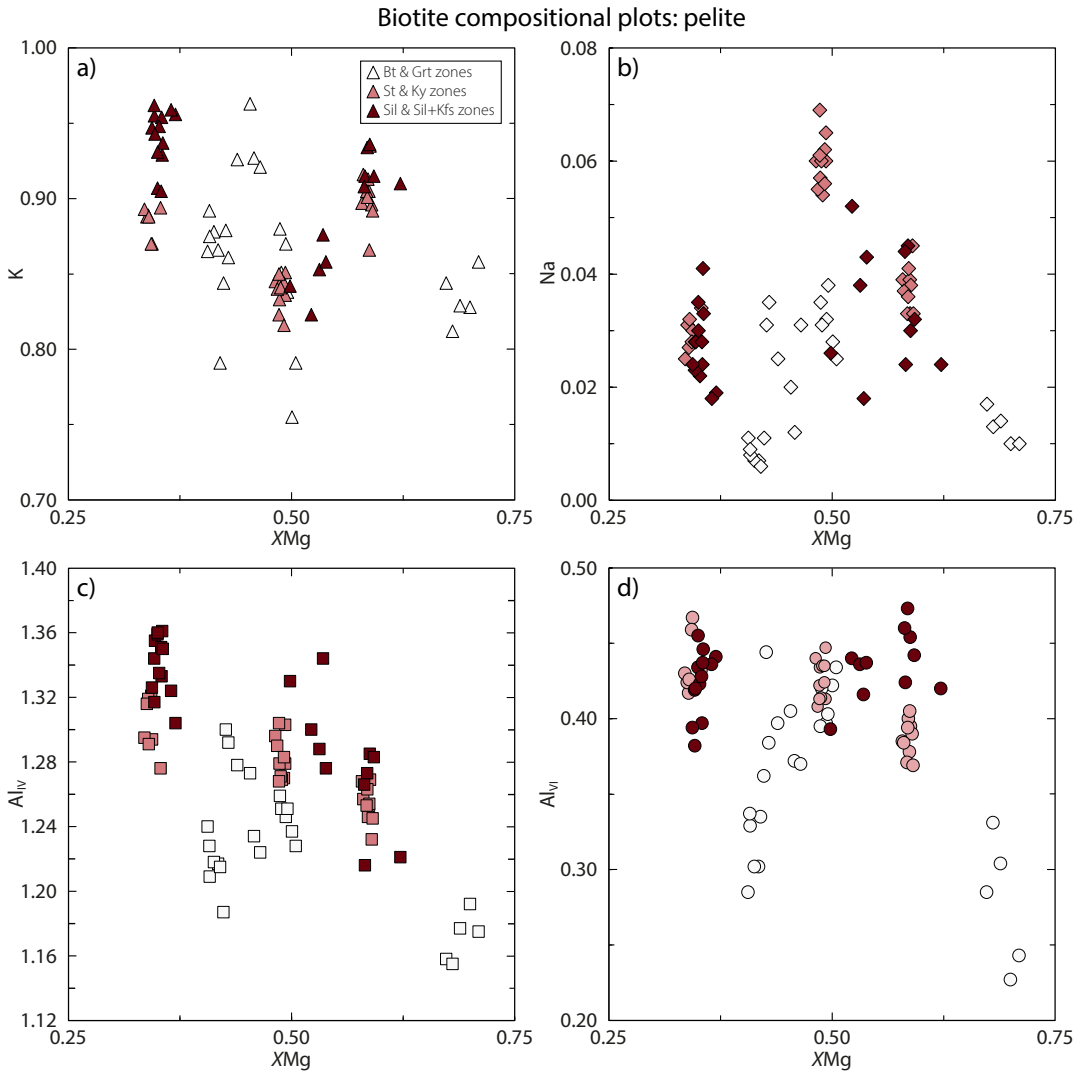


Fig. 3.16 Major substitutions in biotite grouped by metamorphic grade (biotite & garnet zones; staurolite & kyanite zones, sillimanite & sillimanite+K-feldspar zones). Trends display variation in bulk composition and/or metamorphic grade for X_{Mg} vs a) K, b) Na, c) $\mathrm{Al_{IV}}$, and d) $\mathrm{Al_{VI}}$ apfu.

2. Tschermak substitution Al-(Fe,Mg)-Si for eastonite away from the ideal phlogopite-annite end-members (Fig. 3.16c, d & 3.17c). It occurs with the contemporaneous substitution of Al $\rightarrow$ (Fe,Mg) in the trioctahedral site and is balanced by Al $\rightarrow$ Si in the tetrahedral site. Al_{IV}, a proxy for Si, shows a negative correlation with X_{Mg} and thereby positive correlation with increasing grade. Al_{VI} shows a weak negative correlation with X_{Mg} and slight increase at higher grades. Si and total Al are inversely correlated whilst $\mathrm{Fe^{2+}}$+Mg and Si are positively correlated (Fig. 3.17c). Although it is generally inferred to be related to bulk-composition, an indirect metamorphic grade dependence can be observed (Fig. 3.17c).

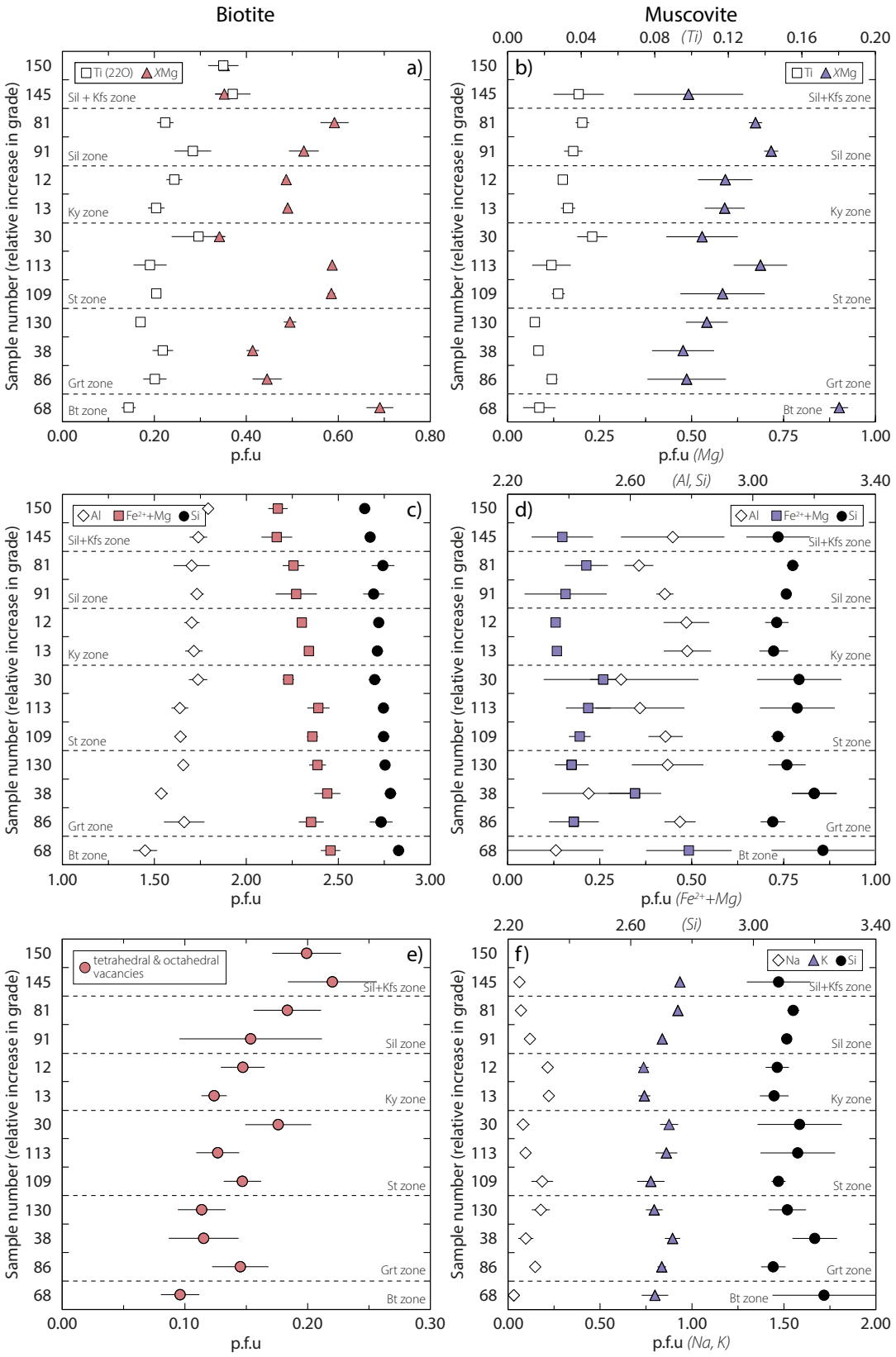


Fig. 3.17 Biotite and muscovite compositional variation plotted against increasing metamorphic grade: a, b) Ti apfu and X_{Mg}; c, d) Al, Fe^{2+} + Mg, and Si apfu; e) tetrahedral and octahedral vacancies in biotite, and f) Na, K, and Si apfu in muscovite. *N.b.* Ti-in-biotite is plotted according to 22 oxygens, in accordance with the calibrations of Henry *et al.* (2005); Wu & Chen (2015), and muscovite according to 11 oxygens.

3. Na-K substitutions in the interlayer site (e.g., Phlogopite to Na-phlogopite; Fig. 3.16a, b). Ignoring low-K values in the biotite zone, K cations are inversely correlated with X_{Mg} and show an overall increase from low- to high-grade. Na is positively correlated with X_{Mg} and shows an overall increase from the biotite zone to kyanite zone and then decreases as grade increases into the sillimanite and sillimanite+K-feldspar zone.

4. A series of "fake" end-members also exist in the thermodynamic dataset to represent the influence of other cations on biotite composition. A key example would be Ti-biotite (White *et al.*, 2014b), which accounts for Ti substitution in octahedral sites. The method by which this charge is compensated is debated (Dymek, 1983; Guidotti, 1984; Waters & Charnley, 2002). A statistical approach presented by Waters & Charnley (2002) shows that introduction of Ti involves de-protonation of two OH groups per Ti, and replacement of some octahedral Al by Ti is balanced by increases in K and/or Si from other sites. Ti content shows an overall increase with relative increase in grade, in contrast to X_{Mg} (Guidotti *et al.*, 1977). This correlation is used to define the Ti-in-biotite thermometer (e.g., Henry *et al.*, 2005).

5. The solution model parameters for biotite as used in White *et al.* (2014b) require that all sites are filled with no vacancies, meaning the octahedral and tetrahedral cations must sum to 7 exactly. However, natural samples show that vacancies in the octahedral and tetrahedral sites are common and are directly proportional to a relative increase in metamorphic grade (Fig. 3.17e). Furthermore in this solution model scheme, silicon is not directly calculated and Al_{IV} is not evaluated - this commonly results in a systematic mismatch of natural and modelled values between Si and Al (e.g., Waters, 2019).

3.2.2.6 Muscovite

Muscovite chemistry was plotted to document key cation substitutions. White mica has the following major end-members for which there are thermodynamic

data:

$KAl_2\,[AlSi_3]\,O_{10}(OH)_2$: muscovite

$NaAl_2\,[AlSi_3]\,O_{10}(OH)_2$: paragonite

$CaAl_2\,[Al_2Si_2]\,O_{10}(OH)_2$: margarite

$K[MgAl]\,[Si_4]\,O_{10}(OH)_2$: Mg-Al-celadonite

$K[FeAl]\,[Si_4]\,O_{10}(OH)_2$: Fe-Al-celadonite

White mica compositions can be treated as ternary solid solution between K-Na-Ca (Coggon & Holland, 2002; Smye *et al.*, 2010). Ca-substitution is not considered, as muscovite compositions contain very low Ca and margarite is rarely seen in nature (White *et al.*, 2014b). A variety of substitutions takes place between the end-members as well as other variations with grade and/or bulk composition:

1. The tschermak substition, AlAl for Si(Fe,Mg), or as more appropriate for muscovite - the phengite substitution, is the dominant substitution of interest for thermobarometric calculations. This substitution results in celadonite end-members and forms a range of compositions known as phengites. Celadonite content in phengites are monitored by Si content, which is 3 in pure muscovite and up to 3.9 in Si-rich phengites. Phengite substitution (increasing Si) results in less Al-rich compositions. Higher grades generally have slightly lower Si contents, and lower associated Fe^{2+}+Mg. These are inversely correlated with increasing Al. This is observed in Figure 3.17d, and Figure 3.18c which show a positive correlation between Si and Mg (e.g., Mg-Al-celadonite). Fe^{2+} does not correlate as strongly as Mg (Fig. 3.18d; e.g., Fe-Al-celadonite). This may result from Fe^{3+} substitution for Al on octahedral sites. Fe^{3+} cannot be distinguished from Fe^{2+} on the EPMA nor reliably recalculated from Fe^{2+}. High levels of Mg and Fe at low-grade samples (Fig. 3.18c, d) may be attributable to celadonite or ferri-muscovite, though may also relate to inter-layer chlorite at low-grades.

2. The other key substitution relating to phengite is paragonite content (represented by Na cations). There is a negative correlation between Na content and Si, this is a result of the incompatibility of Na in phengite (Guidotti, 1984), such that as phengite content increases, paragonite content increases. The substitution towards the end-members is documented on Figures 3.17f and 3.18a, b. Na content increases from biotite zone to kyanite zone, but then reduces in the sillimanite and sillimanite+K-feldspar zones in line with paragonite becoming destabilised (in line with decreasing plagioclase

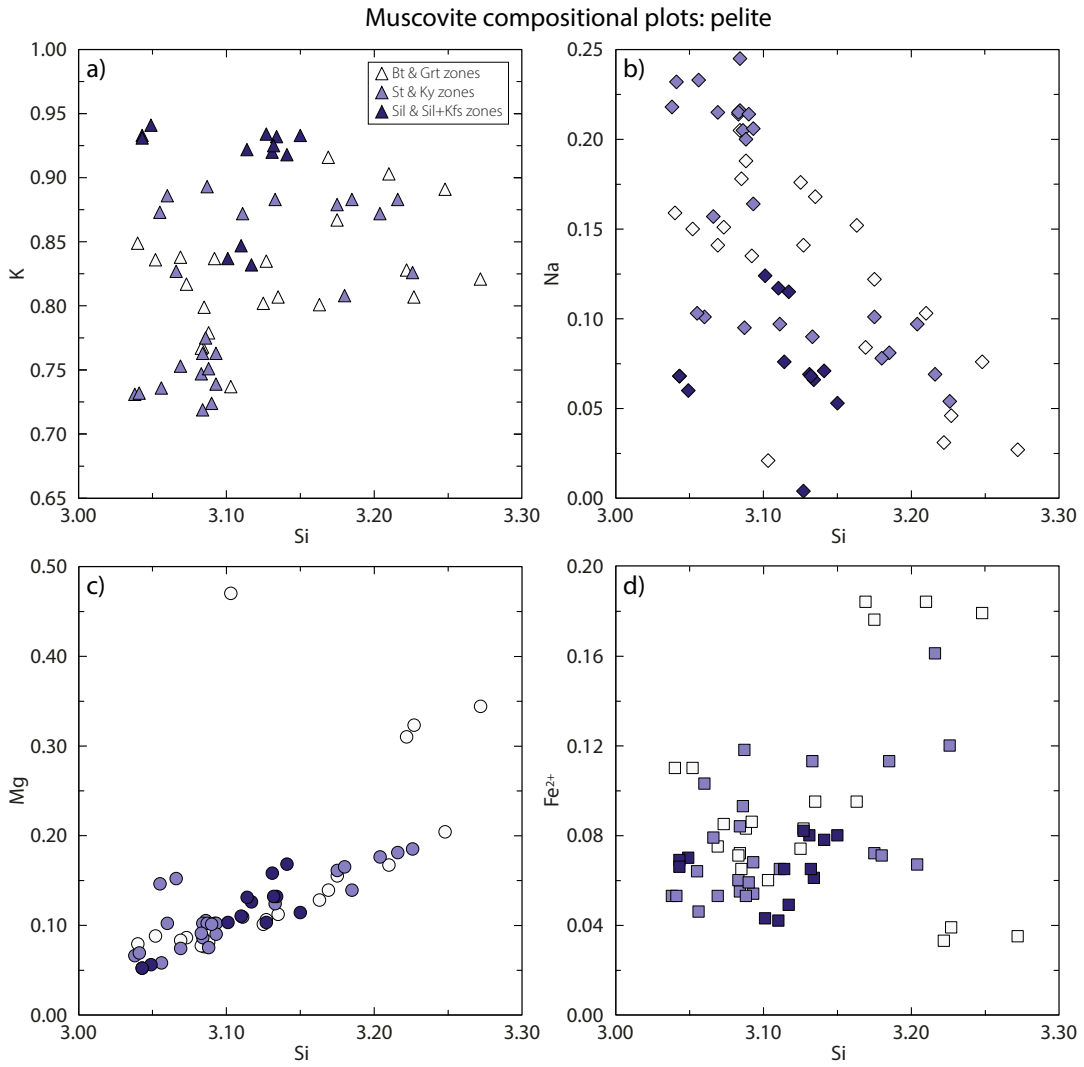


Fig. 3.18 Major substitutions in muscovite with data grouped by metamorphic grade (biotite & garnet zones; staurolite & kyanite zones, sillimanite & sillimanite+K-feldspar zones). Trends display variation in bulk composition and/or metamorphic grade, for Si vs a) K, b) Na, c) Mg, and d) Fe^{2+} apfu.

content). The result is that K is therefore inversely correlated with Na content, but positively correlated with Si content (Figures 3.17 & 3.18a).

3. Similar to biotite, muscovite shows a regular decrease in X_{Mg} with grade with a negative correlation to increasing Ti. Ti concentrations are about ~4–7 times lower than those for biotite from the same samples. 2 SD on X_{Mg} in muscovite shows considerably more variation than in biotite, though mean values appear to show overall less bulk compositional variation than documented for biotite.

3.2.3 Metabasic units

3.2.3.1 Amphibole

Changes in the chemistry of amphibole is useful for detecting change in metamorphic grade as amphiboles are ubiquitous and volumetrically significant in a metabasic sequence. A generalised chemical formula for the amphibole mineral group (e.g., Leake, 1978; Hawthorne *et al.*, 2012) is expressed as:

$$A_{0-1}\ B_2C_5\ T_8O_{22}\ W_2$$

Where:

$A : \square$ (vacancies), Na, K, Ca, Pb, Li

$B : Na, Ca, Mn^{2+}, Fe^{2+}, Mg, Li$

$C : Mg, Fe^{2+}, Mn^{2+}, Al, Fe^{3+}, Mn^{3+}, Cr^{3+}, Ti^{4+}, Li$

$T : Si, Al, Ti^{4+}, Be$

$W : (OH), F, Cl, O^{2-}$

C in the formula corresponds to the octahedral sites: M1, M2, M3, and B corresponds to M4. M13 represents two M1 and one M3. A version more relevant to the amphiboles of this study would be:

$$A_{0-1}M4_2M13_3M2_2T_8O_{22}(OH)_2$$

Where:

M2 (small octahedron): $Al, Cr, Fe^{3+}, Ti, Fe^{2+}, Mg$

M1 + M3 (medium octahedra): Fe^{2+}, Mg, Mn

M4 (larger cation site): Ca, Na, Mn, Fe^{2+}, Mg

Amphibole structure is generally monoclinic though some amphiboles lack A-site cations and contain Fe and Mg in all M-sites, creating an orthorhombic structure. The majority of compositional variation in amphiboles from the transitional greenschist–amphibolite facies to upper amphibolite facies relate to changes in the cations within the A, M2, M1+M3, M4 (C), and T sites. The common coupled vector and homovalent substitutions for monoclinic amphiboles are:

$$\text{Tschermakite vector} = {}^{\text{C}}\text{Al}^{\text{T}}\text{Al}^{\text{C}}\text{Mg}^{\text{T}}_{-1}\text{Si}_{-1}$$
$$\text{Edenite vector} = {}^{\text{A}}\text{Na}^{\text{T}}\text{Al}^{\text{A}}\square^{\text{T}}_{-1}\text{Si}_{-1}$$
$$\text{Glaucophane vector} = {}^{\text{B}}\text{Na}^{\text{C}}\text{Al}^{\text{B}}\text{Ca}^{\text{C}}_{-1}\text{Mg}_{-1}$$
$$\text{Mg}^{2+} \leftrightarrows \text{Fe}^{2+}$$
$$\text{Al}^{3+} \leftrightarrows \text{Fe}^{3+}$$
$$\text{Al}^{3+} \leftrightarrows [\text{Fe}_{0.5}\text{Ti}_{0.5}]^{3+}$$

These substitutions can be quantified relative to end-member tremolite. Site allocations and amphibole classification follow Hawthorne *et al.* (2012). The resulting substitutions and classification diagrams are plotted in Figure 3.19. Amphiboles from select samples can be classified as follows in the various isograd zones: hornblende zone varies from actinolite–magnesiohornblende in composition, oligoclase zone from magnesiohornblende–pargasite (limited sample set), and garnet+plagioclase zone which contains 'hornblende' of the composition magnesiohornblende, pargasite, tschermakite, and minor ferrotschermakite. The compositional change from actinolite to hornblende in the hornblende zone is defined by an increase in the A-site occupancy (also defining the edenite vector), as well as Al, Fe^{3+}, Ti (C-site occupancy), and a decrease in X_{Mg} and Si. The tschermakite component shows a considerable increase over the hornblende zone with the growth of hornblende concurrent with smaller increases in the edenite and small increases in the glaucophane component (Na in M4). Similar compositional trends across the greenschist–amphibolite facies transition are also noted by Starr *et al.* (2020). In the oligoclase zone and garnet+plagioclase zone the A-site occupancy (also defining edenite component) shows an overall increase from hornblende in the hornblende zone, and continued increase of the tschermakite component (trending towards pargasite). Hornblende from the oligoclase and garnet+plagioclase zones have a fairly consistent glaucophane component with the exception of one sample in the garnet+plagioclase zone (ICSV144), which shows low glaucophane values. This samples is distinct in location, corresponding to the sillimanite zone of the pelitic sequence (i.e., lower-pressure); and microstructure, displaying hornblende growth as a late corona around clinopyroxene. X_{Mg} values are slightly lower than analyses of hornblende from the hornblende zone, though they show a greater variation. Si values overlap with those from the hornblende zone though are dominantly lower as grade increases.

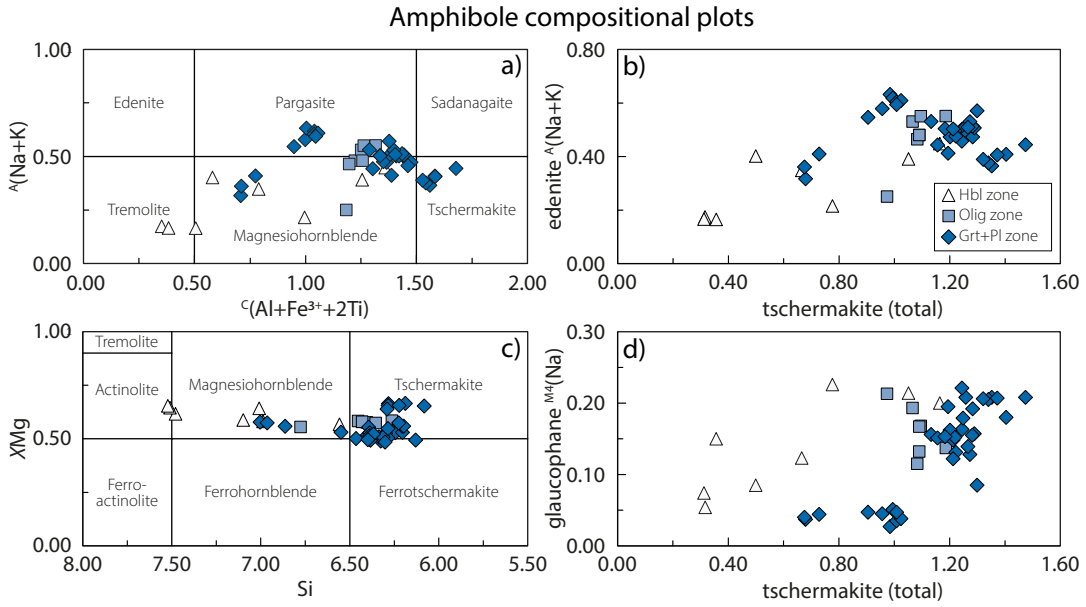


Fig. 3.19 Amphibole compositional plots with data grouped by metamorphic grade (hornblende, oligoclase, and garnet+plagioclase zones. a) ^{C}(Al+Fe^{3+}+2Ti) vs ^{A}(Na+K) amphibole classification diagram, b) tschermakite vector vs edenite vector, c) Si apfu vs X_{Mg} amphibole classification diagram, and d) tschermakite vector vs glaucophane vector. Fields for amphibole classification follow Hawthorne *et al.* (2012).

3.2.3.2 Garnet

Bulk composition variations at lower grades locally produce unique garnet-bearing amphibolites in the hornblende zone. However, garnet is dominantly only present in metabasic rocks in the garnet+plagioclase zone. As a result, only a small subset of garnet zoning profiles are documented. Zoning profiles are presented in Figure 3.20. A comparison of core and rim values, separated by metamorphic grade, is documented on Figure 3.21. Selection of representative points is consistent with the outlined procedure for pelitic assemblages.

The greatest compositional zoning is recorded at lower grades, with minimal composition zoning in garnet in the garnet+plagioclase zone. Based on these observations, and consistent with higher X_{Sps}, it is possible that garnet locally grew early in ICSV50 as no other sample at these grades contains garnet, thereby allowing for a more prolonged period of garnet growth. Therefore, in the higher-grade garnet+plagioclase zone, garnet likely grew late and record a homogenous composition such that core and rim domains are likely both within error of metamorphic "peak". This interpretation is preferred over diffusion and late

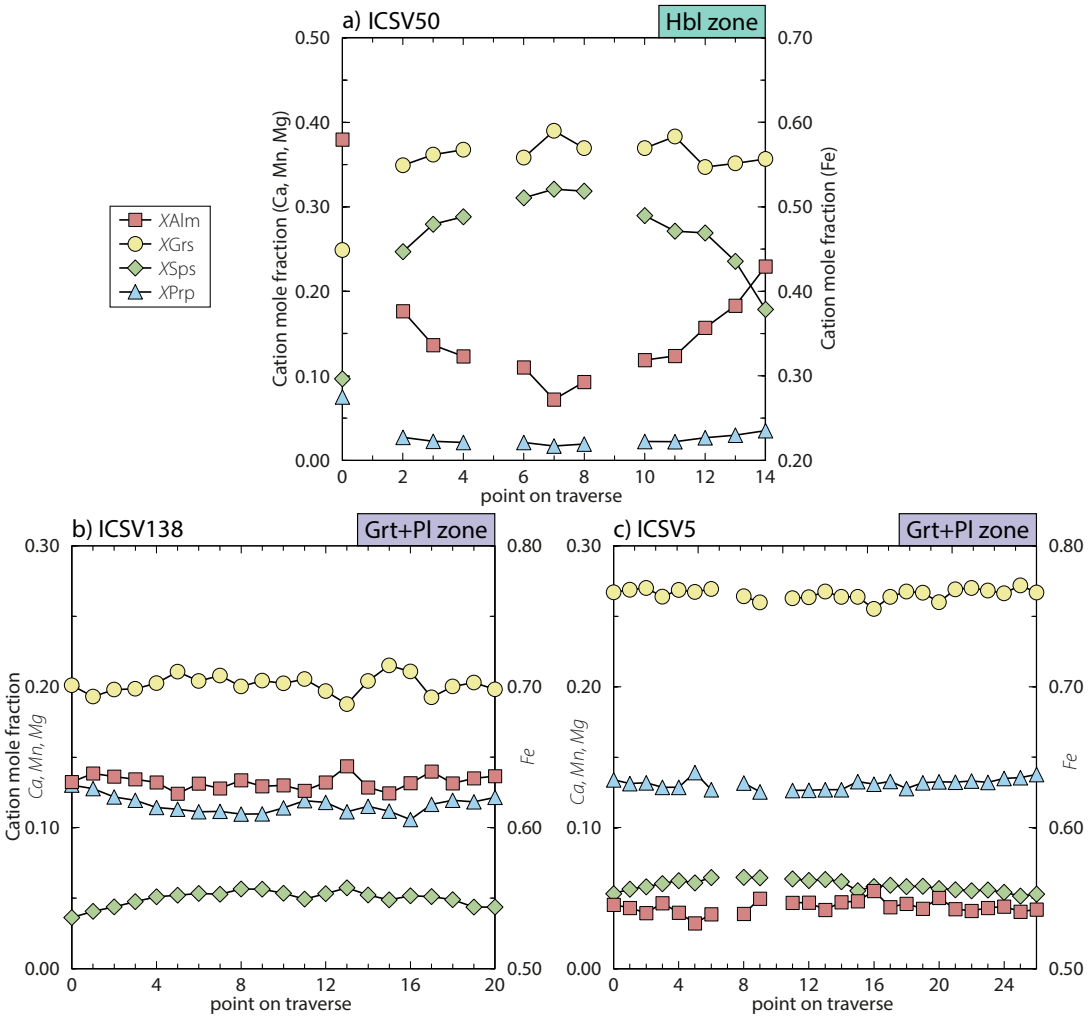


Fig. 3.20 Representative garnet compositional profiles from a) hornblende-zone, and b, c) garnet+plagioclase-zone samples. Line profiles are non-continuous due to traverses crossing over inclusions and fractures, such points are excluded from the profiles. *N.b.* Hornblende-zone samples contain albite rather than "plagioclase" which is used in this study to refer to samples without albite compositions, $X_{\mathrm{Na}} < 0.90$. Furthermore the sample records a high spessartine content, which is anomalous within the dataset. This differentiates the sample from those located in the garnet+plagioclase zone.

resorption given no upward Mn inflections are observed in any samples, particularly those at lower grades.

3.2.3.3 Plagioclase

The variation in feldspar composition with grade is plotted in Figure 3.22. In the hornblende zone, feldspar is albitic in composition ($Ab_{99–97}$). Progressing to the oligoclase isograd, plagioclase becomes progressively more calcic (as determined

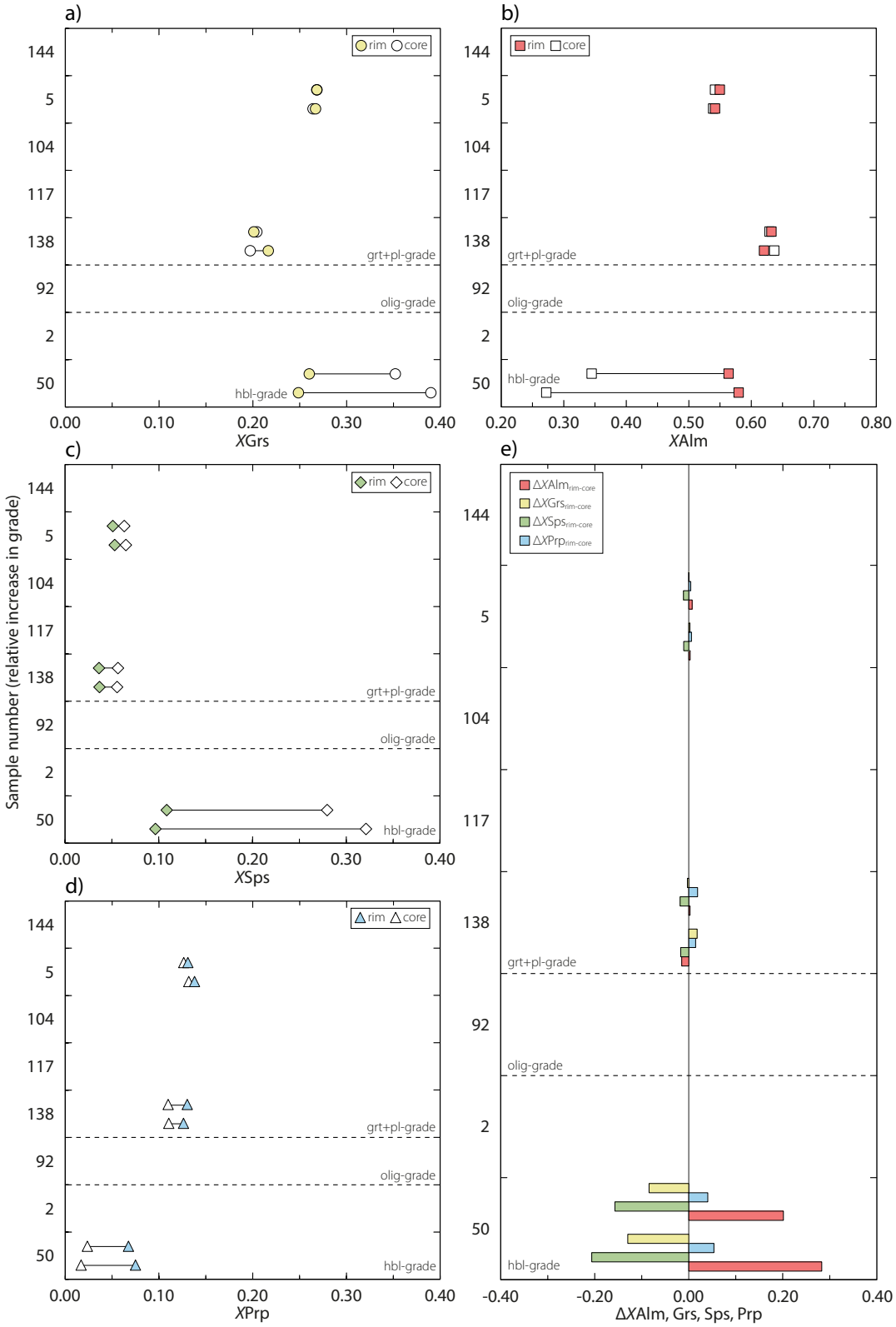


Fig. 3.21 Garnet core and rim values for a) X_{Grs}, b) X_{Alm}, c) X_{Sps}, and d) X_{Prp} plotted for increasing grade with relative grade denoted by dashed line between samples. e) The $\Delta_{\mathrm{rim-core}}$ for each end-member against increasing metamorphic grade.

through optical means). Only one sample was analysed from the oligoclase zone and the chemical composition is Ab_{83}. At higher grade plagioclase becomes progressively more calcic, such that in the garnet+plagoclase zone it is defined by a oligoclase–andesine composition ($Ab_{79–66}$). 2 SD of samples shows an approximate increase with relative increase in metamorphic grade. At higher grade, locally albitic compositions are present in both peak and retrograde assemblages depending on the given sample. The first andesine composition is within the garnet+plagioclase zone and is largely equivalent to the kyanite isoagrad in the pelitic sequence (Figs. 2.15 and 2.16). When clinopyroxene becomes stable in the assemblage the composition is consistently andesine in composition, as also documented by Honegger (1983). In the high-grade clinopyroxene bearing assemblages, K-feldspar is stabilised and composition is Or_{96}.

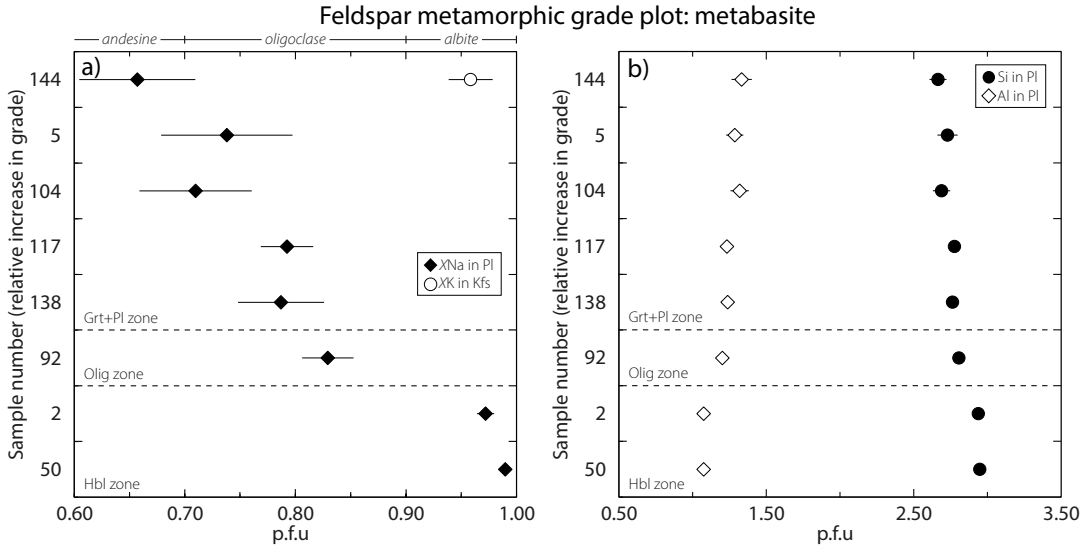


Fig. 3.22 Variation in feldspar composition with increasing metamorphic grade. a) X_{Na} and X_K for plagioclase and K-feldspar respectively and b) Si and Al apfu in plagioclase.

3.2.3.4 Chlorite

Chlorite from metabasite samples are plotted in Figure 3.23. Si cations vary from 2.64–2.88, with the greatest range expressed by samples in the garnet+plagioclase zone and samples from lower grades showing more restricted ranges. Octahedral Al varies from 1.21–1.53, showing a minor decrease in values with increasing grade and showing a weak inverse correlation with Si. Fe^{2+} shows the opposite relationship with a range of values from 1.13–2.31 apfu (Fig. 3.23a). As consitent with trends in other micas, chlorite shows a weak decrease in X_{Mg} (0.75–0.48)

with grade and minor increase in Ti concentrations (0.003–0.013 apfu). Overall chlorite shows less distinct compositional trends with metamorphic grade than observed in other micas. Compositionally chlorite is ripidolite in the hornblende zone and ripidolite or pycnochlorite in the oligoclase and garnet+plagioclase gzones, based on the classification scheme of Hey (1954).

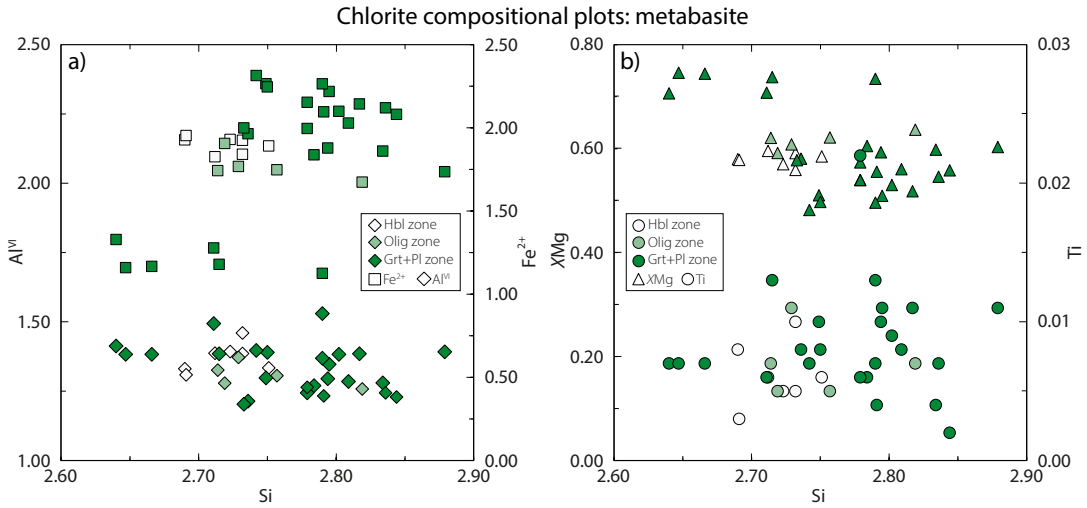


Fig. 3.23 Compositional scatter plots for chlorite within metabasite: a) Al^{VI} or Fe^{2+} apfu vs Si apfu and b) X_{Mg} or Ti apfu vs Si apfu. Chlorite from the hornblende zone is interpreted as prograde–peak, while chlorite from the oligoclase zone and garnet+plagioclase zone is interpreted as metastable and/or retrograde.

3.2.3.5 Biotite

Similar substitutions and cation grade variations occur in biotite from the metabasites as those documented in biotite from the pelitic sequence. ICSV138 and ICSV104 contain only minor ragged biotite and EPMA results suggest two populations of biotite that are best defined by variations of Ti. The microstructural context of grains and chemical variation was used to define a dominant and minor phase for each sample. It is inferred that those with lower Ti as well as a small and ragged shape in ICSV138 represent an earlier phase of growth prior to peak, whilst those in ICSV104 with higher Ti may represent late biotite growth after ilmenite, though the latter are poorly equilibrated. These minor growth phases are plotted with smaller symbols in Figures 3.24 and 3.25.

1. Phlogopite to annite substitution (Fe-Mg) shows biotite becoming more Mg-rich and Fe-poor resulting in a slight overall decrease to X_{Mg} (Fig. 3.25). X_{Mg} varies from sample means of 0.55 in the hornblende zone, 0.58

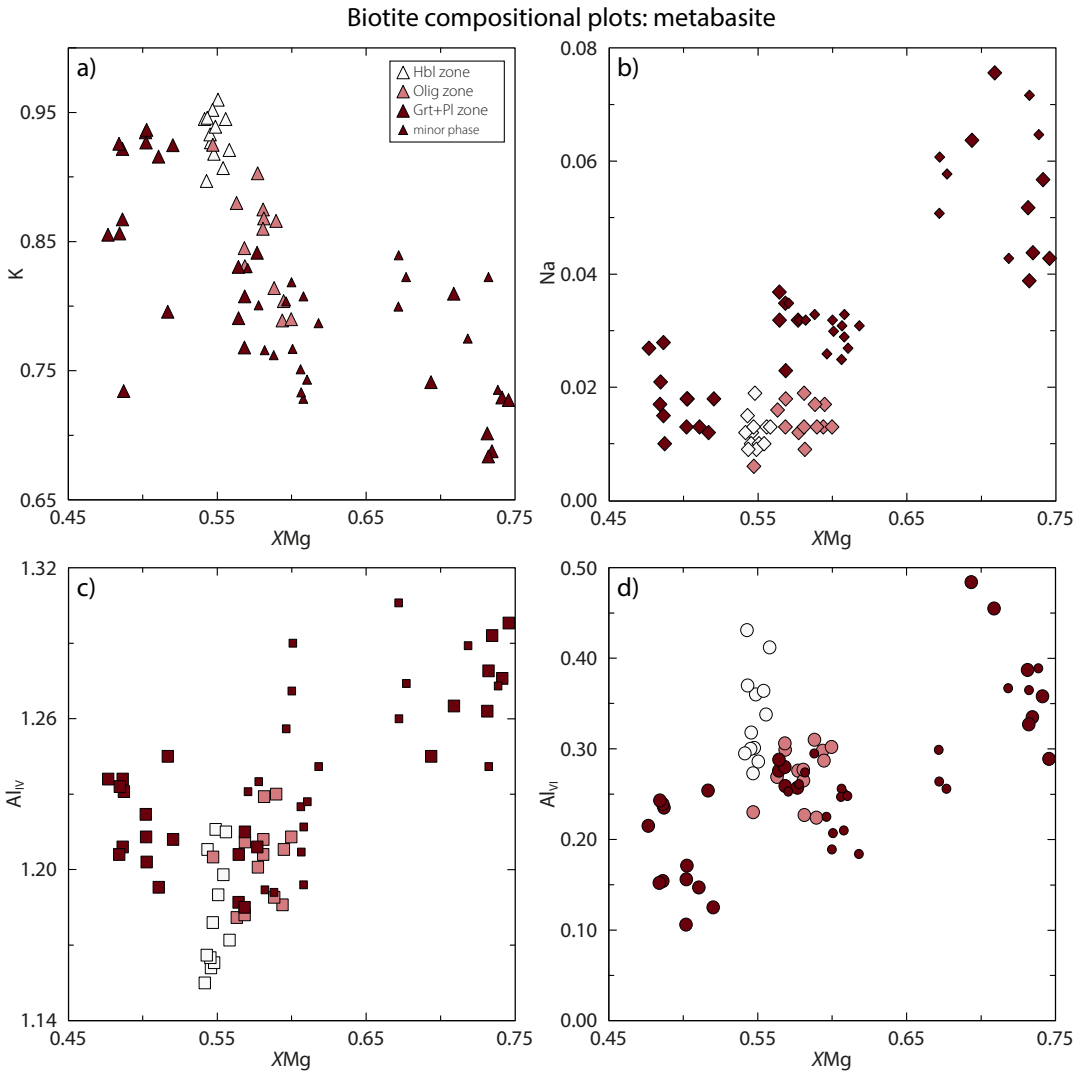


Fig. 3.24 Major substitutions in biotite in metabasite grouped by metamorphic grade (hornblende, oligoclase, and garnet+plagioclase zones). Trends display variation in bulk composition and/or metamorphic grade for X_{Mg} vs a) K, b) Na, c) $\mathrm{Al_{IV}}$, d) $\mathrm{Al_{VI}}$ apfu.

in the oligoclase zone (one sample), 0.57–0.49 in the garnet+plagioclase zone with one high sample at 0.70. This results in two clear X_{Mg} groupings as separated by samples within the greenschist–amphibolite transition zone and lower amphibolite facies (hornblende and oligoclase zones) vs upper amphibolite facies (garnet+plagioclase zone). This drop in X_{Mg} at higher-grades could relate to garnet growth, however, not all samples contain garnet. Notably most samples containing biotite do not contain garnet, and vice versa, implying that nucleation of garnet comes at the expense of biotite growth by sequestering the Fe and Mg required for biotite, or

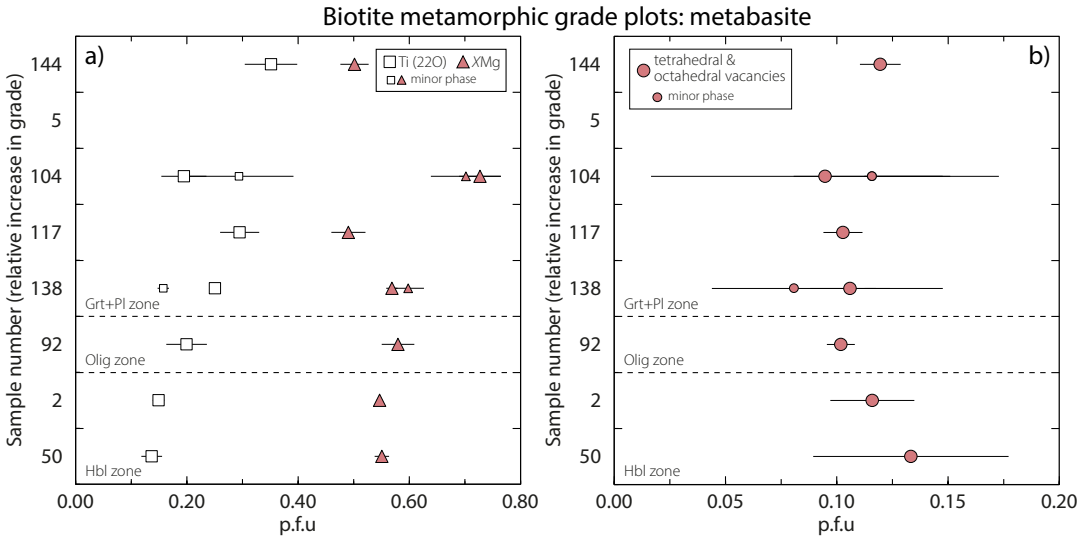


Fig. 3.25 Variation in biotite composition plotted against increasing metamorphic grade: a) Ti apfu and X_{Mg}, b) tetrahedral and octahedral vacancies. *N.b.* Ti-in-biotite is plotted according to 22 oxygens (in accordance with the calibrations of Henry *et al.* (2005); Wu & Chen (2015).

breaking down biotite to form garnet. Significant variation at higher grades may also relate to varying bulk composition.

2. Tschermak substitution (Al-(Fe,Mg)-Si) is recorded as grade increases with Al content decreasing in exchange for Fe+Mg, Si. Al_{IV}, a proxy for Si, shows a negative correlation with X_{Mg} and shows an increase moving to higher grades (Fig. 3.24c). Al_{VI} shows a positive correlation with X_{Mg}, both decreasing as grade increases (Fig. 3.24d). Si and total Al are inversely correlated whilst Fe^{2+}+Mg and Si are positively correlated.

3. Na-K substitutions in the interlayer site (Fig. 3.24a–b). K-cations are inversely correlated with X_{Mg}. Na is positively correlated with X_{Mg}. No significant trends can be deconvolved with grade owing to the large spread in X_{Mg} compositions in the garnet+plagioclase zone.

4. Ti shows a consistent increase with grade and is inversely correlated with decreasing X_{Mg} (Fig. 3.25a).

5. There is no consistent relationship observed between an increase in metamorphic grade and octahedral and tetrahedral vacancies. It appears vacancies first decrease with increasing grade from the hornblende zone to the start of the garnet+plagioclase zone. With increasing metamorphic conditions in the garnet+plagioclase zone, octahedral and tetrahedral vacancies then

increase (Fig. 3.25b). Large variation in vacancies are associated with the analyses of biotites from samples ICSV138 and ICSV104.

3.2.3.6 Epidote

Epidote is stable in metabasic assemblages until a few kilometres beyond the oligoclase isograd where it disappears. ICSV92, coinident with the staurolite isograd in the pelitic sequence, is the last analysed sample before epidote-out. The dominant compositional variation observed within epidote bearing metabasites of the Suru valley region is expressed through the exchange of Fe^{3+} and Al (this may therefore be expressed as $X_{\mathrm{Fe}}\left(\frac{\mathrm{Fe}^{3+}}{\mathrm{Al}+\mathrm{Fe}^{3+}}\right)$. Weak exchange of Mn with Al, Fe^{3+} also occurs, though Mn concentrations are generally very low (locally piemontite has been identified). Al shows an overall decrease with increasing grade, whilst it is exchanged for increasing Fe^{3+}. Compositional zoning in epidote is common with X_{Fe} rich cores and X_{Fe} poorer rims.

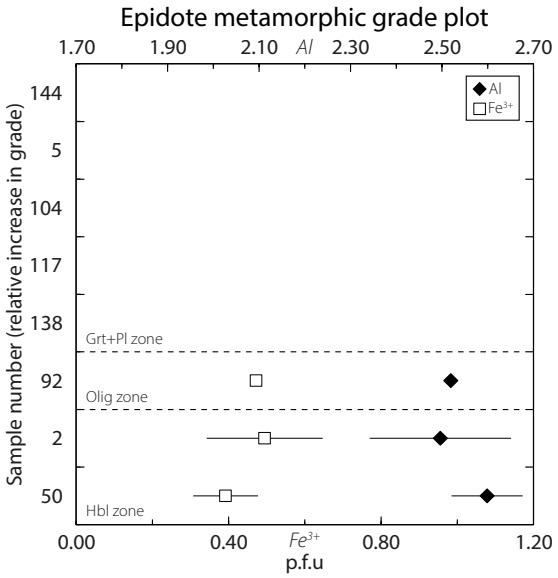


Fig. 3.26 Epidote substitution (Fe^{3+} and Al apfu) plotted against increasing metamorphic grade. Sample ICSV92 does not include 2 SD error as only one spot analysis was collected.

3.3 Comparison of pelitic and metabasic mineral chemistry and textures

Prominent changes in the assemblage and chemistry of mineral phases occur during progressive metamorphism in pelitic sequences (Albee, 1968; Guidotti,

1974; Labotka, 1980; Hiroi, 1983; Lang & Rice, 1985) and metabasic sequences (Cooper, 1972; Maruyama *et al.*, 1983; Bégin, 1992; Powell *et al.*, 1995; Starr *et al.*, 2020). Locally, these changes have also been documented together in metamorphic terrains: including Sanbagawa Belt, Japan (Banno & Sakai, 1989); Isua Greenstone Belt, Greenland (Hayashi *et al.*, 2000; Komiya, 2002; Arai *et al.*, 2015); Dharwar Craton, India (Raase *et al.*, 1986); Andes, Colombia (Ríos *et al.*, 2003); Scandinavian Caledonides (Boyle, 1986); Aegean, Greece (Katagas, 1980); Banda Arc, Indonesia (Kadarusman *et al.*, 2010); and Iberian Massif, Spain (Egufluz & Abalos, 1992). However, few studies have integrated and compared these changes over a complete greenschist- to amphibolite-facies metamorphic sequence. Using both rock sequences allows an assessment of what may be reliably integrated from the rock sequences.

Pelites show significant changes in mineral assemblage over greenschist- to amphibolite-facies conditions, however mineral assemblage changes in metabasite are concentrated over the greenschist- to amphibolite-facies transition zone, but otherwise remain constant. In comparison, metabasic bulk rock compositions remain remarkably consistent, yet display continuous mineral chemical changes (e.g., Raase *et al.*, 1986; Labotka, 1987; Starr *et al.*, 2020). Protolith composition exerts an important control on the chemistry of mineral phases. The timing, mechanism and rate of growth of different minerals also varies. Therefore, whilst not all mineral chemistry and textures are directly comparable in pelitic and metabasic assemblages, a comparison of the relative chemical trends and stability of phases, emphasises the key substitutions and reactions that take place and whether they are dominantly impacted by bulk composition and/or increasing metamorphic grade. Furthermore, treating the Suru Valley region as an analog for regional metamorphic sequences, emphasises what information may reliably be extracted from pelitic and metabasic units across varying grades. The following points of comparison can be highlighted:

1. Both pelitic and metabasic assemblages show an overall slight decrease in X_{Mg} for all plotted minerals excluding garnet with increasing grade (Fig. 3.27a, c). Garnet rims generally shows a slight increase in X_{Mg}, sequestering Fe from the system. The X_{Mg} of major Fe-Mg bearing matrix phases in the metabsites (Amph, Bt, Chl) are closely correlated, implying larger shifts in X_{Mg} (e.g., ICSV104) relate to varying bulk composition. In certain pelitic samples the X_{Mg} of muscovite is less strongly correlated to the X_{Mg} of other micas. This may relate to the inability to reliably calculate and distinguish Fe^{3+} from Fe^{2+}.

Comparing the activities and contents of major phases in feldspars and 'interlayer' components in micas and amphiboles shows an overall decrease in Na contents in exchange for Ca in feldspars, and decrease in Na in exchange for K in biotite (decreasing X_{K}). This is buffered by a slight increase in Na content in muscovite in the pelitic sequence (increasing X_{K}) and an increase in A-site substitution in the amphiboles in the metabasitic units (Fig. 3.27b, d).

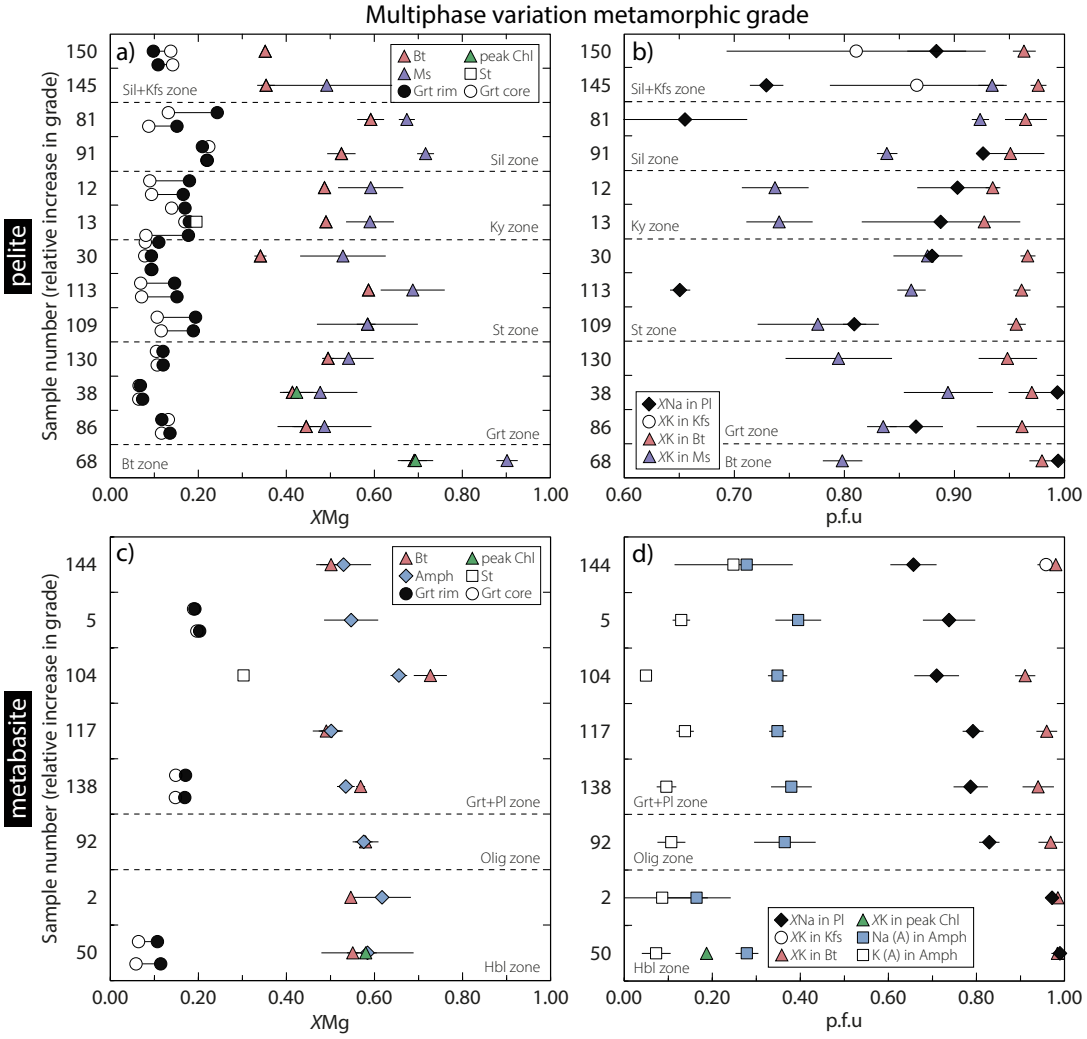


Fig. 3.27 Multiphase compositional variation plotted against relative increase in metamorphic grade for pelite and metabasite. Pelite: a) X_{Mg} vs relative increase in metamorphic grade for garnet rim and core, staurolite, biotite, muscovite, and prograde–peak chlorite. b) X_{Na} in plagioclase, and X_{K} in K-feldspar, muscovite, and biotite. Metabasite: c) X_{Mg} vs relative increase in metamorphic grade for garnet rim and core, amphibole, staurolite, biotite, and prograde–peak chlorite, and d) X_{Na} in plagioclase; X_{K} in K-feldspar, chlorite, and biotite; and A-site Na and K contents in amphibole. Chlorite does not include the 2 SD error bars as they are large and make plot readability limited.

2. As garnet is stable across most of the pelitic sequence, but only stable at higher grades in the metabasic sequence, the scale of comparison is limited. Microstructurally, garnets in the pelitic sequence show a range of sizes, often correlated with the lithology, and at higher grades can show obvious core and rim structures. In comparison the metabasic sequence dominantly records garnets on the scale of 0.5–2.0 cm with no obvious core and rim structures. Both pelitic and metabasic sequences are dominated by the almandine end-member, however, the metabasic sequence has notably higher X_{Grs}. The pelitic sequence shows the expected trend of garnet compositional zoning, whereby the difference between core and rim compositions increase to a maximum at the kyanite zone, with higher grades subject to progressive diffusion re-equilibration of the core compositions. Metabasic units show limited compositional zoning, with greatest compositional zoning recorded in the lowest-grade garnet-bearing metabasic sample. Medium- to high-grade garnet-bearing samples record dominantly flat zoning (Fig. 3.20 & 3.21). Bulk composition has minimal impact on the relative stability of garnet after the garnet isograd in pelitic sequences but has more significant control over the presence or absence of the mineral in metabasites in the garnet+plagioclase zone.

3. Plagioclase is present across all grades in the pelitic and metabasic sequence and K-feldspar is locally present in the highest grade samples from both units (Fig. 3.28). Plagioclase consistently occurs as a matrix phase in both pelitic and metabasic assemblages. Locally plagioclase also occurs as porphyroblasts in the garnet and staurolite zones in the pelitic sequence and in the hornblende zone in the metabasic sequence. In the pelitic sequence plagioclase porphyroblasts overgrow the main fabric in the staurolite zone whilst porphyroblasts at lower grades in the pelitic sequence and metabasic sequence are notably sheared and form augen. Metabasic samples show a consistent decrease in feldspar X_{Ab} with increasing grade. Pelitic samples also show an overall decrease in X_{Ab} with increasing grade, but plagioclase composition is marked by significant variation between samples. For example, the staurolite zone is characterised by compositions ranging from ($\mathrm{Ab}_{0.88–0.65}$). The distribution of compositions within individual grades in the pelitic sequence could be due to greater variation in bulk composition in comparison to metabasic samples. More calcic compositions at these grades may also relate to late porphyroblastic growth of plagioclase that is better equilibrated with the surrounding matrix volume. A comparison

of plagioclase compositions from the pelitic sequence to isopleths of other peak mineral compositions in P-T space may resolve this issue.

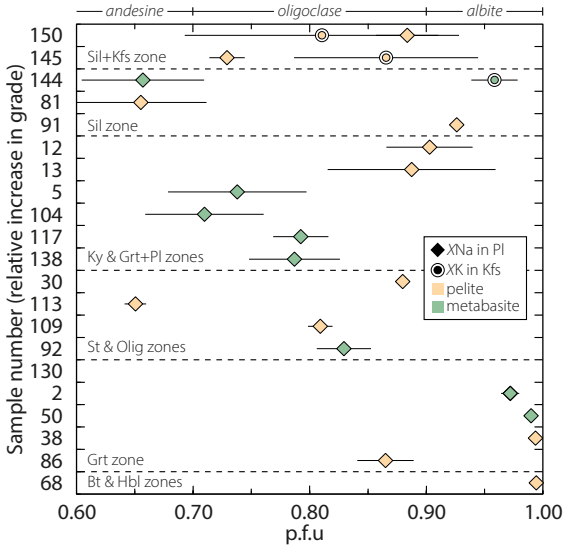


Fig. 3.28 Variation in feldspar composition in both pelitic and metabasic sequence plotted against relative increase in metamorphic grade for X_{Na} and X_{K} for plagioclase and K-feldspar respectively.

4. Chlorite is only stable as a peak phase up to garnet-grade in the pelitic sequence, whilst it is stable into the garnet+plagioclase zone in the metabasic sequence. Prograde chlorite occurs as tabular grains in the pelitic sequence and metabasic sequence at low-grades. At oligoclase- and garnet+plagioclase zone in the metabasic sequence it may occur as mm-scale grains with ragged crystal habit. Chlorite is also abundant as a retrogressive phase across most grades in the pelitic sequence, where it grows in replacement of biotite or during garnet breakdown. Retrograde chlorite is only variably present in the metabasic sequence. Prograde chlorite is dominantly classified as ripidolite (with minor pycnochlorite) and shows similarly weak compositional trends in both rock suites (Figs. 3.15 & 3.23).

5. Biotite is stable across most samples in the pelitic and metabasic sequence as a dominant matrix phase. Biotite occurs as matrix fabric-defining tabular grains in both rock sequences, however, in the metabasite sequence it notably also regularly occurs as coarse mm- to cm-scale porphyroblasts in the hornblende and oligoclase zones. In the garnet+plagioclase zone of the metabasic sequence it is locally present as minor ragged grains (e.g., ICSV138 & ICSV104). A comparison of biotite compositional trends plotted against increasing metamorphic grade is shown in Figure 3.29.

X_{Mg} shows the greatest range and variation across grade in the pelitic sequence, likely resulting from a more variable bulk composition, and thereby mineral composition (Fig. 3.27). The one exception to this is ICSV104, which shows notably elevated X_{Mg} and Ti when compared to the set of metabasite samples, and given the presence of aluminous-rich minerals more commonly associated with pelitic assemblages (e.g., St and Ky), this sample may not be representative of the sequence. In contrast to the pelitic sequence, X_{Mg} of biotite in the metabasic sequence does not appear to show a distinct drop with the nucleation of garnet at the garnet+plagioclase isograd, suggesting other minerals in the sequence may buffer this change, diffusional re-equilibration is limited and/or new biotite does not grow at these grades. X_{Mg} appears more strongly inversely correlated with Ti content in the pelitic sequence than in the metabasic sequence, and this may impact the calibration of Ti-in-biotite thermometers. Ti content shows a more consistent increase in the metabasic sequence compared to the pelitic sequence, again likely owing to the more variable bulk composition in the latter.

Tetrahedral & octahedral vacancies show a relatively consistent increase with grade in the pelitic sequence (Fig. 3.29b). In comparison, the metabasic sequence shows a relative decrease towards oligoclase-grade followed by a minor increase.

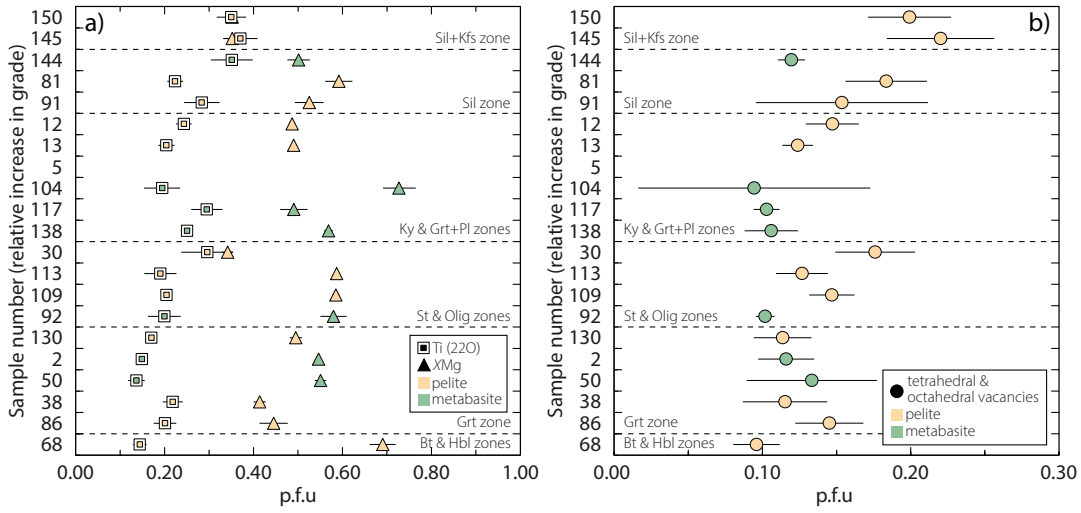


Fig. 3.29 Biotite compositions in both pelitic and metabasic sequence plotted against relative increase in metamorphic grade for a) X_{Mg} and Ti apfu, and b) octahedral and tetrahedral vacancies. Biotite analyses from ICSV138 and ICSV104 exclude minor phases.

6. Other minerals: Ti-oxides are documented in all samples across the pelitic and metabasic suite with the exception of the sillimanite+K-feldspar zone in the pelitic sequence where they are variably documented. In the pelitic sequence, titanite is present as porphyroblastic phase in some lithologies in the biotite zone (Fig. 3.2d), before it is replaced by ilmenite as the dominant Ti-oxide phase across garnet-zone samples. Rutile and ilmenite are dominant across the staurolite, kyanite, and sillimanite zones with ilmenite locally replacing rutile cores. Rutile is commonly observed in kyanite porphyroblasts with a rutile+ilmenite- or ilmenite-dominated matrix (Fig. 3.4b). Ti-oxide relationship is also consistent in high-grade metabasites where rutile (locally ilmenite) is commonly shown in garnet porphyroblasts with rutile or rutile+ilmenite in the matrix. In garnet+plagioclase-zone samples, rutile may be documented in garnet cores with ilmenite in the matrix (e.g., Fig. 3.6e).

   Locally titanite is preserved in garnet cores in kyanite-zone pelitic samples. In the metabasic sequence, fine titanite crystals are aligned to foliation planes in the hornblende zone. In oligoclase- and garnet+plagioclase-zone samples, all three Ti-oxide phases are stable in the assemblage but they are not all inferred to represent metamorphic peak. Where rutile and/or ilmenite are part of the peak metamorphic assemblage, titanite generally occurs as a late polycrystalline phase (Fig. 3.6d) that wraps earlier growth of rutile and/or ilmenite. Unlike the pelitic sequence, ilmenite or titanite are rarely preserved in garnet cores which suggests later growth of garnet in the metabasic sequence and is consistent with the flat compositional profiles of garnets in metabasic rocks(Fig. 3.20). At the highest-grade domain of the garnet+plagioclase zone (equivalent to sillimanite zone of the pelitic sequence), titanite locally occurs as a porphyroblastic phase with primary magmatic textures (see Chapter 5).

   Staurolite is only locally present in staurolite and kyanite zone-samples in the pelitic sequence and locally present in one sample at garnet+plagioclase grade in the metabasic sequence. Staurolite from the metabasites are less Fe-rich resulting in higher X_{Mg} (0.30 vs 0.20).

   Muscovite is locally present in the metabasic sequence, generally as fine (mm- to sub-mm grains), though it is dominant in the sample set across the pelitic sequence up to the sillimanite+K-feldspar zone.

These results suggest that compositional variation may be documented from low- to high-metamorphic grade in pelitic units through trends in garnet and biotite, whilst metabasite show consistent trends in amphibole, biotite, and plagioclase. For subsolidus conditions, mineral assemblage, textural and chemical variation show strongest changes (independent of bulk composition) moving upwards from first the garnet isograd and then kyanite isograd in pelitic sequences. In comparison, in metabasic sequences, significant mineral assemblage and textural change occurs across the hornblende and oligoclase zones, (equivalent to the garnet and staurolite zones in the pelitic sequence), but shows minimal consistent assemblage change after the garnet+plagioclase isograd. Compositional variation of key phases (amphibole, biotite and plagioclase) show consistent chemical trends across all metamorphic grades. Metabasites may be more effective at constraining the relative changes in metamorphic grade over the greenschist–amphibolite facies transition than pelites, whilst the reverse may be true for the amphibolite facies. Effectively documenting and integrating the changes in mineral assemblage, textures and compositional variation of both pelitic and metabasic units across a subsolidus metamorphic sequence will yield significantly greater relative and quantitative information to use in methods of P-T determination.

Chapter 4

Phase Equilibrium Modelling



Folded carbonates at Donara

The techniques use to recover the Pressure-Temperature (P-T) evolution of metamorphic sequences have made significant advancements in recent decades, now allowing for the integration of petrological information from rock sequences recording distinct mineral assemblage changes. Prior metamorphic constraints from the Suru Valley region are dominantly based on amphibolite-facies assemblages and pelitic compositions (e.g., Searle *et al.*, 1992; Walker *et al.*, 2001). The aim of this chapter is to resolve the P and T conditions of prograde–peak metamorphism in the Suru Valley region over greenschist- to amphibolite-facies assemblages by integrating information from both pelitic and metabasic sequences. In particular, this study aims to (1) detail how P-T information is recovered from rocks using thermodynamic principles and what uncertainties are associated with these methods; (2) explain how this study accounts for uncertainties; (3) describe the petrographic relationships, compositions of phases, and a given equilibrium assemblage for each sample; (4) present the thermobarometric constraints from pelitic and metabasic samples across a range of metamorphic grades; and (5) synthesise the contribution and relative rates of the driving tectonic forces, and discuss the implications for Himalayan tectonics and orogenic processes.

4.1 Principles of thermobarometry

4.1.1 Equilibrium

Metamorphism aims to minimise a rock's internal free energy to achieve chemical and textural equilibrium. Reaching equilibrium can be achieved with mechanisms such as growth of new minerals through chemical reactions or recrystallisation of minerals due to changing external conditions (e.g., stress). A given mineral assemblage is a function of specific P-T conditions, further constrained by bulk rock composition.

The P-T path of a metamorphic rock is a reflection of continuous changes in P and T. Documenting segments of this path, requires that equilibrium be partially or totally preserved in a rocks mineral assemblage. Preservation of a mineral assemblage tends to coincide with the maximum T on the P-T path, known as the metamorphic or thermal peak. Fluid along grain boundaries play a pivotal role during metamorphism in promoting equilibration between minerals by catalysing reactions and promoting mass transfer (Guiraud *et al.*, 2001). During prograde metamorphic reactions, fluid is liberated through mineral dehydration, maintaining equilibrium. These fluids are typically lost from the rock volume due

to compaction and deformation, leading to fluid-poor retrograde metamorphic reactions (unless externally reintroduced) with minimal assemblage changes (Powell & Holland, 2010). Equilibrium thermodynamics can therefore be employed to constrain the P-T conditions during metamorphic peak. When combined with geochemical analysis and petrological observations of mineral zoning patterns, inclusion suites, and replacement reactions; the prograde and retrograde history of a metamorphic rock can be disentangled. Using petrological techniques on metamorphic rocks represents a inverse modelling approach. Through an iterative process, model parameters are adjusted to simulate metamorphic processes, aiming to converge on the P-T-X conditions that best replicate the conditions at which the observed mineral assemblage formed.

All modern studies assume equilibrium on some time- or length-scale and those studies using phase diagrams, geothermometry and/or geobarometry are based on this assumption. Regional metamorphism appears to be well accounted for by an equilibrium view (e.g., Yardley, 1977) in which deformation and long time-scales assist in maintaining equilibrium.

Although the equilibrium view of thermodynamics represents a fundamental concept in the study of metamorphic processes, it is not always universally applicable. Disequilibrium processes that require consideration of kinetics can play an important role in metamorphism (e.g., Pattison & Spear, 2018; Pattison & Tinkham, 2009; Starr & Pattison, 2019; Waters & Lovegrove, 2002). Furthermore, disequilibrium processes often provide more insightful interpretations, as a rock preserving a state of perfect chemical and textural equilibrium provides limited interpretation of the P-T path. This study, largely adopts the equilibrium view, but with a critical perspective. A comprehensive understanding of mineral relationships, whether reflecting equilibrium or disequilibrium processes, is crucial for accurately interpreting P-T conditions at which the rock equilibrated and the trajectory of the P-T path travelled. In order to calculate the P-T conditions, knowledge of underlying thermodynamic principles is required, following Spear (1993).

4.1.2 Thermodynamics

Definitions

1. System: collection of phases under investigation.

2. Phase: any portion of a system that is physically separable (e.g., a mineral, silicate melt, fluid). Phases are comprised of components.

3. Component: the constituents needed to define the compositions of phases (e.g., end-members, oxides, or cations and anions).

4. Intensive variables: those that are independent of the size of the studied system and share the same value for all phases in equilibrium with each other.

5. Extensive variables: those that are dependent on the size of the studied system and have different values for each phase.

6. Gibbs free energy: thermodynamic potential to do work.

4.1.2.1 Gibbs free energy

In a multiphase system, the governing factor dictating the thermodynamic state is the potential for performing work. In the context of state variables such as temperature (T), pressure (P), and the number of moles of components (η_i), this particular thermodynamic potential is commonly referred to as the Gibbs free energy (G). The Gibbs free energy is the thermodynamic potential that determines which phase assemblage is most stable under a set of physical conditions defined by these state variables. At a singular P-T point for a given bulk rock composition, a multitude of potential phase combinations could conceivably coexist. In this scenario, the Gibbs free energy of the system (G_{sys}) would exhibit distinct values for each assemblage. The assemblage with the lowest G_{sys} value represents the stable assemblage, with other assemblages with higher values of G_{sys} representing metastable assemblages. The constituent phases of metastable assemblages will normally react to reduce the G_{sys} in order to achieve chemical and textural equilibrium with reference to the ambient P-T-X of the system, thereby driving metamorphic change.

The basis for thermodynamic calculations is that all phases have an associated Gibbs free energy of formation (ΔG_f) and the Gibbs free energy of reaction (ΔG_R) quantifying the energy changes during a chemical reaction. ΔG_R can be calculated by summing the energies of the products and subtracting the energies of the reactants. When $\Delta G_R < 0$, the reaction proceeds, as lower energy configurations are more stable. Since the ΔG_f of a mineral varies with changes in P-T-X, the ΔG_R for any reaction will also vary with these parameters. This

variation allows reactions to be plotted on phase diagrams, where $\Delta G_R = 0$ along reaction lines. When there is no free energy difference between reactants and products, the system is at equilibrium, and the sum of the chemical potentials (μ) is also zero:

$$\Delta G_R = 0 = \sum_{j=1}^{m} \nu_j \mu_j \tag{4.1}$$

Here, ν_j denotes the stoichiometric coefficient of each phase component (j) in a reaction where there are m phase components. μ_j is the chemical potential or reactive energy of phase component j. Where a phase is impure and exhibits solid solution between multiple end-members, the chemical potential μ_j may be expressed as:

$$\mu_j = \mu_j^\circ + RT \ln(a_j) \tag{4.2}$$

where μ_j° is the chemical potential of phase component j in a pure end-member, R is the gas constant (8.314 J $K^{-1}mol^{-1}$), T is temperature (in Kelvins), and a_j is the activity of component j in a given phase.

4.1.2.2 Activity

Many minerals are impure and exhibit a solid solution between multiple end-members. The thermodynamic property of activity is a value that describes how reactive an end-member component is for a given mineral composition. This is expressed as a_j which is the activity (or effective amount) of component j in a given phase (i). Thus for a pure phase, the activity of any component in that phase equals 1 (ideal behaviour), and if the phase is not present in any amount it equals 0. The compositions of minerals in solid solutions are reported in mole proportions of end members. This is not equivalent to activity, unless mixing is ideal. For example aluminosilicate garnet ($X_3Al_2Si_3O_{12}$) is a solid solution between 4 major end-members, X represents a divalent cation: (Fe) almandine, (Mg) pyrope, (Ca) grossular and (Mn) spessartine. Because this is not ideal mixing, end member activities of garnet are determined by an ionic model describing the mixing of cations over the crystallographic sites. For ideal mixing of α cations on a single site, the activity of each component relates to the mole fraction by:

$$a_j = (X_j)^{\alpha} \tag{4.3}$$

Here, the activity of component j equals the mole fraction of cation for phase component j to the power of α which is the number of sites over which the cation may exchange. Therefore activity of a component increases as the mole fraction increases. For the activity of almandine ($Fe_3Al_2Si_3O_{12}$):

$$a_{\mathrm{Alm}} = (X_{\mathrm{Alm}})^3 = \left(\frac{\mathrm{Fe}^{2+}}{\mathrm{Fe}^{2+} + \mathrm{Ca} + \mathrm{Mg} + \mathrm{Mn}}\right)^3 \tag{4.4}$$

However, activity-composition (a-X) diagrams generally often show non-ideal behaviour for a given phase where the activities of endmembers are often greater than the mole fraction. In such scenarios, an activity coefficient term (γ_j) needs to be introduced, which corrects for this non-ideal behaviour:

$$a_j = \gamma_j {X_j}^{\alpha} \tag{4.5}$$

γ_j is determined by thermodynamic calculations and experimental studies. The coefficient varies depending on P, T, and X. Mineral end members display near ideal behaviour at very low and very high mole fractions and as such activity is approximately equal to the mole fraction. Ideal behaviour is dominantly also observed at higher temperatures, and non-ideal behaviour at lower temperatures, where immiscibility can be observed. Activity-composition (a-X) models therefore calculate activities under a wide range of conditions and determine the correction required such that Equation 4.5 is fulfilled. a-X models provide thermodynamic descriptions of the phases in terms of the thermodynamic properties of the end-members and energetics of how end-members are combined to form phases. These models therefore form the underlying input for all thermodynamic calculations used to determine the P-T path of the rock.

4.1.2.3 Fundamental equations

Combining Equations 4.1 and 4.2 produces the following relationship:

$$\Delta G_r = 0 = \Delta G^{\circ} + RT \ln K_{eq} \tag{4.6}$$

Here ΔG° is the change in Gibbs free energy between end-members in a reaction and K_{eq} is the equilibrium constant of a reaction. K_{eq} is the product of the activities of the products divided by the product of the activities of reaction of the reactants each raised to the power of its coefficient.

$$aA + bB \leftrightarrow cC + dD \tag{4.7}$$

$$K_{eq} = \frac{(aC)^c + (aD)^d}{(aA)^a + (aB)^b} \tag{4.8}$$

Expanding ΔG° in Equation 4.6 gives the complete relationship between P, T, and X:

$$\begin{aligned} \Delta G_R = 0 = \Delta H_{298,1} + \int_{298}^{T} \Delta C_P \, \mathrm{d}T + \int_{1}^{P} \Delta V \, \mathrm{d}P - \\ T\left(\Delta S_{298,1} + \int_{298}^{T} \frac{\Delta C_P}{T} \, \mathrm{d}T\right) + RT \ln K_{eq} \end{aligned} \tag{4.9}$$

Here H, C_p, V and S correspond to enthalpy, heat capacity, volume and entropy of a reaction and these thermodynamic properties are given at the standard state of 298 K and 1 bar, as displayed by the subscripts and limits. The integrals adjust the values to the P and T of interest. Using the requisite thermodynamic data and a range of values, this Equation enables the calculation of a reaction curve for any P-T-X condition. A loci of points at which $\Delta G_R = 0$ creates a curve in P-T-X space the separates fields of stability of different mineral assemblages.

For sub-solidus volatile-absent reactions Equation 4.9 can be simplified to remove C_p as it is usually very small for solids and ΔV can be assumed to be constant. This provides the following linear approximation:

$$0 = \Delta H + P\Delta V - T\Delta S + RT \ln K_{eq} \tag{4.10}$$

Which can be expressed as a thermometer (Equation 4.11) or barometer (Equation 4.12):

$$T = \frac{P\Delta V + \Delta H}{\Delta S - R \ln K_{eq}} \tag{4.11}$$

$$P = \frac{T\Delta S - RT \ln Keq - \Delta H}{\Delta V} \tag{4.12}$$

Values of ΔH, ΔS, and ΔV may be calculated from experimental measurements for the phases of interest. K_{eq} may be calculated from measured or assumed compositions of reactants and products. This enables an univariant line representing a particular equilibrium to be positioned in P-T space, the slope of which is described the Clausius-Clapeyron equation and associated derivations for pure phases (Equation 4.13) and those with solid solutions (Equation 4.14):

$$\frac{\delta P}{\delta T} = \frac{\Delta S}{\Delta V} \tag{4.13}$$

$$\frac{\delta P}{\delta T} = \frac{\Delta S - R \ln K_{eq}}{\Delta V} \tag{4.14}$$

4.1.3 Geothermometry

The Clausius-Clapeyron equation indicates that effective geothermometers require a large ΔS and/or a small ΔV resulting in a steep slope that is highly T sensitive (Fig. 4.1a). Reactions that are typically suitable involve cation exchange between phases, thereby shifting composition without changing the phases. Although cation exchange reactions have a small ΔS, they have a comparably smaller ΔV. A useful example is Fe-Mg exchange between garnet and biotite:

$$\begin{aligned} &\text{almandine} + \text{phlogopite} = \text{pyrope} + \text{annite} \\ &\mathrm{Fe_3Al_2Si_3O_{12}} + \mathrm{KMg_3AlSi_3O_{10}(OH)_2} = \\ &\qquad\qquad \mathrm{Mg_3Al_2Si_3O_{12}} + \mathrm{KFe_3AlSi_3O_{10}(OH)_2} \end{aligned} \tag{4.15}$$

If ideal mixing is assumed for the garnet-biotite thermometer then the equilibrium constant and simplified distribution coefficient (K_D) can be written as:

$$K_{eq} = \left(\frac{X^{\mathrm{Bt}}_{\mathrm{Fe}} X^{\mathrm{Grt}}_{\mathrm{Mg}}}{X^{\mathrm{Bt}}_{\mathrm{Mg}} X^{\mathrm{Grt}}_{\mathrm{Fe}}} \right)^3 \tag{4.16}$$

$$K_D = \frac{X_{\mathrm{Fe}}^{\mathrm{Bt}} X_{\mathrm{Mg}}^{\mathrm{Grt}}}{X_{\mathrm{Mg}}^{\mathrm{Bt}} X_{\mathrm{Fe}}^{\mathrm{Grt}}} = \frac{(\mathrm{Mg/Fe})^{\mathrm{Grt}}}{(\mathrm{Mg/Fe})^{\mathrm{Bt}}} = (K_{eq})^{1/3} \tag{4.17}$$

Experimental investigation of the partitioning of Fe and Mg between synthetic garnet and biotite at constant pressures quantifies K_D across P-T space (Fig. 4.1a; Ferry & Spear, 1978).

4.1.3.1 Geobarometry

The Clausius-Clapeyron equation indicates that effective geobarometers require a small ΔS and/or a large ΔV resulting in a shallow slope that is highly P sensitive (Fig. 4.1b). Although cation exchange reactions are mostly T sensitive, in net-transfer reactions the consumption and production of mineral species across terminal or crossed tie-line reactions may be strongly P sensitive. Sensitivity to pressure requires product and reactant assemblages to possess different molar volumes. A useful example is the garnet-aluminosilicate-silica-plagioclase (GASP) barometer that involves the exchange of Ca between garnet and plagioclase through the terminal reaction:

$$\begin{aligned} 3\ \text{anorthite} &= \text{grossular} + 2\ \text{aluminosilicate} + \text{quartz} \\ 3\mathrm{CaAl_2Si_2O_8} &= \mathrm{Ca_3Al_2Si_3O_{12}} + 2\mathrm{Al_2SiO_5} + \mathrm{SiO_2} \end{aligned} \tag{4.18}$$

Assuming ideal mixing, the equilibrium reaction constant can be calculated:

$$K_{eq} = \frac{X_{\mathrm{grs}}^{\mathrm{Grt}} (X_{\mathrm{Al_2SiO_5}}^{\mathrm{Ky}})^2 X_{\mathrm{SiO_2}}^{\mathrm{Qtz}}}{(X_{\mathrm{an}}^{\mathrm{Pl}})^3} = \frac{X_{\mathrm{grs}}^{\mathrm{Grt}}}{(X_{\mathrm{an}}^{\mathrm{Pl}})^3} \tag{4.19}$$

Aluminosilicate and quartz both exhibit negligible solid solution, as such their activities may be set to 1 to simplify the calculation. Experimental data allows contouring of P-T space for K_{eq} (e.g., Holdaway, 2001, Fig. 4.1b). This allows the pressure of equilibration to be calculated for a particular temperature (thereby requiring an independent geothermometer). For a rock containing pure phases of anorthite, grossular, kyanite, and quartz, the activity of all phases may be unity, therefore the reaction (Equation 4.18) would take place at high-pressure along the $K_{eq} = 1$ isoline (Fig. 4.1b). Solid solution and reduced activities are more common. Where activities of grossular in garnet and anorthite in plagioclase are smaller, the reaction may be defined by a smaller value of K_{eq}, and therefore higher P.

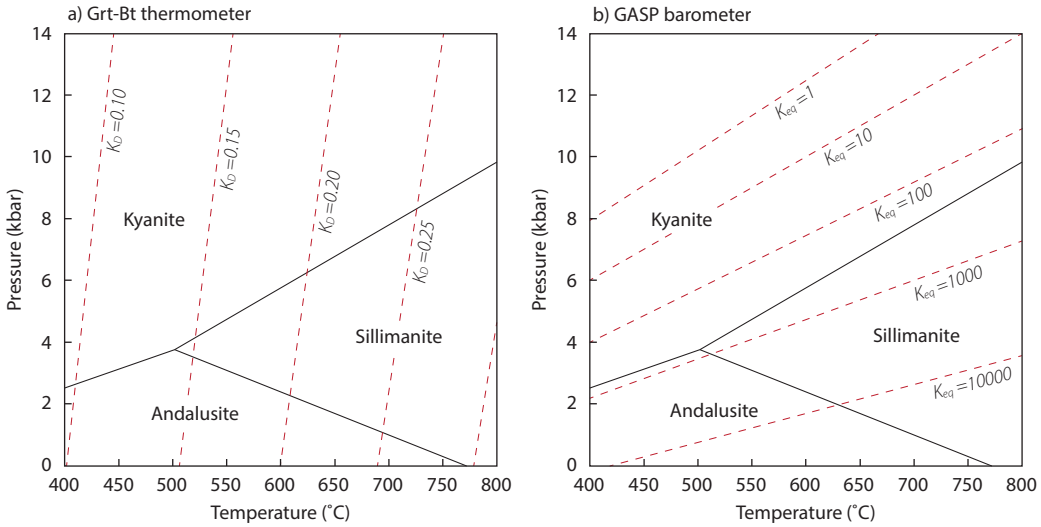


Fig. 4.1 *P-T* space contoured for the simplified distribution coefficient and equilibrium constant for example thermobarometers. (a) Grt-Bt thermometer. Contoured for K_D following Ferry & Spear (1978). (b) GASP barometer. *P-T* space is contoured for K_{eq} following Holdaway (2001).

4.1.3.2 Single phase concentration thermobarometry

In contrast to cation exchange and net transfer reactions described above, single phase concentration thermobarometry or single element thermobarometry uses P or T sensitive saturation concentration of a minor element in a single mineral. In the last two decades, several new empirical and experimental calibrations of trace element thermometers, including Ti-in-biotite (Henry *et al.*, 2005), Zr-in-rutile (e.g., Tomkins *et al.*, 2007; Kohn, 2020), Zr-in-titanite (Hayden *et al.*, 2008), Ti-in-zircon (e.g., Watson *et al.*, 2006; Ferry & Watson, 2007), and Ti-in-quartz (e.g., Thomas *et al.*, 2010, 2015; Wark & Watson, 2006). For a review of trace element thermometers see Cruz-Uribe *et al.* (2018). Example barometers include the Al content of hornblende (Anderson & Smith, 1995), and Ti-in-phengite (Auzanneau *et al.*, 2010). Saturation conditions must be satisfied (e.g., the appropriate mineral assemblage present to buffer the thermometer), or the activities of the relevant compounds must be constrained for the calibration to provide accurate crystallisation conditions (Cruz-Uribe *et al.*, 2018). For the Ti in biotite thermometer, if results are taken in the absence of a Ti-saturating phase, the Ti content of the biotite is not maximised and such a result would represent a minimum temperature of crystallisation.

4.1.3.3 Multi-equilibrium thermobarometry

Thermometer and barometer calibrations do not always agree. Calibrations of thermometers and barometers were made based on natural datasets (e.g., Ghent, 1976; Hodges & Spear, 1982) and detailed experimental studies documenting element fractionation between minerals (e.g., Ferry & Spear, 1978). However, the exponential growth of several P- and T-sensitive equilibria (e.g., Essene, 1989; Spear *et al.*, 2016), and different calibrations of the same equilibria (e.g., garnet-biotite) resulted in multiple *P-T* conditions for the same sample using different calibrations. This led to some difficulty in assessing the precision and accuracy of each *P-T* result and calibration. Simple thermometer-barometer intersections have been criticised for failing to incorporate all the *P-T* information available in a given assemblage and/or for not using the same activity models for mineral end-members (Powell & Holland, 2008; Waters, 2019). The introduction of multi-equilibrium thermobarometry solved the problems associated with conventional thermobarometry by using internally consistent thermodynamic databases (e.g., Powell & Holland, 1994) and their associated solution models to estimate *P-T* conditions using all possible equilibria between minerals in a rock (Berman, 1991). Simultaneous solution of both geothermometers and geobarometers allows for a *P-T* range to be determined for the intersection of equilibria for independent reactions. An example of this approach is the AvPT function of THERMOCALC. Specifically, the process considers the activities of the end-members of phases to be variable within a range of uncertainties, defining *P-T* bands that are then correlated with each other. The average point is then determined using a least-squares approach for every reaction line. The method's statistical approach is advantageous as it means the variation required for the activity of end-members to transect a single point can be assessed. Where fit indices exceeded the maximum value for 95% confidence, the end-member with the worst fit (largest e^*) is removed and the calculation re-run until all indices conform (the χ^2 test, Powell & Holland, 1994). Influential results may also be assessed and removed accordingly. Similarly, mineral assemblages that also give little or no thermobarometric constraints are recognised and caution advised. The same approach applies for AvP and AvT calculations, which are often favoured as they can be calculated directly without iteration (Powell & Holland, 1988).

AvPT, AvP and AvT can be performed in a fluid-absent environment or over a range of fluid compositions ($a\mathrm{H_2O} = \mathrm{H_2O}/(\mathrm{H_2O}+\mathrm{CO_2})$). Although the pseudo-section modelling approach (see next section) has become the favoured method in

the metamorphic community, multi-equilibrium thermobarometry remains useful if an assemblage involves unconstrained factors such as the presence/absence of fluid and unknown activities of H_2O and CO_2, which would be difficult to apply in a pseudosection modelling approach (Powell & Holland, 2008). Similarly, conventional thermobarometry may still be useful for assemblages where there are significant additional phases and/or elements that pseudosections cannot calculate. However, although multi-equilibrium thermobarometry reduces many of the problems found in conventional thermobarometry and petrogenetic grids (see next section) by using an internally consistent thermodynamic dataset, large uncertainties still remain (± 50 °C, greater than 1 kbar; Spear *et al.*, 2016).

The AvPT method is broadly optimised for pressure calculations. Activities for each end-member phase of a mineral species is calculated outside THERMOCALC resulting in certain equilibria, notably cation-exchange thermometers lacking cancellation of site terms that occurs in the calculation of K_D. For example, the K_D for the garnet-biotite thermometer (Equation 4.17) is calculated from the Fe and Mg mole fractions (small uncertainty), whereas THERMOCALC uses the activity of all other sites (more contributing uncertainty). Using the activities of each end-member rather than the overall K_D results in uncertainties on certain geothermometer equilibria becoming significantly overestimated (Waters, 2019). Another associated error that commonly arises is that well-constrained equilibria in a system have similar slopes resulting in a cigar-shaped uncertainty ellipse along this slope (Powell & Holland, 1994). This is common for the H_2O-absent equilibria used by THERMOCALC for most pelites. These errors allow the mean P-T point within the ellipse to be pushed up or down T into a zone which does not overlap with the modelled assemblage. Tightly constrained equilibria with steep P-T slopes are generally devolatilisation reactions which depend inherently on $a\mathrm{H_2O}$. Fluid is commonly considered to be pure H_2O in such systems, but there are many situations where this is not the case (see discussion in Waters, 2019). As such T determination is strongly dependent on $a\mathrm{H_2O}$. Using AvPT and AvT over a wide range of fluid compositions can therefore lead in a wide spread of calculated temperatures.

A recommended approach is to determine AvP at a series of temperatures (termed the P locus). Such temperatures should equate to the likely temperature range of the peak mineral assemblage (Powell & Holland, 1994). Temperatures are usually known better than pressures (e.g., general phase relationships), hence the focus on AvP. If pressures are better constrained, then the inverse approach may be used. Using a thermometer which is not constrained by $a\mathrm{H_2O}$ and orthogonal

to the system used for modelling the rock, can help to independently determine the T of the system and thereby the $a\mathrm{H_2O}$ for each particular sample (Powell & Holland, 2008; Walker *et al.*, 2001). Ti-in-biotite and Zr-in-rutile are useful examples of such thermometers and are employed in this study as such. A similar approach is also emphasised in Powell & Holland (1994, 1988) where one can investigate the dependence of results on fluid composition and thereby select an average fluid composition that corresponds to a minimum σ_{fit} in P-T-X space (see Fig. 4.2).

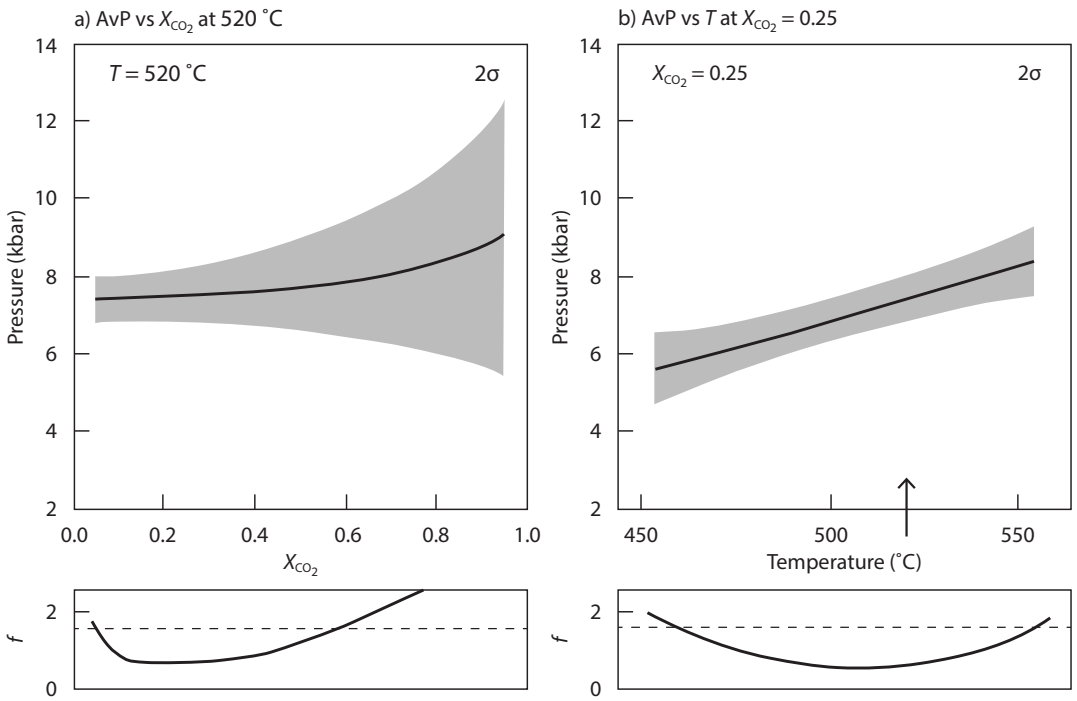


Fig. 4.2 After Figure 8 of Powell & Holland (1988), summary of AvP calculations for sample RP13. a) P vs $X\mathrm{CO_2}$ at 520 °C. b) P vs T at $X\mathrm{CO_2}$ of 0.25. The χ^2 test for AvP fails for $f > 1.61$ (dashed line) under these run conditions, thus averaging is valid for 95% confidence in a) in the range $X\mathrm{CO_2} = 0.05$–0.6 and in b) for $T = 460$–555 °C.

4.1.3.4 Elastic Thermobarometry

When a crystal entraps an inclusion there is conceptually no differential stress or strain. The volume of the inclusion matches the volume of the host void space. However, during cooling and exhumation from peak P-T conditions the volumes of host and inclusion experience differential thermal expansivities and compressibilities. These different changes in volume result in compressive or tensile stresses are determined by measuring the shift in Raman spectra between an inclusion and a standard (e.g., Kohn *et al.*, 2023). Quantification of these

local stresses has allowed entrapment P at assumed T or entrapment T at assumed P to be calculated. This has recently given rise to the field of elastic thermobarometry. Elastic thermobarometry (physical measurements) differs fundamentally from conventional thermobarometry (chemical measurements). Although both methods seek to determine the P-T conditions of mineral formation, conventional thermobarometry is based on thermodynamic inversion of mineral chemical composition. In contrast, elastic thermobarometry relies on elastic inversion of mineral physical properties.

Quartz-in-garnet barometry has been used to determine the pressure at which garnet entrapped quartz during prograde metamorphism (Enami *et al.*, 2007; Kohn, 2014b; Spear *et al.*, 2014; Thomas & Spear, 2018; Wolfe *et al.*, 2021). The assumption of unmodified volume and geometry of the inclusion since entrapment has been questioned, with the recognition that post entrapment shape change of quartz may also be controlled by the host garnet (Zhong *et al.*, 2020; Cesare *et al.*, 2021). Furthermore, differential local stresses may be affected by inelastic processes, anisotropic expansivities and compressibilities (for non-cubic crystals), inclusion shape, and proximity to other inclusions or surfaces (Kohn *et al.*, 2023). Recent experiments have attempted to quantify and correct for these features (see review in Kohn *et al.*, 2023).

4.1.4 Phase equilibrium modelling

Conventional thermobarometry is dependent on mineral composition (inverse modelling), which may not always record preserved equilibrium (e.g., retrograde cation Fe-Mg exchange; Fitzsimons & Harley, 1994). Quantitative phase equilibrium modelling is not explicitly dependent on observed mineral compositions, rather it involves forward modelling of a selected system. This provides graphical context by which equilibrium relationships between phases in a model system, mineral compositional data and modes can be compared. This progress has been firmly rooted in the continuing development of ever-improving thermodynamic data for end-member minerals, fluid and melt, a-X models and software packages (Connolly, 1990, 2005; Dale *et al.*, 2005; de Capitani & Brown, 1987; de Capitani & Petrakakis, 2010; Diener *et al.*, 2007; Diener & Powell, 2012; Green *et al.*, 2007, 2016; Holland & Powell, 1985, 1990, 1998, 2011; Holland *et al.*, 2022; Powell & Holland, 1988; White *et al.*, 2000; White *et al.*, 2001, 2007, 2014b). Phase equilibrium modelling is now viewed as the most powerful and reliable thermobarometric

tool (Powell & Holland, 2008), allowing for improved quantitative constraints on the condition of formation of metamorphic rocks.

4.1.4.1 Gibbs Phase Rule

The Gibbs Phase rule provides the foundation for defining the chemical state of a system and predicting the equilibrium relation of phases present in a system relating to the physical conditions. It also represents the basis for constructing phase diagrams. The Gibbs Phase rule describes how many variables (e.g., P and T) can be independently changed in a heterogeneous system without altering the state of the system (i.e. the number of phase components and their compositions remaining constant). The total number of phase components (N_K; e.g., end-members) in the system can be written as:

$$N_K = \sum_{j=1}^{N_i} N_{i(j)} \tag{4.20}$$

Where N is the number, j is a given phase component, K are phase components in a system (such that N_K defines the total number of phase components), and i are phases in a system (such that N_i is the total number of phases). However, for each phase component, e.g., for j, there are $N_{i(j)} - 1$ phase components, because the mole fractions of the phase components in each phase are not all independent such that:

$$N_K - N_i = \sum_{j=1}^{N_i} N_{i(j)} - 1 \tag{4.21}$$

The other variables in the system are P and T. Therefore, the total number of variables in the system may be expressed as:

$$N_{\text{variables}} = N_K - N_i + 2 \tag{4.22}$$

The number of constraints on a heterogeneous system can be based on the number of linearly independent reactions defining the system. This is defined as: number independent reactions = total number of phase components − number of system components.

$$N_{\text{reactions}} = N_K - C \tag{4.23}$$

Where C is the number of system components. C represents the number of chemical components necessary to constitute all system phases, in comparison the total number of phase components N_K which represents the chemical components required to describe the variability of a phase.

The variance, or degrees of freedom (F), of a system is then calculated by the difference between the number of variables and number of constraints:

$$F = (N_K - N_i + 2) - (N_K - C) \tag{4.24}$$

Substituting N_i for P gives the Gibbs Phase rule:

$$\begin{aligned} P + F &= C + 2 \\ F &= C + 2 - P \end{aligned} \tag{4.25}$$

4.1.4.2 Duhem's theorem

The Gibbs Phase rule accounts for intensive variables, but does not include extensive variables. Bulk composition, an extensive variable, is essential in modelling to determining the stability of phases over a space defined by intensive variables. Mass balance equations are used to incorporate the bulk composition of the rock in terms of the constituent minerals.

The molar amount of an oxide (e.g., SiO_2) in a rock containing phases A, B, and C is equal to:

$$m_{\text{SiO}_2} = n^A_{\text{SiO}_2} M^A + n^B_{\text{SiO}_2} M^B + n^C_{\text{SiO}_2} M^C \tag{4.26}$$

Where m_j is moles of system component j in the rock, n^i_j is the number of moles of component j in phase i, and M^i is the number of moles of phase i in the rock. The number of mass balance equations (one for each system component) will be equal to C. The new variables introduced are M^i of which there are P (one for each phase) and m_j of which there are C (one for each phase component). The new variance may now be calculated by adding the variables and subtracting

the constraints — with a fixed bulk composition m_j and thereby C is known and P is unknown:

$$F = (C - P + 2) + (P - C) = 2 \tag{4.27}$$

This states that the number of degrees of freedom in a system for which the bulk composition is fixed is 2. Therefore, where two independent variables are specified, the state of the system is determined, including the composition of phases (X) and modal abundances (M). P-T-X-M plots can be produced where P-T space is contoured by X-M.

4.1.4.3 Types of phase diagrams

Once a model chemical system and phases of interest have been been defined, there are a variety of ways these may be presented graphically. A *total phase diagram* contains all the phase equilibrium within a specific system and displays all possible stable assemblages at all P-T-X conditions. The number of axes for a total phase diagram depends on the number of system components whereby the number of components in an n-component system would have axes of pressure, temperature and $n-1$ independent compositional axes (thereby $n+1$ for the total system). A 3-D representation of such a combination of axes is challenging, resulting in 2-D representations being favoured. The most common lower-dimensions constructions are projections, sections, and pseudosections.

A total phase diagram can be projected on a reference plane. An example of this would be a projection from compositional variables onto P-T space to create a P-T projection or petrogenetic grid (e.g., Spear & Cheney, 1989), which displays all possible equilibria considered in P-T space. Petrogenetic grids represent a series of univariant reactions that divide P-T space into areas within which different mineral phase assemblages are stable (Spear, 1993). The limitation of such model systems are that: 1) in order to keep them simple enough to interpret they are typically restricted to the KFMASH chemical system and do not account for important components such as Mn, Ca, Na, and Fe^{3+} (Spear *et al.*, 2016); 2) natural systems containing a specific bulk composition would only experience a small number of the total possible equilibria; and 3) they do not provide information on continuous reactions.

Total phase diagrams may also be sectioned with respect to an intensive (P, T, μ_i) or extensive (S, V, or n_i) variables. When sectioned for intensive variables, calculated assemblages lie on the plane of the section as the value of any intensive value is equal in all phases. Whereas, for extensive variables, calculated assemblages do not lie on a single sectioned plane and the calculated phase diagram is thereby referred to as a *pseudosection*. The most common pseudosections are sectioned for bulk composition (n_i), with the remaining variable axes plotted as P and T, creating a P-T pseudosection.

A P-T pseudosection will produce a "map" of equilibrium mineral assemblages relative to the specified chemical bulk composition, thereby adhering to Duhem's Theorem. A T-X or P-X pseudosection, holds P or T constant, respectively, for a chemical composition vector. The composition vector can be used to explore mineral assemblages through poorly constrained variables such as $M\mathrm{H_2O}$, $X_{\mathrm{Fe^{3+}}}$, the addition of fluids, or to span a range of actual rock compositions. These pseudosections provide additional thermobarometric constraints for situations when additional minerals join the phase assemblage, minerals are unstable, and a fluid may alter the stability of certain minerals. More complex modelling of the P-T evolution of a rock during its burial-heating history can be undertaken using garnet zoning (a ubiquitous feature in amphibolite-facies pelites) to determine a the P-T path over which garnet grew and pin down a segment of the rock's P-T evolution (Gaidies *et al.*, 2008; George & Gaidies, 2017; Moynihan & Pattison, 2013). Determining equilibrium assemblages for a sample-specific bulk composition makes pseudosections a powerful tool to simultaneously examine the different stages of a rock's evolution.

This thesis uses a combination of pseudosections, with constraints from conventional, single-phase and multiphase equilibria thermobarometers to investigate the metamorphic evolution of rocks from the Suru Valley region.

4.1.5 Limitations and uncertainties

A requirement of any calculation is that the result includes an assessment of uncertainties that arise from uncertainties on the input information (Powell & Holland, 1994, 2008). In order to accommodate these uncertainties, it is essential to first consider the individual sources of uncertainties that may arise. Previous summaries of uncertainties in thermobarometry are outlined in the studies of Hodges & McKenna (1987); Powell & Holland (1988, 1994); Kohn & Spear

(1991a,b) and Worley & Powell (2000). Error may be systematic or random, and can be separated into geological, analytical, parameter and model uncertainties.

4.1.5.1 Geological error

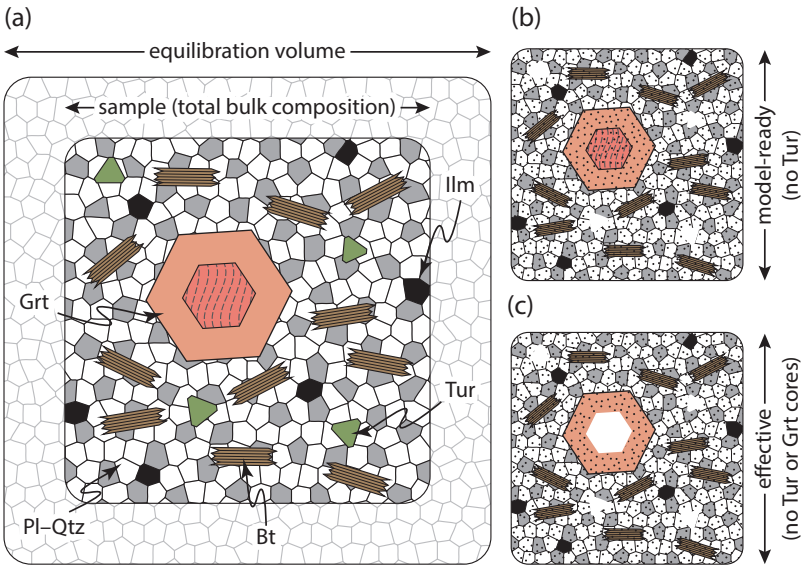


Fig. 4.3 From Palin *et al.* (2016), graphical sketch of various bulk composition nomenclature. Note that although minerals such as tourmaline do contain components not present in the model system, they may form part of the effective bulk composition, however, are not treated as such for modelling purposes.

A fundamental source of error arises from non-analytical bias in sample selection, and interpretations during petrological investigation. Sampling bias has an inherent contribution to the measured (or calculated) bulk composition through petrological differences (e.g., varying mineral abundances) between samples. As well as this inherent variation, the method of bulk composition determination can differ depending on the interpreted scale and degree to which equilibrium has been achieved in a mineral assemblage. XRF analysis assumes equilibrium is achieved on the 'rock' scale and creates a 'total' bulk composition (Fig. 4.3). However, many metamorphic rocks preserve chemical zoning of porphyroblasts and therefore a calculation using an 'effective' bulk composition selected from thin sections may be more more appropriate (Fig. 4.3). The topology of a given pseudosection can vary significantly based on the method applied to determine bulk composition (Fig. 4.4; e.g., Stüwe, 1997; Guevara & Caddick, 2016; Palin *et al.*, 2016; Lanari & Engi, 2017). Equally, accounting for fractionation of zoned porphyroblasts has shown to not produce significant differences in calculated P-T conditions (Zuluaga *et al.*, 2005).

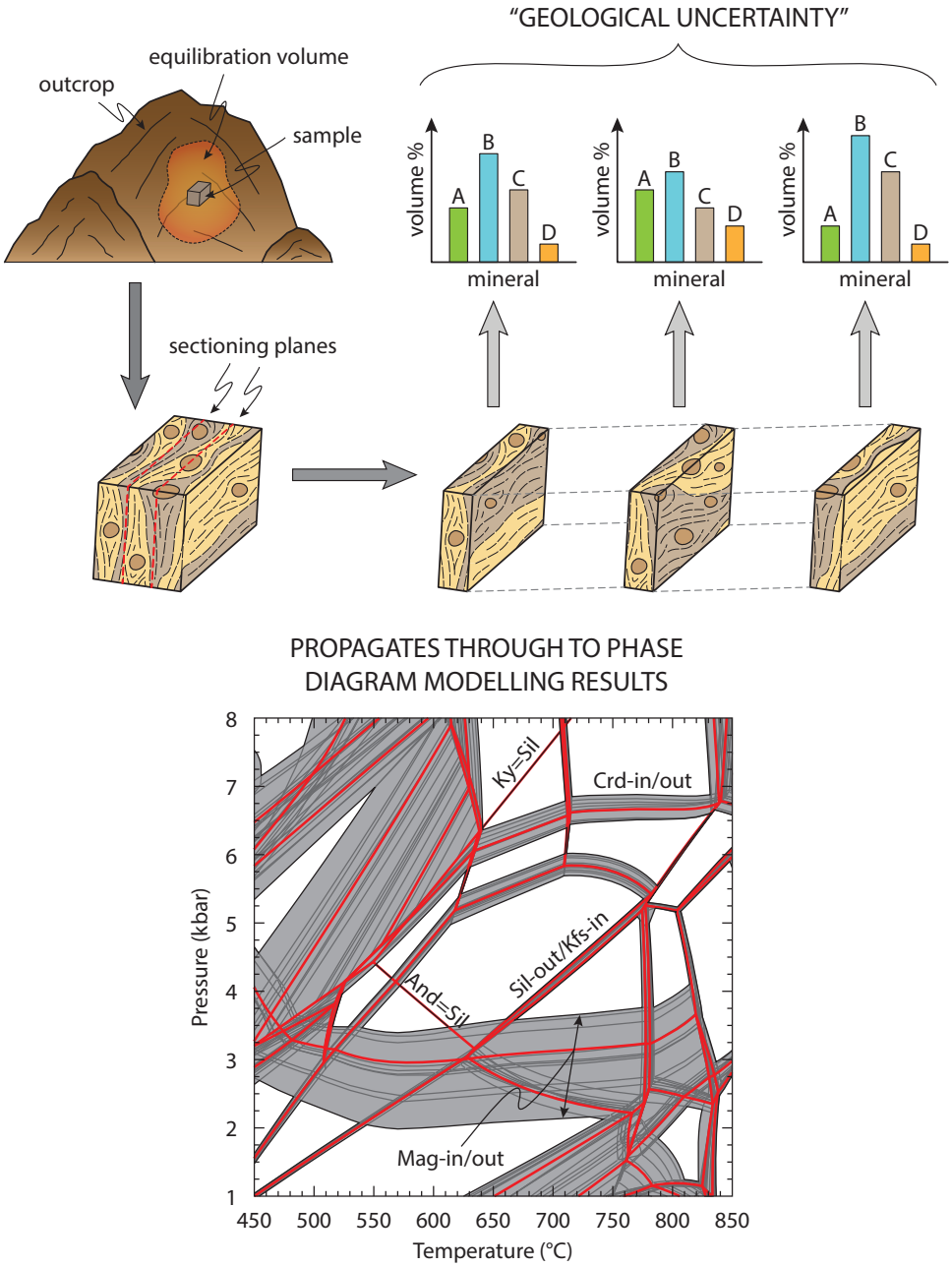


Fig. 4.4 From Palin *et al.* (2016), sketch illustration of the propagation of geological uncertainty originating from petrological variation on the hand sample- and thin section scale to phase equilibrium modelling results.

Although the equilibrium view of thermodynamics represents a fundamental concept in the study of metamorphic processes, it is not always universally applicable. Disequilibrium processes that require consideration of kinetics can play an important role in metamorphism (e.g., Waters & Lovegrove, 2002; Pattison & Tinkham, 2009; Pattison & Spear, 2018; Starr & Pattison, 2019). Furthermore, disequilibrium processes often provide more insightful interpretations, as a rock preserving a state of perfect chemical and textural equilibrium provides

limited interpretation of the P-T path. Forward modelling the consequences of metamorphic transformation at a fixed pressure (P), temperature (T), and bulk composition (X) is resolved by computations based on the concept of equilibrium thermodynamics, yet studies by necessity must accommodate various scales of disequilibrium and consider the appropriate volume for which equilibrium can be applied. While the discussed errors are non-systematic, statistical approaches have been advocated by Steltenpohl & Bartley (1987); Hodges & McKenna (1987); Palin *et al.* (2016) to assess the impact on resulting P-T conditions. Uncertainty related to natural petrographic variation produces displacements the order of ± 1 kbar for only a moderate degree of uncertainty in modal proportions (Fig. 4.4 Palin *et al.*, 2016).

4.1.5.2 Analytical error

Analysis of mineral compositions for thermobarometric calculations involves uncertainties on the measured weight percent oxides. This is derived from counting statistics, standardisation, and correction procedures on the electron microprobe. The contribution is predicted to be normally distributed. As measured weight % oxides are normalised to individual mineral formula, then may be normalised again to calculate mineral mole fractions, the resulting uncertainties on weight % oxides are not equivalent to uncertainties on mole fractions (Worley & Powell, 2000). A Monte Carlo procedure may be incorporated to estimate uncertainties on calculated mole fractions (Hodges & McKenna, 1987; Kohn & Spear, 1991b), while analytical uncertainties associated with standardisation and correction procedures are likely insignificant if undertaken at a single analytical facilitiy (Worley & Powell, 2000).

4.1.5.3 Parameter error

Modelling a rock sample requires a variety of choices and input parameters that may significantly impact the resulting uncertainty on P-T conditions. Firstly, the appropriate database, a-X models and model system must be selected to best represent the rock. While ds6.2 (Holland & Powell, 2011) represents a significantly expanded and improved dataset for reliable calculations for petrological modelling, there is disagreement over which thermodynamic database and associated a-X models best reproduce natural observations. At low P, it has been found that ds6.2 is not capable of reproducing widely developed mineral assemblages as documented

in natural sequences (Pattison & DeBuhr, 2015; Pattison & Goldsmith, 2022). At high temperatures, Gervais & Trapy (2021) has demonstrated that ds5.5 and the biotite solution model of Tajčmanová *et al.* (2009) better reproduce data from experiments. The result of this is that several authors still model pelitic assemblages using older thermodynamic datasets and a-X models (e.g. George & Gaidies, 2017; Pattison & Spear, 2018; Waters, 2019). The choice of appropriate a-X models and a model system is also critical to inferred P-T conditions and topology of pseudosections. A model system that is smaller than one better representing the controlling equilibria may not adequately reproduce the observed rock assemblage, as well as mineral composition and modal abundance (White *et al.*, 2007). A current limitation is the reliance on a necessarily simplified system, thereby omitting elements that may occur in natural systems (e.g., Mn in garnet, Zn in staurolite), which may significantly impact modelled stability of certain minerals. Where it is possible to compare the impact of these omissions, the presence of absence of Mn in the model system is shown to strongly impact the appearance of garnet with changing P-T conditions (Tinkham *et al.*, 2001).

As as well as the petrologist appropriately defining the appropriate equilibration volume and bulk composition, a variety of other decisions are required as input parameters for petrological modelling. This includes a decision on bulk rock $X_{Fe^{3+}}$ as well as fluid abundance and composition (aH_2O). Apparent Oxidation state, is generally considered in most rocks as the ratio of ferrous (FeO, Fe^{2+}) to ferric (Fe_2O_3, Fe^{3+}) iron due to the overwhelming abundance of iron in comparison to other multivalent elements. This ratio ($X_{Fe^{3+}}$) may influence the location of phase equilibria and is now recognised as a key parameter in phase equilibrium modelling (Forshaw & Pattison, 2021). However, in the absence of costly and non-standard methods such as wet chemical titration, Mössbauer spectroscopy or X-ray absorption near edge structure (XANES) spectroscopy, bulk composition defining XRF and EPMA analyses are unable to distinguish between Fe^{3+} and Fe^{2+}. Charge balance techniques may be used to estimate Fe^{3+} and Fe^{2+} for some minerals based on EPMA analyses, but not for those containing vacancies. The lack of bulk rock $X_{Fe^{3+}}$ constraints can be partially mitigated by using P-X and T-X pseudosections to explore the dependence of phase equilibria on the input $X_{Fe^{3+}}$ ratio, and/or matching the predicted X_{Mg} values of silicate minerals to observed values (e.g., Doukkari *et al.*, 2018; Schorn & Diener, 2019). Assuming fluid-present conditions, phase equilibrium modelling of mineral assemblages formed at sub-solidus conditions may commonly infer pure H_2O. However, where fluid composition-dependent conditions may be implicated a lower aH_2O may be

necessary (e.g., Ohmoto & Kerrick, 1977), which could have a significant impact on the temperature of mineral assemblage boundaries (e.g., Weller *et al.*, 2013).

4.1.5.4 Model error

A major source of uncertainty in thermobarometry comes from the underlying model data used for calculations. This includes the thermodynamic data and activity-composition relations. Single-reaction and multi-reaction thermobarometry are both associated with uncertainties in thermodynamic data. For thermometers and barometers, these uncertainties are dominantly expressed by the precision of the experimentally determined end-member reactions used in calibrating the given thermometer or barometer (Hodges & McKenna, 1987; Kohn & Spear, 1991a; Worley & Powell, 2000). However when considering multi-reaction thermobarometry, experimental techniques and machine precision vary between different laboratories worldwide, with the result that thermodynamic parameters for individual phases determined during such experiments (e.g., H, S and V) are subject to random and systematic uncertainty. For internally consistent datasets, the calibrations used will adjust slightly within error brackets to ensure values are internally consistent (Holland & Powell, 1998, 2011). In this approach the uncertainties and correlations on the enthalpies of formation are determined by least-squares derivation from the experimental data, while other thermodynamic properties are inferred to be well-known. Such uncertainties and correlations can be propagated through the dataset onto calculated values of P and T.

a-X models are simplification of natural phases, for example, ideal behaviour may be assumed for a phase that actually behaves in a non-ideal manner. More sophisticated models may use additional terms (e.g., activity coefficients and interaction parameters; Green & Usdansky, 1986) to describe the excess Gibbs free energy of mixing. The difficulty in constraining these terms experimentally means large uncertainties are carried over for a-X relations during phase equilibrium modelling. Measured activity-composition relations are few in number and thus uncertainties are difficult to constrain (Powell & Holland, 1988). An attempt to account for these uncertainties is included in the AvPT method where analytical and a-X uncertainties are combined empirically to produce an uncertainty on the activity which is strongly weighted towards the a-X contribution.

Recognising the possible sources of error within P-T calculations, allows petrologists to minimise these where possible, and record associated errors where it is not. Powell & Holland (2008) and Palin *et al.* (2016) suggested that a realistic

assessment of absolute uncertainty in *P-T* estimates should be a minimum of ± 1 kbar and ± 50 °C (2σ).

4.2 Thermobarometry methods

4.2.1 Pseudosection setup

Pseudosections are the preferred method of investigation for the *P-T* path of metamorphic rocks (Powell & Holland, 2008), and were chosen as the main interpretative tool for the metamorphic rocks of the Suru Valley region. Several programs are available to calculate pseudosections, with the main difference being those that minimise Gibbs free energy (e.g., Theriak-Domino), thereby creating fields, and those that solve non-linear equations (e.g., THERMOCALC), thereby calculating field boundaries. All pelite pseudosections were constructed using Theriak-Domino (de Capitani & Brown, 1987; de Capitani & Petrakakis, 2010, version 25th May 2021, modified by D. Tinkham) using a converted version of ds6.2 (Holland & Powell, 2011, version td-ds62-mp50-v05 from 11th March 2022, modified by D. Tinkham). All metabasite pseudosections were constructed also in Theriak-Domino using a later version (version 11th June 2023) to incorporate the latest compositional models (e.g., FSP4TR; Holland *et al.*, 2022) integrated into ds6.2 (version td-ds62-mb50-v07 from 24th Dec 2022, modified by D. Tinkham). Select metabasite samples containing garnet or other phases better suited to an integrated dataset used a custom version of the pelite and metabasite dataset.

Phase diagrams were computed in the 11-component MnNCKFMASHTO system (MnO-Na_2-CaO-K_2-FeO-MgO-Al_2O_3-SiO_2-H_2O-TiO_2-O_2) for pelitic assemblages and NCKFMASHTO for metabasic assemblages. Pelitic garnet-bearing assemblages were modelled with the addition of MnO, as Mn has been shown to have a large effect on garnet stability (Mahar *et al.*, 1997; White *et al.*, 2014a).

For MnNCKFMASHTO in pelitic systems, the following solid-solution models were used: silicate melt, garnet, biotite, muscovite, margarite, orthopyroxene, cordierite, staurolite, chlorite, chloritoid (White *et al.*, 2014b), feldspar (Holland *et al.*, 2022), stipnomelane, minnesotaite, prehnite, pumpellyite, epidote (Holland & Powell, 2011), sapphirine (Wheller & Powell, 2014), ilmenite and hematite, magnetite (subsolidus model; White *et al.*, 2000).

For NCKFMASHTO in metabasic systems, the following solid-solution models were used: silicate melt, hornblende, actinolite, glaucophane, jadeite-omphacite-

diopside clinopyroxene, muscovite (Green *et al.*, 2016), feldspar (Holland *et al.*, 2022), epidote, olivine (Holland & Powell, 2011), garnet, biotite, orthopyroxene, chlorite (White *et al.*, 2014b), ilmenite and hematite, magnetite (subsolidus model; White *et al.*, 2000).

For MnNCKFMASHTO in select metabasite samples, the following solid-solution models were used: silicate melt, garnet, biotite, muscovite, margarite, orthopyroxene, cordierite, staurolite, chlorite, chloritoid (White *et al.*, 2014b), feldspar (Holland *et al.*, 2022), minnesotaite, prehnite, pumpellyite, epidote, corundum (Holland & Powell, 2011), sapphirine (Wheller & Powell, 2014), ilmenite and hematite, magnetite (subsolidus model; White *et al.*, 2000). Mn-bearing ilmenite was selected such that the maximum number of Mn-bearing phases were activated such that garnet was not artificially stabilised.

Additional phases with no solid solution include H_2O, andalusite, kyanite, sillimanite, corundum, H2O, quartz, rutile, and titanite.

Calculating pseudosections requires some form of idealised bulk composition as an input. Theriak-Domino accepts molar amounts (extensive properties) of elements in any order. In comparison, THERMOCALC requires this to expressed in molar proportions of oxide components, in a fixed order. Because XRF data was chosen as the preferred method for bulk composition, samples that were mainly composed of phases that could be represented in the model system were preferentially selected. The following modifications were made to weight % XRF data to make it suitable for input to Theriak-Domino:

1. P_2O_5 was removed from the bulk and a proportional adjustment was made to total CaO to correct for the contribution of apatite ($Ca_5(PO_4)_3(OH,F,Cl)$). For each mole of P_2O_5 removed, 10/3 moles of CaO were removed multiplied by the proportion of original P_2O_5 residing in apatite. This was approximated by inspection in thin section to the relative proportion of apatite versus monazite. For the presence of both apatite and monazite only a half-correction was made, where only apatite was present a fully correction was made.

2. For pelitic compositions a value of $X\mathrm{Fe}_{3+}$ was set using Fe-Ti-oxide minerals present as a guide of oxidation state (Diener & Powell, 2010; Forshaw & Pattison, 2021). Diener & Powell (2010) showed that within pelitic assemblages it is just ilmenite present at $X\mathrm{Fe}_{3+} < 0.05$ (very reduced conditions) with magnetite or hematite stabilised at $X\mathrm{Fe}_{3+} > 0.05$. It

reflects the observation that with the exception of biotite and chlorite (and to a smaller degree white mica and staurolite), silicate minerals do not host large amounts of Fe_{3+}, so changes in $X_{Fe^{3+}}$ are best indicated by the oxide mineralogy (Diener & Powell, 2010; Forshaw & Pattison, 2021). Adopting this measure helps ensure that the whole rock $X_{Fe^{3+}}$ used for the modelling is broadly consistent with the thermodynamic dataset and a-X models chosen. For metabasic compositions Fe_2O_3 is distributed across multiple phases, as such the use of Fe-Ti-oxides are less useful in determining the oxidation state. An important reservoir for Fe_{3+} is hornblende which represents the modally dominant mineral in all samples, with the exception of ICSV2, which contains both large amounts of both actinolite and hornblende. As such a mean of amphibole $X_{Fe^{3+}}$ was used for bulk rock $X_{Fe^{3+}}$. This was calculated using the mineral recalculation scheme defined by an in-house spreadsheet (D.J. Waters). This scheme differs from AX in two points. Firstly, it applies a deprotonation substitution involving half the Ti content of hornblende in accordance with Green *et al.* (2016), this correction is applied to the oxygen total (and therefore total cations). Secondly it allows for Mn to be allocated preferentially to the M4 site as introduced in the Hawthorne *et al.* (2012) stoichiometry. The difference to the AX recalculation scheme is minor but appears to bring results better into alignment with the Green *et al.* (2016) model thus was chosen solely for defining $X_{Fe^{3+}}$ as this choice impacts the bulk rock estimate. It is important to note that this method produces results similar to measured $X_{Fe^{3+}}$ estimates from similar metabasic sequences (Starr *et al.*, 2020), where an average value of 16.9% was used.

3. H_2O was set in excess for all sub-solidus regions (in this case MH_2O was set to 20), to simulate prograde metamorphism (Guiraud *et al.*, 2001). For supra-solidus regions, water content was estimated from mineral modes and compositions of hydrous phases Groppo *et al.* (2013); Waters (2019), see further details below.

4.2.2 Thermometry

Thermometry was undertaken based on a variety of mineral phases using both single-phase concentration and mineral pair thermometry techniques including Zr-in-rutile (Kohn, 2020; Tomkins *et al.*, 2007), Ti-in-Ca-amphibole (Liao *et al.*, 2021), Zr-in-titanite (Hayden *et al.*, 2008), and Ti-in-biotite (Henry *et al.*, 2005; Wu & Chen, 2015). The Ti-in-biotite thermometer of (Henry *et al.*, 2005) and

hornblende-plagioclase exchange therometer of Holland & Blundy (1994) were used as the independent temperature constraints in this study, with the other calibrations used to validate the temperatures. The Ti-in-biotite thermometer was selected for pelitic rocks because biotite is present in all modeled pelite samples. Furthermore, this thermometer was specifically calibrated for graphitic pelites that contain either ilmenite or rutile as the Ti-dominant phase, both of which are abundant across all grades in the sample set. Interleaved metabasic lithologies also contain biotite in all but two modelled samples, allowing for comparison of predicted temperatures between rock types. For metabasic compositions the hornblende-plagioclase exchange thermometer was used as the independent thermometry result as the pre-requisite assemblage is present in all metabasite samples and it has been successfully applied in calcic-amphibole bearing assemblages in numerous metamorphic and igneous studies.

For thermometers with pressure-dependency, calculations are undertaken at 10 kbar for all samples except for ICSV68 and ICSV142 (9 kbar), ICSV144 (7 kbar), and ICSV148 (6 kbar). This pressure range was selected based on the range of previous pressure constraints from the region (e.g., Searle *et al.*, 1992; Walker *et al.*, 2001); the recorded metamorphic grade and microstructures; and preliminary tests of the AvP. A pressure uncertainty range of $\pm$ 2 kbar is propagated through the temperature calculations to assess dependency on initial input.

For each thermometer an average value is used with population distribution assessed via a 2 SD uncertainty (including pressure uncertainty where present in the calibration). Where therometry results are paired to multi-equilibrium barometry, calibration error (where given) is used for final reporting of temperature results. Compositional data are filtered in each technique as follows: for Hornblende-plagioclase, Ti-in-Ca-amphibole, and Ti-in-biotite, electron microprobe spot analyses are excluded consistent with the selected compositions for mineral chemistry. Analyses are discarded based on stoichiometry, excursions of particular elements suggesting more than one phase was analysed, and/or microstructural relationships. For analyses undertaken specificly for thermometry (Zr-in-rutile and Zr-in-titanite), a different approach was used, outlined below for the given techniques.

4.2.2.1 Zr-in-rutile

Rutile compositional analysis were completed on a Cameca SX5-Fe electron microprobe with a tungsten tipped field emission gun at the Department of Earth Sciences, University of Oxford. Carbon coated, polished thin sections, ~30 µm thick were analysed using the spectrometer setup and operating parameters included in the appendix. A matrix correction was applied to all analysis assuming a composition 59 % Ti. The primary standard used was R632 (4294 ± 196 ppm; Axelsson *et al.*, 2018). Synthetic TiO_2 was used as a blank. Data showing excursions in Fe, Ca and Si content, or near detection limit for Zr were excluded.

The Zr-in-rutile thermometer was first calibrated empirically (Zack *et al.*, 2004), then experimentally (Watson *et al.*, 2006; Tomkins *et al.*, 2007), and has since been refined by Kohn (2020). The Tomkins *et al.* (2007) calibration has been most-widely applied owing to the incorporated pressure-dependence. However, experimental calibrations use very high temperatures (~1150 °C), which are both higher than most-rutile bearing rocks, and significantly higher than the temperatures in this study. Subsequent refinement of the thermometer by Kohn (2020) using bootstrapped, weighted, linear regressions that incorporate both experimental data and natural data at lower temperatures, is used for the present study, comparison to the Tomkins *et al.* (2007) calibration is given for reference.

4.2.2.2 Hornblende-plagioclase and Ti-in-Ca-amphibole

Electron microprobe wavelength dispersive spectrometer spot analyses for mineral compositional data of Ca-amphibole and plagioclase follows the procedure detailed in Section 3.2.1.

For the hornblende-plagioclase NaSi-CaAl exchange thermometer the calibration of Holland & Blundy (1994) with corrections from Dale *et al.* (2000) are used in this study, this includes preventing non-stoichiometric Ca distribution onto the M13-site. For compatibility with the Green *et al.* (2016) amphibole model an in-house spreadsheet is used where half of the Ti substitution is treated as deprotonation. Results are given for the edenite-tremolite thermometer. Since, the exchange thermometer should be used with X_{Na} range of 0.1–0.9, results outside this range can only be viewed as minimum temperature estimates. Subsequent re-assessment of the exchange thermometer and calibrations by Molina *et al.* (2021) require an even more restricted range of X_{Na} (< 0.8) and is therefore not applicable to this study.

For the Ti-in-Ca-amphibole thermometer, the calibration of Liao *et al.* (2021) is applied to amphibole analyses from metabasic rocks.

4.2.2.3 Zr-in-titanite

Trace element data for titanite was collected by laser ablation at the British Geological Survey, detailed procedure for this technique is included in Section 5.2.2. Data outside an IQR for each sample are excluded. A resulting mean and 2 SD is calculated. Zr-in-titanite temperatures were calculated using the calibration of Hayden *et al.* (2008). Zircon and quartz commonly coexist with titanite in the analyzed samples, however, rutile is rarely present. TiO_2 activation energy must therefore be lower than 1, but higher than the plausible lower limit in typical crustal rocks of 0.5 (Chambers & Kohn, 2012; Ferry & Watson, 2007; Ghent, 1976; Hayden & Watson, 2007). A value of a_{TiO_2} 0.75 was used with a conservative uncertainty of ± 0.25. Given there is no calibration error, reported uncertainties are the propagated 2 σ uncertainties of the Zr concentrations, selected pressure (± 2 kbar) and a_{TiO_2}.

4.2.2.4 Ti-in-biotite

Electron microprobe wavelength dispersive spectrometer spot analyses for mineral compositional data of biotite follows the procedure detailed in Section 3.2.1.

Ti-in-biotite thermometry can use the calibration of Henry *et al.* (2005) or the empirical recalibation of Wu & Chen (2015). The Wu & Chen (2015) recalibration incorporates pressure dependence and Fe and Al^{VI} into the equation (originally solely dependent on the input X_{Mg} and Ti contents). The Henry *et al.* (2005) calibration is suitable for X_{Mg} = 0.275–1.000, Ti = 0.02–0.30 apfu, and T = 480–800 °C, whereas the Wu & Chen (2015) thermometer is suitable for a more restricted compositional range 1–19 kbar, Ti = 0.02–0.14 and 450–840 °C. Ti contents are reported throughout for 11 oxygens, with calculations undertaken using 22 oxygens. This study contains biotite with a Ti compositional range of 0.07–0.19 apfu which is outside the reported parametrisation for the Wu & Chen (2015) calibration. Furthermore, the Wu & Chen (2015) calibration lacks a strict thermodynamic and crystallographic foundation — and as such the Henry *et al.* (2005) calibration was selected for this study, comparison to the Wu & Chen (2015) calibration is given for reference.

4.2.3 Constraining $a\mathrm{H_2O}$ and pseudosection construction

Although the locating fields approach is recommended as the first method of *P-T* determination, other thermobarometric constraints are favoured where an assemblage involves unconstrained factors (e.g., activities of H_2O and CO_2; Powell & Holland, 2008). Initial pseudosection reconaissance assuming dominant pure H_2O for a large proportion of the sample set resulted in no field match across large *P-T* ranges for the observed pelitic assemblage for the given bulk composition. Partial assemblage matches were displayed in melt-bearing fields, but only a small sub-set of samples have field-observations supporting *in-situ* migmatisation. Therefore $a\mathrm{H_2O}$-independent thermometry and/or thermobarometry constraints may be used to to constrain $a\mathrm{H_2O}$ of the system (Walker *et al.*, 2001; Powell & Holland, 2008). The Ti-in-biotite thermometer (Henry *et al.*, 2005), as used for pelite, and hornblende-plagioclase exchange thermometer (Holland & Blundy, 1994), as used for metabasite, are not constrained by $a\mathrm{H_2O}$ and are orthogonal to the system used for modelling. These thermometers were used with an $a\mathrm{H_2O}$-dependent AvP result to inform the $a\mathrm{H_2O}$ for phase equilibrium modelling or were paired with an $a\mathrm{H_2O}$-independent AvP result, to provide an independent constraint for phase equilibrium modelling. The effect of adjusting $a\mathrm{H_2O}$ is analysed in Section 4.4.3.

AvP was run until all indices conformed (the χ^2 test, Powell & Holland, 1994). If 1) the 95 % confidence interval was achieved for a calculated pressure over a temperature range, and 2) the given temperature range overlapped the boundaries of the thermometer mean result and associated calibration error, then the result was accepted. If the temperature range was too high and did not overlap with the independent thermometer result, then the $a\mathrm{H_2O}$ was reduced in increments of 0.1 to achieve an acceptable result. Although, this approach helped to initially constrain an appropriate $a\mathrm{H_2O}$, where possible final AvP results were calculated using $a\mathrm{H_2O}$-independent equilibria (e.g., by removing paragonite and albite). For samples where AvP was not possible due to insufficient constraining equilibria, a best guess of pressure was obtained using a peak assemblage match and/or mineral compositional data as detailed below.

The $a\mathrm{H_2O}$ used in AvP calculations was set within the thermodynamic database of Theriak-Domino used for pixel mapping routine (detailed in Section 4.2.4) and phase equilibrium diagrams. Pseudosection modelling was undertaken over an appropriate interval that could be inferred from the *P-T* data obtained from multi-equilibria barometry and independent thermometery. Generally the

interpreted peak assemblage and intersection of independent thermobarometer was thus obtained. Where the AvP result was constrained by reactions with no free fluid phase, then pixelmapping was undertaken with progressive reductions of $a\mathrm{H_2O}$ (0.1) to achieve reasonable agreement between the necessary components of the peak assemblage field, best-fit of mineral compositions (Section 4.2.4) and $a\mathrm{H_2O}$-independent thermobarometer intersection. For AvP results that contained a free fluid phase in equilibria reactants or products but where pixelmaps or phase equilibrium diagrams did not show an agreement of the peak assemblage field, modelled mineral compositions and the thermobarometer intersection, further adjustments were necessary. As above, pixelmapping with progressive reductions of $a\mathrm{H_2O}$ was undertaken to achieve agreement between the necessary components. AvP results were also adjusted such that parameter values were consistent.

Departure from the above method must be outlined for supra-solidus samples. A variable approach of defining $a\mathrm{H_2O}$ was not applied and all samples were modelled without a fixed $a\mathrm{H_2O}$. This approach was applied given the recognition that $a\mathrm{H_2O}$ decreases moving towards anhydrous melting. Adjusting $a\mathrm{H_2O}$ also has a significant impact of the location of the solidus (Weller *et al.*, 2013). Hydrous equilibria can be defined by changes in T rather than P, resulting in a vertical solidus when P-T are displayed on y-x axes accordingly. A variety of methods for defining the water content are possible, see discussion in Waters (2019). The $\mathrm{H_2O}$ content in the bulk rock composition was estimated by combining mineral modes and compositions of hydrous phases, following the approach of Groppo *et al.* (2013) and Waters (2019). In such cases where biotite is the near-dominant hydrous phase, $\mathrm{H_2O}$ is therefore estimated using the Ti-H substitution scheme of White *et al.* (2007). Overestimation of biotite, owing to its tabular nature, was avoided by using sections cut perpendicular to the foliation. Furthermore, several point counts of biotite were conducted to ensure robust counting.

Components of the peak assemblage field that were not considered essential were phases such as ilmenite, haematite, rutile and magnetite. This is based on relative uncertainty over the location of phase transitions in P-T space. Ti-oxides may be poorly preserved during decompression and retrogression of the assemblage. Equally, it must be acknowledged that in the absence of inferred retrogression, the current models of White *et al.* (2000) do not always perfectly reproduce the natural observed Ti-oxides. However, P-X and T-X pseudosections were used to explore the dependence of phase equilibria on the input $X_{\mathrm{Fe^{3+}}}$ ratio. This step was performed last as this variable has a minimal impact on the stability of major phases. In pelitic compositions an appropriate $X_{\mathrm{Fe^{3+}}}$ value was selected

to best represent the interpreted peak Fe-Ti-dominant phase with values chosen to match the modelled composition rather than the observed composition (Forshaw & Pattison, 2021). For metabasites, $X_{Fe^{3+}}$ was set by the appropriate value calculated by the modally dominant amphibole.

4.2.4 Grid-search non-linear inversion

Quantitative *P-T* constraints and estimate of uncertainty in the modelled system was undertaken with a series of MATLAB scripts using grid-search non-linear inversion. Two main inputs for the scripts are required. 1) Forward models, generated using Theriak-Domino for *P-T* points within the range of interest (pixel mapping). This approach used phase compositions (and locally modal volumes). 2) Observed data corresponding to the modelled variables, in this case mean values and associated 2 SD uncertainty of EPMA mineral analyses. Three main scripts then define the routine which can be undertaken in any 2-dimensional space of (e.g., *P-T*, *P-X*, *T-X*). Dominantly this was *P-T* space, and is referred to as such, with the recognition that other combinations are possible. A coarse 30 × 30 grid was generally applied during reconnaissance of 2-dimensional space followed by a 100 × 100 grid for the final result.

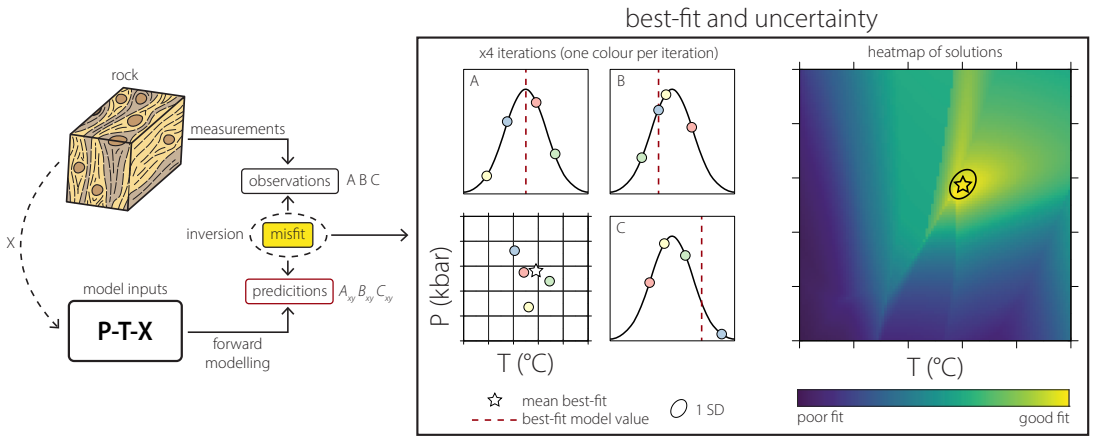


Fig. 4.5 Schematic of grid-search non-linear inversion workflow showing determination of best-fit statistic and associated uncertainty from resampling. Thin setion schematic taken from Palin *et al.* (2016).

1. Overlapping contoured isopleths: The first script plots the *P-T* interval over which the observed values for each selected compositional variable is modelled to be stable. Variables can be added and subtracted, allowing initial filtering to select those that produce reasonable overlap with other compositional information within the *P-T* range of interest.

2. Grid-search non-linear inversion: The second script calculates the value of an objective function at each point in the *P-T* grid. The objective function is a scalar value that shows how well the observed data fits the modelled data. A large value indicates a poor fit (i.e., a large misfit), whereas a small value indicates a good fit. The "best fit" *P-T* solution for the observed data is the point in *P-T* space with the lowest objective function value (smallest misfit). Consequently, the script plots a misfit map of the observed values for the selected compositional variables in modelled space. The 2-dimensional space is coloured or contoured with a heatmap to display the zone of minimum misfit between the mean value of each variable (lower values preferable). This produces a global minimum across the calculated *P-T* range. The more variables used generally results in an overall higher range of misfit values but a more clustered result. This method is known as grid-search inversion, and is often used for non-linear inverse problems, where the goal is to find the set of model variables by iteratively minimising the difference between the observed data and the data predicted by the model.

3. Bootstrapping: In order to determine the distribution and uncertainty on the best-fit statistic (i.e., bootstrapping), the final script randomly resamples (Monte Carlo simulation) each observed compositional variable from a normal distribution space with a SD of 10 % from the mean observed value. The script runs 500 simulations, and the best-fit solution is calculated for each simulation. Statistical analysis is then performed on the cluster of results. A peak point is calculated for the greatest cluster using a normalised 2D gaussian distribution. A 1 SD uncertainty ellipse is given using the individual peak points defined by each Monte Carlo simulation.

This approach was broadly used to define 1) garnet core compositions where significant compositional zoning was observed and/or 2) all phases or zones of phases inferred to be in equilibrium at "peak".

The reliability of the result is dominantly dependent on the selected compositional variables (assuming an appropriate *P-T* range and grid density is used). variables that showed good *P-T* dependence were chosen, with a preference towards using site fractions or ratios. The aim was to create a set of variables that were broadly independent. As such only 3 out of the 4 possible garnet end-members were used. Almandine was removed as it represents the largest mole fraction in this sample set, thefore its absolute value is more strongly

influenced by variation among the other phase components (Waters, 2019). For pelitic compositions the following variables were used: Si, X_{Mg}, Ti in biotite; Si, X_{Pa}, X_{Cel} in muscovite; X_{Grs}, X_{Sps}, X_{Prp}, X_{Mg} in garnet; X_{Mg} in chlorite; X_{Na} in plagioclase and X_{K} in K-feldspar.

In metabasic compositions the same constraints were used with the addition of $X\mathrm{Fe}^{3+}$ in epidote; tschermakite (Al(T)-Na(A)-K(A)), edenite (Na(A)+K(A)), glaucophane (Na(M4)) vectors and Ti in amphibole; Al, X_{Mg}, Ca and X_{Jd} in clinopyroxene. The use of vectors in amphibole was deemed essential to reduce dependency of the result on regularly overestimated (Al and A-site Na) or underestimated (Si, Ca and A-site K) cations (Forshaw *et al.*, 2019).

4.2.5 X-ray fluorescence

XRF whole-rock data was acquired at the XRF laboratory within the Institute of Geosciences at the University of Mainz. The laboratory is equipped with a MagiXPro spectrometer from Panalytical. Excitation was achieved on fused glass beads from representatively-sized powdered samples. Loss on ignition (LOI) was determined during formation of glass beads at a temperature of ~1050 °C. The results of the chemical analysis and LOI are shown in Appendix tables, with all Fe reported as Fe^{3+}. Sample ICSV144 was subsequently analysed at the School of Earth and Environmental Sciences at University of St Andrews using a SPECTRO XEPOS HE ED-XRF. The routine is broadly consistent with that listed above.

4.3 Sample descriptions

Rock names are based on relevant indicator minerals in pelitic and metabasic assemblages. In general, porphyroblastic minerals of increasing grade and key indicator minerals are discussed first followed by matrix phases. A primary assemblage infers the given phases formed during prograde–peak metamorphism and dominantly preserve textural and chemical equilibrium. Key metamorphic porphyroblasts (e.g., garnet) are documented as syn- or post-tectonic with respect to the main crustal thickening fabric (Fig. 2.17), emphasising a Himalayan origin. Petrographic description includes all garnet grains in the sample. All garnet compositional information is given from core–rim unless specified otherwise. Only the garnet grain selected for modelling (defined for subsolidus grains as

the grain that has the greatest X_{Sps} in the core) is discussed in the context of compositional zoning. Accessory minerals are not discussed unless deemed relevant (e.g., Ti-oxide phases). Ti contents in biotite are given to 11 oxygens in this chapter, consistent with use in the *a-X* models of White *et al.* (2014a), where the Ti-in-biotite thermometer is used, Ti contents use 22 oxygens. Sample locations are shown in Figure 4.6.

4.3.1 Pelite

4.3.1.1 Garnet zone: ICSV86, ICSV38, ICSV130

ICSV86: Garnet-biotite schist ICSV86 contains the primary assemblage quartz, muscovite, biotite, plagioclase, and garnet (Fig. 4.7a). Accessory phases include apatite, ilmenite, tourmaline, allanite, and monazite. Retrogressive phases include chlorite. This sample is part of the mixed psammite, pelite, and semipelite lithology.

Garnet forms irregularly sized subhedral to anhedral elongate poikiloblasts, ranging from sub-mm to 6 mm in size. Grains host abundant quartz, ilmenite, biotite, and allanite inclusions that are well distributed throughout. Smaller grains typically contain fewer inclusions. Heavily fractured garnet grains exhibit chlorite growth along fractures and ragged grain boundaries (Fig. 4.7a). These features can locally be associated with partial resorption and growth of chlorite, biotite and plagioclase along garnet rims. Garnet is generally weakly- to moderately-zoned, the selected compositional profile does not transect the true core (Fig. 4.8a). Garnets are Fe-rich ($X_{Mg} = \frac{\mathrm{Mg}}{\mathrm{Fe^{2+}+Mg}} = 0.12$–$0.14$) with the centres of the selected garnet grain having slightly lower almandine and pyrope content ($X_{\mathrm{Alm}} = 0.77$, $X_{\mathrm{Prp}} = 0.10$) relative to rims ($X_{\mathrm{Alm}} = 0.80$, $X_{\mathrm{Prp}} = 0.13$). Spessartine and grossular contents are slightly elevated in the core relative to the rim ($X_{\mathrm{Sps}} = 0.03$–0.01, $X_{\mathrm{Grs}} = 0.09$–0.07).

Biotite is present as subhedral to euhedral tabular grains (~0.1–3.0 mm). It occurs as coarse matrix grains, appearing as a primary phase, or is intergrown with muscovite occurring as fine grains along cleavage and grain boundaries. In the latter scenario, growth may have been in replacement of muscovite. Biotite contains minor variation of X_{Mg} of 0.43–0.46 and Ti (11 O) of 0.09–0.11 apfu.

Muscovite occurs in a variety of forms. It is mostly present as subhedral to euhedral tabular grains, ranging from sub-mm to 2 mm in length, and as the

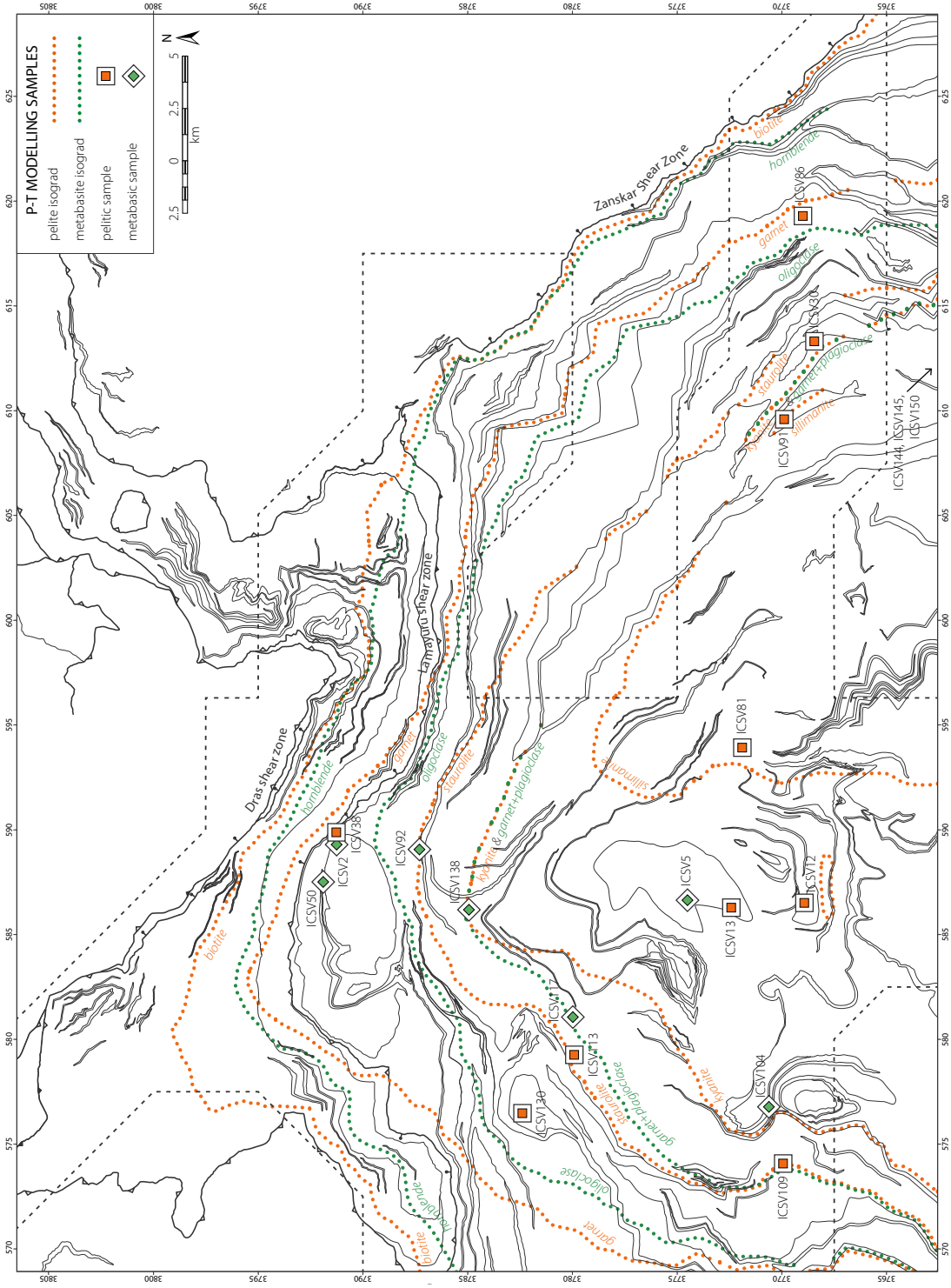


Fig. 4.6 Form-line map of major lithological and tectonic features of the Suru Valley area, NW India, overlain with pelitic and metabasic isograd sequences with highlighted locations for the studied sample set.

dominant fabric defining phase. Muscovite also occurs as a coarse porphyroblastic phase that locally define weakly developed mica-fish. Grains are generally subhedral to anhedral and may be fringed by biotite and/or late chlorite, with the latter

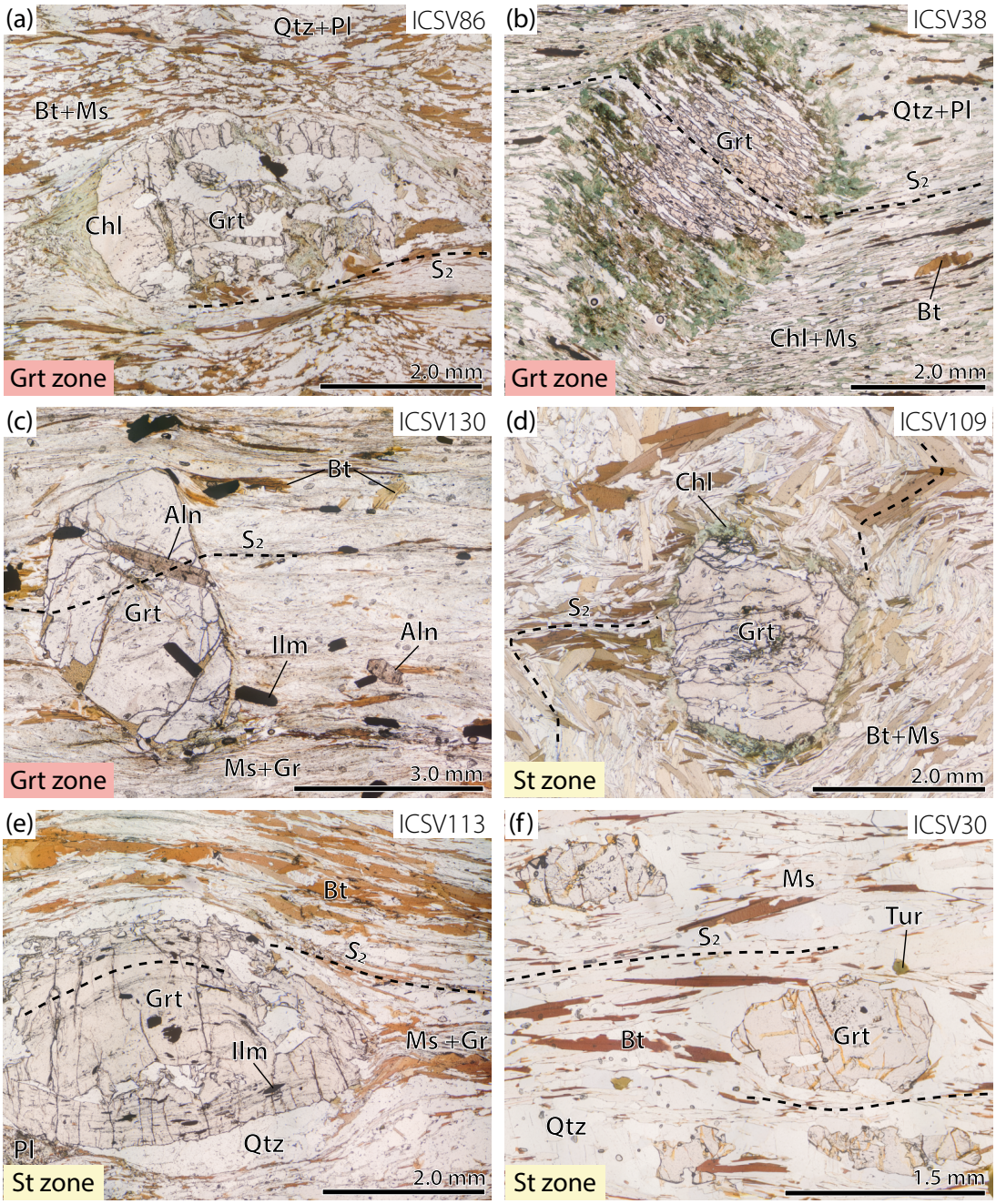


Fig. 4.7 Petrographic images of characteristic textures and mineral assemblages in a–c) garnet-zone, and d–f) staurolite-zone samples.

also present along cleavage. There are also some smaller (~0.3 mm) euhedral crystals that are unoriented with respect to the main fabric. Matrix grains are slightly more Si-rich than porphyroblastic grains (3.07–3.10 vs 3.04–3.05 apfu, respectively). X_{Na} contents show negligible difference between microstructural location and vary from 0.14–0.16.

Plagioclase occurs as prismatic to oval subhedral to anhedral grains (between $\leq$ 0.1 and 0.4 mm). Largely, plagioclase occurs in the interstices between matrix

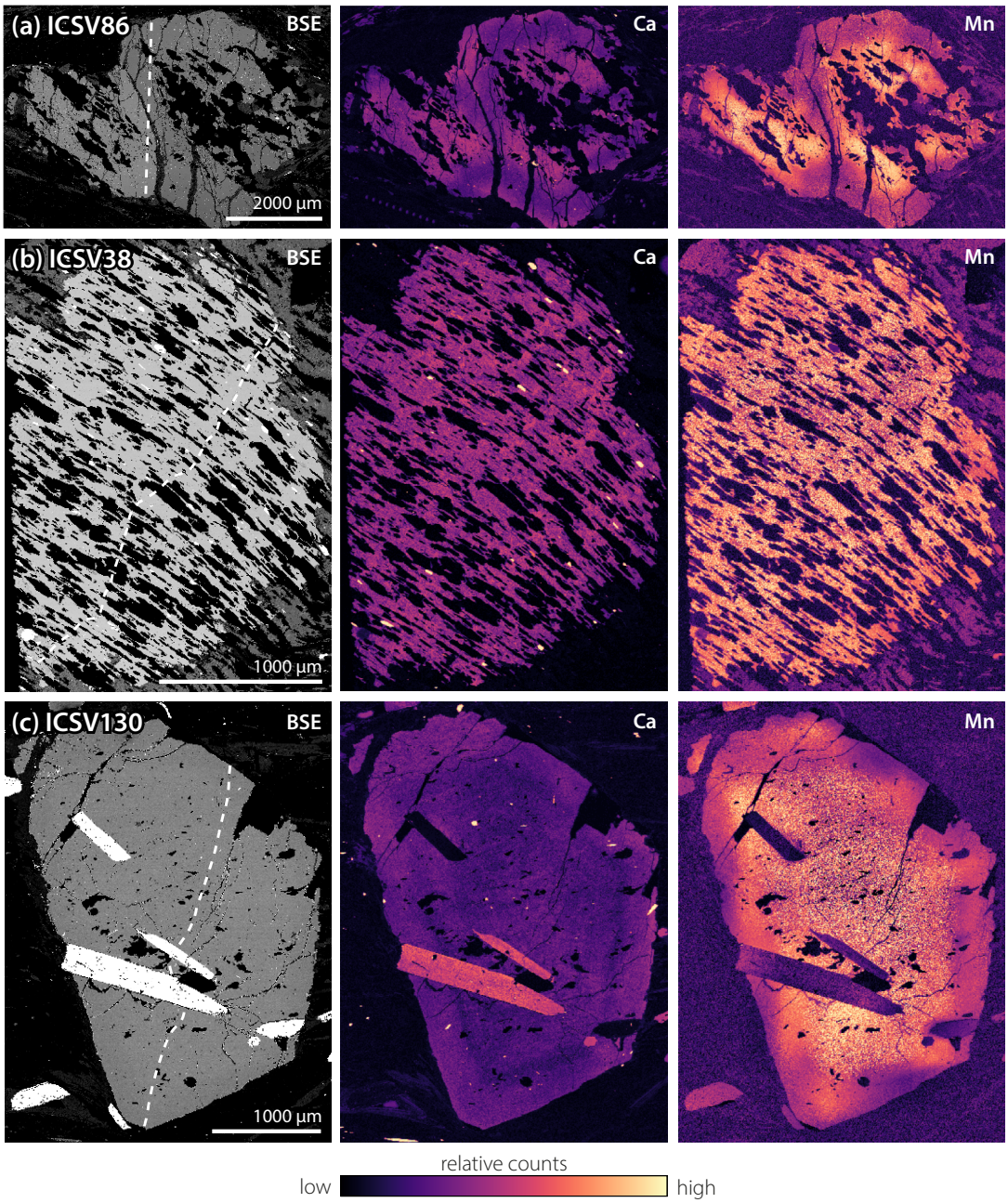


Fig. 4.8 Garnet BSE images and Ca and Mn X-ray compositional maps for garnet-zone samples.

phases in semipelitic layers, or is well-distributed but modally minor with quartz in psammitic layers. Plagioclase shows minor variation in the oligoclase range (X_{Na} 0.84–0.90).

Quartz occurs as rounded to oval flattened grains of variable size. Quartz grains found as inclusions in garnet are coarse (up to 2.5 mm in length) with no evidence of recrystallisation and only minor evidence of recovery. Matrix grains are smaller (~$\leq$ 0.1 to 0.6 mm), displaying bulging at grain boundaries and

sweeping undulose extinction. C' bands developed in the rock record significant sub-grain rotation. The periphery of garnet augen are also defined by sub-grain rotation in quartz.

Ilmenite generally occurs as prismatic to angular euhedral grains aligned with the main matrix fabric and also concentrated in garnet cores.

ICSV38: Garnet-biotite schist ICSV38 contains the primary assemblage quartz, muscovite, chlorite, garnet, biotite, and plagioclase (Fig. 4.7b). Accessory phases include ilmenite, sulphides and apatite. Retrogressive phases include chlorite. This sample is part of the mixed psammite, pelite, and semipelite lithology.

Garnet forms rounded euhedral to subhedral grains, ranging between 3.5 to 6.0 mm in size. Grains host abundant parallel equigranular inclusions of elongate quartz and ilmenite. Inclusions are well distributed throughout the grain and display ~25–40° of rotation from the matrix fabric (Fig. 4.7b). Garnet displays ~0.5–1.0 mm thick corona of unoriented Fe-rich chlorite, with minor biotite and white mica (Fig. 4.7b). This corona texture is interpreted to represent late resorption and replacement by mica. Garnet is generally weakly zoned (Fig. 4.8b). Garnet grains are Fe-rich ($X_{\mathrm{Mg}} = 0.07$) with the cores having slightly lower almandine content relative to rims ($X_{\mathrm{Alm}} = 0.58$–0.59). Spessartine contents are slightly elevated in the core relative to the rim ($X_{\mathrm{Sps}} = 0.16$–0.13). Pyrope contents show a fairly flat profile ($X_{\mathrm{Prp}} = 0.04$) , whereas grossular varies between point analysis and shows a slight increase from core to rim ($X_{\mathrm{Grs}} = 0.22$–0.24). Garnet grains from ICSV38 are more grossular rich than other samples (Fig. 3.12a).

Chlorite dominantly occurs as primary tabular euhedral to subhedral grains (~0.1–1.0 mm in length) intergrown with muscovite (Fig. 4.7b). X_{Mg} varies between 0.41–0.44. Chlorite at garnet rims is compositionally consistent with matrix grains, which matches observations from Figure 3.15 showing no obvious compositional variation between prograde or retrograde chlorite. This is inconsistent with the darker blue colour (commonly Fe-rich) of chlorite on garnet rims.

Biotite occurs as tabular euhedral to subhedral grains intergrown or overgrowing matrix chlorite (~0.2–2.0 mm in length; Fig. 4.7b) and as porphyroblasts/mica-fish. All analysed grains are homogenous with an X_{Mg} of 0.41–0.42 and a Ti content of 0.10–0.11 apfu.

Muscovite occurs as fine tabular euhedral matrix grains intergrown with chlorite. It is the dominant mica and is well distributed throughout the sample. Compositionally grains show some variation (Si = 3.17–3.25 apfu, $X_{\mathrm{Na}} = 0.08$–0.12).

Plagioclase is present as oval subhedral grains (between ≤ 0.1 and 0.4 mm in size) in the interstices between matrix phases and is well-distributed throughout the sample. Plagioclase is homogenous, with the composition of albite ($X_{\mathrm{Na}} = 0.99$).

Quartz occurs as flattened grains and is largely equigranular throughout the section showing variation in size between ≤ 0.1 and 1.0 mm. Grains display minimal evidence of recovery and recrystallisation as expressed through minor undulose extinction and local bulging at grain boundaries.

Ilmenite generally occurs as oval to prismatic euhedral grains (up to 0.2 mm in size) aligned with the main matrix fabric and present both in the matrix and garnet cores. Sulphides are locally present as thin elongate grains aligned with the main fabric.

ICSV130: Garnet-biotite schist ICSV130 contains the primary assemblage muscovite, quartz, biotite, plagioclase, graphite, and garnet (Fig. 4.7c). Accessory phases include ilmenite, allanite, ilmenite, and apatite. Retrogressive phases include chlorite. This sample is part of the mixed psammite, pelite, and semipelite lithology.

Garnet forms angular euhedral to subhedral pokiloblasts ranging in size from 2.0–4.0 mm. Ilmenite, allanite, quartz, and graphite are the dominant inclusions present, and inclusion trails are concordant with the matrix fabric, implying post-tectonic growth of garnet (Fig. 4.7c). Locally garnet rims are mantled by misoriented chlorite, interpreted to represent retrogression, otherwise garnet shows minimal evidence of resorption or breakdown at rims (Fig. 4.7c). This is in agreement with garnet chemistry, which displays moderate compositional zoning (Fig. 4.8c). Garnet cores are Fe-rich ($X_{\mathrm{Mg}} = 0.12$–0.11) have moderately lower almandine and slightly lower pyrope content relative to rims ($X_{\mathrm{Alm}} = 0.72$–0.77, $X_{\mathrm{Prp}} = 0.08$–0.11). Spessartine in the core is elevated relative to the rim ($X_{\mathrm{Sps}} = 0.09$–0.02). Grossular content shows a fairly flat profile ($X_{\mathrm{Grs}} = 0.10$).

Biotite is intergrown with muscovite to define the dominant matrix fabric. Biotite occurs as tabular subhedral grains that lie with cleavage sub-parallel or

oblique to the main fabric (Fig. 4.7c). The latter locally results in the development of mica fish. Grains vary from ~0.1–3.0 mm in length. All biotite grains are compositionally homogenous with an intermediate Fe-Mg composition (X_{Mg} of 0.49–0.50) and a Ti content of 0.08–0.09 apfu.

Muscovite is the dominant mica in this sample and is abundant throughout the sample as a fine intergrown fibrous micaceous layer, with grains up to 1.0 mm in length (Fig. 4.7c). Together with graphite, muscovite preserves a crenulation cleavage, axial planar to the now dominant fabric. Locally unoriented sub-mm euhedral muscovite overgrows the dominant fabric. Si content varies from 3.08–3.16 apfu and X_{Na} varies from 0.14–0.21 across all grains.

Locally, quartz-rich lenses alternate with the micaceous fabric on a sub-mm scale. Quartz is present as rounded to flattened grains and is generally equigranular varying in size from $\leq$ 0.1 to 0.5 mm. Some grains display sweeping undulose extinction and minor bulging at grain boundaries. Where present as inclusions in garnet the grains are largely undeformed.

Ilmenite occurs as euhedral rounded to prismatic grains sub-parallel to the main fabric and up to 1.0 mm in length. Ilmenite is present in both the matrix and as inclusions in garnet (Fig. 4.7c).

4.3.1.2 Staurolite zone: ICSV109, ICSV113, ICSV30

ICSV109: Garnet biotite schist ICSV109 contains the primary assemblage biotite, muscovite, quartz, plagioclase, and garnet (Fig. 4.7d). Accessory phases include apatite, allanite, rutile, tourmaline, monazite, and zircon. Retrogressive phases include chlorite. This sample is part of the mixed psammite, pelite, and semipelite lithology.

Garnet is present as angular subhedral poikiloblasts (~2.0–4.0 mm in diameter) containing ilmenite, allanite and abundant quartz inclusions in the core. The rim is inclusion-poor though does contain some rutile, and quartz. Grains contain a thin (0.3 mm) corona of chlorite that overgrows biotite (Fig. 4.7d). Garnet is strongly zoned (Fig. 4.9a). Garnet cores are Fe-rich ($X_{\mathrm{Mg}} = 0.11$–0.19) displaying significantly lower almandine and pyrope content ($X_{\mathrm{Alm}} = 0.62$, $X_{\mathrm{Prp}} = 0.07$) with respect to rims ($X_{\mathrm{Alm}} = 0.71$, $X_{\mathrm{Prp}} = 0.17$). Spessartine and grossular contents are significantly higher in the core ($X_{\mathrm{Sps}} = 0.10$, $X_{\mathrm{Grs}} = 0.20$) when compared to the rim ($X_{\mathrm{Sps}} = 0.01$, $X_{\mathrm{Grs}} = 0.11$).

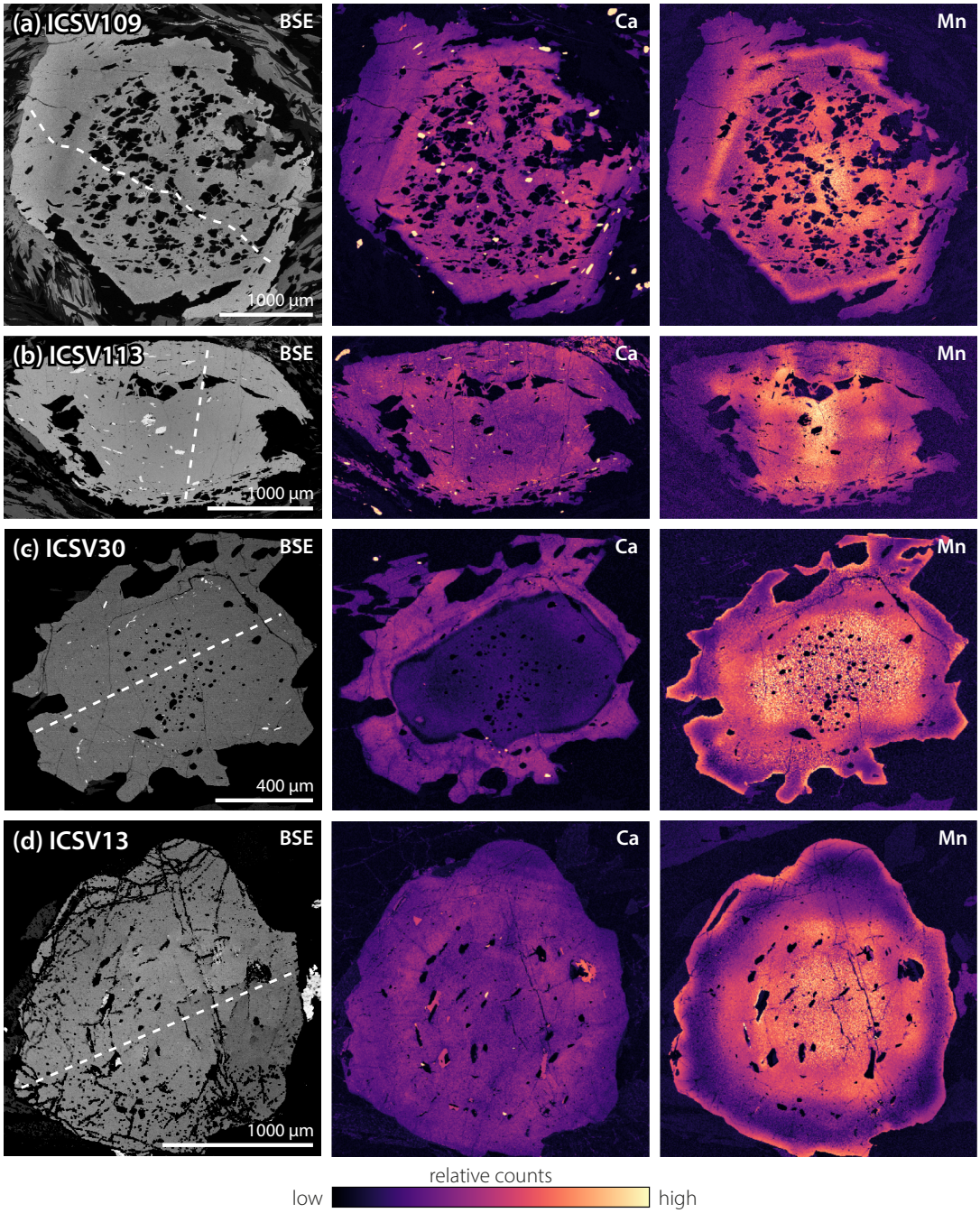


Fig. 4.9 Garnet BSE images and Ca and Mn X-ray compositional maps for a–c) staurolite-zone and d) kyanite-zone samples.

Biotite comprises the dominant matrix fabric together with muscovite, with both micas recording a strong crenulation cleavage (Fig. 4.7d). Biotite and muscovite are present as tabular subhedral to euhedral grains varying from 0.2–4.0 mm in length. Biotite grains show tightly clustered X_{Mg} (0.58–0.59) and Ti (0.10–0.11 apfu) compositions. Inclusions of monazite, allanite, and zircon are common. Muscovite Si contents are equally homogenous (3.07–3.09 apfu) with

slightly more variation in X_{Na} (0.16–0.22), largely resulting from variation in Na and Ca apfu contents.

Plagioclase occurs as oval subhedral equigranular grains, ranging from 0.1–0.5 mm in size. Plagioclase is dominantly present in semipelitic layers and has the composition of oligoclase with an X_{Na} of 0.78–0.81.

Quartz varies from 0.1–2.0 mm in size, recovery is expressed through patchy extinction and recrystallisation through minor bulging at grain boundaries. Psammitic layers in the section are dominated by coarser quartz grains, whereas semipelitic layers host smaller grains.

Ilmenite is dominantly present in garnet cores, whereas rutile occurs at garnet rims and in the rock matrix. Ilmenite is dominantly prismatic and rutile occurs as both oval and rounded grains. Allanite occurs as prismatic grains in both garnet cores and as polycrystalline aggregates and rounded grains in micaceous layers of the rock matrix.

ICSV113: Garnet biotite schist ICSV113 is characterised by the primary assemblage muscovite, quartz, biotite, garnet, and plagioclase (Fig. 4.7e). Accessory phases include rutile, ilmenite, tourmaline, zoisite, apatite, graphite and monazite. Retrogressive phases include chlorite. This sample is part of the mixed psammite, pelite, and semipelite lithology.

Garnet occurs as elongated poikiloblasts of moderate size (~1.5–6.0 mm) hosting inclusions of graphite, ilmenite, quartz, allanite, and tourmaline. Garnet rims are locally serrated (Fig. 4.7e). Compositionally the selected grain shows moderate zoning (Fig. 4.9b). The grain is strongly Fe-rich (X_{Mg} = 0.07–0.15). Almandine, pyrope, spessartine and grossular contents all vary from core to rim (X_{Alm} = 0.59–0.67, X_{Prp} = 0.04–0.11, X_{Sps} = 0.10–0.01, X_{Grs} = 0.26–0.22). One garnet grains is locally replaced by misoriented chlorite grains. Other grains show no evidence of breakdown.

Biotite occurs as elongate tabular subhedral grains defining the dominant planar fabric with sizes varying from 0.2–6.0 in length (Fig. 4.7e). Grains host inclusions of graphite, zircon, rutile and tourmaline. Locally grains occur as mm-scale rounded porphyroblasts or mica fish. Biotite grains have an X_{Mg} of 0.59 and Ti of 0.08–0.10 apfu.

Muscovite is the other dominant fabric-forming phase in the rock. It occurs as intergrown mats with individual tabular grains that varying from 0.1–2.0 mm

in length (Fig. 4.7e). It is commonly associated with graphite, and has inclusions of rutile and tourmaline. Grains locally preserve crenulation cleavage of the now dominant fabric. Muscovite Si contents and X_{Na} are largely homogenous (Si = 3.06–3.20 apfu, X_{Na} = 0.09–0.11).

Plagioclase poikiloblasts (range from 1.0–3.0 mm in length) locally overgrow muscovite rich layers and are rich in biotite inclusions (Fig. 4.7e). Grains have an anhedral form and are oval to prismatic in shape and habit. X_{Na} is homogenous across grains (X_{Na} = 0.65), and corresponds to andesine in composition.

Quartz rich layers and lenses are well distributed throughout the sample and are generally sub-mm in thickness (Fig. 4.7e). Boundaries between quartz grains are curvilinear, whereas they are sharp with bracketed micaceous layers. Grains show patchy or undulose extinction and bulging at grain boundaries.

Rutile occurs as the dominant Ti-oxide matrix phase, grains are oval and oriented parallel with the fabric. Ilmenite rims are locally developed on matrix grains. Rutile does not occur inside garnet, where instead prismatic ilmenite grains are stable.

ICSV30: Garnet biotite schist ICSV30 is a high-Al pelite characterised by the primary assemblage muscovite, quartz, biotite, and garnet (Fig. 4.7f). Accessory phases include tourmaline, plagioclase, apatite, ilmenite, and monazite. This sample is part of the mixed psammite, pelite, and semipelite lithology.

Garnet occurs as flattened elongate subhedral poikiloblasts (~0.75–3.0 mm in diameter; Fig. 4.7f). The core contains abundant rounded fine (< 0.1 mm) inclusions, whereas the rim contains fewer coarser inclusions of quartz, ilmenite and/or muscovite. Ilmenite is concentrated in some grains at the core–rim boundary which is well-defined and suggestive of more than one phase of growth. The selected grain is Fe-rich and shows fairly constant X_{Mg} from core–rim (0.09–0.10). Strong zonation is documented by the garnet end-members (Fig. 4.9c). Almandine shows strong core to rim zonation (X_{Alm} = 0.71–0.77), whereas pyrope contents show only a minor increase from core–rim (X_{Prp} = 0.07–0.08). Spessartine and grossular contents are both strongly zoned, with elevated core (X_{Sps} = 0.19) and reduced rim contents (X_{Sps} = 0.05). Grossular shows inverse zonation patterns and records lower core contents to the rim (X_{Grs} = 0.04–0.11), which combined with the discrete core–rim microstructure, may be suggestive of multiple growth phases with a more calcic second phase of growth at peak conditions.

Biotite is present as tabular euhedral to subhedral grains that vary from 0.2–2.0 mm in length. Grains host inclusions of ilmenite, monazite and zircon. Biotite occurs as a matrix phase of dispersed flakes intergrown with muscovite to define the main fabric (Fig. 4.7f). Biotite grains have an X_{Mg} of 0.34–0.35 and moderately variable Ti of 0.12–0.17 apfu.

Muscovite occurs as tabular euhedral grains that are well distributed throughout the sample. Grains occur as intergrown mats with individual grains up to 5.0 mm in length (Fig. 4.7f). Muscovite is often fringed by biotite or shows biotite growth along cleavage domains. Ilmenite occurs as an inclusion in muscovite. Compositionally muscovite grains vary from an Si of 3.06–3.21 apfu and X_{Na} of 0.05–0.10.

Plagioclase is sparse, occurring as flattened subhedral to anhedral grains of ~0.5 mm in length. Plagioclase has the composition of oligoclase with an X_{Na} of 0.86–0.87.

Quartz occurs in semipelitic layers throughout the sample with anhedral grains that vary from 0.1–1.5 mm in size, recovery is expressed through patchy extinction and recrystallisation through minor bulging at grain boundaries.

Ilmenite is dominantly present in garnet cores and is locally present throughout the rock matrix as fine prismatic grains aligned to the main fabric.

4.3.1.3 Kyanite zone: ICSV13, ICSV12

ICSV13: Kyanite-staurolite schist ICSV13 contains the primary assemblage muscovite, biotite, quartz, kyanite, garnet, staurolite, and plagioclase (Fig. 4.10a). Accessory phases include apatite, rutile, ilmenite, graphite, tourmaline, and monazite. Chlorite is present as a retrogressive phase. This sample is part of the pelite lithology.

Garnet is present as rounded to flattened subhedral poikiloblasts generally 1.0–2.0 mm in diameter (Fig. 4.10a). Where flattened, grains show a prominent strain cap defined by matrix mica. Garnet is host to inclusions of rutile, ilmenite, quartz, graphite, monazite, and tourmaline. Grains often display an inclusion-poor rim whilst the mantle and/or core are inclusion-rich. The selected grain is Fe-rich with increasing ratio of Mg to Fe from core–rim (X_{Mg} = 0.08–0.18). All end-members show strong compositional zoning (Fig. 4.9d), X_{Alm} = 0.60–0.76, X_{Prp} = 0.05–0.16, X_{Sps} = 0.19–0.02, X_{Grs} = 0.16–0.06.

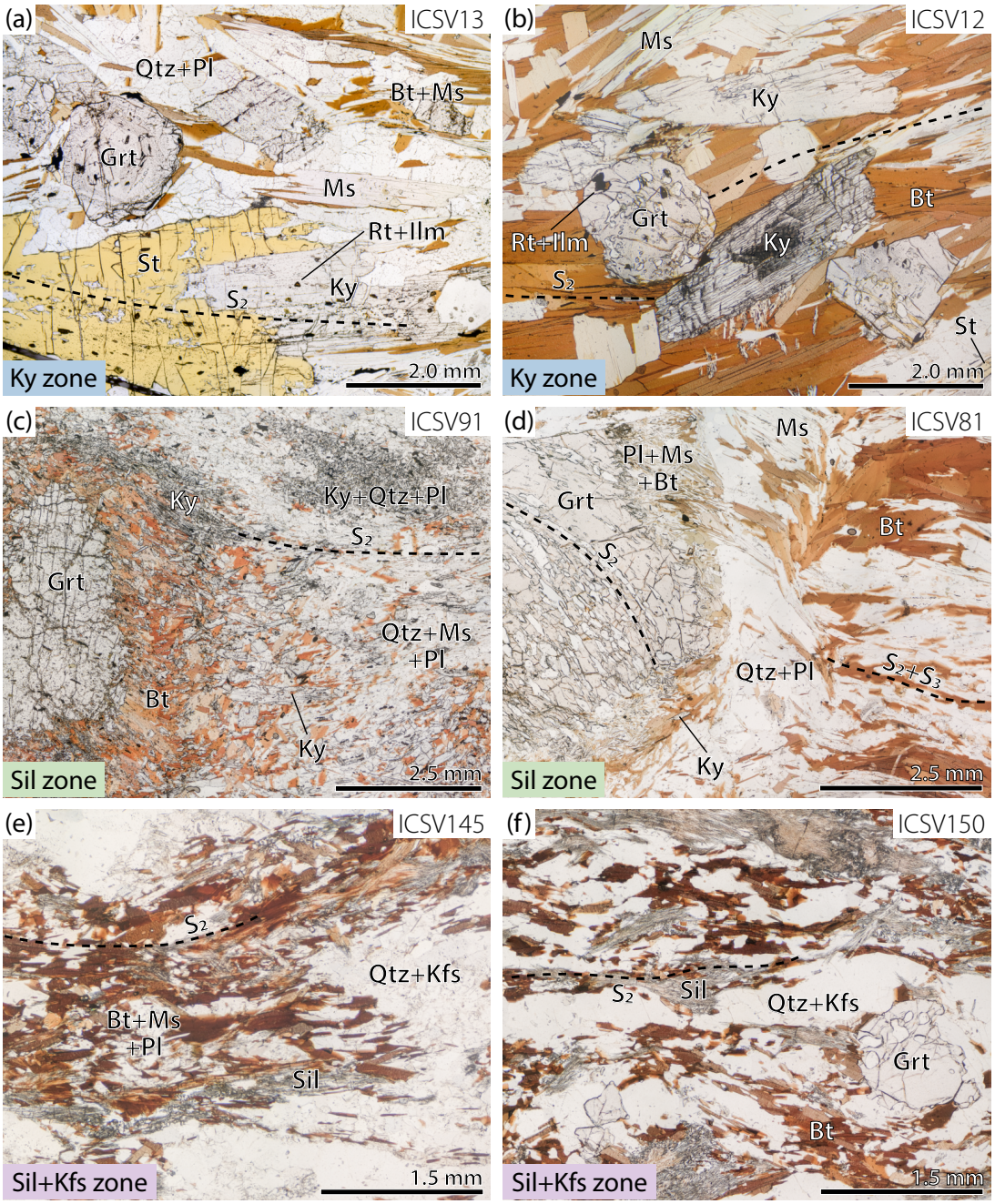


Fig. 4.10 Petrographic images of characteristic mineral assemblages and textures in a–b) kyanite-zone, c–d) sillimanite-zone, and e–f) sillimanite+K-feldspar-zone samples.

Staurolite appears as a singular large prismatic poikiloblast (~15.0 mm) containing inclusions of rutile, graphite, ilmenite, tourmaline, quartz, and monazite. Inclusions are concentrated in the core of the grain and are generally oriented parallel with the fabric (Fig. 4.10a). X_{Mg} and Ti are consistent across the grain (X_{Mg} = 0.19–0.20, Ti = 0.14–0.15 apfu). Kyanite occurs as prismatic subhedral poikiloblasts throughout the section ranging from ~0.6–7.0 mm and host to inclu-

sions of rutile, ilmenite, monazite, biotite, and tourmaline. It locally wraps grains of garnet. Locally staurolite and kyanite appear with impinged grain boundaries, defined by the boundary of the other grain (Fig. 4.10a). A concordant inclusion trail extends from one mineral to the other. The microstructure and inclusion suite is suggestive of concurrent or similar relative timing and conditions of growth.

Biotite is present as 0.2–4.0 mm long tabular subhedral grains intergrown with muscovite to define the dominant matrix fabric (Fig. 4.10a). Analysed biotite grains are compositionally homogenous with an X_{Mg} of 0.49 and a Ti content of 0.09–0.11 apfu. A biotite inclusion in kyanite records slightly elevated Ti contents (0.12 apfu). Muscovite is the dominant mica, with tabular mats of grains that vary from 0.2–3.0 mm in length. Compositionally grains vary from (Si = 3.04–3.09 apfu, X_{Na} = 0.21–0.25). Locally weakly oriented to unoriented chlorite overgrows biotite.

Plagioclase occurs as oval subhedral to anhedral grains in the interstices between matrix phases and is locally present in semipelitic or psammitic layers (~0.4–1.5 mm; Fig. 4.10a). Plagioclase shows some variation across the albite–oligoclase compositional boundary (X_{Na} 0.84–0.92), overall showing Na-rich compositions for the metamorphic grade.

Quartz occurs as flattened grains that vary from 0.1–3.0 mm and is well distributed throughout the section. Grains show evidence of recovery and recrystallisation as expressed through minor undulose extinction and bulging at grain boundaries.

Ilmenite is the dominant Ti-oxide in the matrix and is often concentrated as coarser grains (up to 1.5 mm) at the boundary of kyanite or garnet grains. Rutile and ilmenite are both stable as inclusions in a variety of porphyroblastic phases (Fig. 4.10a).

ICSV12: Kyanite-garnet schist ICSV12 is characterised by the primary assemblage muscovite, biotite, quartz, kyanite, garnet, and plagioclase (Fig. 4.10b). Accessory phases include apatite, ilmenite, rutile, monazite, and staurolite. Chlorite occurs as a retrogressive phase. This sample is part of the pelite lithology.

Garnet occurs as rounded to subangular poikiloblasts of variable size (0.1–3.0 mm). Locally grains are fractured and split into multiple fragments. Garnet cores are rich in quartz, rutile, ilmenite, monazite, epidote and rounded fluid inclusions,

whereas rims are generally more inclusion-poor (Fig. 4.10b). X_{Mg} varies from 0.09–0.18 from core–rim and strong compositional zoning is documented across the grain (Fig. 4.11a). The core of the selected grains records significantly lower almandine and pyrope content content ($X_{\mathrm{Alm}} = 0.67$, $X_{\mathrm{Prp}} = 0.07$) to rims ($X_{\mathrm{Alm}} = 0.77$, $X_{\mathrm{Prp}} = 0.17$). Spessartine and grossular contents are significantly higher in the core ($X_{\mathrm{Sps}} = 0.14$, $X_{\mathrm{Grs}} = 0.13$) when compared to rim contents ($X_{\mathrm{Sps}} = 0.02$, $X_{\mathrm{Grs}} = 0.04$).

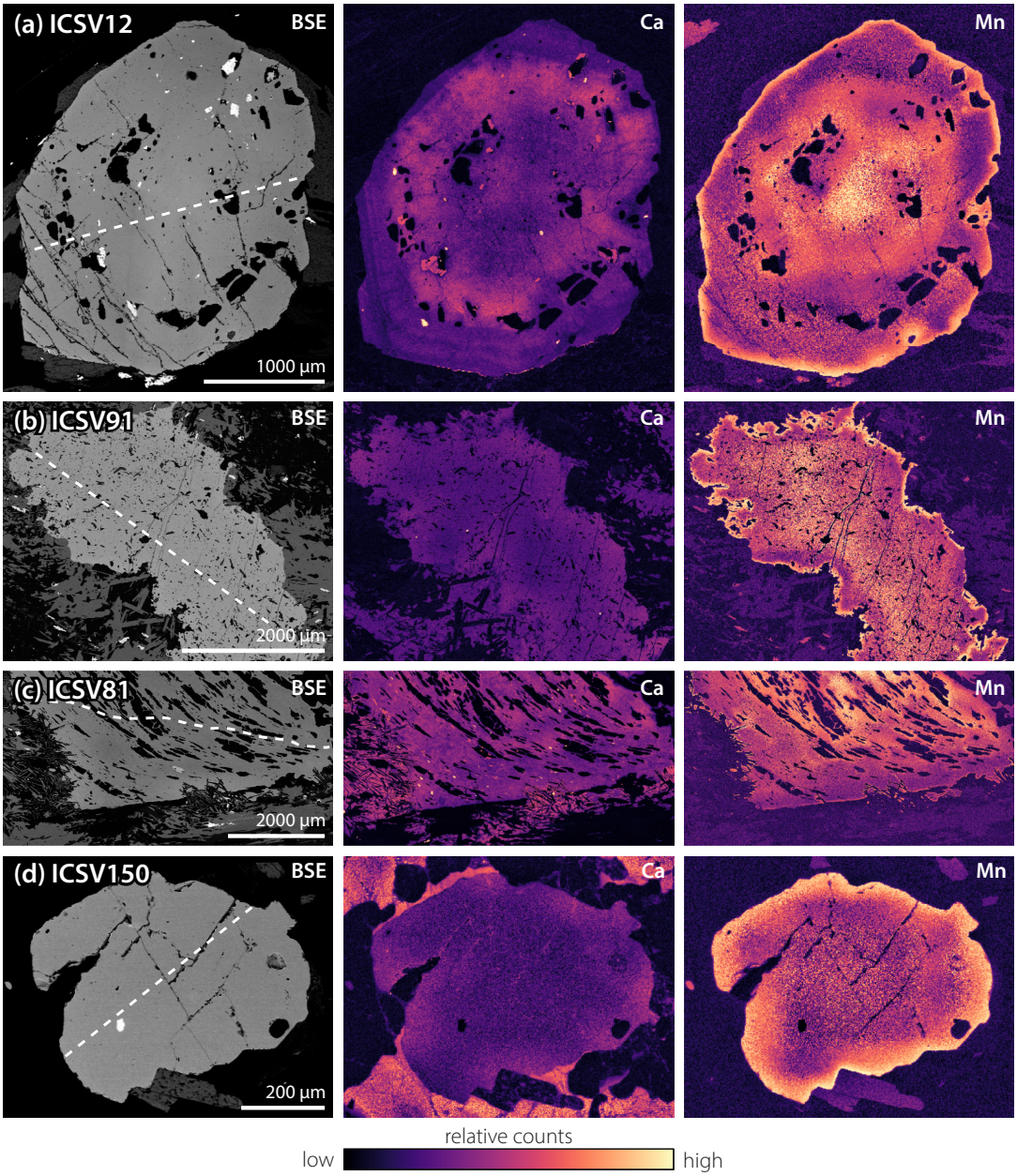


Fig. 4.11 Garnet BSE images and Ca and Mn X-ray compositional maps for a) kyanite-zone; b, c) sillimanite-zone; and d) sillimanite+K-feldspar-zone samples.

Kyanite occurs as coarse prismatic subhedral poikiloblasts ranging from ~1.0–12.0 mm (Fig. 4.10b). Locally kyanite occurs in direct contact with garnet rims and appears to entrap garnet. Kyanite contains inclusions of rutile, ilmenite, biotite, apatite, monazite, and tourmaline. Staurolite is locally present in the matrix, but shows no relative relationship in timing of growth with respect to kyanite or garnet.

Biotite is present as 0.2–4.0 mm long tabular subhedral grains intergrown to define a micaceous fabric along with muscovite (Fig. 4.10b). Analysed biotite grains are compositionally homogenous with an X_{Mg} of 0.48–0.49 and a Ti content of 0.12–0.13 apfu. Unoriented to weakly oriented chlorite interlayed with ilmenite overgrow biotite.

Muscovite is the volumetrically dominant mica in the matrix and also occurs as an intergrown matt of subhedral grains. Individual grains vary from 0.2–4.5 mm in length and compositionally show minimal variation (Si = 3.06–3.09 apfu, X_{Na} = 0.21–0.24).

Plagioclase occurs as coarse anhedral prismatic poikiloblasts 3.0–13.0 mm in length. Plagioclase is dominantly found within muscovite rich layers and includes small inclusions of tabular biotite and muscovite. Mica inclusions are concordant to the matrix fabric suggesting late precipitation of plagioclase on micaceous layers. Rutile rimmed by ilmenite are also present as inclusions. Plagioclase is interstitial to other matrix grains, for example, kyanite is locally embayed where in contact with plagioclase and shows a thin muscovite film. Plagioclase grains commonly show wedged twins. Plagioclase compositions cross the albite–oligoclase boundary (X_{Na} 0.88–0.92).

Quartz varies from 0.2–1.5 mm in size, recovery is expressed through undulose–patchy extinction and recrystallisation through minor bulging at grain boundaries.

Rutile and ilmenite both occur as inclusions within garnet (Fig. 4.10b), whereas rutile (locally with ilmenite rims) occur as inclusions within kyanite and plagioclase poikiloblasts. In the matrix ilmenite is the dominant Ti-oxide with rare rutile cores preserved.

4.3.1.4 Sillimanite zone: ICSV91, ICSV81

ICSV91: Kyanite-garnet schist ICSV91 contains the primary assemblage quartz, biotite, muscovite, kyanite, plagioclase, and garnet (Fig. 4.10c). Accessory

phases include tourmaline, rutile, ilmenite and titanite. This sample is part of the mixed psammite, pelite, and semipelite lithology.

Garnet is present as heavily fractured large oval poikiloblasts (~4.0 mm) with prominent corona of biotite, kyanite, plagioclase, quartz, rutile and ilmenite (Fig. 4.10c). Edges of grains are serrated where the corona assemblage impinges on the garnet grain boundary. Locally, a rounded cluster of the corona assemblage is present which is interpreted to represent the total breakdown of a former garnet grain. Garnet is rich in inclusions of acicular kyanite, rutile, ilmenite, and tourmaline that are evenly distributed from core to rim. Inclusion trails are approximately concordant with the external matrix fabric (Fig. 4.10c). Garnet shows relatively flat compositional profiles (Fig. 4.11b), a result of increasing diffusional homogenisation moving up grade (Tracy, 1982). The selected grain records X_{Mg} of 0.22. Core values of end-members are: $X_{\mathrm{Alm}} = 0.66$, $X_{\mathrm{Prp}} = 0.19$, $X_{\mathrm{Sps}} = 0.09$, $X_{\mathrm{Grs}} = 0.05$, and rim compositions are: $X_{\mathrm{Alm}} = 0.69$, $X_{\mathrm{Prp}} = 0.20$, $X_{\mathrm{Sps}} = 0.04$, $X_{\mathrm{Grs}} = 0.06$.

Kyanite occur as prismatic to acicular grains ranging in size from < 0.1 to 2.0 mm in length (Fig. 4.10c). In garnet, kyanite occurs as fine needles with minor coarsening from garnet core to rim. Kyanite located within garnet corona varies from unoriented to weakly oriented sub-parallel with the matrix fabric. Kyanite in the matrix is kinked and generally weakly aligned with the mica-defined fabric. Finally, augen of clustered unoriented kyanite with quartz and plagioclase are common in the matrix (Fig. 4.10c). Such augen are biotite and muscovite absent. Texturally the rock sample is hornfelsic and cordierite is observed in neighbouring samples. The mineral assemblage of the clusters suggests kyanite growth is not related to garnet breakdown with the overall lack of mica suggesting another primary mineral must be responsible for the clustered growth. These clusters are interpreted to represent a pseudomorph after cordierite.

Biotite is present as tabular subhedral grains ranging from 0.1–1.5 mm in length. Where present in the matrix, it dominantly occurs as smeared rims on coarser unoriented muscovite. Differing microstructure for biotite shows no distinct difference in chemistry, as such biotite is inferred to represent a single equilibrated population. Analysed grains record an X_{Mg} of 0.50–0.54 and a Ti content of 0.13–0.15 apfu.

Muscovite is the main mica and occurs in two microstructural contexts. It occurs dominantly as an intergrown matt of grains defining the main fabric (Fig. 4.10c). It also occurs as coarser euhedral grains that are not aligned with the

fabric and are often oriented at angles of ~60 or 120 ° to each other. There likely represent relic grains of a crenulation cleavage or late unoriented growth of mica on the fabric. The dominant matrix group of muscovite is compositionally homogenous (Si = 3.10–3.12 apfu, X_{Na} = 0.12–0.13).

Plagioclase is present as subhedral to anhedral oval grains up to 1.0 mm in size. Compositionally the plagioclase is albite and it shows a homogenous chemistry (X_{Na} = 0.92–0.93).

Quartz, together with plagioclase, shows a weak granoblastic texture in the matrix. Quartz shows little evidence of dynamic recrystallisation.

Rutile and ilmenite are both present as inclusions in garnet and in garnet coronas, often with cores of ilmenite and rims of rutile. The matrix is dominated by rutile, locally with thin ilmenite rims.

ICSV81: Sillimanite-kyanite-garnet schist ICSV81 contains the primary assemblage quartz, muscovite, biotite, plagioclase, garnet, and kyanite (Fig. 4.10d). Accessory phases include rutile, titanite, ilmenite, monazite, apatite, and sillimanite. Retrogressive phases include chlorite. This sample is part of the mixed psammite, pelite, and semipelite lithology.

Garnet is present as large skeletal rounded poikiloblasts (~4.0–8.0 mm; Fig. 4.10d). Grains have a prominent corona of biotite, muscovite, plagioclase, ilmenite and locally kyanite. Skeletal cores are rich in inclusions of quartz, titanite, rutile, ilmenite and epidote–clinozoisite. Rims are inclusion-poor, though contain the same inclusions, with the exception of titanite which is not present. X_{Mg} varies from 0.09 in the core to 0.16 in the rim. The grain shows moderate zoning following some diffusional homogenisation (Fig. 4.11c). The core has lower almandine and pyrope content (X_{Alm} = 0.63, X_{Prp} = 0.06) to rims (X_{Alm} = 0.69, X_{Prp} = 0.13). Spessartine and grossular contents are higher in the core (X_{Sps} = 0.04, X_{Grs} = 0.27) when compared to rim contents (X_{Sps} = 0.01, X_{Grs} = 0.18).

Kyanite occurs as prismatic grains that are locally skeletal in nature. Grain length varies from 0.2–5.0 mm. Kyanite appears within garnet corona, with matrix kyanite locally associated with corona-assemblages of biotite, muscovite, and plagioclase (Fig. 4.10d). It is thus indicated that kyanite growth follows progressive garnet breakdown. Kyanite appears both aligned and misaligned relative to the developed S_3 fabric. Sillimanite locally occurs as fibrolitic mats

overgrowing biotite. It is rare within the given sample though is locally more abundant within neighbouring outcrops.

Biotite is present as tabular subhedral grains ranging from 0.2–6.0 mm in length (Fig. 4.10d). It is intergrown with muscovite and defines the matrix fabric. Biotite within corona around garnet is acicular and ragged in nature, and is locally green. Matrix biotite shows chemistry ranging from X_{Mg} of 0.58–0.62 and Ti from 0.11–0.12 apfu. Biotite in the corona dominantly shows variable X_{Mg} (0.53–0.56) and Ti (0.07–0.12 apfu), with the green biotite measuring elevated X_{Mg} (0.66–0.71) and minor increase in Ti (0.12–0.13 apfu). Locally chlorite replaces biotite along cleavage domains.

Muscovite is intergrown in a fibrous network in the matrix with individual grains ranging up to 3.5 mm in length (Fig. 4.10d). Muscovite in the corona around garnet is acicular and dominantly unoriented. Si ranges from 3.11–3.14 apfu and X_{Na} from 0.07–0.08.

Plagioclase is present as subhedral to anhedral interstitial oval grains up to 1.0 mm in size and located both within the matrix and the garnet corona (Fig. 4.10d). Compositionally grains are dominantly andesine in composition, with matrix grains measuring $X_{\mathrm{Na}} = 0.66$–0.70 and grains in the garnet corona measuring X_{Na} 0.63–0.65.

Quartz occurs as rounded to flattened grains up to 4.0 mm in length that dominantly display patch undulose extinction. In areas this develops into near-chessboard type extinction.

Titanite is the dominant Ti-oxide in garnet cores and occurs as small rounded grains (< 0.1 mm), whereas rutile and ilmenite dominate the mantle and rim as oval grains with no titanite. Ilmenite (+sulphides) is dominant in the garnet corona, in contrast rutile is dominant in the matrix (though few grains are present) with elongate habit (locally with fine ilmenite rims). This pattern suggests a clockwise *P-T* path through the Ti-oxides, from titanite, to ilmenite+rutile during garnet growth, to rutile during peak conditions with late ilmenite during garnet breakdown.

4.3.1.5 Sillimanite+K-feldspar zone: ICSV145, ICSV150

ICSV145: Sillimanite-K+feldspar migmatite ICSV145 contains the primary assemblage quartz, K-feldspar, biotite, plagioclase, and sillimanite (Fig.

4.10e). Accessory phases include muscovite and monazite. This sample is a migmatite and contains the following domains. 1) Fine-grained biotite-rich domains, containing weakly oriented biotite that defines a discontinuous foliation and is associated with fibrolitic and prismatic sillimanite, minor muscovite, quartz, and plagioclase feldspar. 2) Coarse-grained quartzo-feldspathic domains consisting of recrystallised quartz, K-feldspar porphyroblasts, plagioclase (locally myrmekite), and radiating fibrolitic sillimanite. These domains are shown in Figure 4.10e.

Sillimanite occurs as prismatic and fibrous acicular grains in both the palaeosome and leucosome. Leucosomal grains are dominantly radiating fibrolite, whereas prismatic grains are dominantly located in biotite rich domains where grains extend up to 2.0 mm in length (Fig. 4.10e). Sillimanite is present in a variety of orientations that are both aligned to the dominant fabric (likely representing epitaxial growth as discussed in Section 2.7.1), and displaying no distinct orientation. End-sections of sillimanite are common suggesting grains are not consistently aligned relative to a stretching lineation. Sillimanite is commonly fractured perpendicular to the long axis and is locally replaced by fine polycrystalline muscovite.

Biotite occurs as red–dark brown subhedral to anhedral grains that are concentrated in the palaeosome and vary from $<$ 0.1–2.0 mm in length (Fig. 4.10e). Grain boundaries are commonly embayed by quartzo-feldspathic domains. Biotite shows low X_{Mg}, consistent with the colour, and varies from 0.34–0.37 and records high Ti contents of 0.17–0.20 apfu.

Muscovite is present in two main forms, as weakly oriented euhedral grains in biotite-rich domains and as ragged subhedral to anhedral grains in quartzo-feldspathic domains (Fig. 4.10e). These domains are often associated with K-feldspar and likely developing through back-reaction with aqueous fluid or residual melt (Waters, 2019). Muscovite from biotite-rich domains contains Si contents from 3.04–3.05 apfu and X_{Na} from 0.06–0.07, whereas muscovite from the quartzo-feldspathic domains contain slightly elevated Si contents from 3.13–3.15 apfu and X_{Na} from 0.05–0.06.

K-feldspar forms coarse poikiloblasts in quartzo-feldspathic leucocratic domains (up to 3.5 mm in width; Fig. 4.10e). Grains regularly contain coarse rounded quartz inclusions, fine tabular muscovite and locally, minor biotite and sillimanite. Grains boundaries are often fringed by late muscovite growth and may also be embayed by myrmekitic integrowths of plagioclase and quartz. Grains record a variable X_{K} from 0.78–0.90.

Plagioclase occurs in two microstructural locations: as small (~0.5 mm) subhedral grains within biotite-rich domains (Fig. 4.10e) and as myrmekitic intergrowths embaying K-feldspar within leucocratic domains. Myrmekitic plagioclase may also be associated with prismatic sillimanite. Plagioclase from biotite-rich domains display prominent oscillatory compositional zoning. Grains are oligoclase in composition, with those from biotite-domains measuring $X_{\mathrm{Na}} = 0.73$–0.74 and one grain from the leucocratic domain measuring $X_{\mathrm{Na}} = 0.72$.

No Ti-oxide phases are present in this sample.

ICSV150: Sillimanite-K+feldspar-garnet migmatite ICSV150 contains the primary assemblage quartz, K-feldspar, plagioclase, biotite, sillimanite, and garnet (Fig. 4.10f). Accessory phases include monazite and ilmenite. This is a migmatite with mm-scale layering alternating between leucocratic ribbons and biotite+sillimanite-rich layers defining a discontinuous foliation (Fig. 4.10f).

Garnet forms rounded euhedral to embayed anhedral grains from ~0.5–2.0 mm in diameter (Fig. 4.10f). Garnet is hosted in both biotite+sillimanite-rich domains and in leucocratic domains. In leucocratic domains it is commonly surrounded by a rim of K-feldspar, plagioclase and/or quartz. In more mesocratic domains, wavy biotite+sillimanite-rich layers wrap around garnet and/or sites of former garnet. Garnet cores are commonly inclusion-poor whereas rims are commonly corroded and grain boundaries are surrounded by biotite, sillimanite and quartz. Garnet from both domains contain inclusions of fine sillimanite, lobate quartz, biotite and rarely ilmenite. Locally sillimanite inclusions are concordant with matrix sillimanite, suggesting garnet overgrew a sillimanite-aligned fabric. However, given the grain size and small amount of the mineral present as inclusions within garnet rims, it seems likely that garnet first grew in a sillimanite-absent environment then continued growth when the rock contained low modal % of sillimanite. Garnet grains from ICSV150 display prominent reverse zoning patterns (Fig. 4.11d), with X_{Mg} ranging between 0.14–0.10. Core commpositions are: $X_{\mathrm{Alm}} = 0.80$, $X_{\mathrm{Prp}} = 0.13$, $X_{\mathrm{Sps}} = 0.06$, and $X_{\mathrm{Grs}} = 0.02$. The rim compositions are: $X_{\mathrm{Alm}} = 0.74$, $X_{\mathrm{Prp}} = 0.08$, $X_{\mathrm{Sps}} = 0.16$, and $X_{\mathrm{Grs}} = 0.02$. A mantle zone occurs inboard of the rim with: $X_{\mathrm{Alm}} = 0.76$, $X_{\mathrm{Prp}} = 0.10$, $X_{\mathrm{Sps}} = 0.11$, $X_{\mathrm{Grs}} = 0.02$. Uniform X_{Mg} in the garnet core ($X_{\mathrm{Mg}} = 0.14$) is typical of high-temperature diffusional homogenisation which obliterates Fe-Mg growth zoning (e.g., Groppo *et al.*, 2010). Therefore the core is likely the most representative zone of the garnet for peak-temperature determination.

Sillimanite is mostly present as thick fibrous mats epitaxially aligned with the matrix fabric (Fig. 4.10f) but with coarser grains (up to 1.0 mm in length) displaying a variety of radiating orientations. Locally fibrous knots are also developed. Grains are present within both leucocratic and mesocratic domains, though prismatic sillimanite is concentrated in the latter.

Biotite occurs as subhedral grains with ragged grain boundaries < 0.1–1.0 mm in length, intergrown with sillimanite (Fig. 4.10f). Coarser biotite with a well-defined crystal habit is commonly located at garnet grain boundaries. Grain boundaries are commonly embayed by quartz or feldspar. Biotite is compositionally homogenous with low X_{Mg} (0.35–0.36), consistent with the red-brown colour, and high Ti contents (0.17–0.19 apfu).

K-feldspar forms flattened oval grains (0.2–1.5 mm in length) well distributed throughout both leucocratic and mesocratic domains (Fig. 4.10f). Grains commonly display weak micro-perthitic exsolution and locally contain fine biotite, muscovite and rarely sillimanite inclusions. Grains vary from subhedral to anhedral where they are interstitial between other quartz and feldspar grains. Grains record a variable X_{K} from 0.72–0.87.

Plagioclase occurs as small ($\leq$ 0.5 mm) subhedral to anhedral grains locally host to inclusions of rounded to lobate quartz (suggesting myrmekitic intergrowth), and fine biotite. Compositionally grains are dominantly oligoclase measuring X_{Na} = 0.87–0.90.

Ilmenite locally occurs as inclusions in garnet. One grain is present in the matrix, though it is hosted in the core of a coarse biotite grain in contact with corroded garnet rim. The grain is also cross cut by sillimanite. This is interpreted to represent a relic inclusion from the corroded garnet and is therefore not interpreted as a stable part of the observed assemblage.

Interpretation of migmatite microstructures Samples from the migmatite domain show well-preserved evidence of microstructures and assemblages indicative of high-temperature, low-pressure conditions, as well as melt-producing and consuming reactions:

1. Lobate quartz inclusions in garnet suggest growth during partial melting (Waters, 2001). Some grains of garnet therefore represent a peritectic phase.

2. The partial replacement of garnet in mesocratic domains likely represents decompression and retrograde-related features (Waters, 2019). A possible melt-consuming process for this could be:

$$\text{garnet} + \text{K-feldspar} + \text{melt}/\text{H}_2\text{O} = \text{biotite} + \text{sillimanite} + \text{quartz} \quad (4.28)$$

3. The presence of sillimanite inclusions in garnet suggest that garnet rims locally grew in the sillimanite stability field.

4. Rarely, thin films and beads of weakly cuspate quartz, K-feldspar or plagioclase are present at grain boundaries between K-feldspar, quartz or biotite. Such films are interpreted as pseudomorphs of liquid filled pores (e.g., Holness & Sawyer, 2008), and suggests melt crystallisation between grains. However, the rocks have also experienced significant static recrystallisation, likely obscuring significant evidence of melt film at phase boundaries.

5. In sample ICSV145, coarse-grained K-feldspar poikiloblasts contain abundant inclusions of rounded quartz, minor plagioclase and at rims, prismatic sillimanite. This suggests K-feldspar may have grown at the expense of these minerals and might be a peritectic phase (e.g., Sawyer, 2008). Given prismatic sillimanite is also observed to embay K-feldspar grain boundaries, it suggests sillimanite was likely volumetrically minor prior to K-feldspar poikiloblast growth. Myrkmekitic plagioclase and sillimanite corroding K-feldspar poikiloblasts are interpreted to represent back-reaction between melt and solid phases during final melt crystallisation. These observations support sillimanite growth being a K-feldspar consuming reaction after earlier phase(s) of melting.

4.3.2 Metabasite

4.3.2.1 Hornblende zone: ICSV50, ICSV2

ICSV50: Garnet-actinolite amphibolite The primary assemblage in ICSV50 is hornblende, actinolite, chlorite, biotite, albite, epidote-clinozoisite, and garnet (Fig. 4.12a). Accessory phases include quartz, titanite, and chlorite. Retrogressive phases include chlorite. This sample, as well as all other metabasites modelled here are part of the group A metavolcanic rock unit.

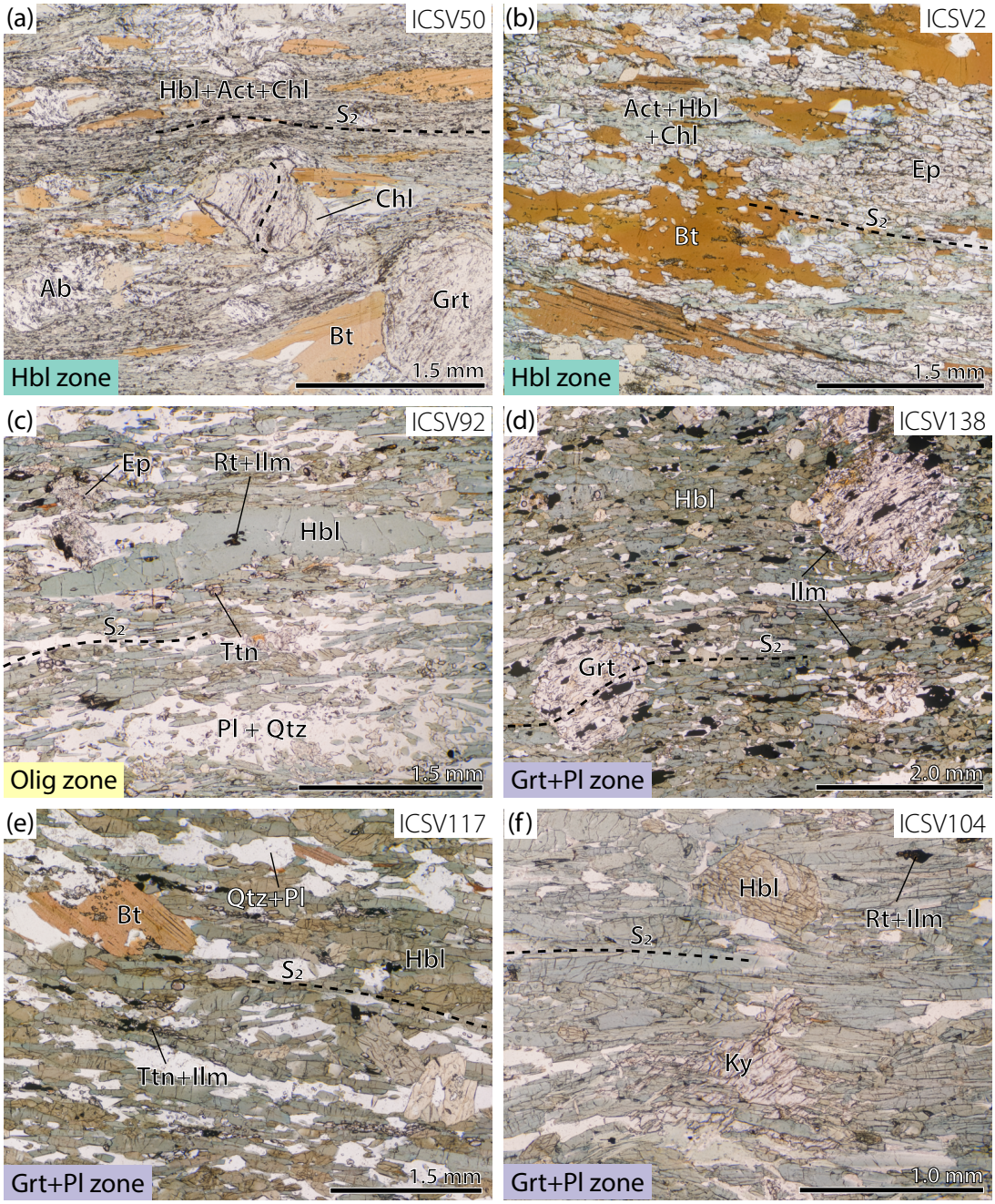


Fig. 4.12 Petrographic images of characteristic mineral assemblages and textures in samples from the a–b) hornblende zone, c) oligoclase zone, and d–f) garnet+plagioclase zone.

Garnet occurs as poikiloblastic euhedral grains that are locally serated and fractured (Fig. 4.12a). Two garnet grains are present with a diameter of 1.75 and 0.75 mm. Both grains contain S-shaped inclusion trails of epidote-clinozoisite and polycrystalline titanite (Fig. 4.12a). Chlorite corona occur at garnet rims with mimetic replacement of euhedral garnet shape, growth also develops along garnet fractures. Garnet X_{Mg} ranges from 0.06–0.11. Strong compositional zoning is

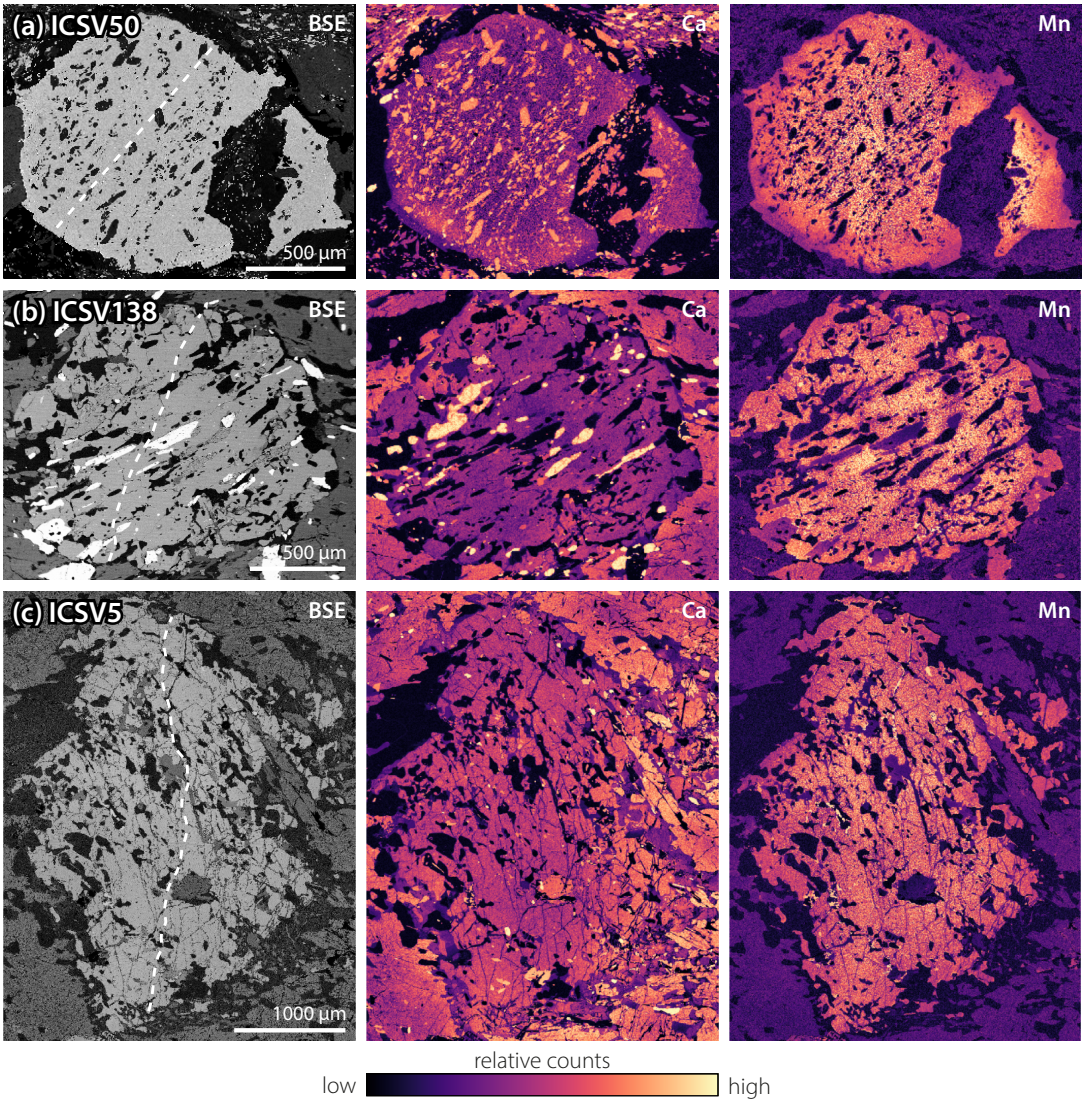


Fig. 4.13 Garnet BSE images and Ca and Mn X-ray compositional maps for a) hornblende-zone; and b, c) garnet+plagioclase-zone samples. *N.b.* Hornblende-grade samples contain albite rather than "plagioclase" which is used in this study to refer to samples without albite compositions, $X_{\mathrm{Na}} < 0.90$. Furthermore the sample records a high spessartine content, which is anomalous within the dataset. This differentiates the sample from those located in the garnet+plagioclase-zone.

recorded (Fig. 4.13a): the core has lower almandine and pyrope content ($X_{\mathrm{Alm}} = 0.27$, $X_{\mathrm{Prp}} = 0.02$) to rims ($X_{\mathrm{Alm}} = 0.58$, $X_{\mathrm{Prp}} = 0.08$). Spessartine and grossular contents are higher in the core ($X_{\mathrm{Sps}} = 0.32$, $X_{\mathrm{Grs}} = 0.39$) when compared to rim contents ($X_{\mathrm{Sps}} = 0.10$, $X_{\mathrm{Grs}} = 0.25$). The spessartine-rich composition is inferred to account for the relatively early growth of garnet.

Amphibole occurs as fine acicular subhedral to euhedral grains that form thick mats defining the dominant S_2 fabric (Fig. 4.12a). Locally, they also preserve crenulation cleavage. Analysed grains are dominantly magnesiohornblende

(Hawthorne *et al.*, 2012) with vectors varying as follows: tschermakite from 0.78–1.16, edenite from 0.22–0.45, and glaucophane from 0.20–0.23. Significant composition variation reflects the recognition that actinolite are also identified from field and petrographic constraints, and that compositional variation is reflected through progressive transition to dominant hornblende growth.

Prograde chlorite occurs as fabric aligned tabular–fibrous grains intergrown with amphibole and in the strain shadows of feldspar augen (Fig. 4.12a). X_{Mg} varies from 0.56–0.59. Retrograde chlorite occurs as grains of varying orientations in replacement of garnet grain boundaries.

Biotite occurs as fabric aligned euhedral–subhedral tabular grains or as matrix poikiloblasts (Fig. 4.12a). Grains vary from 0.2–2.0 mm in length. Biotite is observed to overgrow matrix chlorite and crenulation cleavage. Furthermore, grains display local impingement of garnet grain boundaries. Chlorite at garnet rims (inferred retrograde) and biotite do not impinge or overgrow one another (Fig. 4.12a). This suggests only garnet shows relatively instability during the retrograde evolution of the rock resulting in chlorite growth that replaces garnet but does not replace biotite. This agrees with the recognition of multiple chlorite generations. Biotite X_{Mg} varies from 0.54–0.56 and Ti from 0.06–0.08 apfu.

Plagioclase is present as rounded grains up to a diameter of 0.5 mm in diameter (Fig. 4.12a). Grains are poikiloblastic and contain S-shaped inclusion trails dominantly comprised of fine acicular actinolite and epidote–clinozoisite. Microstructure suggests syn-tectonic growth with respect to dominant matrix S_2 fabric. Compositionally grains are albite with homogenous chemistry ($X_{\mathrm{Na}} = 0.99$).

Epidote-clinozoisite occur as prismatic elongate to rounded euhedral grains, dominantly < 0.3 mm in length (Fig. 4.12a). The long axis of grains is consistently aligned with the main fabric and occur as inclusions in a variety of phases. Analysed grains contain two main groupings: pistacite content varies from 0.12–0.14 and 0.34–0.44, likely reflecting observed compositional zoning. The lower values are selected as the main grouping.

Titanite forms the only Ti-oxide phase where it occurs in the matrix as angular grains, locally partially included in albite. Polycrystalline titanite is also located as inclusions in garnet.

ICSV2: Hornblende-actinolite amphibolite ICSV2 contains the primary assemblage: biotite, actinolite, hornblende, epidote-clinozoisite, quartz, and albite (Fig. 4.12b). Accessory phases include titanite.

Amphibole occurs as acicular to prismatic subhedral to euhedral grains up to 1.0 mm in length (Fig. 4.12b). Grains are dominantly aligned and define the matrix fabric, although they are also observed to cross-cut the fabric. Locally grains record actinolite cores and hornblende rims. Amphibole varies from tremolite-actinolite to magnesiohornblende (Hawthorne *et al.*, 2012) with the following vectors: tschermakite varies from 0.31–0.67, edenite from 0.17–0.40, and glaucophane from 0.07–0.15.

Biotite grows as coarse subhedral poikiloblasts and fabric aligned grains that range in legnth from 0.5–10.0 mm (Fig. 4.12b). Poikiloblastic grains have inclusions of epidote and strings of polycrystalline titanite aligned parallel to the main fabric. Epidote is slightly coarser grained in the matrix than as inclusions. Biotite grains show homogenous compositions, with an X_{Mg} of 0.54–0.55 and Ti from 0.07–0.08 apfu.

Plagioclase is strongly albitic (X_{Na} of 0.97–0.98) and occurs as rounded subhedral grains ≤ 0.5 mm in size. Grains are often host to fine acicular epidote.

Epidote occurs as prismatic to rounded euhedral grains varying from < 0.1 to 0.5 mm in size (Fig. 4.12b). The long axis of grains is consistently aligned with the main fabric and epidote occur as inclusions in all phases. X_{Fe} (pistacite content) varies from 0.13–0.19 in the cores of analysed grains.

Quartz is present as anhedral grains interstitial to the dominant matrix forming minerals. No significant recovery or dynamic recrystallisation textures are observed.

Titanite forms the only Ti-oxide phase and occurs as very fine polycrystalline grains commonly forming a string-of-beads that is aligned to the main fabric.

4.3.2.2 Oligoclase zone: ICSV92

ICSV92: Hornblende-oligoclase amphibolite ICSV92 contains the primary assemblage hornblende, oligoclase, quartz, and epidote-clinozoisite (Fig. 4.12c). Accessory phases include: rutile, ilmenite, titanite, apatite and biotite. Chlorite occurs as a retrogressive phase commonly associated with primary biotite.

Amphibole dominantly occurs as coarse acicular prismatic grains that are euhedral and range from 0.1–5.0 mm in length (Fig. 4.12c). Repeated layering of amphibole define a prominent foliation. Cores of larger grains contain inclusions of rutile with ilmenite fringes. Actinolite is modally minor and occurs as fine acicular grains up to 0.2 mm in length, dominantly observed as inclusions within feldspar poikiloblasts. The inclusion assemblage, suggests the actinolite–hornblende miscibility gap was likely passed prior to poikiloblast growth of feldspar. Actinolite is therefore interpreted to be metastable as has been documented in accordance with reported disequilibrium behaviour of actinolite in the oligoclase zone of Starr & Pattison (2019). Analysed hornblende is characterised as magnesiohornblende–pargasite (Hawthorne *et al.*, 2012) with vectors varying as follows: tschermakite from 0.97–1.19, edenite from 0.25–0.55, and glaucophane from 0.12–0.21.

Biotite occurs as an accessory phase as fine tabular grains up to 0.4 mm in length. Dominantly grains occur at hornblende grain boundaries, aligned to the main fabric. X_{Mg} varies from 0.55–0.60 and Ti from 0.09–0.12 apfu.

Plagioclase occurs as rounded poikiloblasts (up to 2.0 mm in length) and as prismatic subhedral matrix grains generally < 1.0 mm (Fig. 4.12c). Matrix grains also locally contain inclusions. Inclusions in feldspar are euhedral small hornblende, acicular actinolite, epidote and rounded quartz. Inclusion trails in poikiloblastic phases are S-shaped or discordant suggesting pre- to syn-tectonic growth of feldspar with respect to the dominant hornblende-defined fabric. Plagioclase grains are oligoclase in composition ($X_{\mathrm{Na}} = 0.82$–0.85).

Epidote occurs as rounded ragged anhedral grains 0.1–1.0 mm in size that are well distributed throughout the matrix (Fig. 4.12c). Grains show prominent compositional zoning. Only one spot was analysed with a pistacite content of 0.15.

Quartz occurs in flattened quartzo-feldspathic layers with grains dominantly 0.2-0.5 mm in length. Grains display patchy to undulose extinction and minor bulging at grain boundaries.

Ti-oxides record a consistent growth sequence with rutile sequentially rimmed by ilmenite and then titanite. Locally rutile and titanite are in direct contact, suggesting ilmenite and rutile were likely co-stable. Titanite occurs as polycrystalline rims around previous phases of Ti-oxide. Only rutile and ilmenite are found within the cores of larger hornblende grains (Fig. 4.12c). Titanite

dominantly forms as polycrystalline rims at amphibole grain boundaries and at rims of rutile-ilmenite rims.

4.3.2.3 Garnet+plagioclase zone

ICSV138: Garnet-Hornblende amphibolite ICSV138 contains the primary assemblage of hornblende, quartz, plagioclase, garnet, and ilmenite (Fig. 4.12d). Accessory phases include biotite, apatite, titanite and sulphides. Retrogressive phases include chlorite and titanite.

Garnet occurs as poikiloblastic rounded subhedral grains around ~0.5–1.5 mm. Grains contain matrix concordant inclusion trails of ilmenite, quartz and epidote/clinozoisite (Fig. 4.12d). Corona of thin plagioclase and minor titanite growth are associated with grain margins. The selected grain records X_{Mg} of 0.15–0.17 (core–rim). Endmember composition zoning profiles are relatively flat (Fig. 4.13b). X_{Alm} is 0.63 from both core–rim and X_{Prp} is 0.11–0.13. X_{Sps} is 0.06–0.04 and X_{Grs} consistent at 0.20.

Amphibole is present as moderately sized acicular prismatic grains from 0.2–1.5 mm in length (Fig. 4.12d). Foliation is defined by repeated laying of aligned hornblende crystals. Analysed hornblende is classified as magnesiohornblende–pargasite (Hawthorne *et al.*, 2012) with the vectors varying as following: tschermakite from 1.19–1.29, edenite from 0.41–0.51, and glaucophane from 0.16–0.22.

Biotite occurs as an accessory phase as fine tabular grains up to 0.3 mm in length. Dominantly grains are aligned with the main fabric. Chemistry shows two dominant groups defined by varying Ti content. One group shows X_{Mg} range of 0.57–0.62 and Ti of 0.07 apfu, whereas the second group shows X_{Mg} varying from 0.56–0.58 and Ti from 0.12–0.13 apfu. One grain analysed in 7 spots shows both populations suggesting the variation is most likely resorption or diffusion at grain boundaries rather than growth of different populations. Alternatively, incipient chloritisation of biotite rims and cleavage may result in partial Ti loss. Grains with higher Ti (analysed from larger, less ragged grains) were selected as preferred analyses.

Plagioclase occurs as rounded to serrated prismatic grains less than 1.0 mm in length. The long axis is aligned with the fabric, with amphibole and ilmenite overgrowing feldspar. Grains are oligoclase in composition (X_{Na} of 0.76–0.81).

Quartz occurs as elongate polycrystalline ribbons or as interstitial grains. Patchy extinction is common representing subgrain development with minor bulging at grain boundaries.

Ilmenite forms the dominant Ti-oxide and is aligned with the foliation throughout the sample (Fig. 4.12d). Titanite locally occurs as fine inclusions in garnet or is developed as polycrystalline growth at garnet rims. The former are interpreted as prograde growth and the latter as retrograde (locally associated with fractured fluid pathways).

ICSV117 ICSV117 contains the following primary assemblage: hornblende, plagioclase, biotite, and quartz (Fig. 4.12e). Accessory phases include titanite, apatite, and ilmenite. Chlorite is the main retrogressive phase.

Amphibole occurs dominantly as coarse acicular prismatic grains that are euhedral and range from 0.2–2.0 mm in length (Fig. 4.12e). Repeated layers of amphibole define the prominent S_2 foliation. Analysed amphibole is classified as magnesiohornblende–pargasite (Hawthorne *et al.*, 2012). Vectors vary as follows: tschermakite from 0.97–1.19, edenite from 0.25–0.55, and glaucophane from 0.12–0.21.

Biotite is present as coarse subhedral poikiloblasts to fine tabular grains (0.5–4.0 mm in length; Fig. 4.12e). Poikiloblastic grains have matrix fabric concordant inclusions of angular to rounded quartz, plagioclase and amphibole. Biotite defines the S_2 fabric along with repeated layering of amphibole. Biotite grains record a homogenous composition (X_{Mg} of 0.48–0.52, Ti of 0.14–0.16 apfu).

Plagioclase occurs as oval to angular prismatic euhedral–subhedral grains. Grains are dominantly less than 1.0 mm in size, with the long axis aligned with the main fabric. Locally plagioclase contains inclusions of fine-grained hornblende crystals and apatite. Strong concentric compositional zoning is observed. Plagioclase is defined as oligoclase (X_{Na} of 0.77–0.81).

Quartz occurs as interstitial grains well distributed throughout the sample. Together with feldspar it may be locally concentrated into quartz+feldspar-rich lenses (Fig. 4.12e). Patchy subgrain development and extinction textures are common, with minor bulging at grain boundaries.

Ilmenite and titanite are the main Ti-oxide phases. Ilmenite form individual crystals, whereas titanite form polycrystalline string-of-beads textures, with both phases aligned to the main fabric (Fig. 4.12e). Ilmenite occur as cores to titanite

rims, though both are in contact with the matrix. Ilmenite grain boundaries is defined by shape habit of amphibole, whereas titanite, commonly forming along amphibole grain boundaries, may impinge on amphibole crystals.

ICSV104 ICSV104 contains the primary assemblage of amphibole, plagioclase, quartz, and kyanite (Fig. 4.12f). Accessory phases include staurolite, ilmenite, rutile and apatite. Retrogressive phases include chlorite.

Amphibole occurs as coarse prismatic and euhedral grains that range from 0.2–3.5 mm in length (Fig. 4.12f). Foliation is defined by repeated layering of aligned amphibole crystals, though amphibole also cuts across this fabric. Analysed hornblende is classified as tschermakite (Hawthorne *et al.*, 2012) with the vectors varying as following: tschermakite from 1.32–1.47, edenite from 0.37–0.44, and glaucophane from 0.18–0.21.

Staurolite appears as a singular grain anhedral grain with ragged grain boundaries, ~0.2 mm in size. Composition is consistent across the grain (X_{Mg} = 0.29–0.31, Ti = 0.12–0.13 apfu). Kyanite occurs more regularly throughout the sample as anhedral ragged grains either aligned with or at angle to the S_2 fabric (Fig. 4.12f). Grain size ranges up to 2.0 mm.

Plagioclase is present as euhedral–subhedral angular grains generally less than 1.5 mm in size, the long axis of grains is generally aligned parallel with the main fabric. Concentric compositional zoning is common. Plagioclase is defined as oligoclase–andesine (X_{Na} of 0.68–0.75).

Biotite is an accessory phase and occurs as fine ragged grains generally less than 0.1 mm in length. Grains are more commonly associated with kyanite and also with late chlorite. Chemistry shows two dominant groups (X_{Mg} range of 0.69–0.75 and Ti of 0.08–0.11 apfu and X_{Mg} varying from 0.67–0.74 and Ti from 0.12–0.18 apfu). The second group is defined by a larger range of chemistry and appears poorly equilibrated. Grains are not compositionally zoned, different grains are associated with different groups. This suggests the more chemically homogenous group within the thin-section volume was better equilibrated at peak metamorphic conditions . This composition is therefore used in subsequent petrological modelling.

Quartz is dominantly interstitial and display a long axis aligned with the main fabric. Patchy to sweeping undulose extinction is visible. Grains shows little evidence of dynamic recrystallisation

Rutile and ilmenite are the only Ti-oxides, both are be found as inclusions in amphibole, and are well distributed throughout the matrix (Fig. 4.12f). Ilmenite is common at the fringes of rutile, though associations of ilmenite cores and rutile rims are also present. It is likely that both were stable during prograde–peak metamorphism.

ICSV5: Garnet-Hornblende amphibolite ICSV5 contains the primary assemblage hornblende, plagioclase, and garnet (Fig. 4.14a). Accessory phases include quartz, titanite, ilmenite, rutile, zircon, and biotite. Retrograde growth of chlorite is documented along garnet fractures and in the matrix.

Garnet occurs as heavily fractured rounded grains around ~3.0 mm in diameter. Grain boundaries are ragged and serrated and defined by a corona of plagioclase (with hornblende inclusions), ilmenite and locally fine biotite crystals (Fig. 4.14a). Grains contain inclusions of ilmenite and late chlorite and green biotite. The selected garnet records X_{Mg} of 0.20 at both core and rim. Compositional zoning across the grain is weak, with relatively flat profiles (Fig. 4.13c). X_{Alm} and X_{Prp} are constant from core to rim (0.54 and 0.13–0.14, respectively). Grossular contents are similarly flat (0.26–0.27, core–rim), whereas spessartine shows slightly higher relative compositional zoning from 0.07–0.05.

Amphibole occurs dominantly as coarse acicular prismatic grains that are euhedral and range between 0.2–3.5 mm in length (Fig. 4.14a). Foliation is defined by repeated layering of aligned hornblende grains. Ilmenite (locally with fine rutile cores) are hosted within larger hornblende crystals. Analysed hornblende show magnesiohornblende–pargasite compositions (Hawthorne *et al.*, 2012) with the vectors varying as following: tschermakite from 1.21–1.30, edenite from 0.50–0.57, and glaucophane from 0.16–0.17.

Plagioclase occurs as oval to angular prismatic grains and are generally less than 1.0 mm in size (Fig. 4.14a), the long axis of grains are mostly aligned parallel to the main fabric. Locally plagioclase contains inclusions of fine-grained hornblende crystals. Grains dominantly show concentric compositional zoning. Plagioclase has the composition of oligoclase ($X_{\mathrm{Na}} = 0.70$–0.76), refractive indices also suggest some andesine compositions.

Similar to other samples, all Ti-oxides are present in varying microstructural contexts. Consecutive growth of rutile, ilmenite and then titanite is identified. Titanite occurs dominantly as polycrystalline rims around earlier grown Ti-oxides (Fig. 4.14a). Ilmenite is the only Ti-oxide associated with garnet-resorption,

indicating that breakdown of garnet was either coincident with "peak" conditions or happened soon thereafter during decompression. Titanite growth must therefore occur during later stages of decompression. The long-axis of matrix associated Ti-oxides are all aligned to the main fabric.

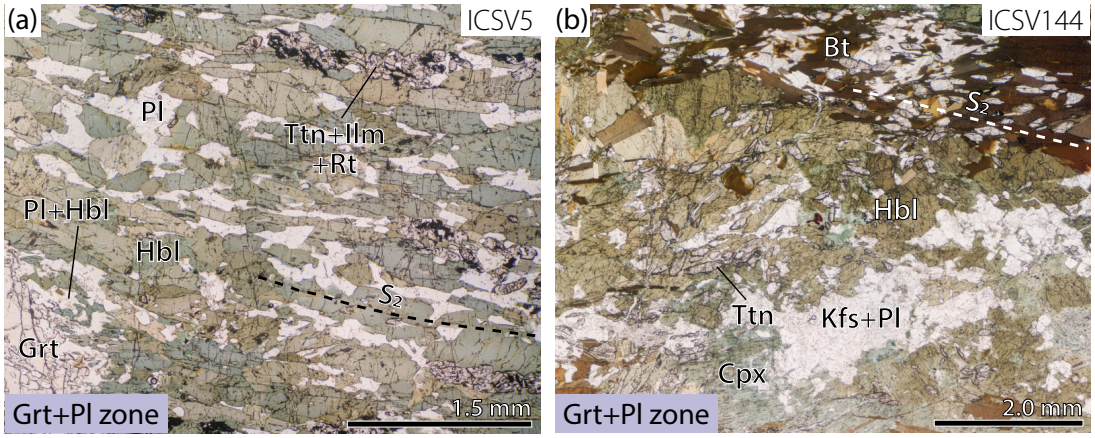


Fig. 4.14 Petrographic images of characteristic mineral assemblages and textures in garnet+plagioclase-zone samples.

ICSV144: Clinopyroxene-hornblende amphibolite ICSV144 contains the primary assemblage hornblende, andesine, biotite, titanite, clinopyroxene, and quartz (Fig. 4.14b). Accessory phases include apatite and zircon. Chlorite is locally present as a retrogressive phase.

Clinopyroxene occurs as anhedral grains often located at the cores of hornblende poikiloblasts or as ragged grains in contact with hornblende (Fig. 4.14b). Grains vary from 0.5–7.0 mm in diameter. Inclusions include titanite, biotite and quartz. Clinopyroxene chemistry shows moderate variation with X_{Mg} ranging from 0.56–0.67, X_{Jd} from 0.01–0.06, and Al 0.05–0.32 apfu.

Amphibole occurs as coarse poikiloblastic to prismatic subhedral to anhedral grains grains that range from 0.5–8.0 mm in length (Fig. 4.14b). Grain boundaries are dominantly impinged by feldspar. The inclusion assemblage comprises titanite, biotite, quartz, plagioclase and apatite. Biotite and titanite inclusions are dominantly misoriented parallel to the matrix fabric. Microstructurally, coarse hornblende poikiloblasts form coronas around embayed and resorbed clinopyroxene grains. Inclusions of titanite show noticeable coarsening from clinoproyxene cores to hornblende rims. Prismatic amphibole is aligned within the biotite-defined foliation. Compositionally amphibole varies from magnesio-hornblende to pargasite (Hawthorne *et al.*, 2012), with the majority of grains clustered in

the pargasite compositional field. Amphibole vectors range from 0.68–1.01 for tschermakite, 0.32–0.63 for edenite and 0.03–0.05 for glaucophane.

Biotite defines the main fabric, and is present as subhedral tabular grains between 0.3–4.0 mm in length (Fig. 4.14b). Biotite wraps coarse feldspars and hornblende-clinopyroxene poikiloblasts. Titanite and apatite occur as inclusions within biotite. Biotite is noticeably more ragged in contact with K-feldspar grains. X_{Mg} varies from 0.48–0.52 and Ti from 0.15–0.19 apfu.

Plagioclase is present as rounded to oval subhedral grains that range dominantly from 0.2–1.5 mm in size (Fig. 4.14b). Plagioclase is host to quartz and biotite inclusions. Quartz inclusions are lobate to rounded, locally with myrmekitic cores. Plagioclase has the composition of andesine (X_{Na} = 0.62–0.69).

K-feldspar occur as prismatic grains up to 3.0 mm in length (Fig. 4.14b). Grains are host to inclusions of quartz, titanite, and occasionally hornblende. Grains show strong perthitic exsolution and often display minor sericitisation. Grains have K-rich compositions, with X_{K} of 0.94–0.97.

Quartz is modally minor and dominantly occurs as rounded to lobate interstitial grains in the matrix. Flattened grains up to 1.0 mm in length are also present. Bulging recrystallisation is observed at grain boundaries and grains show patchy undulose extinction.

Titanite is the only Ti-oxide and occurs as euhedral to subhedral rounded to angular elongate grains generally between 0.1–0.4 mm in length (Fig. 4.14b), with grain size increasing from the inclusions in poikiloblasts to matrix grains. The long axis of grains is generally aligned parallel to the foliation.

4.4 *P-T* results

4.4.1 Single phase concentration and mineral pair thermometry

Geothermometry was undertaken based on a variety of mineral phases using both single-phase concentration and mineral pair thermometry techniques including Zr-in-rutile (Kohn, 2020; Tomkins *et al.*, 2007), Ti-in-Ca-amphibole (Liao *et al.*, 2021), Zr-in-titanite (Hayden *et al.*, 2008), and Ti-in-biotite (Henry *et al.*, 2005; Wu & Chen, 2015). The results are presented in Figures 4.15, 4.16, and 4.17. All figures show the mean result and 2 SD uncertainty rather than the calibration error. The 2 SD variation is generally smaller than the calibration error, however,

larger variation locally occurs. The 2 SD uncertainty is therefore displayed to see how well equilibrated grain populations are. Calibration errors of mean populations are then subsequently used when paired results with P data (Table 4.1). Mineral compositional data for all calibrations employed are provided in the Appendix.

4.4.1.1 Zr-in-rutile

Mean temperatures using the Kohn (2020) calibration range from 524-618 °C from the garnet and oligoclase zones to the sillimanite and garnet+plagioclase zones (Fig. 4.15a). 2 SD for samples, including the propagated pressure uncertainty (± 2 kbar), vary from ± 23 °C to ± 47 °C. Zr-in-rutile temperatures calculated using the Tomkins *et al.* (2007) calibration range from 554–664 °C and with mean calulations for each sample 22–30 °C higher than those calculated using the Kohn (2020) calibration at the selected pressure (Fig. 4.15a). The possible reasons for these discrepancies will be discussed in a later section (Section 4.4.1.5).

Rutile shows a variety of microstructural locations within pelitic samples, which includes in the matrix, hosted within porphyroblasts (garnet, staurolite, and kyanite), and hosted within decompression-type corona textures on garnet. Minimal temperature variation is present between microstructural locations, though is consistent with the sequence of crystallisation in regional metamorphic environments. Calculated temperatures from grains hosted within kyanite porphyroblasts are on average 9 °C higher than those hosted within garnet. Staurolite-hosted grains are 5 °C higher than those in garnet. Grains found within garnet corona are slightly higher (4–6 °C) than garnet-hosted or matrix grains in ICSV91, but are 20 °C lower than garnet-hosted grains in ICSV81. Matrix-hosted grains are either consistent with garnet-porphyroblast results or 3-4 °C lower, with the maximum difference between peak porphyroblastic phase and matrix grains documented in the kyanite-grade samples (-14 °C lower in ICSV6). These results suggest that kyanite-grade samples are subject to minor Zr loss, likely coincident with precipitation of ilmenite rims or rutile grains, and/or minor diffusional re-equilibration during decompression. Overall, the degree of variation is minor, suggesting such effects are minimal. Results from all microstructural locations were averaged and an integrated uncertainty was used over the pressure range of ± 2 kbar from the selected pressure to compare with other thermometers in Figure 4.17.

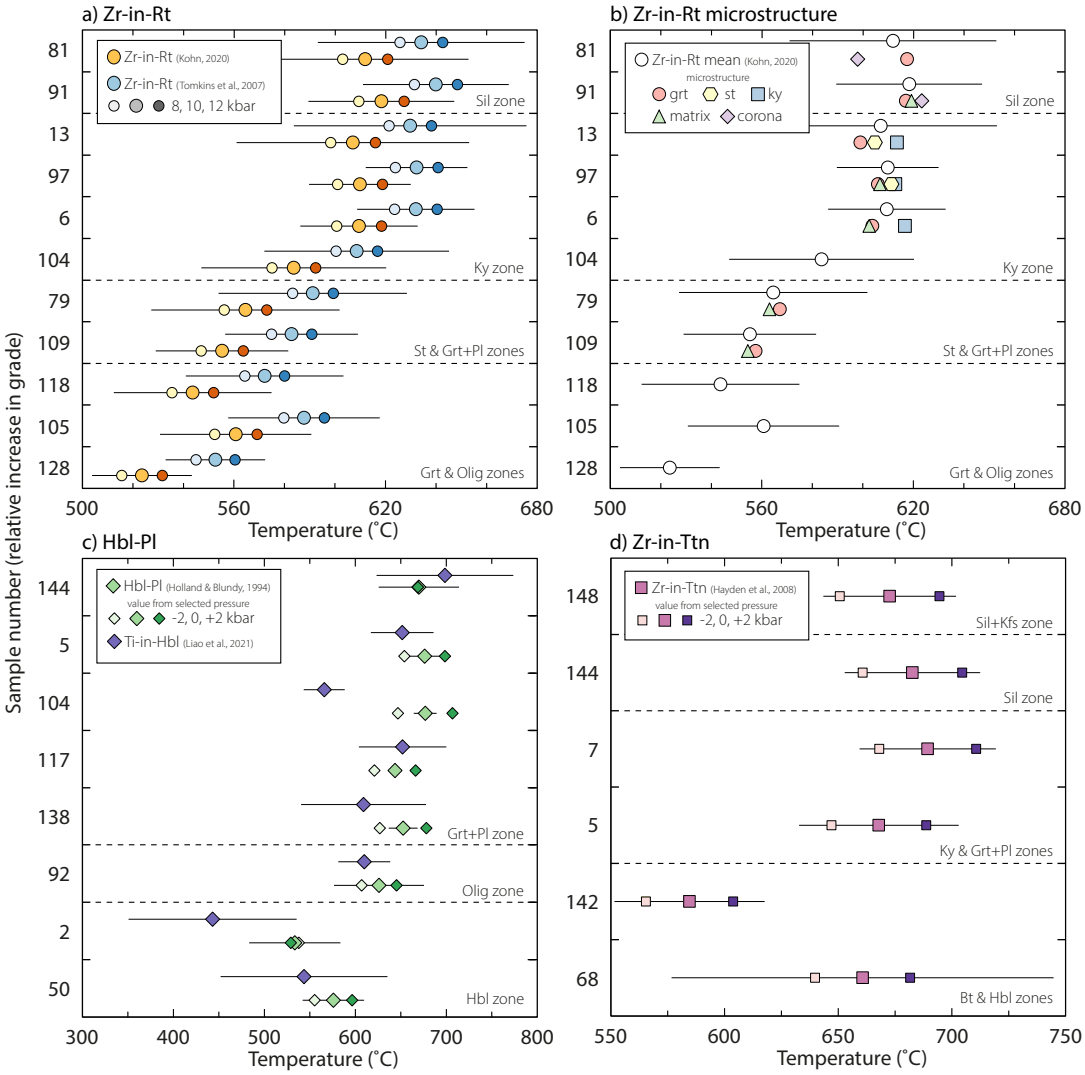


Fig. 4.15 Thermometry results for a-b) Zr-in-rutile, c) hornblende-plagioclase exchange, and d) Zr-in-titanite. Where values have a pressure dependence the selected pressure is 10 kbar for all samples except for ICSV68 and ICSV142 (9 kbar), ICSV144 (7 kbar), and ICSV148 (6 kbar).

4.4.1.2 Hornblende-plagioclase and Ti-in-Ca-amphibole

Mean hornblende-plagioclase temperatures range from 533–677 °C for samples from the hornblende to garnet+plagioclase zones (Fig. 4.15c). 2 SD for samples, including the propagated pressure uncertainty (± 2 kbar), varies from ± 33 °C to ± 54 °C. The Ti-in-Ca-Amphibole thermometer of Liao *et al.* (2021), dominantly shows good agreement with the hornblende-plagioclase exchange thermometer, recording a mean range of 443–698 °C (Fig. 4.15). Results in individual samples vary from +8 to -110 °C from the hornblende-plagioclase temperature, with a mean variation of -35 °C. Removing two discrepant results (ICSV2 and ICSV104), likely

due to partitioning of Ti into other phases, the average variation is significantly reduced to -13 °C.

4.4.1.3 Zr-in-titanite

Mean Zr-in-titanite temperatures range from 585–689 °C (Fig. 4.15d). 2 SD for samples, including the propagated pressure uncertainty (± 2 kbar) and a_{TiO_2} uncertainty (± 0.25), varies from ± 43 °C to ± 46 °C (excluding ICSV68, see below). Results from the kyanite to sillimanite+K-feldspar zone and garnet+plagioclase zone show minimal variation in temperature, whereas crystallisation of titanite from the biotite and hornblende zones show widely variable results. Results from ICSV68 have a significant 2 SD of ± 86 °C and show temperatures far in excess of equivalent thermometry results for this grade. Given the low-grade of the sample, it is possible that the analysed population represents mixing between an inherited and subsequent metamorphic rim domain, such that the lowest range of calculated temperatures is likely coincident with crystallisation of metamorphic rims. Alternatively the grain has suffered trace element disequilibrium (Cruz-Uribe *et al.*, 2018). Given the uncertainty, this result was not collated in Figure 4.17.

4.4.1.4 Ti-in-biotite

Mean Ti-in-biotite temperatures from the Henry *et al.* (2005) calibration are 517–686 °C across pelitic and metabasic lithologies. At lower grades in the biotite, garnet, and hornblende zones, the Ti-in-biotite results are higher in the pelitic sequence than the metabasic sequence by 35–76 °C (Fig. 4.17). Although in the staurolite, kyanite and garnet+plagioclase zones results are consistent in the lower part of the sequence (e.g., ICSV109 and ICSV92), at higher grades (kyanite zone and into the central parts of the garnet+plagioclase zone) significant variation is observed between the higher temperatures recorded in ICSV104 vs lower temperatures in ICSV13 and ICSV12, a difference of 40-73 °C (Fig. 4.16b). This suggests that either the calibration is unsuitable for metabasites, that peak conditions may not be well preserved within certain pelitic samples from the kyanite-zone, or that the calibration should not be applied at the given pressure range.

Both calibrations of the Ti-in-biotite thermometer successfully distinguish systematic changes in temperature through a regional metamorphic sequence.

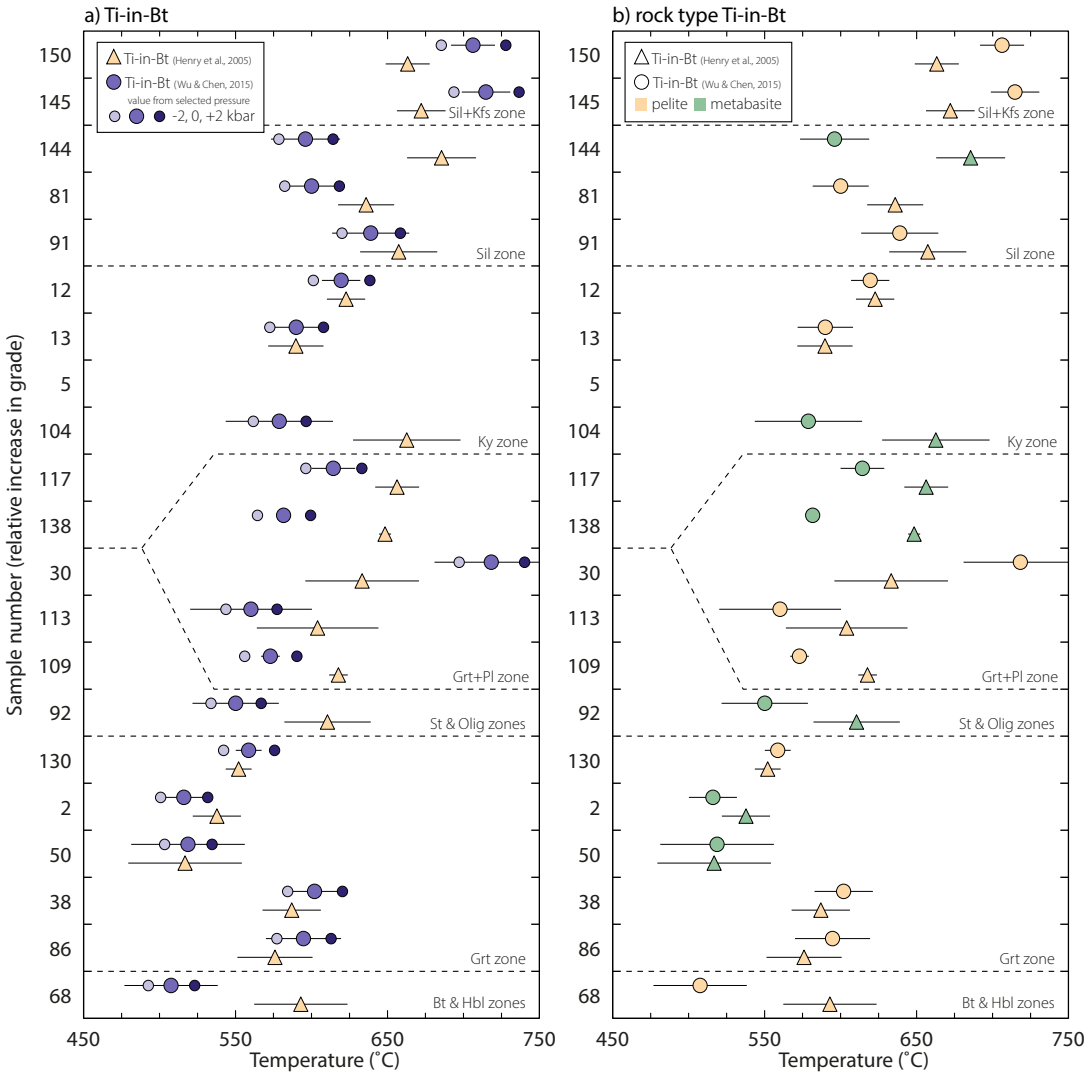


Fig. 4.16 a) Results for the Ti-in-biotite calibrations of Henry *et al.* (2005) and Wu & Chen (2015) plotted with relative increase in metamorphic grade. The Wu & Chen (2015) thermometer is pressure dependent thus uses a selected pressure of 9 kbar for ICSV68, 7 kbar for ICSV144 and 6 kbar for ICSV145 and ICSV150. All other samples are calculated with a selected pressure of 10 kbar. The 2 SD uncertainty range is plotted for the selected pressure and for results from the Henry *et al.* (2005) calibration. b) Ti-in-biotite thermometry results plotted against relative increase in metamorphic grade for pelite and metabsite. The selected pressure of 10 kbar is used for the Wu & Chen (2015) calibration. Intersection of the kyanite- and garnet+plagioclase-grade lines relate to map patterns displayed on Fig. 4.6.

The pressure dependent calibration of Wu & Chen (2015) produce calculated temperatures ranging from 554–664 °C at the selected pressure, with mean calulations for each sample varying from +86 °C to −89 °C than those calculated using the Henry *et al.* (2005) calibration. Significant variation between the two calibrations are reported for ICSV68, ICSV30, ICSV104, ICSV144, ICSV145 and ICSV150

with the calibration of Henry *et al.* (2005) showing a more consistent trend of temperatures over increasing metamorphic grade without localised increases or decreases in temperature. This is likely related to varying mineral chemistry, a result of the additional chemistry incorporated into the Wu & Chen (2015) calibration.

4.4.1.5 Multiphase thermometry summary and limitations

Figure 4.17 presents a collation of the preferred thermometry calibrations for Zr-in-rutile (Kohn, 2020), Ti-in-biotite (Henry *et al.*, 2005), hornblende-plagioclase (Holland & Blundy, 1994), and Zr-in-titanite (Hayden *et al.*, 2008). The Zr-in-rutile results from the Kohn (2020) calibration consistently record the lowest temperatures. This is commensurate with the timing of rutile growth, which commonly occurs in the core of peak porphyroblast phases, or in the mamtrix with rims of subsequent ilmenite or ilmenite and titanite overgrowth, suggesting rutile forms during prograde–peak or peak metamorphism. The Zr concentration of rutile may equilibrate when temperature reaches peak (e.g., Penniston-Dorland *et al.*, 2018; Kohn, 2020). However, the overall sequence of reported Zr-in-rutile temperatures compared to higher temperatures from all other thermometers implies this discrepancy may result from 1) only partial equilibration at thermal-peak conditions, 2) partial re-equilibration during retrograde metamorphism, or 3) inaccuracy of the current calibration, when compared to higher temperatures recorded in the previous (Tomkins *et al.*, 2007) calibration. Partial re-equilibration on the retrograde path is unlikely to impact the results owing to the fact that this effect is only documented in the outer 10–20 µm of individual crystals and has dominantly been documented for thermal peaks at greater than 700 °C followed by re-equilibration at amphibolite-facies conditions (i.e., < 700 ° C Kohn *et al.*, 2016). The Kohn (2020) calibration is inferred to be the more robust approach owing to the use of the pressure-dependence missing from the original Zack *et al.* (2004) calibration and not contingent on experimental data performed in high-temperature experiments as per the Tomkins *et al.* (2007) calibration. Zr-in-rutile temperatures show a consistent change in temperature with increasing grade, though they do not show significant temperature variation between the lowest- and highest-grade samples analysed.

Ti-in-biotite results for pelitic rocks generally record higher temperatures than Zr-in-rutile, though are lower than Ti-in-biotite, and hornblende-plagioclase results from metabasic rock. The use of the Henry *et al.* (2005) calibration is widespread,

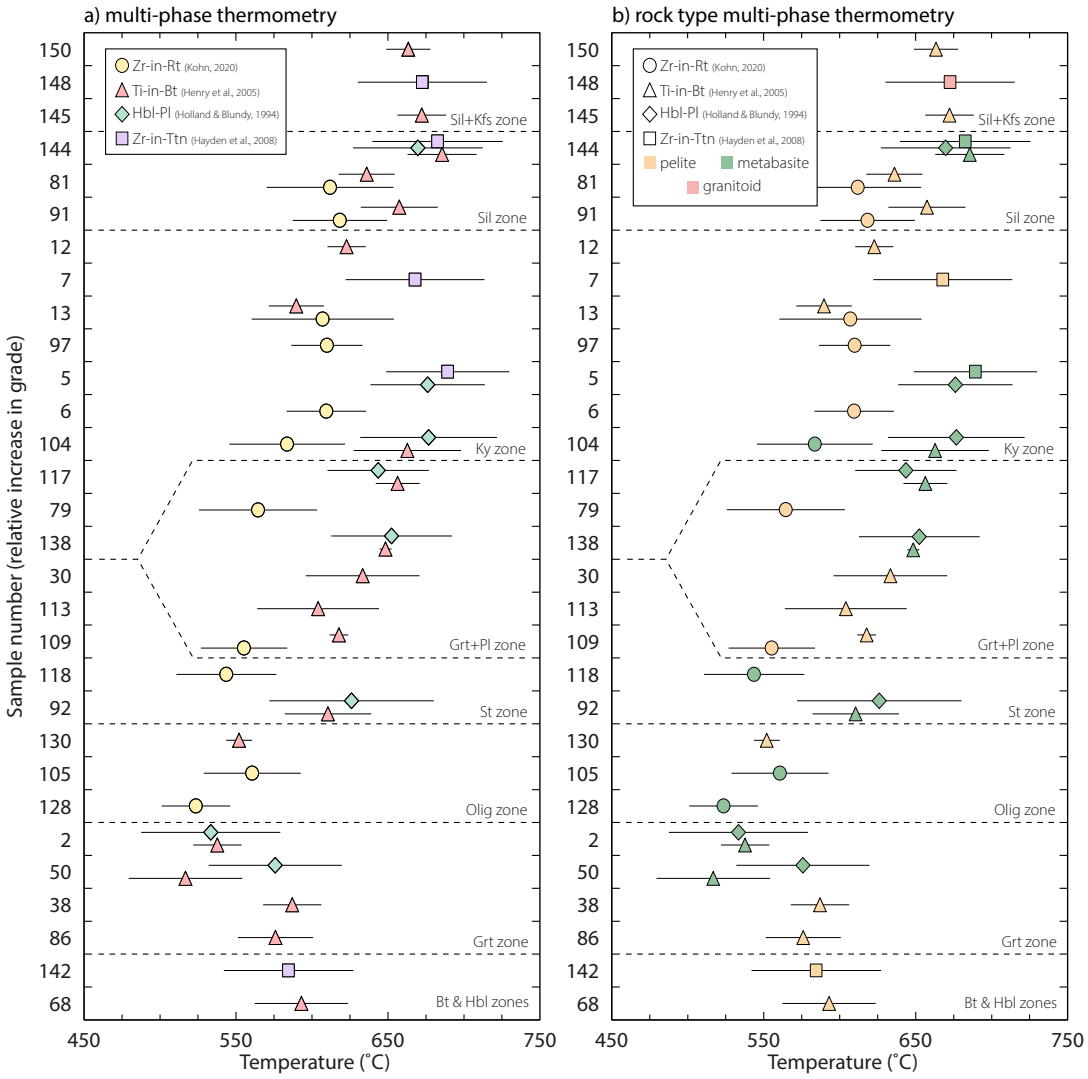


Fig. 4.17 a) Comparison of multiphase thermometry results using the preferred calibration for each thermometer. b) Comparison of thermometry results for pelitic and metabasic rocks (including one granitic sample). ICSV68 Zr-in-Ttn result is not displayed in either plot, given significant associated 2 SD (see previous discussion). Intersection of the kyanite- and garnet+plagioclasee-grade lines relate to map patterns displayed on Fig. 4.6.

though some limitations must be emphasised. Firstly, continuous changes in biotite composition with increasing grade has been well documented (Henry & Guidotti, 2002), however, it should also be considered that equilibration may occur episodically associated with periods of reaction (e.g., isograd boundaries; Pattison *et al.*, 2011). Secondly, the calibration is based on a detailed natural prograde sequence from New England, Maine, combined with the petrogenetic grid of Spear *et al.* (1999). The result is that it is only based on a limited, albeit excellently studied and exposed, natural database. Although incorporation of the petrogenetic grid greatly expands its reliability to other sequences, such

visualisations are necessarily simplified. Third, the thermometer was calibrated over the narrow pressure range of 4–6 kbar. It is worth noting that the Ti-biotite results of metabasic rocks generally show good agreement (particularly in the oligoclase and garnet+plagioclase zones) with the hornblende-plagioclase exchange thermometer. Although the Henry *et al.* (2005) Ti-in-biotite thermometer has been calibrated for pelitic systems this emphasises a series of points. 1) Ti-in-biotite results from metabasic rocks show reproducible results with other thermometers calibrated for metabasic systems, implying an accurate and/or well–equilibrated result is recorded. 2) For Ti-in-biotite, thermal-peak may be better preserved in metabasic rocks than in pelitic rocks, the latter potentially recording minor re-equilibration during decompression or retrogression from peak conditions. This may be representative of the whole-sample rather than the systematics of Ti-in-biotite. 3) The thermometer remains robust at higher pressure kyanite- and garnet+plagioclase-grade assemblages despite the narrow and lower pressure range of calibration.

Hornblende-plagioclase exchange thermometer shows a continuous increase in temperatures with relative increase in metamorphic grade and most samples show good agreement with Ti-in-biotite and Zr-in-titanite results where such phases are stable in the same sample or in neighbouring samples. Despite not being calibrated for albitic compositions in ICSV50 and ICSV2, thermometry values are in good agreement with Ti-in-biotite thermometry values where the pre-requisite criteria have been met. Despite this, thermometry values from these samples should be treated with caution and represent only minimum estimates for peak temperature.

Zr-in-titanite is in good agreement with hornblende-plagioclase and Ti-in-biotite results. However, large discrepancy between calculated temperatures are observed between kyanite-grade samples. ICSV7 records Zr-in-titanite results from porphyroblast hosted titanite that is 48–78 °C higher than neighbouring matrix Ti-in-biotite results from ICSV12 and ICSV13 (590–620 °C). This discrepancy might be explained by: 1) Ti-in-biotite results not representing thermal peak in these samples and have been subject to re-equilibration during decompression from peak, 2) Zr-in-titanite results are subject to disequilibrium trace element partitioning (Cruz-Uribe *et al.*, 2018). Equilibrium trace element partitioning will be maintained when the rate of mineral growth is slower than the rate of matrix diffusion for said trace element. When the rate of matrix diffusion is faster, disequilibrium partitioning will occur. Disequilibrium uptake of Zr into titanite has been well documented at lower temperatures, where it has been

cautioned that the thermometer may produce erroneous results for rocks that have equilibrated below 600 °C (Cruz-Uribe *et al.*, 2018). However, in scenarios where cooling rapidly from higher temperature conditions, reaction rates may outpace Zr matrix diffusion, yielding temperatures not in equilibrium with peak conditions (Cruz-Uribe *et al.*, 2018). Relevant titanite from ICSV7 are located as inclusions within garnet porphyroblasts thus do not directly diffuse Zr with the matrix. However, given the implied prograde microstructural context (i.e., inclusions), it suggests that Zr re-equilibrated at peak, similar to Zr-in-rutile systematics, or subjected to decompression and cooling from higher temperatures.

4.4.2 Multi-equilibrium barometry

Geobarometry was undertaken using the AvP mode from THERMOCALC and the results of the AvP calculations are presented in Fig. 4.18 where pressure values are plotted for a selected T value as informed from peak thermometry results (Fig. 4.17). These results are collated in Table 4.1. Garnet-grade samples record average peak pressures from 9.0–11.1 kbar (-0.9/+1.5), whereas hornblende-grade samples record pressures from 7.4–10.1 kbar (-1.8/+1.3). Samples ICSV38, ICSV50 and ICSV2 are all taken adjacent to the Sankoo metagranite. These samples broadly lie along strike from each other within an along-strike distance of 2.5 km (representing similar metamorphic grade) yet result in significant variation of pressures from 7.4–11.1 kbar (-1.8/+1.5), though uncertainty ranges all overlap. One oligoclase-grade sample (lying on the staurolite isograd) records higher pressures (12.0 ± 1.0 kbar) than equivalent staurolite-grade samples which show well clustered results (9.4–10.6 kbar, -1.3/+1.1). Kyanite samples (ICSV12 and ICSV13) record pressures between 9.4–9.8 kbar (± 0.9). Metabasite samples from the garnet+plagioclase zone that overlap with the staurolite- and kyanite-zone samples, record pressures largely clustered at 10.0–10.9 kbar ($-2.23/+1.0$), with significantly higher pressures recorded in ICSV117 at 14.8 kbar (± 2.31). Pressure conditions remain relatively isobaric or preserve slightly higher pressures moving up grade into the sillimanite-zone (10.0–12.7 kbar $-1.0/+1.1$). Decompression is recorded in the highest grade samples of the garnet+plagioclase zone (7.6 kbar ± 1.3). AvP recorded significant uncertainties for samples from the sillimanite+K-feldspar zone. ICSV145 only contains end-members for the phases biotite, muscovite, plagioclase and K-feldspar, which calculated a pressure of 3.9 kbar (± 0.5) for the selected temperature. ICSV150, in addition to the above assemblage, includes garnet but lacks muscovite, yielding 7.7 ± 2.2 kbar for the selected temperature.

Table 4.1 Paired thermometry and AvP results for the sample set. Ti-in-biotite and hornblende-plagioclase are the selected thermometers for all samples with the exception of ICSV145 and ICSV150 where thermometer criteria are not met and represent a minimum estimate. The thermometry results from neighbouring samples are thereby averaged to produce a best estimate of ~680 °C. All pressure-dependent thermometers use a pressure of 10 kbar for all samples except ICSV144 which uses 7 kbar.

Sample	**Grade**	**Ti-in-Bt (°C)**	**Hbl-Pl (°C)**	**Zr-in-Rt (°C)**	**Zr-in-Ttn (°C)**	**Selected T (°C)**	**T uncertainty (°C)**	**AvP (kbar)**	**1 SD (kbar)**	**$a\mathbf{H_2O}$**	**Removed**
ICSV86	grt	576				576	24	9.0	0.9	*	-pa -ab
ICSV38	grt	587				587	24	11.1	1.5	1.0	-daph -ames
ICSV50	hbl	517	576			576	40	7.4	1.8	1.0	-parg -gl -cel -pa
ICSV2	hbl	538	533			533	40	10.1	1.3	1.0	-gl
ICSV130	grt	552				552	24	9.8	1.4	*	
ICSV92	olig	611	626			626	40	12.2	1.1	1.0	-parg -gl
ICSV109	st	618		555		618	23	10.6	1.1	*	-pa -ab
ICSV113	st	604				604	23	9.6	0.9	*	-pa -ab
ICSV30	st	633				633	23	9.4	1.3	*	-pa -ab -phl -ann
ICSV138	grt+pl	648	652			652	40	10.6	1.1	0.7	-parg -gl
ICSV117	grt+pl	656	644			644	40	13.6	2.4	0.7	-parg -gl
ICSV104	grt+pl	663	677	584		677	40	10.0	2.2	1.0	-parg -gl
ICSV5	grt+pl		676		689	676	40	10.7	1.0	0.7	-parg
ICSV13	ky	590		607		590	23	9.3	0.9	*	-mst -fst -pa -ab
ICSV12	ky	623				623	23	9.8	0.9	*	-pa -ab
ICSV91	sil	657		618		657	23	12.6	1.0	*	-pa -ab
ICSV81	sil	636		612		636	23	10.0	1.1	*	-pa -ab -ky
ICSV144	grt+pl	686	670		683	670	40	7.5	1.3	1.0	-cat -ab
ICSV145	sil+Kfs	672				680	23	4.1	0.7	1.0	-ab -pa
ICSV150	sil+Kfs	663				680	23	7.7	2.2	1.0	-ab -san

*$a\mathrm{H_2O}$ independent using anhydrous equilibria (no free fluid phase)

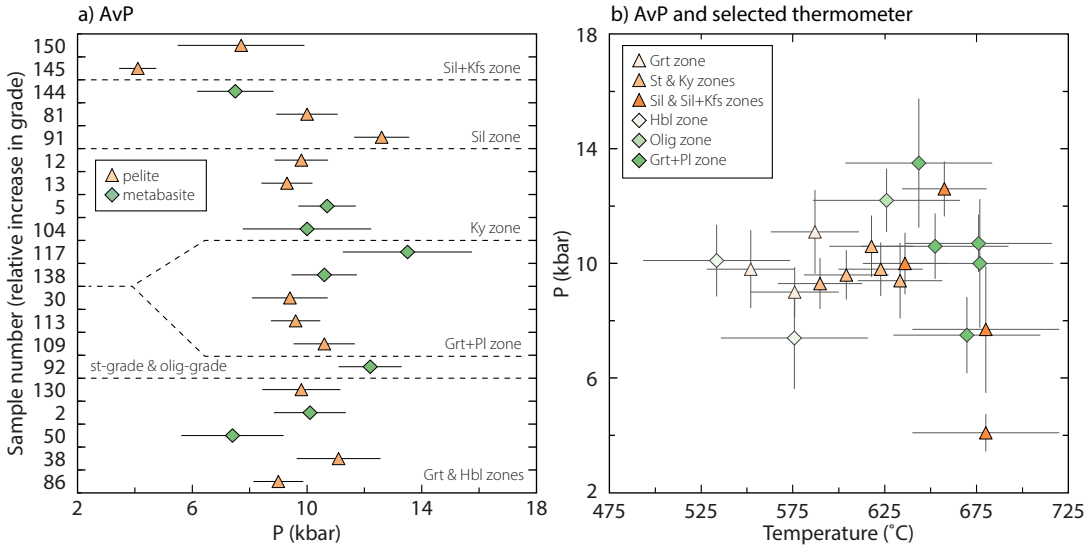


Fig. 4.18 a) AvP results at the preferred thermometry result and associated SD as calculated in THERMOCALC for pelite and metabasite. ICSV68 did not produce a result. a) AvP results at the selected temperature value. Orange colours used for pelite and green for metabasite, colour shifts represent increase in metamorphic grade.

4.4.3 Impact of $a\mathbf{H_2O}$

The procedure for determining $a\mathrm{H_2O}$ was discussed in section 4.2.3. In this section the impact of adjusting $a\mathrm{H_2O}$ on the stability of mineral phases in P-T space is explored.

Assuming fluid-present conditions, phase equilibrium modelling of mineral assemblages formed at sub-solidus conditions commonly infer pure $\mathrm{H_2O}$. However, where fluid composition-dependent conditions can be implicated, a lower $a\mathrm{H_2O}$ could be necessary. Petrographic observations record graphite in the cores of some porphyroblasts or as a dominant matrix phase in select samples. $a\mathrm{H_2O}$ can be set as low as 0.7–0.9 where graphite is present, implying that the coexisting metamorphic fluid may have been diluted with $\mathrm{CO_2}$ (Ohmoto & Kerrick, 1977). However, although graphite is abundant in samples from the western portion of the mapped area (e.g., ICSV130), graphite is not ubiquitous across the full sample set. Yet assuming pure $\mathrm{H_2O}$ sub-solidus equilibria in graphite-poor or graphite-absent samples produces calculated temperatures using the MATLAB routine significantly in excess of independent thermometry results. While graphite is not ubiquitous across the area, aqueous metamorphic fluids contain high salinity this may also result in a reduction of $a\mathrm{H_2O}$ (Aranovich & Newton, 1998) or alternatively graphite could act as a reactant during prograde metamorphic

reactions. Given that an aH_2O of unity can produce unreasonable results (even in graphite-absent conditions), the dependence of P-T results on the variable is explored in two pelitic samples, one from the garnet zone and one from the kyanite zone. Both samples contain graphite-poor or graphite-absent assemblages. This also serves to demonstrate the preferred procedure for handling determination of aH_2O.

4.4.3.1 ICSV86 (garnet zone) and ICSV13 (kyanite zone)

AvP Figures 4.20 and 4.19 shows the approach of using AvP mode in THERMOCALC to vary aH_2O to align the Ti-in-biotite thermometry results with the calculated T range over which P results are statistically robust. align pressure results that are dependent on aH_2O conditions to match that of Ti-in-biotite geothermometer. The functionality of AvP mode is detailed earlier in Section 4.1.3.3). To attain a result with no free fluid phase in the balancing reactions with the typical assemblage garnet-feldspar-biotite-muscovite, paragonite (and thus albite) may be removed. This produces a fluid composition independent result (as attained in ICSV86). The presence of staurolite in ICSV13 introduces a fluid dependence with shallow pressure gradients.

For a mean Ti-in-biotite temperature of 576 °C in ICSV86, AvP values range from 6.6 kbar (1 SD of 1.5 kbar) at aH_2O of 1.0 to 8.4 kbar (1 SD of 1.0 kbar) at aH_2O of 0.5. A fluid-composition independent result produces a pressure of 9.3 kbar (1 SD of 0.89 kbar). The results, with a 95 % confidence margin, as depicted in Fig. 4.19b, fall within the mean Ti-in-biotite range (± 24 °C) for water activities ranging from 0.8 to 0.5. The plateau of these results broadly occur at temperatures in excess of 650 °C. The fluid composition independent result passes the 95 % confidence across the possible 200 °C temperature range.

For a mean Ti-in-biotite temperature of 590 °C, AvP values range from 9.9 kbar (1 SD of 0.9 kbar) at aH_2O of 1.0 to 9.3 kbar (1 SD of 0.8 kbar) at aH_2O of 0.5. A fluid-composition independent result produces a pressure of 9.3 kbar (1 SD of 0.9 kbar). The results, with a 95 % confidence margin, as depicted in Fig. 4.20b, fall within the mean Ti-in-biotite range (± 24 °C) for water activities ranging from 1.0 to 0.5. The plateau of these results aligns most closely with the independent thermometer at $aH_2O = 0.7$ to 0.5. The fluid composition independent result passes the 95 % confidence test across the given 200 °temperature range.

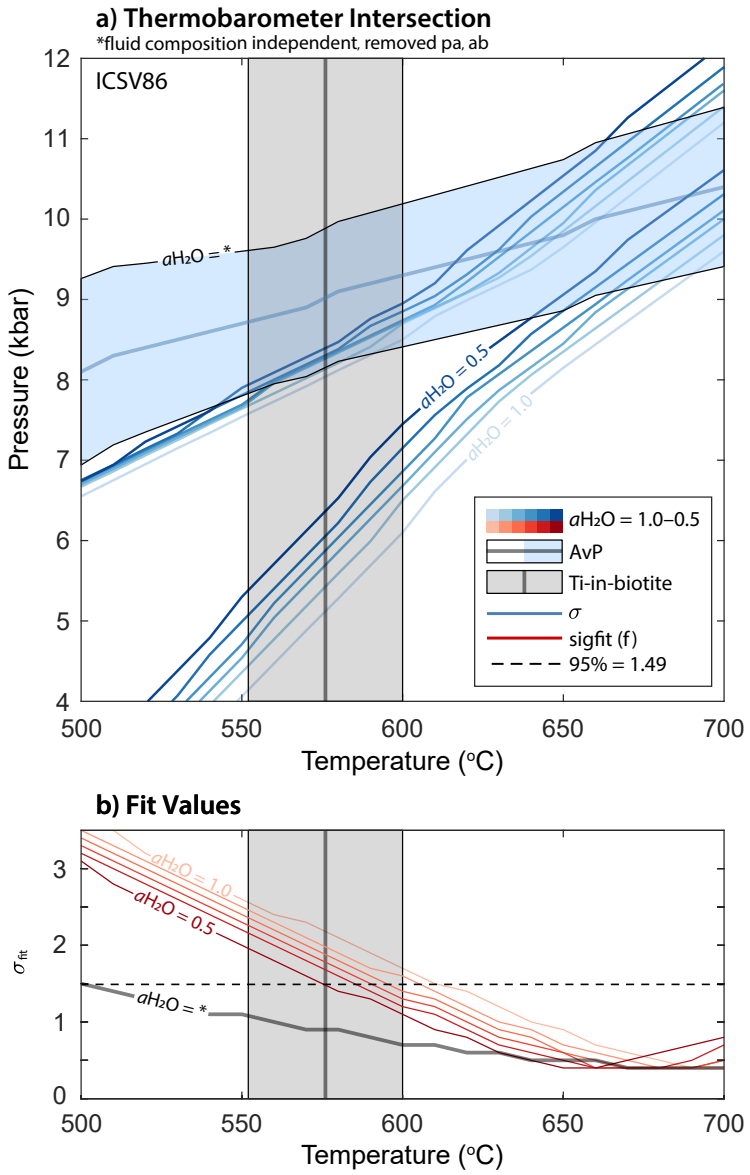


Fig. 4.19 a) ICSV86 Ti-in-biotite and AvP intersection plotted in P-T space. All fields and points vary from an aH_2O of 1.0 (lighter shade) to 0.5 (darker shade). The final AvP result is independent of aH_2O by excluding the listed phases. b) AvP fit values. For a result with 95 % confidence, sigfit must be less than the listed value.

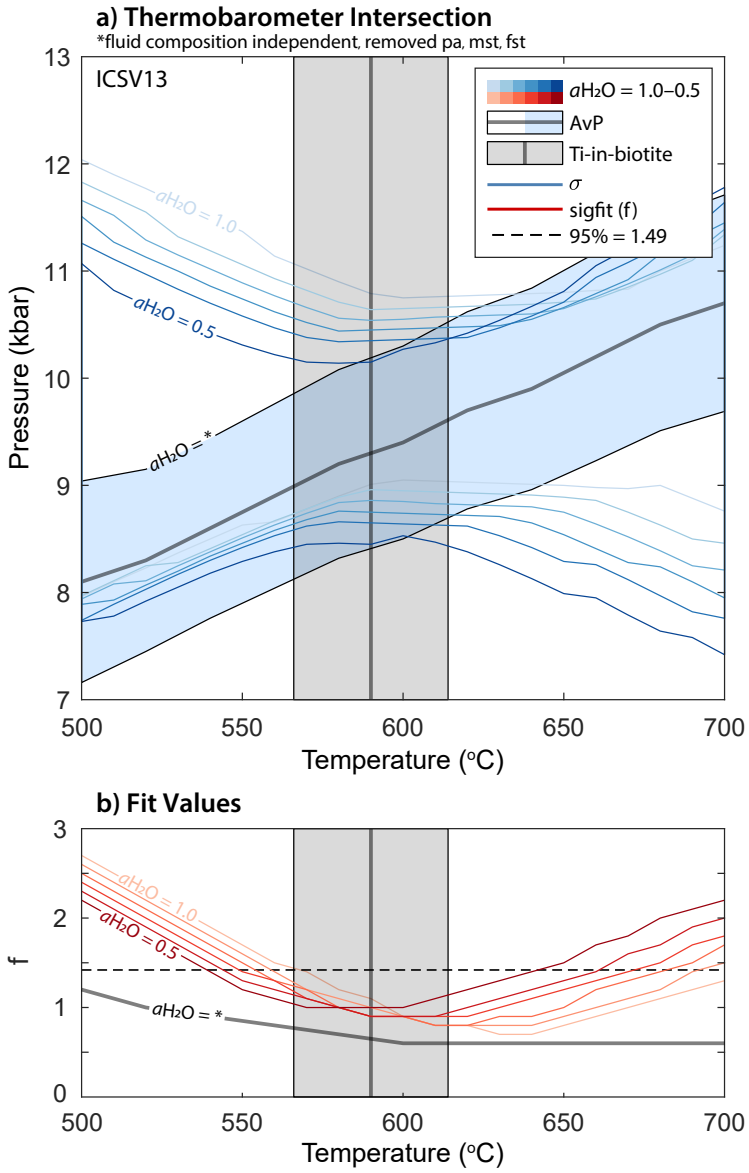


Fig. 4.20 a) ICSV13 Ti-in-biotite and AvP intersection plotted in P-T space. All fields and points vary from an aH_2O of 1.0 (lighter shade) to 0.5 (darker shade). The final AvP result is independent of aH_2O by excluding the listed phases. b) AvP fit values. For a result with 95 % confidence, sigfit must be less than the listed value.

Determining the fluid composition that corresponds to a minimum σ_{fit} in P-T-X space, is one approach suggested by Powell & Holland (1994). However, given a preferable fluid independent geothermometery result, this study follows the approach suggested by Powell & Holland (2008, see Section 4.2.3). However, the lowest fit values overall are attained at $a\mathrm{H_2O}$ of 1.0 in ICSV13. Suggesting smaller fit values are preferable to larger ones is 'dangerous' where both results have passed the χ^2 test (Powell & Holland, 1988). Therefore the aim should be to ensure that the range of results passing the χ^2 test are within range of the chosen thermometry result and its associated calibration error.

Modelling of both samples show better agreement between AvP results and independent thermometers using an $a\mathrm{H_2O}$ of less than 1.0. A result that's independent of fluid, achieved by eliminating end-members associated with fluid-liberating reactions, provides a result with 95 % confidence throughout the temperature range of the study and is therefore the preferred option whenever feasible, even if it leads to a larger uncertainty.

Phase equilibrium modelling The next stage involves using the peak field to achieve a match between the thermobarometer intersection of Ti-in-biotite and the fluid composition independent AvP results and associated uncertainties. Figures 4.21 and 4.22 depict the modelled peak assemblage field and variation of phase stability boundaries by varying $a\mathrm{H_2O}$ from 1.0–0.5. It is possible to see that in ICSV86 almost no overlap is achieved at an aH2O of 1.0 and increasing overlap progressing to lower $a\mathrm{H_2O}$. For ICSV13 overlap is achieved between the peak field and thermobarometer intersection at $a\mathrm{H_2O}$ of 0.6 and 0.5. This suggests it is indeed required to reduce the $a\mathrm{H_2O}$ for these samples.

Adjusting $a\mathrm{H_2O}$ results in significant displacements to phase boundaries, consistent with Le Chatelier's principle (system at equilibrium adjusts to counteract applied changes). Reducing the activity of $\mathrm{H_2O}$ expands $\mathrm{H_2O}$ bearing fields such that dehydration reactions, which liberate $\mathrm{H_2O}$ on the high temperature side, will move to lower temperatures. Furthermore, melt producing reactions that consume $\mathrm{H_2O}$ (low-temperature side) will move up temperature. Kyanite, staurolite, stilpnomelane, paragonite, epidote, garnet, chlorite, and titanite all move to lower temperatures, whereas cordierite and the liquidus move to higher temperatures (Figs 4.21 and 4.22). Certain phases may be involved in both types of reactions (muscovite, garnet, biotite, plagioclase and K-feldspar), and as such may expand in both directions. The liquidus shows considerable change across the P-T range. For both samples the liquidus changes from weakly negatively

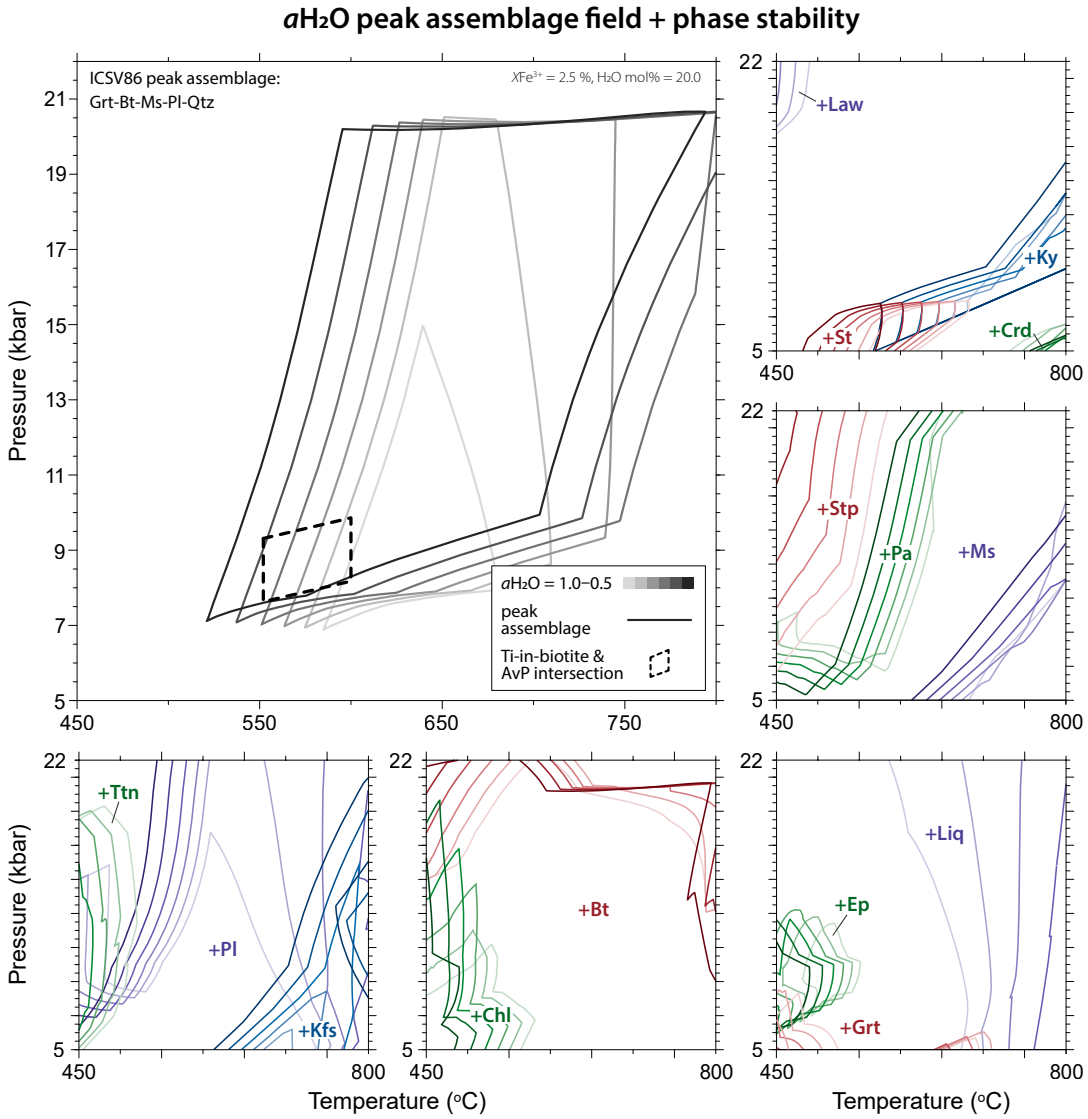


Fig. 4.21 Top left: ICSV86 peak assemblage field varying from an aH_2O of 1.0 (lighter shade) to 0.5 (darker shade). Overlap of thermobarometer intersection and peak assemblage field occurs at aH_2O = 0.9–0.5. Right and below: Stability of mineral phases across *P-T* space for the given bulk composition varying from aH_2O of 1.0 (lighter shade) to 0.5 (darker shade).

sloping at ~675 °C at aH_2O of 1.0 to gradual clockwise rotation of the slope to become weakly positively sloping at temperatures in excess of 750 °C by aH_2O of 0.7. By aH_2O of 0.6 the liquidus is absent on ICSV86 across the modelled temperature range (500–700 °C) and by aH_2O of 0.6 on ICSV13 for the range of 500–800 °C.

Although displacements to phase boundaries are most pronounced with shifts up- or down-temperature, some mineral phase boundaries expand up-pressure

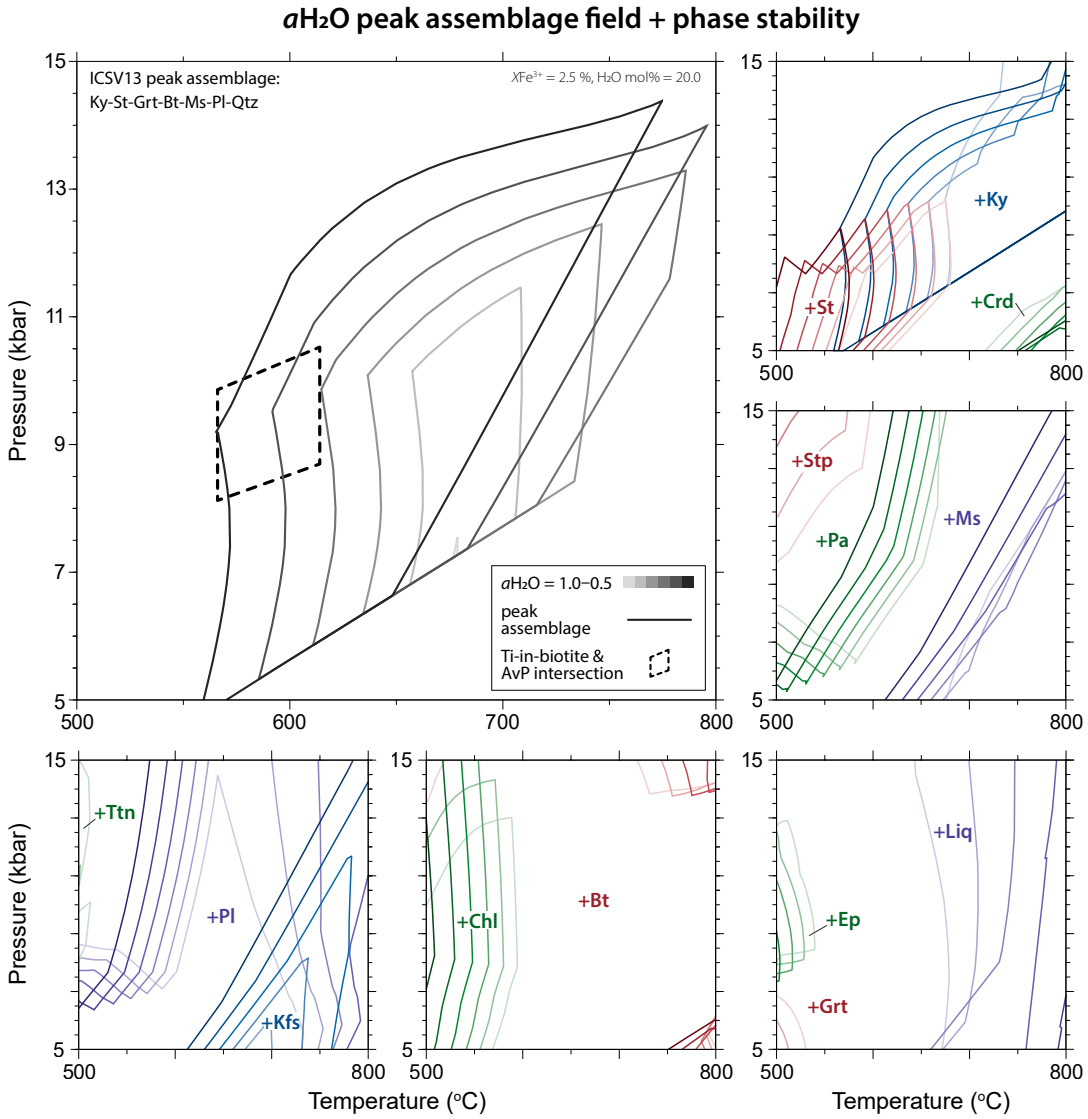


Fig. 4.22 Top left: ICSV13 peak assemblage field varying from an $a\mathrm{H_2O}$ of 1.0 (lighter shade) to 0.5 (darker shade). Overlap of thermobarometer intersection and peak assemblage field occurs at $a\mathrm{H_2O} = 0.6$–0.5. Right and below: Stability of mineral phases across P-T space for the given bulk composition varying from $a\mathrm{H_2O}$ of 1.0 (lighter shade) to 0.5 (darker shade).

and/or down-pressure (e.g., plagioclase and K-feldspar), with more minor changes in pressure of micas, staurolite and kyanite.

Mineral chemistry The optimal choice for $a\mathrm{H_2O}$ may be further constrained through matching isopleth mineral chemistry to the peak assemblage field and/or thermobarometer intersection. Mineral chemistry can also be dependent for certain phases on the selected $X\mathrm{Fe^{3+}}$ of the system. As such an appropriate value for $X\mathrm{Fe^{3+}}$ is calculated using a P-$X\mathrm{Fe^{3+}}$ plot at the T fixed by the Ti-in-biotite

thermometer, and/or T-$X\mathrm{Fe}^{3+}$ plot at the P fixed by the AvP result. This can be calculated with an estimate of the preferred $a\mathrm{H_2O}$ based on the AvP and phase equilibrium modelling. A clear example of the variation of the mineral chemistry can be observed by the activity of titanium in biotite, which equates to Ti contents apfu (11 oxygens). Ti content is located significantly up temperature of the thermobarometer intersection for an $a\mathrm{H_2O}$ of 1.0 but shows a closer match or overlaps with the thermobarometer intersection at a reduced $a\mathrm{H_2O}$. Using all mineral chemistry variables a best match with the thermobarometer intersection is distinguished at a reduced $a\mathrm{H_2O}$ of 0.6 in ICSV86 or 0.5 in ICSV13.

Reducing the $a\mathrm{H_2O}$ commonly predicts both peak conditions, reaction history and mineral chemistry more accurately than $a\mathrm{H_2O} = 1.0$ for the sample set. For the following parts of the workflow the preferred ranges of $a\mathrm{H_2O}$ may be discriminated, a) AvP and the indendent thermometer: 0.8–0.5 in ICSV86 or 0.7–0.5 in ICSV13, b) peak assemblage field and thermobarometer intersection: 0.9–0.5 in ICSV86 or 0.6–0.5 in ICSV13, c) mineral chemistry: 0.6 in ICSV86 and 0.5 in ICSV13. The relative implications of a reduced $a\mathrm{H_2O}$ to conditions for melt-formation and abundance in the Himalaya are explored in Section 4.4.8.

4.4.4 Pelite

For each modelled sample the following diagrams are generally displayed. a) A pseudosection displaying the stability of phase assemblages across P-T space coloured by variance, P-T pseudosections are overlain by the thermobarometer intersection defined by AvP and Ti-in-biotite thermometer using the calibration of Henry *et al.* (2005). In the subsequent section for metabasic samples (Section 4.4.5) the hornblende-plagioclase exchange thermometer of Holland & Blundy (1994) is employed. b) P-T pseudosection boundaries overlain on a diagram displaying the relative misfit between the range of modelled mineral chemistry variables. A lower misfit value indicates a more robust result, visualized using a heatmap (color map representing data in a matrix to convey intensity and facilitate pattern recognition). Overlaid is the bootstrapped result (Monte Carlo simulation), displaying mean best-fit result with a 1 SD uncertainty ellipse. c) A box plot displaying the median and interquartile range (IQR) of T and P results defined by the spread of the resampled data. The grey background of these boxplots are coloured by the minimum and maximum T and P range shown on the thermobarometer intersection. The median result is the preferred result for all samples. d) A 10x10 bin plot of the bootstrapping result displaying distribution

in P and T space. e) A pixel density plot of compositional isopleth ranges for garnet core or rim compositions.

Figures 4.23–4.32 show the results of pseudosection modelling and best-fit calculation for each of the studied pelitic samples. Grey phase boundaries are used for transition into or between Ti-oxides to indicate the lack of certainty on location of boundaries in P-T space. Interpreted peak assemblages are therefore first defined by major constituent silicate minerals, and then attempts to reproduce Ti-oxides and compositional variables are undertaken using T- or P-$X\mathrm{Fe}^{3+}$ plots. If the observed Ti-oxides cannot be reproduced, the best estimate for the peak assemblage is selected based on the dominant constituent minerals with the $X\mathrm{Fe}^{3+}$ that most closely produces the Ti-oxide (e.g., rutile + ilmenite vs ilmenite).

4.4.4.1 Garnet zone

Pseudosection diagrams for samples from the garnet zone located along the Parkachik–Rangdum transect (ICSV86) and the Shanshin Nala transect (ICSV130; Fig. 4.6) are presented in Figures 4.23 and 4.24.

Diagrams for ICSV86 and ICSV130 show a similar topology and sequence of mineral reactions across temperature, but differ in regards to the stability of phases over the modelled pressure ranges. Garnet and biotite are broadly stable across most P-T conditions on both diagrams. ICSV86 is distinct with a broad field of epidote stability between ~450–525 °C and ~7.0–12.0 kbar, which is only stable at low P-T conditions on ICSV130 (~450 °C and ~6.5 kbar). ICSV130 shows an expanded field of staurolite stability that extends up to 10.5 kbar, which is higher than for the other samples from the region. The paragonite-out boundary is also pushed up P in ICSV130 and is characterised by a shallower slope. Significantly, ICSV130 only features stability of plagioclase at higher temperatures and pressures, with a moderately inclined slope of stability across the diagram, in good agreement with the plagioclase-absent assemblage.

ICSV86 shows significant overlap between the thermobarometer intersection and observed peak assemblage (Grt-Bt-Ms-Pl-Qtz-Ilm) for an $a\mathrm{H_2O}$ of 0.7 at conditions of 552–600 °C and 7.8–10.2 kbar (Fig. 4.23a). The peak field is delimited at lower temperatures by paragonite stability, and at higher temperatures by the appearance of kyanite, whereas down pressure is constrained by staurolite and up-pressure by the rutile-in boundary. The best fit of observed and modelled mineral chemistry variables producecs a result of 575 °C (+8/−10 °C) and 7.72

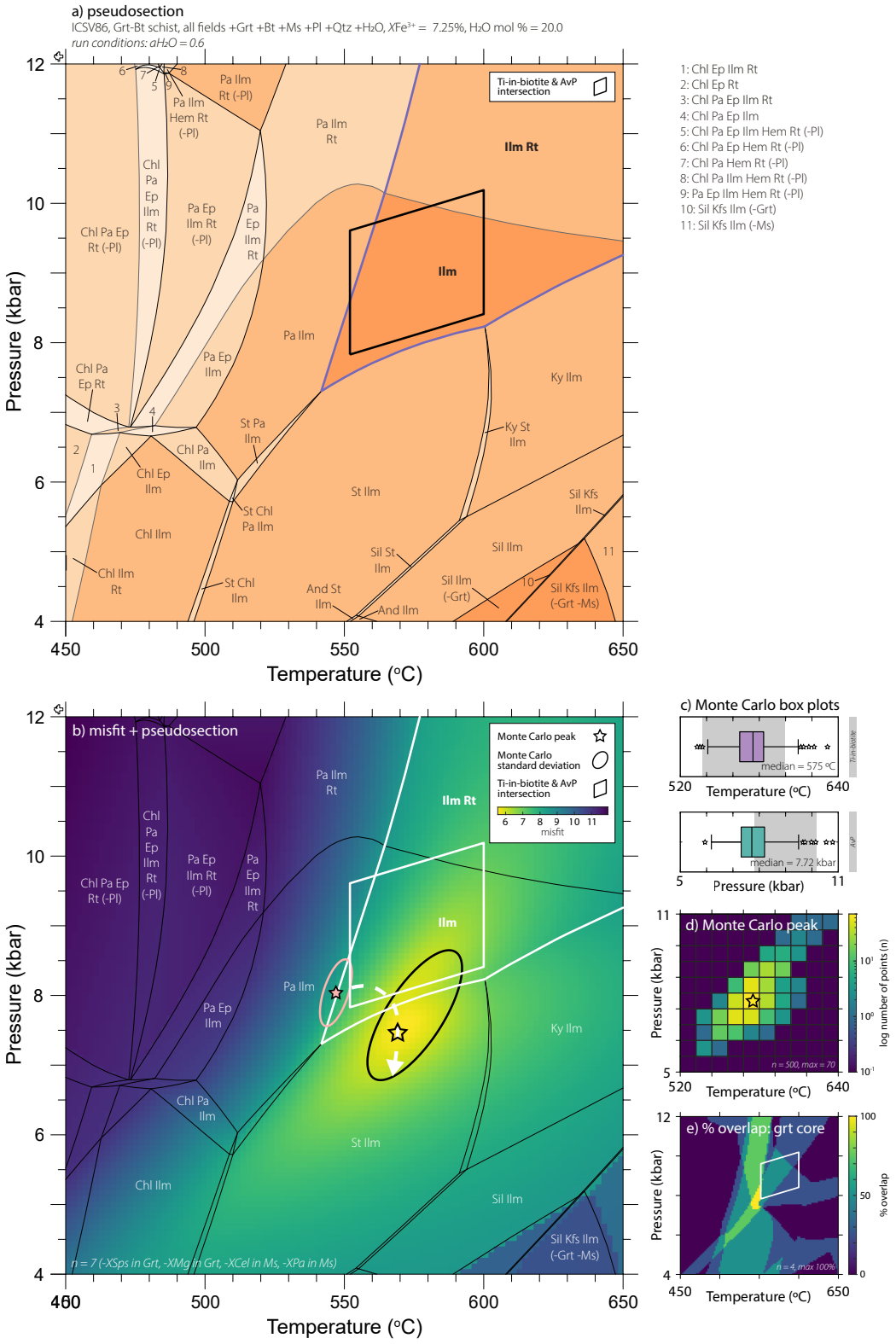


Fig. 4.23 ICSV86 a) pseudosection, b) heatmap showing the misfit of mineral chemistry variables, overlain with the bootstrapped mean best-fit result and the corresponding pseudosection, c) boxplots of bootstrapped T and P estimates with the grey bar indicating the range of the selected thermometer and AvP results, d) log-scaled 2D-histogram bin-plot of the boostrapped data with mean best-fit result marked by the star, e) % overlap of garnet core compositional isopleths.

kbar (+0.49/−0.40 kbar), which does not lie in the thermobarometer intersection or peak field, however, 1 SD of this result does intersect both features (Fig. 4.23b–d). Uncertainty on the best fit shows considerable variation over P space (~5.5–11.0 kbar) as a result of sub-parallel, steeply sloping, intersecting isopleths; whereas T is well constrained (~520–640 °C; Fig. 4.23d). The best estimate of temperature constrained from mineral compositional information is consistent with the Ti-in biotite thermometry result, whereas the pressure estimate lies on the low-P boundary of the AvP result range (Fig. 4.23c). Notably, the peak result lies in a staurolite bearing field. X_{Mg} was removed to reduce the dependence of the result on garnet rim chemistry, which preferentially lies at the upper boundary of the staurolite bearing field. Although this might suggest later growth of garnet rims, the core chemistry similarly shows minimal pressure difference, with a calculated P-T of 546 °C (+4/−2 °C) and 8.04 kbar (+0.24/−0.32 kbar; Fig. 4.23b). Garnet shows asymmetric weak compositional zoning (Fig. 3.10), however, the broad garnet stability field across the pseudosection but narrow temperature interval between garnet-core and peak compositional results (Fig. 4.23b, e) suggests a true core composition is not recorded by the analysed grain. Alternatively, the garnet has been subsequently diffusionally modified, as the theoretical 'core' chemistry should lie down P and T towards the garnet-in line.

ICSV130 provides a thermobarometer result with a large SD on a near isobaric AvP range. The interpreted peak assemblage of Grt-Bt-Ms-Qtz-Ilm is best approximated by the highlighted field in Fig 4.24a. This field contains rutile as a stable phase, which is not present in the observed assemblage. The boundary of the field can be constrained at lower temperatures, and higher pressures, by chlorite and paragonite. It may also be constrained at higher temperatures by the appearance of plagioclase or disappearance of ilmenite, and lower pressures by staurolite. Overlap between the thermobarometer intersection and the peak field occurs at 528–576 °C and 9.6–11.2 kbar. Very poor overlap occurs between the calculated peak of selected compositional variables (excluding all garnet variables, and X_{Cel} in Ms, 541 +14/−16 °C and 8.44 +1.11/−0.91 kbar) and the peak assemblage field (Fig. 4.24b). The calculated temperature is in relative agreement with the Ti-in-biotite thermometry result, whereas the calculated IQR of pressures just overlaps with the lower P boundary of the AvP result. The calculated peak shows considerable variation over both T and P (Fig. 4.24d). Garnet variables were removed from the calculation procedure as they do not agree with other variables and plot at consistently lower pressures and temperatures (Fig. 4.24b). The core composition produces a best fit at 503 ± 12 °C and 6.22 ± 0.30 kbar,

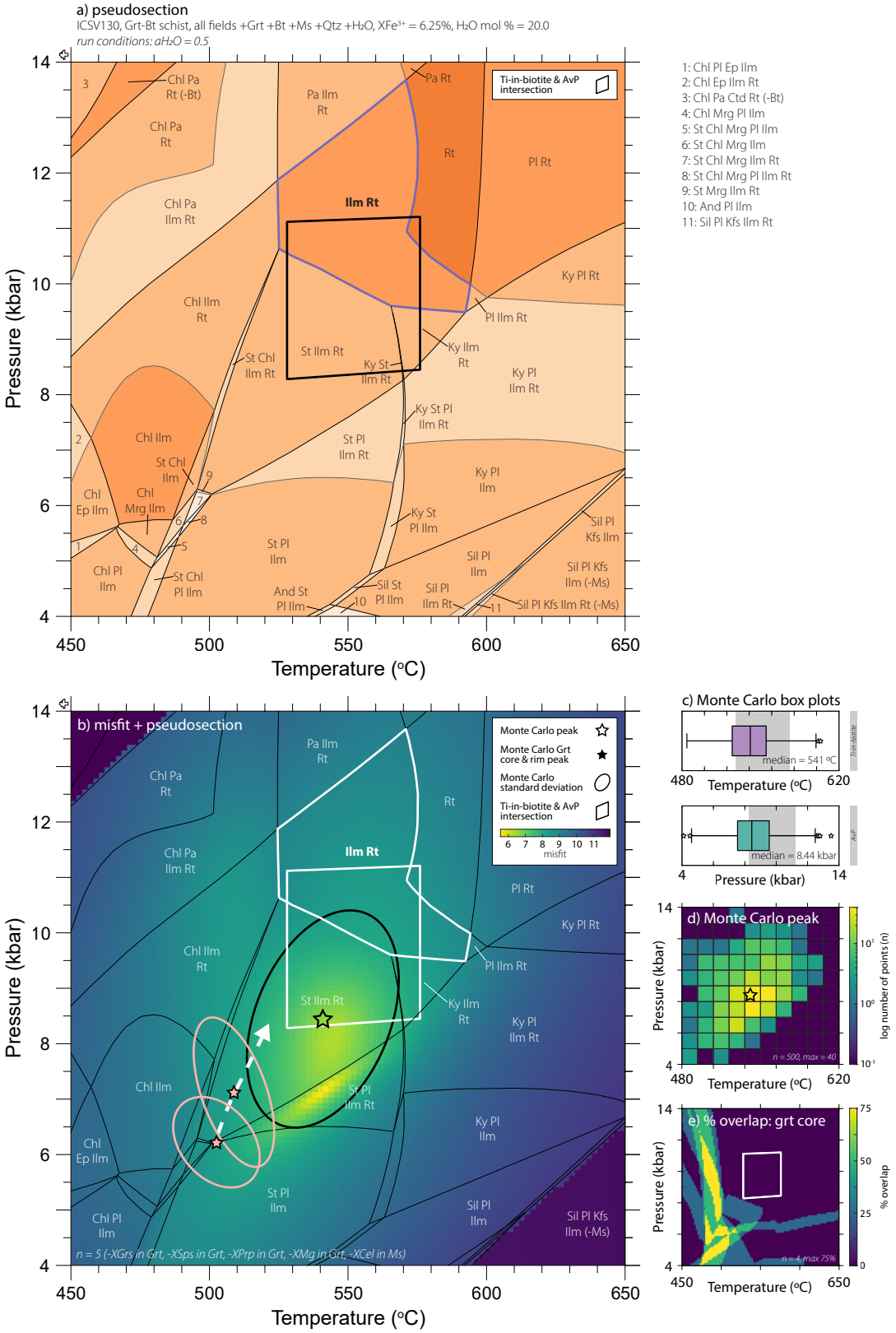


Fig. 4.24 ICSV130 a) pseudosection, b) heatmap showing the misfit of mineral chemistry variables, overlain with the bootstrapped mean best-fit result and the corresponding pseudosection, c) boxplots of bootstrapped T and P estimates with the grey bar indicating the range of the selected thermometer and AvP results, d) log-scaled 2D-histogram bin-plot of the boostrapped data with mean best-fit result marked by the star, e) % overlap of garnet core compositional isopleths.

and the rim at 509 ± 10 °C and 7.13 +0.61/−0.81 kbar (Fig. 4.24b). Several issues are present with the garnet results. Firstly, the modelled range of observed compositions from the garnet core show poor overlap (Fig. 4.24e). Secondly, although the best fit of garnet core and garnet rim implies near isothermal burial during garnet growth, microstructural evidence indicates garnet overgrows the S_2 fabric, suggesting garnet growth after burial. Additionally, despite the absence of post-peak diffusional modification and prominent compositional zoning measured in the garnet grain uncertainty ranges of chemical variables for core and rim plot show significant overlap (Fig. 4.24b). Consequently, the modelled disequlibrium between garnet mole fractions, the implied timing of garnet growth, and narrow chemical zonation patterns, do not adequetely align with the natural observations and data. The discrepancy between modelled peak conditions and the peak assemblage suggests the peak result may can be represented at the upper uncertainty range of ~10.0 kbar and 550 °C, concomitant with the thermobarometer intersection and peak assemblage field.

Temperature estimates for the two garnet-zone samples suggest conditions of 525–583 °C (minimum and maximum IQ-range) for the calculated mineral assemblages and 528–600 °C as suggested by the thermobarometer intersection and peak field. Pressure conditions show more significant variation between 7.32 to 9.55 kbar as per calculated compositional variables, or 7.8 to 11.2 kbar suggested by the intersected range of AvP and peak field intersection. The range of pressure results suggested by the peak field are not deemed reliable by themselves given the poor constraints on the upper pressure phase boundaries.

4.4.4.2 Staurolite zone

Pseudosection diagrams for samples from the staurolite zone located along the Shanshin Nala and Chellong Nala transects (ICSV109 and ICSV113, respectively; Fig. 4.6) are displayed in Figures 4.25 and 4.26.

Both diagrams show a similar topology, with identical peak assemblage fields, and similar assemblages defining the low-temperature and low-pressure boundaries. Garnet and biotite are largely stable across the modelled *P-T* range for ICSV109 and ICSV113, with garnet absent at low pressures and higher temperatures on ICSV109 and biotite absent at high pressures and low temperatures in ICSV113. In ICSV109, paragonite stability extends to higher temperatures (~600 °C), in comparison to the range of ~400–500 °C for ICSV113. Plagioclase only becomes unstable over the *P-T* range for ICSV109 in domains where paragonite

is stable, whereas for ICSV13, plagioclase is not stable until ~600 °C. The higher temperature at which plagioclase joins the assemblage in ICSV113, is in agreement with late poikiloblastic plagioclase overgrowing the S_2 fabric. The garnet-zone sample from the same transect along Shanshin Nala (ICSV130) documents a plagioclase-absent assemblage and records delayed plagioclase stability until higher temperatures as shown in Fig. 4.24. Both samples have low Na_2O bulk rock compositions (0.45 and 0.80 wt % for ICSV113 and ICSV130, respectively).

ICSV109 displays significant overlap between the thermobarometer intersection and the observed peak assemblage (Grt-Bt-Ms-Pl-Qtz-Rt) for an aH_2O equal to 0.7 between 594 and 642 °C and 9.1–11.8 kbar (Fig. 4.25a). The peak field extends to greater P and T than the modelled range. Large peak assemblage field boundaries, often extending over a significant pressure range, are common across the modelled sample suite (e.g., Fig. 4.21). Down temperature the peak field is delimited by the presence of paragonite, and down pressure by staurolite or kyanite stability fields. Selected mineral chemical variables show a best-fit median result at 599 °C (+6/−9 °C) and 9.04 kbar (+0.71/−0.51 kbar; Fig. 4.25b–d). This result lies just outside the thermobarometer intersection and peak field but the 1 s.d of the Best fit result does intersect both features (Fig. 4.25b). Uncertainty on the best fit shows considerable variation over P space (~7.0–15.0 kbar) as a result of sub-parallel, steeply sloping, intersecting isopleths, whereas T is well constrained (~560–660 °C; Fig. 4.25d). The best estimate of temperature from mineral chemistry constraints is consistent with the Ti-in-biotite thermometer result, whereas the pressure estimate overlaps with the low-P boundary of the AvP result range (Fig. 4.25c). X_{Mg} was removed to reduce the dependence of the result on garnet rim chemistry, which preferentially lies at the upper boundary of the staurolite bearing field, in contrast other variables (X_{Sps}, X_{Cel} and X_{Pa} in muscovite) were removed due to poor fit, sitting at higher pressures than the dominant cluster of results. Garnet core compositional isopleths intersect to produce a best-fit result at 502 °C (+0/−3 °C) and 7.02 kbar (+0.20/−0.10 kbar; Fig. 4.25b,e).

ICSV113 shows moderate overlap between the thermobarometer intersection and observed peak assemblage at aH_2O of 0.6 between 587–627 °C and 9.0–10.7 kbar (Fig. 4.25b). The peak assemblage is best represented with plagioclase included, given the observation that plagioclase porphyroblasts overgrow the main fabric, with the peak assemblage of Grt-Bt-Ms-Pl-Qtz-Rt. Ilmenite rims on rutile are present in the thin section but cannot be reproduced in the P-T domain of interest. Growth of the rims may represent a decompression feature.

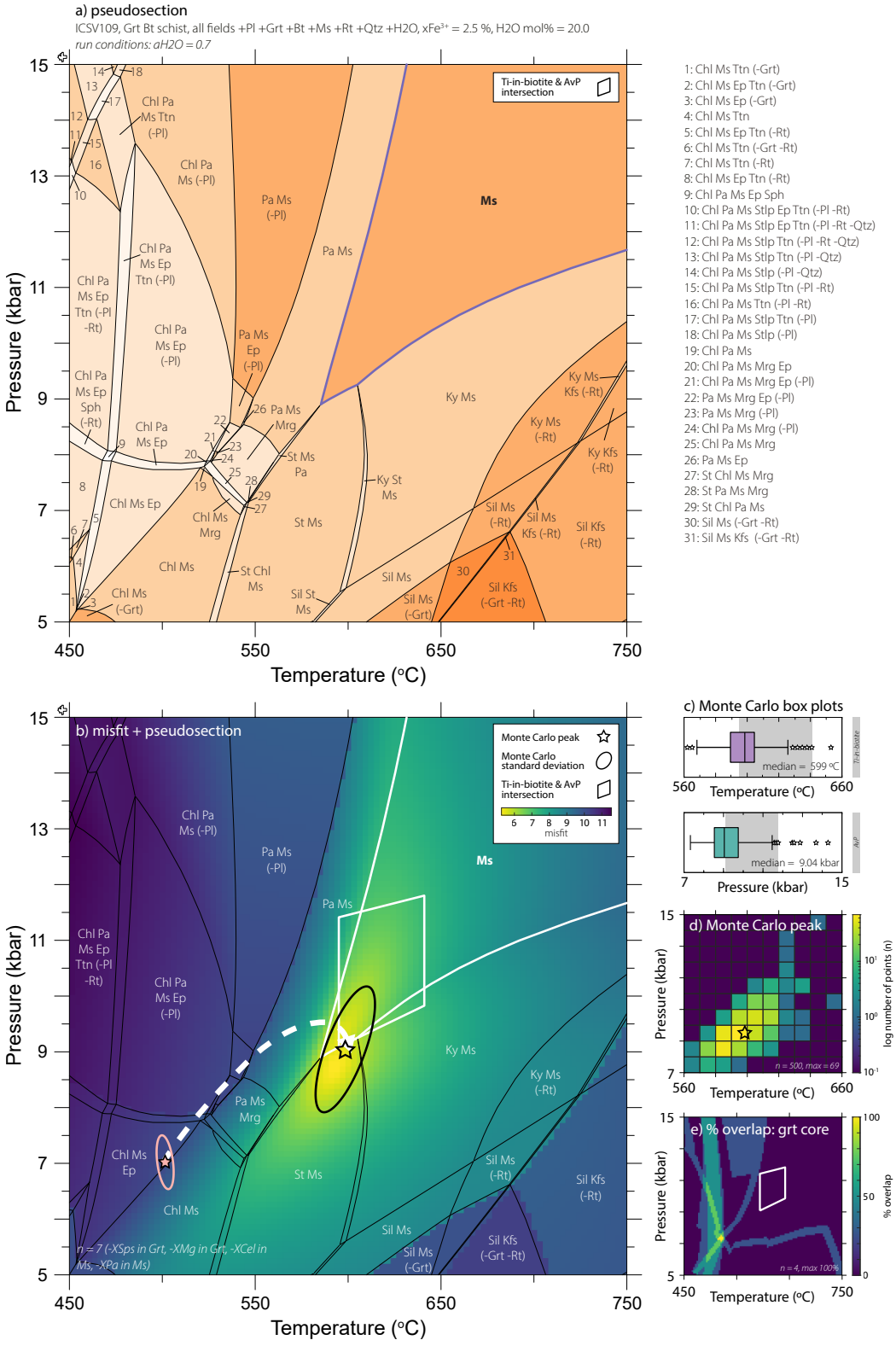


Fig. 4.25 ICSV109 a) pseudosection, b) heatmap showing the misfit of mineral chemistry variables, overlain with the bootstrapped mean best-fit result and the corresponding pseudosection, c) boxplots of bootstrapped T and P estimates with the grey bar indicating the range of the selected thermometer and AvP results, d) log-scaled 2D-histogram bin-plot of the boostrapped data with mean best-fit result marked by the star, e) % overlap of garnet core compositional isopleths.

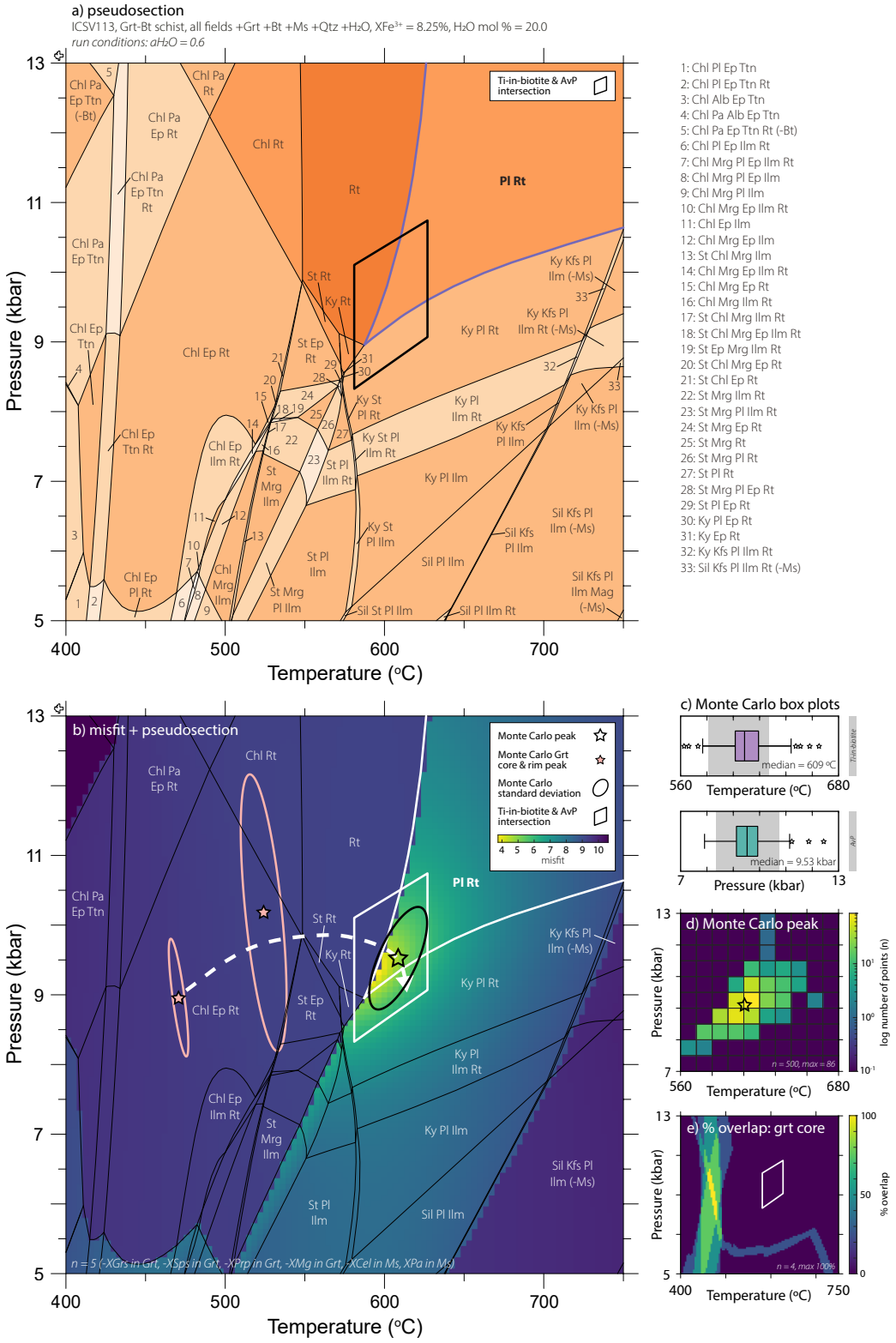


Fig. 4.26 ICSV113 a) pseudosection, b) heatmap showing the misfit of mineral chemistry variables, overlain with the bootstrapped mean best-fit result and the corresponding pseudosection, c) boxplots of bootstrapped T and P estimates with the grey bar indicating the range of the selected thermometer and AvP results, d) log-scaled 2D-histogram bin-plot of the boostrapped data with mean best-fit result marked by the star, e) % overlap of garnet core compositional isopleths.

The peak field extends to greater temperatures and pressures than documented on the phase equilibrium diagram, however, the addition of K-feldspar is inferred to mark the high-temperature boundary at 750–800 ~°C. The peak field is defined at low-temperatures by a plagioclase-absent assemblage and lower-pressures by kyanite-bearing assemblages. Mineral chemical variables ($n = 5$) produce a best-fit result at 609 °C (+12/−6 °C) and 9.53 kbar (± 0.40 kbar), with both the peak and associated uncertainty dominantly lying within the thermobarometer intersection and peak assemblage field (Fig. 4.26b–c). The range of the bootstrapped results shows a steep *P*-*T* slope, with a maximum range of uncertainty between ~7.5–13.0 kbar, with good constraint over *T* space in the range of ~560–670 °C. Garnet variables were removed as the resulting peak (524 +7/−4 °C and 10.17 +1.29/−1.46 kbar) was not in alignment with those based on other compositional variables. The garnet core compositions produce a best fit at 471 °C (± 4 °C) and 8.96 kbar (+0.40/−0.49 kbar; Fig. 4.26b,e). Garnet chemistry does not document resorbed rims contrary to the earlier growth history suggested by modelled mineral chemistry. However, poor overlap between the compositional variables alternatively implicates that garnet may have been an earlier phase that did not fully re-equilibrate at peak. Garnet does not contain rutile or epidote inclusions (chlorite unlikely to be preserved) though does contain allanite, of which epidote may have grown as a precursor.

P-*T* estimates from both staurolite zone samples are in agreement. Constraints from mineral chemistry place the peak temperature at 590–621 °C (IQR) and 587–627 °C as defined by the overlap of thermobarometer intersection and peak field. Pressure shows more variation between 8.53 to 9.93 kbar suggested by calculated compositional variables or 9.0 to 11.8 kbar based on the AvP and peak field intersection. The range of pressure results suggested by the peak field are not deemed suitable on their own given the large *P*-*T* range of the compositional field.

4.4.4.3 Kyanite zone

Pseudosection diagrams for samples from the kyanite zone located on the Sankoo–Parkachik transect (Fig. 4.6) are displayed in Figures 4.27 and 4.28.

ICSV13 and ICSV12 are topologically similar with a steeply sloping domain of kyanite stability, ~100–150 °C wide, that extends to high pressures. In ICSV12 this zone widens considerably to ~200 °C at high pressures. The range of kyanite stability in these samples is distinct from phase equilibrium diagrams from

staurolite- and garnet-zone samples where kyanite is absent at higher pressures. Plagioclase joins the stable assemblage with a moderate-steeply sloping boundary at ~550 °C in both samples for the pressure of interest. Staurolite is stable up to ~9.5 kbar in ICSV13 and to ~13.0 kbar in ICSV12 where it overlaps with chloritoid stability. Chloritoid is only stable on the pseudosection for ICSV12, where it is present from ~450–500 °C across the modelled pressure range. Garnet and biotite are present across the *P-T* range on both diagrams. Garnet is locally unstable at temperatures between ~400–450 °C in ICSV12, coincident with the chloritoid stable zone.

ICSV13 contains the peak assemblage Ky-St-Grt-Bt-Ms-Pl-Qtz-Ilm-Rt, which is best outlined on Figure 4.27 by the highlighted staurolite-absent field. An approximation of the peak field could also be represented by either 1) the staurolite-stable field or 2) the temperature-restricted kyanite- and staurolite-stable field. It has been documented that the free energy difference for staurolite vs kyanite nucleation is minimal, such that within the staurolite-bearing field kyanite may grow earlier through chlorite-consuming reactions (Pattison & Spear, 2018). However, given that nearby assemblages only contain kyanite rather than kyanite-staurolite (Fig. 2.15), the staurolite-present field is discounted as representative of the peak assemblage. The zone of co-existence of staurolite and kyanite on phase equilibrium diagrams is minimal in contrast to the common coexistence in natural Barrovian sequences. Furthermore, staurolite records metastable persistence until or into the sillimanite zone (Pattison & Spear, 2018). The kyanite-bearing field on Figure 4.27 is thus chosen to best represent the peak assemblage and for sluggish reaction dynamic to account for the metastable persistence of staurolite. The chosen peak field is delimited at high pressures by the loss of ilmenite and at high temperatures by the addition of K-feldspar. The lower bounds are defined by staurolite at low temperatures and at low pressure by the loss of rutile or addition of sillimanite. The peak field constrains temperature between ~575–700 °C, whereas pressure is poorly constrained owing to the dependence on the Ti-oxide phases to constrain the phase boundaries. A large area of overlap at $a\mathrm{H_2O}$ of 0.5 between the thermobarometer intersection and peak field is observed between 569–614 °C and 8.20–10.5 kbar. The mineral chemical variables (excluding X_{Cel} in Ms and X_{Pa} in Ms) yield a best-fit median result at 582 $+9/-6$ °C and 9.61 $+0.16/-0.24$ kbar (Fig. 4.27b–d). The peak of this result lies within the peak assemblage field and the thermobarometer intersection. The 1 SD of this result lies entirely within the thermobarometer intersection and dominantly within the peak assemblage field. These features show excellent agreement between

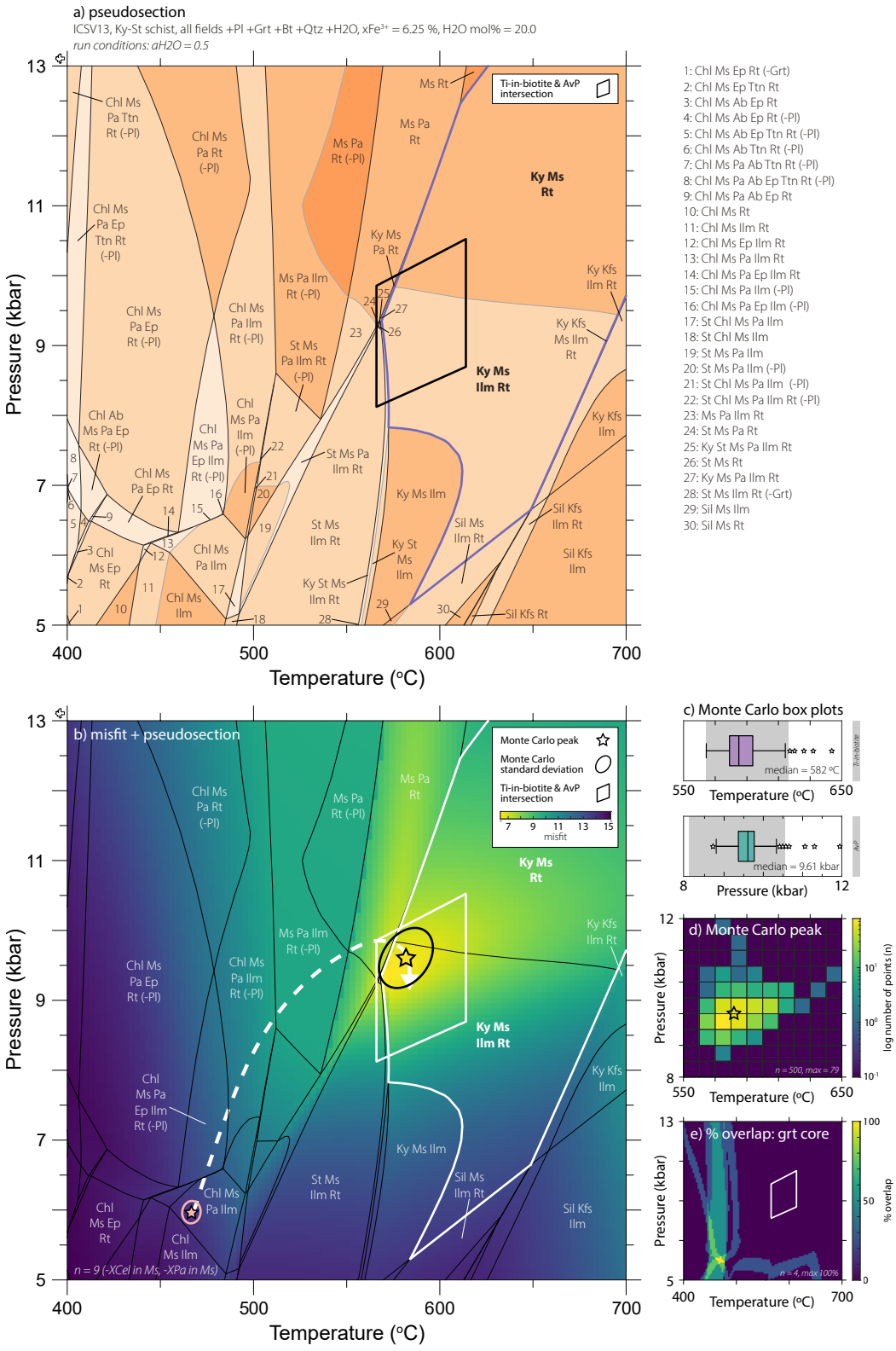


Fig. 4.27 ICSV13 a) pseudosection, b) heatmap showing the misfit of mineral chemistry variables, overlain with the bootstrapped mean best-fit result and the corresponding pseudosection, c) boxplots of bootstrapped T and P estimates with the grey bar indicating the range of the selected thermometer and AvP results, d) log-scaled 2D-histogram bin-plot of the boostrapped data with mean best-fit result marked by the star, e) % overlap of garnet core compositional isopleths.

the independent AvP result and the dependent mineral chemistry peak and pseudosection (Fig. 4.27b–c). Uncertainty on the best fit shows good constraint over T and P space with a rounded shape suggesting a well distributed angle of intersection for the selected mineral compositional variables, constraining the results over a narrow temperature range (~100 °C) and moderate pressure range (~3.5 kbar; Fig. 4.27d). Garnet core compositional isopleths intersect to produce a tight region of overlap, producing a best-fit result of 467 °C (± 3 °C) and 5.97 kbar (± 0.08 kbar; Fig. 4.27b,e).

At $a\mathrm{H_2O} = 0.5$, overlap between the peak assemblage field and thermobarometer intersection in sample ICSV12 occurs over 600–646 °C and 8.59–11.0 kbar (upper boundary constraint is a Ti-oxide phase stability change). The assemblage field, representing the assemblage Ky-Grt-St-Bt-Ms-Pl-Qtz-Ilm-Rt, is again chosen with a staurolite-absent field for the reasons suggested above. The boundaries are defined at high pressures by the absence of biotite, and at low pressure by a change in stability of Ti-oxide phases. At higher temperatures, K-feldspar becomes stable, and staurolite and/or paragonite are stable at lower temperatures. The mineral chemical variables produce a best-fit result at 633 $+14/-11$ °C and 9.35 $+0.40/-0.30$ kbar, which overlaps with both the peak field and thermobarometer intersection. The 1 SD uncertainty lies outside the thermobarometer intersection at higher temperatures and lower pressures (Fig. 4.28b, c) and shows a rounded uncertainty envelope resulting from the larger number of available chemical variables ($n = 8$) and presence of both shallowly and steeply sloping contours. There is more variation in pressure between ~7.5–11.0 kbar in comparison to ~120 °C of variation in the peak result calculation (Fig. 4.28c, d). Garnet core compositional isopleths intersect to produce a best fit at 474 $(+4/-0)$ °C and 5.87 kbar (± 0.35 kbar; Fig. 4.28e).

Kyanite-zone samples show excellent agreement for P-T estimates for samples from the Sankoo–Parkachik transect. Constraints from mineral chemistry place the peak temperature at 576–647 °C (IQR) and 569–646 °C as suggested by the thermobarometer intersection and peak field. Pressure conditions show more variation between 9.05 to 9.77 kbar suggested by calculated compositional variables (IQR) or 8.2 to 11.0 kbar suggested by the overlap of AvP and peak field intersection.

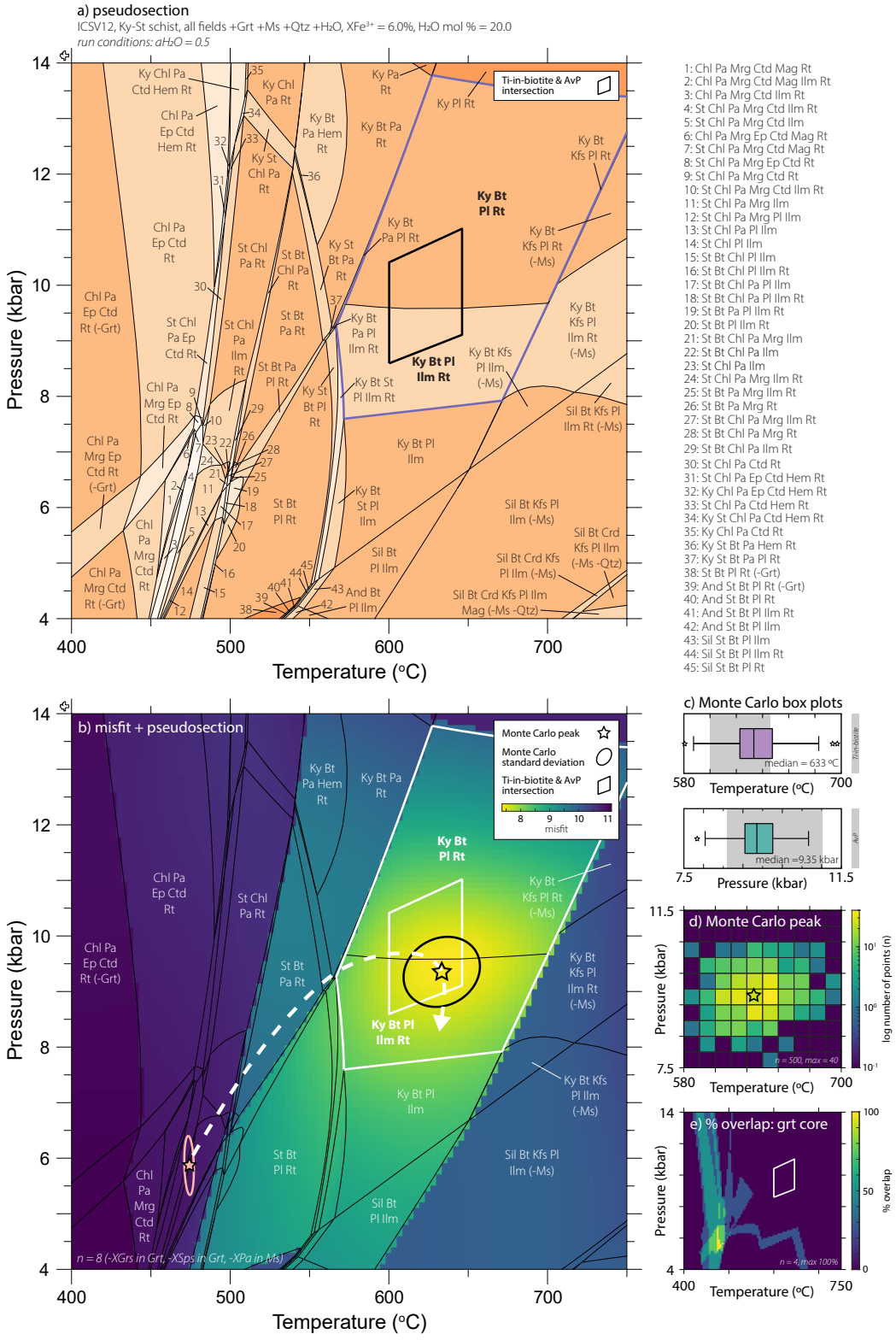


Fig. 4.28 ICSV12 a) pseudosection, b) heatmap showing the misfit of mineral chemistry variables, overlain with the bootstrapped mean best-fit result and the corresponding pseudosection, c) boxplots of bootstrapped T and P estimates with the grey bar indicating the range of the selected thermometer and AvP results, d) log-scaled 2D-histogram bin-plot of the boostrapped data with mean best-fit result marked by the star, e) % overlap of garnet core compositional isopleths.

4.4.4.4 Sillimanite zone

Pseudosection diagrams for samples from the sillimanite zone located on the Parkachik–Rangdum transect (Fig. 4.6) are displayed in Figures 4.29 and 4.30.

ICSV91 is constrained by few phase boundaries over a large range of pressures and moderate range of temperatures, whereas ICSV81 shows considerable variation over a similar P-T range due to a number of high-variance assemblages as defined through margarite and varying Ti-oxides. Despite the higher pressures modelled for ICSV91, where kyanite and/or staurolite would normally be absent in other modelled samples from the pelitic sequence (Figs. 4.23–4.26), kyanite is stable throughout most of the diagram, and staurolite is stable until at least 10.0 kbar. In comparison, in ICSV81 assemblages above 9.0 kbar are kyanite absent. The other key differences include: the presence of chlorite and epidote in ICSV81 (absent in ICSV91), and the slope of the K-feldspar-in boundary which is shallower in ICSV81. Garnet, biotite, plagioclase and quartz are present throughout most of the diagram except where excluded in relevant areas (e.g., muscovite in K-feldspar-stable assemblages, and plagioclase in paragonite-bearing assemblages). Garnet also becomes unstable at higher pressures in ICSV91 (below ~10.0–7.0 kbar) than in ICSV81 (below ~7.0–4.0 kbar).

ICSV91 has a large peak assemblage field spanning more than ~10.0 kbar and ~100–150 °C, representing the observed assemblage (Ky-Grt-Bt-Ms-Pl-Qtz-Rt; Fig. 4.29a). Fine fibrolitic sillimanite was observed in hand-specimen and is observed in thin-section in neighbouring samples. Ilmenite rims are locally present on rutile grains or within the garnet corona, these are interpreted as a decompression feature. The field is delimited at lower temperatures by paragonite stability, at higher temperatures by K-feldspar-in and at lower pressures by garnet-absent assemblages. The thermobarometer intersection overlaps entirely within the delimited stability field and encompasses a range of 634–680 °C and 11.33–13.93 kbar (Fig. 4.29a). The selected mineral chemical variables produce a best fit at 665 °C (+20/−18 °C) and 12.15 kbar (+2.22/−2.53 kbar) with the peak lying within both the thermobarometer intersection and peak assemblage field Fig. 4.29b, c). The result produces a large 1 SD (Fig. 4.29b) owing to the few variables used ($n = 4$). The bootstrapped results display significant variation over the modelled P range and ~575–750 °C (Fig. 4.29d). Garnet variables were not included in the peak as the peak of rim compositions produce a best-fit result of 586 °C (± 5 °C) and 10.54 kbar (+0.15/−0.30 kbar; Fig. 4.29b,e). However, it should be emphasised that garnet rims are commonly resorbed and broken

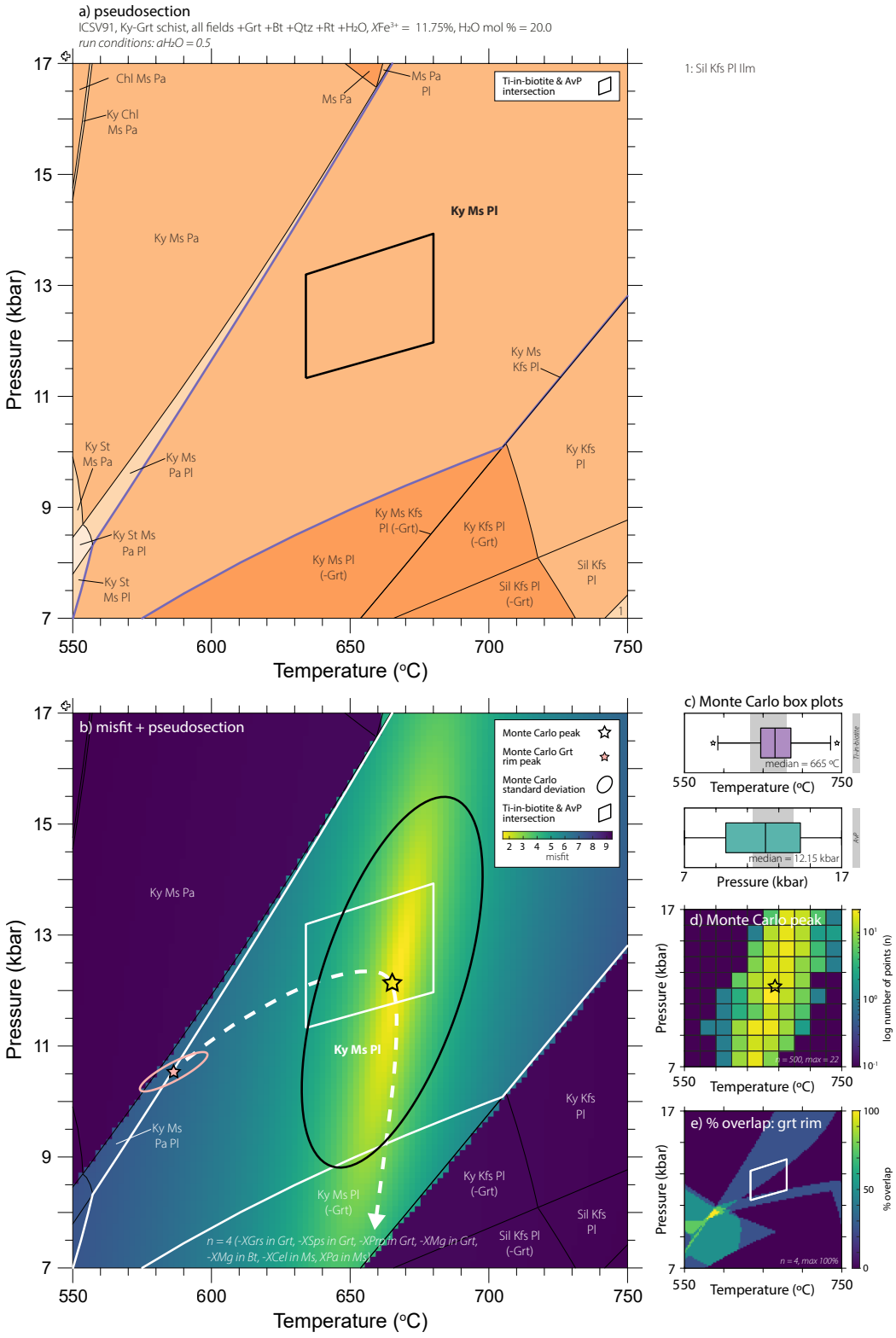


Fig. 4.29 ICSV91 a) pseudosection, b) heatmap showing the misfit of mineral chemistry variables, overlain with the bootstrapped mean best-fit result and the corresponding pseudosection, c) boxplots of bootstrapped T and P estimates with the grey bar indicating the range of the selected thermometer and AvP results, d) log-scaled 2D-histogram bin-plot of the boostrapped data with mean best-fit result marked by the star, e) % overlap of garnet core compositional isopleths.

down to mica-plagioclase-kyanite. The implication of this is that a "true" rim composition likely exists in *P-T* space between the best fit of the garnet-rim compositions and the best fit of the multiphase assemblage.

ICSV81 has a peak field matching the observed assemblage Grt-Bt-Ms-Pl-Qtz-Rt (Fig. 4.30b). Kyanite growth is associated with resorption of garnet rims. Decompression features such as ilmenite growth within coronas around garnet localised ilmenite rims on matrix rutile, and precipitation of fibrolitic sillimanite on biotite, are reproduced in the modelled assemblage. The peak field spans ~580–700+ °C and ~8.5–14.0+ kbar. The field is delimited at lower temperatures by the presence of epidote and paragonite, and at lower pressures by the presence of kyanite and/or staurolite. The thermobarometer intersection shows overlap of the peak field between 9.1–11.4 kbar and 612–660 °C. The mineral chemical variables yield a best fit at 639 +14/−18 °C and 9.96 +0.61/−0.71 kbar with the calculated peak lying both within the peak field, and thermobarometer intersection (Fig. 4.30b, c). Bootstrapped results vary over ~540–700 °C and a wide pressure range of ~4.0–14.0 kbar. Garnet variables were not included in the peak as rim compositions produce a best-fit result of 559 °C (± 6 °C) and 7.94 kbar (+0.40/−0.30 kbar; Fig. 4.30e). Garnet mode decreases between the calculated garnet rim conditions and the peak of matrix phases. Together with the prominent corona texture suggest garnet rim compositions are also not coincident with thermal peak. A "true" rim composition likely exists in *P-T* space between the garnet peak and matrix assemblage peak.

Sillimanite-zone samples show peak temperature from mineral chemistry constraints constraints 621–685 °C (IQR), and 612–680 °C as suggested by the thermobarometer intersection and peak field. Pressure conditions show large range, 9.25 to 14.37 kbar suggested by calculated compositional variables (IQR) or 9.1 to 13.93 kbar suggested by the overlap of AvP and peak field intersection.

4.4.4.5 Sillimanite+K-feldspar zone

Samples from the sillimanite+K-feldspar zone are located in Lalung Valley, outside the main mapped region, these occur ~20 km south of the marker for ICSV86 (Fig. 4.6). Pseudosections are displayed in Figures 4.31 and 4.32. The MATLAB routine for these samples differed in that following *in-situ* partial melting, it is assumed that the system has lost melt, therefore the current *P-T* conditions reflect the bulk and mineral composition at the end of melting. This can be distinguished as a point near or on the solidus curve. As such, distinguishing a *P-T* point

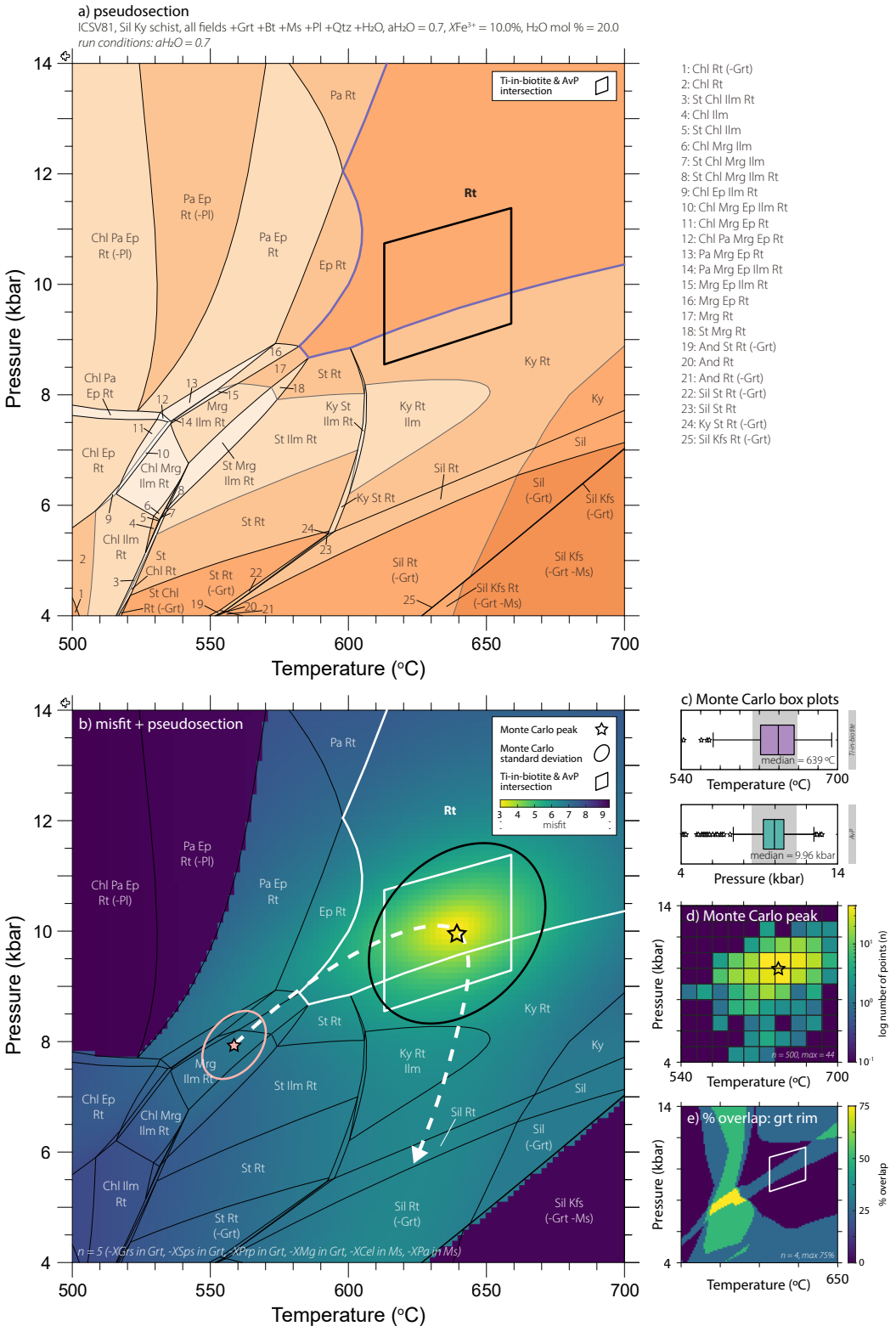


Fig. 4.30 ICSV81 a) pseudosection, b) heatmap showing the misfit of mineral chemistry variables, overlain with the bootstrapped mean best-fit result and the corresponding pseudosection, c) boxplots of bootstrapped T and P estimates with the grey bar indicating the range of the selected thermometer and AvP results, d) log-scaled 2D-histogram bin-plot of the boostrapped data with mean best-fit result marked by the star, e) % overlap of garnet core compositional isopleths.

within the suprasolidus or sub-solidus would not reflect the final composition. Instead overlap of the mineral chemical variables and modal abundances define the point of equilibration along the solidus curve. Discussion of pseudosections does not include sub-solidus conditions.

ICSV145 and ICSV150 record a similar topology across the modelled *P-T* range (Figs. 4.31a and 4.32a), ICSV150 records more numerous phase assemblage changes coincident with the larger modelled *T* and *P* range (+50 °C +2 kbar). Both sections display a positively sloping solidus curve that intersects free hydrous phases at ~670–675 °C and ~4.5 kbar. Owing to the similar modal proportion of biotite in these samples, it is reflected in similar molar % of H_2O and similar solidus curves. Sillimanite is stable across most *P-T* ranges but becomes absent at low pressures, whereas cordierite becomes stable at low pressures. Prominent differences across the pseudosections largely results from stability of garnet, in ICSV145 garnet occurs as a stable phase at temperatures greater than ~710 °C and broad range of pressures, whereas in ICSV150 garnet occurs at most *P-T* conditions greater than ~3.0 kbar. Plagioclase is stable at all *P-T* conditions above the solidus in ICSV145 but become absent at temperatures in excess of ~740 °C in ICSV150. Biotite is similarly absent at higher temperatures in this sample coincident with the greater modelled temperature range.

ICSV145 shows few phase changes over the modelled temperature range. The peak assemblage field is best defined by the point on the solidus curve containing muscovite. This ranges from ~680–710 °C and ~5.0–6.5 kbar. This is delimited above the solidus by the absence of muscovite, and at lower and higher pressures by rutile and garnet-present assemblages, respectively. The *P-T* result may therefore be approximated at the percentage overlap defined over the solidus curve at ~700 °C and ~6.0 kbar (Fig. 4.31b). This assemblage is in agreement with the muscovite-rich domains present throughout the thin section. Muscovite is preserved in the rock in biotite rich domains, reflecting the rock likely crossed over at the first muscovite-melting curve and did not progress to temperatures significantly in excess of the solidus. Muscovite is associated with K-feldspar, likely developing as a late back-reaction with aqueous fluid or residual melt (e.g., Waters, 2019). Moving from higher *P-T* to lower *P-T* conditions, late growth of myrmekitic plagioclase in replacement of K-feldspar rims is reflected by increasing plagioclase volume % towards the solidus, whereas K-feldspar volume % decreases (Fig. 4.31c). Sillimanite volumes remain broadly consistent and biotite shows a slight increase to the solidus intersection.

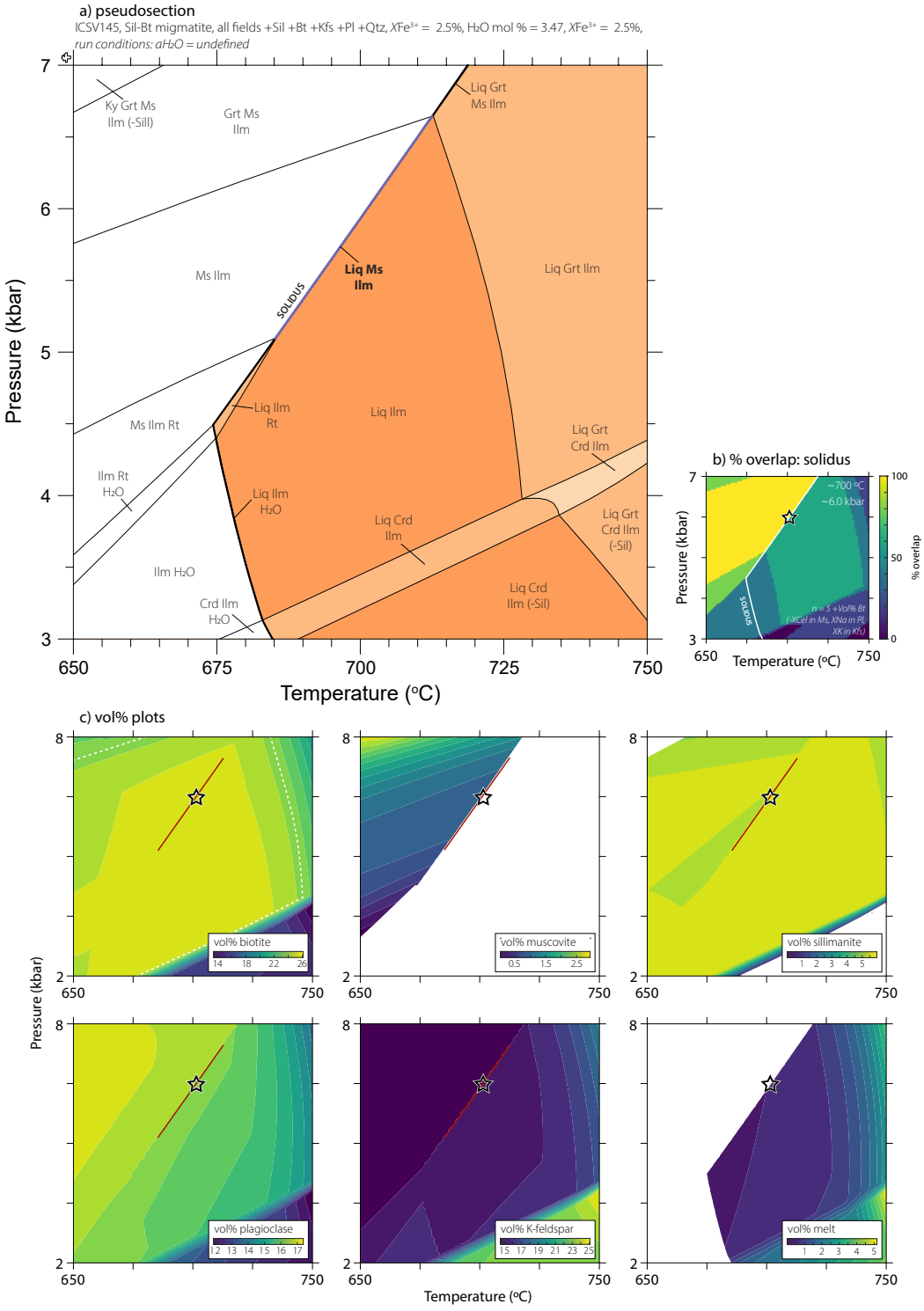


Fig. 4.31 ICSV145 a) pseudosection, b) % overlap of mineral chemical variables for the solidus and c) volume % plots for dominant mineral phases.

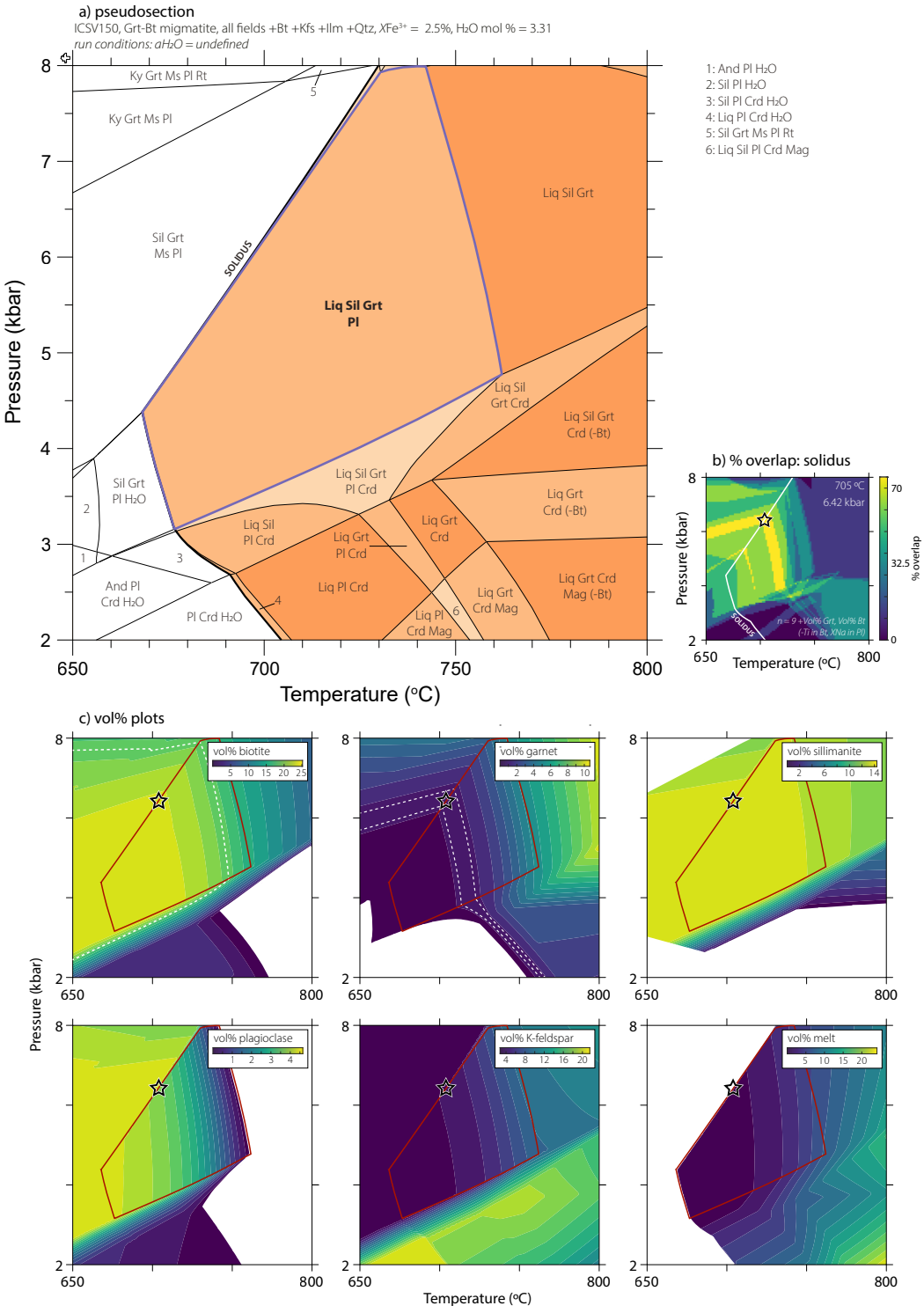


Fig. 4.32 ICSV150 a) pseudosection, b) % overlap of mineral chemical variables for the solidus and c) volume % plots for dominant mineral phases.

ICSV150 records the observed assemblage as Qtz-Kfs-Pl-Bt-Sil-Grt-Ilm (+Liq) as highlighted over the *P-T* range of ~670–760 °C and ~3.0–8.0 kbar. This is delimited at higher temperatures by plagioclase-absent assemblages and at lower pressures by cordierite-present assemblages. An equilibrated assemblage at the solidus can be estimated at ~705 °C and ~6.4 kbar defined by the overlap of 9 variables (Fig. 4.32b). Volume % from garnet and biotite were added to better constrain the *P-T* conditions because the relative proportions of garnet, K-feldspar, and fluid reduce concomitant with an increase in biotite and sillimanite, reflecting Equation 4.28. Moving from higher *P-T* conditions to lower *P-T* conditions towards the solidus intersection these modal changes are observed over the volume % plots (Fig. 4.32c). Plagioclase volume % also increases, likely reflecting myrmekitic growth in replacement of K-feldspar margins.

Broadly similar *P-T* conditions of final melt-loss occurs is constrained in both samples from the sillimanite+K-feldspar zone to occur at ~700 °C and 6.0–6.5 kbar.

4.4.5 Metabasite

Figures 4.33–4.39 show the results of pseudosection modelling and best-fit calculation for the studied metabasic sample suite. *P-T* pseudosections are overlain by the thermobarometer intersection defined by AvP and hornblende-plagioclase exchange thermometer using the calibration of Holland & Blundy (1994) with the corrections by Dale *et al.* (2000). Dashed lines are used for boundaries where the pre-requisite criteria of the thermometry or barometry values are not met. Consistent with the modelled pelites, grey phase boundaries are used for transition into or between Ti-oxides. Within the metabasites, it must be noted the modelled Ti-oxides rarely match the observed oxides inferred to represent peak. Part of this appears to relate to the broad overstability of titanite across phase boundaries at moderate to high grades. As such, in scenarios where the Ti-oxide phase is not produced within the approximate range of the thermobarometer result, a conservative approach is used and a peak assemblage field is defined irrelevant of the Ti-oxide phase. Where it is produced the assemblage field may be constrained in all field where the pre-requisite assemblage is met and contain the stable Ti-oxide phase (as well as other possible Ti-oxide phases). Furthermore, the presence or absence of clinopyroxene is not deemed relevant to phase boundaries in clinopyroxene-absent assemblages (all samples except ICSV144) owing to its well-documented overstability in modelled metabasic systems (Forshaw *et al.*,

2019). Phases on assemblage diagrams that are marked in red within square brackets are those that were not reproduced within the selected peak field and are discussed where relevant for each sample. Absence of Fe-Ti oxides is not indicated.

4.4.5.1 Hornblende zone

Pseudosection diagrams for samples ICSV50 and ICSV2 from the hornblende zone located south of Sankoo along the Sankoo–Parkachik transect (Fig. 4.6) are displayed in Figures 4.33 and 4.34. Samples are located less than 5 km from each other along strike.

Pseudosections for ICSV50 and ICSV2 show vastly different stability of actinolite and hornblende within the given P-T ranges. Hornblende is stable across most of the P-T range for ICSV50 except at temperatures lower than 470–540 °C where actinolite and barroisite are stable at low and high pressures, respectively. In comparison actinolite is the dominantly stable amphibole for ICSV2 across the modelled P-T range except at ~480–560 °C and ~5.0–9.5 kbar where hornblende is locally stabilised along with actinolite. ICSV50 uses an Mn-bearing database whereas ICSV2 uses an Mn-absent database owing to the presence of strongly zoned garnet in ICSV50 which is not stabilised at pressures below ~12.0 kbar in an Mn-absent database. Switching database is observed to have minimal shift on phase boundaries. The result is that garnet is stabilised across the whole P-T range in ICSV50 whereas it is only observed at conditions in excess of ~520 °C and ~9.5 kbar in ICSV2. Phase stability of chlorite is similar and extends to lower pressures in ICSV50 and slightly higher temperatures. Plagioclase is stable over a similar range of temperatures in both samples though is largely restricted to lower pressures in ICSV2 ($\sim<$ 7.5 kbar). The peristerite gap and presence of albite occurs at ~450 °C and ~9.0 kbar in ICSV50. The absence of Na-rich feldspar within the best estimate of the peak assemblage field is problematic in both samples.

ICSV50 contains the interpreted peak assemblage Hbl-Act-Bt-Chl-Ab-Ep-Qtz-Ttn which is best represented by the albite- and actinolite-absent field highlighted. Thermometer constraints from multiphase thermometry constrain ICSV50, ICSV2, and ICSV38 (all lying within an along strike distance of 2.5 km) to record temperatures of equilibration from 517–587 °C (mean thermometry values). The range of calculated temperatures reflect the largest spread of thermometry data, which in these samples this is defined by the the Ti-in-biotite thermometry

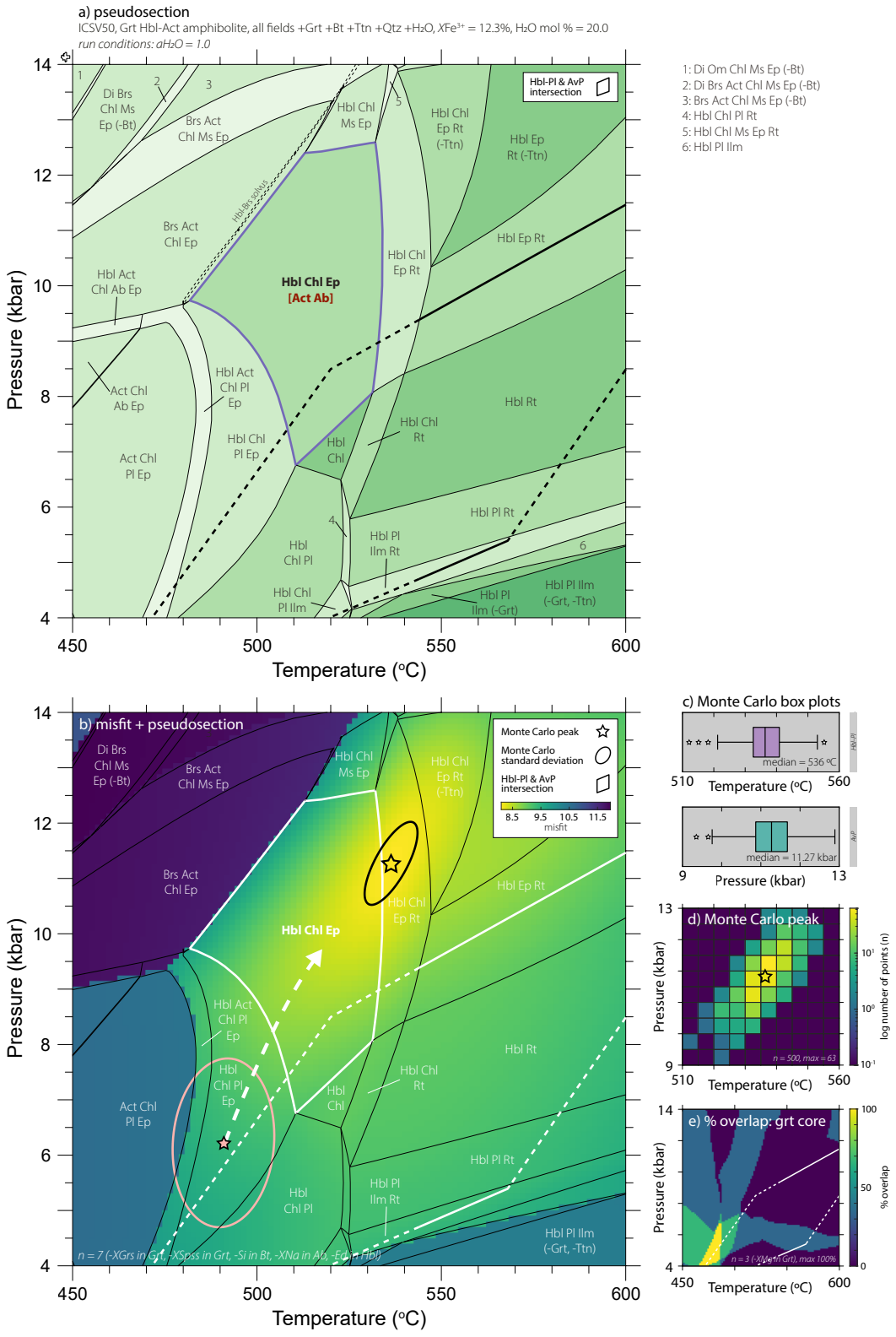


Fig. 4.33 ICSV50 a) pseudosection, b) heatmap showing the misfit of mineral chemistry variables, overlain with the bootstrapped mean best-fit result and the corresponding pseudosection, c) boxplots of bootstrapped T and P estimates with the grey bar indicating the range of the selected thermometer and AvP results, d) log-scaled 2D-histogram bin-plot of the boostrapped data with mean best-fit result marked by the star, e) % overlap of garnet core compositional isopleths.

results. A conservative and thereby large range of thermometry values was used to help infer the possible metastability of minerals within the primary assemblage. Albite poikiloblasts have a composition of X_{Na} 0.99 and are sheared by the main fabric. Based on the narrow field of stability of modelled albite compositions at temperatures of ~450 °C (which are distinctly lower than the range of possible thermometer values), it is likely that either a) albite is metastable, or b) the peristerite gap of the FSP4TR models (Holland *et al.*, 2022) do not match natural data. Actinolite is identified through field and petrographic observations. Only a limited number of amphibole analyses produced stoichiometrically appropriate results (n = 3), and give compositions of hornblende. However, petrographic criteria are also deemed robust, and are consistent with compositional analyses of actinolite found within ICSV2 from the same structural horizon. It is inferred that actinolite is present in the assemblage, though may be metastable as is well documented across the greenschist–amphibolite facies transition (Starr & Pattison, 2019). None of those temperature constraints overlap with an actinolite stable field until pressures of ~13.0 kbar owing to the positive slope of the actinolite-out boundary. It is therefore suggested that actinolite is metastable in this sample. Owing to the uncertainty over the stability range of actinolite and albite, the peak assemblage field should be treated with appropriate uncertainty.

The thermobarometer intersection for ICSV50 relies on a hornblende-plagioclase exchange result using albite rather than a more Ca-rich plagioclase, and thus should be treated with caution. The AvP result shows a significant positive slope over the calculated temperature range, and these pressures are significantly lower than nearby samples as discussed previously. It should be noted that AvP passes the χ^2 test at temperatures between 550–590 °C. Therefore there is no overlap between the thermobaromter intersection and peak assemblage field. The peak assemblage field is delimited on the low-temperature side by by plagioclase-present or epidote-absent assemblages at lower pressures and by muscovite-present or Na-rich Ca-amphibole assemblages at higher pressures. The high-temperature side is delimited by the presence of rutile. The selected mineral chemical variables produce a best fit at 536 °C (+5/−4) and 11.27 kbar (± 0.40 kbar) with the compositionally defined peak lying within the thermometry and barometry results when defined indvidually (Fig. 4.33b, c). The SD of the best fit overlaps with the peak field (Fig. 4.33b). Select garnet variables were excluded: The range of X_{Grs} was broadly stable towards the low-pressure boundary of the phase diagram and X_{Sps} at pressures at the upper boundary of the phase diagram. Other variables did overlap well with clustered results from other variables (X_{Na} in Ab), did not

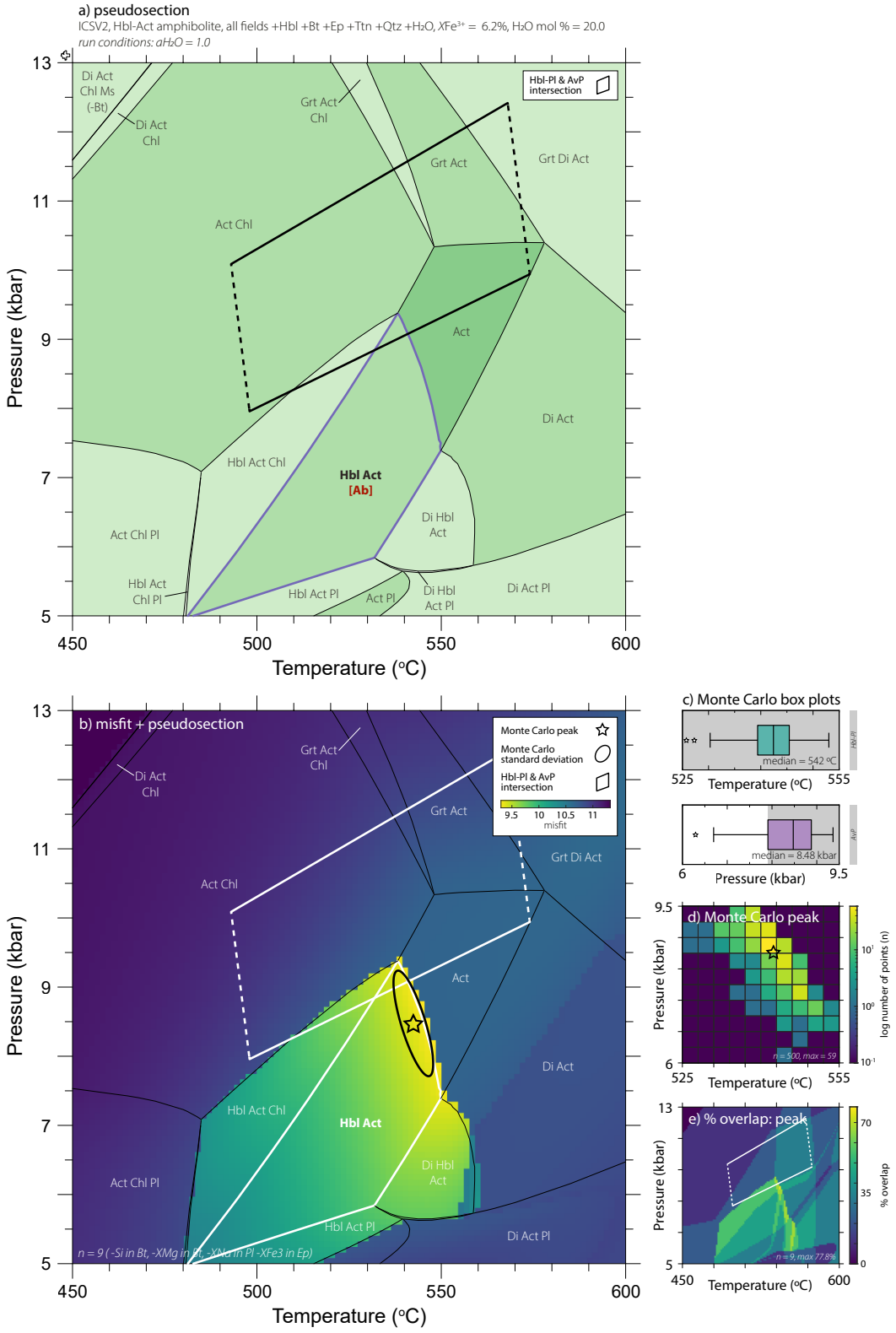


Fig. 4.34 ICSV2 a) pseudosection, b) heatmap showing the misfit of mineral chemistry variables, overlain with the bootstrapped mean best-fit result and the corresponding pseudosection, c) boxplots of bootstrapped T and P estimates with the grey bar indicating the range of the selected thermometer and AvP results, d) log-scaled 2D-histogram bin-plot of the boostrapped data with mean best-fit result marked by the star, e) % overlap of observed mineral compositional variables.

plot within the *P*-*T* range (Si in biotite) or produced significant skew of the *P* range (Ed in Hornblende). Garnet core compositional data yielded a best-fit result at 491 °C (+6/−8 °C) and 6.22 kbar (± 0.81 kbar; Fig. 4.33b,e).

ICSV2 contains the peak assemblage of Act-Hbl-Ep-Bt-Ab-Qtz-Ttn which is defined by the highlighted field spanning ~480–550 °C and ~5.0–9.5 kbar. The peak field is delimited at low temperatures by chlorite-bearing assemblages and at high temperatures by hornblende-absent or diopside-present assemblages at a low pressures by a plagioclase-present assemblage. Similar to ICSV50, albite must be inferred as metastable or the result of a peristerite gap that doesn't match natural data. The peak assemblage field locally overlaps the AvP results over a limited range of 532–541 °C and 8.84–9.08 kbar. The selected mineral chemical variables (n = 9) produce a best fit at 542 °C (± 3 °C) and 8.48 kbar (+0.40/−0.57) °C (Fig. 4.34c). The best-fit result lies within the temperature range of the AvP calculation, which passes the χ^2 test across the range displayed. The AvP uncertainty range and *P* best-fit result show minor overlap (Fig. 4.34c). The SD of this result (Fig. 4.34b) and range of the resampled data (Fig. 4.34d) provide narrow temperature constraints and larger *P* constraints, with the result sitting at the hornblende-out boundary on the high-temperature side. This implies other chemical variables may record higher temperatures (Fig. 4.34e) but are forced to the boundary by the modelled boundary of hornblende.

Hornblende-zone samples show good agreement for *T* estimates but very poor agreement for *P* estimates. Constraints from mineral chemistry place the peak temperature at 532–545 °C (IQR, both samples) and 532–541 °C (only ICSV2) as suggested by the overlap of thermobarometer intersection and peak assemblage field. Peak pressure is calculated for a best-fit between 7.91–11.67 (IQR, both samples) and overlap of AvP and peak assemblage field between 8.84–9.08 kbar (only ICSV2). ICSV50 shows a peak assemblage field with the range of 482–534 °C and 6.78–12.61 kbar and AvP statistically significant result at 4.66–9.0 kbar over the range of 550-590 °C.

4.4.5.2 Oligoclase zone

Sample ICSV92 is the only modelled sample from the oligoclase zone, and is located along the Sankoo–Parkachik transect just south of the oligoclase isograd (Fig. 4.6).

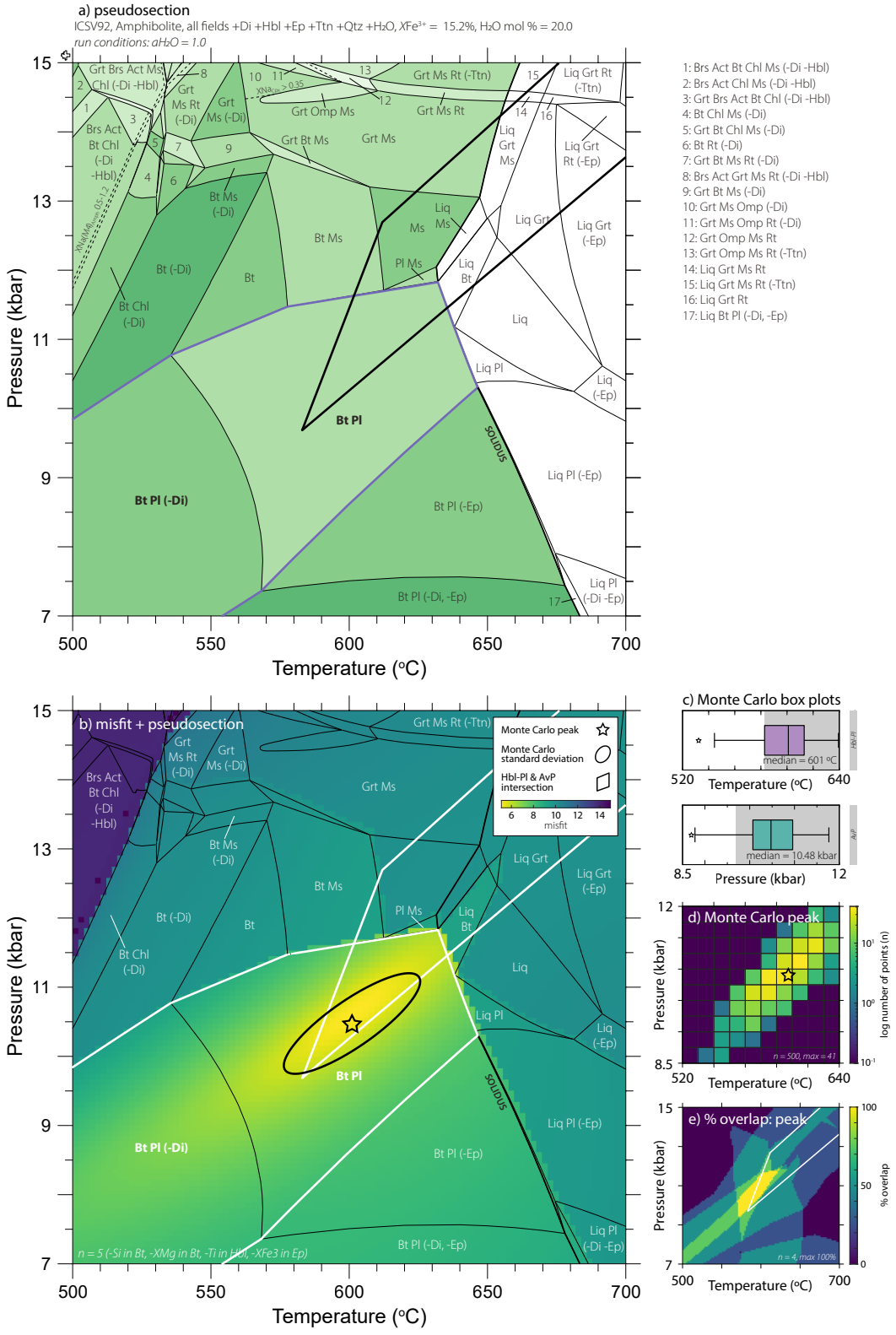


Fig. 4.35 ICSV92 a) pseudosection, b) heatmap showing the misfit of mineral chemistry variables, overlain with the bootstrapped mean best-fit result and the corresponding pseudosection, c) boxplots of bootstrapped T and P estimates with the grey bar indicating the range of the selected thermometer and AvP results, d) log-scaled 2D-histogram bin-plot of the boostrapped data with mean best-fit result marked by the star, e) % overlap of observed mineral compositional variables.

ICSV92 contains the peak assemblage of Hbl-Pl-Qtz-Ep-Bt-Ilm-Rt which is represented by the highlighted assemblage field (excluding the relevant Ti-oxide phases; Fig. 4.35a). The boundary is marked at low pressures by epidote-absent assemblages and at high pressures by plagioclase-absent assemblages. At high temperatures the boundary is marked by the solidus. The lower T boundary of the field extends beyond the modelled P-T range. The peak assemblage field overlaps the therobarometer result at 583–636 °C and 9.69–11.83 kbar (Fig. 4.35a). The mineral chemistry variables constrain peak conditions at 601 °C (+13/−18) and 10.48 kbar (+0.49/−0.40) showing agreement with both the thermobarometer intersection and peak assemblage field (Fig. 4.35b, c). The simulations produce result over a range of ~530–640 °C and ~8.5–12.0 kbar with a strong positive slope, parallel to the slope of the AvP result. This results from the dominance of positive slope mineral variables showing shallow angles of intersection, with the exception of one variable (Ti in biotite) which provides the dominant constraint on temperature in this sample (Fig. 4.35e). The lack of any evidence of *in-situ* melting in this sample, combined with the modelled mineral chemistry and thermobarometer intersection, strongly suggests the P-T of equilibration are located in the highest-P-T range of the peak assemblage field.

The maximum range for the oligoclase zone may therefore be defined from this sample as 583–614 °C and 10.08–10.97 kbar defined from mineral chemistry, and 583–636 °C and 9.69–11.83 kbar from overlap of thermobarometer intersection and peak assemblage field.

4.4.5.3 Garnet+plagioclase zone

Samples ICSV138 and ICSV5 are located along the Sankoo–Parkachik transect, ICSV117 along Shanshin Nala transect and ICSV144 along Lalung Valley transect, south of the mapped region (Fig. 4.6). Pseudosection diagrams are displayed in Figures 4.36–4.39.

Samples ICSV138, ICSV117, and ICSV5 document higher pressure assemblages and thus may be more meaningfully compared, in contrast, ICSV144 documents lower pressure assemblage ICSV117 and ICSV5 display a broadly similar topology across a largely consistent modelled P-T range. ICSV138 appears more distinct, with minimal variation across the modelled P-T range, other than Fe-Ti-oxides and the stability of diopside. Plagioclase is only stabilised at low pressures and high temperatures with a composition of labradorite–bytownite (X_{Na} of 0.30–0.38), compositions that are inconsistent with observed oligoclase (X_{Na} of 0.79). It is

inferred that underestimation of Ca and overestimated of A-site Na in amphibole (Forshaw *et al.*, 2019) impacts the stability of Na-rich plagioclase compositions, and where plagioclase is stabilised results in overly Ca-rich compositions. Ca in garnet is similarly impacted resulting in X_{Grs} stabilised at significantly lower pressures than other garnet end-members. In ICSV117 and ICSV5 higher-variance assemblages are recorded at higher pressures with peak fields defined across low- to moderate-variance assemblages. Low pressures and temperatures are broadly defined by diopside-absent assemblages, lower temperature and higher pressures by epidote-present assemblages and higher temperatures by plagioclase-bearing assemblages. Muscovite is broadly preserved at high pressures, locally coincident with biotite-absent assemblages (e.g., ICSV5). Garnet stability is variable across the modelled samples (owing the respective presence and absence of the mineral). Hornblende is stable across the entire *P-T* range and biotite broadly stable across most *P-T* ranges.

In ICSV138 the peak assemblage field is poorly constrained across the *P-T* range owing to the lack of phase stability change for modally dominant minerals. The observed peak assemblage is Hbl-Grt-Qtz-Pl-Ilm-Bt, however, owing to the significant difference in modelled vs measured plagioclase composition, plagioclase is rejected as a constraint for this sample; and given Ti oxides absent from the observed assemblages are present in the best-estimate of the assemblage field, then fields containing the observed Ti-oxide (ilmenite) are selected. No constraints are placed on the assemblage field at low and high temperatures, extending across a range of ~200 °C. At high pressures, ilmenite is no longer stable and at low pressures the field is delimited by garnet-absent or Ca-rich plagioclase-bearing assemblages. The thermobarometer intersection mostly overlaps within the selected peak field at 600–723 °C and 9.02–11.98 kbar (Fig. 4.36a). The mineral chemical variables produce a best fit at 671 ±16 °C and 9.88 +1.70/−1.40 kbar with the peak field lying within both the thermobarometer intersection and peak field (Fig. 4.36b, c)). This result shows significant variation over a range of ~110 °C and ~5.0 kbar (Fig. 4.36d), producing a large 1 SD uncertainty ellipse. The modelled range of X_{Grs} is broadly stable towards the low-pressure boundary of the phase diagram, consistent with significant issues in the assignment of Ca ratios stemming from issues with the amphibole compositional information. X_{Mg} in Grt was removed to remove dependence of the result on garnet which dominantly suggests higher temperatures than other variables (Fig. 4.36e). Other variables did not plot within the *P-T* range of interest or did not produce sufficient overlap.

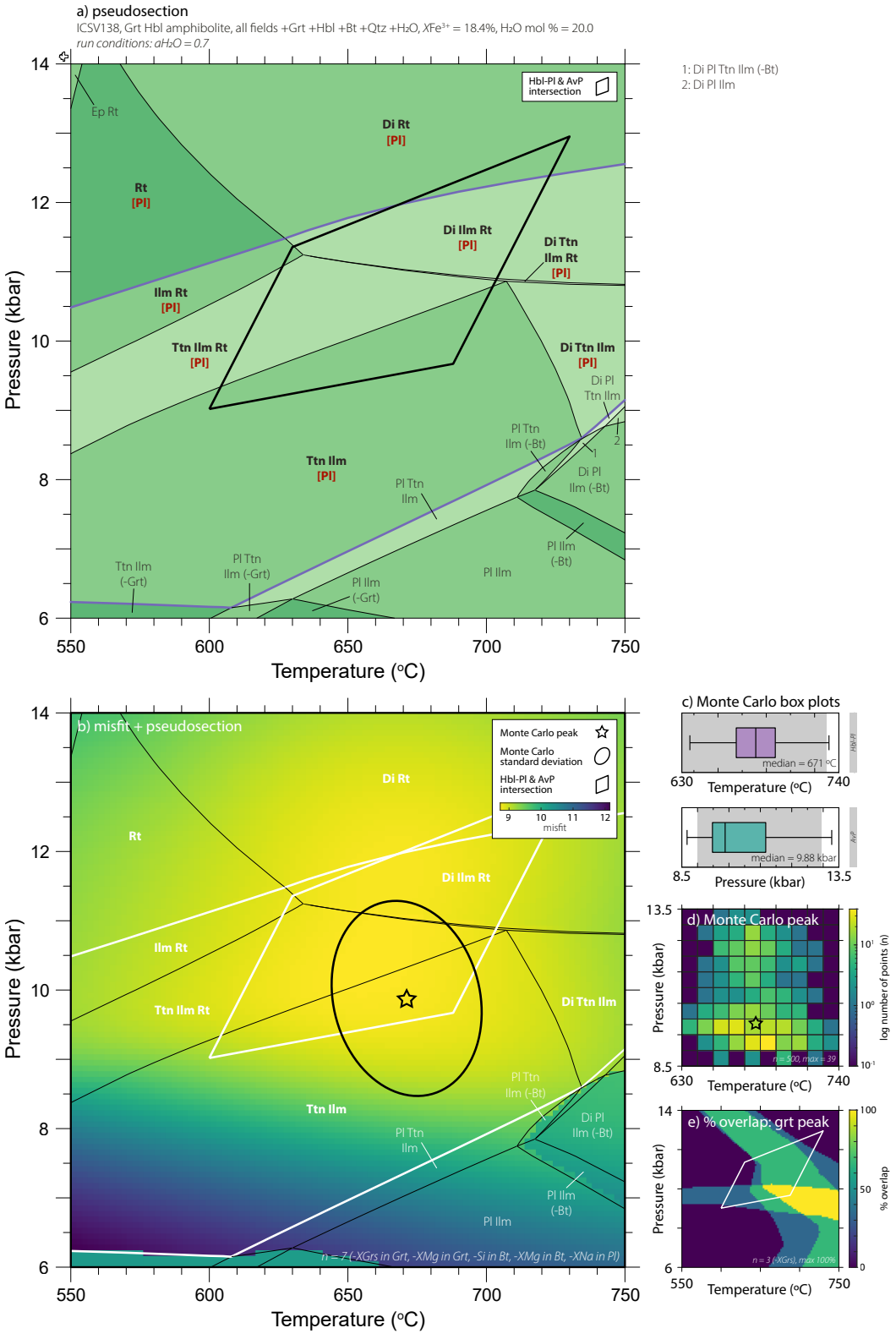


Fig. 4.36 ICSV138 a) pseudosection, b) heatmap showing the misfit of mineral chemistry variables, overlain with the bootstrapped mean best-fit result and the corresponding pseudosection, c) boxplots of bootstrapped T and P estimates with the grey bar indicating the range of the selected thermometer and AvP results, d) log-scaled 2D-histogram bin-plot of the boostrapped data with mean best-fit result marked by the star, e) % overlap of garnet rim compositional variables.

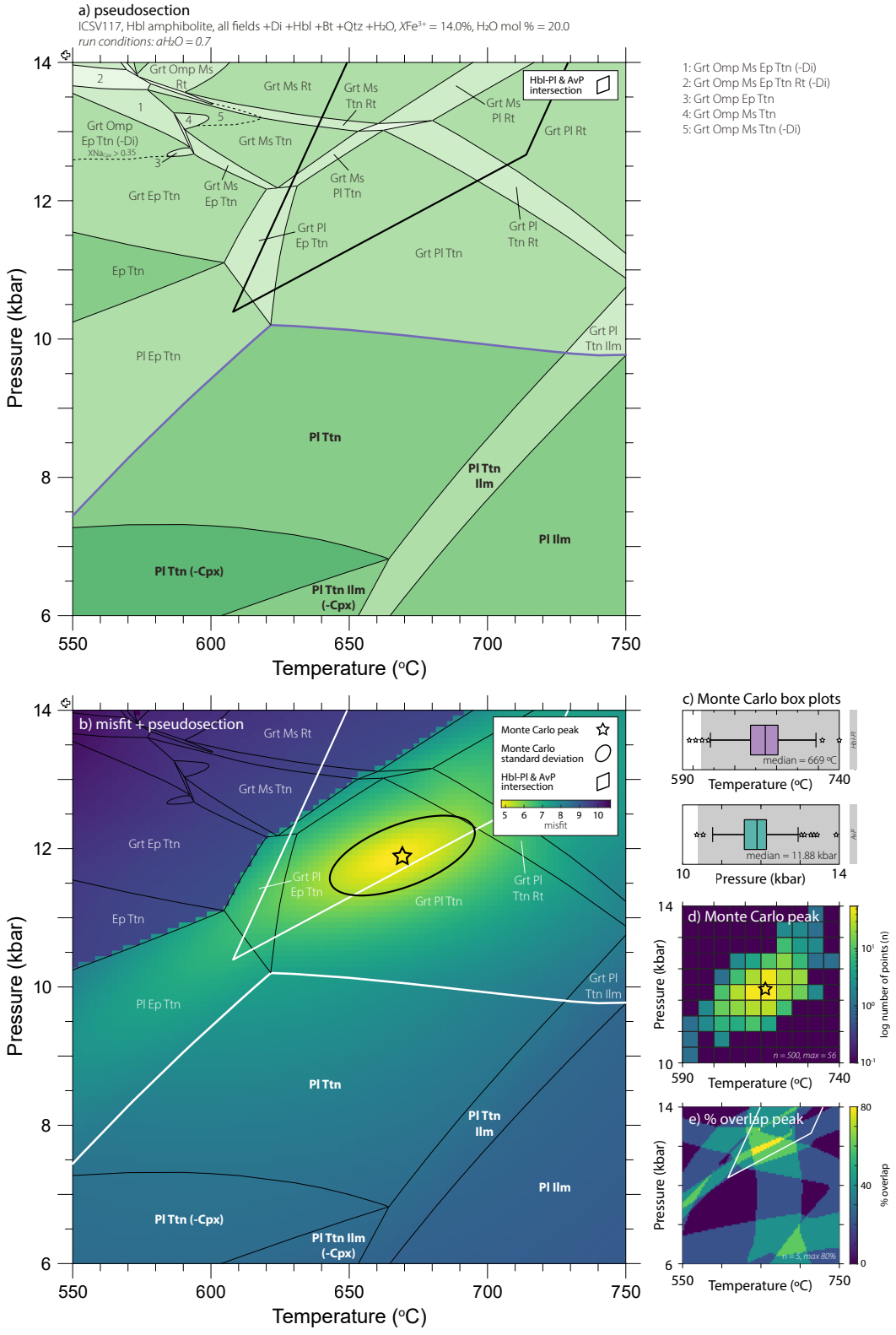


Fig. 4.37 ICSV117 a) pseudosection, b) heatmap showing the misfit of mineral chemistry variables, overlain with the bootstrapped mean best-fit result and the corresponding pseudosection, c) boxplots of bootstrapped T and P estimates with the grey bar indicating the range of the selected thermometer and AvP results, d) log-scaled 2D-histogram bin-plot of the boostrapped data with mean best-fit result marked by the star, e) % overlap of observed mineral compositional variables.

ICSV117 defines a broad zone of possible peak assemblages that extends for a greater range of temperatures than modelled (550–750 °C) and to lower pressures than modelled but up to ~10.0 kbar (Fig. 4.37a). The observed peak assemblage is Hbl-Pl-Bt-Qtz-Ilm-Ttn. Titanite growth dominantly post-dates ilmenite growth. Petrographic criteria in this sample are unclear whether titanite represents peak conditions or growth occurs during decompression from peak conditions. The relationship of Ti-oxide phases is not reproduced in a clockwise *P-T* path on the modelled diagram. The high-pressure boundary is delimited on the resulting peak assemblage field by garnet and at lower temperatures by epidote stability. The thermobarometer intersection shows no overlap with the peak assemblage field, temperatures show agreement but pressures are in excess of ~10.0 kbar for AvP results (Fig. 4.37b). The mineral chemical variables produce a best fit at 669 °C (+12/−14 °C) and 11.90 kbar (Fig. 4.37c), in agreement with the thermobarometer intersection but not for the peak assemblage field. The calculated *P-T* result shows a spread from ~590–740 °C and ~10.0–14.0 kbar (Fig. 4.37d). Despite lacking garnet in the observed assemblage, the calculated result lies within a garnet bearing field. The pressure of the result is largely defined by the amphibole compositional vectors, and Ca-dependent compositional information from plagioclase (X_{Na} plagioclase). These variables show shallowly sloping *P-T* gradients (Fig. 4.37e).

ICSV5 shows a range of possible assemblages as phase changes are broadly defined by changing stability of Fe-Ti-oxide phases across the *P-T* range (Fig. 4.38a). The observed peak assemblage is: Hbl-Pl-Grt-Qtz-Bt-Ilm-Rt. The selected field shows a temperature range from ~550-780 °C though the boundary extends to lower temperatures and pressures than modelled. Upper pressure range extends to a maximum of ~13.5 kbar. The high-pressure boundary is broadly delimited by: the presence of epidote, muscovite, or K-feldspar. The high-temperature boundary is set as the solidus. The thermobarometer intersection in encompassed within the peak assemblage field over the range of 628–741 °C and 9.33–11.23 kbar. The mineral chemical variables produce a best fit at 691 ± 15 °C and 11.09 +0.28/−0.24 kbar (Fig. 4.38c). This result may vary across a range of ~140 °C and ~2.5 kbar (Fig. 4.38d), with the SD ellipse producing a relatively narrow uncertainty range on both temperature and pressure (Fig. 4.38b). These results agree with other thermobarometric constraints (Fig. 4.38b). Consistent with other samples garnet peak results result in slightly higher temperature constraints than other variables (Fig. 4.38e).

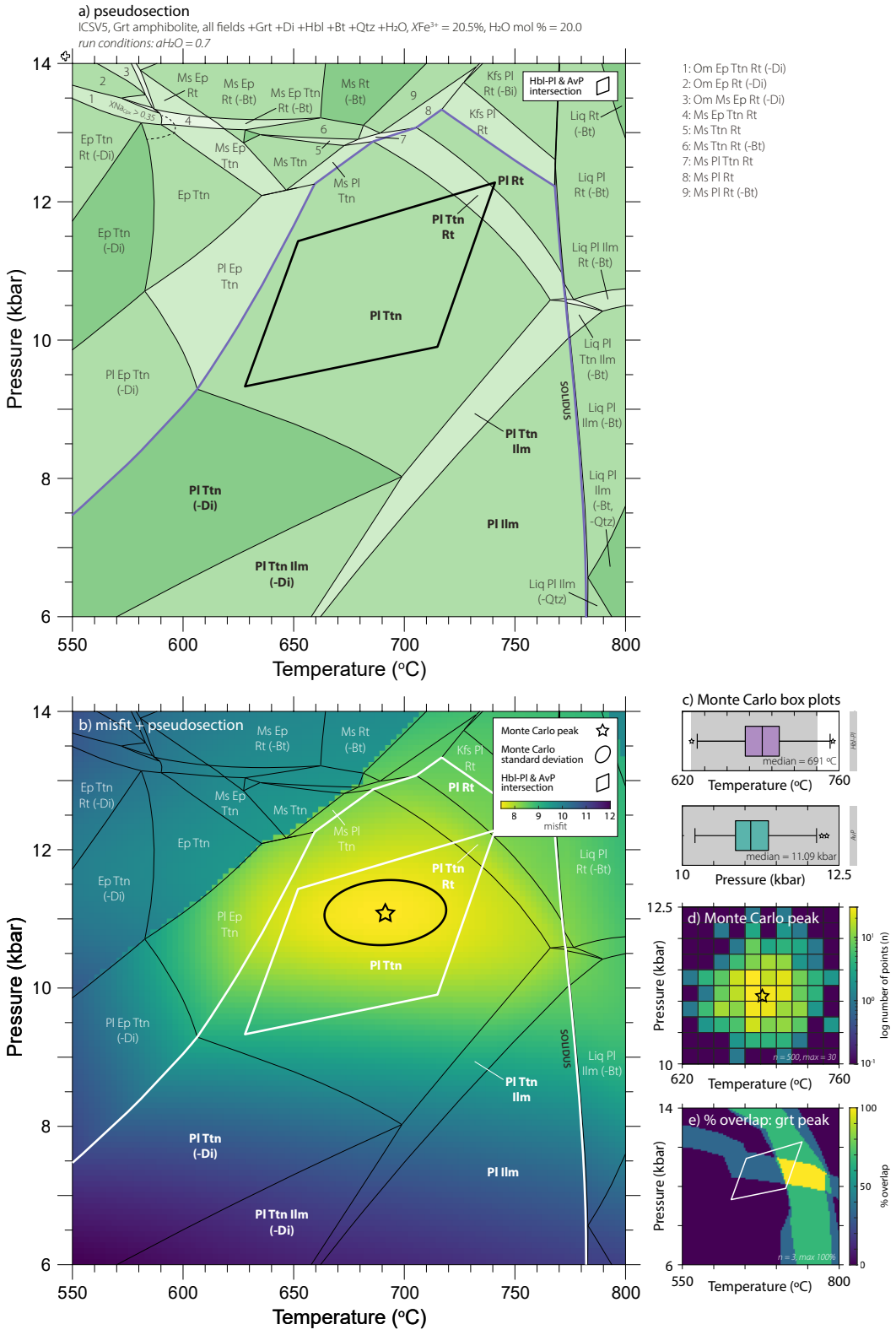


Fig. 4.38 ICSV5 a) pseudosection, b) heatmap showing the misfit of mineral chemistry variables, overlain with the bootstrapped mean best-fit result and the corresponding pseudosection, c) boxplots of bootstrapped T and P estimates with the grey bar indicating the range of the selected thermometer and AvP results, d) log-scaled 2D-histogram bin-plot of the boostrapped data with mean best-fit result marked by the star, e) % overlap of observed garnet rim compositional variables.

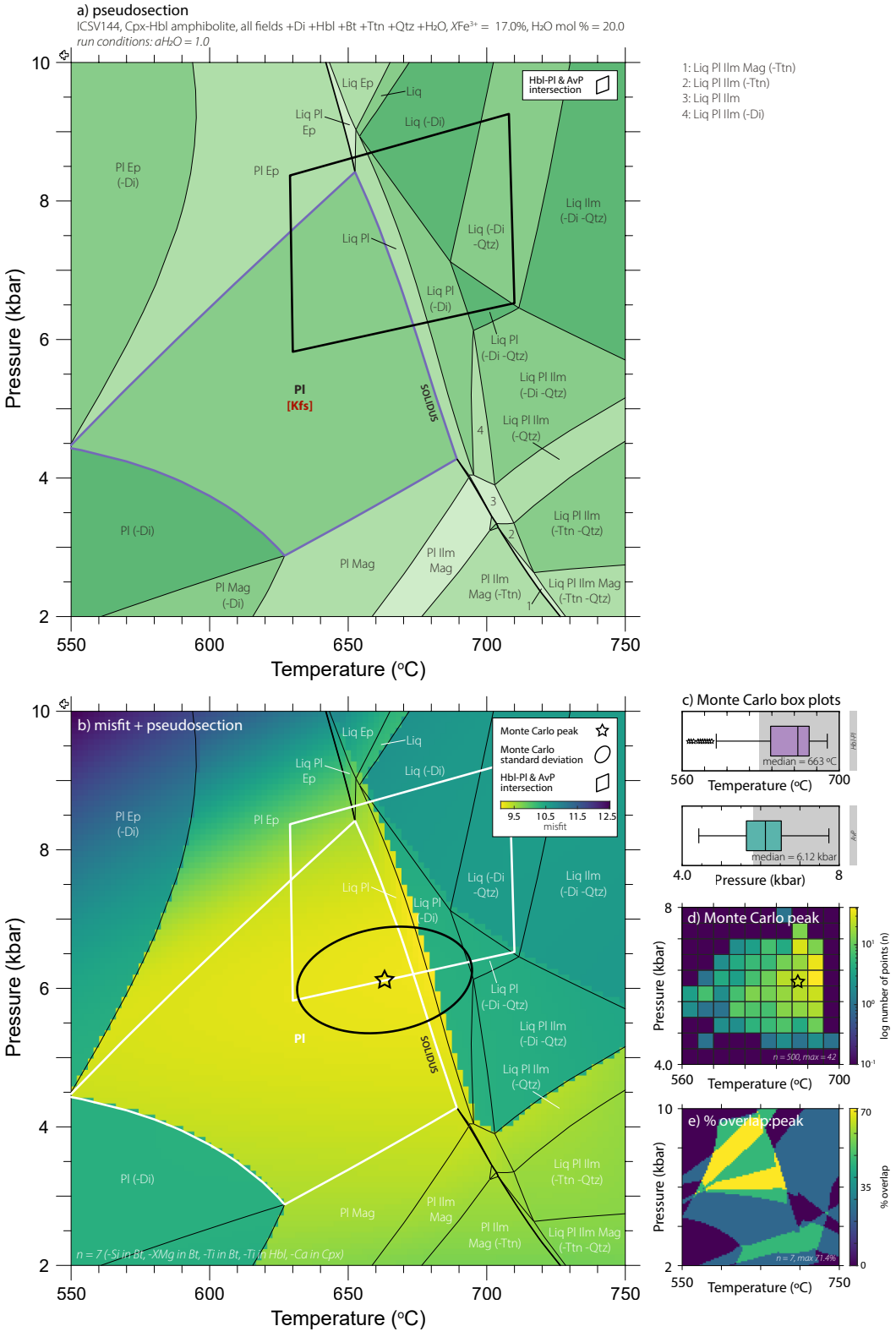


Fig. 4.39 ICSV144 a) pseudosection, b) heatmap showing the misfit of mineral chemistry variables, overlain with the bootstrapped mean best-fit result and the corresponding pseudosection, c) boxplots of bootstrapped T and P estimates with the grey bar indicating the range of the selected thermometer and AvP results, d) log-scaled 2D-histogram bin-plot of the boostrapped data with mean best-fit result marked by the star, e) % overlap of observed mineral compositional variables.

ICSV144 represents the highest grade sample modelled in the metabasite set. It also lies outside the main mapped region within the garnet+plagioclase isograd or the equivalent sillimanite-grade conditions of the pelitic assemblage. The observed peak assemblage of this sample is: Hbl-Pl-Bt-Ttn-Cpx which occurs in the modelled result at ~550–690 °C and ~3.0–8.5 kbar (Fig. 4.39a). The thermobarometer intersection overlaps with this field over the range of 629–674 °C and 5.82–8.43 kbar (Fig. 4.39b). Using the selected mineral compositional variables a result of 663 °C (+10/−24 °C) and 6.12 kbar (+0.40/0.48 kbar) is calculated as the best-fit result (Fig. 4.39c). The resampling calculates a maximum range of ~560–700 °C and ~4.0–8.0 kbar by varying the mineral compositions. These results show an asymmetric distribution towards the upper temperature range (Fig. 4.39c, d). The maximum temperature boundary is constrained by the stability of diopside, with diopside-absent assemblage at higher temperatures displaying higher misfit (Fig. 4.39b). Biotite compositional variables and Ti-in-hornblende showed stability of observed compositions above the solidus, and Ca-in-clinopyroxene did not plot within the modelled *P-T* range. These variables were thus excluded from calculation. The final result has a higher misfit than other samples (Fig. 4.39b), and poor overlap of compositional variables (Fig. 4.39e). However, the result is in agreement with the lower pressure range of the thermobarometer intersection and upper temperature range of modelled peak assemblage.

The highest grades of the garnet+plagioclase zone are defined by peak T at 655–706 °C (IQR) and P at 9.48–11.58 kbar as defined from mineral chemistry. Overlap of thermobarometer intersection and peak assemblage field produces a temperature range of 600–741 °C and pressure range of 9.02–11.98 kbar (from ICSV138 and ICSV5). No overlap is recorded in ICSV117 which extends to pressures in excess of 14.0 kbar. The highest metamorphic grade, equivalent to the sillimanite zone, records *P-T* conditions from mineral chemistry at 653–687 °C and 5.64–6.52 kbar or 629–674 °C and 5.82–8.42 kbar from overlap of thermobarometer intersection and peak assemblage field.

4.4.6 Comparison of pelitic and metabasic *P-T* results

The accurate determination of a prograde *P-T* path is the most diagnostic parameter in determining the thermal and tectonic history of orogenic sequences (Copley & Weller, 2022). Exhumed orogenic sequences expose rocks of varying structural levels, and owing to the steep nature of dehydrations reactions in

P-T space (Guiraud *et al.*, 2001), preserved metamorphic assemblages tend to relate to the peak temperature conditions rocks have experienced. An accurate representation of a *P-T* path may therefore be best defined by the *P-T* loci of T_{max} for rocks of all exposed structural levels, termed the metamorphic field gradient.

The techniques use to recover the *P-T* evolution of metamorphic sequences have made significant advancements in recent decades, now allowing for the integration of petrological information from pelitic and metabasic rocks using internally consistent datasets (e.g., Dale *et al.*, 2005; Holland & Powell, 2011; White *et al.*, 2014b; Diener & Powell, 2012; Green *et al.*, 2016). However, the number of studies that have thus far undertaken this opportunity is very few (e.g., Valli *et al.*, 2004; Bousquet, 2008; Gross *et al.*, 2009; Ugwuonah *et al.*, 2017; Faak *et al.*, 2012). Where it has been applied, it often uses a limited sample set, and/or compare results over a narrow range of *P-T* conditions. A study of metabasites by Kunz & White (2019) in the Ivrea Zone (NW Italy) also compares calculated *P-T* results with pelite results from Redler *et al.* (2012) along the same transect over an amphibolite to granulite facies transition. Kunz & White (2019) suggest that when analysed together, both rock types may more precisely constrain the thermal gradient of the region, than individual analysis. Furthermore, the study shows good agreement in *P-T* conditions using the applied Green *et al.* (2016) and White *et al.* (2014b) *a-X* models. It should be noted that although reported pressures and temperatures from both rock compositions show good overlap within given uncertainty ranges across the transect, the metabasites consistently predict slightly hotter conditions (see Fig. 9 of Kunz & White, 2019). The Suru Valley region provides a broader sample set across several transects from a wider range of metamorphic grades and techniques with which to develop the comparison between *P-T* estimates from pelite and metabasite. First the relative difference between the *P-T* conditions in pelites and metabasites are quantified for each technique, then the preferred results using the latest *a-X* models are integrated to inform the metamorphic field gradient and deconvolve the *P-T* evolution of the region.

Figure 4.41 provides a comparison of the different *P-T* determinations obtained for both pelitic and metabasic units. The thermobarometer intersection method shows a wider temperature range for metabasic compositions than pelitic compositions. This in part relates to the large associated calibration uncertainty (± 40 °C), and acute angle between the pressure-sensitive hornblende-plagioclase exchange calibration of Holland & Blundy (1994) and AvP array. Ignoring the

Table 4.2 Best-fit *P-T* results from the MATLAB bootstrapping routine. Approximate results from mineral chemistry overlap at the solidus are also included for ICSV145 and ICSV150.

Sample		Grt core				Grt rim				Peak			
		T (°C)	**uncertainty (°C)**	**P (kbar)**	**uncertainty (°C)**	**T (°C)**	**uncertainty (°C)**	**P (kbar)**	**uncertainty (°C)**	**T (°C)**	**uncertainty (°C)**	**P (kbar)**	**uncertainty (°C)**
ICSV86[p]	Grt-	546*	+4/−2	8.04*	+0.24/−0.32					575	+8/−10	7.72	+0.49/−0.40
ICSV130[p]	Grt-	503	± 12	6.22	± 0.30	509	± 10	7.13	+0.61/−0.81	541	+14/−16	8.44	+1.11/−0.91
ICSV109[p]	St-	502	+0/−3	7.02	+0.20/−0.10					599	+6/−9	9.04	+0.71/−0.51
ICSV113[p]	St-	471	± 4	8.96	+0.40/−0.49	524	+7/−4	10.17	+1.29/−1.46	609	+12/−6	9.53	± 0.40
ICSV13[p]	Ky-	467	± 3	5.97	± 0.08					582	+9/−6	9.61	+0.16/−0.24
ICSV12[p]	Ky-	474	+4/−0	5.87	± 0.35					633	+14/−11	9.35	+0.40/−0.30
ICSV91[p]	Sil-					586*	± 6	10.54*	+0.15/−0.30	665	+20/−18	12.15	+2.22/−2.53
ICSV81[p]	Sil-					559*	± 6	7.94*	+0.40/−0.30	639	+14/−18	9.96	+0.61/−0.71
ICSV145[p]	Sil+Kfs-									700		6	
ICSV150[p]	Sil+Kfs-									705		6.42	
ICSV50[m]	Hbl-	491	+6/−8	6.22	± 0.81					536	+5/−4	11.27	± 0.40
ICSV2[m]	Hbl-									542	± 3	8.48	+0.40/−0.57
ICSV92[m]	Olig-									601	+13/−18	10.48	+0.49/−0.40
ICSV138[m]	Grt+Pl-									671	± 16	9.88	+1.70/−0.40
ICSV117[m]	Grt+Pl-									669	+12/−14	11.9	+0.32/−0.24
ICSV5[m]	Grt+Pl-									691	± 15	11.09	+0.28/−0.24
ICSV144[m]	Grt+Pl-									663	+10/−24	6.12	+0.40/−0.48

* petrographic or compositional data suggest result not indicative of "true" core or rim
[p] pelite
[m] metabasite

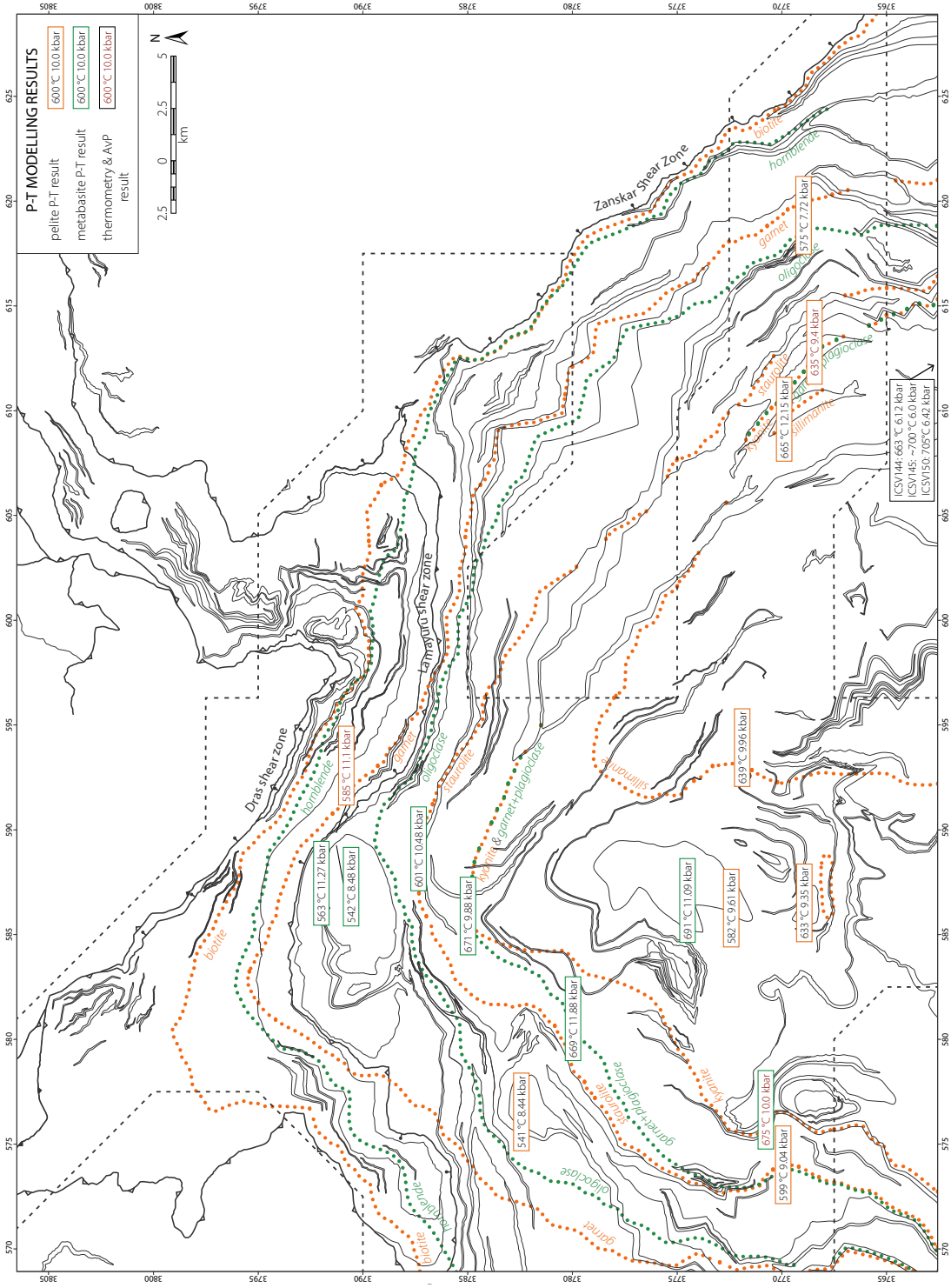


Fig. 4.40 Form-line map of major lithological and tectonic features of the Suru Valley area, NW India, is overlain pelitic and metabasic isograd sequences and the calculated best-fit results from the MATLAB routine shown for the analysed samples. Samples which were not selected for the routine or were unsuccessful have the selected thermometer and AvP values displayed.

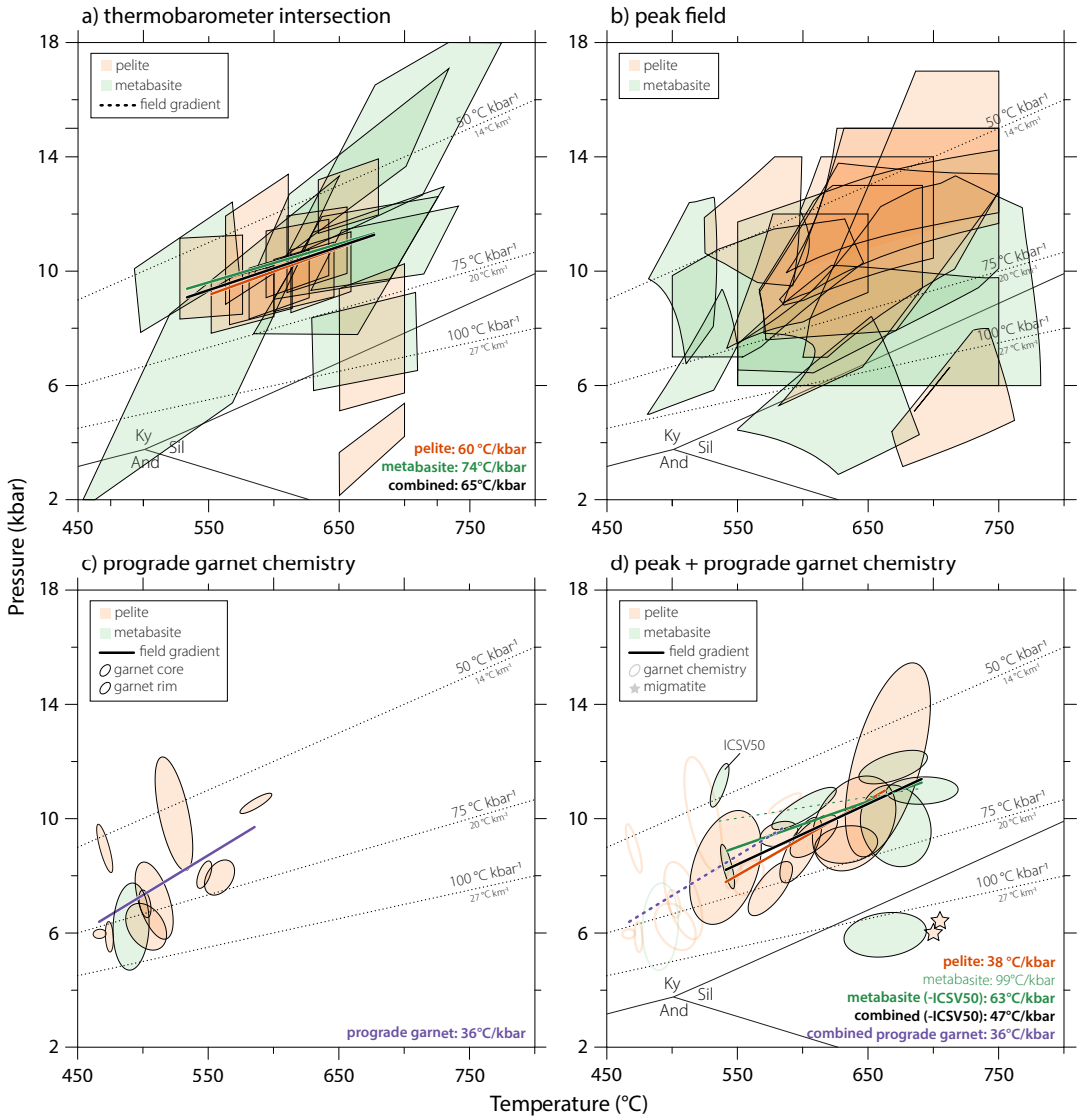


Fig. 4.41 Comparison of P-T results from pelitic and metabasic assemblages for the Suru Valley region. Resulting metamorphic field gradients are displayed with a linear regression, and calculated values displayed at bottom right of each plot. a) AvP and selected thermometer intersection, results in Table 4.1, b) pseudosection selected peak field, results in figures 4.23–4.39, c, d) best fit between selected chemical variables for both prograde garnet and peak mineral chemistry with 1 SD ellipses created using MATLAB routine, results in Table 4.2. For pseudosection peak assemblage fields that show large ranges, upper T and P boundaries are often denoted by the plotted range. For migmatites, ICSV145 and ICSV150, a star denotes the location of highest percentage overlap of observed chemistry along the solidus line, indicative of the location where the bulk composition finished losing melt. Calculation of metamorphic field gradient uses all samples from higher-pressures, thereby excluding ICSV144, ICSV145 and ICSV150 located in the sillimanite stability field. Thermal gradients assume a crustal density of 2750 kg m^{-1} and are drawn through the origin.

calibration and SD uncertainties on these techniques and using paired *P-T* points (Table 4.1), metabasite temperatures extend from 533–677 °C and in pelite from 552–657 °C (shown by the length of the metamorphic field gradient line in Fig. 4.41). Although these results overlap within their uncertainty ranges, the larger range of temperatures recorded in metabasite is shown by multiple samples and thermometry techniques (Fig. 4.17b). Pressures are broadly consistent across techniques, though with slightly higher pressures recorded in AvP results, owing to the use of steeply sloping equilibria reactions involving H_2O as a free phase. The wider temperature range of *P-T* determinations from metabasic compositions is similarly displayed by the peak assemblage fields approach (Fig. 4.41b). Samples from the hornblende zone and garnet+plagioclase zone extend to lower and higher temperatures, respectively, than equivalent grade samples from the pelites. However, pelitic assemblages extend to higher pressures, largely due to the lack of phase assemblage change (i.e. larger field boundaries) noted in pelitic pseudosections broadly above 9 kbar (excluding Fe-Ti-oxides). Calculated peak conditions using mineral chemistry yield similar trends to the thermobarometer intersection with lower temperatures recorded at lower grades and higher temperatures at higher grades. Only one garnet amphibolite had a zoned garnet profile (owing to the unusual X_{Sps} rich composition) but appears in good agreement with results from pelitic samples (Fig. 4.41c).

Metamorphic field gradients are higher in metabasite than in pelite for the thermobarometer intersection approach (74 and 60 °C kbar^{-1} for pelite and metabasite, respectively; Fig. 4.41a). Gradients are also concordant to the approximate slope of the dominant P-sensitive equilibria used in AvP calculations (thereby showing a difference of only 14 °C kbar^{-1}). Metamorphic field gradients are not identified for *P-T* determinations from peak assemblage fields owing to the size of peak fields that therefore permit a range of possible metamorphic field gradient slopes. *P-T* estimates from the best-fit of mineral chemistry shows significant disagreement between pelite and metabasite metamorphic field gradients: 38 °C kbar^{-1} for pelite and 63 °C kbar^{-1} for metabasite (Fig. 4.41d). ICSV50 is excluded from the metabasite result owing to the anomalously high-pressure value inconsistent with *P* values from nearby samples and due to the limited number of metabasite samples modelled at lower grades (thereby significantly skewing the result: 99 °C kbar^{-1}; Fig. 4.41d). Pelite results are broadly closer to the trend of prograde garnet chemistry, which records a gradient of 36 °C kbar^{-1} (Fig. 4.41c, d).

Given the variation in rate and degree of assemblage change during progressive metamorphism in pelite and metabasite (see Chapters 2 and 3), integrating the thermobarometric results from these rock sequences produces a potentially more representative metamorphic field gradient, suggesting the prograde conditions occur at a steeper gradient of 36 °C kbar^{-1}, whereas the trajectory towards peak conditions followed a shallower *P-T* gradient (47 °C kbar^{-1}). The latter produces a shallower *P-T* gradient than that suggested solely considering pelitic assemblages.

4.4.7 *P-T* record of the Suru Valley region and implications for GHS

The classic model of nested, clockwise *P-T* loops display a metamorphic field gradient that is broadly concave relative to the T-axis, polychronic and at a steep angle to *P-T* paths of individual samples (Fig. 4.42a; England & Thompson, 1984; Spear, 1993; Weller *et al.*, 2013). The modelling parameters used to produce such loops are that in scenario 1 (Fig. 4.42a), rapid burial is followed by erosion during which $T_{\max}$ is generally attained during decompression. Alternatively, in scenario 2 (Fig. 4.42b), if a rock sequence experiences slow burial, then thermal equilibration is approached during compression, resulting in convergence between *P-T* paths and metamorphic field gradients (England & Thompson, 1984). In such a scenario, $P_{\max}$ and $T_{\max}$ are broadly concurrent, such that $\frac{\delta t}{\delta T}$ is low, where δt is the difference between time achieved at $P_{\max}$ and $T_{\max}$. *P-T* predictions from certain Barrovian environments are better reproduced by a scenario encompassing thermal convergence between *P-T* paths and metamorphic field gradients (e.g., Weller *et al.*, 2013). However, slower burial is not distinctly required throughout the prograde–peak *P-T* cycle in order to achieve this. Fast burial followed by thermal relaxation without concomitant erosion (scenario 3; Fig. 4.42c) or fast burial followed by slow burial prior to attainment of maximum pressure conditions (scenario 4; Fig. 4.42d) will produce convergence between the *P-T* path and metamorphic field gradient for peak conditions. This convergence is broadly achieved by relatively isobaric conditions between $P_{\max}$ and $T_{\max}$. These may be disparate (large $\frac{\delta t}{\delta T}$) or occur near concurrently (small $\frac{\delta t}{\delta T}$).

Several features in the Suru Valley cannot be accounted for by scenario 1 or 2 in Figure 4.42a, b. Chapter 2 demonstrated that thermal peak is attained syn- to post-tectonic with respect to the main phase of crustal thickening, with post-tectonic growth dominant at lower structural levels (Fig. 2.17). These observations suggest thermal equilibration likely occurred after rather than during compression,

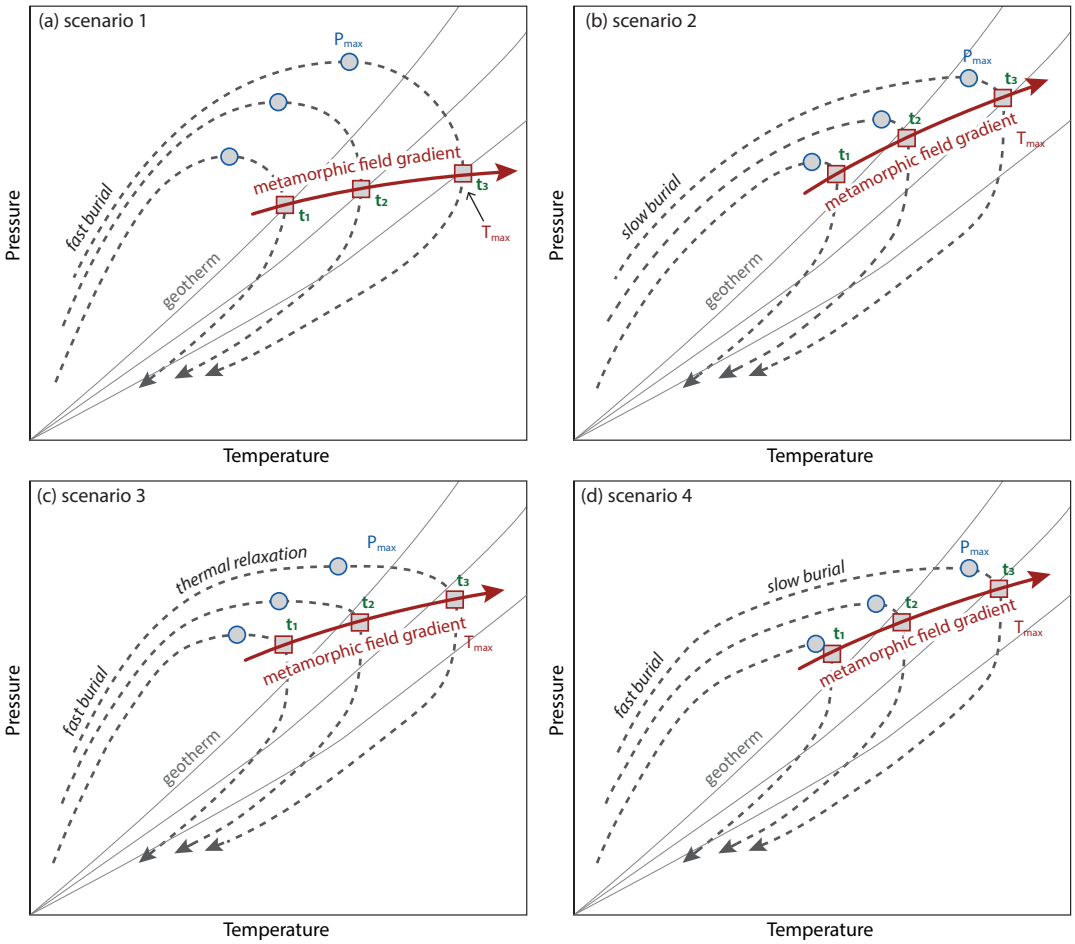


Fig. 4.42 Schematic of P-T paths for 3 hypothetical samples during thickening of the crustal sequence. $T_{\max}$ for each P-T path defines a pinning point for the metamorphic field gradient. a) Classic P-T path experienced during Barrovian metamorphism, where the metamorphic field gradient is concave relative to the T-axis, polychronic and at a steep angle to the P-T paths defining the gradient (England & Thompson, 1984; Spear, 1993). b) Displays a variation experienced during slower burial where P-T paths and field gradients are sub-parallel and progressively merge (England & Thompson, 1984). c-d) variations of scenario 1 and 2 displaying fast then absent burial and/or heterogenous rates of burial. Figure modified from Weller *et al.* (2013) after England & Thompson (1984); Spear (1993).

discounting consistent slow burial throughout prograde–peak conditions. Peak temperatures are attained at high pressures in samples from the staurolite to sillimanite zones and oligoclase to garnet+plagioclse zones (~9.0–12.0 kbar). P-T paths recorded in this study do not suggest significant difference in pressure between $P_{\max}$ and $T_{\max}$ (e.g., Fig. 4.30), which cannot be accounted for in scenario 1. Furthermore, owing to the propensity of preserved metamorphic assemblages that relate to the peak temperatures attained (e.g., Guiraud *et al.*,

2001), the lack of lower-pressure assemblages is notable. Even within the mapped sillimanite zone, kyanite remains the volumetrically dominant aluminosilicate, with only localised growth of fibrolite and preserved peak *P-T* conditions sit within the kyanite field (Fig. 4.41). This suggests that decompression does not drive attainment of thermal peak. In order to preserve the dominance of kyanite-grade conditions, temperatures must not have increased significantly during decompression. Therefore, the initial stages of exhumation must occur along a *P-T* array within the kyanite stability field. Alternatively, the fluid budget was consumed at high pressures. This relative lack of lower pressure assemblages also suggests that the process(es) driving decompression only exerted a minor influence on the metamorphic record in the Suru Valley region. It is likely that during decompression, the *P-T* path only entered sillimanite-nucleating conditions for a limited period and/or under fluid-absent conditions. The driving processes enabling decompression were not active across most structural levels during the prograde to peak metamorphic evolution of the region, only initiating during the later stages of the metamorphic cycle.

Determining a metamorphic field gradient from an oblique crustal section requires that thermal and tectonic characteristics are constant across the region of consideration (Harte & Dempster, 1987). The relative consistency of the mapped mineral isograd pattern in the Suru Valley suggests the thermal architecture is consistent across the region. The calculated thermal gradients are therefore considered representative for the region with the recognition that any given field gradient has a finite extent with notable lateral variation in heat flow and age of metamorphism across orogenic sequences (Weller *et al.*, 2013, 2021). Although discussion of burial rates require integration of quantitative age constraints, this section reasonably assumes that the slope of the *P-T* gradient may broadly relate to the rate of burial or exhumation. Relative comparisons of slopes are therefore used to inform the processes constraining the *P-T* evolution at different points. During prograde metamorphism significantly lower thermal gradients are recorded (34 °C kbar^{-1}), consistent with faster rates of burial compared to peak conditions that are attained at shallower thermal gradients (47 °C kbar^{-1}). This suggests that following initial rapid burial *P-T* paths become more isobaric across decreasing structural levels. These gradients are consistent with heterogenous burial rates or rapid burial followed by a dominant phase of thermal relaxation, and do not require exhumation driven processes prior to attainment of high-pressure thermal peak (Fig. 4.42c, d).

It must also be noted that higher-pressure Barrovian terrains cannot reach such pressures solely by crustal thickening though folding, and require concurrent or subsequent underthrusting beneath a thickened cover sequence (e.g., Tethyan thrust belt Corfield & Searle, 2000) and/or continental plate (e.g., DeCelles *et al.*, 2002). It is possible that underthrusting in combination with significant folding may help to account for rapid thickening of the crust and initially steeper metamorphic field gradients. T_{max} at peak-pressure assemblages and lower-pressure assemblages are broadly consistent (e.g., sillimanite-grade assemblages), suggesting only minimal variation of the slope of decompression profile (near-isothermal). A period of very rapid exhumation is required for such a decompression profile, this may be accounted for by mechanical erosion and tectonic unroofing along the footwall of the ZSZ (Searle *et al.*, 1999b).

The following *P*-*T* constraints and a schematic model for *P*-*T* evolution of the Suru Valley region (Fig. 4.43) may be summarised from lowest to highest metamorphic grades:

1. At the lowest metamorphic grade (garnet zone; hornblende zone), samples have equilibrated at temperatures between 525–583 °C. Pressures are dominantly recorded between 7.32–9.55 kbar though may extend as high as 11.61 kbar in one sample. The prograde evolution of these samples occurs at faster burial rates of 36 °C kbar^{-1} when compared to peak conditions (Fig. 4.43)

2. At moderate metamorphic grade (staurolite and kyanite zones; oligoclase and garnet+plagioclase zones) temperatures range from 576–647 °C in pelitic samples but from 583–706 °C in metabasic samples. Pressures in pelitic samples range from 8.52–9.93 kbar (using mineral chemistry constraints, ranging from 8.2–11.8 kbar using alternate techniques) and from 9.48–11.58 kbar in metabasites. The metamorphic field gradient shows progressive shallowing concomitant with the end of crustal thickening to 47 °C kbar^{-1}, followed by a stage of thermal relaxation (or slow burial; Fig. 4.43).

3. The rocks that have decompressed to the lowest pressures (sillimanite and sillimanite+K-feldspar zones; garnet+plagioclase zone) were buried and heated during thermal relaxation up to conditions of 621–684 °C and 9.25–14.37 kbar but decompress to conditions of 653–700 °C and 5.64–6.52 kbar on a near-isothermal path. Final loss of melt from migmatites occurs around 700 °C and 6.0–6.5 kbar. A progressive overturning of the decompression path occurs from lowest–highest metamorphic grade such that T_{max} may

occur at lower pressures at sillimanite grade and sillimanite+K-feldspar grade (Fig. 4.43).

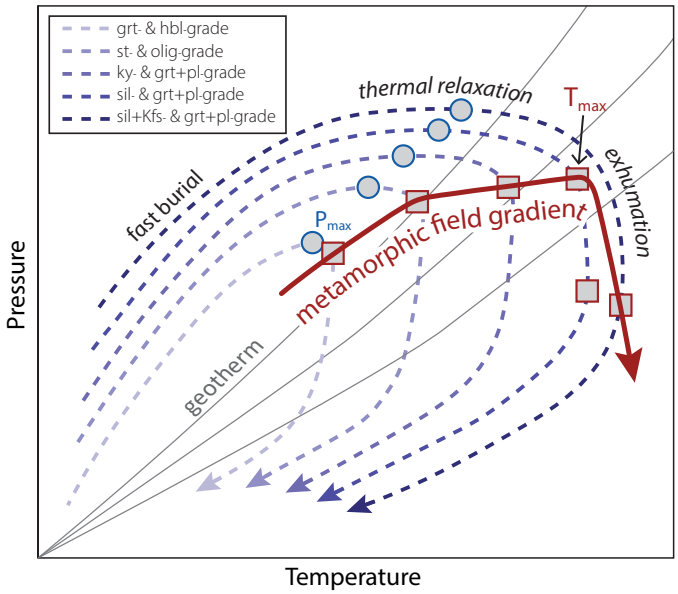


Fig. 4.43 Schematic of *P-T* paths of all metamorphic grades of the Suru Valley region accounting for rapid burial followed by thermal relaxation (or slow burial) and finally isothermal exhumation driven by rapid erosion and/or normal-sense shearing.

4.4.8 Implications of reduced $a\mathrm{H_2O}$

Constraining the metamorphic evolution of crustal rocks relies on key variables such as bulk rock, mineral, and fluid composition. $a\mathrm{H_2O}$ is commonly assumed to be unity in most subsolidus prograde–peak metamorphic environments given the recognition that dehydration reactions prevail. However, studies in the GHS have treated $a\mathrm{H_2O}$ as an undefined variable (e.g., Waters, 2019; Long *et al.*, 2017; Yakymchuk & Godin, 2012; Imayama *et al.*, 2010; Groppo *et al.*, 2017). The results of this study show the significance that a reduced $a\mathrm{H_2O}$ may impart on the stability of mineral phases, determination of peak assemblage and temperature conditions at which the solidus may be transected. Reducing the activity of $\mathrm{H_2O}$ expands $\mathrm{H_2O}$ bearing fields: dehydration reactions, which liberate $\mathrm{H_2O}$ on the high-temperature side, will move to lower temperatures; and $\mathrm{H_2O}$-consuming reactions (e.g., wet solidus) will move to higher temperatures. This reflects the principle that reducing the activity of a solid solution stabilises that solid solution. Furthermore, melt producing reactions that consume $\mathrm{H_2O}$ (low-temperature side) will move up temperature. The liquidus shows significant displacements towards

higher temperatures at reducing $a\mathrm{H_2O}$ and the liquidus shows clockwise rotation from negatively to positively sloping curves. On a clock-wise path samples that isothermally decompress are less likely to transect the solidus curve until lower pressures once the shape has established a positive slope, suggesting reduced melt volume at peak conditions. Sample specific determination of P-T conditions that most accurately predict the observed rock compositional information vary by $a\mathrm{H_2O}$. Thus, considering $a\mathrm{H_2O}$ as a variable in appropriate circumstances, where a reduction may be implicated by petrographic or lithological criteria, may significantly impact the determined metamorphic field gradient, and thereby the thermal and tectonic history of the region (Copley & Weller, 2022). The Suru Valley shows a regional trend of reduced $a\mathrm{H_2O}$ that matches the observations and data obtained from natural samples. The relative implications of a reduced $a\mathrm{H_2O}$ to Himalayan tectonics is herein considered.

Previous studies have identified $\mathrm{CO_2}$ rich fluid inclusions in the GHS across the Himalaya (Pêcher, 1979; Sauniac & Touret, 1983; Craw, 1990; Boullier *et al.*, 1991; Sachan *et al.*, 2013; Montemagni *et al.*, 2016). Similarly these are identified in the crystalline units of Garhwal Himalaya (Sachan *et al.*, 2001; Pandey *et al.*, 2004) and in the North Himlayan gneiss domes (Li *et al.*, 2022). Saline fluid inclusions have also been identified (Sachan *et al.*, 2013; Li *et al.*, 2022). Origin of such fluids may occur as metamorphic fluids during the prograde–peak evolution of a sample (e.g., Boullier *et al.*, 1991; Pandey *et al.*, 2004; Montemagni *et al.*, 2016; Rapa *et al.*, 2017) or may occur during exhumation and shearing (e.g., Pêcher, 1979; Sauniac & Touret, 1983; Craw, 1990). The latter is often attributed with increasing $\mathrm{CO_2}$ content towards the bounding shear zone (e.g., Pêcher, 1979). The relative source of this fluid may vary, though decarbonation of calc-silicate rocks or impure marbles during metamorphic reactions may act as a significant source of the given $\mathrm{CO_2}$ content in fluid (Groppo *et al.*, 2017; Rapa *et al.*, 2017). Marly intercalations within pelitic sedimentary sequences (carbonate-poor) are inferred to produce greater $\mathrm{CO_2}$ during prograde metamorphism than carbonate-rich sedimentary rocks (Groppo *et al.*, 2017). The Suru Valley region is abundant in carbonate-poor (locally graphite rich metasedimentary rocks) with modally minor carbonate-dominant sediments, regularly intercalated across the metamorphic sequence and at all metamorphic grades. Carbonates, calc-silicates and calc-pelites occur in the GHS across the orogen (e.g., Jessup *et al.*, 2008; Cottle *et al.*, 2011; Kellett & Grujic, 2012; Parsons *et al.*, 2016c; Groppo *et al.*, 2017; Rapa *et al.*, 2017; Walters & Kohn, 2017). $\mathrm{CO_2}$ (and saline fluids) may therefore be derived from these lithologies in combination with graphite-present

metasedimentary rocks), and suggests the relative impact of a reduced $a\mathrm{H_2O}$ to Himalayan tectonics warrants consideration.

Application of thermal models to the metamorphic evolution of the Himalayan orogen place a crucial dependence on widespread partial melting in the GHS to accommodate the required reduction in viscosity (e.g., Beaumont *et al.*, 2001; Grujic, 2006). The presence of melt in a few volume percent, may reduce viscosity and halve the strength of a rock (Beaumont *et al.*, 2004; Rosenberg & Handy, 2005). The propensity of a given sample to cross the modelled solidus on a clockwise *P-T* path in intrinsically linked to the fluid composition driving devolatilisation reactions. Although lithologic units observed in individual tectonostratigraphic units across the Himalaya may appear remarkably constant, the relative proportions of these lithologies show significant variation (Le Fort, 1975; Upreti, 1999; Yin, 2006), which is likely to result in orogen-parallel variation of viscosity during metamorphic evolution (Parsons *et al.*, 2016c). We suggest this is not only driven by a density contrast owing to the varying proportions of lithologies, but also by the resulting devolatisation reactions from differing rock types, which may significantly impact the fluid composition during the metamorphic cycle. This may significantly reduce the propensity of melt producing reactions to take place. Without the prerequisite drop in rock strength, this exerts significant control over the likelihood for viscous flow (Rosenberg & Handy, 2005).

4.4.9 Uncertainty on *P-T* measurements

The preferred routine in this study places quantitative constraints on *P-T* measurements and geological uncertainty between natural systems and predictive modelling. This routine shows significant benefit to determining *P-T* constraints for samples with few phase assemblage changes and/or large field boundaries. Placing statistical constraints on *P-T* results in modelling is the first step towards accurately determining robust *P-T* paths and relative discrepancy between natural and modelled systems. Through first accurately quantifying the appropriate $a\mathrm{H_2O}$, the relative uncertainty on peak *P-T* measurements in a Barrovian metamorphic sequence defined by a range of *P-T* conditions and bulk compositions is 12 °C and 0.63 kbar. These results consider solely mineral compositional uncertainty. Uncertainty on $a\mathrm{H_2O}$ may increase the temperature uncertainty further (~25 °C).

4.5 Conclusion

The following conclusions can be drawn regarding the metamorphic evolution of the Suru Valley region and orogenic sequences.

1. At the lowest metamorphic grade (garnet zone; hornblende zone), samples have equilibrated at temperatures between 525–583 °C. Pressures are dominantly recorded between 7.32–9.55 kbar. At moderate metamorphic grade (staurolite and kyanite zones; oligoclase and garnet+plagioclase zones), temperatures range from 576–647 °C in pelitic samples and from 583–706 °C in metabasic samples. Pressures in pelitic samples range from 8.52–9.93 kbar and from 9.48–11.58 kbar in metabasites. Rocks that have decompressed to the lowest pressures (sillimanite and sillimanite+K-feldspar zones; garnet+plagioclase zone) are buried and heated during thermal relaxation up to conditions of 621–684 °C and 9.25–14.37 kbar but decompress to conditions of 653–700 °C and 5.64–6.52 kbar on a near-isothermal path.

2. Incorporating pelite and metabasite thermobarometry yields a shallower metamorphic field gradient than solely considering pelitic assemblages, implying that the trajectory towards peak conditions follows a more isobaric path. Using the quantitative information from both rock types may yield more representative P-T constraints in orogenic sequences.

3. Attainment of thermal peak in the Suru Valley region is demonstrably driven by burial mechanisms and is not driven by decompression, in contrast to other regions across the Himalaya.

4. Classical models for the thermal evolution of Barrovian sequences are not deemed appropriate to resolve the thermal evolution of the Suru Valley region. Fast burial occurs during early prograde conditions of garnet growth at a metamorphic field gradient of 38 °C kbar^{-1}. However, during attainment of thermal peak, after the dominant stage of garnet growth, slower burial rates and/or a dominant stage of thermal relaxation (47 °C kbar^{-1}) in the absence of mechanical erosion and tectonic unroofing better reproduce the metamorphic field gradient. Progressing from lower–higher metamorphic grades the decompression profile progressively trends from steeply positively sloping to steeply negatively sloping. Initiation of melting, rapid erosion, and/or normal-sense shearing are required to initiate decompression along this near-isothermal path.

5. The regional signature of a reduced $a\mathrm{H_2O}$ may result from the regular interleaving of impure carbonates, calc-silicates, and calc-pelites within the observed rock sequence. Decarbonation reactions during prograde metamorphism may dilute the hydrous fluid with CO_2. The shift of the solidus uP-Temperature may account for the low volumes of melt recorded in the area and result in a more rigid portion of the GHS. This in turn allows for better preservation of the higher-pressure kyanite-grade conditions abundant in the region.

6. Establishing statistical constraints on P-T modelling represents a crucial initial step for precise determination of P-T paths and understanding the divergence between natural and modelled systems. The uncertainty in peak P-T measurements for modelling a Barrovian metamorphic sequence over a diverse range of metamorphic grades and bulk compositions is 12 °C and 0.63 kbar.

Chapter 5

Multiphase U-(Th)-Pb geochronology



Last rays of light along Shanshin Nala

5.1 Principles of radioisotopic dating

5.1.1 Equations of decay

Radioactive decay describes the probability that a given particle within the nucleus of an atom will surpass the potential energy barrier binding it to the nucleus, thereby forming a new nuclide. The rate at which decay occurs is both exponential and independent of varying physical or chemical conditions (Rutherford & Soddy, 1902)). The rate of decay of any parent atom is proportional to the number of those atoms present in the system N at any time t:

$$\frac{\mathrm{d}N}{\mathrm{d}t} \propto N \tag{5.1}$$

dN/dt is negative because N is decaying. Variation in the rate of decay of different elements may be associated by the decay constant, λ, which is assumed to have remained unchanged throughout Earth's history. Therefore:

$$\frac{\mathrm{d}N}{\mathrm{d}t} = -\lambda N \tag{5.2}$$

$$\int_{N_0}^{N} \frac{1}{N}\mathrm{d}N = \int_{t_0}^{t} -\lambda \mathrm{d}t \tag{5.3}$$

$$\ln\left(\frac{N}{N_0}\right) = -\lambda(t - t_0) \tag{5.4}$$

At the start of decay, $t_0 = 0$, simplifying the equation to:

$$N = N_0 e^{-\lambda t} \tag{5.5}$$

This relates to the number of parent atoms after initiation of decay (N) to the initial number of parent atoms at initiation of decay (N_0). However, as N_0 is usually unknown, the number of radiogenic daughter isotopes, D^*, can be substituted:

$$D^* = N_0 - N \tag{5.6}$$

Modifying equation 5.5:

$$D^* = N\left(\mathrm{e}^{\lambda t} - 1\right) \tag{5.7}$$

The age, t, can then be calculated if the number of decayed daughter atoms, D^* and number of parent atoms present since initiation of decay, N, are known. However, the number of daughter atoms present in a system D_t must also include those initially present, D_0, and those produced by decay:

$$D_t = D_0 + D^* \tag{5.8}$$

Substituting this into equation 5.7,

$$D_t = D_0 + N\left(\mathrm{e}^{\lambda t} - 1\right) \tag{5.9}$$

This is the fundamental relationship that relates the number of parent and daughter atoms in a system with the time since decay started. D_0 is still unknown, but this equation is linear and solvable. To overcome the uncertainty associated with D_0, a non-radiogenic, non-radioactive isotope of the same element may be used as a reference (X). X is assumed to have remained constant over time. Isotopic ratios are therefore used to normalise:

$$\frac{D_\mathrm{t}}{X} = \frac{D_0}{X} + \frac{N}{X}\left(e^{\lambda t} - 1\right) \tag{5.10}$$

Analysis of a sample using mass spectrometry allows measurement of D_t and N. Assuming the decay constant λ for the measured radioactive isotope is known, the equation can be solved for t, the age since decay initiated:

$$t = \ln\left(\frac{D_t - D_0}{N} + 1\right)\lambda^{-1} \tag{5.11}$$

This equation provides a practical and reliable method for calculating the age of a system based on the measured quantities of daughter and parent isotopes. The logarithmic term in the equation accounts for the decay process, and the normalisation with X ensures the consideration of initial conditions, making it a robust formula for age determination in the context of radioactive decay.

5.1.2 U-Th-Pb systematics

The 'age' of a rock is dependent on a variety of factors, key of which is the radioisotopic system used. A framework to constrain isotopic ages of geological units is that of closure temperature (Dodson, 1973). Closure temperature, a

fundamental concept in geochronology, delineates the temperature threshold at which isotopic diffusion within a mineral or rock system becomes negligible. At elevated temperatures, atoms within the crystal lattice of minerals can migrate, leading to isotopic diffusion and potential changes in isotopic ratios. If a mineral undergoes cooling through the closure temperature it becomes "closed" to isotopic exchange or diffusion, preserving the evolving isotopic ratios of the system. Once below this threshold, the mineral "records" the time spent below the closure temperature by recording the changing parent to daughter isotopic ratios with time. Different minerals exhibit unique closure temperatures for various isotopic systems, providing a key parameter for understanding the thermal history of rocks and minerals. Two main systems are used in this study: U-Pb and Th-Pb, appropriate to determining the high-temperature igneous and metamorphic record (e.g., Parrish, 1990).

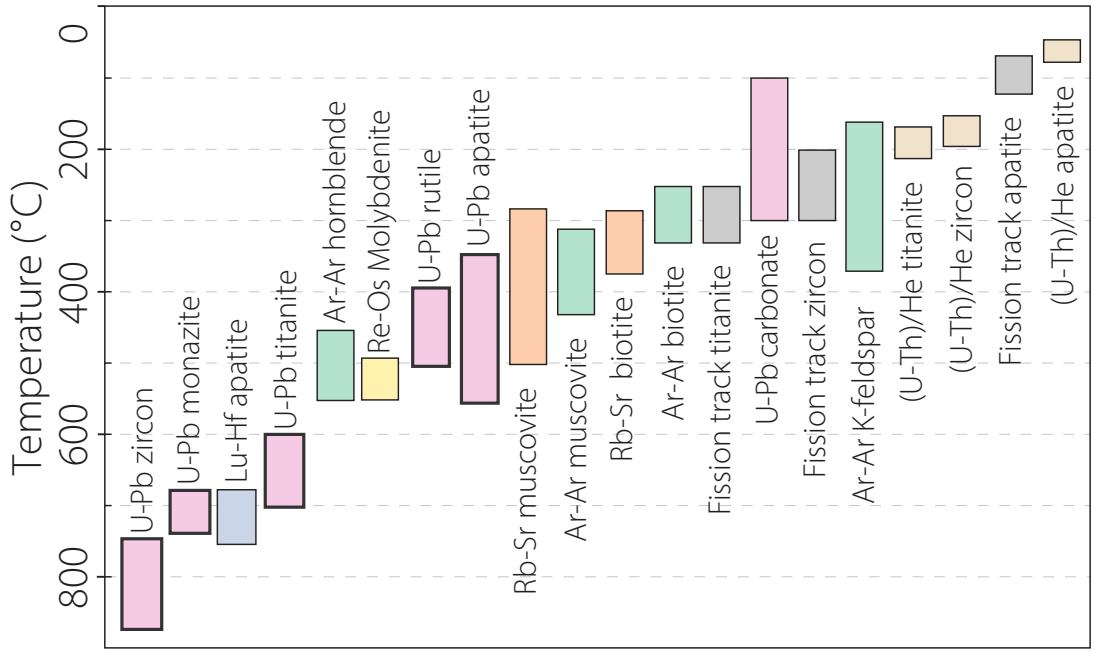


Fig. 5.1 Effective closure temperatures for commonly used thermochronometers, modified from Chew & Spikings (2015). Isotopic system and accessory phases analysed in this study are highlighted with a thick stroke.

Uranium comprises three naturally occurring radioactive isotopes: ^{238}U, ^{235}U, and ^{234}U; ^{238}U and ^{235}U are abundant enough for geochronology applications through Earth's entire history. These two parent isotopes (^{238}U and ^{235}U) undergo decay processes, leading to the formation of stable daughter isotopes ^{206}Pb and ^{207}Pb through the uranium series and actinium series, respectively. ^{234}U serves as an intermediate nuclide exclusively within the uranium series, and can be used

for dating young material (< ka). In contrast, thorium predominantly exists as ^{232}Th producing stable daughter isotope ^{208}Pb (thorium series).

The overall decay scheme for each involves the emission of multiple α and β particles and energy release (Q):

$$\begin{aligned} {}_{92}\mathrm{U}^{238} &= {}_{82}\ \mathrm{Pb}^{206} + 8\alpha + 6\beta + \mathrm{Q} \\ {}_{92}\mathrm{U}^{235} &= {}_{82}\ \mathrm{Pb}^{207} + 7\alpha + 4\beta + \mathrm{Q} \\ {}_{90}\mathrm{Th}^{232} &= {}_{82}\ \mathrm{Pb}^{208} + 6\alpha + 4\beta + \mathrm{Q} \end{aligned} \tag{5.12}$$

Despite the existence of intermediate daughters, the half-lives of the parent U and Th isotopes are much larger compared to the production rate of stable Pb isotopes. Therefore, the production rate of stable Pb isotopes is primarily limited by the rate at which the parent isotopes decay, not by the intermediate steps in the decay sequence. Once significantly beyond the realm of U-series geochronology, which is limited to < 600 ka, U and Th can be considered to decay directly to Pb, in a state that is termed secular equilibrium.

Substituting each decay scheme into equation 5.9 using the only naturally occurring non-radiogenic isotope of Pb (^{204}Pb) as a normalising reference:

$$\left(\frac{^{206}\ \mathrm{Pb}}{^{204}\ \mathrm{Pb}}\right)_t = \left(\frac{^{206}\ \mathrm{Pb}}{^{204}\ \mathrm{Pb}}\right)_0 + \left(\frac{^{238}\mathrm{U}}{^{204}\ \mathrm{Pb}}\right)_t \left(e^{\lambda_{23x} t} - 1\right) \tag{5.13}$$

$$\left(\frac{^{207}\ \mathrm{Pb}}{^{204}\ \mathrm{Pb}}\right)_t = \left(\frac{^{207}\ \mathrm{Pb}}{^{204}\ \mathrm{Pb}}\right)_0 + \left(\frac{^{235}\mathrm{U}}{^{204}\ \mathrm{Pb}}\right)_t \left(\mathrm{e}^{\lambda_{235} t} - 1\right) \tag{5.14}$$

$$\left(\frac{^{208}\ \mathrm{Pb}}{204\ \mathrm{Pb}}\right)_t = \left(\frac{^{208}\ \mathrm{Pb}}{^{204}\ \mathrm{Pb}}\right)_0 + \left(\frac{^{2332}\mathrm{Th}}{^{204}\ \mathrm{Pb}}\right)_t \left(e^{\lambda_{232} t} - 1\right) \tag{5.15}$$

Three independent ages may therefore be obtained when solving these equations for time. These ages should be within error (concordant) if certain conditions are met. This includes decay constants are known, the mineral has remained a closed system below its closure temperature, correct values for the initial Pb isotope ratios are used, and analytical procedures are accurate. Where such ages do not agree (are discordant), a range of responsible factors can be considered.

5.1.3 Interpretation and visualisation of U-(Th)-Pb data

All age calculation and plotting is conducted in IsoplotR (Vermeesch, 2018). The minerals dated here contain variable degrees of common Pb (except for zircon where it is largely absent), and thus the Tera-Wasserburg plot (derived from the total Pb/U plot of Ludwig, 1998) is more suitable than the traditional Wetherill concordia plot. On Tera-Wasserburg plots, the age is calculated as the lower intercept with concordia, and the upper intercept reflects the initial Pb (common Pb) composition. Due to the change in scale as a function of the exponential correlation between ratio and age, the Tera-Wasserburg is generally more useful for common Pb bearing or absent data such as for 'young' Himalayan-aged data rather than Wetherill plot. However, the Wetherill plot remains useful for 'older' data or zircon data that have recorded lead-loss.

To date, most analysts rely on either the U-Pb or Th-Pb system, the choice of which depends on the mineral, with only monazite being more commonly dated with Th-Pb. However, if both systems are measured, then data from each decay chain can be used to inform about the age and initial Pb composition. Vermeesch (2020) employed algorithms into the plotting and age calculation package (IsoplotR) for this purpose. Where appropriate, the combined U-Th-Pb approach is variably used for certain minerals. The lack of ^{208}Pb and ^{232}Th measurement on some instrumentation due to detector arrays (i.e., the Nu Plasma HR) precludes this approach.

Allanite, apatite, and rutile analyses are displayed on Tera-Wasserburg plots and ages quoted are lower intercept ^{238}U-^{206}Pb ages comprising U-Pb measurements only. Titanite analyses are shown using Tera-Wasserburg plots and ages quoted are lower intercept ^{238}U-^{206}Pb ages from combined U-Th-Pb measurements. Zircon uses the U-Pb system only and are plotted and calculated as Wetherill or Tera-Wasserburg plots based on the age ranges. Detrital zircon ages are also plotted as kernel density plots calculated in IsoplotR. Monazite use the combined U-Th-Pb approach and are displayed on Tera-Wasserburg (or locally Wetherill plots), along with the addition of: 1) Th-Pb vs U-Pb plots of common-lead corrected data to assess the concordance between these systems; and 2) rank order plots of common lead corrected Th-Pb ages. Monazite can contain significant excess ^{206}Pb derived from ^{230}Th, the intermediary decay product of the ^{238}U-^{206}Pb decay chain. Excess ^{206}Pb results in measured ^{238}U-^{206}Pb ages older than true crystallisation. Where appropriate, plots are colour-coded by trace element data

using the in-built colour-scaling in IsoplotR. All data and ages are shown and quoted at 2σ.

5.2 Analytical approach

5.2.1 Sample selection and preparation

Accessory minerals were analysed *in situ* in thin section and as separates in epoxy resin mounts. For select samples, heavy mineral separation procedures were undertaken at National Environmental Isotope Facility (BGS, Keyworth, UK). Whole rock was separated into constituent minerals using a SELFRAG (selective fragmentation machine). Heavy and light material was separated on a Roger's table, and further partitioning undertaken using a Frantz magnetic separator. If appropriate (e.g., zircon), the remaining non- magnetic or weakly magnetic-fraction was then then separated using a diodomethane heavy liquid. Accessory phases were then picked in ethanol and mounted into 25 mm epoxy resin discs. Polishing was then undertaken to reveal a broadly equatorial section of the mineral grains

In preparation for geochronological analysis, examination of chemical and textural features of selected accessory phases was undertaken at the University of Oxford Earth Science Department on a Cameca SX5-Fe electron microprobe with a tungsten tipped field emission gun. Analyses were conducted on carbon coated, polished thin sections *ca.* 30 µm thick, augmented by additional analyses on carbon-coated epoxy resin mounts for select samples. Full spectrometer setup and operating parameters are included in the appendix.

For apatite and rutile no dominant chemical zonation was observed, and inspection of crystals during picking shown them to be inclusion-poor; therefore for thin sections, petrography and BSE images were used to highlight microstructural context and grain consistency, and for mounted grains no imaging techniques were employed. For monazite, and to a lesser degree titanite and allanite, internal compositional domains were identified through examination of enhanced contrast on BSE images and wavelength dispersive X-ray spectrometry element maps. Al, Ce, Fe, Nb, Ti maps were collected for titanite, and Ce, La, Th, U, Y for monazite and allanite. Zircon was imaged with a cathodoluminescence detector on a FEI Quanta 600 environmental scanning electron microscope at the British

Geological Survey (BGS), Keyworth using a 15 kV electron beam, and a working distance of 10 mm.

5.2.2 Mass spectrometry

A Nu Plasma HR multi-collector inductively coupled plasma mass spectrometer (MC-ICP-MS) with a mixed multi-ion-counter/faraday array was used for two early analytical sessions due to instrument availability. Rutile was collected over two sessions during November and December 2021 (ICSV6, ICSV12, ICSV96, ICSV97, ICSV113) while apatite was collected over one session in November 2021 (ICSV6, ICSV12). Instrument parameters are shown in the Appendix tables (A.3).

Titanite, allanite, monazite, zircon, rutile, and apatite were analysed for U-(Th)-Pb geochronology using a Nu Instruments Attom single collector inductively coupled mass spectrometer (SC-ICP-MS). Measurement was conducted in e-scan mode with a fixed magnet and a fast peak-hopping routine. Isotopes and dwell times are provided in the analytical tables. Large ion beams cannot be measured on the single ion counter, thus an attenuation grid is employed that divides the beam by approximately 260 times. Use of this attenuation grid varied for each mineral, but is especially crucial for monazite where the ^{232}Th and ^{208}Pb signals were sufficiently large to be attenuated. To avoid incorrect mass bias correction, reference materials (RMs) were measured using the same protocol as the samples - i.e., isotopes that are attenuated must match. For minerals with large signals on ^{238}U, ^{235}U is measured instead, and ^{238}U is calculated using an assumed ^{238}U/^{235}U ratio of 137.818 (Heiss *et al.*, 2012). The Attom was tuned to achieve < 0.5 % on both ThO/Th and UO/O. In addition to U-Th-Pb isotopes, the maximum mass dispersion in peak-hopping mode allows measurement down to the middle of the REE range. To potentially distinguish between multiple age populations and/or to help understand protracted ages, ^{163}Dy and ^{172}Yb were also measured in most sessions. Instrument parameters are shown in the Appendix tables (A.3).

Trace elements were measured stand-alone in titanite, and for monazite in tandem with U-Pb (via split-stream) using an Agilent 7500 series quadropole ICP-MS. Tuning was conducted to achieve < 2 % CeO/Ce and < 4% 70/140.

Two New Wave Research (now Elemental Scientific Lasers) 193nm excimer laser ablation systems were used depending on the analytical session, either coupled to a 193UC New Wave Research 193UC excimer laser ablation system

fitted with a TV32 cell, or a 193ImageGeo fitted with a TV3 cell. Both have washout times of less than 1 second, and use He as a carrier gas, which is mixed with Ar downstream before the torch using a y-piece. Static ablation spots were used for all analyses, with spot sizes varying between 12 and 35 µm, fluence varying between 2 and 3.5 Jcm^{-2}, repetition rate generally being 7 or 10 Hz, and ablation times being 20 to 30 seconds. For each session, the same ablation conditions were maintained for all samples and RMs, but initial set-up was dependent on the mineral zonation and typical signal sizes on the ICP-MS. Ablation conditions are provided in further detail in the Appendix tables (A.3).

5.2.3 Data reduction

A standard-sample bracketing routine was employed for analyses. A 60 to 100 second background was taken before every block of analyses. A 5 second wait time between ablations was given to ensure sample washout. Ablation runs were regularly separated with ablation of several matrix-matched RMs. For rutile Sugluk (1719 ± 14; Bracciali *et al.*, 2013) was used as the primary RM for all sessions, with PCA (1865 ± 7.5; Bracciali *et al.*, 2013), R10 (1095.2 ± 4.7 Ma; Luvizotto *et al.*, 2009), and R19 (489.5 ± 0.9 Ma; Zack *et al.*, 2011) used as secondary RMs. For apatite, Madagascar (475 ± 0.7 Ma; Chew *et al.*, 2014) was used as the primary RM, with McClure (523.51 ± 2.09; Schoene & Bowring, 2006) and Durango (32.716 ± 0.072; Paul *et al.*, 2021) used as secondary RMs. For allanite, Tara (418.7 ± 44.2 Ma; Gregory *et al.*, 2007) was used as the primary RM, with 40010 (2735 ± 226 Ma; Smye *et al.*, 2014), Bona (30.1 ± 0.1 Ma; von Blackenburg, 1992) and Daibosatsu (*ca.* 13 Ma; McFarlane & McCulloch, 2007) run as secondary RMs. For titanite, Ontario-2 (1053.3 ± 3.1 Ma; Spencer *et al.*, 2013b), Khan River (516.3 ± 1.3 Ma; Mazoz *et al.*, 2022) and Fish Canyon Tuff (28.402 ± 0.023 Ma Schmitz & Bowring, 2001) were run as RMs, with the primary RM of either Khan River or Ontario-2 for different sessions (based on optimal performance). Monazite 44069 (424.86 ± 0.36 Ma; Aleinikoff *et al.*, 2006) served as the primary RM, and monazites FC-1 (55.7 textpm 1.3 Ma Horstwood *et al.*, 2003) and Bananeira (507.7 textpm 1.3 Ma Gonçalves *et al.*, 2016) were run as secondard RMs. For zircon, GJ1 (601.86 ± 0.47 Ma; Jackson *et al.*, 2004) was used as the primary RM, and Temora 2 (416.78 ± 0.33 Ma; Black *et al.*, 2004) and BB9 (± 0.4 Ma; Santos *et al.*, 2017) were used as secondary RMs.

Laser conditions for each mineral phase are listed in Tables in Appendix tables (A.3). Data reduction used two primary methods, partly due to the transfer of

data reduction from an excel-based procedure to standardised procedure using the Iolite software during the course of the PhD. The first procedure uses the Attolab time-resolve software, with a NICE file for calculating mean counts and mean ratios of counts, followed by an Excel spreadsheet for drift correction, normalisation and uncertainty propagation. Using this method, downhole correction of the U-Th-Pb data assumes equivalent behaviour between samples and RMs. This procedure was used for rutile and titanite, and follows a two-step normalisation, with Pb/Pb ratios normalised to NIST glass, followed by Pb/U ratio normalisation to the matrix-matched mineral (e.g., Roberts *et al.*, 2017). The second method takes the raw time-resolved data and uses the standard U-Pb or VisualAge DRS to reduce the data in Iolite4 (e.g., Paton *et al.*, 2011). Zircon and monazite, with concordant RMs use the U-Pb Geochronology data reduction scheme. Rutile and apatite use the VisualAge data reduction scheme with NIST glass (typically NIST612) used for normalisation of Pb/Pb ratios and the matrix-matched RM used for normalisation of the U/Pb ratios. For trace elements, the time-resolved data output from the Agilent ICP-MS were normalised using the standard Trace Element data reduction scheme in Iolite4, with titanite standardisation assuming 22.45 wt % P in monazite and 19.25 wt% Ca in titanite. Zr-in-titanite temperatures were calculated using the calibration of Hayden *et al.* (2008), using the approach outlined in Section 4.2.2.3. Full trace element data are given in Appendix tables (A.3).

Uncertainty propagation follows the principles of random and systematic uncertainties as defined by (Horstwood *et al.*, 2016). Weighted mean or pooled ages comprise additional systematic uncertainties - decay constant uncertainty, RM uncertainty, and long-term excess variance. The latter is generally estimated since it is difficult to accurately measure with common-Pb bearing minerals that have heterogeneous RMs. Based on zircon, which can be assumed to be a best-case scenario, excess variance on the Attom is typically *ca.* 1.0 to 1.5 % at 2σ. Common-lead-corrected dates and uncertainties quoted from individual analyses do not include components for systematic uncertainties.

Analyses on the Nu-Attom SC-ICP-MS collect both U-Pb and Th-Pb data, thereby allowing independent age determinations to be made in either decay system. Th can be preferentially incorporated during crystallisation in place of U. Therefore, for monazite ^{232}Th-^{208}Pb ages and associated uncertainties are quoted. Titanite, allanite, rutile and apatite are all reported using the standard ^{238}U-^{206}Pb. Older zircon ages are reported using upper intercepts with concordia, or individual ^{207}Pb-^{206}Pb ages. All data and ages are shown and quoted at 2σ.

All common-lead-corrected ages use the algorithms contained within IsoplotR (Vermeesch, 2018). Common lead correction assumes concordance in the $^{238}U/^{206}Pb$ and $^{235}U/^{207}Pb$ systems; the common lead contribution is also assumed to have a composition equivalent to the terrestrial lead model of (Stacey & Kramers, 1975). The correction is similar to a simple ^{207}Pb based correction, which calculates the ratio of common ^{207}Pb to radiogenic ^{207}Pb, based upon the measured $^{207}Pb/^{206}Pb$ ratios compared to an assumed age. The assumed age is derived from the lower intercept age and the model common lead compositions are derived from Stacey & Kramers (1975) at that assumed age. The correction is conducted iteratively. In the case of the common lead corrected monazite dates presented here ($^{208}Pb/^{232}Th$), use the common to radiogenic lead contribution measured in U-Pb space, and calculate the proportion of common ^{208}Pb based on the assumed Stacey & Kramers (1975) composition; again, all dates assume concordance.

5.2.4 Data quality control

The reproducibility (i.e. precision) and accuracy of the U-Th-Pb data can be assessed by use of the secondary RMs run during each session. A summary of the pooled ages from across all sessions and key plots for each RM are provided in the Appendix (A.3). Uncertainties on the weighted mean, or intercept ages of each RM are less than 2 % in all cases, except for the common-lead-rich Bona allanite. However, these are standard error uncertainties are thus not an ideal representation of true reproducibility. The Mean Squared Weighted Deviation (MSWD) in RMs varies from 0.52 to 4.8. An MSWD of *ca.* 1 indicates that uncertainties have been accurately portrayed, and that the RM is itself homogeneous at levels suitable for the method. The high MSWDs recorded here may indicate that some uncertainties have been underestimated; however, many of these RMs are in fact heterogeneous as evidenced by ID-TIMS data, such as Bananeira monazite, Sugluk and PCA rutile, and 40010 allanite. MSWDs of primary RMs across the pooled session are always *ca.* 1, as the propagated uncertainties are estimated using multiple RMs and/or the co-analysed NIST glass or zircon. Offsets from the true age, an indication of accuracy, are generally less than 1 % or better than 2 % depending on the mineral. A few outliers include: Bona allanite, which had a very imprecise age estimate, and FC1 monazite. The latter is reverse discordant, and the true Th-Pb age is unknown; if closer to the $^{207}Pb/^{235}U$ age, then the age offset would be reduced. Overall, the RM data indicate that the sample data presented are generally both reproducible and

accurate to better than 2%. For uncertainty propagation of quoted ages on pooled on mean dates, a systematic uncertainty component of 2% (2 σ) is added to account for long-term reproducibility.

5.2.5 Nu-Attom and Agilent (LASS)

Analysis of monazite separates from three samples (ICSV12, ICSV18 and ICSV151) were undertaken during a single session in March 2023 using a split-stream set-up. The Nu Attom and laser were configured and run as described above. In addition, an Agilent 7500 quadrupole ICP-MS was used to measure specific trace elements; isotopes and dwell times are provided in the analytical protocol table (A.3), and the total sweep time equated to 2 seconds. The Agilent was tuned to achieve < 3 % CeO/Ce (i.e., oxides) and < 2 % 70/140 (i.e., doubly charged species). After leaving the laser cell, the He carrier gas was combined with Ar gas from a Nu Instruments DSN-1000 desolvating unit. This was split at a Y-piece to feed both ICP-MS instruments. Prior to entering the torch, the gas line was merged again at a Y-piece with another source of Ar carrier gas from each instrument's internal mass flow controller. This setup allowed independent control of the He to Ar ratio for each ICP-MS, and the ability to adjust the signal for a solution aspirated through the desolvating unit. The setup is illustrated in Figure 5.2.

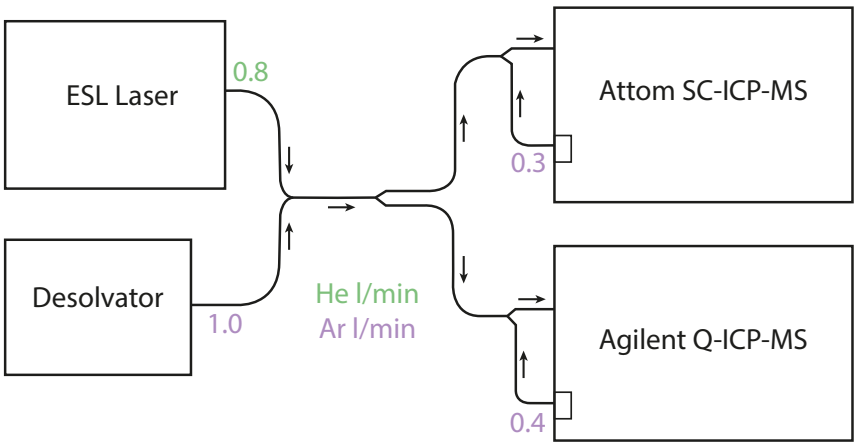


Fig. 5.2 LASS setup using an Elemental Scientific Lasers 193nm excimer ImageGeo laser ablation system, Nu Instruments DSN-1000 desolvating unit, Nu Instruments Attom single collector ICP-MS, and Agilent 7500 quadropole ICP-MS

Data reduction of the U-Th-Pb data followed the procedures outlined above, using Iolite4 (Paton *et al.*, 2011) and the U-Pb Geochronology data reduction scheme. Data reduction of elemental concentrations from the Agilent also used Iolite4 with the standard Trace Elements data reduction scheme. Internal stan-

dardization used ^{31}P assuming 22.45 wt% for all sample and RM analyses. Data were normalised to Bananeira monazite, using a combination of values from Gonçalves *et al.* (2016); Kylander-Clark *et al.* (2013), and in-house assessment. Reproducibility of the monazite validation RMs was < 10 % standard deviation for most elements. Concentrations of monazites 44069 and FC-1 broadly overlap with data published in previous papers (Gonçalves *et al.*, 2016; Kylander-Clark *et al.*, 2013; Holder *et al.*, 2015).

5.3 Titanite

5.3.1 Results

Titanite grains are hosted in a variety of lithologies and displays different microstructural associations and age groupings. Results are thereby discriminated on the basis of lithology, microstructure and metamorphic grade where relevant. Results are broadly reported from oldest to youngest. For all analysed samples, including other phases, locations for each sample are shown in Figure 5.3. BSE images were collected for all grains. Owing to the size of the dataset, X-ray compositional maps were not collected for all samples. Where such maps have been collected, relevant zoning is discussed. All ages are given as Tera-Wasserburg lower intercept ages.

Magmatic titanite grains are commonly euhedral with large crystal faces and often display patchy or oscillatory zoning (Kohn, 2017). Metamorphic titanite (either recrystallised or neocrystallised) are often subhedral to anhedral, with more lobate to rounded grain boundaries (Kowallis *et al.*, 2022). Metamorphic titanite commonly displays less consistent zoning pattern and varies from unzoned to patchy zonation. Recrystallised titanite exhibits features of both of the above characteristics.

5.3.1.1 Group 1: low-grade porphyropblastic titanite (*ca.* 38–30 Ma)

Samples ICSV139, ICSV68, ICSV142 and ICSV58 are located in the biotite zone of the metasedimentary Lamayuru Complex (Fig. 5.3), with ICSV58 located immediately down-temperature from the garnet isograd. These samples form part of the pelite, psammite, and semipelite unit (locally calcitic in psammite layers). Porphyroblastic euhedral to subhedral titanite ($\sim\leq$ 0.1–1.0 mm) is

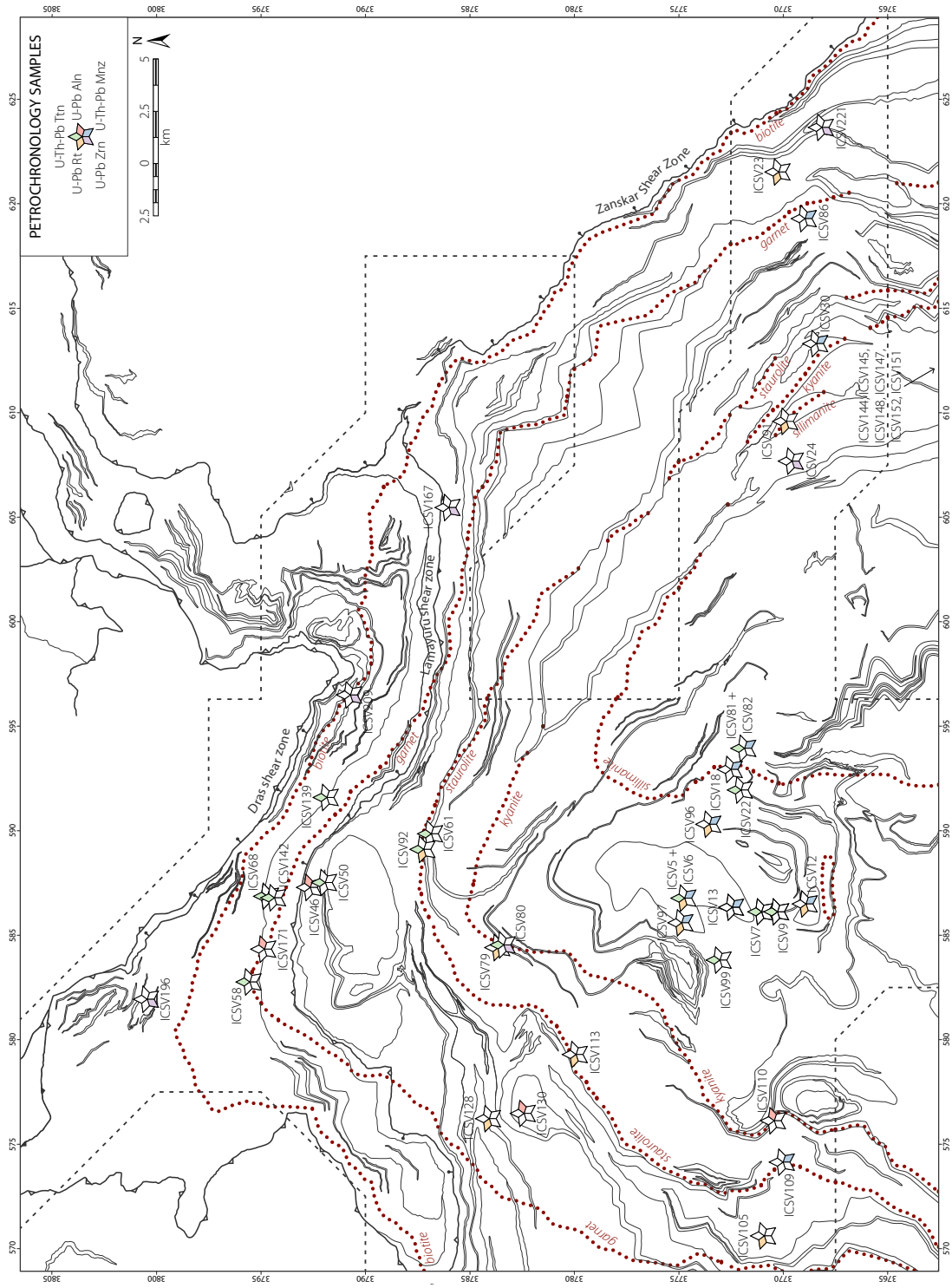


Fig. 5.3 Form-line map of major lithological, tectonic and metamorphic features of the Suru Valley area overlain with the samples used for multiphase geochronology. Coloured points on each star identify the analysed phases and isotopic system in each sample. Grid references are truncated, with the final three zeroes omitted.

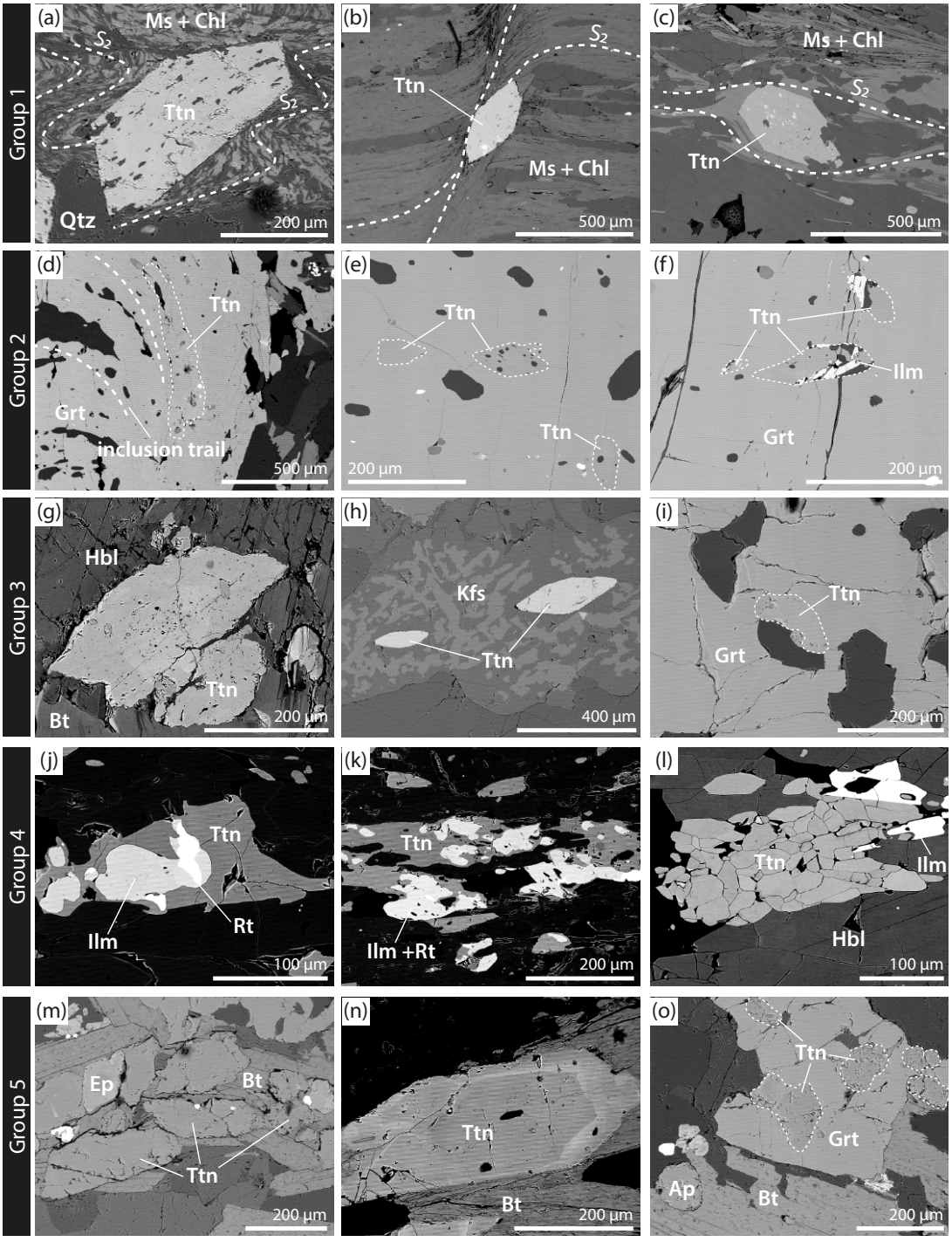


Fig. 5.4 BSE images of titanite from analysed samples documenting different microstructural associations for each group discussed in the text. Group 1 shows syn- and post-D_2 growth of titanite in biotite-grade samples. Group 2 comprises titanite within syn-D_2 garnet cores from the kyanite zone and the sillimanite zone. Group 3 shows porphyroblastic titanite in the matrix of metabasite and metamorphosed granite, titanite also locally occurring in metagranite garnet cores. Group 4 features polycrystalline titanite rims on earlier Ti-oxide phases in metabasite in the oligoclase and garnet+plagioclase zones. Group 5 shows coarse matrix titanite and titanite as inclusions in garnet.

located in pelite and semipelite layers. Samples show a dominant S_2 fabric with locally developed D_3 crenulations. Titanite dominantly overgrows the matrix S_2 fabric with matrix concordant inclusion trails, though it can be re-oriented into alignment with S_3 (Fig. 5.4a, b). This suggests inter-tectonic growth. ICSV142 also locally shows titanite wrapped by the S_2 fabric with concentric inclusion traces suggesting concurrent fabric development and porphyroblast growth (Fig. 5.4c). Titanite growth at these structural levels is therefore defined as syn- to post-D_2.

BSE images show grains with thick inclusion-rich cores that transition to thinner inclusion-poor rims. Cores are locally slightly lighter than rim domains. X-ray element concentration maps generally show minor compositional zoning. Locally grains are host to patchy Ti depleted and Al enriched cores, and Nb zoning is documented (Fig. 5.5a). This zoning is interpreted to reflect compositional variation during growth (Holder *et al.*, 2019).

All samples contain low to moderate U concentrations (0.7–143.8 ppm), and common Pb (^{238}U-^{206}Pb dominantly ranges from ~0–21), resulting in moderate to large age uncertainties. The following ^{238}U-^{206}Pb intercept ages were measured: in ICSV139, 108 analyses on 12 grains yield an age of 36.4 ± 9.8 Ma (MSWD = 0.71); in ICSV68, 170 analyses on 23 grains yield an age of 34.3 ± 4.1 Ma (MSWD = 2.7); in ICSV142, 57 analyses on 9 grains yield an age of 37.6 ± 7.6 Ma (MSWD = 1.1); and in ICSV58, 87 analyses on 6 grains yield an age of 30.2 ± 6.8 Ma (MSWD = 0.71; Fig. 5.7). In each sample a single age population is measured, although minor mixing is observed in ICSV68, resulting in a higher MSWD (2.8) possible indicating an older age component.

5.3.1.2 Group 2: porphyroblast hosted titanite(*ca.* 46–37 Ma)

Sample ICSV7 is located in the kyanite zone and ICSV82 in the sillimanite zone with both part of the mixed psammite, pelite, and semipelite unit (Fig. 5.3). Both samples host titanite within coarse euhedral to rounded garnet grains, and with ilmenite or rutile being the matrix Fe-Ti-oxide phase.

Titanite in ICSV7 is characterised by fine–coarse elongate grains with cuspate grain boundaries. Garnet grains have helicitic to snowball inclusions trails with titanite aligned with the trace of inclusions (Fig. 5.4d). The dominant matrix fabric is S_2. Garnet grains locally show minor continued growth after development of strain caps. Titanite grain size shows a relative increase from core to rim. In

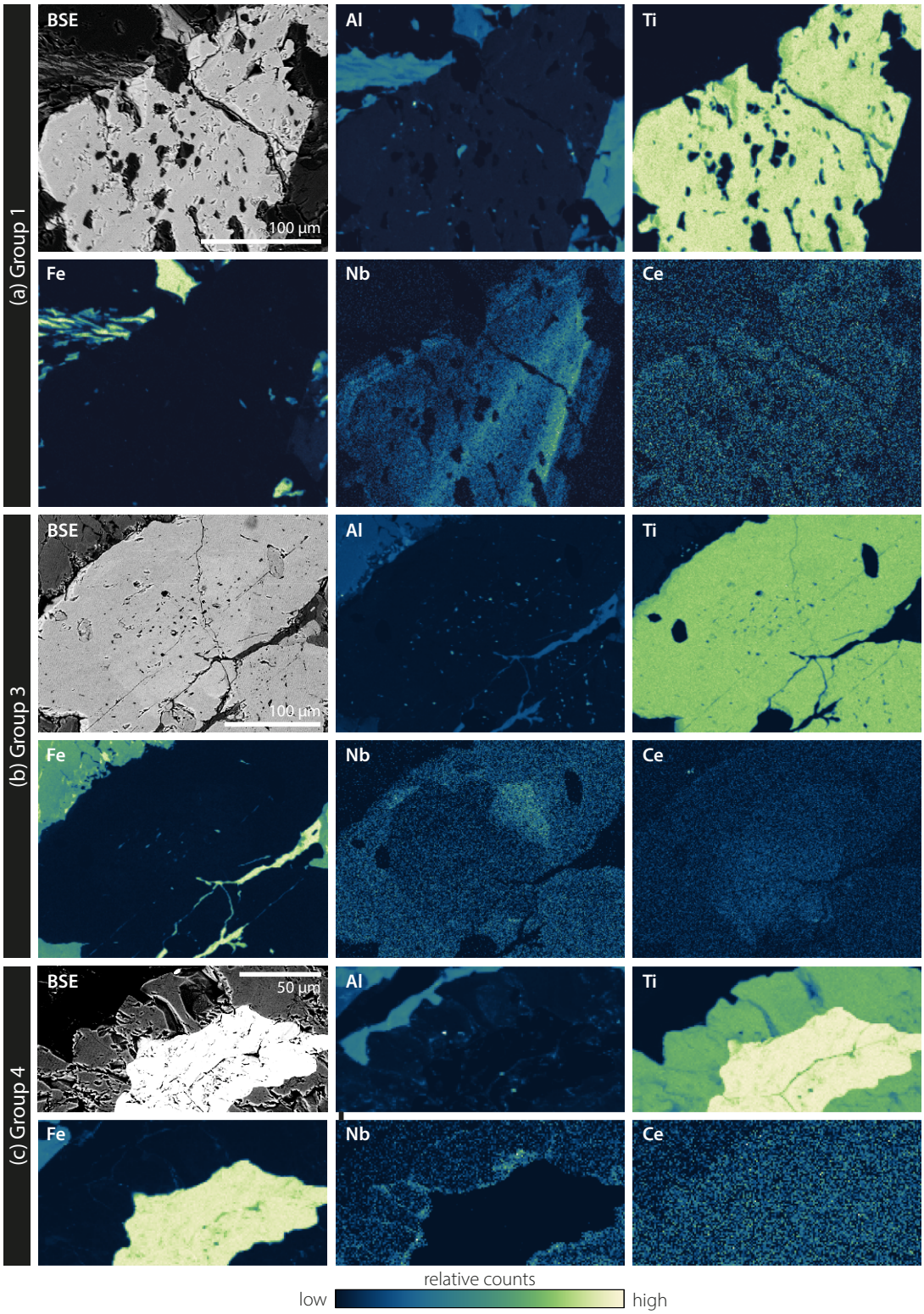


Fig. 5.5 X-ray compositional zoning maps of titanite grains in group 1, 3 and 4 titanite. Grains are from samples ICSV58, ICSV144 and ICSV99 respectively.

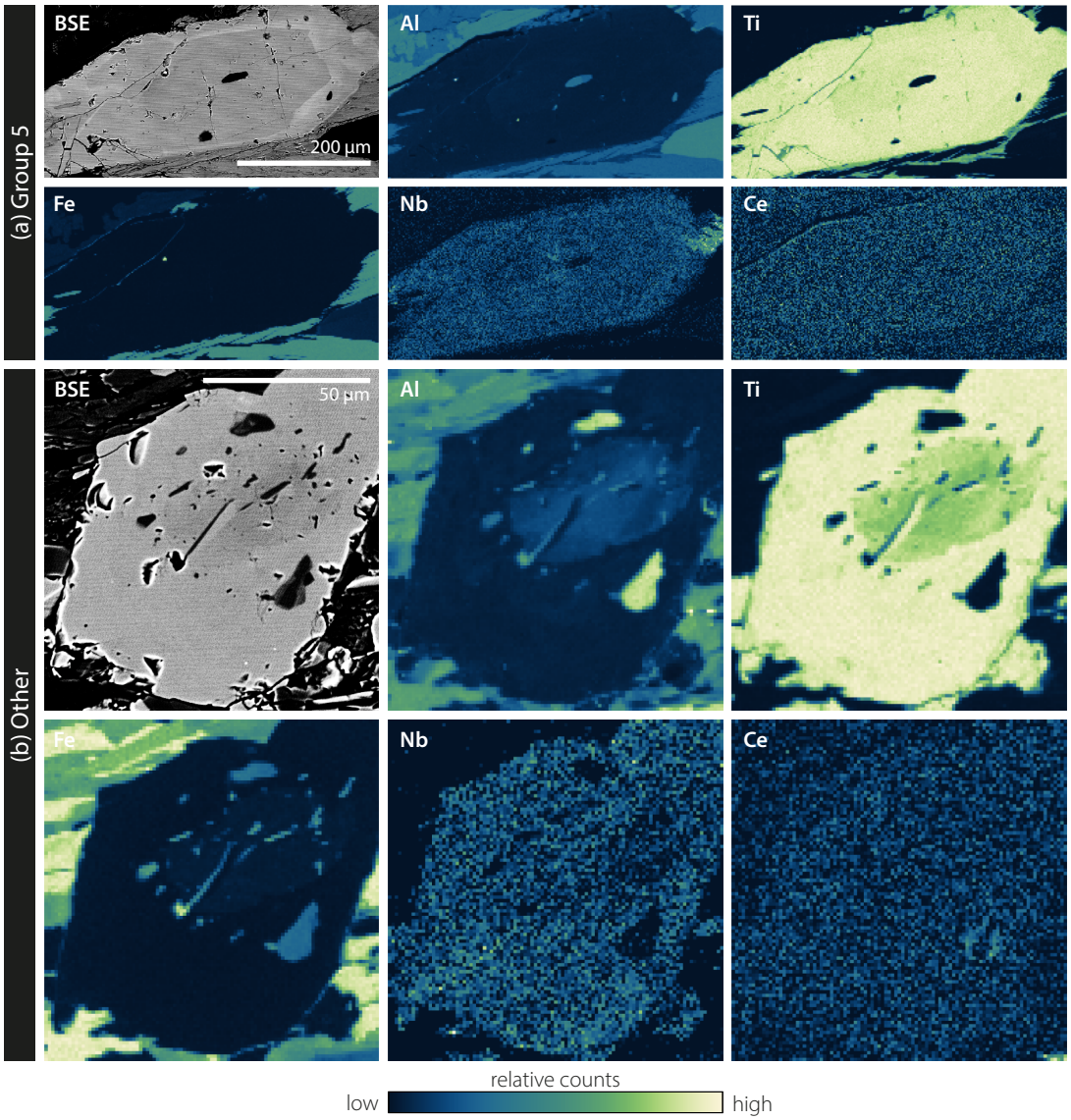


Fig. 5.6 X-ray compositional zoning maps of titanite grains in group 5 (sample ICSV9) and ICSV50.

domains of continued growth ilmenite locally mantles titanite or is the dominant Ti-oxide within the garnet rims. These observations suggest titanite growth either predated garnet growth or was concurrent with dominantly syn-D_2 garnet. Titanite is locally fractured and contain small rounded inclusions (Fig. 5.4d), no compositional zoning was recorded in BSE.

ICSV82 contains highly fractured garnet, with one grain preserving abundant small (60–100 µm in length) euhedral titanite grains within inclusion-rich garnet cores. Garnet cores dominantly show straight inclusion trails that are disjunctive with the dominant matrix S_3 fabric. Garnet rims are inclusion poor with a sharp core to rim boundary suggesting distinct phases of garnet growth. Titanite grains

contain small rounded quartz grains and in BSE show patchy brighter cores (Fig. 5.4e, f). Where titanite is adjacent to fractures, ilmenite growth occurs as a replacement of titanite rims, although this does not extend past the fractured domain, suggesting that titanite was the only Ti-oxide present during garnet growth (Fig. 5.4f).

Both samples contain low–moderate U concentrations (1.5–115.0 ppm) and abundant common Pb (^{238}U-^{206}Pb ratio of ~1–19) leading to large age uncertainties. In ICSV7, 137 analyses yield an ^{238}U-^{206}Pb intercept age of 46 ± 10 Ma (MSWD = 0.83). In ICSV82, 16 analyses from 13 grains yield an ^{238}U-^{206}Pb intercept age of 36.6 ± 10.6 Ma (Fig. 5.7).

5.3.1.3 Group 3: high-grade coarse titanite (*ca.* 22–21 Ma)

Samples ICSV144 and ICSV148 are located in the highest-grade sillimanite (or garnet+plagioclase, ICSV144) and sillimanite+K-feldspar zones (ICSV148; Fig. 5.3). ICSV144 is a metabasite of group A metavolcanic rock and ICSV148 is a metamorphosed granite. Both samples preserve moderate–coarse grained euhedral titanite that is dominantly hosted in the matrix; in ICSV148 titanite is also located in the cores of poikiloblastic garnet.

Titanite within ICSV144 occurs as coarse euhedral to oval grains hosted in the matrix. In BSE, cores are locally brighter (Fig. 5.4g) and X-ray compositional maps display minor compositional zoning in select grains with Nb-poor cores and patches of Nb-enriched domains in the mantle. Locally Ce is enriched adjacent to fractures (Fig. 5.5b). Dominantly grains show minimal to no zoning profiles. Titanite in ICSV148 vary from euhedral to rounded grains located in the matrix or within poikiloblastic garnet. BSE images consistently shows thin brighter rims on most matrix and garnet hosted-titanite phases. Locally titanite hosted within K-feldspar grains shows no obvious variation between core and rim.

ICSV144 displays a single age population with grains displaying a cluster at the common lead intercept (0.5–0.9) and another with higher ^{238}U-^{206}Pb ratios (3.6–10.8). U concentrations are low–moderate (3.5–137.2 ppm) A series of points show potential mixing towards an older domain (Fig. 5.7). 68 analyses from 9 grains yield a ^{238}U-^{206}Pb interept age of 20.8 ± 4.8 Ma (MSWD = 0.77, Fig. 5.7). ICSV148 is characterised by a single age population, 35 analyses fromm 11 grains yield a ^{238}U-^{206}Pb age intercept of of 21.8 ± 0.7 Ma. Analyses show a

consistent trend of moderately radiogenic ^{238}U-^{206}Pb ratios (between ~47–213), and moderate–high U concentrations (159.2–1777.1 ppm); Fig. 5.7).

5.3.1.4 Group 4: polycrystalline matrix titanite (*ca.* 21 Ma)

Metabasic samples from the oligoclase zone (ICSV92, ICSV61) and the garnet+plagioclase zone (ICSV117, ICSV99, ICSV5; Fig. 5.3) display abundant polycrystalline to oval matrix titanite dominantly aligned parallel to the main metamorphic fabric and mantling rutile and/or ilmenite grains (Fig. 5.4j–l). Titanite forms dominantly along grain boundaries, and locally impinges into amphibole crystals. BSE images show no consistent zoning with dominantly homogenous grains. X-ray maps show no pronounced zoning with only Nb locally enriched adjacent to rutile (Fig. 5.5c).

Most samples are dominated by common Pb with ^{238}U-^{206}Pb ratios varying from ~0–24 with low U concentrations (0.0–24.0 ppm), resulting in significant uncertainty on the intercept ages in Tera-Wasserburg space. The following ^{238}U-^{206}Pb intercept ages were measured: in ICSV92, 23 analyses yield an age of 17 ± 17 Ma (MSWD = 0.65); in ICSV61, 24 analyses yield an age of 8.6 ± 30.4 Ma (MSWD=0.58); in ICSV117, 45 analyses yield an age of 28 ± 26 Ma (MSWD = 0.82); in ICSV99, 48 analyses yield an age of 2.6 ± 26.4 (MSWD = 0.6); and in ICSV5, 67 analyses yield an age of 20.9 ± 3.3 (MSWD = 0.78). Tera-Wasserburg plots are shown in Figures 5.7 and 5.8.

5.3.1.5 Group 5: coarse matrix and porphyroblast hosted titanite (17-16 Ma))

Granite samples ICSV9 and ICSV22 are located within the kyanite and garnet+plagioclase zones (Fig. 5.3). Titanite occurs as coarse euhedral grains in both the matrix, dominantly hosted within biotite-rich layers, and locally within garnet porphyroblasts. Certain grains show upper and lower grain boundaries relative to the long axis of the mineral that are flat against biotite grain boundaries or cleavage domains (Fig. 5.4n). These observations imply that the orientation of biotite influenced titanite growth. Titanite found within garnet porphyroblasts is commonly lobate and rounded (Fig. 5.4o). Grains display prominent oscillatory magmatic zoning textures, locally defining a possible recrystallisation front on grain margins (Fig. 5.6a).

Both ICSV9 and ICSV22 are contain low–moderate U concentrations (1.7–223.3 ppm) with a spread of ^{238}U-^{206}Pb ratios from ~1–60. In ICSV9, 7 analyses on titanite grains trend towards an older intercept age with minor mixing toward the dominant trend of analyses. The remaining 79 analyses fromm 6 grains yield an ^{238}U-^{206}Pb intercept age of 15.9 ± 1.5 Ma (MSWD = 1.2). ICSV22 also shows scattering of 11 analyses that lie below the regression from common Pb in a triangular envelope, possibly reflecting an older age component; 35 analyses across 7 grains yield a ^{238}U-^{206}Pb intercept age of 17.3 ± 2.5 Ma (MSWD = 1.2, Fig. 5.8).

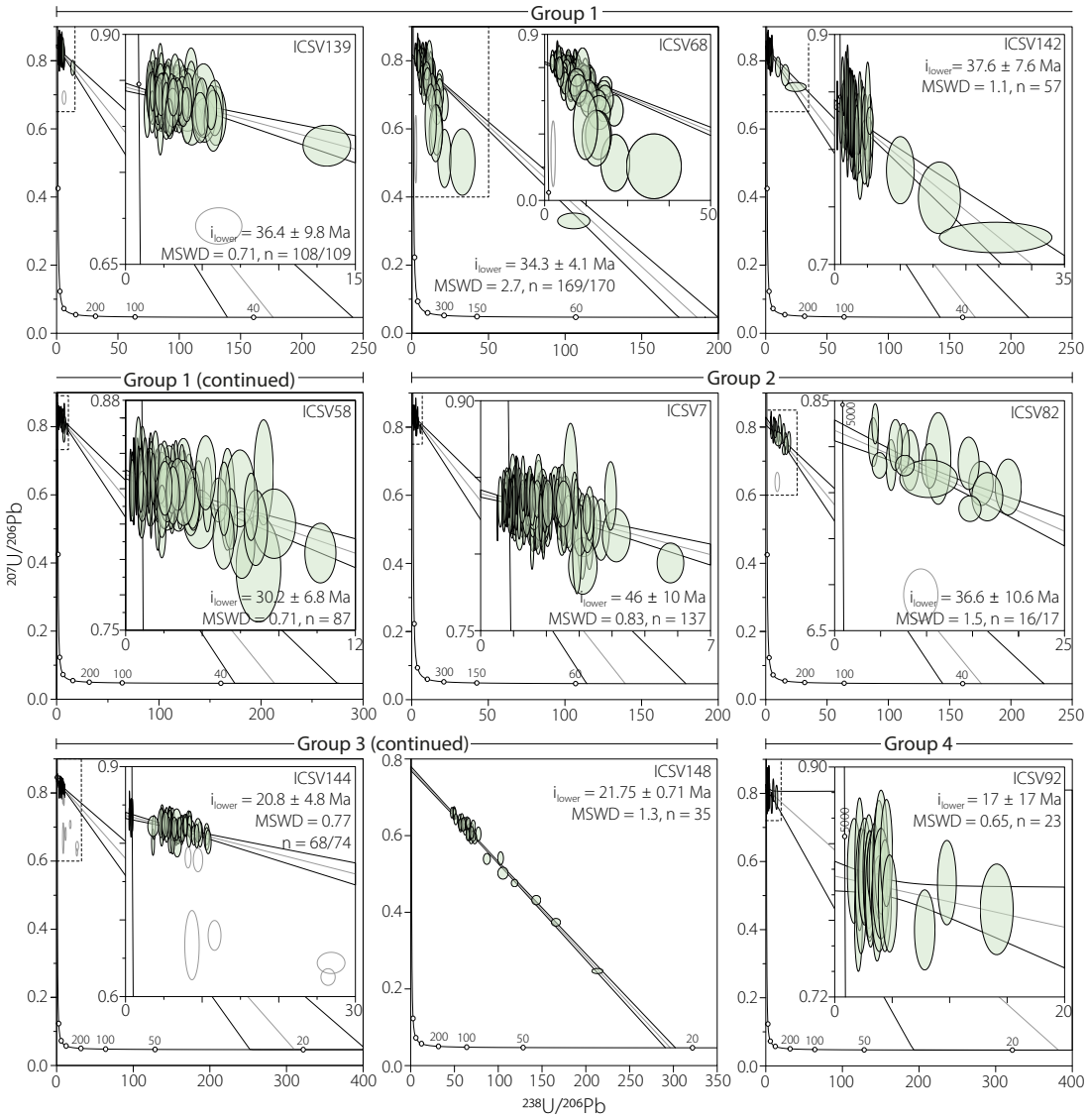


Fig. 5.7 Tera-Wasserburg plots for analysis of titanite from groups 1–4. Ages quoted are lower intercept ^{238}U-^{206}Pb ages from combined U-Th-Pb measurements.

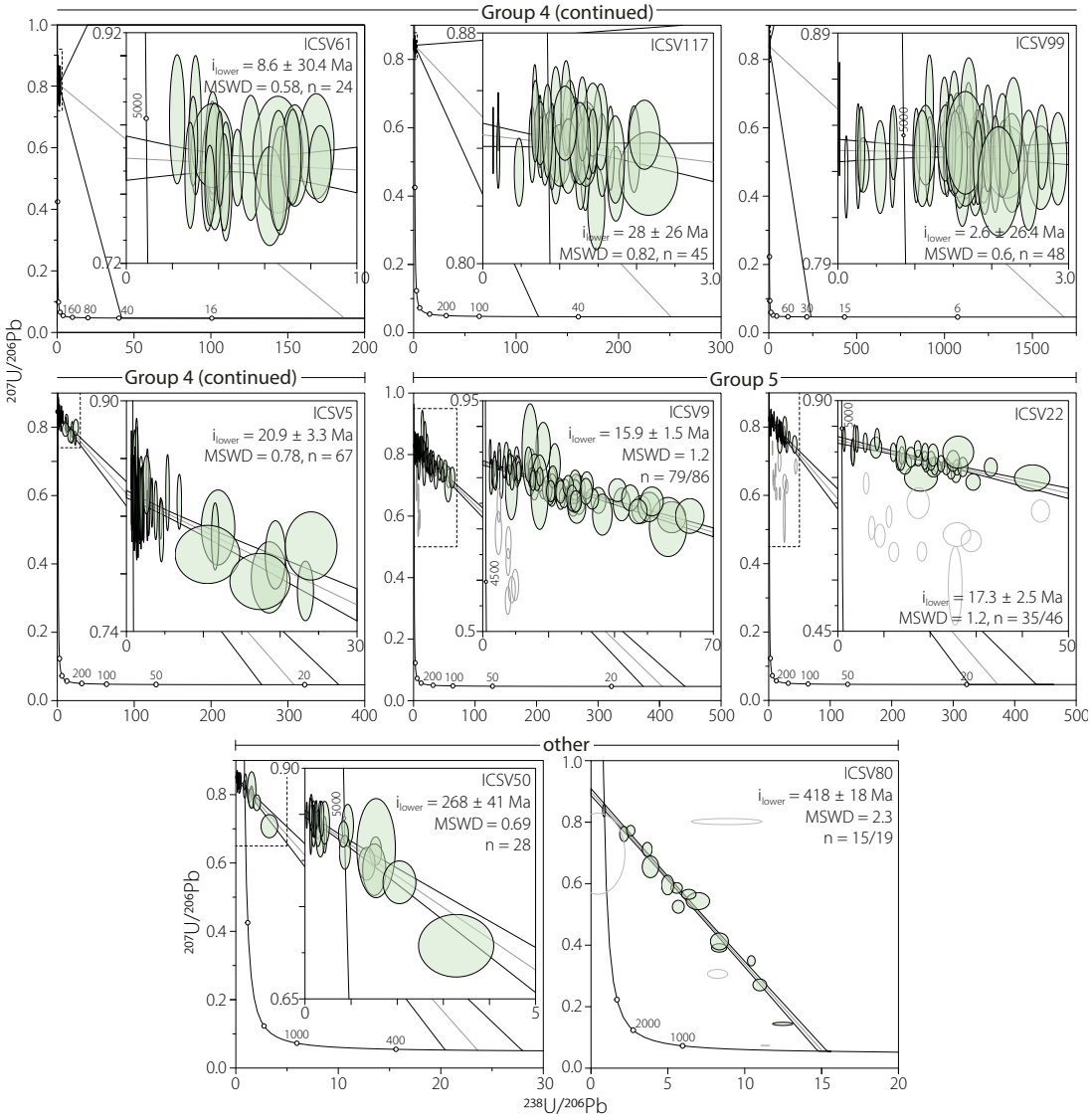


Fig. 5.8 Tera-Wasserburg plots for analysis of titanite from groups 4–5 and remaining samples. Ages quoted are lower intercept ^{238}U-^{206}Pb ages from combined U-Th-Pb measurements.

5.3.1.6 Other

The remaining samples do not conform to a consistent microstructural context or age grouping and are therefore discussed separately.

ICSV50 ICSV50 is a metabasic rock from the hornblende zone (Fig. 5.3). Titanite occurs as small euhedral to subhedral angular grains with fine inclusion-rich cores. Cores display darker oval to patchy zones in BSE. X-ray element concentration maps show consistent zoning patterns across grains. Grains records patchy to oval Ti depleted, Al- and Fe-enriched cores. Nb and Ce show no

prominent zonation, locally Nb is enriched adjacent to grain boundaries or inclusions (Fig. 5.6b).

Titanite from ICSV50 has low U concentrations (0.3–16.5 ppm) and is dominated by common Pb (^{238}U-^{206}Pb ratios betweem ~0–3), producing significant uncertainty on the regression. 28 analyses across 13 grains yield a ^{238}U-^{206}Pb intercept age of 268 ± 41 Ma (MSWD: 0.69; Fig. 5.8).

ICSV80 ICSV80 is a psammite in the staurolite zone (Fig. 5.3). Titanite is well distributed throughout the sample but occurs as fine rounded grains with angular to lobate grain boundaries. Select grains display minor patchy zonation, exhibited by lighter BSE domains; however, most grains appear homogenous.

Titanite from ICSV80 has a spread of U concentrations (12.2–643.4 ppm). Analyses from 15 spots across 12 grains yields a ^{238}U-^{206}Pb intercept age of 418 ± 18 Ma (MSWD = 2.3; Fig. 5.8), a few scattered outliers were rejected from the regression.

5.3.1.7 Zr-in-titanite and trace element discrimination

Estimates of the closure temperature of titanite (temperature at which titanite closes thermally mediated volume diffusion of Pb) vary significantly (400–800 °C, based on both empirical and experimental studies (Mattinson & Echeverria, 1980; Cherniak, 1993; Scott & St-Onge, 1995; Pidgeon *et al.*, 1996; Verts *et al.*, 1996; Kohn & Corrie, 2011; Spencer *et al.*, 2013b). Kohn (2017) reviews the issue and argues that the higher estimates are more robust and that titanite is able to record metamorphic or hydrothermal growth or recrystallisation at temperatures above 700 °C. The idea that titanite will consistently record younger ages than other high temperature minerals (e.g., zircon and monazite which are fully retentive to Pb at these temperatures; Rasmussen *et al.*, 2013), has been replaced by studies arguing that titanite ages merely record primary metamorphic growth at high temperatures, followed by fluid mediated alteration and reprecipitation at lower temperatures (Stearns *et al.*, 2016; Holder *et al.*, 2019; Holder & Hacker, 2019; Mottram *et al.*, 2019).

Common Pb and/or low U concentrations in titanite can result in poorly constrained age regressions and/or make it difficult to discriminate between different geological events or crystallisation conditions. In a sample with two (re-)crystallisation events, a given mineral with abundant common Pb will record a

triangular envelope making discrimination of distinct events difficult. Crystallisation conditions can also be discriminated using various trace element information (e.g., Stearns *et al.*, 2016; Holder *et al.*, 2019; Holder & Hacker, 2019; Olierook *et al.*, 2019; Walters *et al.*, 2022).

Due to grain size constraints and the analytical approach undertaken in this study, is was not possible to effectively constrain both age relationships and trace element systematics with relation to the same spot analyses used for U-(Th)-Pb analyses. Thus, trace elements were collected in similar spot locations to inform on general trends in (re-)crystallisation events within each sample. The results of Zr-in-titanite thermometry and trace element discrimination for samples ICSV142, ICSV68, ICSV7, ICSV5, ICSV144 and ICSV148 are discussed below.

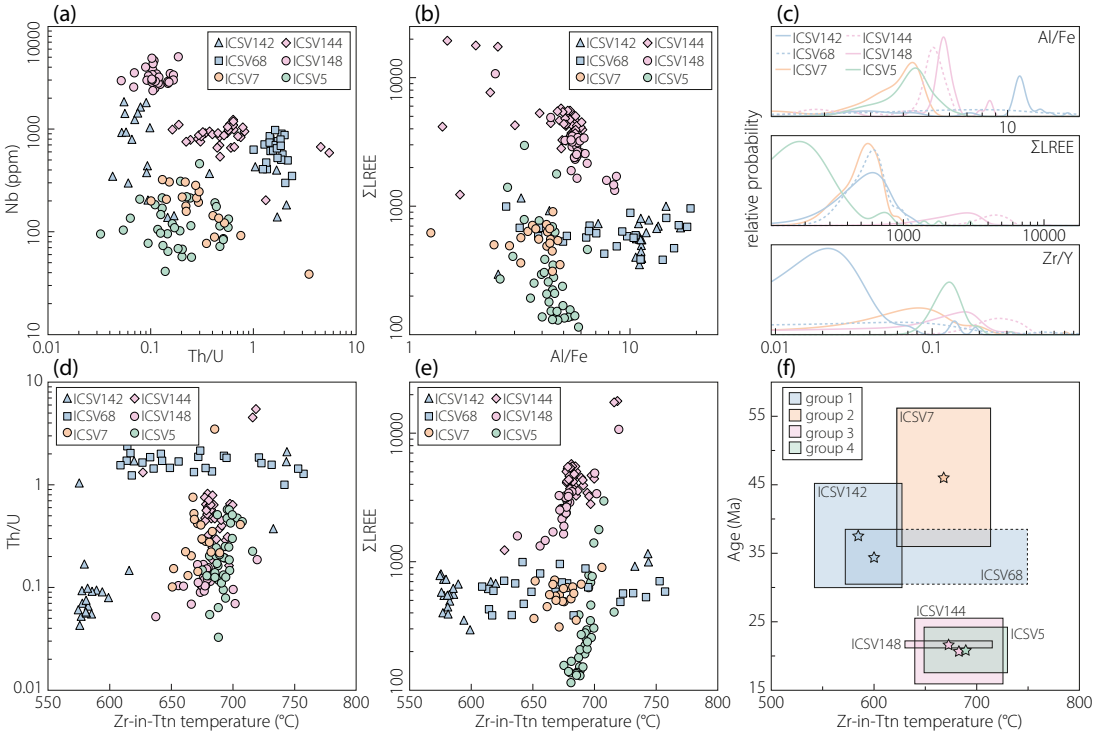


Fig. 5.9 Titanite trace element discrimination indices a) Nb vs Th/U, b) ΣLREE vs Al/Fe, c) kernel density plots for Al/Fe, ΣLREE and Zr/Y, d) Zr-in-titanite temperature vs Th/U, e) Zr-in-titanite temperature vs ΣLREE and f) Zr-in-titanite temperature vs ^{238}U-^{206}Pb-^{207}U-^{206}Pb intercept ages. The different colours correlate to groups 1–4 discussed in the text.

Zr-in-titanite thermometry results and trace element discrimination diagrams are presented in Figure 5.9. Previous studies have shown trace elements to be useful in discriminating between igneous, recrystallised and metamorphic grains, and in discriminating host rock (Olierook *et al.*, 2019; Scibiorski & Cawood, 2022). The following discriminates are used in this study:

1. Nb: Nb and other high field strength elements (HFSEs) generally occupy the octahedral Ti lattice site. Nb may substitute by $2Ti^{4+} \leftrightarrow Nb^{5+} + (Al, Fe)^{3+}$ (Vuorinen & Hålenius, 2005), with variations in metamorphic titanite potentially relating to fluid composition or source rock (Chen & Zheng, 2015; Kowallis *et al.*, 2022).

2. Th/U: Partition coefficients of Th and U vary in different co-crystallising minerals in magmatic and metamorphic systems, allowing differentiation by Th/U ratios (Tiepolo *et al.*, 2002; Olierook *et al.*, 2019).

3. Al/Fe: Al^{3+} and Fe^{3+} can substitute for Ti^{4+} in the octahedral site, with Al^{3+} generally favoured with increasing pressure (Smith, 1981). Al/Fe (or Fe/Al) has therefore been assigned as a discriminant between metamorphic and igneous titanite (Kowallis *et al.*, 2022; Scibiorski & Cawood, 2022). Al/Fe ratios of $> 2{:}1$ are characteristic of igneous phases and $< 2{:}1$ for most metamorphic phases, though discrimination is mostly achieved at the 1:1 boundary (Kowallis *et al.*, 2022).

4. ΣLREE: Igneous and metamorphic titanite can be discriminated based on ΣLREE (Scibiorski & Cawood, 2022). LREE is defined here as La–Sm; excluding Pm (not analysed). Fluid or melt composition may exert primary control on the ability of trace elements to substitute for mineral-forming elements at different *P-T* conditions. Igneous titanite can crystallise late, resulting in incompatible elements and REE concentrated in the residual melt; these may subsequently be incorporated into titanite (Kohn, 2017). Igneous and recrystallised titanite can display concentric REE zoning patterns (Olierook *et al.*, 2019). Metamorphic fluids serve as a dominant source of trace elements for metamorphic titanite. It has been argued that fluids possess a more uniform chemical composition compared to magma, therefore, metamorphic titanite normally appears relatively homogenous (Olierook *et al.*, 2019). Trace elements may also be liberated through the breakdown of precursor minerals; however, when these elements are bound up or partitioned among other phases, they become inaccessible for the formation of newly crystallizing metamorphic titanite (Scibiorski & Cawood, 2022).

5. Zr-in-titanite: Zr^{4+} substitutes for the octahedral Ti site (similar to Nb). The degree of substitution is dominantly temperature and pressure controlled but shows sensitivity to deformation and co-crystallisation of other Si-, Ti- and Zr-bearing phases (Hayden *et al.*, 2008).

Figure 5.9a shows that the greatest Nb values are recorded in titanite from groups 1 and 3 which are hosted within calc-pelite, granitic and metabasic bodies. Samples from group 1 and 3 consistently display notably weak Nb-zonation patterns that increase from core–rim in X-ray elemental concentration maps. Th/U broadly cluster as both the lowest and highest values in group 1, with the highest values recorded in ICSV68 which displays consistent heterogeneity across Zr-in-titanite temperatures (Fig. 5.9c). High Th/U is attributed to recrystallised or igneous titanite. A Th/U ratio of > than 1 has previously been used to discriminate igneous (>1) from metamorphic titanite (<1), however, used in isolation has shown to have variable success (Scibiorski & Cawood, 2022). The significant variation within group 1 samples is notable owing to the near identical, mineral assemblage, texture, structural level, and lithology. ICSV142 is found 300 m up grade and across strike from ICSV68, yet ICSV68 preserves a range of Zr-in-titanite temperatures extending to higher temperatures. It is inferred that this significant variation in trace element discriminators may be indicative of recrystallisation, which is supported by high Th/Pb ratios documented during U-(Th)-Pb analyses (Olierook *et al.*, 2019), decoupling between trace element tracers and U-Pb age (Cherniak, 2015), or smearing of growth zonation as expressed by Nb variation (e.g., Holder *et al.*, 2019).

Discrimination between igneous and metamorphic titanite using the approach of Scibiorski & Cawood (2022) as shown in Figure 5.9b, c shows that all samples are largely dominated by moderate–high Al/Fe ratios and moderate to low ΣLREE consistent with metamorphic and/or recrystallised titanite. Select analyses in group 3 (dominantly ICSV144) have low Al/Fe and high ΣLREE trending towards the igneous discriminator boundary. Groups 3 and 4, despite both containing metabasite samples (ICSV144 and ICSV5) record vastly different ΣLREE (Fig. 5.9b, c), consistent with their varying microstructural characteristics. LREE are preferentially incorporated over HREE at higher temperatures, however, despite consistent rock type and Zr-in-titanite temperatures, ΣLREE varies significantly. This suggests trace element mobility or availability during crystallisation or recrystallisation conditions differed considerably. ICSV5 shows irregular lobate titanite growth around precursor Fe-Ti-oxides, whereas ICSV144 preserves coarse wedge-shaped matrix titanite. Based on shape, zoning patterns and the triangular envelope recorded in ICSV144 (Figs 5.4 & 5.7), titanite is most convincingly interpreted as magmatic in origin, with subsequent recrystallisation during metamorphism. The shape and homogenous zoning pattern of titanite in ICSV5 are more consistent with a neocrystallised metamorphic titanite. Ow-

ing to the high ΣLREE in ICSV5, and rutile cores on which titanite nucleates, and relatively depleted source of REE rutile represents, an external or different internal fluid source is required. Breakdown of epidote, garnet or amphibole during decompression would provide an appropriate REE budget for titanite (Zhao *et al.*, 2023). Epidote is only preserved to peak pressures in one group 4 sample (ICSV92) and garnet locally shows thin minor decompression rims with no obvious association to titanite growth. Titanite is observed to impinge on amphibole grain boundaries, as such it is cautiously inferred that amphibole acts as a source for titanite REE concentrations in group 4 samples.

For the suite of samples analysed the following discriminations prove most effective. Group 1 is discriminated based on low Th/U ratios, moderate–high Al/Fe and low Zr-in-titanite temperatures. Group 2 is best discriminated based on low–moderate values of nearly all characteristics, and can be best distinguished from similar composition of group 4 by documenting relatively lower Zr/Y concentrations (Fig. 5.9c) and higher ΣLREE. Group 3 is distinguished by moderate–high Nb, high ΣLREE and moderate Al/Fe with localised low Al/Fe analyses. Group 4 contains similar characteristics to group 3 and can be discriminated using the aforementioned criteria.

A summary of Zr-in-titanite temperatures correlated with the measured age of each sample are presented in Figure 5.9f and show 3 prominent distributions. Owing to the following characteristics of ICSV68: 1) the uncertainty over the distribution of trace element discriminators and Zr-in-titanite thermometer age, and 2) the proximity and similarity of samples ICSV142 and ICSV68, the intersection of the two samples is taken as a more accurate representation of the conditions of titanite (re-)crystallisation in ICSV68. Group 1 is best defined by the youngest age population and temperatures. Although group 2 records even younger ages, the 10 Ma uncertainty must be taken into account. Furthering this uncertainty, are unreasonably high Zr-in-titanite thermometry results. Based on the consistency of thermometry results across the full dataset (Fig. 4.17), Zr-in-titanite thermometry results are coincident with a thermal peak for adjacent samples (e.g., ICSV5). Temperatures do not match the well-defined prograde conditions that may be inferred from the given microstructural context. It is suggested that Zr-in-titanite thermometry does not represent crystallisation conditions for this sample. This requires either decoupling of U-Pb age and trace element systematics from deformation (e.g., Gordon *et al.*, 2021; Kavanagh-Lepage *et al.*, 2023), or continuous equilibration of Zr concentrations when temperature increases to peak, similar to Zr-in-Rt thermometry (e.g., Penniston-Dorland *et al.*, 2018; Kohn,

2020). The final grouping of samples correlates with recrystallised magmatic titanite and neocrystallised metamorphic titanite occurring at high temperatures at well-defined overlapping ages *ca.* 21 Ma.

5.3.2 Interpretation

5.3.2.1 Pre-Himalayan metamorphism and magmatism

The oldest age is recorded in sample ICSV80 which yields 418 ± 18 Ma. It is inferred that titanite is originally metamorphic and may relate to the well documented Cambro-Ordovician event at *ca.* 490–460 Ma (Cawood *et al.*, 2007; Palin *et al.*, 2018). Localised patchy BSE zones at grain boundaries of rounded titanite grains, and slight dispersion of analyses in Tera-Wasserberg space, suggests subsequent partial recrystallisation during the Himalayan metamorphic cycle has disrupted the U-Pb systematics.

A Permian age is recorded by ICSV50 (268 ± 41 Ma). The limited number of titanite analayses (n = 28), reflecting the small grain size; the low U concetration; and dominance of common-Pb, has produced significant uncertainty on the regression. This age broadly correlates to a known Permian rifting event (Shellnutt *et al.*, 2011; Shellnutt, 2018). This is documented by the volcanic rocks of the voluminous Panjal Traps, found throughout Kashmir and western Zanskar - locally dated at 289 ± 3 Ma (U-Pb zircon; Shellnutt *et al.*, 2011) and 288.2 ± 0.3 Ma (U-Pb zircon, CA-ID-TIMS; Chen *et al.*, 2023). The occurrence of Permian granites across Zanskar is now well documented, with ages ranging from *ca.* 284–268 Ma (this study; Horton & Leech, 2013; Noble *et al.*, 2001; Spring *et al.*, 1993). ICSV50 structurally overlies the Sankoo monzogranite dated at 268 ± 5 Ma (U-Pb zircon Noble *et al.*, 2001). Mixing and regressions towards similar age brackets can be inferred for select analyses in ICSV9, ICSV22 and ICSV144. ICSV9 and ICSV22 and can be defined by the lowest bracket of the triangular envelope trending back towards *ca.* 280 Ma, consistent U-Pb zircon ages from these localities (Horton & Leech, 2013; Walker *et al.*, 2001). Mixing of ages in ICSV144 is less obvious, but given a consistent lithostratigraphic unit to ICSV50, it is inferred that a Permian magmatic age might be indicated prior to Himalayan recrystallisation.

Older ages are also recorded within titanite from Group 1 owing to the triangular envelope of spot analyses trending from common Pb (e.g., ICSV68). Taking the densest population of age spots (those located within the inset on

Fig. 5.7) would produce a regression of 57.3 ± 5.2 Ma overlapping with the onset of collision between India-Asia (see summary in Parsons *et al.*, 2020). However, taking a subset of spot analyses at the lower base of the triangular envelope would produce a regression towards *ca.* 125 Ma, near the timing of thrusting and suturing of the Dras Arc (see summary in Bhat *et al.*, 2019a). Given the proximity of the sample to the Dras Arc, the older titanite spectra might relate to the thrusting of the Dras Arc onto the Indian shelf sequence, further analysis is required to deconvolve the relationship. It is worth noting that calc-silicate samples commonly record partial recrystallisation of older phases (Mottram *et al.*, 2019).

5.3.2.2 Prograde–peak

Prograde to peak metamorphic ages are recorded in group 1 and group 2 samples. Group 1 samples record overlapping ages from three samples at 36.4 ± 9.8 Ma, 34.3 ± 4.1 Ma (using the preferred age from ICSV68), and 37.6 ± 7.6 Ma, along with one other sample at 30.2 ± 6.8 Ma. Although varying age populations may be distinguished in ICSV68, it must also be recognised that other samples from group 1 show syn- or post-tectonic relationships to the main S_2 fabric and are clearly re-oriented by S_3 (Fig. 5.4a–c), suggesting single age populations are likely coincident with metamorphic growth. ICSV142 records the oldest age at 37.6 ± 7.6 Ma and is the only sample to preserve syn-D_2 titanite. Other samples all contain post-D_2 titanite. D_2 may therefore be interpreted to be waning at these structural levels by *ca.* 38 Ma. Zr-in-titanite temperature of 585 °C (± 43 °C) is taken as a broadly representative temperature of crystallisation at these structural levels.

Group 2 titanite occurs within garnet cores. Cores are interpreted to represent syn-D_2 growth, with titanite in ICSV7 showing syn-tectonic growth and titanite in ICSV81 associated with the syn-D_2 garnet growth domains constraining D_2 between 46 ± 10 and 36.6 ± 10.6 Ma. Similarly, titanite is not the Ti-oxide phase preserved in the matrix, suggesting the ages are associated with prograde conditions. A Zr-in-titanite temperature of 668 °C (± 46 °C) in ICSV7 is inferred to be consistent with thermal peak rather than crystallisation conditions.

ICSV7 is located in the kyanite zone and ICV82 in the sillimanite zone, and thus the age gap may represent the progression of metamorphic conditions down structural level. However, owing to the large uncertainty, it is likely that this occured over significantly less than a 10 Ma period. Post-tectonic growth of

garnet rims, and therefore thermal peak in the sillimanite zone (which may not be coincident with sillimanite-growth, see Chapter 4), must occur after *ca.* 37 Ma.

These ages represent some of the oldest titanite dates from the metamorphosed Indian sedimentary sequence. In Nepal, the oldest titanite ages in the HMC generally cluster from *ca.* 31–29 Ma (Johnson *et al.*, 2021; Mottram *et al.*, 2019; Rapa *et al.*, 2017; Walters & Kohn, 2017). However, a study by Kohn & Corrie (2011) record protracted ages spanning from *ca.* 37–24 Ma.

5.3.2.3 Decompression

Group 3 titanite are located within metamorphic grades (sillimanite and sillimamnite+K-feldspar zones) reflecting decompression from thermal peak. Group 3 samples are interpreted as magmatic grains that recrystallised at 20.8 ± 4.8 Ma and 21.8 ± 0.7 Ma. Zr-in-titanite temperatures are clustered at 673–683 °C (± 43 °C). Titanite grains in ICSV148, a sample located at the highest metamorphic grade (sillimamnite+K-feldspar zone), are found in both the matrix and as inclusions in garnet and yet comprise a consistent age population. Garnet shows angular boundaries against both matrix and inclusion phases, with these observations being inconsistent with textures expected for a peritectic phase (Waters, 2001), therefore titanite growth might occur prior to garnet growth. Consistent with the lithology (granitoid), titanite growth is likely magmatic. This is supported by grain habit, zoning patterns, higher U concentrations (indicative of an older age), BSE textures and microstructural context.

Rutile rimmed by titanite is a commonly identified decompression features in high-pressure terranes (e.g., Harlov *et al.*, 2006; Cruz-Uribe *et al.*, 2014; Lucassen *et al.*, 2010; Zhao *et al.*, 2023) and is clearly documented in group 4 samples (Fig. 5.4j–k). Nb enrichment at titanite-rutile boundaries indicate Nb back-diffusion to rutile (Cruz-Uribe *et al.*, 2018; Lucassen *et al.*, 2010). ICSV5 records an age of 20.9 ± 3.3 Ma and crystallisation temperature of 689 ± 41 °C, in agreement with the group 3 ages and Zr-in-titanite temperatures. Similar microstructural and textural features for ICSV92, ICSV61, ICSV117 and ICSV99, suggest they would likely record similar ages to ICSV5 if more U has been incorporated into the crystallising titanite. The dominance of Rt and/or Ilm as the Ti-oxide phase in un-zoned garnet, where garnet chemistry is indicative of the thermal peak, corroborates that titanite growth must occur after the thermal peak. The common occurrence of titanite rims on rutile attest to P-T paths that evolved with relative

increases in temperature or decreases in pressure. The consistency of temperature conditions between Hbl-Pl thermometry and Zr-in-titanite thermometry (Fig 4.17) suggest that this documents dominantly isothermal decompression.

5.3.2.4 Recrystallisation and cooling

Group 5 samples display significant patchy recrystallisation at grain margins (Fig. 5.4). Ages are recorded at 17.3 ± 2.5 and 15.9 ± 1.5 Ma. Despite a similar structural level as ICSV5, these ages are noticeably younger. Grain shape, zoning patterns, and age distribution suggest magmatic grains subject to significant late retrograde recrystallisation. Recrystallisation and or re-equilibration of these samples provide the youngest age recorded from titanite in the Suru Valley region.

5.4 Allanite

5.4.1 Results

Locations for the four analysed samples are shown on Figure 5.3 with microstructural context and X-ray maps in Figures 5.10 and 5.11, and U-Pb Tera-Wasserburg plots are in Figure 5.12.

5.4.1.1 Biotite- & garnet-zone pelite: porphyroblastic allanite

ICSV171 ICSV171 is a part of the semipelite, psammite, and pelite unit of the Lamayuru Complex (Fig. 5.3). Samples ICSV142, ICSV68, ICSV139 and ICSV58 (analysed for titanite) are also from this unit. ICSV171 contains both porpyhyroblastic titanite and allanite. Titanite shows a similar post-D_2 origin as detailed previously. Allanite from ICSV171 occurs as oval euhedral to subhedral grains with reaction halos (Fig. 5.10a). Allanite shows similar relations to titanite, with no obvious perturbation of the matrix fabric with respect to allanite grains and associated reaction halos. Grains show minor realignment along developing D_3 crenulation cleavages. BSE images commonly exhibit patchy linear compositional zoning. X-ray compositional maps show minor zoning for the analysed elements (Y, La, Ce, Th, U; Fig. 5.10g). Y displays minor patchy zoning. Th and U contents of grains are very low or below detection limits. Minor Th enrichment is recorded as thin discontinuous rims. Grains contain low La concentrations with minor increase in rim domains. Ce shows the reverse zoning

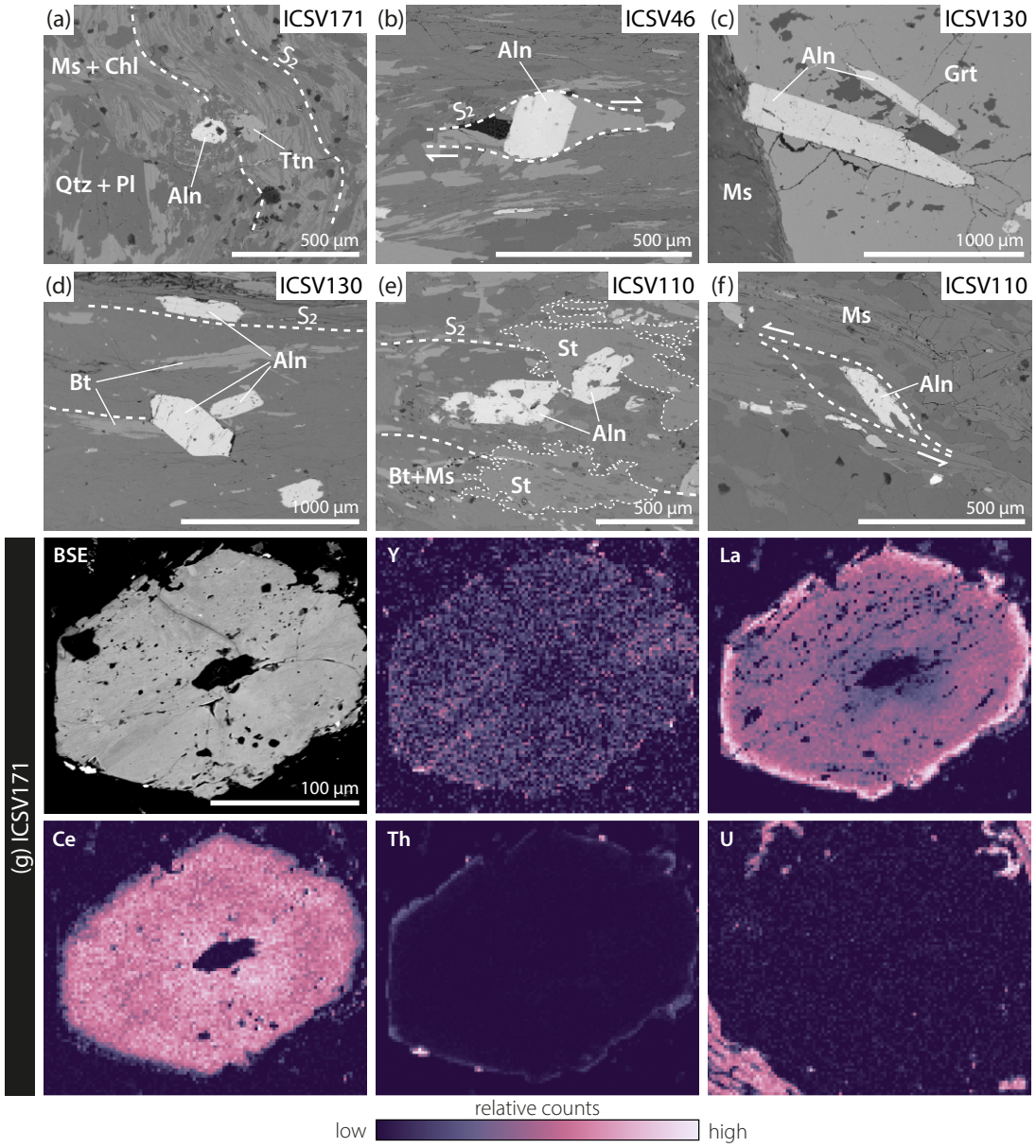


Fig. 5.10 BSE images of the various microstructural context of allanite, as well as BSE images and X-ray compositional maps of allanite grains from sample ICSV171

pattern. Thin Ce-depleted rims are not inferred to represent epidote owing to lack of variation denoted on BSE images.

41 analyses on 7 grains yields a $^{238}U/^{206}Pb$ age intercept of 15 ± 19 Ma (MSWD = 0.86). Low–moderate U concentrations (29–253 ppm) and/or abundant common Pb ($^{238}U/^{206}Pb$ ratios of ~2–10) produce significant uncertainty on the regression (Fig. 5.12).

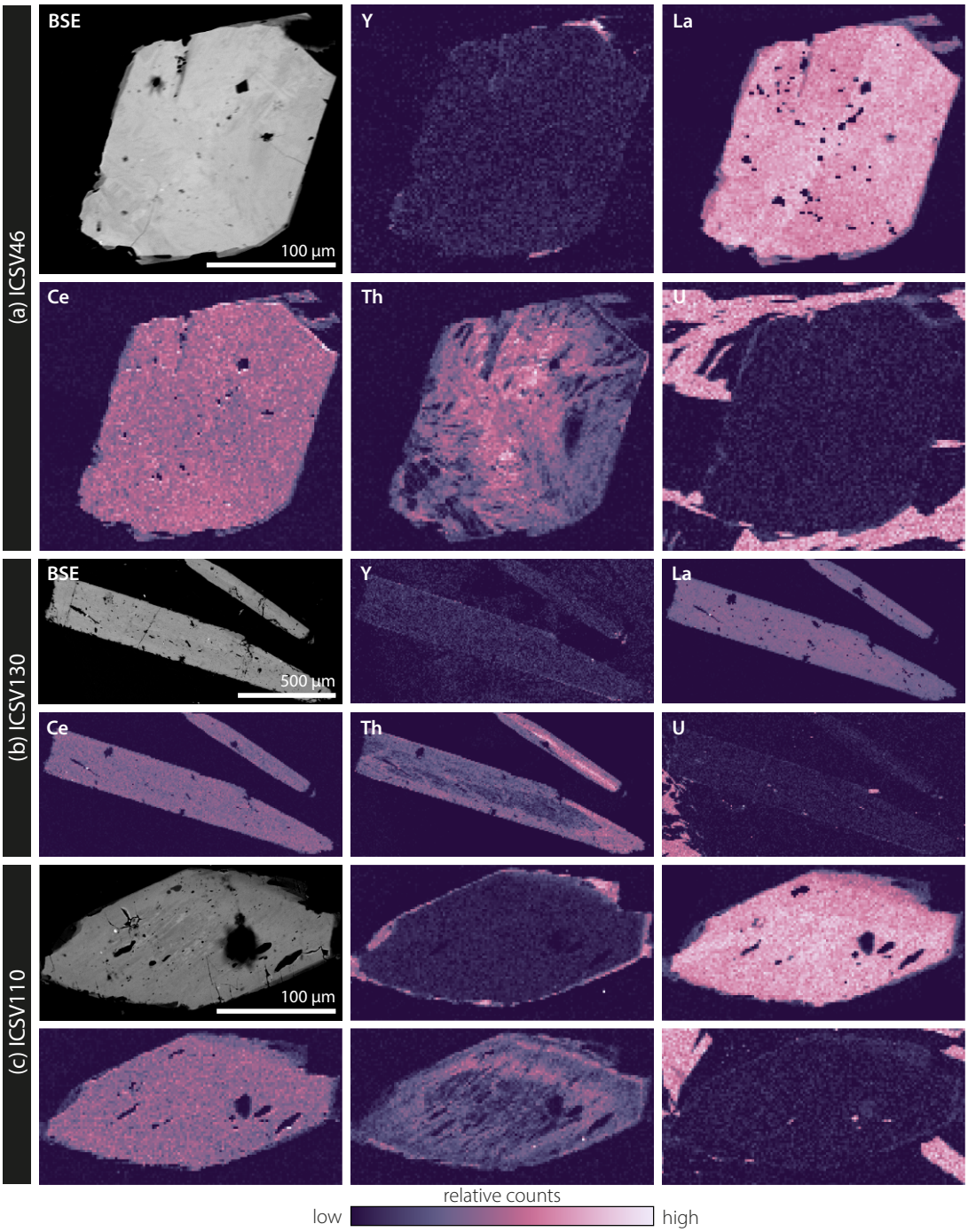


Fig. 5.11 BSE images and X-ray compositional maps for allanite grains within samples ICSV46, ICSV130 and ICSV110.

ICSV46 ICSV46 is located in the mixed psammite, pelite, and semipelite unit within the garnet zone (Fig. 5.3). Allanite in ICSV46 preserves small to coarse euhedral prismatic grains that range up to 1000 µm in length. Long prismatic grains are aligned to the matrix S_2 fabric and display S-shaped matrix concordant inclusion trails producing a weak S-C fabric. Shearing also produces augen with inclined allanite porphyroblasts (σ-type) wrapped by the S_2 fabric

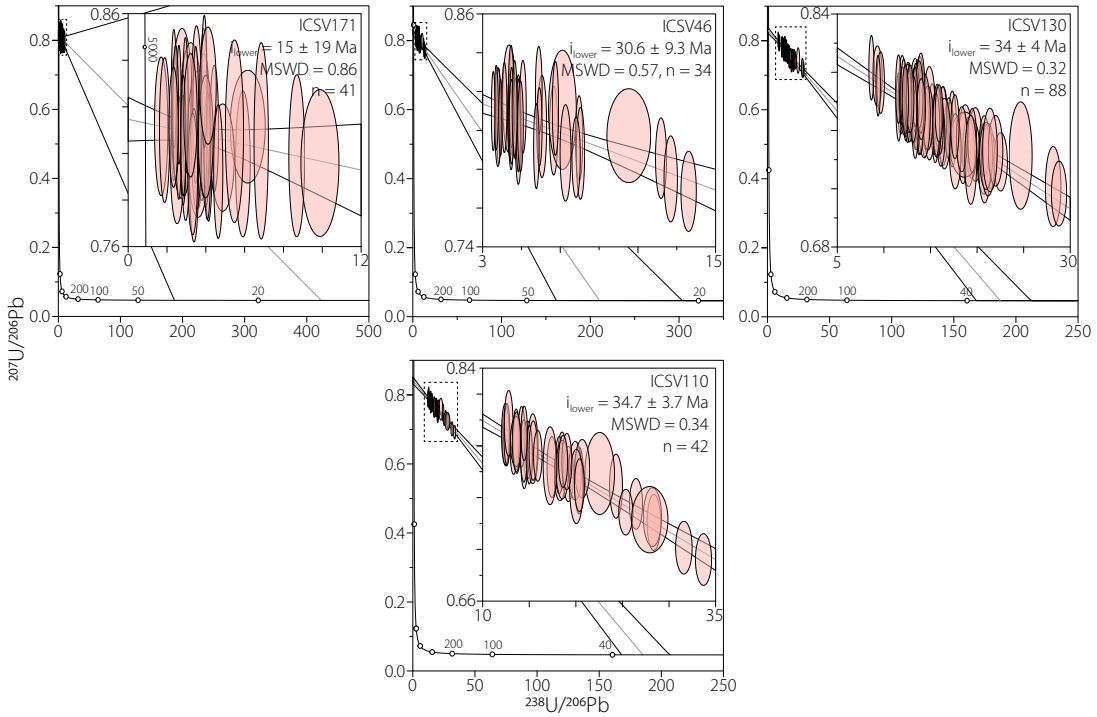


Fig. 5.12 Tera-Wasserburg plots for analysed allanite samples. Ages quoted are lower intercept ^{238}U-^{206}Pb ages.

(Fig. 5.10b). Sheared garnet porphyroblasts are also present in ICSV46 with matrix-continuous S-shaped inclusion trails and consistent with partial rotation and shearing during growth. BSE images show patchy–striped zoning textures distributed across grains. A thin discontinuous darker rim is present around grains. X-ray compositional maps show relatively homogenous Y, Ce and U distribution across the grain. La displays weak sector zoning and Th shows patchy compositional zoning. Locally a Th-enriched inner rim (prior to the dark BSE rim domains) is present. Thin darker rims in BSE are reflected by higher Y and U, and lower La and Ce.

Allanite is abundant in the sample though it is generally too small or inclusion-rich to allow for spot locations. Consequently, only three sufficiently large grains were analysed. 34 analyses across 3 allanite grains yields a ^{238}U/^{206}Pb intercept age of 30.6 ± 9.3 Ma (MSWD = 0.57; Fig. 5.12). U concentrations range from 1084–3138 ppm and ^{238}U/^{206}Pb ratios range from ~4–14.

5.4.1.2 Garnet- & kyanite-zone graphite-rich pelite: porphyroblast- or coarse matrix-hosted

ICSV130 ICSV130 occurs in the mixed psammite, pelite, and semipelite unit within the garnet zone (Fig. 5.3). Allanite in ICSV130 forms coarse euhedral prismatic grains, 250–1400 µm in length. Grains often contain oval lobate to rounded inclusions. Grains occur partially or fully encapsulated within garnet or as porphyroblasts within the matrix. Allanite grains hosted in garnet are equally coarse as matrix grains, with the largest allanite grain in the sample mostly contained within garnet (Fig. 5.10c). Garnets within ICSV130 overgrow the S_2 fabric and display matrix concordant inclusion trails. Matrix allanite grains appear to cross-cut S_2 or are aligned length-wise (Fig. 5.10d). BSE images and compositional zoning are broadly consistent in both microstructural contexts. BSE show patchy compositional zoning distributed throughout the grain. Locally dark BSE discontinuous rims are present in matrix grains but are less prominent or absent in garnet-hosted grains. X-ray compositional maps show prominent zoning for select elements. Y, Ce, and U generally display minimal zoning across the grain though locally show relative depleted or enriched thin discontinuous rims. La appears unzoned or displays sector zoning. Th varies from striped patches of elevated and depleted zones to concentric zoning patterns (Fig. 5.11b). Cores are more often Th depleted than rims, though this pattern is inconsistent.

88 analyses from 7 grains yields an $^{238}U/^{206}Pb$ intercept age of 34 ± 4 Ma (MSWD = 0.32; Fig. 5.12). High U concetrations (1581–4579 ppm) and moderate spread of $^{238}U/^{206}Pb$ ratios (~9–29) were measured. No variation in age population is noted for the contrasting microstructural contexts.

ICSV110 ICSV110 occurs in the mixed psammite, pelite, and semipelite unit and is located at the kyanite isograd (Fig. 5.3). Allanite in sample ICSV110 occurs as subhedral to euhedral angular to elongate prismatic grains up to 1500 µm in length. Grains are often inclusion-rich with small to moderately sized oval to angular inclusions. Grains are all found within the matrix, though locally grains are partially wrapped by staurolite porphyroblasts that overgrow the S_2 fabric (Fig. 5.10e). This microstructural association is tracked by S_2 concordant graphite-rich inclusion trails in staurolite. The sample also contains garnet and kyanite, both as porphyroblastic phases. Kyanite also overgrows the S_2 fabric and kyanite-allanite show the same relationships as staurolite-allanite. Garnet contains inclusions of both coarse kyanite and staurolite grains. The inferred

crystallisation sequence has allanite pre-dating staurolite+kyanite, followed by coarse garnet growth. Most matrix grains are aligned with S_2 and locally shear fabrics produce σ-porphyroblasts (Fig. 5.10a).

BSE images show patchy zoning textures exhibiting linear variations between lighter and darker domains (Fig. 5.11c). X-ray compositional maps show similar zoning textures to ICSV130. Y, Ce and U show homogenous zoning across the grain except at the outer rim where relatively enriched or depleted domains may occur. La is weakly zoned or unzoned, and where zoned may display sector zoning (Fig. 5.11c). Th is strongly zoned and displays concentric or patchy zoning patterns (Fig. 5.11c). No consistent trends are observed for relative enrichment or depletion between core and rim, though Th is often enriched in cores with progressive reduction in concentrations towards rims.

42 analyses on 7 grains yields a $^{238}U/^{206}Pb$ intercept age of 34.7 ± 3.7 Ma (MSWD = 0.34; Fig. 5.12). ICSV110 is the highest-grade allanite-bearing sample, and records the highest $^{238}U/^{206}Pb$ ratios, ranging between ~12–34, and high U concentrations (820–2712 ppm).

5.4.2 Interpretation

5.4.2.1 Timing of fabric development

Allanite broadly shows syn- or post-tectonic mineral growth at varying structural levels. However, converse to a typical prograde sequence where prograde–peak metamorphic minerals can occur syn-tectonic at lower grades and post-tectonic at higher grades, in this sequence at lowest-grade allanite growth appears dominantly post-D_2 while garnet- and kyanite-zone allanite growth is dominantly syn-D_2 with tentative late or post-tectonic growth recorded in ICSV130. Allanite from the lowest grade sample (ICSV171) is from a different lithology and tectonic group than the other samples (Lamayuru Complex vs GHS). A bulk compositional variation, or variation in reacting fluid composition may have a more significant impact on stability than the *P-T* conditions (Budzyń *et al.*, 2011).

Allanite in ICSV130 (syn- to post-D_2 crystallisation; garnet grade) and ICSV110 (syn-D_2 crystallisation; kyanite grade) record overlapping ages of 34 ± 4 Ma and 34.7 ± 3.7 Ma. As D_2 is interpreted as the dominant event driving tectonic thickening of the crust in the study area, these ages show D_2 was active at *ca.* 34 Ma at these structural levels. A slightly younger age for ICSV130 and lower

metamorphic grade is consistent with the syn- to post-D_2 relationship unique to this sample. It is therefore suggested that at *ca.* 34 Ma D_2 was waning at these structural levels. ICSV46 also records syn-D_2 allanite but records a potentially younger age (30.6 ± 9.3 Ma) despite also located within the garnet zone. This may suggest D_2 was still active by *ca.* 30 Ma at the sampled structural level, however, there is a large uncertainty associated with this age means it overlaps the older ages.

5.4.2.2 Timing of porphyroblast growth

The absolute timing of growth for peak porphyroblastic phases can vary as a function of metamorphic grade. Therefore inclusion-host relationships between dateable phases and porphyroblast growth do not determine an absolute age for the given microstructure across the entire metamorphic sequence. However, the relationship of phases to fabric helps track the development of the thermal culmination as indicated by the relative relationship between metamorphic fabric and porphyroblast. Below, the timing of porphyroblast growth at varying structural levels is constrained with the recognition that bulk composition may influence the timing of nucleation and rate of mineral phase growth.

Porphyroblast growth and relationship to fabric development show notable similarities across the metamorphic sequence. ICSV46 records both syn-D_2 garnet and allanite growth (Fig. 5.10b). An age of 30.6 Ma ± 9.3 Ma from the allanite can therefore be interpreted as coincident with the timing of crustal thickening (syn-D_2). ICSV130 and ICSV110 both contain porphyroblasts that grew at or near thermal-peak at the given metamorphic grade. In ICSV130, allanite contained in post-D_2 garnet is as equally coarse as matrix grains, with the largest grain occurring as an inclusion in garnet. This possibly suggests garnet growth only began after allanite growth had terminated, providing a maximum age of 34 ± 4 Ma for post-D_2 garnet growth in the garnet zone. Allanite in ICSV110 grows prior to post-D_2 staurolite. A similar microstructural context for both staurolite and kyanite (garnet-hosted) suggests they crystallise at a similar time. Therefore, 34.7 ± 3.7 Ma constrains a maximum age for staurolite and kyanite growth within the kyanite zone. Post-tectonic growth of garnet in ICSV130 and post-tectonic growth of staurolite & kyanite in ICSV110, inferred to be coincident with thermal peak, suggests that *ca.* 35–34 Ma represents a maximum age for attainment of thermal peak at these structural levels.

5.5 Monazite

5.5.1 Results

The location for all analysed monazite samples is shown in Figure 5.3 and U-Th-Pb diagrams for all analysed monazite grains are shown in Figures 5.16–5.20. From left to right the figures show a Tera-Wasserburg (or for select samples with older age distributions, a Wetherill plot), a common-Pb corrected ^{232}Th-^{208}Pb vs ^{238}U-^{206}Pb, and a common-Pb corrected ^{232}Th-^{208}Pb age ranked plot. For most samples the discussion centres on the common-Pb corrected ^{208}Pb/^{232}Th age range. The mean age is generally not considered as monazite growth is interpreted as continuous rather than a single growth episode. This is further discussed as required below. Samples are described by the dominant age range recorded by the sample, with ranges of age groupings distinguishable by microstructural context as detailed in a later section.

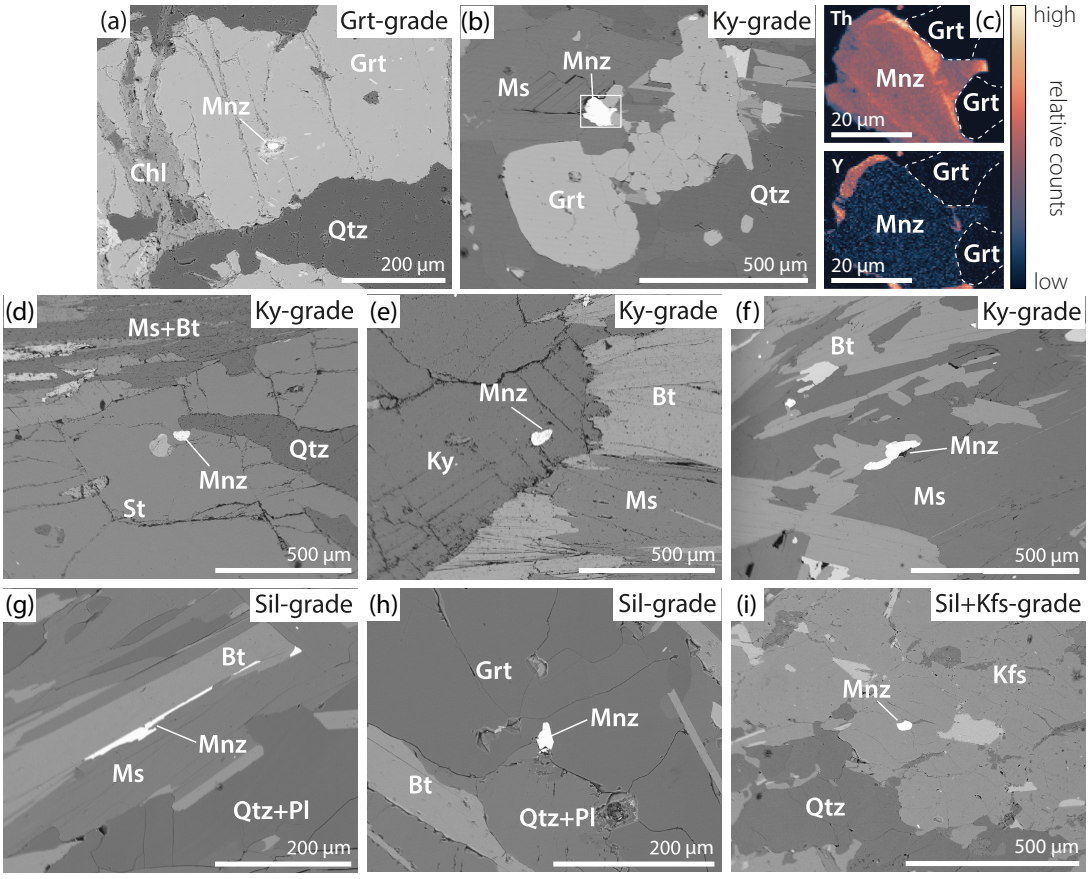


Fig. 5.13 BSE images and X-ray compositional maps of different microstructural contexts for monazite at different metamorphic grades.

5.5.1.1 Garnet zone

ICSV86 is the only analysed sample from the garnet zone. One monazite grain is preserved as an inclusion in garnet (not shown on Figure 5.16), with all other grains hosted in mica-rich layers in the matrix. The monazite inclusion is oval and subhedral, the grain shows patchy internal Th zoning with relatively enriched cores. Y and U are depleted in cores and enriched in thin discontinuous rims. Monazite inclusions from the matrix show patchy to striped Th enriched cores and thin rims, whereas Y records weaker zoning with elevated cores progressing to thin depleted rims (Fig. 5.14).

The single spot analysis from the inclusion yields a $^{208}Pb/^{232}Th$ age of *ca.* 407.6 ± 28.0 Ma. Garnet is fractured between the matrix and inclusion (Fig. 5.21a). 11 analyses from 4 grains yield $^{208}Pb/^{232}Th$ ages between *ca.* 24.6–22.4 Ma.

5.5.1.2 Staurolite zone

Monazite of sufficient grain size is only present in the matrix of samples ICSV109 and ICSV30. ICSCV30 also preserves monazite grains (< 15 µm) in garnet but these were too small or irregular to accommodate ablation spots. In ICSV109, monazite is preserved as small anhedral to lobate grains. Allanite is locally present within the matrix. ICSV30 preserves elongate subhedral grains often with sharp grain boundaries to adjacent micas. For monazite from the staurolite zone, Th commonly displays patchy to striped weak zoning with locally enriched cores or rims. Y commonly shows strongest zoning with depleted cores and discontinuous enriched rims in ICSV30, and patchy enriched cores in ICSV109. Ce locally shows strong rim enrichment adjacent to uneven surfaces, thus is not inferred to represent meaningful zoning patterns. La zoning is commonly enriched in the core and decreases progressively towards the rim (Fig. 5.14).

From the staurolite zone, $^{208}Pb/^{232}Th$ ages range between *ca.* 29.2–21.9 Ma. In ICSV109, 10 analyses from 3 grains yield $^{208}Pb/^{232}Th$ ages between *ca.* 26.7–21.9 Ma. In ICSV30, 47 analyses from 6 grains yield $^{208}Pb/^{232}Th$ ages between *ca.* 28.2–22.7 Ma.

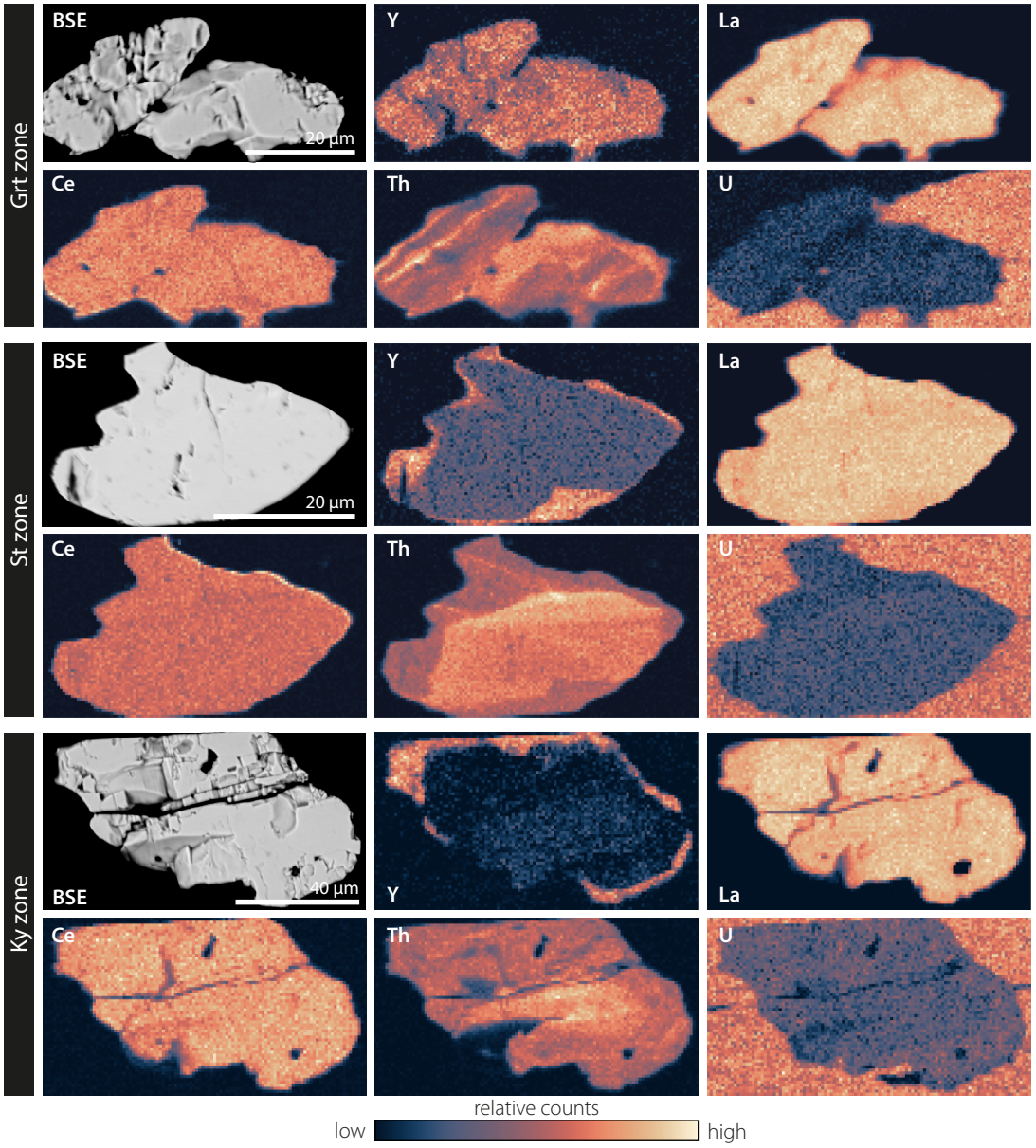


Fig. 5.14 High contrast BSE images and X-ray compositional maps for monazite grains from the garnet–kyanite zones.

5.5.1.3 Kyanite zone

Monazite grains in kyanite zone samples (ICSV6, ICSV97, ICSV13, ICSV12, ICSV96, and ICSV18) occur in a variety of petrographic settings. Monazite occurs as inclusions in kyanite or staurolite or in the matrix (Fig. 5.13b–f). No samples contain monazite within garnet; however, garnet rims and satellite garnet grains (garnet II) can be seen to locally embay monazite rims (Fig. 5.13b–c). Zoning patterns are not constrained by garnet grain boundaries (indicating growth prior to garnet; Fig. 5.13c). Inclusion grains in staurolite and kyanite

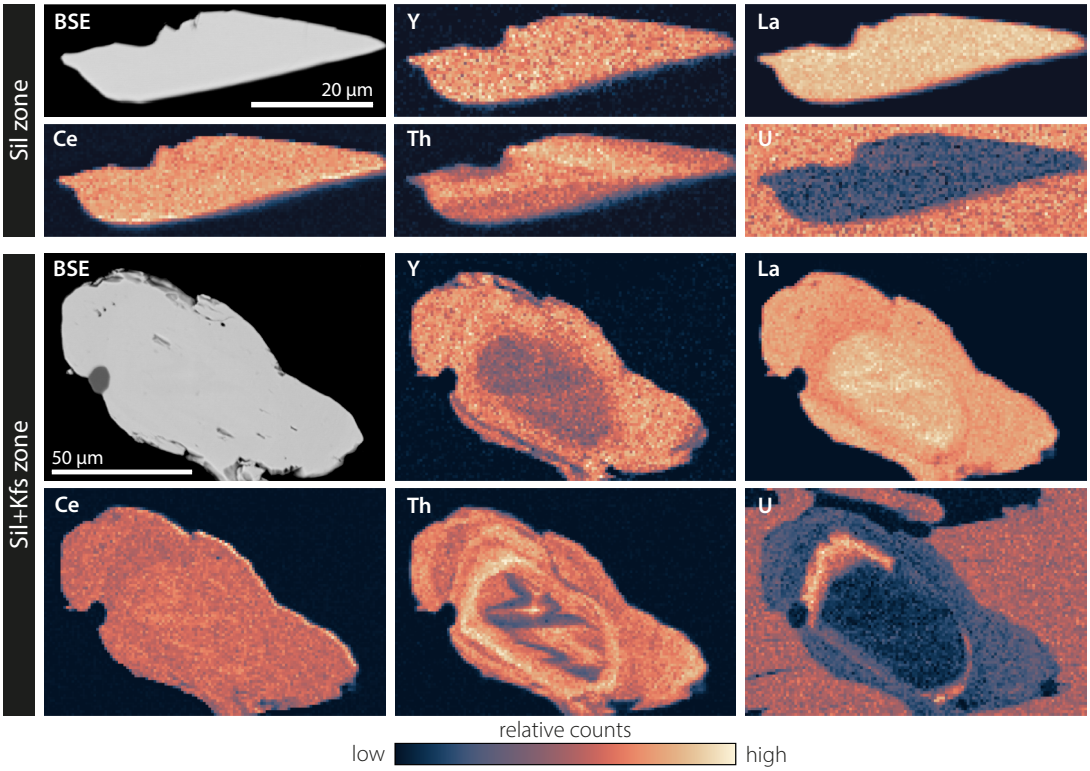


Fig. 5.15 High contrast BSE images and X-ray compositional maps for monazite grains in sillimanite- and sillimanite+K-feldspar-zone samples.

are generally smaller (*ca.* 20 µm in length) than matrix grains (up to 150 µm in length). All monazite grains vary from subhedral to euhedral and may show heavy fracturing. Grains generally show no significant zoning under BSE. X-ray compositional maps show significant and complex internal zoning. The following trends are most commonly observed: Y commonly shows depleted cores and thin discontinuous to locally thick continuous enriched rims. Grains locally show concentric patterns with both Y enriched cores and thin rims with depleted mantles. Th zonation is complex, with patchy to linear zonation in cores. Rims are generally weakly depleted relative to cores, though this varies significantly. Other elements are weakly zoned. U often displays lower concentrations in cores and non-continuous rims with slightly higher relative concentrations. Ce may show slight variation between depleted cores progressing to enriched rims, with the opposite trend observed for La (Fig. 5.14).

Monazite analysed in kyanite-zone samples yield $^{208}Pb/^{232}Th$ ages between *ca.* 33.4–18.2 Ma. $^{208}Pb/^{232}Th$ ages are as follows from each sample: in ICSV6, 56 analyses from 16 grains yield ages between *ca.* 23.7–18.7 Ma; in ICSV97, 57 analyses from 8 grains yield ages between *ca.* 32.7–20.1 Ma; in ICSV13, 37 analyses from 7 grains yield ages between *ca.* 31.3–23.3 Ma; in ICSV12, 43

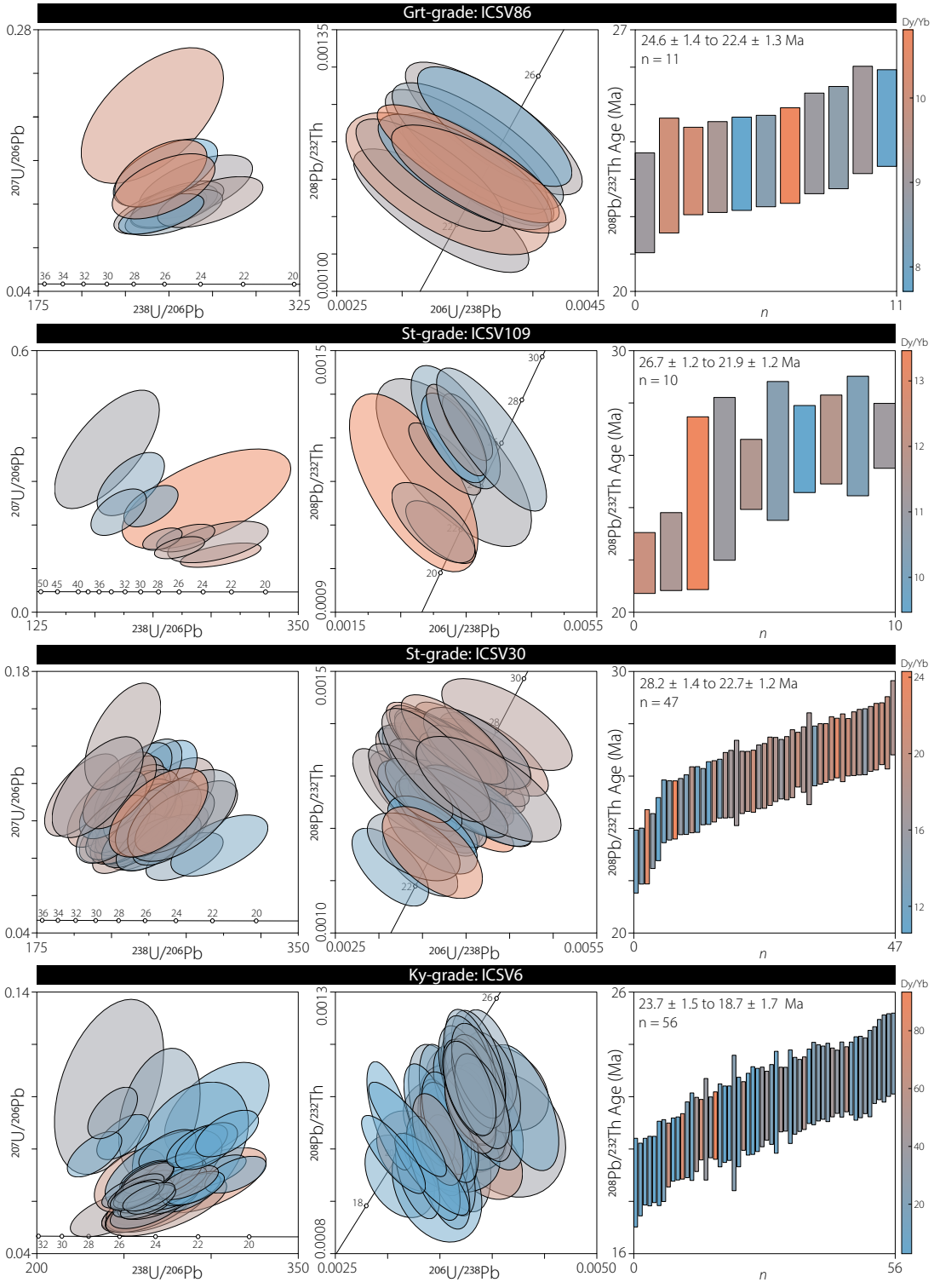


Fig. 5.16 U-(Th)-Pb results from monazite hosted in garnet-zone, staurolite-zone and kyanite-zone samples. From left to right the figures show a Tera-Wasserburg, a common-Pb corrected ^{232}Th-^{208}Pb vs ^{238}U-^{206}Pb, and a common-Pb corrected ^{232}Th-^{208}Pb age ranked plot.

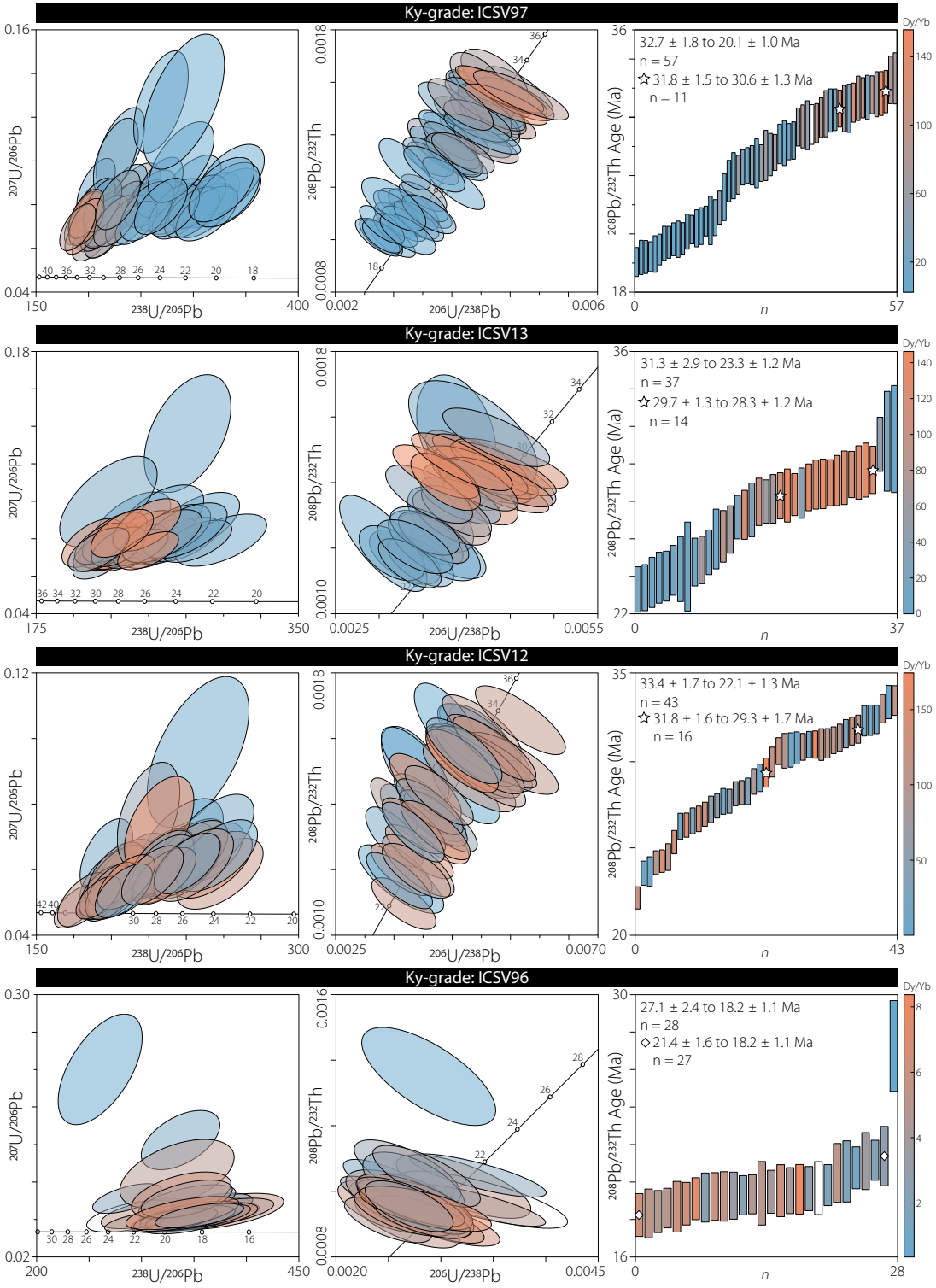


Fig. 5.17 U-(Th)-Pb results for monazite in kyanite-zone samples. From left to right the figures show a Tera-Wasserburg, a common-Pb corrected ^{232}Th-^{208}Pb vs ^{238}U-^{206}Pb, and a common-Pb corrected ^{232}Th-^{208}Pb age ranked plot. Stars on age ranked plots correlate to elevated domains of Dy/Yb.

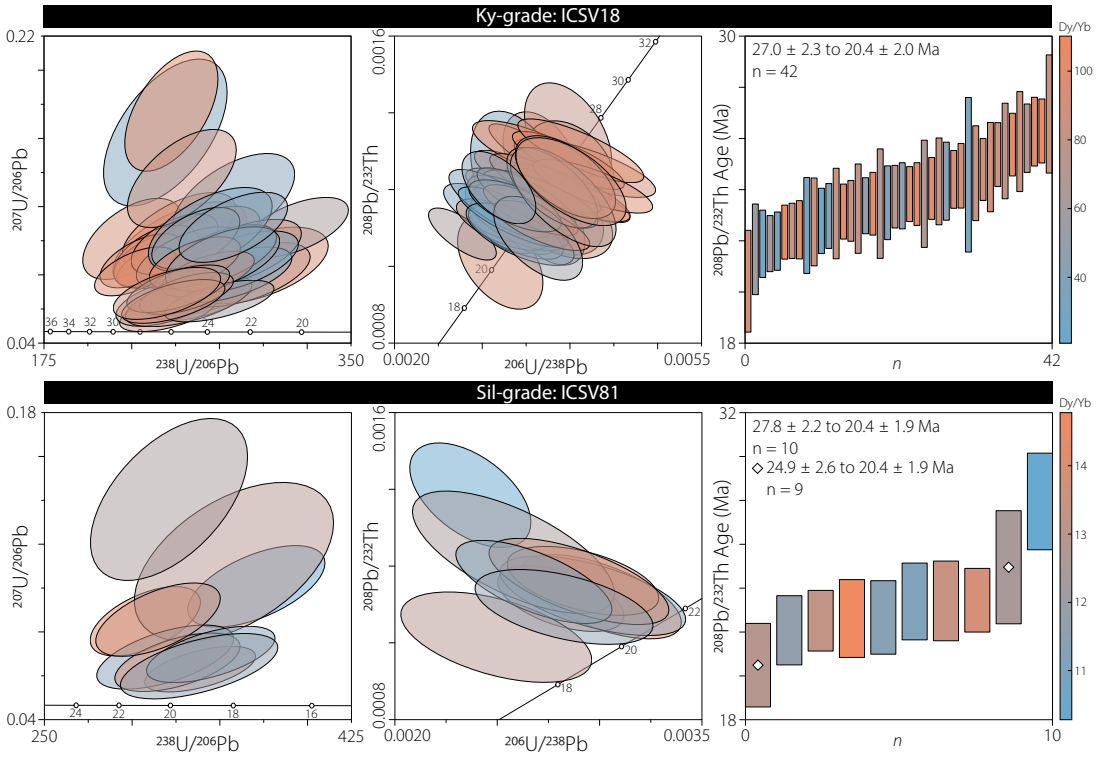


Fig. 5.18 U-(Th)-Pb results for kyanite- and sillimanite-zone samples. U-(Th)-Pb results from monazite hosted in garnet-zone, staurolite-zone and kyanite-zone samples. From left to right the figures show a Tera-Wasserburg (and Wetherill in ICSV91), a common-Pb corrected ^{232}Th-^{208}Pb vs ^{238}U-^{206}Pb, and a common-Pb corrected ^{232}Th-^{208}Pb age ranked plot. Stars on the age ranked plot in ICSV91 approximate the dominant age range in the sample.

analyses fromm 8 grains yield ages beetween *ca.* 33.4–22.1 Ma; in ICSV96, 28 analyses fromm 6 grains yield ages between *ca.* 27.1–18.2 Ma; in ICSV18, 42 analyses from 5 grains yield ages between 27.0–20.4 Ma.

5.5.1.4 Sillimanite zone

Only one sample from the sillimanite zone contained enough monazite of sufficient size for analysis. In ICSV81, monazite have a high length-width aspect ratio producing angular to rectangular subhedral grains (Figs. 5.13e and 5.15). Monazite shape can be defined by mica cleavage or grain boundaries that define S_3 fabric. BSE images and X-ray maps show minimal to no zonation patterns. Weak Th enrichment in cores is observed in select grains (Fig. 5.15).

In ICSV81, 10 analyses over 6 grains yield ^{208}Pb/^{232}Th ages between *ca.* 27.9–20.4 Ma. The oldest spot yields an age of 27.9 ± 2.2 and the most clustered 9 spots produce an age range of *ca.* 24.9–20.4 Ma.

5.5.1.5 Sillimanite+K-feldspar zone

Monazite from sillimanite+K-feldspar-zone samples show distinct textural differences with monazite from lower-grade samples. Monazite occurs as large oval euhedral to subhedral grains ranging between 20–200 µm in length. Grains are found within the matrix and locally within coarse K-feldspar porphyroblasts. Monazite shows complex internal zoning, which varies from oscillatory to patchy, and is marked by sharp core to rim boundaries (Fig. 5.15). In high-contrast BSE images, grains are homogenous or display patchy zonation. X-ray compositional maps show zoning within all analysed elements. Y shows depleted inner cores and relatively enriched outer cores. These can be subsequently zoned with a low Y domain and thin discontinuous Y rich rims. La and Ce show moderate zonation often displaying weakly enriched cores relative to rims. Th shows complex internal zoning in the inner core and enriched mantle–rim. Finally, U shows depleted cores and relatively weakly enriched mantle–rim. A high Th and U rich domain often occurs at the boundary between core and mantle. (Fig. 5.15).

Monazite analyses generally lie on concordia at ages between *ca.* 500–450 and *ca.* 20 Ma with discordant analyses between these two clusters (Fig. 5.19). S-shaped age distributions are recorded on the ranked age plots. The oldest analyses are found in ICSV150 which record $^{208}Pb/^{232}Th$ ages as old as *ca.* 900 Ma. Filtering for discordance (-4 to +5.6) produces the following weighted mean $^{208}Pb/^{232}Th$ ages for Cambro-Ordovician age populations. In ICSV145, 19 analyses yield an age of 499.0 ± 11.5 (MSWD = 0.96) and 11 analyses yield an age of 471.7 ± 11.9 Ma (MSWD = 0.93); in ICSV150, 23 analyses yield an age of 467.3 ± 13.8 Ma (MSWD = 7.9); in ICSV147, 43 analyses yield an age of 453.1 ± 11.0 (MSWD = 3.1); and in ICSV152, 40 analyses yield an age of 483.8 ± 11.8 (MSWD = 3.6). An insignificant age distribution is recorded between *ca.* 400-40 Ma, interpreted as mixing between two age populations. Himalayan age populations are recorded in ICSV145 and ICSV152. In ICSV145, analysis on low Y-mantle–rim and thin discontinuous Y-rich rims (n = 14), yields a $^{208}Pb/^{232}Th$ age of 24.1 ± 1.5 Ma, but with a high MSWD (9.5) or a $^{208}Pb/^{232}Th$ age range of 12 analyses between *ca.* 27.5–21.5 Ma. In ICSV152, ages do not record an apparent plateau, thus a single age population or age distribution are not relevant. 5 analyses yield a $^{208}Pb/^{232}Th$ age between *ca.* 28.4–21.1 Ma.

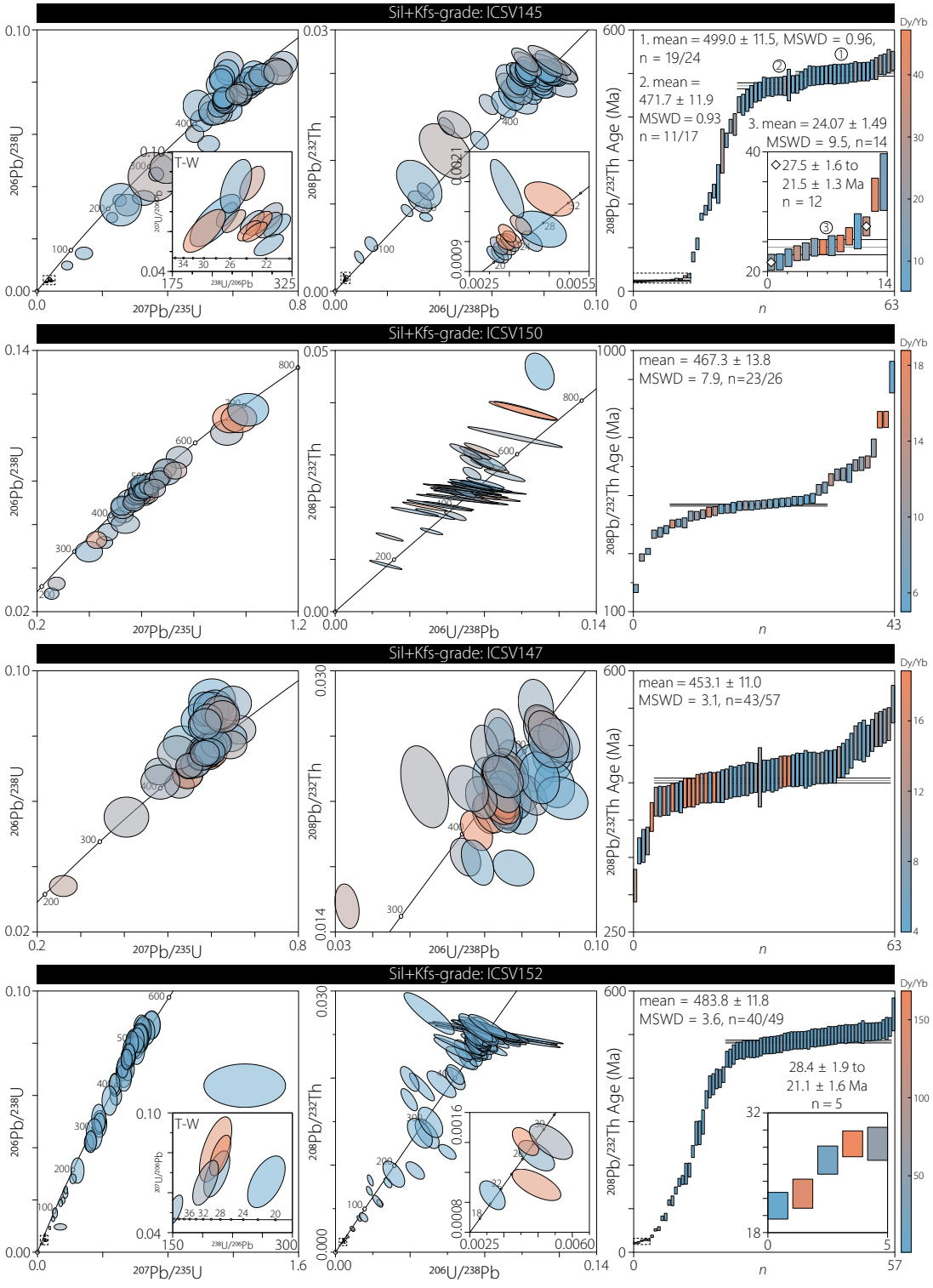


Fig. 5.19 U-(Th)-Pb results for monazite analysed in sillimanite+K-feldspar-zone samples. From left to right the figures show a Wetherill (and inset Tera Wasserberg in ICSV145 and ICSV152), a common-Pb corrected ^{232}Th-^{208}Pb vs ^{238}U-^{206}Pb, and a common-Pb corrected ^{232}Th-^{208}Pb age ranked and/or mean weighted plot. Discordance filter from concordia is applied to all mean weighted ages with a range of -4 and +5.6 (excluding the Himalayan-aged population in ICSV145 where it was unsuccessful).

5.5.1.6 LASS

Select samples were analysed on a split-stream setup to allow discrimination of ages by trace element ratios and concentrations, which is further discussed in a later section. The U-(Th)-Pb age plots are also presented here for comparison. Samples ICSV12 and ICSV18 (also run using the *in-situ* setup described above) are from the kyanite zone, whereas ICSV151 (not run *in situ*) is from the sillimanite+K-feldspar zone.

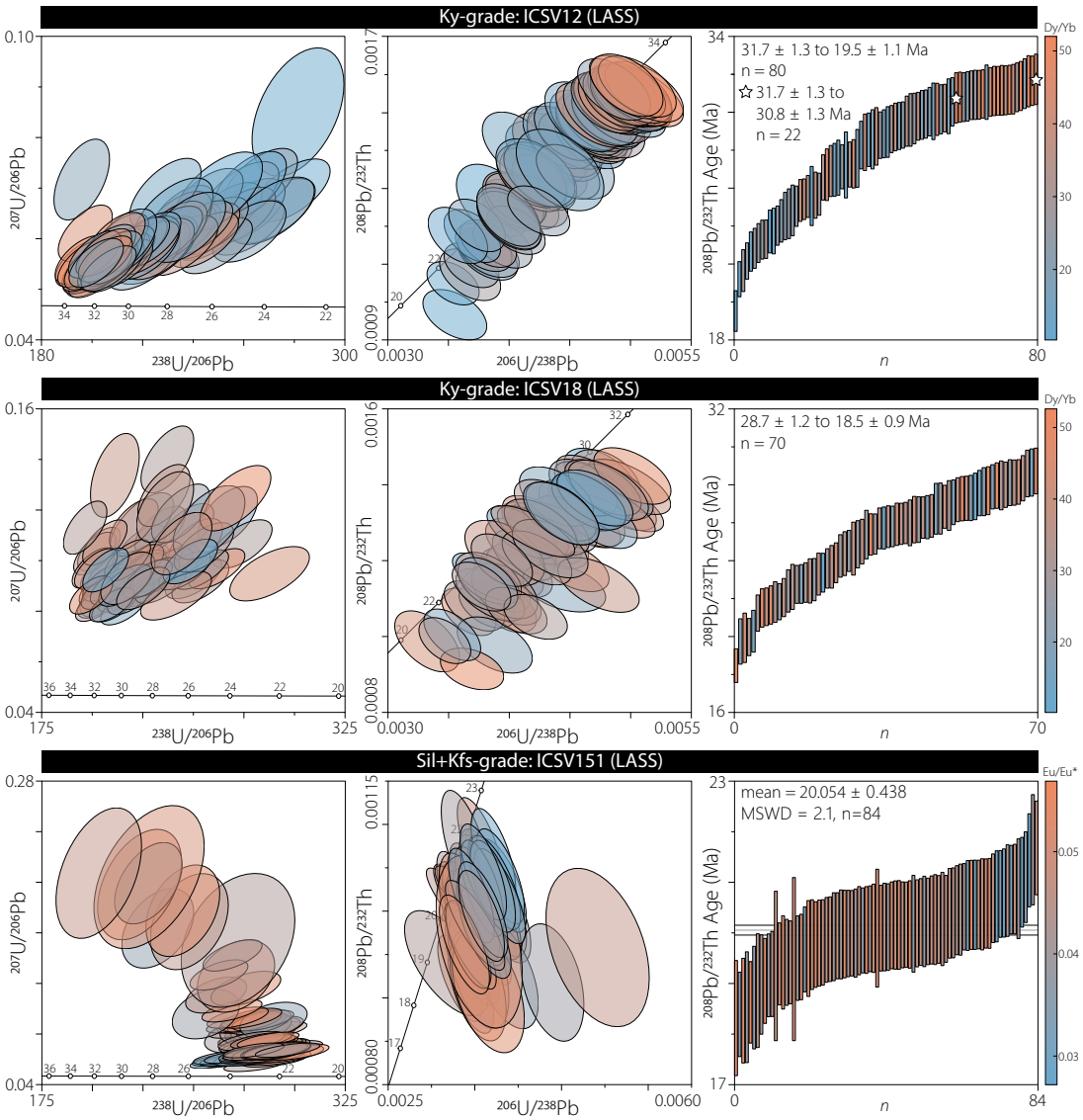


Fig. 5.20 U-(Th)-Pb results for analysed monazite separates from kyanite- and sillimanite+K-feldspar-zone samples analysed using the LASS setup. From left to right the figures show a Tera-Wasserburg, a common-Pb corrected ^{232}Th-^{208}Pb vs ^{238}U-^{206}Pb, and a common-Pb corrected ^{232}Th-^{208}Pb age ranked or mean weighted plot.

ICSV12 Monazite separates from ICSV12 share the same characteristics as previously described from BSE images and X-ray compositional zoning maps. Use of mineral separates allowed overall larger grains to be selected that showed more prominent zoning textures that could be well targeted during analysis. A well distributed age population is again recorded. 80 analyses from 10 grains yield $^{208}Pb/^{232}Th$ ages between *ca.* 31.7–19.5 Ma. A dominant clustering of ages recorded between *ca.* 31.7–30.8 Ma and concurrent with high Dy/Yb ratios (Fig. 5.20).

ICSV18 Separates in ICSV18 show consistent zonation textures as discussed for the *in-situ* analysis of kyanite-zone samples. 70 analyses from 11 grains yield $^{208}Pb/^{232}Th$ ages between *ca.* 28.7–18.5 Ma (Fig. 5.20).

ICSV151 Monazite from ICSV151 was not described above, thus the grain textures are discussed in greater detail than for the previous two samples. ICSV151 is a coarse grained leucogranite from the sillimanite+K-feldspar zone. The sample displays only weak deformation textures, expressed through undulose patchy extinction in quartz. Monazite separates generally occur as rounded to oval subhedral grains (100–200 µm) locally with small rounded to lobate inclusions. BSE images show lighter lobate to patchy domains. X-ray compositional maps show abundant complex lobate zoning textures that are generally broadly distributed across the grain. Y maps display wispy to lobate zoning patterns with greater enrichment generally recorded in the core relative to the rim. Ce generally display minimal zoning, with weak depletion in cores relative to rims. La shows lobate zoning patterns with weakly enriched cores and rims and depleted mantle domains. U is weakly zoned with lobate to patchy zoning. Finally, Th generally displays angular to lobate zoning patterns with no consistent core–rim patterns of enrichment-depletion.

Analysis of 84 spots from 9 grains yields a weighted mean $^{208}Pb/^{232}Th$ age of 20.1 ± 0.4 Ma. The mean age has a MSWD = 2.1, greater than a single age population (MSWD = ~1), suggesting minor spread of ages and/or underestimationg of uncertainties. The data show a progressive increase in the size of the negative Eu anomaly with younger ages (Fig. 5.20).

5.5.1.7 Microstructure-age relationship

Figure 5.21 displays age ranked plots discriminated by petrographic context for the analysed monazite grains. Plots are presented in order of increasing metamorphic grade and are discussed in the order of porphyroblast growth in a standard Barrovian reaction sequence. It should be noted that all porphyroblast hosts contain fractures, suggesting grains are susceptible to recrystallisation.

Only one analysis of a garnet inclusion is recorded and shows no relationship to an early syn-D2 microstructural context (19.1 ±1.3 Ma; Fig. 5.21a). The presence of monazite within garnet is limited; however, matrix grains may also be in contact, partially engulfed, or embayed by garnet rims (garnet II). An example of this is recorded by one large grain in ICSV18 (Fig. 5.13b, c), which records an age range between *ca.* 26.3–23.7 Ma (Fig. 5.21e), and in a single spot on one grain in ICSV81 (Fig. 5.13h) at 23.4 ± 1.5 Ma (Fig. 5.21f). This produces an asymmetric age population peaking at *ca.* 24 Ma, and broadly extending to *ca.* 26 Ma (Fig. 5.21g).

Ages from staurolite inclusions are bimodal, older populations are broadly distributed in ICSV97 (*ca.* 30.0–29.4 Ma) and ICSV13 (*ca.* 28.4–24.9 Ma) with the youngest population recorded in ICSV18 (*ca.* 23.8–21.9 Ma). Collated results produce a dominant probability peak at *ca.* 22 Ma and a broadly distributed asymmetric peak at *ca.* 29 Ma. Petrography of ICSV18 shows that garnet cores (garnet I) are slightly corroded at grain boundaries coincident with the presence of staurolite. Garnet rims (garnet II) are discontinuous around garnet cores and grain boundaries of garnet II and staurolite are both incised where in mutual contact (Fig. 5.21e). Garnet rims are also present in strain contacts defined by mica and staurolite. Staurolite is constrained to have grown between the two phases of garnet growth or to have grown after garnets I and II, accompanied by partial corrosion of both phases.

Monazite inclusions in kyanite from ICSV6 are distributed over a large age range (*ca.* 22.7–18.8 Ma) with no prominent clustering of ages. More clustered results in ICSV13 and ICSV12 produce age ranges from *ca.* 31.2–28.0 and *ca.* 30.7–26.2 Ma, respectively (Fig. 5.21c, d). However, monazite analyses within kyanite are distributed across all age ranges (*ca.* 33.3–18.8 Ma; Fig. 5.21g). A broadly distributed age peak is recorded at *ca.* 28 Ma for the collation of these analyses (including ICSV6).

Similar to kyanite inclusions, monazite in the matrix records a broad range of ages with wide peaks at *ca.* 31 and 23 Ma (Fig. 5.21g).

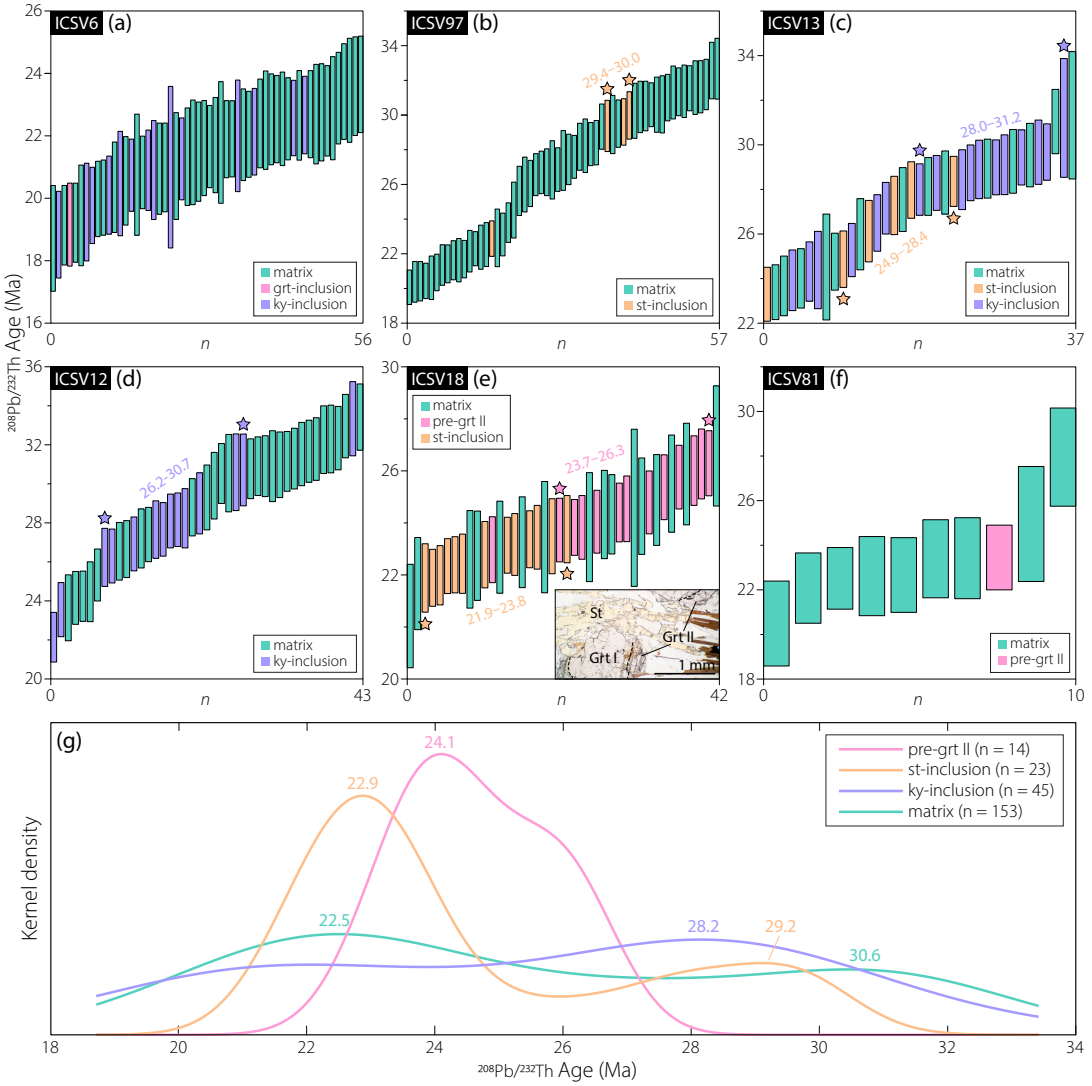


Fig. 5.21 Ranked Th-Pb ages for kyanite-zone (a–e) and sillimanite-zone (f) samples separated by varying microstructural context. Stars denote the major population of analyses for a given microstructural context. Figure e) contains an inset of a PPL thin section photomicrograph showing the relationship between garnet and staurolite - garnet I appears to be corroded at grain boundaries and staurolite contains abundant quartz inclusions, while garnet II appears to have grown after staurolite as it locally embays staurolite grain boundaries. Figure g) displays Kernel Density Estimate (KDE) plots for monazite that began to crystallise prior to garnet II, and occurs as staurolite and kyanite inclusions and matrix grains.

5.5.1.8 Laser Ablation Split-Stream (LASS) petrochronology

Monazite commonly reacts multiple times during a given metamorphic cycle, thus preserving evidence for multiple (re-)crystallisation episodes (e.g., Foster *et al.*, 2002). Thus consideration of trace element concentrations, may help to discriminate distinct growth phases. Monazite is suitable for petrochronological study due to its ability to easily take up a broad range of elements during (re-)crystallisation (Foster *et al.*, 2002), participation in numerous reactions (Pyle & Spear, 1999), and its proclivity at being preserved as an inclusion within porphyroblasts (Bell & Welch, 2002). Although Dy/Yb and Th/U ratios were collected during all analyses, select samples were selected for mineral separation and LASS U-Th-Pb geochronology.

The following discriminators are generally used to help link monazite growth to the petrological evolution of the host rock:

1. Th and U enter monazite through coupled substitution with Ca or with Si (Williams *et al.*, 2007). Th and U concentrations can be linked to fluid availability facilitating monazite recrystallisation. Th is generally thought to be insoluble in fluids; monazite recrystallised in the presence of fluids may act as a sink and show Th-enrichment (Seydoux-Guillaume *et al.*, 2002). The result is that monazite rims commonly have higher concentrations of Th and higher Th/U ratios than cores. Intra-sample Th/U in monazite is also shown to increase with metamorphic grade, diverging at high temperature conditions to produce high ratios indicative of partial melting (Yakymchuk & Brown, 2014; Taylor *et al.*, 2016; Yakymchuk *et al.*, 2018). Furthermore, extraction of thorium-rich melt from the system may leave progressively thorium depleted rims (Dumond *et al.*, 2015).

2. Y and HREE content (e.g., Dy/Yb or Dy/Lu). Y content between monazite and garnet can act as a quantitative thermometer and due to the competition for Y between the minerals, Y content of monazite may be linked to prograde and retrograde reactions involving garnet (e.g., Pyle *et al.*, 2001). Y is commonly regularly grouped with HREE. Both garnet and monazite incorporate REE during crystallization, with garnet preferentially incorporating the middle–heavy REEs and monazite LREE (e.g., Ayres & Harris, 1997). Monazite growth in the presence of garnet is relatively Y+HREE depleted in comparison to monazite growth during garnet-breakdown or in garnet-absent assemblages. During partial melting, monazite can dissolve

while further garnet crystallisation can occur. Melt crystallisation and retrogression (garnet breakdown) may trigger growth of new high-Y+HREE monazite as new grains or as recrystallisation on older cores (e.g., Kohn *et al.*, 2004, 2005). The result is that Y+HREE rich cores with older ages can be interpreted as forming before garnet (prograde growth), low Y+HREE mantles forming in the presence of garnet (prograde–peak), and high Y+HREE rims forming during recrystallisation or post-melt crystallisation (Kohn *et al.*, 2004; Regis *et al.*, 2016; Tobgay *et al.*, 2012; Štípská *et al.*, 2015).

3. Variability in the Eu anomaly ($Eu/Eu^* = Eu_N/\sqrt{Sm_N \times Gd_N}$) is commonly attributed to the growth and breakdown of feldspar (Rubatto *et al.*, 2013; Mottram *et al.*, 2014b; Dumond *et al.*, 2015). Changes in Eu/Eu* also reflect changes in fO_2, the stability of monazite, or other minerals that may partition Eu^{2+} or Eu^{3+} (Holder *et al.*, 2020).

The trace-element budget of a rock is governed by complex relationships between the major and accessory phases, and the trends described above are unlikely to be consistent in all scenarios (Holder *et al.*, 2020; Mottram *et al.*, 2014b; Warren *et al.*, 2019; Weller *et al.*, 2020). The availability of, and competition for different trace elements is likely to vary during the metamorphic cycle. For example, the distribution of Y+HREE between monazite and garnet must also account for other Y and REE rich phases such as zircon, xenotime, allanite and apatite. With the exception of xenotime, all these phases are documented in this study. All REE ratios use concentrations normalised to chondrite (McDonough & s. Sun, 1995).

ICSV12 records relatively flat Th/U ratios across the analysed grains (Fig. 5.22a), though when viewed as an individual sample, it shows a gradual decrease in Th/U values after *ca.* 30 Ma (Fig. 5.23a). Trace elements for the remaining phases can be discriminated in two ways. Approach 1: shows a prominence of ages between *ca.* 32.0–30.5 Ma, which display High Dy/Lu values and broadly distributed Y values (overall dominated by lower values), and lower Eu/Eu* values. These analyses suggest monazite growth in the presence of a HREE+Y rich phase (e.g., allanite, garnet, xenotime) and plagioclase stable conditions. Alternatively, these results can be treated as progressive trends between *ca.* 32–29 Ma: a decrease in Dy/Lu, increase in Y, and weak increase in Eu/Eu* are observed with decreasing age (Fig. 5.22b–d). Relative decreases in Dy/Lu or increases in Y must therefore be attributed to progressive breakdown of a given HREE+Y rich

phase. These changes are also accompanied by a minor reduction in the negative Eu anomaly (Eu/Eu* < 1) with decreasing age. A reduction in the anomaly is an increase in Eu/Eu* (Figs. 5.22e, 5.23b), which could relate to a relative decrease in feldspar content. Breakdown of garnet is generally associated with plagioclase rims, thus implication of garnet breakdown at *ca.* 32–29 Ma may not be applicable. Figure 5.23a appears to support stepped changes in trace element data: with high Dy/Lu values, low Y and low Eu/Eu* between *ca.* 32–30.5 Ma. Older age populations broadly appear to be preferentially enriched in HREE and less enriched in LREE. All analyses have a moderate Eu anomaly, which shows minor decrease in the anomaly with younger ages (Fig. 5.23b).

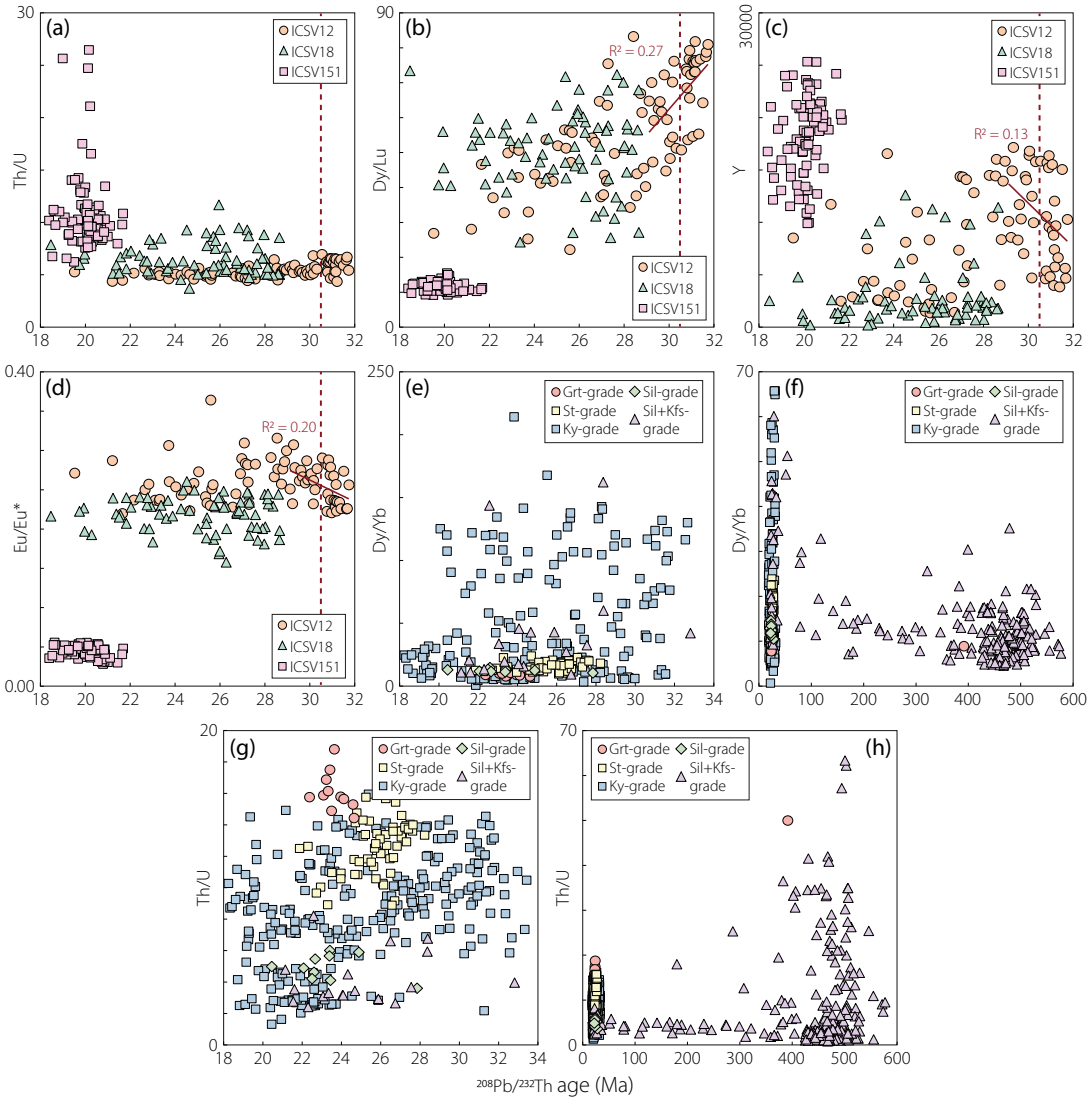


Fig. 5.22 Trace element discrimination ratios or concentrations vs $^{208}Pb/^{232}Th$ age for samples analysed using the LASS setup (a–d) and the standard Nu-Attom setup (e–h).

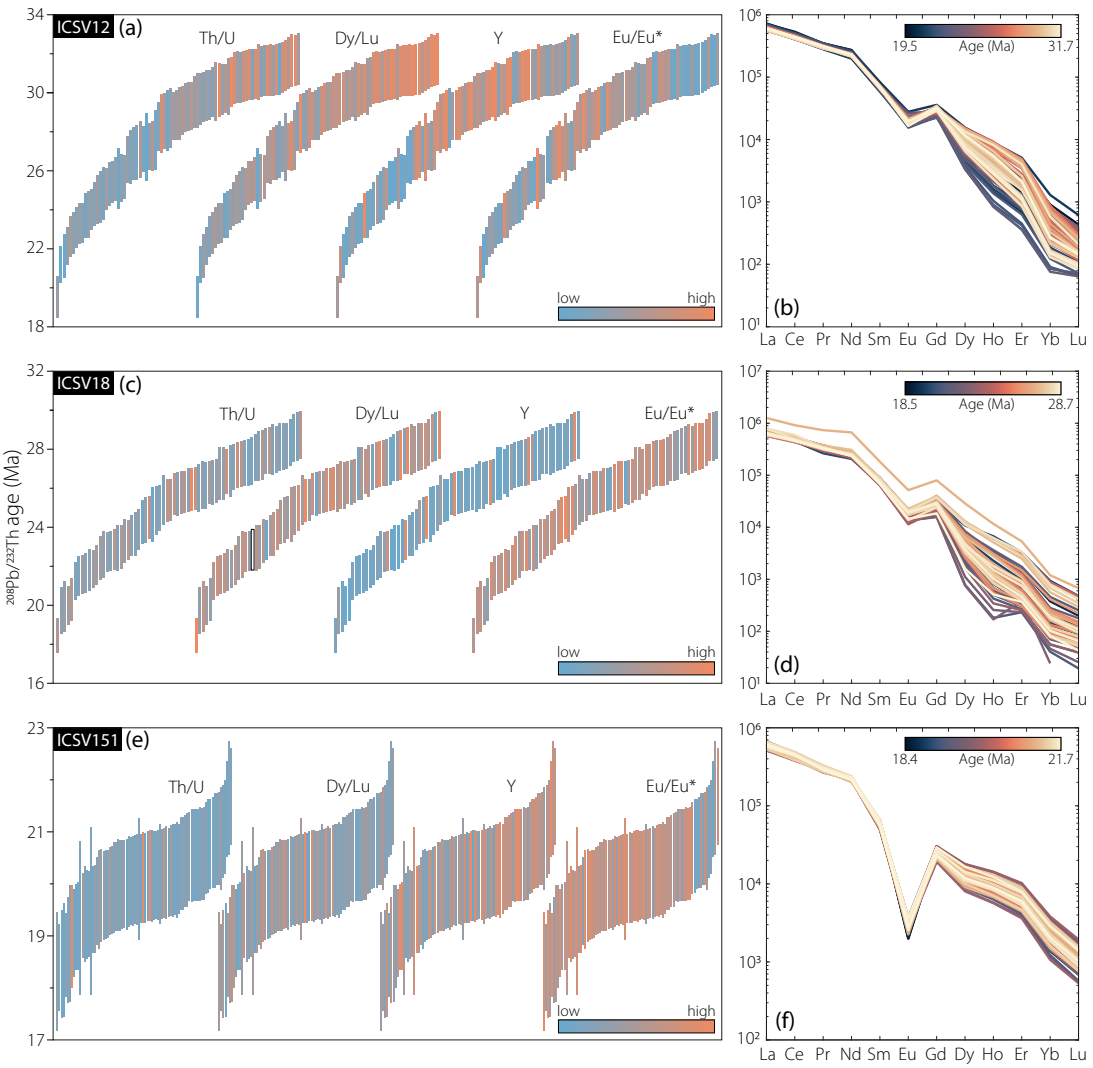


Fig. 5.23 Age ranked or mean weighted $^{208}Pb/^{232}Th$ analyses coloured by Th/U, Dy/Lu, Y & Eu/Eu* and chondrite-normalised REE plots for ICSV12 (a, b), ICSV18 (c, d) and ICSV151 (e, f).

ICSV18 shows few consistent trends between trace element data and age population. Th/U, Y and Eu/Eu* record relatively flat trends with associated scatter across varying age populations (Figs. 5.22a, c, d and 5.23b). Significant scatter is recorded in Dy/Lu values with no discernable trend (Fig. 5.22b, 5.23b). Older-middle ages show slightly more enriched HREE and MREE concentrations but no discernable difference is observed in LREE. (Fig. 5.23d)).

ICSV151 shows broad ranges of Th/U values (5-35) and Y concentrations (10000–25000). Both Th/U and Y are relatively elevated in comparison to values from ICSV18 and ICSV12. Elevated Y values are supported by the lack of co-crystallising HREE+Y phases present in the assemblage. Dy/Lu and Eu/Eu* values are relatively low compared to other samples. The most significant trends

are a slight decrease in Y values coincident with a relative increase in the Eu anomaly (Eu/Eu*; Fig. 5.23e). Eu concentrations similarly show a relative decrease (increasing anomaly) with decreasing metamorphic age in Figure 5.23f.

Th/U and Dy/Yb (representative of the MREE/HREE ratio) are measured using the principal Nu-Attom monazite method. Thus, a comparison of metamorphic age, Th/U and Dy/Yb ratios can also be discussed. The highest Dy/Yb values are dominantly found in kyanite-zone samples, with scattered higher ratios also documented for ablations from the sillimanite+K-feldspar zone. Dy/Yb values generally do not extend higher than 150 between *ca.* 33–20 Ma and are broadly lower than 30 from from *ca.* 20–18 Ma. Garnet-, staurolite- and sillimanite-zone samples dominantly record Dy/Yb values between 5-20. Overall, all grades document weak correlations with overall decreases in Dy/Yb ratios with decreasing metamorphic age. Older age populations show relatively low Dy/Yb ratios, with progressive increase in values where mixing between Himalayan and older age populations. Th/U concentrations are overall relatively low in Himalayan aged metamorphic populations. The following approximate ranges of Th/U analyses are shown for each metamorphic zone: 14-20 for garnet, 8-16 for staurolite, 2-16 for kyanite, 4-6 for sillimanite, and 2-8 for sillimanite+K-feldspar. An overall decrease in Th/U values is thus documented with relative increase in metamorphic grade. Within grades, an overall weak decrease in Th/U ratios with decreasing age is observed (Fig. 5.22g). Older age populations show a significantly higher range of Th/U values dominantly ranging from 0-40 with a relative decrease for mixed age populations trending between Himalayan and older metamorphic events. However, as a generalisation, only relative intra-sample changes rather than absolute ratios between samples are meaningful (Weller *et al.*, 2020).

5.5.2 Interpretation

5.5.2.1 Pre-Himalayan metamorphism

Samples from higher metamorphic grades are dominated by Cambro-Ordovician monazite ages. Two main age groups cluster between *ca.* 499–484 Ma and *ca.* 472–453 Ma. All samples are plotted as weighted mean plots and dominantly show one apparent Cambro-Ordovician age population. A slight variation is recorded by ICSV145, which potentially shows two apparent Cambro-Ordovician age populations (Fig. 5.20). Owing to the larger MSWD on the one age population

(MSWD = 7.1) compared to the two apparent age populations (MSWD = 5.1 and 0.93), it is suggested that two age plateaus fit a bimodal age distribution. Polyphase metamorphism is also consistent with the Kernel Density Estimate (KDE) plots with discordant filtered age populations (Fig. 5.24a) that show peaks at *ca.* 501 and *ca.* 467 Ma.

5.5.2.2 Prograde–peak

Monazite from the Suru Valley region records a protracted phase of metamorphic growth between *ca.* 33–18 Ma. The following age ranges are bracketed for each metamorphic grade: *ca.* 25–22 Ma at garnet grade, *ca.* 27–22 Ma at staurolite grade, *ca.* 33–18 Ma at kyanite grade, *ca.* 28–21 Ma at sillimanite grade, and *ca.* 28–21 at sillimanite+K-feldspar grade, which may be further discriminated by peaks on KDE plots. This produces three prominent groupings: the first group is from *ca.* 28–26 Ma, which is interpreted to either post-date M_1 or be representative of M_1, a second peak occurs at *ca.* 24–23 Ma, inferred to relate to M_2. Finally, the last peak occurs at *ca.* 21–20 Ma coincident with leucogranite crystallisation during the waning stages of M_2.

Monazite in the matrix shows a broader range of ages and commonly records the oldest age populations compared to monazite inclusions in porphyroblasts. This suggests that matrix grains preserve prograde growth despite continued growth and/or recrystallisation during progressive metamorphism. Given the largest grains are commonly located in the matrix, it suggests that for this sample set grain size exerts a stronger influence on preservation of prograde growth than the microstructural location. The frequent fracturing of porphyroblasts aligns with the broad age ranges measured from individual monazite grains, implying that fluid infiltration can result in continuous recrystallisation of monazite during progressive metamorphism. However, the preservation of the largest age populations in matrix monazite necessarily implies microstructural context and/or chemistry is essential to deconvolving the age spectra.

The rareity of Himalayan-aged monazite inclusions in garnet cores is suggestive that monazite growth broadly post-dates growth of garnet cores. Monazite growth displays relationships suggestive of partial growth prior to garnet rims. Which produces a dominant age population between *ca.* 26–24 Ma. This can be tested against the relative timing of staurolite crystallisation and microstructural relationship with respect to monazite in ICSV18 (Fig. 5.21e). Age populations from monazite in different microstructural contexts suggest garnet rims pre-

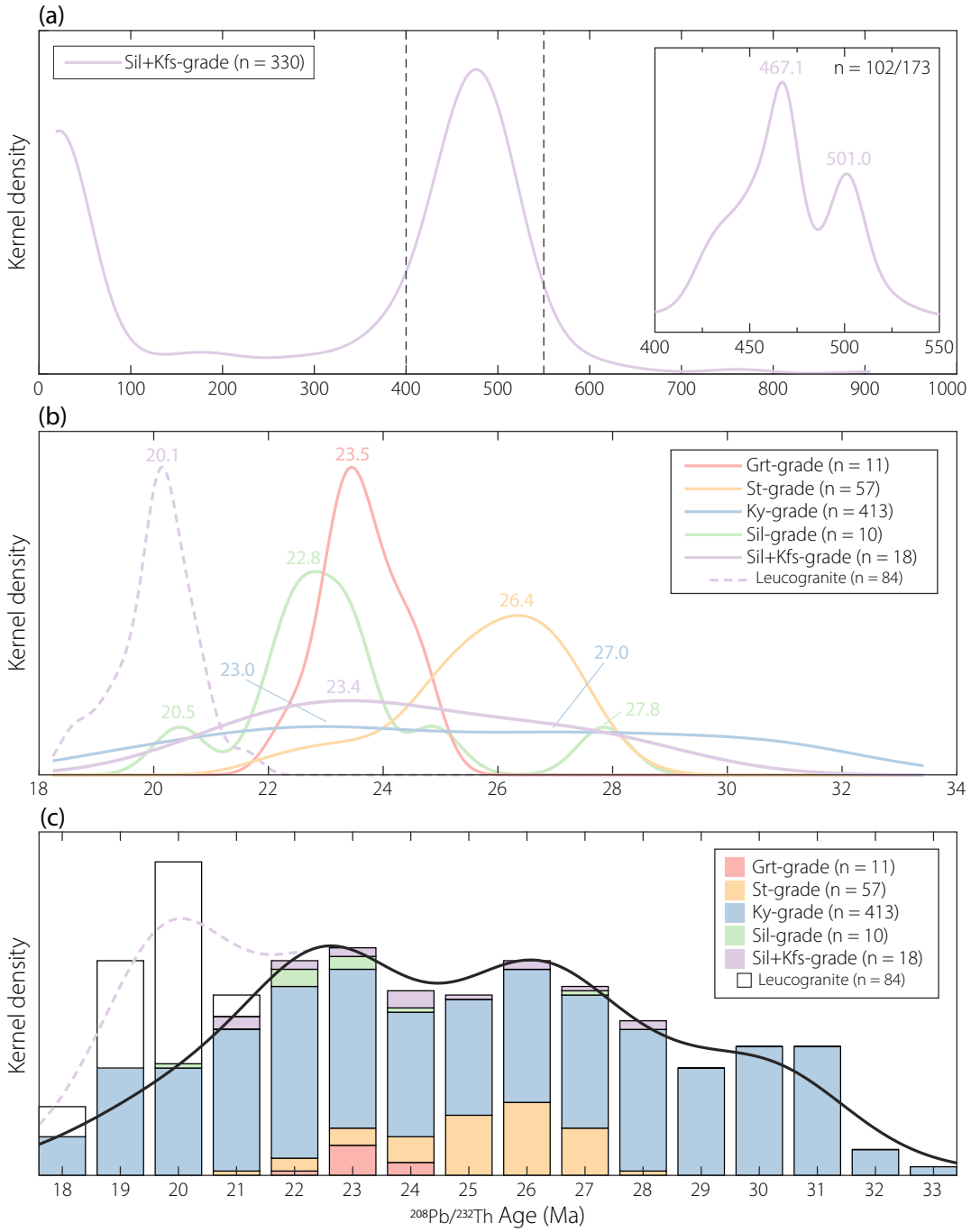


Fig. 5.24 KDE plots for the monazite dataset partitioned by metamorphic grade for a) pre-Himalayan metamorphism (Cambro-Ordovician) and b) Himalayan metamorphism. Owing to a prominent single age population on leucogranite, it is rescaled to the maximum probability of other populations. Inset in figure a) displays sillimanite+K-feldspar zone results between 400-550 Ma with discordance filter of -4 and +5.6 showing a bimodal peak during the Bhimphedian metamorphic event. c) KDE plot and histogram for all Himalayan ages monazite. Dashed line represents results including single-age leucogranite results and solid line excluding these results.

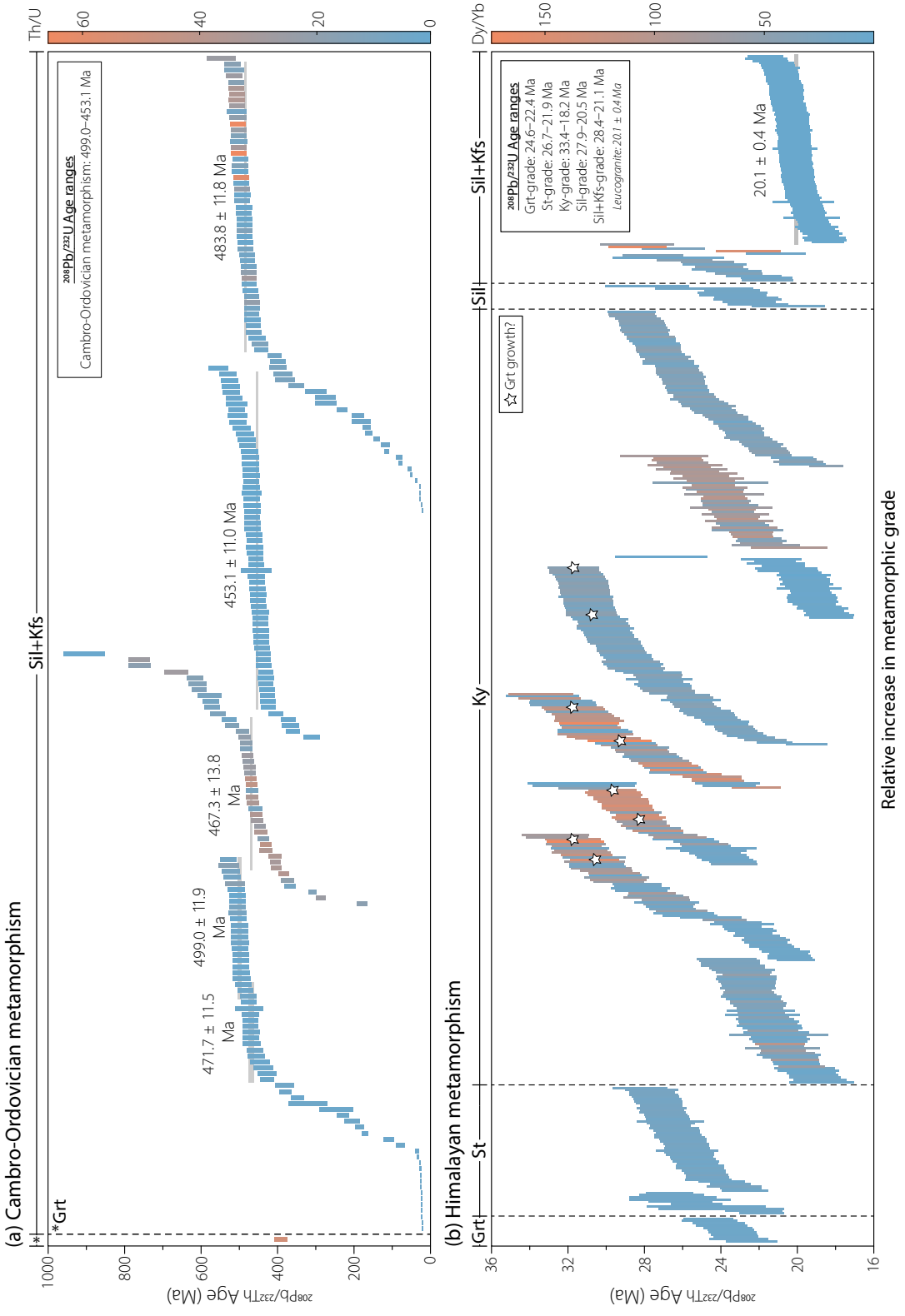


Fig. 5.25 Collation of mean-weighted $^{208}Pb/^{232}Th$ analyses for the entire monazite dataset separated for a) Cambro-Ordovician and b) Himalayan metamorphic episodes .

date staurolite growth, which is consistent with microstructural interpretations with partial resorption of garnet rims by staurolite. However, ages from these microstructural locations are consistently younger than those from other samples (The monazite grain that shows partial pre-garnet rim growth is notably the largest grain in the sample, and the oldest ages from this grain (back to *ca.* 26.3 Ma) could be consistent with the relative size of the analysed grain that is less susceptible to penetrative recrystallisation.

Age populations from other staurolite bearing samples suggest growth of staurolite at lower structural levels during or after *ca.* 30–25 Ma. Kyanite growth may occur concurrent or subsequent to age determinations ranging between *ca.* 31–26 Ma. Comparison of a minimum age for kyanite growth (*ca.* 31–28 Ma) and minimum age for staurolite growth (*ca.* 28–25 Ma) suggests that growth of staurolite could post-date kyanite-growth. Microstructural analysis reveals that grain boundaries between the two minerals are incised at their points of contact. Both minerals exhibit post-D_2 growth and contain similar inclusion suites, indicating that they likely grew near contemporaneously. Subsequent growth of staurolite is possible though would require more convincing evidence owing to the overlap of age distributions in ICSV13 and overlap of minimum kyanite growth range in ICSV13 (*ca.* 31–28 Ma) with the minimum staurolite growth range in ICSV97 (*ca.* 30–29 Ma; Fig. 5.21b, c).

Owing to the recognition of post-tectonic growth of kyanite and staurolite, at thermal peak conditions, documented age clusters broadly constrain minimum ages for attainment of thermal peak. Although age ranges provide a minimum estimate for relative growth, normalised density distribution (KDE) could better reflect pulsed stages of monazite growth across the sample set. Relative age peaks for staurolite and kyanite that are associated with peak conditions at *ca.* 29–28 Ma (Fig. 5.21g) are inferred as the timing of thermal peak metamorphism in kyanite-zone samples.

Finally, prograde–peak conditions can also be constrained by trace-element geochemistry. High Dy/Yb ratios in kyanite-zone samples are documented between *ca.* 33–28 Ma (Fig. 5.25b) and suggest that monazite growth was concurrent with the growth or presence of a significant HREE+Y sink (interpreted as garnet). This record is only captured in certain grades and rock compositions, as the oldest age documented in lower Dy/Yb samples from the staurolite zone is 28.2 ± 1.4 Ma, suggesting the dominant growth stage of a HREE+Y sink possibly occurs to this age at these structural levels.

5.5.2.3 Decompression

The highest metamorphic grades preserve metamorphic assemblages, reaction textures, and *P-T* conditions attributed to decompression from peak pressures. Analysis of monazite from sillimanite- and sillimanite+K-feldspar-zone samples show population peaks at *ca.* 23 Ma and 24 Ma, respectively. These ages are inferred to broadly relate to the M_2 peak. Limited monazite growth documented at *ca.* 28–27 Ma, could coincide with M_1 peak conditions, or initial monazite growth at the onset of decompression, through the release of HREE from garnet rim resorption. 28–27 Ma is therefore set as a maximum age for the onset of decompression.

The waning stage of M_2 is recorded by monazite ages in weakly-deformed leucogranite, and the youngest age populations of sillimanite- and sillimanite+K-feldspar-zone monazite at *ca.* 21–20 Ma.

5.6 Zircon

The results of zircon isotopic dating can be considered by lithological group, owing to the propensity of zircon to be of detrital, magmatic and/or metamorphic origin. The lithological groups include psammite, metavolcanic rock (group B), and metamorphosed granite & leucogranite. Wetherill concordia and Tera-Wasserburg plots are presented in Figure 5.27.

5.6.1 Results

5.6.2 Psammite

Samples ICSV167 and ICSV80 are psammite horizons within the mixed psammite, pelite, and semipelite unit. The extracted zircon population in ICSV167 are oval euhedral grains that show minor fracturing (~200 µm). Regular polygon oscillatory zoning is observed, and in addition to locally patchy zoning (Fig. 5.26a). Along fractured domains or grain margins, darker zones of recrystallisation are present. Grains extracted from ICSV80 are commonly oval subhedral–euhedral grains (~100–300 µm) often displaying concoidal fracturing. Zoning is dominantly oscillatory or patchy with brighter homogeneous overgrowth along fractures. The analysis of zircon was performed on the darker domains (Fig. 5.26b).

57 analyses from zircons in ICSV167 and 25 analyses from zircons in ICSV80 yield prominent $^{207}Pb/^{206}Pb$ age peaks at *ca.* 1200–800 Ma (Fig. 5.27). Smaller $^{207}Pb/^{206}Pb$ age peaks range back to *ca.* 3000 Ma in ICSV80 and *ca.* 3500 Ma in ICSV167. ICSV80 records another $^{207}Pb/^{206}Pb$ age peak at *ca.* 700 Ma and *ca.* 300 Ma whilst ICSV167 record peaks from *ca.* 700–400 Ma. Broadly, the samples record a prominence of Proterozoic signatures locally extending up into to the Palaeozoic. The youngest detrital populations, as defined by the average $^{207}Pb/^{206}Pb$ ages from of the three youngest grains, are Ediacaran: *ca.* 604 Ma (ICSV167) and *ca.* 610 Ma (ICSV80).

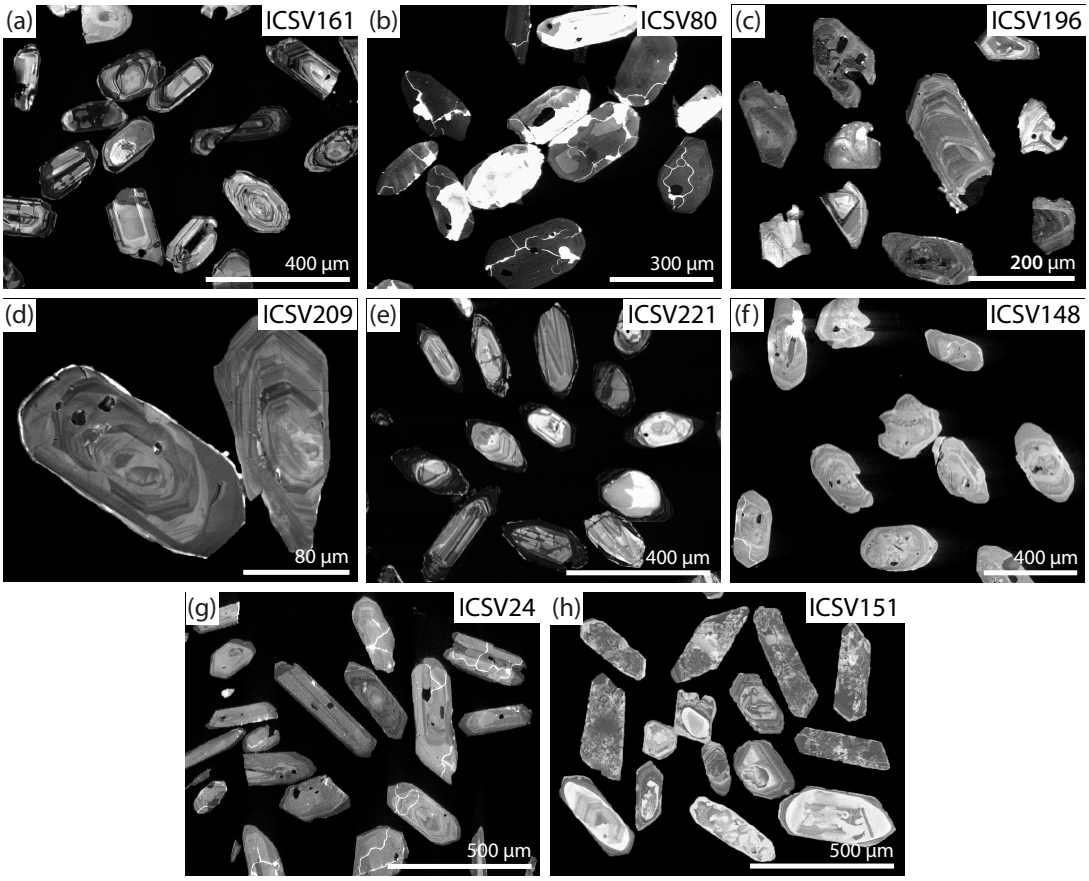


Fig. 5.26 Cathodoluminescence image of representative zircon grains from analysed populations for each sample.

5.6.3 Metavolcanic rock

Samples ICSV196 and ICSV209 are metavolcanic rocks within the Lamayuru Complex. Owing to their mafic-rich nature, few grains were recovered during mineral separation. Analysed populations display polygon concentric zoning

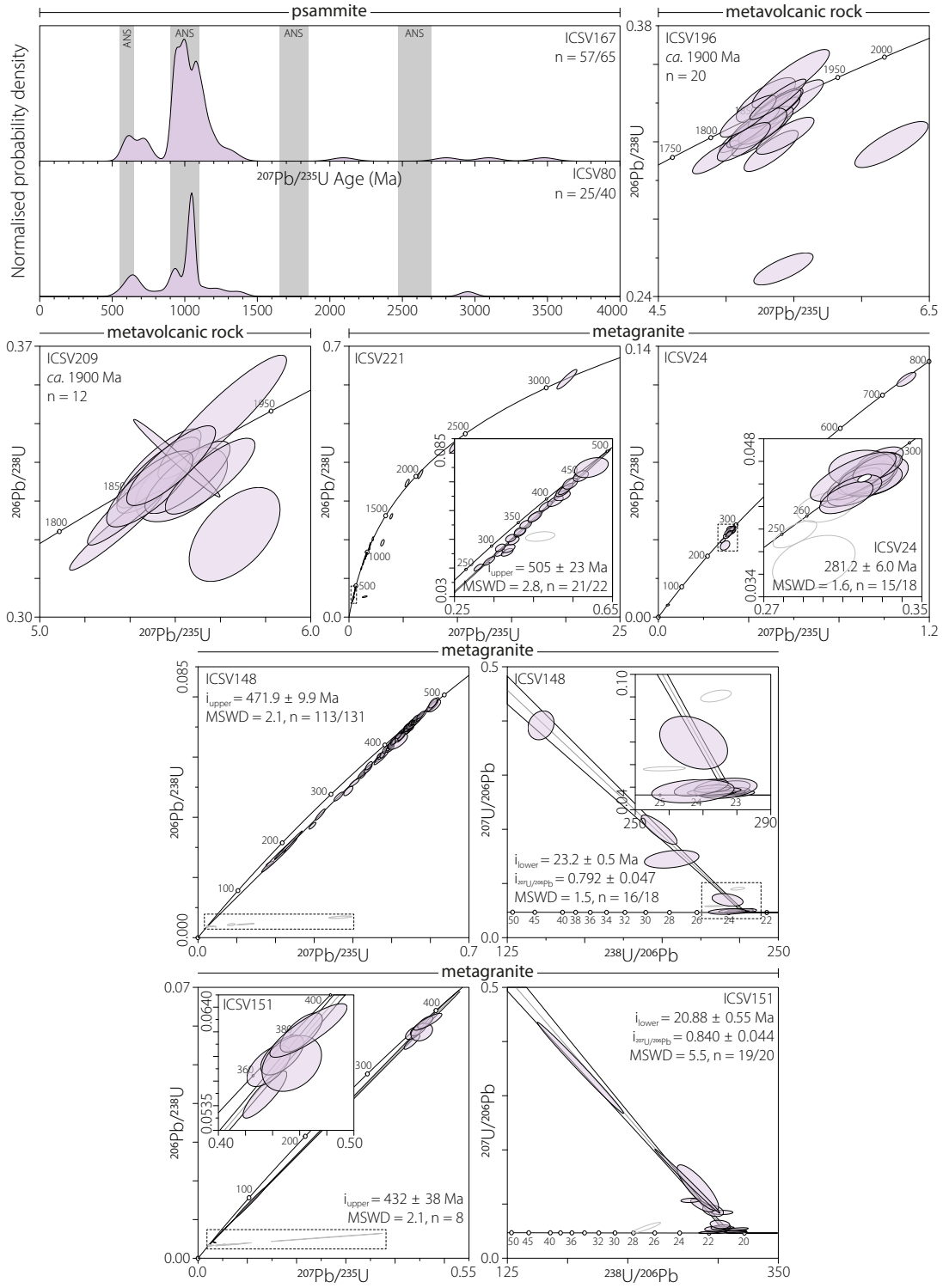


Fig. 5.27 U-Pb analyses of zircon separates from select samples from psammite, metavolcanic rock and metamorphosed granite samples. KDE plots use analyses that passed -4 and +5.6 discordance filtering from concordia. ANS equates to the Arabian-Nubian Shield with subpopulations of 2700–2470, 1850–1650, 1100–900 and 650–550 from Avigad *et al.* (2003).

patterns (Fig. 5.26c, d). Grains are dominantly euhedral (~100–200 µm) though locally display rounded corners and may be split across cores.

20 analyses from 10 grains in ICSV196 and 12 analyses from 2 grains in ICSV209 yield $^{207}Pb/^{206}Pb$ discordant ages that cluster at *ca.* 1900 Ma on concordia for both samples (Fig. 5.27).

5.6.4 Metamorphosed granite & leucogranite

The granitic units can be differentiated into Cambro-Ordovician granite, Permian granite, and Miocene leucogranite. ICSV221 and ICSV148 are Cambro-Ordovician granites. ICSV221 is a metamorphosed syenogranite with euhedral zircons (~100–300 µm) that display prominent striated to oscillatory zoned xenocrystic cores with growth zoned rims. ICSV148 is a metamorphosed granite with various intersecting *in-situ* and layered melt domains. It contains subrounded grains with recrystallised or convolutely zoned cores with oscillatory zoning in the rims. ICSV24 is a Permian granite with grains ranging between ~100–600 µm in length with euhedral angular shapes. Grains display oscillatory zoning (locally patchy). Conchoidal fracturing develops in select grains leaving high cathodoluminescence (CL) homogenous zones of recrystallisation. ICSV151 is a coarse grained leucogranite with minimal deformation (undulose patchy extinction in quartz). Recovered zircon displays euhedral–subhedral angular to subrounded grains (~150–400 µm) that display xenocrystic oscillatory zoned or recrystallised cores with oscillatory zoned overgrowths. Recrystallised cores were not targeted during analysis.

21 analyses of zircon grains in ICSV221 yield a $^{207}Pb/^{206}Pb$ upper intercept at 505 ± 23 Ma (MSWD = 2.8). Across the total 40 analyses from 23 grains, concordant results cluster at *ca.* 1000–800 Ma with both discordant and concordant analyses trending back to *ca.* 3100 Ma (Fig. 5.27).

113 analyses of zircon grains in ICSV148 yield a $^{207}Pb/^{206}Pb$ upper intercept at 471.9 ± 9.9 Ma (MSWD = 2.1; Fig. 5.27). 16 analyses on an uncorrected Tera-Wasserburg plot yield a $^{238}Pb/^{206}Pb$ lower intercept at 23.2 ± 0.5 Ma (MSWD = 1.5; Fig. 5.27).

15 analyses of zircon grains in ICSV24 from yield a $^{207}Pb/^{206}Pb$ concordia age of 281.2 ± 6.0 Ma (MSWD = 1.6; Fig. 5.27). Two analyses also lie on concordia with an older and a younger age of *ca.* 752.1 and *ca.* 41.2 Ma, respectively.

8 analyses of zircon grains in ICSV151 show discordance trending back to an upper $^{207}Pb/^{206}Pb$ intercept of 432 ± 38 Ma (MSWD = 2.1). 19 analyses yield a dominant $^{207}Pb/^{206}Pb$ age population at 20.9 ± 0.6 Ma (MSWD = 5.5; Fig. 5.27).

5.6.5 Interpretation

5.6.5.1 Detrital record

The prominence of *ca.* 1100–900 Ma zircon population has been used by previous studies to suggest that Himalayan detritus may be sourced from the East African Orogen and the Arabian-Nubian Shield (e.g., DeCelles *et al.*, 2000; Myrow *et al.*, 2010; Spencer *et al.*, 2013a; Dyck *et al.*, 2019). The overlap of kernel density estimates with analysed detrital zircon populations from the Arabian-Nubian Shield supports the existing interpretation. Older grains show less overlap with these sources, and possibly pertain to older orogens involving Palaeoproterozoic and Archaean crust and interpreted to have been exposed in Gondwana (e.g., Myrow *et al.*, 2010). The dominance of the 1100–900 age signature matches well with detrital age spectra from the GHS in Sutlej Valley (Webb *et al.*, 2011), Garhwal (Spencer *et al.*, 2012), Nepal (Dyck *et al.*, 2019), Sikkim (Mottram *et al.*, 2014a), and Bhutan (McQuarrie *et al.*, 2008; Long & Mcquarrie, 2010). The younger age population at *ca.* 750–600 Ma are observed in the GHS composite of Gehrels *et al.* (2011, and references therein), however, the relative presence and/or dominance of this peak across the orogen appears inconsistent, suggesting variation of detritus source across-strike as suggested by Spencer *et al.* (2012).

The moderate span of time between the youngest detrital $^{207}Pb/^{206}Pb$ age population (*ca.* 610–604 Ma) and oldest crystallisation age (505 ± 21 Ma) suggests that the nature of the sediment load is consistent with a passive margin stratigraphy (Cawood *et al.*, 2012).

5.6.5.2 Igneous activity

Discordant ages from samples ICSV196 and ICSV209 do not produce a meaningful age regression owing to the limited number of analysed grains; however, both cluster near concordia at 1900 Ma (Fig. 5.27). Metavolcanic rocks are interlayered within the Triassic–Upper Cretaceous Lamayuru Complex deposited on the north Indian margin (Robertson & Degnan, 1993); thus, a magmatic age of *ca.* 1900

Ma is unlikely in the given sedimentary depositional ages. Ages *ca.* 1900–1800 Ma are recorded in the orthogneiss of the Ama Drime massif (Cottle *et al.*, 2009a; Wang *et al.*, 2017); and in the LHS or GHS granite gneisses (e.g., Kohn *et al.*, 2010; Mottram *et al.*, 2014a) and mafic units (Miller *et al.*, 2000). This widespread seemingly Palaeoproterozoic magmatic event has been attributed to rifting processes (Bhat *et al.*, 1994, 1998; Ahmad *et al.*, 1999; Sakai *et al.*, 2013), or a continental volcanic arc on the northern margin of the Indian plate active during the early aggregation of the supercontinent Nuna (Kohn *et al.*, 2010). A psammitic sample from the Lamayuru Complex went through mineral separation techniques, though no zircon was recovered. The age correlation between volcanosedimentary Lamayuru Complex (forming part of the suture zone) and Paleoproterozoic magmatic ages within other lithotectonic domains requires further investigation.

Metamorphosed granites and leucogranites from the HMC record three dominant age populations. A Cambro-Ordovician magmatic age is recorded at *ca.* 505–472 Ma and a Permian magmatic age at 281.2 ± 6.0 Ma. Metamorphic rims in a Cambro-Ordovician granite and igneous rims on zircon in the leucogranite yield ages of 23.2 ± 0.5 Ma and 20.9 ± 0.6 Ma, respectively. The HMC contains voluminous Cambro-Ordovician granitic bodies formed during the early Paleozoic Bhimphedian orogeny, largely between *ca.* 520–470 Ma (Cawood *et al.*, 2007, 2021). The ages recorded in this study are in agreement with this age range.

Permian igneous activity is largely recorded as volcanism in the voluminous Panjal Traps sequence across western Zanskar and eastern Kashmir (Shellnutt, 2018). However, small Permian granitic bodies have been locally documented in NW India and Pakistan (e.g., Anczkiewicz *et al.*, 2001; Noble *et al.*, 2001). Previous analysis of smaller granites in the Suru Valley have recorded Permian U-Pb zircon ages: the Sankoo granite at *ca.* 270 Ma (Noble *et al.*, 2001), Parkachik granite at 268 ± 5 Ma (Noble *et al.*, 2001) and 284 ± 4.4 Ma (Horton & Leech, 2013). A thin alkali granite dyke further SE in Zanskar records an age of 284 ± 1 Ma (Spring *et al.*, 1993). The granite dated in this study shows excellent agreement with these age populations.

Sample ICSV148 and ICSV151 are both located in the sillimanite+K-feldspar zone, and thus Miocene ages on metamorphic and igneous rims respectively may be directly attributed to metamorphism. An age of 23.2 ± 0.5 Ma is linked with the M_2 event, and concurrent partial melting. A younger age is recorded in the

leucogranite, consistent with the final stage of melt crystallisation at 20.9 ± 0.6 Ma.

5.7 Rutile

5.7.1 Results

5.7.1.1 Metacarbonate

ICSV23 ICSV23 is sampled from a thick layer of metamorphosed carbonate within the ZSZ. It displays prominent normal-sense shear criteria and a penetrative shear fabric. Rutile growth in thin-section appears broadly concurrent with the S_3 fabric. Analysed grains from ICSV23 are separates and occur as angular and moderate–coarse grains.

36 analyses from 7 grains yield a $^{238}U/^{206}Pb$ intercept of of 22.5 ± 0.8 Ma (MSWD = 2.1; Fig. 5.28).

5.7.1.2 Pelite

Pelitic samples host rutile in a variety of microstructural settings in the 7 samples analysed. With increasing grade the samples are from the staurolite zone (ICSV113, ICSV79), kyanite zone (ICSV6, ICSV97, ICSV12, ICSV96) and the sillimanite zone (ICSV91; Fig. 5.3). This broadly equates with the documented stability of rutile in the study area. Rutile is rarely observed at garnet grade and not observed in the sillimanite+K-feldspar zone. Rutile grains dominantly range from 50–200 µm in size and occur as rounded to oval grains locally with ragged or incised grain boundaries. Locally it is intergrown or rimmed by ilmenite. Rutile is generally aligned to the main fabric in analysed samples. BSE images show no variation in brightness across grain margin.

Within all analysed samples there exists no variation in age population as a result of microstructural context. For staurolite-zone samples $^{238}U/^{206}Pb$ ages are as follows: in ICSV113, 10 analyses from 5 grains yield an age of 15.1 ± 6.2 Ma (MSWD = 0.4); and in ICSV79, 9 analyses yield an age of 18.5 ± 1.9 Ma (MSWD = 1.5; Fig. 5.28). For kyanite-zone samples $^{238}U/^{206}Pb$ ages are as follows: in ICSV6, 16 analyses from 6 grains yield an age of 15.0 ± 1.0 Ma (MSWD = 0.81), in ICSV97, 34 analyses from 6 grains yield an age of 18.9 ± 1.0 (MSWD = 1.1);

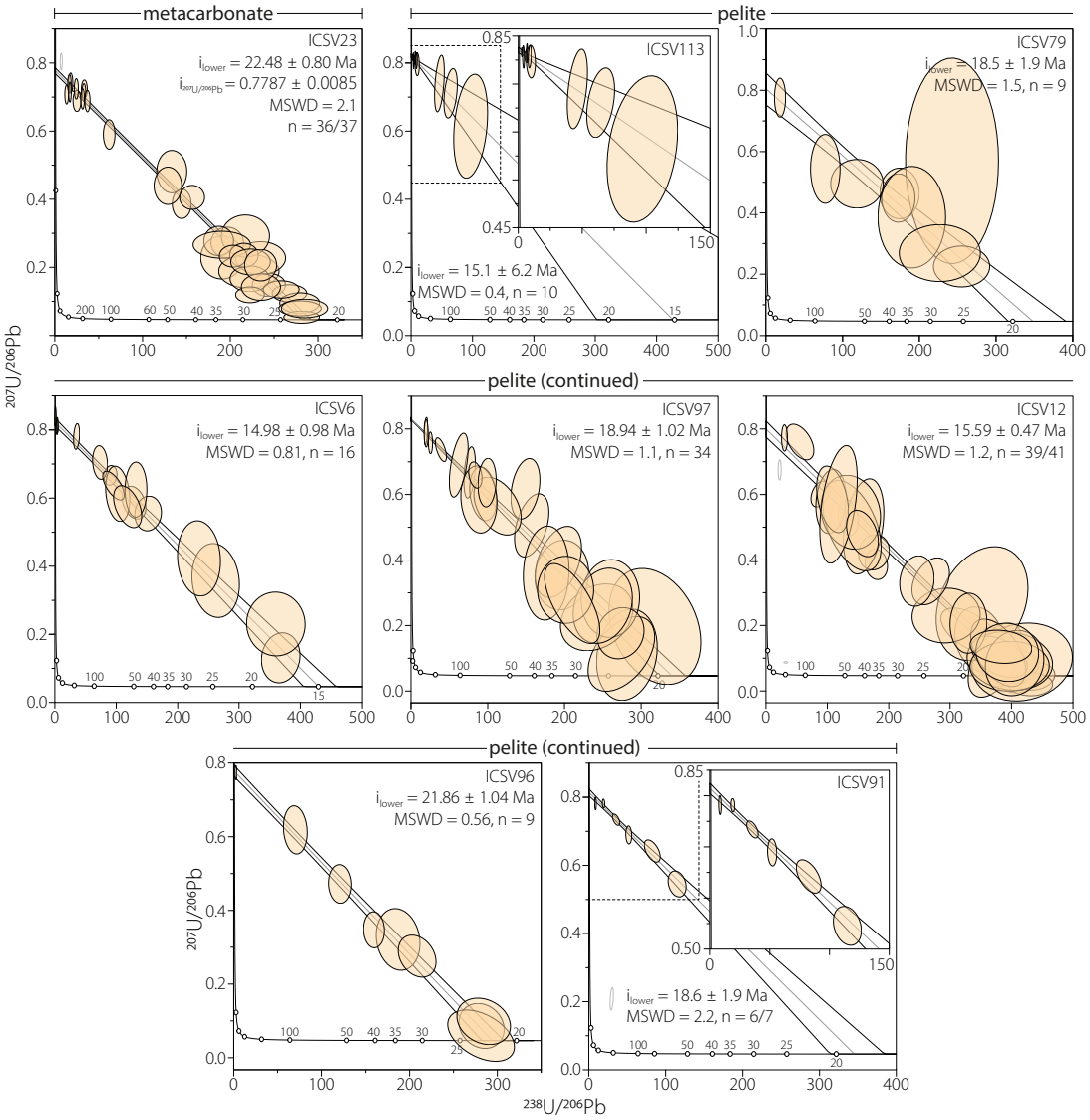


Fig. 5.28 U-Pb results for analysis of rutile from metacarbonate and pelite samples on Tera-Wasserburg plots with age regression using model-1.

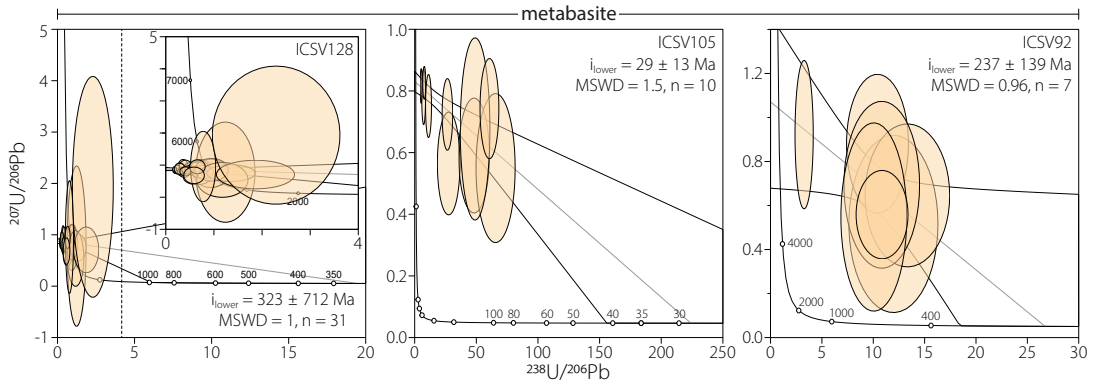


Fig. 5.29 U-Pb results for analysis of rutile in metacarbonate and pelite samples on Tera-Wasserburg plots with age regression using model-1.

in ICSV12, 39 analyses from 7 grains yield an age of 15.6 ± 0.5 Ma (MSWD = 1.2), in ICSV96, 9 analyses from 5 grains yield an age of 21.9 ± 1.0 Ma (MSWD = 0.56; Fig. 5.28). In the sillimanite zone, 6 analyses from 4 grains in ICSV91 yield an $^{238}U/^{206}Pb$ age of 18.6 ± 1.9 Ma (MSWD = 2.2; Fig. 5.28).

5.7.1.3 Metabasite

Although petrographic analysis indicates rutile commonly equates with peak pressures in metabasite samples, grains are poorly preserved owing to the relative rareity of porphyroblast phases until higher grades (where garnet growth is also dependent on bulk composition). Ilmenite (and/or titanite) commonly mantle rutile, and/or replace the grain entirely. Rutile is generally aligned with the main fabric in analysed samples. Three samples (ICSV128, ICSV105 and ICSV92) are from metabasic rocks, which are all located in the oligoclase zone (Fig. 5.3). ICSV128 and ICSV92 contain lobate to oval single or polycrystalline grains ranging from 50–500 µm in size. Fine acicular needles of ilmenite in patchwork patterns locally occur within grains. Rutile grains in ICSV128 are skeletal in nature. ICSV105 shows grains ranging from 40–160 µm in size that are rounded to angular in shape.

Two samples of amphibolite (ICSV128 and ICSV92) are dominated by common Pb and produce measured ages with large uncertainties. In ICSV128, 31 analyses from 11 grains yield a $^{238}U/^{206}Pb$ age of 323 ± 712 Ma (MSWD = 1), and in ICSV92, 7 analyses from 6 grains yield a $^{238}U/^{206}Pb$ age 237 ± 139 Ma (MSWD = 0.96; Fig. 5.29). These samples record uncertainties in excess or near to the absolute value of the measured age, these ages are not geologically meaningfull and are not discussed further. ICSV105 contains a layer of both amphibolite and mixed metamorphosed volcanosedimentary layer. Rutile is dominantly hosted in the amphibolite layer, where grains contain abundant coarse biotite in comparison to the previous samples that contain little to no biotite. 10 analyses from 9 grains in ICSV105 yield an $^{238}U/^{206}Pb$ age of 29 ± 13 Ma (MSWD = 1.5; Fig. 5.29).

5.7.2 Interpretation

For the sample closest to the upper contact of the ZSZ (ICSV23; Fig. 5.3) the microstructural context of the rutile and the measured age of 22.5 ± 0.8 Ma could either represent: 1) a (re-)crystallisation age for rutile coincident with S_3 fabric development and shearing, or 2) a cooling age. Recognising that this sample occurs

within the biotite zone and assuming an approximate closure temperature of 600 °C for grains of 100 µm (Cherniak, 1993), suggests that rutile likely crystallised below the closure temperature, and therefore dates crystallisation. Even assuming a lower limit for closure temperature of *ca.* 490 °C that may apply to rutile rims (e.g., Kooijman *et al.*, 2010), it is likely that the rutile cooled through the closure temperature near biotite-grade conditions (assuming isothermal decompression). The ZSZ may therefore be interpreted to be active at or earlier than *ca.* 23 Ma.

The ages from the pelitic samples at higheer-grade conditions are inferred to represent cooling as there are no obvious signs in BSE to indicate recrystallisation fronts on analysed rutile. Ages broadly span between *ca.* 22–15 Ma in the relevant metamorphic grades, with analysed staurolite-zone rutile yielding the youngest age range between *ca.* 19–15 Ma although there appears to be no consistent relationship between metamorphic grade and relative age. Within closely spaced kyanite-zone samples the ages range between *ca.* 22–15 Ma indicates significant heterogeneity in the timing at which "cooling" is recorded. The reasons for this variation are inferred to relate to grain size (e.g., Kooijman *et al.*, 2010) or relative abundance of porphyroblasts within samples hosting rutile. Importantly, these ages show that indendent of sample variation, cooling through ~600–490 °C was underway dominantly between *ca.* 20–15 Ma (though it may have occurred as early as *ca.* 22 Ma). Given the significant uncertainty associated with the measured age for ICSV105 (29 ± 13 Ma), which overlaps with these ages, it is possible that a younger age of cooling may be more representative, however, accounting for this uncertainty this result is not incorporated into any tectonic interpretations.

5.8 Apatite

5.8.1 Results

5.8.1.1 Group B volcanic rock

One sample was collected from the group B (meta)volcanic rock unit outside the main mapped region located by the NE corner of the map. This sample is from the Lamayuru Complex and is laterally continuous with similar samples analysed in the main mapped region that are metamorphosed to low grades (e.g., ICSV197 and ICSV209). Apatite separates from this sample comprise prismatic euhedral grains with locally fractured ends. Grains range from 75–200 µm and appear

inclusion free with no obvious zoning under BSE. Analysis of 33 spots from 10 grains yield a $^{238}U/^{206}Pb$ age of 165 ± 19 Ma (MSWD = 2.4).

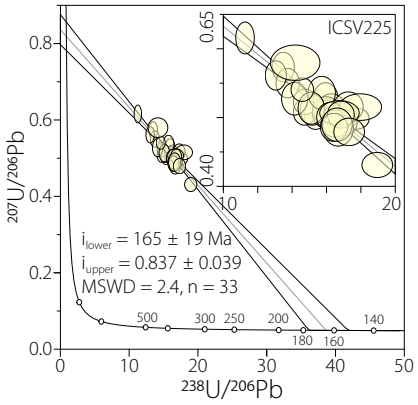


Fig. 5.30 U-Pb results for analysis of apatite separates from ICSV225 on Tera-Wasserburg plots with age regression using model-1.

5.8.2 Interpretation

Owing to the unmetamorphosed (or at minimum sub-greenschist facies) nature of the sampled volcanic horizon and well preserved euhedral habit of the apatite grains, this age is interpreted to correlate to a crystallisation age for apatite during volcanism. Previous stratigraphic studies from the Lamayuru Complex have dated radiolarian cherts in volcaniclastic material and produced a mid–late Jurassic age (Sutre, 1990) inferring depositional contacts with the volcanic flows. Suggested but unquantified ages of late Triassic–early Jurassic were given by Honegger (1983). The 'overlying' pelagic limestones above volcanic horizons contain *Globotruncana* that are late Cretaceous (Sutre, 1990). This age is in agreement with the stratigraphic work and places tighter constraints on alkaline activity and relative constraints on sedimentation on the Indian passive margin. Given the well preserved passive margin stratigraphy of the Lamayuru Complex documented in this study and in other studies Sutre (1990); Robertson & Degnan (1993), it is proposed that volcanic reactivation of the margin took place during the mid–late Jurassic Sutre (1990), or as constrained here at around 160 Ma.

5.9 Summary of multiphase geochronology

A map containing the collated age results for all analysed samples is shown in Figure 5.31.

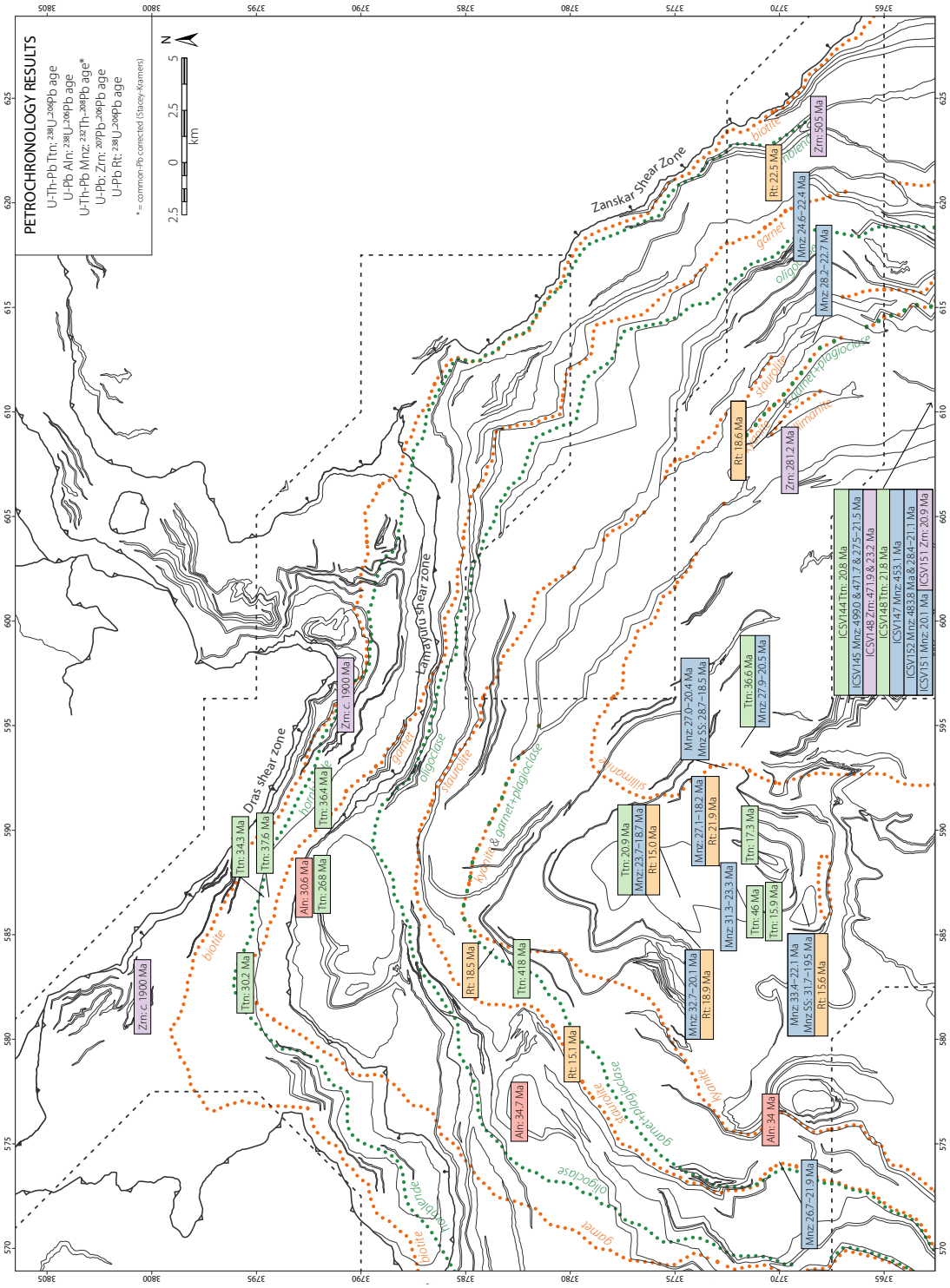


Fig. 5.31 Form-line map of major lithological, tectonic and metamorphic features of the Suru Valley area overlain with analysed samples and collated age data. Colour relates to the phase analysed. Ages with significant uncertainty or no resolvable age spectra are omitted. Grid references are truncated, with the final three zeroes omitted.

5.9.1 Pre-Himalayan magmatism and metamorphism

During the Cambrian, passive margin sedimentation on the Indian plate was well-established, with the youngest pre-orogenic biostratigraphic ages corresponding to the Furongian (Late Cambrian) throughout India, Nepal and Bhutan (Myrow *et al.*, 2016). This includes the Karsha Formation (Gaetani & Garzanti, 1991), Sanctuary and Annapurna Yellow formations (Annapurna; Searle *et al.*, 2003), and the Yellow Band below Everest (Searle & Godin, 2003; Myrow *et al.*, 2009). A biostratigraphic gap between *ca.* 490–460 Ma (maximum 36 Ma, minimum 22 Ma) follows deposition of those units. Postorogenic Late Ordovician mollase-type strata were then deposited above an unconformity (Myrow *et al.*, 2016). The stratigraphic break coincides with Barrovian metamorphism, crustal melting and emplacement of both S- and I-type granites between *ca.* 500–460 Ma (Gehrels *et al.*, 2006; Cawood *et al.*, 2007; Palin *et al.*, 2018; Cawood *et al.*, 2021). This period of orogenic activity has been named the Bhimphedian Orogeny (Cawood *et al.*, 2007), or alternatively the Kurgiakh Orogeny (Myrow *et al.*, 2016; Spencer *et al.*, 2019). The orogeny occurred from Pakistan to the eastern Himalaya and possibly into Afghanistan (Cawood *et al.*, 2007). Metamorphosed granites from the Suru Valley region yield Cambro-Ordovician magmatic ages between *ca.* 505–472 Ma, which are in agreement with the age range denoted in previous collations of this dataset, inferring they represent the same suite of granites (Cawood *et al.*, 2007, 2021).

Pre-Himalayan metamorphism has recently been documented along the length of the Himalayan mountain belt, however, the lateral extent and magnitude of the metamorphic event are poorly constrained is due to poor exposure and/or reworking (e.g., Cawood *et al.*, 2021). Evidence for the early metamorphism are often constrained by cross-cutting or host relationships between Cambro-Ordovician granite and sediment (e.g., Marquer *et al.*, 2000; Johnson, 2003; Thakur & Patel, 2012; Robyr, 2023). In NW India, relics of granulitic assemblages and textures in mafic bodies hint at a high temperature metamorphic event predating the Himalayan greenschist to amphibolite facies metamorphic event (Pognante & Lombardo, 1989; Wyss *et al.*, 1999; Thakur, 2014), as do staurolite inclusions reported in greenschist facies garnets (Robyr, 2023). The early Himalayan Cambro-Ordovician metamorphic event has also been constrained by geochronology in: Pakistan (482.4 ± 7.9 Ma and 464.5 ± 4.0 Ma, U-Pb monazite; Palin *et al.*, 2018), Himachal Pradesh (485 ± 19 Ma and 473 ± 14 Ma, Sm-Nd Grt; Bhargava *et al.*, 2016), Garhwal (Mohan *et al.*, 2022) (467 ± 3 Ma, Sm-Nd Grt; 534 ± 24 Ma,

Sm-Nd Grt; 465 ± 6.4 Ma, U-Pb zircon; Argles *et al.*, 1999; Foster *et al.*, 2000; Mohan *et al.*, 2022), Central Nepal (445 ± 16 Ma, Th-Pb Aln; 436 ± 8 Ma and 548 ± 17 Ma, Th-Pb Mnz; Catlos *et al.*, 2000, 2002a), and in Sikkim (*ca.* 480 Ma $^{40}Ar/^{39}Ar$; Grujic *et al.*, 2017).

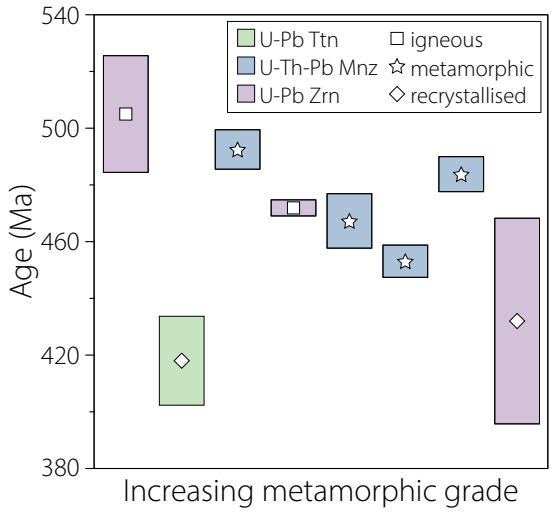


Fig. 5.32 Summary of multiphase geochronology of Cambro-Ordovician age signatures in U-Th-Pb titanite, monazite and U-Pb zircon analysis.

Samples analysed in this study show metamorphic mineral growth between *ca.* 499–484 Ma and *ca.* 472–453 Ma. Alternatively, plotted as a KDE produces prominent peaks at *ca.* 501 and *ca.* 467 Ma (Fig. 5.24a). These age groups are similar to the pre-Himalayan kyanite-grade and sillimanite-grade metamorphism constrained by U-Pb monazite ages at 482.4 ± 7.9 and 464.5 ± 4.0, respectively (Palin *et al.*, 2018). It may be that monazite growth occured in two main stages during the Bhimphedian Orogeny in Pakistan and NW India, recording two metamorphic events.

The recognition that the Bhimphedian Orogeny is associated with widespread metamorphic signature orogen has been underappreciated. In certain lithologies, structural levels, and/or accessory phases the metamorphic record is dominated by Cambro-Ordovician ages (e.g., Palin *et al.*, 2018) and this has repurcussions for models constraining the metamorphic evolution of the Himalaya, in that a widespread pre-Himalayan orogenic event may exert significant control over the subsequent Himalayan architecture. Voluminous Cambro-Ordovician granite along the length of the Himalaya will thermally weaken the crust through redistribution of radioactive elements from lower to higher crustal levels during granite formation and emplacement (i.e., elevated radiogenic heat production; Cunningham, 2013). This leads to the following question: what level of control does the

relative distribution of pre-Himalayan granite across the Himalaya exert over the thermal architecture or melt-production in the HMC? Cambro-Ordovician monazite is notably restricted to sillimanite- and sillimanite+K-feldspar-zone samples. In addition, there is a close structural relationship between leucogranites formed during the final phase of Himalayan anatexis and pre-Himalayan granites. These observations suggest that such links warrant further investigation. Other relevant factors include relative distribution of older tectono-metamorphic fabrics and structural features, which represent potential locus points for subsequent deformation or control the relative orientation of superposed structures. Inherited mechanical, rheological and structural weaknesses have previously been identified as important and interrelated controls on the accommodation of stress through the lithosphere (Raimondo *et al.*, 2014; Butler, 2017).

The recognition that not all metamorphic minerals are Himalayan in origin (e.g., Argles *et al.*, 1999; Robyr, 2023; Lihter *et al.*, 2022) could result in erroneous petrological modelling without sufficient context. In the Suru Valley region, key metamorphic porphyroblasts are documented as syn- or post-tectonic with respect to the main crustal thickening fabric, emphasising a Himalayan origin; however, without such context, the misuse of partially recrystallised or inherited Cambro-Ordovician minerals imparts significant error on calculated *P-T* conditions. This emphasises the necessity of careful field observations and petrographic constraints integrated with geochronology when deconvolving polymetamorphic sequences.

A second magmatic pulse is documented in the Suru Valley region during the Permian. Across Western Zanskar and Kashmir, the Panjal Traps are emplaced (Shellnutt, 2018), with smaller granitic bodies documented with U-Pb zircon analyses yielding ages between *ca.* 284–268 Ma (Spring *et al.*, 1993; Noble *et al.*, 2001; Horton & Leech, 2013). The Shafat granite dated in this study falls in this range (281.2 ± 6.0 Ma). Importantly this body represents the volumetrically largest granite thus dated, with an along strike distance of greater than 30 km. This analysis builds on the growing evidence that magmatic ages in NW India cannot be inferred to be dominated by Cambro-Ordovician ages and that the scale of Permian magmatism could be greater than currently recorded. A significant pulse of plutonic activity may act as a further heat source in the crust.

Possible thermal activity during the Permian has also been documented by two studies. Monazite inclusions in garnet from staurolite schists of the Pakistan Himalaya produce U-Pb monazite ages of 267 ± 5 Ma and 273 ± 2 Ma (Palin *et al.*, 2018), which are broadly coeval to Permian magmatic activity (this study;

Spring *et al.*, 1993; Noble *et al.*, 2001; Horton & Leech, 2013; Chen *et al.*, 2023). This was used to suggest that intrusions into the lower crust during Neo-Tethyan rifting may have provided the heat for crustal melting (Palin *et al.*, 2018). This is in agreement with the significant pulse of magmatic activity recorded in the Suru Valley region with the Shafat granite. Lu-Hf garnet ages in the Kanchenjunga region of eastern Nepalese Himalaya document Permian ages at 291.3 ± 1.4 Ma and 293.3 ± 1.4 Ma, with a third sample recording a lower age at 230.9 ± 2.3 Ma (Lihter *et al.*, 2022). The latter sample may have been resorbed following a similar Permian age of crystallisation or be affected by late diffusive Lu re-uptake (Kelly *et al.*, 2011). These ages have been similarly attributed to Neo-Tethyan rifting during the breakup of Gondwana (Lihter *et al.*, 2022). This suggests that the record of Permian magmatism and metamorphism across the Himalaya might invariably be documented in future studies.

5.9.2 Constraints on burial, fabric development and metamorphism

Figure 5.33 and Tables 5.1 and 5.2 show a summary of the key observations, interpretations and constraints regarding the timing of M_1 and M_2 events and fabric development in the Suru Valley region. The M_1 and M_2 events are part of a petrological continuum in the metamorphic evolution of a region such that relative thermal peaks or maxima will occur at different structural levels (and thereby metamorphic grade) at different times. The following key constraints and interpretations can thus be summarised (note that results here do not include the significant uncertainty range present on select analyses):

1. At high structural levels (biotite zone) prograde M_1 conditions occur at *ca.* 38 Ma with peak conditions between *ca.* 36–35 Ma (titanite). Prograde metamorphic growth occurs at garnet-grade conditions at $<$ *ca.* 35 Ma (allanite), likely coincident with the onset of thermal peak conditions around *ca.* 31–30 Ma (allanite and titanite). A maximum age for initiation of garnet growth at these structural levels is also $<$ 35 Ma. D_2 was waning by *ca.* 38 Ma and had broadly terminated by M_1 peak around *ca.* 36–35 Ma at biotite grade and by *ca.* 30 Ma near the start of garnet-grade conditions.

2. At moderate to low structural levels (staurolite and kyanite zones, and oligoclase and garnet+plagioclase zones) the following constraints are provided. In the kyanite zone, prograde conditions and garnet growth in select Ca-rich compositions might have initiated as early as *ca.* 46 Ma (titanite), with

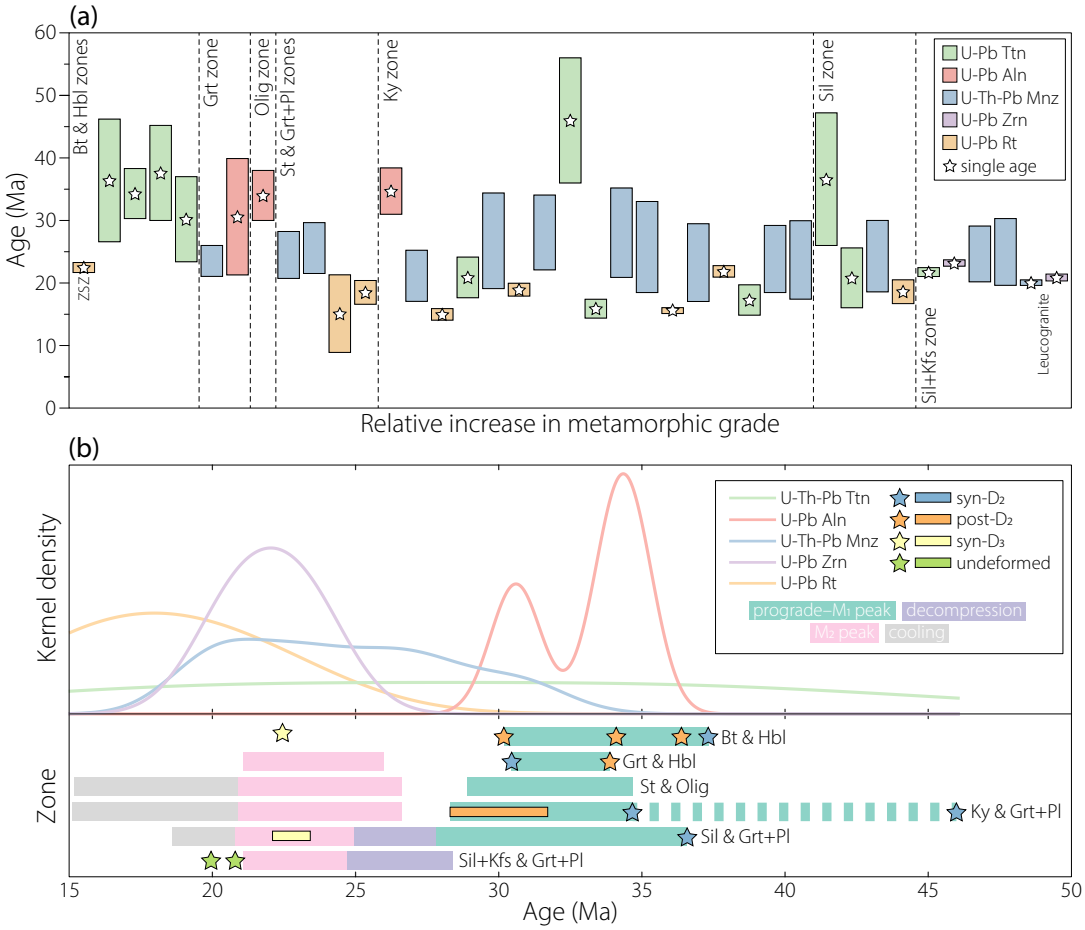


Fig. 5.33 Summary of multiphase petrochronology based on U-Th-Pb titanite, U-Pb allanite, U-Th-Pb monazite, U-Pb zircon and U-Pb rutile analyses. a) analyses plotted by increasing metamorphic grade with pelitic and metabasic isograds indicated, b) KDE plots for multiphase analyses.

the dominant stage of prograde development occurring closer to *ca.* 35 Ma (allanite). Both are synchronous with S_2 fabric development, and pre-date the thermal peak. Monazite growth initiated at staurolite grade-conditions *ca.* 27–26 Ma, likely concomitant or post-dating peak M_1 (the reasons for this are discussed in a later section). Garnet growth initiated in most kyanite-zone samples *ca.* 33 Ma and terminated *ca.* 28 Ma. Thermal peak M_1 conditions are broadly constrained *ca.* 31–28 Ma with burial having largely terminated prior to these ages.

3. Sillimanite-grade conditions show prograde M_1 development at *ca.* 37 Ma (titanite). Decompression from M_1 thermal peak likely occurs < *ca.* 28–27 Ma in sillimanite and sillimanite-K-feldspar-grade conditions (monazite).

4. Attainment of peak M_2 conditions likely occurs at the following ages moving up metamorphic grade: *ca.* 24 Ma (garnet grade), *ca.* 25–21 Ma (kyanite

grade), *ca.* 23–21 Ma (sillimanite & garnet+plagioclase grade), and *ca.* 23 Ma (sillimanite+K-feldspar grade).

5. The ZSZ and associated normal-sense movement is active at 22.5 ± 0.8 Ma based on U-Pb analyses of rutile associated with S_3 fabrics. At sillimanite grade, recrystallisation (or neocrystallisation) of monazite may be driven by S_3 reactivation (concomitant with fluid mobilisation) of earlier fabrics, suggesting D_3 is also active around 23 Ma.

6. Leucogranite emplacement and the end of M_2 occurs at 21–20 Ma, best constrained by a monazite mean age of 20.1 ± 0.4 Ma. The near-undeformed state of the leucogranite suggests the main phase of movement on the ZSZ was completed by *ca.* 20 Ma — however, S_3 is also not homogeneously distributed.

Broadly, the youngest monazite ages (*ca.* 20–18 Ma) and titanite ages (*ca.* 17–16 Ma) are interpreted as retrogressive, relating to progressive fluid dominated recrystallisation during uplift. These may be combined with U-Pb rutile analyses which record ages betweeen *ca.* 20–15 Ma, interpreted to represent uplift through a conservative estimate for the closure temperature for rutile of *ca.* 600–490 °C (e.g., Cherniak, 2000; Kooijman *et al.*, 2010)

Table 5.1 Petrochronological constraints on development of metamorphic fabrics and M_1

Information	**Petrochronological interpretation**
Phase: Ttn Age: 36.4 ± 9.8 Ma, 34.3 ± 4.1 Ma, 37.6 ± 7.6 Ma, 30.2 ± 6.8 Ma Sample: ICSV139, ICSV68, ICSV142, ICSV58 Zone: Bt Context: matrix, syn- to post-D_2 and pre-D_3	• Syn- to post-D_2 (dominantly post-D_2) Ttn interpreted to represent M_1 peak (*ca.* 38–30 Ma). • Syn-D_2 Ttn (ICSV142) records oldest age (*ca.* 38 Ma), while post-D_2 Ttn (other samples) document post-D_2 growth (*ca.* 36-30 Ma). D_2 was waning by *ca.* 38 Ma and had terminated by *ca.* 36–30 Ma. • Reorientation of grains by D_3 crenulations provides a maximum age for D_3. • ICSV58 located less than 100 m from the Grt isograd, indicates initiation of garnet-grade conditions at *ca.* 30 Ma.

Table 5.1 - continued

Information	**Petrochronological interpretation**
Phase: Aln Age: 30.6 ± 9.3 Ma Sample: ICSV46 Zone: Grt Context: matrix, syn-D_2	• Syn-D_2 Aln and peak porphyroblast index minerals (Grt) document syn-D_2 growth and indicate that the crystallisation age of *ca.* 31 Ma dates the M_1 peak.
Phase: Aln Age: 34 ± 4 Ma Sample: ICSV130 Zone: Grt Context: matrix and Grt inclusion, syn- to post-D_2	• Peak porphyroblast index mineral (Grt) exhibits post-D_2 growth and post-dates syn- to post-D_2 Aln. Crystallisation age points to prograde-peak growth with M_1 peak (and Grt growth) occurring after *ca.* 34 Ma.
Phase: Mnz Age: *ca.* 26.7–26.1 Ma Sample: ICSV109 Zone: St Context: matrix	• Matrix Aln corroded and not in equilibrium with matrix, small matrix Mnz grains present. Oldest monazite ages inferred to occur following matrix Aln breakdown. Oldest ages (*ca.* 27-26 Ma) may correlate with M_1 peak.
Phase: Aln Age: 34.7 ± 3.7 Ma Sample: ICSV110 Zone: Ky Context: matrix, syn-D_2, pre-St growth	• Syn-D_2 Aln indicates S_2 development at *ca.* 35 Ma; termination of crustal thickening occurs after *ca.* 35 Ma. Aln is partially engulfed by peak index porphyroblasts (St) which are post-D_2. M_1 metamorphic peak must occur after *ca.* 35 Ma.
Phase: Ttn Age: 46 ± 10 Ma Sample: ICSV7 Zone: Ky Context: syn-D_2 inclusions in Grt	• Inclusions documenting syn-D_2 growth of garnet. S_2 fabric development, associated crustal thickening and prograde metamorphism ongoing at *ca.* 46 Ma. Peak M_1 postdates *ca.* 46 Ma. Garnet growth as early as *ca.* 46 Ma?
Phase: Mnz Age: 33.4–28.3 Ma Sample: ICSV97, ICSV13, ICSV12 Zone: Ky Context: matrix, Ky and St inclusions	• High middle–heavy REE ratios suggest Grt growth between *ca.* 33-28 Ma. Grt cores commonly syn-D_2 with rims post-D_2. Peak porphyroblast phases (Ky and St) are post-D_2. Grt rims show varying relative timing of growth to pre- or post-Ky growth, broadly suggesting concurrent growth. Youngest ages of the given range (*ca.* 31-28 Ma) likely correlate with Grt rim growth = M_1 peak conditions.

Table 5.1 - continued

Information	**Petrochronological interpretation**
Phase: Mnz Age, context, sample: *ca.* 30.0–29.4 Ma (St inclusions, ICSV97); *ca.* 31.2–28.0 Ma (Ky inclusions, ICSV13); *ca.* 28.4–24.9 Ma (St inclusions, ICSV13); *ca.* 30.7–26.2 Ma (Ky inclusions, ICSV12) Age peaks: *ca.* 29.2 Ma (St inclusion); *ca.* 28.2 Ma (Ky inclusion) Zone: Ky	• Monazite from St inclusions dated between *ca.* 30-25 Ma and those in Ky inclusions between *ca.* 31–26 Ma, providing minimum ages of crystallisation of peak porphyroblast phases. Normalised peak distribution of ages from St- and Ky inclusions between *ca.* 29–28 Ma which can broadly correlate with the M_1 peak.
Phase: Mnz Age peaks, sample: *ca.* 29.8 Ma (ICSV97), *ca.* 28.6 Ma (ICSV13), *ca.* 30.8 Ma (ICSV12), *ca.* 30.3 Ma (ICSV12 SS) Zone: Ky	• Ky-zone samples characterised by phase of Mnz growth between *ca.* 31–29 Ma indicating major metamorphic event (M_1).
Phase: Ttn Age: 36.6 ± 10.6 Ma Sample: ICSV82 Zone: Sil Context: inclusions in syn-D_2 Grt core	• Ttn inclusions in syn-D_2 garnet core suggests S_2 fabric development and prograde M_1 ongoing at *ca.* 37 Ma. Peak M_1 postdates *ca.* 37 Ma.

Table 5.2 Petrochronological constraints on development of metamorphic fabrics and M_2

Information	**Petrochronological interpretation**
Phase: Rt Age: 22.5 ± 0.8 Ma Sample: ICSV23 Zone: Bt Context: Rt growth associated with S_3, analysed grains are separates	• Rt growth syn-D_3 indicating ZSZ was active by *ca.* 23 Ma.

Table 5.2 - continued

Information	**Petrochronological interpretation**
Phase: Mnz Age: *ca.* 24.6–22.4 Ma Age peak: *ca.* 23.5 Ma Sample: ICSV86 Zone: Grt Context: Matrix	• Matrix Mnz growth was late or experienced late recrystallisation (chemical zoning). Absence of Himalayan aged Mnz inclusions in Grt core and rim suggests Mnz growth post-dates Grt growth. Ages are coincident with M_2 event.
Phase: Ttn Age: 20.9 ± 3.3 Ma Sample: ICSV5 Zone: Grt+Pl Context: Matrix, polycrystalline rims around Rt+Ilm	• Post-peak Fe-Ti-oxide phases document late growth which could correspond to decompression or retrograde growth following peak-pressure conditions = coincident with M_2 thermal peak.
Phase: Ttn Age: 15.9 ± 1.5 Ma, 17.3 ± 2.5 Ma Sample: ICSV9, ICSV22 Zone: Ky & Grt+Pl Context: Matrix (ICSV9 & ICSV22) and locally Grt inclusions (ICSV22)	• BSE images suggest recrystallisation, U-Pb ages support recrystallisation likely during or following uplift. Ages provide minimum constraint on M_2 conditions. Older age in ICSV22 may relate to partial preservation of Ttn in Grt porphyroblasts shielding grains from subsequent recrystallisation.
Phase: Mnz Age peaks, sample: *ca.* 22.0 Ma (ICSV6), *ca.* 24.6 Ma (ICSV13), *ca.* 20.9 Ma (ICSV96), *ca.* 24.6 Ma and *ca.* 23.5 Ma (ICSV18), *ca.* 26.6 Ma (ICSV18 SS) Zone: Ky Context: Matrix; Grt, St & Ky inclusions	• Ky-zone samples dominated by second stage of Mnz growth between *ca.* 25–21 Ma, suggesting a younger metamorphic event (e.g., M_2). ICSV18 is located on the boundary with the Sil zone. A maximum age from ICSV18 defined by the separates analysed via SS is interpreted as a maximum age for the onset of decompression (*ca.* 27 Ma).
Phase: Mnz Dominant age range: *ca.* 24.9–20.4 Ma Age peak: *ca.* 22.8 Ma Sample: ICSV81 Zone: Sil Context: Matrix	• Mnz habit defined by mica cleavage coincident with S_2 reactivation and incipient S_3 development, such grains dated between *ca.* 25–21 Ma = S_3 development. Sample exhibits breakdown of Grt rims coincident with Ky growth. No petrographic relationship between Grt rim reaction products and Mnz growth and no relative decrease in HREE with age, inferred growth concurrent with late localised Sil growth between *ca.* 25–21 Ma (M_2).

Table 5.2 - continued

Information	Petrochronological interpretation
Phase: Ttn Age: 20.8 ± 3.8 Ma Sample: ICSV144 Zone: Grt+Pl Context: Euhedral matrix grains	• Euhedral shape and X-ray compositional zoning textures suggest magmatic growth with subsequent metamorphic growth/recrystallisation. Ages interpreted to constrain peak M_2 conditions *ca.* 21 Ma.
Phase: Ttn & Zrn Age: 21.8 ± 0.7 Ma (Ttn) 23.2 ± 0.5 Ma (Zrn) Sample: ICSV148 Zone: Sil+Kfs & Grt+Pl Context: Euhedral matrix grains and Grt inclusions (Ttn). Metamorphic rims on igneous cores (Zrn)	• Euhedral shape and texture of titanite in BSE images suggest magmatic growth with subsequent metamorphic recrystallisation. Analysed rims on zircon interpreted to be metamorphic based on CL zoning textures. Ages interpreted to constrain dominant phase of metamorphic recrystallisation/growth at peak M_2 conditions between *ca.* 23–22 Ma.
Phase: Mnz Age range and sample: *ca.* 27.5–21.5 Ma (ICSV145), *ca.* 28.4–21.2 Ma (ICSV152) Age peak (ICSV145 & ICSV152): *ca.* 22.8 Ma Zone: Sil+Kfs Context: Matrix	• Analysed inner rims record high Dy/Yb ratios relative to Cambro-Ordovician cores suggests concurrent growth of Himalayan Grt. Few spots and multiple phases of Grt growth make constraining Grt growth difficult. Mnz dated at *ca.* 23 Ma are coincident with M_2 peak. Decompression may initiate as early as *ca.* 28 Ma though equally may represent prograde–peak growth (i.e. M_1).
Phase: Mnz & Zrn Mean age: 20.1 ± 0.4 Ma (Mnz), 20.9 ± 0.6 Ma (Zrn) Sample: ICSV151 Zone: Sil+Kfs Context: Matrix (analysed grains are separates), igneous rims analysed on Zrn	• Single age of 20.1 ± 0.4 Ma in Mnz and 20.9 ± 0.6 Ma in Zrn constrains crystallisation age of leucogranite in final stage of M_2. *ca.* 21 Ma acts as a minimum age for M_2 thermal peak conditions.

5.9.3 Comparison to timing of events in NW Indian Himalaya

The range of ages from different structural levels and metamorphic grades fall within the spread of ages documented in the NW Indian Himalaya by previous studies (Fig. 2.3 Noble & Searle, 1995; Dèzes *et al.*, 1999; Vance & Harris, 1999; Walker *et al.*, 1999; Robyr *et al.*, 2006, 2012; Thöni *et al.*, 2012; Finch *et al.*, 2014;

Robyr *et al.*, 2014; Horton & Leech, 2013; Stübner *et al.*, 2014; Horton *et al.*, 2015; Robyr & Lanari, 2020; Štípská *et al.*, 2020).

5.9.3.1 Burial and prograde–peak metamorphism

Constraints on early tectonic burial and associated fabrics are provided in the Himachal Pradesh region by the youngest monazite inclusions, *ca.* 26 Ma in garnet and *ca.* 25 Ma in staurolite, which are interpreted as marking the end of burial (U-Th-Pb Mnz; Stübner *et al.*, 2014). Further east, in the amphibolite facies metamorphosed components of the THS, burial is documented to end by *ca.* 30 Ma (U-Pb Mnz; Chambers *et al.*, 2009) by the youngest monazite inclusions in garnet. Two stages of burial have been proposed for the Gianbul dome region of Zanskar (Štípská *et al.*, 2015; Robyr & Lanari, 2020). Ages from U-Pb monazite analyses in Štípská *et al.* (2020) fall between *ca.* 44–37 Ma and *ca.* 31–27 Ma, in agreement with U-Pb monazite age trends from Robyr & Lanari (2020) that cluster between *ca.* 43–41 Ma and *ca.* 29–28 Ma, progressing from higher to lower structural levels. Despite such age trends younging with decreasing structural height, fabric orientation and vergence suggest NE-directed folding and thrusting, superposed by SW-directed folding and thrusting (Robyr & Lanari, 2020). Other mechanisms have also been invoked to explain the presence of NE-directed structures (local heterogeneities, late backfolding, doming etc. Frank *et al.*, 1987; Singh, 2012; Fuchs & Linner, 1995; Dèzes *et al.*, 1999; Horton *et al.*, 2015). Prograde metamorphism (i.e., burial) in the Gianbul dome region is also documented from *ca.* 37–30 Ma (U-Th-Pb Mnz; Horton *et al.*, 2015). Timing of development of specific fabrics associated with SW-vergent folding and thrusting are largely unconstrained in other regions.

Petrochronology of inclusions is an essential technique for constraining prograde-metamorphic conditions. U-Th-Pb analysis of allanite and monazite inclusions in garnet from sillimanite-zone samples in the SE Zanskar region (Gianbul dome) are interpreted to date greenschist–amphibolite facies conditions between *ca.* 39–35 Ma and *ca.* 30–29 Ma respectively (Robyr *et al.*, 2012). Samples analysed in Robyr & Lanari (2020) show consistent age populations for monazite located in the matrix and occurring as inclusions. This indicates that the isotopic system was not reset after monazite crystallisation such that the ages of *ca.* 41 Ma and *ca.* 29 Ma (Robyr & Lanari, 2020) broadly correlate to peak conditions. From the same region, the following results are documented in Štípská *et al.* (2020) using LA-ICP-MS U-Pb dating. In a kyanite-garnet migmatite, garnet

growth is bracketed by monazite inclusions that yield ages between *ca.* 44–41 Ma; and kyanite growth by monazite inclusions with ages between *ca.* 44–38 Ma. In a kyanite-staurolite schist, inclusions in staurolite bracket staurolite growth between *ca.* 40–36 Ma, with *ca.* 36 Ma interpreted as the metamorphic peak. Samples that preserve younger age populations (garnet-staurolite schists) show inclusions of monazite and xenotime in garnet constraining the age of garnet growth between *ca.* 32–29 Ma. In staurolite from these samples, monazite ages of *ca.* 31-27 Ma are documented with a prominent peak at *ca.* 29 Ma. Analysis of metamorphic schists from SE Zanskar (Gumburanjum) and NW Himachal Pradesh (Upper Lahul) regions by Walker *et al.* (1999) provided concordant ages of *ca.* 32–29 Ma in monazite (U-Pb), while a single reversely discordant grain had a $^{207}Pb/^{235}U$ age of *ca.* 35.3 Ma. Combined with monazite ages from pegmatites, this led Walker *et al.* (1999) to interpret Barrovian metamorphism as occurring between *ca.* 37–30 Ma. Prograde metamorphic monazite (re)crystallisation dates is documented between *ca.* 37–33 Ma in the Gianbul dome (Horton *et al.*, 2015). In central Himachal Pradesh, monazite inclusions in garnet and kyanite show that prograde conditions occurred at *ca.* 38 and 39 Ma, respectively (U-Th-Pb Mnz; Stübner *et al.*, 2014). Analyses from monazite cores indicate prograde growth initiated as early as *ca.* 41 Ma. Peak metamorphic conditions are constrained between *ca.* 37–36 Ma, though high grade metamorphic conditions could have lasted until *ca.* 27–26 Ma (Stübner *et al.*, 2014). In the eastern Himachal Pradesh region (lower THS), monazite inclusions in garnet yield ages between *ca.* 34–29 Ma, and are used to constrain initiation of garnet growth at *ca.* 34 Ma and termination of growth by *ca.* 28 Ma (U-Pb Mnz; Chambers *et al.*, 2009).

The relative timing of metamorphic conditions in the Suru Valley region was previously constrained by Sm-Nd garnet dating for samples from the kyanite zone generated core–rim ages of *ca.* 33–31 and *ca.* 31–28 Ma (Vance & Harris, 1999). These were interpreted to constrain prograde growth, with peak metamorphism occurring after. However, rim compositions of garnet also coincide with thermal peak (see Chapter 4) - such that rim ages (*ca.* 31–28 Ma) may represent attainment of peak conditions. These results are consistent with the relative timing of documented garnet growth in this study. Metamorphic monazite located at the staurolite isograd yields an age of *ca.* 27 Ma, and is inferred to date near-peak conditions (Horton & Leech, 2013). Finally, $^{40}Ar/^{39}Ar$ hornblende ages of *ca.* 31 Ma from the upper structural levels (located near the garnet isograd) and *ca.* 22 Ma at the lower structural levels (near the kyanite or sillimanite isograd) show that peak metamorphism occurred before these times at these structural levels

(Searle *et al.*, 1992). The dominantly Oligocene–Miocene age populations from previous studies in NW India as well as those previously undertaken in the Suru Valley regioin are in excellent agreement with the results of this study, notably ages for garnet growth at *ca.* 32–29 Ma (Štípská *et al.*, 2020), and *ca.* 34–28 Ma (Chambers *et al.*, 2009), as well as a dominant phase of staurolite growth at *ca.* 29 Ma (Štípská *et al.*, 2020) and peak of monazite crystallisation at *ca.* 29 Ma (Robyr & Lanari, 2020).

The extent and magnitude of memtamorphism during *ca.* 44–37 Ma was substantial enough to induce medium-pressure metamorphic conditions and partial melting (Epard *et al.*, 1995; Robyr, 2002; Robyr & Lanari, 2020; Štípská *et al.*, 2020). The lack of peak metamorphic ages between *ca.* 44–37 Ma in the metamorphic domes as documented in Robyr & Lanari (2020); Štípská *et al.* (2020), suggest that these age ranges are not pervasive nor dominant across the Indian Himalaya. The early NE-directed structures that are proposed by Robyr & Lanari (2020) to account for this early stage of burial are not observed within the Suru Valley region. It has also been proposed that an earlier stage of NE-vergent contractional structures are not required and that these represent earlier phase of extension on the ZSZ that was subsequently domed into opposite vergence prior to the latest stage of normal ZSZ movement (Horton *et al.*, 2015). Prograde monazite ages at *ca.* 40 Ma in the Himachal Pradesh region (Stübner *et al.*, 2014), and between *ca.* 37–30 Ma in SE Zanskar (Walker *et al.*, 1999; Horton *et al.*, 2015) are consistent with the timing of prograde growth obtained in this study, though were determined from higher temperature assemblages or porphyroblasts (e.g., inclusions in kyanite) than those determined for equivalent ages (*ca.* 38–30 Ma) for prograde growth in the Suru Valley region(e.g., matrix titanite or inclusions in garnet, Fig. 5.33a, b).

5.9.3.2 Decompression, Zanskar Shear Zone movement and leucogranite crystallisation

The timing of movement on the Zanskar Shear Zone has been constrained by a number of studies in Zanskar and across NW India. U-Pb dating of monazite from leucogranites in the footwall of the ZSZ indicate that the main extension shearing along the ZSZ initiated before to 22.2 ± 0.2 Ma. Undeformed leucogranite dykes intruding the base of the ZSZ cooled below the closure temperature for Ar diffusion in muscovite between 19.8 ± 0.1 and 19.3 ± 0.1 Ma, indicating cessation of the main phase of ductile deformation. Monazite dating from migmatites in

the southern flank of the Gianbul dome yields a Th-Pb age of 26.58 ± 0.21 Ma (mean SIMS) or U-Pb concordant age of 25.87 ± 0.20 (ID-TIMS; Robyr *et al.*, 2006). These ages were interpreted to pertain to a high-temperature stage of the exhumation history that was linked to the onset of extension along the ZSZ shortly before *ca.* 26.6 Ma. In SE Zanskar, Finch *et al.* (2014) analysed monazite from leucogranite samples sheared during thrusting, normal-movement, and those that were undeformed to constrain the transition from thrust- to normal-sense fabrics. Monazite within leucogranites that display thrust-sense movement and those that display normal-sense movement both record U-Pb ages analysed using SIMS between *ca.* 26–21 Ma. Monazite within thrust-sense samples were interpreted to record continuous metamorphic growth, whilst those in normal-sense samples were inferred to be best represented by an average of 23.0 ± 0.8 Ma, in agreement with U-Pb rutile ages from this study. The waning stage of normal movement is recorded by undeformed leucogranite, which yields a dominant age spectrum between *ca.* 23 and 21.5 Ma. Together, these results were interpreted by Finch *et al.* (2014) to reflect the transition from thrusting to normal movement occuring between an upper range of *ca.* 26–24 Ma and *ca.* 22 Ma, with normal shearing no longer active by *ca.* 20 Ma. Given the overlap of ages, a more conservative estimate is normal movement between *ca.* 26–21 Ma. Rb-Sr geochronology from mylonitic samples in the direct footwall of the ZSZ were interpreted to suggest that ductile deformation was ongoing at *ca.* 26 Ma and continued to *ca.* 16 Ma in some sections (Inger, 1998). Dating of calc-mylonites at Rangdum as sampled for ICSV23 record Rb-Sr ages dominantly between *ca.* 27–26 Ma (Inger, 1998). Muscovite $^{40}Ar/^{39}Ar$ ages from sheared recrystallised or neocrystallised grains adjacent to the ZSZ constrain movement initiation between *ca.* 25–23 Ma and active between *ca.* 25–20 Ma (Vance *et al.*, 1998). Muscovite $^{40}Ar/^{39}Ar$ ages from leucogranite samples in SE Zanskar indicate rapid cooling immediately after intrusion, with ages between *ca.* 21-19 Ma (Dèzes *et al.*, 1999; Walker *et al.*, 1999; Horton & Leech, 2013; Horton *et al.*, 2015). The onset of exhumation in other studies has been constrained through the cessation of prograde–peak conditions at *ca.* 30 Ma (Chambers *et al.*, 2009) or *ca.* 27–26 Ma (Stübner *et al.*, 2014). The termination of burial being commensurate with the onset of exhumation is dependent on the recognition of syn-tectonic growth of peak porphyroblast phases and shape of the *P-T* path. As noted in the Suru Valley region, the relative timing of peak conditions may occur after the dominant phase of burial has ceased at lower structural levels (Fig. 4.43).

Direct constraints on the initiation of M_2 (i.e. metamorphic growth during decompression, broadly equivalent to sillimanite-grade conditions) are dominated by leucogranite isotopic ages. Ages from NW India are as follows: *ca.* 27,*ca.* 22–20 (U-Pb Zrn and U-Th-Pb Mnz; Horton & Leech, 2013); *ca.* 22 Ma (deformed) and *ca.* 21 Ma (undeformed) (Horton *et al.*, 2015); *ca.* 23 Ma (U-Th-Pb Mnz; Robyr *et al.*, 2006, 2012); *ca.* 22 Ma (U-Pb Mnz; Dèzes *et al.*, 1999); *ca.* 26–21 (deformed), and *ca.* 23–21.5 (undeformed) (Finch *et al.*, 2014); *ca.* 21-20 Ma (Noble & Searle, 1995). Migmatites also record prominent stages of monazite (re-)crystallisation defined by single spot ages from *ca.* 27–22 Ma (Robyr *et al.*, 2006). It has largely been argued that initiation of movement on the ZSZ drives decompression (e.g., Robyr *et al.*, 2006; Searle *et al.*, 1999b). This is supported by the recognition of isothermal decompression (i.e., rapid uplift and exhumation) commonly identified in NW India (Dèzes *et al.*, 1999; Searle *et al.*, 1999a). Normal-sense movement on the ZSZ during the Miocene is key to the currently observed tectono-metamorphic architecture of the HMC (e.g., telescoping of isograds adjacent to the shear zone; Searle & Rex, 1989; Searle *et al.*, 1992; Patel *et al.*, 1993; Finch *et al.*, 2014). Age data in this study suggest that the ZSZ activity was contemporaneous with M_2 metamorphism. However, initiation of the ZSZ is not required to drive initial decompression. Unroofing through erosion can equally produce isothermal decompression where the erosion products are removed from the system or there is a large time lag ($>$ 10 Ma) between crustal thickening and initiation of denudation (Whitney *et al.*, 2004). Whilst a time gap of this order is not observed, a gap on the order of *ca.* 5 Ma is possible given the age constraints. Precise isothermal decompression is not required if two factors are met. Firstly, exhumation along the ZSZ must still be invoked after the initial stages of erosion, secondly temperature increase is minimal during erosional driven uplift as a function of both the limited time it is active and the rapid rate at which it must occur. This has been previously suggested at higher to middle structural levels away from ZSZ in the Suru Valley region by Vance & Mahar (1998) based on Ar-Ar dating on metamorphic micas. However, equally they indicate that at lower structural levels isothermal decompression is required, and suggest activity on the ZSZ to drive this. Based on the above assumptions, minimum ages for metamorphic growth associated with decompresssion-associated assemblages or maximum ages for prograde growth are not sufficient to precisely constrain the onset of ZSZ activity, and should solely be used for bracketing. Ideally, the ages used must be directly linked to fabrics associated with shearing during normal exhumation (e.g., Finch *et al.*, 2014).

The results of this study provide an alternative scenario that directly constrains the age of peak M_1 conditions, thereby setting a maximum age for the onset of decompression which may initiate at as early as *ca.* 35–30 Ma at upper structural levels to *ca.* 28–27 Ma at lower structural levels. Given the peak ages of crystallisation of monazite, titanite and zircon between *ca.* 25–21 Ma at medium–lower structural levels, these are interpreted to represent peak M_2 conditions. The development of D_3 fabrics at all structural levels broadly post-date biotite- to kyanite-grade and hornblende- to upper garnet+plagioclase-grade peak porphyroblast phases (Fig. 2.17). S_3 is not associated with significant growth metamorphic phases. Instead S_3 is characterised by retrograde recrystallisation of micas along shear bands (often associated with chlorite). Furthermore, the recognition that breakdown and decompression of peak metamorphic phases initiates in an intertectonic environment (D_2–D_3) and that sillimanite growth is not associated with penetrative D_3 fabric development suggests that initial decompression towards M_2 conditions is not driven by initiation of ZSZ movement. Another mechanism (e.g., denudation) must therefore be invoked during the initial stages of decompression.

5.9.4 Controlling factors on distribution of isotopic ages

The isotopic ages determined for the 49 samples analysed in this study show significant variation in the range, absolute value and accuracy of the age determinations based on the accessory phase analysed, lithology, bulk composition, grain size, shear intensity and fluid distribution etc. Such variation can be expected, particularly with respect to the phase analysed. However, specific discussion and interrogation of these variables can be relevant to deconvolving the metamorphic evolution of a region. While shearing drives fluid transport and aids strain-mediated recrystallisation, the mapped area does not contain significant developed tectonic discontinuities or shear zones away from the major D_3 fault zones. These D_3 structures are located at low grades (biotite and hornblende zones) where few accessory phases are analysed. This section considers the factors deemed most relevant for titanite, allanite, and monazite — which are analysed from a range of structural levels. The relative stability and persistence of zircon in the geological record, combined with the focus on igneous and detrital populations makes this accessory mineral phase less relevant for the present discussion.

5.9.4.1 Titanite

A variety of different lithologies host titanite, with a range of sizes and habits. Although titanite has been grouped in this study based on microstructural context and age clusters, other studies have organised larger titanite datasets relative to lithology (e.g., Mottram *et al.*, 2019). Organising samples by lithology is considered below with reference to the success rate during analysis, and what parts of the metamorphic evolution are recorded. Success rate in this study is variable, largely owing to significant common Pb and low U contents. Due to the relatively young ages recorded by titanite (with the exception of samples ICSV50 and ICSV80), this study defines successful dating to imply a geologically meaningful result, correlating to an error of less than 30 % of the age, MSWD is not considered owing to dominance of samples with well clustered results but defined by significant common Pb (e.g., ICSV61, ICSV117, ICSV99; Fig. 5.7,5.8).

Although metabasite is the lithology that preferentially hosts titanite, it showed a low success rate (43 %, n = 7)), reflecting the low U in the protolith (Mottram *et al.*, 2019). In contrast, calc-pelitic (n = 4), pelite (n = 2) and granite (n = 3) units showed a 100 % success rate. These observations broadly corroborate the larger database of Mottram *et al.* (2019), where success rate is defined as the presence of suitable U/Pb ratios to allow dating. In their study, reconnaissance dating was completed on amphibolites (61 % success rate), 47 calc-gneiss (100 % success rate), garnet-bearing calc-silicates (71 % success rate), and impure marble (100 % success rate).

Lithology also appears to be important when considering the recovered age spectra. Calc-pelites commonly return a single-age spectrum, though certain samples also display mixing with an older phase component. Pelites dominantly displays a single-age spectrum indicative of neocrystallisation. Locally old populations with small grain sizes may show partial recrystallisation. Metabasite display both magmatic grains that show partial recrystallisation, or neocrystallised metamorphic grains. Microstructural context, grain size, zoning patterns and trace elements act as key discriminators between these groups. Granites similarly contain older phases (inferred to be magmatic) that show partial or total recrystallisation dependent on metamorphic grade and/or fluid availability. Lithologies characterised by limited internal fluid capacity in minerals, or likely to nucleate magmatic phases, appear to more consistently preserve older titanite populations.

Bulk composition, fluid availability, deformation-related recrystallisation, grain size and temperature all seem to be key controlling factors in the documented age determinations from titanite (Kirkland *et al.*, 2016; Mottram *et al.*, 2019; Smye *et al.*, 2018). It is clear from this study that incorporating titanite from multiple lithologies and from different microstructural contexts has a stronger chance of deconvolving the metamorphic history a region by using the widest range of age spectra.

5.9.4.2 Allanite

Breakdown of allanite is often coincident with monazite growth and is expected to occur in low-Ca bulk compositions at middle amphibolite-facies (e.g., staurolite) with the reaction possibly facilitated by breakdown of P-rich phases such as apatite (Goswami-Banerjee & Robyr, 2015; Janots *et al.*, 2008; Kohn & Malloy, 2004). However, the relative stability of allanite, and the transition to monazite-bearing assemblages (discussed in the next section) show significant variation as a function of metamorphic grade and bulk rock composition. ICSV110 is from the kyanite zone (defining the kyanite isograd) and contains no monazite and has allanite as a stable phase. High-Ca (and to a lesser degree high-Al) bulk compositions may result in persistence of allanite to higher temperatures (Spear, 2010; Wing *et al.*, 2003). No bulk-compositional data for this sample or major element mineral analyses were collected to test Ca and Al content. However, garnet diameters exceed 1 cm and abundant allanite suggest a higher than average Ca content.

5.9.4.3 Monazite

The high closure temperature for Pb diffusion in monazite (e.g., Seydoux-Guillaume *et al.*, 2002), and ability of the mineral to progressively (re-)crystallise during progressive metamorphism, allows monazite to record different stages on a prograde–peak–retrograde P-T path. Analysis of monazite from different metamorphic grades, in conjunction with careful interrogation of microstructural context and zoning allows for the reconstruction of progressive thermal evolution across a metamorphic sequence from higher to lower structural levels. To accurately constrain this evolution, it is important to first consider the controls on monazite growth and retention of metamorphic ages.

The relative presence and absence of other REE-rich phases (defined by bulk-compositional variation) may exert a control on the ability of monazite to nucleate. The role of allanite was discussed above and is discussed further below. However, the presence or absence of titanite at higher grades may also relate to the presence of monazite. For example, sample ICSV7 from the kyanite zone and ICSV82 from the sillimanite zone, both preserve titanite within garnet cores, with little or no monazite present in the samples. Minerals such as titanite only host a small fraction of the REE concentrations present in monazite, yet notably include similar REE (e.g., Ce, La, Nd, Sm). Titanite is shown to preferentially incorporate middle REE (MREE) over LREE or HREE as recorded at a range of silicate melt compositions (Tiepolo *et al.*, 2002; Prowatke & Klemme, 2005). However, trace element availability during crystallisation of titanite could strongly influence the trace element content incorporated (e.g., Lucassen *et al.*, 2011; Scibiorski *et al.*, 2019). If the REE budget is reduced during titanite crystallisation, as can occur during the co-crystallisation or presence of M–HREE sinks such as garnet, LREE may be preferentially incorporated. Co-crystallisation of titanite and garnet is shown to increase MREE:HREE ratios during titanite growth (Scibiorski *et al.*, 2019). This can be extended further, although garnet preferentially incorporates HREE, it also incorporates substantial MREE during growth and acts as an overall sink such that a range of LREE compositions may be recorded in set compositions. Co-crystallisation of titanite and garnet is shown by ICSV7, and ICSV82 contains titanite inclusions in garnet cores - suggesting similar timing of growth. In the absence of REE-rich fluids, phases such as titanite, which unlike allanite are not directly linked to monazite forming reactions, could exert a dominant control on a given rock's REE budget. Sequestration of REE from host minerals may prevent subsequent monazite nucleation and/or inhibit the scale or rate of growth. This may also explain the younger age population recorded by ICSV81 (taken from the same outcrop locality as ICSV82 and of similar bulk composition) - early titanite growth may limit or preclude monazite growth during M_1. Subsequent breakdown of garnet, follow by fluid mobilisation during S_3 drives neocrystallisation or recrystallisation of monazite, accounting for a more limited age spectra.

As previously discussed, the formation of monazite in metasedimentary rocks is commonly linked to the breakdown of other accessory phases (particularly allanite) during prograde metamorphism (Ferry, 2000; Wing *et al.*, 2003). Thus, the timing of monazite growth may depend on the persistence of allanite which may show significant variation owing to bulk composition. A key example of this

are the differences between ICSV109 and ICSV110. ICSV109 is a staurolite-zone sample that contains small matrix allanite that exhibits features of breakdown, as well as small grain sizes of monazite, both occuring in the matrix. ICSV110 located just 2-km across strike and down structural section into the kyanite zone, contains abundant matrix allanite but no monazite.

Allanite is observed in varying stages of breakdown within certain monazite-bearing staurolite-zone samples (ICSV109). Modelling of the allanite-monazite transition using the average pelitic bulk composition of Shaw (1956), which contains a CaO wt% of 2.17 and CaO/Na_2O ratio of approximately 1.26 shows that this transition lies between 450–550 °C at 5–10 kbar in the MnNCKFMASHPCe system (Spear, 2010). However, these temperatures are slightly too low for reported natural monazite at the staurolite isograd. The thermal peak estimate in ICSV109 of 620 °C (Ti-in-biotite; Fig. 4.16) and the recognition that monazite growth and thereby allanite breakdown occurs around 600 °C in equivalent HMC samples in Zanskar (Goswami-Banerjee & Robyr, 2015) implies that the oldest age populations of monazite from staurolite-zone samples (26.7 ± 1.2 Ma in ICSV109 and 28.2 ± 1.4 Ma in ICSV30) may broadly represent thermal peak (subject to the degree of recrystallisation). However, this assumption relies on consistent bulk composition, which is shown to have a significant impact on the continued stability of allanite. For comparison ICSV109 contains a CaO of 1.19 wt% and CaO/Na_2O of 0.84. The lower CaO content compared to modelled phase relations should increase the stability of monazite, yet monazite grains are both small, show only minor chemical zonation and age population. Furthermore, grains are not thought to have recrystallised to younger ages owing to progressive decrease in Y from core–rim. Alternative explanations must therefore be proposed for the variable stability. This could result from an alternative mechanism of monazite formation. Previous studies have suggested that monazite does not react in an isolated chemical system but rather interacts with a variety of phases present (e.g., Spear & Pyle, 2002; Kohn & Malloy, 2004; Corrie & Kohn, 2008). Garnet profiles from ICSV109 show minimal diffusion re-equilibration at rims and minor retrogressive growth of chlorite at rims, indicating that this took place under late greenschist facies conditions during exhumation (therefore after M_2 peak). The exact mechanism of monazite growth therefore remains elusive in this sample. Defining temperature conditions for monazite growth should only be done within the context of known bulk composition and reaction sequences.

It is also important to consider the impact of grain size on monazite ages. The percent of recrystallisation relative to grain volume is likely to be more pervasive

for smaller grain sizes, thus may impact the preservation of older metamorphic ages, particularly where grains are not armoured by porphyroblasts. Grains within both staurolite samples are small (< 60 µm in length), thereby more susceptible to a higher volume % of recrystallisation. However, as Th is enriched in the cores of staurolite-zone samples rather than rims, this suggests that recrystallisation is not pervasive through the grain (Seydoux-Guillaume *et al.*, 2002).

Fe and Mg content are also known to impact the timing of monazite growth (Fitzsimons *et al.*, 2005). Rocks with elevated Mg- and/or Al-bulk compositions may impact garnet stability and growth such that the garnet-breakdown reaction responsible for amphibolite facies monazite growth is not achieved (Kohn & Malloy, 2004; Fitzsimons *et al.*, 2005). However, other studies have noted that the growth of monazite in low-Ca pelitic schists show consistent age population across a broad range of compositions in AFM space, indicating that variations in bulk composition by AFM may not control the observed age spectra of monazite during amphibolite facies metamorphism in all environments (Rasmussen *et al.*, 2006). The result is that bulk composition could exert an influence on the record of metamorphic ages preserved in monazite, but it's clear this work requires further investigation in other natural sequences.

In the absence of significant retrogression disrupting the established thermal gradient, or subsequent recrystallisation and overprint, lower metamorphic grades will achieve peak metamorphic conditions prior to higher metamorphic grades in a typical prograde metamorphic sequence. In such a sequence a younging of peak metamorphic ages from higher structural levels (lower metamorphic grades) to a lower structural levels (higher metamorphic grades) will occur. Analysis of monazite from the garnet zone produces a peak at *ca.* 24 Ma, which is younger than the peak of results from the staurolite zone at *ca.* 26 Ma. Both preserve a relatively narrow range of metamorphic ages, particularly in garnet-zone samples where the range of garnet ages do not overlap with the peak of staurolite growth. Likely scenarios therefore include: 1) total recrystallisation of monazite following thermal peak or 2) delayed neocrystallisation. Garnet-zone monazite does appear to display minor Th enrichment at rims though cores may also display enrichment. It is possible that recrystallisation mechanisms influenced the record of metamorphic ages within this sample. In a scenario of delayed growth this requires that pre-requisite monazite forming reactions could only occur during decompression, owing to the stability of precursor mineral phases over varying P conditions. Alternatively, if monazite is primarily controlled by T, it implies that temperatures must increase during decompression, contrary

to the recognition that rocks commonly preserve thermal peak (Guiraud *et al.*, 2001). Alternatively, metamorphic peak occurs for garnet-grade conditions at *ca.* 24 Ma. However, it is important to note that sillimanite grade conditions are equally clustered at *ca.* 23 Ma which shows minimal variation from garnet-grade conditions. Given calculated thermal gradients, a temperature increase of this magnitude within the calculated time frame is geologically unlikely in a regional tectonic setting. Sillimanite-grade conditions are broadly constrained by the results of ICSV81 which contains monazite displaying microstructure suggestive of significant recrystallisation (Fig. 5.13g). Late fluid influx during the later M_2 metamorphic event or temperature variation during decompression may drive recrystallisation.

Monazite from kyanite-zone lithologies preserve the widest distribution of ages (Fig. 5.24a). Monazite grains from this grade are larger than lower-grade lithologies, which may influence the age distribution. However, the kyanite zone is also the only metamorphic zone to include outcropping of the pelite lithology. Varying bulk rock composition may impact the mineral reaction sequence, grain size, abundance of porphyroblastic phases, distribution of strain, fluid availability, and fluid composition. Such features may directly or indirectly influence the recovered age distribution from monazite. ICSV6, ICSV97, ICSV12, ICSV13 are pelite in composition *senu-stricto* and monazite from these samples yield ages between *ca.* 33.4–18.7 Ma (Fig. 5.34a, b). Notably, ICSV6 provides the smallest age range between *ca.* 23.7–18.7 Ma while the other three samples range between *ca.* 33.4–20.1 Ma. ICSV6 is located on the gradational boundary of the pelite lithology with the overlying mixed psammite, pelite, and semipelite. In comparison to the other three samples, ICSV6 contains more quartz and feldspar (Fig. 5.34b). ICSV96 and ICSV18 are semipelite in composition (Fig. 5.34b), located within the mixed psammite, pelite, and semipelite lithology, and record ages between *ca.* 28.7–18.2 Ma, with ICSV96 dominated by ages between *ca.* 21.4–18.2 Ma (Fig. 5.34a). Owing to the Fe-, Al-, Mg- rich nature and higher metamorphic grade of kyanite-zone pelite samples, more porphyroblasts (e.g., garnet, staurolite and kyanite) and thus more porphyroblast hosted monazite are present (Fig. 5.34c). Porphyroblasts are shown to have an armouring effect to subsequent dissolution/recrystallisation or Pb-diffusion (Montel *et al.*, 2000; Catlos *et al.*, 2002b; Cherniak *et al.*, 2004). However, although pelite samples preserve a greater volume % of porpyhroblasts (Fig. 5.34a), and have more spot analyses from inclusions than those from semipelite samples (Fig. 5.34c), the oldest ages are found in the matrix (Fig. 5.21), precluding this interpretation.

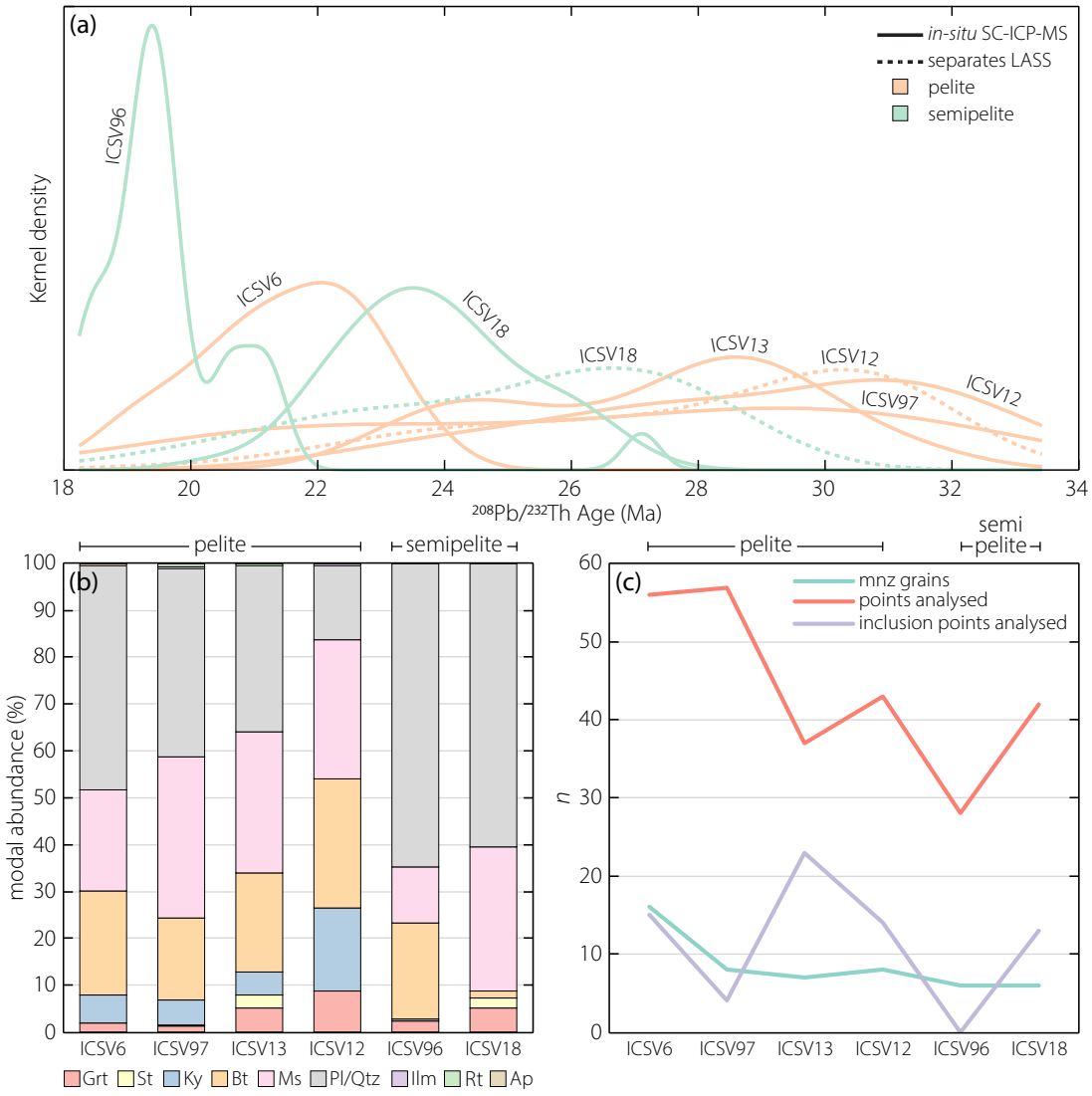


Fig. 5.34 Variation of recovered monazite ages from kyanite-zone samples. a) KDE of single spot $^{208}Pb/^{232}Th$ ages for monazite from pelite and semipelite. b) Volume % stacked histogram of primary mineral phases collected via point counting in kyanite-zone samples. c) Line graph comparing number of monazite grains analysed, spots ablated, and spots ablated as inclusions within garnet, staurolite, or kyanite porphyroblasts.

The number of grains analysed, nor the total number of spot analyses reflect any consistent trend with the range or distribution of ages.

Other factors that may impact the age distribution include strain accumulation and fluid mobilisation. ICSV96 preserves S_3 fabrics (developed through crenulation of S_2), suggesting heterogenous strain distribution during exhumation may drive fluid mobilisation and recrystallisation of monazite. ICSV18 is located near the sillimanite isograd. Resorption of garnet during decompression releases HREE, suitable for monazite crystallisation, and progressive metamorphic reactions may

release fluids and drive mobilisation of REE. The younger age populations within ICSV6, ICSV96 and ICSV18 (< *ca.* 20 Ma) post-date leucogranite crystallisation suggesting that strain and fluids have likely mediated recrystallisation during progressive exhumation of the HMC.

While the kyanite zone records the broadest range of Himalayan metamorphic ages, at higher and lower metamorphic grades more restricted age ranges are recovered (Fig. 5.25b). For the kyanite zone to attain appropriate temperatures to initiate monazite growth sooner than the staurolite zone would require burial of the kyanite zone sooner than the staurolite zone, a suggestion that is inconsistent with NW-SE propagating deformation and metamorphism. Alternatively, the pelite lithology could record a higher proportion of heat-producing elements resulting in heterogeneous heating, however, this is not supported by thermometry results. Neither of these are deemed robust interpretations. It is inferred that the timing of monazite growth reflects complicated interactions between growth and resorption of different REE-rich phases and the broader variations in bulk composition. Such factors exert significant control on when monazite can crystallise (Fitzsimons *et al.*, 2005) and the susceptibility of grains to subsequent processes of recrystallisation (fluid mobilisation, fluid composition etc.).

The final consideration for the relative timing of monazite re(equilibration) involves the thermal evolution of the Suru Valley region compared to other regions in the Himalaya. Figure 2.3 shows that the thermal maximum of the Suru Valley region may be lower than other areas across NW India. This may further preclude earlier prograde growth of monazite in select lithologies, suggesting that the relative timing of prograde metamorphism may show significant diachroneity in scenarios where multiphase geochronology is not used. Owing to the variety of structural grades, transects, lithologies and phases analysed in this study, the compelte lack of age populations between *ca.* 43–38 Ma associated with high-grade conditions of partial melting suggests that these conditions, or possibly even the conditions driving these processes, are not recorded in the Suru Valley valley region. Given the clear documentation of the structural and metamorphic architecture resulting from SW-directed folding and thrusting, it is possible the lack of these ages may be more convincingly explained by invoking a separate phase of burial (e.g., early NE-directed folding and thrusting; Robyr & Lanari, 2020). Multiphase burial is supported by the significant diachroneity of age populations (e.g., Štípská *et al.*, 2020). This study shows the relative benefits of employing a multiphase technique to deconvolve the metamorphic evolution of the Zanskar Himalaya.

5.10 Conclusions

The following conclusions are based on the results of multiphase geochronology in the Suru Valley region with the acknowledgement that deformation and associated metamorphism propagate both spatially and temporally:

1. M_1 metamorphism began at higher structural levels starting at 38 Ma with peak conditions attained at *ca.* 36–30 Ma from biotite- to garnet-grade conditions. Growth of garnet may be constrained within the garnet zone to initiate $<$ *ca.* 35 Ma with garnet-present conditions documented *ca.* 30 Ma. Variations in bulk composition lead to garnet growth at lower structural levels as early as *ca.* 46 Ma coincident with D_2. D_2 was waning by *ca.* 38 Ma and had terminated by *ca.* 36–35 Ma at biotite grade and by *ca.* 30 Ma near the onset of garnet-grade conditions.

2. At lower structural levels garnet growth occurs as early as *ca.* 46 Ma in Ca-rich lithologies, though in most lithologies it occurs at $<$ *ca.* 35 Ma. These ages correspond to prograde (*ca.* 46 Ma) and prograde–peak conditions (*ca.* 35 Ma) respectively. M_1 peak has a maximum constraint of $<$ *ca.* 35 Ma at these structural levels with most ages for peak conditions in kyanite-zone samples ranging between *ca.* 31–28 Ma. The dominant stage of fabric development terminated prior to attainment of peak M_1 conditions.

3. Prograde development in the sillimanite zone occurs as early as *ca.* 37 Ma and decompression may initiate as early as *ca.* 28–27 Ma. This process does not inherently need to be linked to ZSZ initiation. Movement on the ZSZ is constrained to initiate before *ca.* 23 Ma at the highest structural levels. The ZSZ is inferred to be active at sillimanite-grade conditions *ca.* 23 Ma. Attainment of peak M_2 conditions likely occurs at the following times moving up metamorphic grade: *ca.* 24 Ma (garnet), *ca.* 25–21 Ma (kyanite), *ca.* 23–21 Ma (sillimanite & garnet+plagioclase), and *ca.* 23 Ma (sillimanite+K-feldspar). The temporal relationship between ZSZ activity and these ages suggests the dominant phase of normal movement was coincident with M_2 peak. Leucogranite emplacement and waning activity on the ZSZ (evident through limited deformation on leucogranite) occurs at 20.1 ± 0.4 Ma.

4. Multiphase geochronology is key to constraining the metamorphic and magmatic evolution of regions that show significant lithological and bulk

compositional differences. Variations in bulk compositions, and growth of multiple or varying REE dominated phases may impact the available REE budget or relative crystallisation of analysed phases. This could result in large uncertainties in the interpretation of the age data, particularly for areas that underwent multiple metamorphic events and host a variety of rock compositions. Integrating multiple phases allows the relative benefits of each phase based on different closure temperature, susceptibility to recrystallisation, growth zoning etc., to minimise the cumulative effect of these uncertainties and allows untangling of the complete metamorphic evolution of the region.

Chapter 6

Synthesis and Tectonic Implications



Sunset over 'Lama Tupi'

6.1 Integrated *P-T-t-D* evolution of the Suru Valley region

Few areas in the Himalayan mountain belt preserve the early tectonometamorphic record and architecture that developed prior to peak temperature regional metamorphism. This is due to the propensity of younger lower-pressure sillimanite-grade mineral assemblages to characterise the final metamorphic record. The incomplete preservation of the early stages of the orogenic cycle limits our understanding of how crustal thickening and heat propagate spatially and temporally. Furthermore, it hinders our understanding of how the early tectonometamorphic architecture influences the dissipation of potential energy during exhumation. The geology of the Suru Valley region provides extensive evidence of *P-T-t-D* conditions imparted by progressive crustal thickening during the early part of the orogenic cycle. Minimal development of sillimanite-grade assemblages in this area allows for the recognition of three key early attributes: 1) the occurrence of pre-collisional magmatism and metamorphism, 2) the timing and conditions of thermal peak metamorphism with respect to orogenic crustal thickening, and 3) the relationship between post-pressure peak decompression and initiation of the STDS. A schematic summary of *P-T-t-D* relationships as constrained at different peak metamorphic grades in the Suru Valley region is shown on Figure 6.1. For simplicity an average of the prograde and peak *P-T* conditions from both pelitic and metabasic units are used at each grade to define points along the path, the absolute range of these values (rounded to 5 °C and 0.1 kbar) is given in text for reference.

6.1.1 Pre-collisional history

The lithostratigraphic architecture of the Suru Valley region comprises a laterally extensive regional volcano-sedimentary sequence that is intruded by granitic bodies. Despite subsequent Cenozoic polyphase regional metamorphism and deformation, the original stratigraphic sequence remains readily discernible (Chapter 2). The volcano-sedimentary package is dominated at low structural levels by clastic sedimentary strata characterised by abundant Precambrian, mainly Neoproterozoic, detritus. Detrital zircon age determinations from Chapter 5 of *ca.* 1100–900 Ma and *ca.* 750–600 Ma in the Suru Valley region suggest that the Arabian-Nubian Shelf may represent an important source area, consistent with other regional lithostratigraphic studies of the GHS (e.g., DeCelles *et al.*, 2000; Myrow *et al.*, 2010; Spencer *et al.*, 2013a; Dyck *et al.*, 2019). An apparent gap in

sedimentation between *ca.* 490–460 predates the deposition of late-Ordovician molasse-type strata (Myrow *et al.*, 2016), and coincides with Barrovian metamorphism, crustal melting and emplacement of both S- and I-type granites that are dated between *ca.* 500–460 Ma (Gehrels *et al.*, 2006; Cawood *et al.*, 2007; Palin *et al.*, 2018; Cawood *et al.*, 2021). This period of orogenic activity (the Bhimphedian orogeny) is dominated in the Suru Valley region by the emplacement of voluminous granite bodies into the volcano-sedimentary pile, with crystallisation ages of *ca.* 505–472 Ma (U-Pb Zrn). Biphase metamorphic monazite growth (U-Th-Pb) is constrained at *ca.* 499–484 Ma and *ca.* 472–453 Ma (Chapter 5), consistent with U-Pb monazite ages from Pakistan of 482.4 ± 7.9 Ma and 464.5 ± 4.0 Ma, respectively (Palin *et al.*, 2018). Moderate age range between the youngest detrital population (*ca.* 610–604 Ma) and oldest crystallisation age (505 ± 23 Ma) suggests the sediment may be consistent with a passive margin stratigraphy (Cawood *et al.*, 2012).

The Suru Valley region is dominated by a widespread volcano-sedimentary sequence that is preserved at the higher structural levels, and is invariably folded and interlayered with the lower clastic sedimentary strata at all metamorphic grades as a result of subsequent Himalayan folding and thrusting (Chapter 2). The volcanic rocks occur in structural proximity to granite bodies. The Shafat granite dated in this study has a U-Pb zircon age of 281.2 ± 6.0 Ma, and is the volumetrically largest granite dated, extending over an along-strike distance of more than 30 km (Chapter 5). Previous studies have yielded U-Pb zircon ages between *ca.* 284–268 Ma (Spring *et al.*, 1993; Noble *et al.*, 2001; Horton & Leech, 2013) for smaller granite bodies in Zanskar. These granites appear to be temporally associated with a significant period of volcanic activity, dated in this study with a U-Th-Pb titanite age of 268 ± 41 Ma. These ages are recorded in Kashmir in the protolith unmetamorphosed Panjal Traps at 289 ± 3 Ma (U-Pb zircon; Shellnutt *et al.*, 2011) and 288.2 ± 0.3 Ma (U-Pb zircon, CA-ID-TIMS; Chen *et al.*, 2023). The eruption of the volcanic rocks and emplacement of the granitic plutons have been interpreted as recording widespread magmatic activity associated with the break-up of Gondwana (Shellnutt, 2018). The age constraints for the intrusive and extrusive units and the structural association and regular interlayering with siliciclastic and carbonate sedimentary rocks suggest the latter lithologies must also be younger than the Palaeo–Neoproterozoic ages commonly attributed to GHS strata. Searle *et al.* (2007) proposed that the protoliths of the upper GHS could be correlated with the unmetamorphosed Paleozoic–Mesozoic stratigraphy of the Tethyan shelf sequence. The recognition that Permian as well

as Mesozoic strata are folded and interlayered within the GHS and that they all record the same deformation fabrics, and metamorphic mineral growth history is essential in determining that the dominant metamorphic episode recorded by the GHS is Himalayan in origin.

Uniquely the rock record of the Suru Valley region provides temporal constraints on both the response of the Indian margin to the final assembly of Gondwana and its subsequent breakup during the Permian. This is, in spite of the subsequent and pervasive Himalayan metamorphic episode that followed terminal collision of the Indian and Asian plates. Few areas in the Himalaya preserve such a complete record of both early and late metamorphic and magmatic events. The increasing documentation of these events suggest that metamorphic minerals need not necessarily be Himalayan in origin (e.g., Argles *et al.*, 1999; Robyr, 2023; Lihter *et al.*, 2022), failing to account for this might result in erroneous petrological modelling. This emphasises the necessity for: careful field observations and mapping, well-documented porphyroblast growth-fabric development relationships, and regional lithostratigraphic context when deconvolving polymetamorphic terrains.

6.1.2 Crustal thickening and M_1 (> *ca.* 38–28 Ma)

Following the initiation of India-Asia continental collision, deformation is accommodated by significant SW-vergent thrusting and folding (Fig. 6.2a, b). As documented in Chapter 2, SW-verging deformation is recorded in the Suru Valley region by the planar and/or linear structural elements characterising D_1 (greenschist-facies fabrics) and D_2 (greenschist- to amphibolite-facies fabrics). Crenulation of the D_1 fabrics led to the formation of D_2 structural elements, which are dominant regional penetrative fabrics associated with crustal thickening. The obliquity of the D_1 and D_2 mineral stretching lineations to the dip directions imply this was a period of dominantly non-coaxial ductile deformation, as has been documented in other areas of NW India (e.g., Patel *et al.*, 1993; Walker *et al.*, 1999; Wyss *et al.*, 1999; Stephenson *et al.*, 2000; Vannay *et al.*, 2004; Wiesmayr & Grasemann, 2002). Associated F_2 fold structures are tight to isoclinal, are developed in all lithological units (Fig. 6.2b), are perpendicular in orientation to the principal shortening direction (where not disrupted by later refolding), and are documented at the microscale to macroscale. Additionally, the lithostratigraphic units from upper structural levels (Mesozoic siliciclastic and carbonate sedimentary rocks) are infolded with the lithostratigraphic units from the lower

structural levels within the higher-grade mineral zones that form the HMC. These features suggest that the confining stresses exerted by plate convergence during the Himalayan orogenic cycle were both pervasive and penetrative across the region at all scales and directly account for significant thickening and burial of the Indian crust. It should also be noted that higher-pressure Barrovian terrains cannot achieve the high pressures solely by crustal thickening though folding, and that concurrent or subsequent underthrusting beneath a thickened cover sequence and/or continental plate (e.g., Tethyan thrust belt Corfield & Searle, 2000) and/or continental plate (e.g., DeCelles *et al.*, 2002). Indeed, concomitant with pervasive folding, the GHS was underthrust below the THS (thickened cover sequence) along the proto-ZSZ, consistent with the thrust sense S_2 fabrics (e.g., Patel *et al.*, 1993; Dèzes *et al.*, 1999; Robyr, 2002; Finch *et al.*, 2014).

The orientation of the isograd surfaces ranges from sub-parallel to oblique with respect to the principal D_2 planar structural elements (Fig. 6.2b). The final orientation of the metamorphic isograd surfaces during the later stages of shortening, transposition and thickening of the lithostratigraphic sequence, is concurrent with the development of D_2 structures at lower grades and follows the formation of D_2 structural elements at higher grades. Mineral growth in the higher temperature range of the Barrovian sequence shows relationships to the main regional fabric (S_2) that suggests dominantly post-D_2 growth, whereas mineral growth-deformation fabric relationships at lower grades supports growth syn- to post-D_2. Taken as a set, these observations document that peak temperature mineral growth outlasted development of the dominant (S_2) regional fabric (Chapter 2).

The response to crustal thickening as recorded at different structural levels yields the following *P-T-t* record as documented within Chapters 4 and 5 and summarised in Figure 6.2b. At high structural levels (biotite grade), prograde M_1 conditions occur at *ca.* 38 Ma with peak conditions from *ca.* 36–35 Ma (U-Th-Pb titanite). At garnet and hornblende grade, prograde conditions occur at *ca.* 35 Ma with peak conditions at temperatures of 525–583 °C, pressures of 7.3–9.6 kbar and absolute timing bracketed between < *ca.* 35 and 30 Ma (U-(Th)-Pb titanite and allanite). Based on titanite growth and fabric development microstructure relationships, D_2 was waning by *ca.* 38 Ma and had broadly terminated by *ca.* 36–35 Ma (U-Th-Pb titanite) in the biotite zone and by *ca.* 30 Ma (U-Th-Pb titanite) or shortly thereafter in the garnet zone. Prograde garnet growth occurs rates of 36 °kbar^{-1}. In the staurolite and kyanite zones; and oligoclase and garnet+plagioclase zones, garnet rim temperatures range

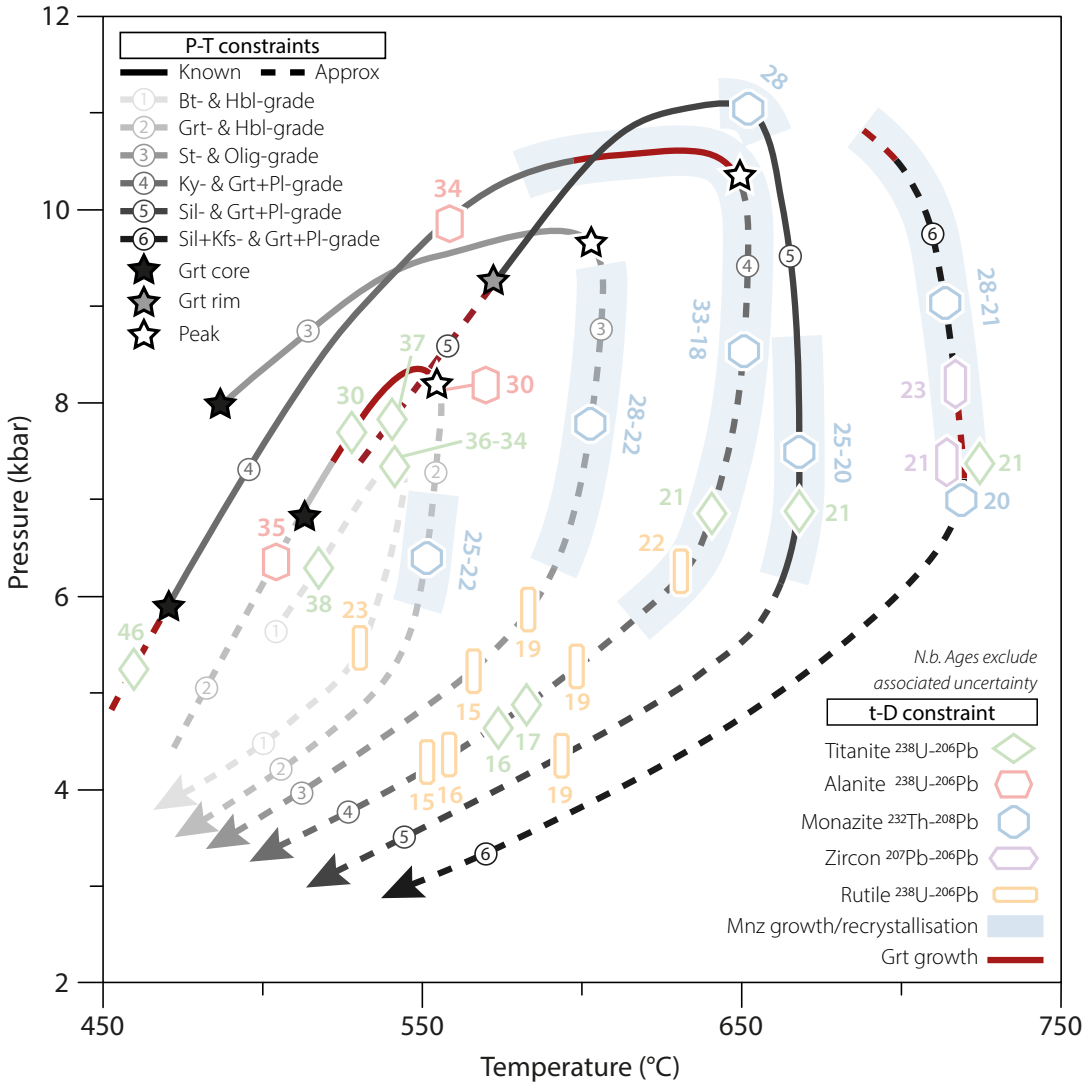


Fig. 6.1 Schematic summary of *P-T-t-D* conditions as determined with metamorphic samples from Suru Valley region. *P-T-t* paths are defined by prograde and peak points recorded. Results represent an average from the most representative pelitic and metabasic samples at each structural level. *P-T* results are shown in table 4.2. Known components of PT paths or relative timing of garnet growth are displayed with solid lines and approximate with dashed lines. The relative location of accessory phase age constraints along specific *P-T-t* paths are best estimates and are not scaled consistently across all paths.

from 575–645 °C in pelitic samples and from 585–705 °C in metabasic samples. Pressures in pelitic samples range from 8.5–10.0 kbar and from 9.5–11.6 kbar in metabasites. S_2 concurrent garnet growth in select Ca-rich compositions and prograde growth of allanite occur at *ca.* 46 Ma (U-Th-Pb titanite) and *ca.* 35 Ma (U-Pb allanite), respectively. Peak M_1 conditions are largely attained from *ca.* 31–28 Ma after termination of D_2. Following earlier prograde conditions, the slope of the metamorphic field gradient shallows at these grades to 47 °C kbar^{-1}

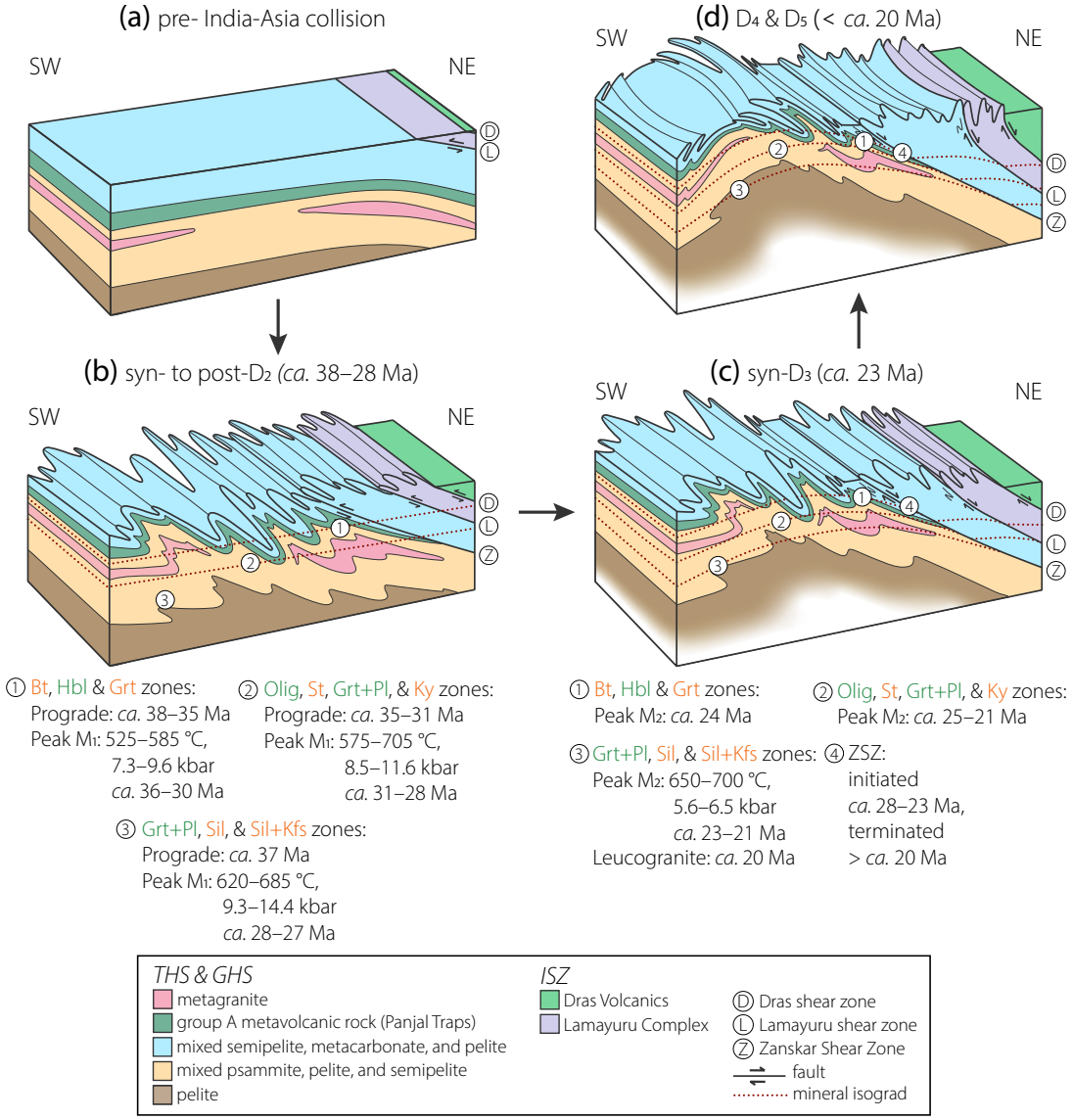


Fig. 6.2 Schematic mid-crustal block diagrams summarising the *P-T-t-D* evolution of the Suru Valley region: a) prior to initiation of India-Asia collision, b) thermal equilibration following progression of D_2 from high to low structural levels between *ca.* 38–30 Ma, c) D_3 reactivation and exhumation of the sequence, coincident with sillimanite-grade metamorphism initiating between *ca.* 28–23 and terminating prior to *ca.* 20 Ma. d) D_{4-5} km-scale open warping of the earlier established lithological, tectonic and metamorphic architecture, occurring after *ca.* 20 Ma. Effects of late D_3 backthrusting are preserved along the Dras, Lamayuru and Zanskar shear zones.

concomitant with termination of crustal thickening. Prograde conditions are recorded in sillimanite-grade rocks at *ca.* 37 Ma (U-Th-Pb titanite) with peak M_1 conditions *ca.* 28 Ma at conditions of 620–685 °C and 9.3–14.4 kbar. The overall temporal trend suggests a younging in the attainment of peak thermal conditions

with decreasing structural level, consistent with SW-propagating metamorphism (e.g., Searle *et al.*, 1992).

6.1.3 Decompression, M_2 and D_3 exhumation (*ca.* 28–20 Ma)

As recorded in Chapter 2, thrust-sense D_2 fabrics are overprinted/reactivated during D_3 to form normal-sense mylonitic fabrics or crenulation cleavage under non-coaxial simple shear. Sub-parallel planar and linear structural elements from D_1 through to D_3 imply a continuous sequence of deformation with a consistent orientation of the major stress direction from early- to late-deformation structures. D_3 fabrics are observed to wrap thermal peak porphyroblasts and realign linear mineral phases. Specifically, sillimanite-growth shows no distinct orientation with respect to D_2, suggesting post-D_2 growth. However, the relative relationship between sillimanite growth and D_3 is unclear: termination of sillimanite growth prior to D_3 is unlikely based on temporal relationships between metamorphic ages from sillimanite- and sillimanite+K-feldspar-zone samples and timing of D_3 activity. Therefore, it is possible sillimanite grew during D_3 at a structural level where D_3 did not develop S_3, or sillimanite growth initiated prior to D_3 and continued during D_3. Tectonic thinning adjacent to D_3 normal faults is evidenced by a reduction in the structural width of the mineral zones (spacing of the isograds) and by the alignment of isograd surfaces parallel to the faults (Fig. 6.2c). In SE Zanskar, shear intensity along the ZSZ is high (Herren, 1987; Dèzes *et al.*, 1999). Whereas, in the NW of the Suru Valley, there is a progressive increase in the spacing of the isograds moving from SE to NW, suggesting a spatial decrease in the intensity of D_3 normal-sense deformation along the length of the shear zone.

The rocks that were decompressed to the lowest pressures (sillimanite and sillimanite+K-feldspar grade; garnet+plagioclase grade) were buried and heated during thermal relaxation up to conditions of 621–684 °C and 9.3–14.4 kbar but decompressed to conditions of 655–700 °C and 5.6–6.5 kbar on a near-isothermal path (Fig. 6.2c). Final loss of melt from migmatites occurred at conditions of approximately 700 °C and 6.5 kbar, coincident with modelled mineral chemistry along the solidus curve. Decompression and onset of M_2 conditions may have initiated as early as *ca.* 28–27 Ma (U-Th-Pb monazite) at the highest metamorphic grade (oldest monazite ages within sillimanite and sillimanite+K-feldspar zone samples) but prior to *ca.* 23 Ma (U-Th-Pb monazite; syn-D_3 monazite recrystallisation). Decompression microstructures, such as late

kyanite growth occurred following breakdown of garnet rims in rocks the display subsequent and minor fibrolite growth. Kyanite grains appear both aligned and misaligned to locally developed S_3 fabric and growth is modelled to occur after thermal peak on a near-isothermal decompression path on phase equilibrium diagrams. These observations suggest that movement along the ZSZ initiated after attainment of thermal peak. At low structural levels in the sillimanite zone, syn-D_3 monazite recrystallisation occurs at *ca.* 23 Ma, while syn-D_3 rutile crystallisation occurs at 22.5 ± 0.8 Ma (U-Pb rutile) at the highest structural levels. Owing to propagation of deformation SW-wards, at the highest structural levels, ZSZ movement initiated after *ca.* 28–27 Ma but prior to *ca.* 23 Ma.

Attainment of peak M_2 conditions is constrained to have occurred at the following times at different metamorphic grades: *ca.* 24 Ma (garnet zone), *ca.* 25–21 Ma (kyanite zone), *ca.* 23–21 Ma (sillimanite zone & garnet+plagioclase zone), and *ca.* 23 Ma (sillimanite+K-feldspar zone) as constrained by U-(Th)-Pb monazite, titanite and zircon analyses (Fig. 6.2c). Peak M_2 is inferred to be concurrent with movement on the ZSZ across all structural levels based on temporal relationship to absolute ages of S_3 activity, and inferred D_3 recrystallisation of monazite in sillimanite zone samples. Near-undeformed leucogranite crystallisation and the end of M_2 occurred at *ca.* 21–20 Ma, and is best constrained by a monazite Th-Pb mean age of 20.1 ± 0.4 Ma. The onset of decompression does not necessarily imply the onset of normal movement along the ZSZ (*cf.* Robyr *et al.*, 2006). Unroofing through erosion during the initial stage of metamorphic decompression, shortly followed by, and then concurrent with rapid ZSZ movement, are inferred to account for isothermal decompression during exhumation of the HMC. These *P-T-t* results are detailed in Chapters 4 and 5.

6.1.4 Continued exhumation, backthrusting and $D_{4–5}$ ()< *ca.* 20 Ma)

In the northern part of the mapped area, the GHS–THS are juxtaposed against the ISZ by a set of long-lived fault structures that record polyphase deformation (Chapter 2). Normal-sense D_3 fabrics are also developed in this region, yet in this instance are defined by a crenulation cleavage (locally penetrative) and meso- to macro-scale folding. The variation in the nature of D_3 is interpreted to represent a transition from penetrative exhumation fabrics along the ZSZ, to spaced regional backfolding and back-thrusting towards the NE (Fig. 6.2c, d), thereby constraining the western termination and extent of the ZSZ *sensu stricto*. Towards the west the STDS does not continue as a separate structure, though

normal sense movement is recorded along the ISZ in Pakistan (Anczkiewicz *et al.*, 2001). In this area, a maximum age for initiation of normal movement is suggested from an Ar-Ar muscovite age on pre- to syn-normal movement leucogranite dykes at *ca.* 28 Ma. This age is broadly consistent with the maximum age constrained by this study, though is slightly older than absolute ages from other studies in Zanskar (e.g., Finch *et al.*, 2014). Local variations both in timing and degree of normal displacement along strike of STDS have previously been documented (Inger, 1998). The present study thereby directly documents the relative temporal and spatial transition of normal movement from the STDS into the ISZ, and a transition to NE-directed backthrusting.

Within the kyanite and garnet+plagioclase zones of the HMC, localised recrystallisation of accessory phases occurs after *ca.* 20 Ma, coincident with cooling ages (Chapters 4 and 5). Monazite records a major stage of recrystallisation at *ca.* 20–18 Ma, associated with Y-rich outer rims, and magmatic titanite within granites record recrystallisation of grains at *ca.* 17–16 Ma (indicated by grain shape, zoning patterns, and age distribution). The fluid source to enable recrystallisation of monazite and titanite, is inferred to be influx of fluids during uplift and/or from partial break-down of host micas driven by retrograde reactions. Measured rutile ages within staurolite- to sillimanite-grade samples dominantly record uplift at temperatures below the *ca.* 600–490 °C closure temperature (e.g., Cherniak, 2000; Kooijman *et al.*, 2010) between *ca.* 20–15 Ma (Fig. 6.1).

The final stage of deformation in the Suru Valley region is expressed as crustal scale open folding, producing a dome and basin interference pattern of pre-existing structural and metamorphic elements (Chapter 2; Fig. 6.2d). Specifically, the structural interference pattern of fold hinges at a high-angle (Ramsay, 1962, 1967) associated with F_4 and F_5 produced the domal architecture. The planar structural elements (S_2 and F_2) that best outline the domal culmination, pre-date the formation of the dome itself, rather than being linked to its formation (cf. Gilbert, 1986; Gapais *et al.*, 1992; Searle *et al.*, 1992).

6.2 Implications for the metamorphic evolution of the Himalaya

This study quantifies the conditions, rates, and absolute timing under which crustal thickening progressed using field mapping, structural, petrological and geochronological constraints, for a poorly constrained period of the Himalayan

orogen. Taken as a whole, the tectonometamorphic architecture along the length of the orogen highlights a noticeable diachroneity in the rock record and/or differing rates and timescales of metamorphism relative to regional deformation. For example, numerous studies of the HMC in other segments of the orogen record a dominance of pre and/or syn-tectonic growth of peak-pressure and peak-temperature metamorphic mineral assemblages relative to the local main fabric: Western Himalaya (Kundig, 1989; Pognante *et al.*, 1993; Stephenson *et al.*, 2000; Finch *et al.*, 2014; Phukon *et al.*, 2019); Central Himalaya (Cottle *et al.*, 2007; Jessup *et al.*, 2008; Larson *et al.*, 2010; Yakymchuk & Godin, 2012; Montomoli *et al.*, 2015; Thakur *et al.*, 2015; Braden *et al.*, 2017; Iaccarino *et al.*, 2017a,b; Soucy La Roche *et al.*, 2018; Carosi *et al.*, 2019; Montemagni *et al.*, 2019; Soucy La Roche *et al.*, 2019; Dyck *et al.*, 2020); and Eastern Himalaya (Goswami *et al.*, 2009; Groppo *et al.*, 2012; Kellett *et al.*, 2013; Smit *et al.*, 2014; Chakraborty *et al.*, 2016; Zhang *et al.*, 2018; Kalita *et al.*, 2022). The Suru Valley region is unique in demonstrably recording post-deformation (D_2) growth of the highest-pressure assemblages and early post-thermal peak (pre- to syn-D_3) decompression assemblages. This unique record might be attributable to lower volumes of crustal melting and development of pervasive normal- sense fabrics associated with ZSZ movement. To achieve the *P-T* conditions documented requires rapid compression (aka burial) during crustal thickening (lower $\delta T/\delta P$), thus outpacing the rate of heating, followed by progressive heating under higher $\delta T/\delta P$. The preservation of the thermal peak (or near thermal peak) assemblages rather than the higher temperature but lower-pressure assemblages requires the following: significantly low or absent erosion and/or normal-sense movement prior to, or near, attainment of thermal peak conditions. If these criteria are not met it would necessarily be reflected by a decrease in pressure during the final stage of heating.

Decompression towards sillimanite-grade conditions initiated prior to the dominant phase of activity on normal-sense D_3 structures that show syn-D_3 crystallisation or recrystallisation of accessory phases *ca.* 23 Ma. Decompression may initially be triggered by overburden and unroofing via erosion, however the dominant phase of ZSZ movement is concurrent with M_2 peak. Minor heating resulting from a transition from a steep decompression profile to one displaying progressively shallower slopes (from weakly positive to weakly negative) may induce melting, providing a reduction in viscosity and the necessary driving force for initiation of movement on the ZSZ (e.g., Finch *et al.*, 2014) However, given the little documented melt in the region, it is possible that focused erosion and thus

differential extrusion rates between the GHS and THS might have alternately initiated a transition to normal-sense movement along the upper bounding and prior thrust (proto-ZSZ).

Any model attempting to replicate the exhumation history of the HMC within the Zanskar Himalaya must account for the following observations as documented in this study:

1. The preservation of an extensive and consistent passive margin-stratigraphy (Chapter 2).

2. The attainment of thermal peak conditions for the highest-pressure assemblages occur after the formation of D_2 deformation fabrics and prior to decompression or exhumation (Chapters 2, 4 and 5).

3. A thick GHS (approximately 55 km across strike from the ZSZ at Rangdum to the northern margin of the Kishtwar Window), that only locally contains modally low volumes of *in-situ* partial melting and leucogranite (implying a high viscosity for the rock package; Chapters 2 and 4)

4. Normal shearing on the ZSZ occurs shortly after the onset of decompression, with mechanical erosion (or another mechanism) required prior to the onset of D_3 normal shearing, after which both mechanisms might have operate in tandem to drive isothermal decompression (Chapters 4 and 5).

5. Relative variation in the penetrative development of D3 fabrics, shear zone width, and displacement across the ZSZ with greenschist facies metamorphic assemblages occurring in both the immediate footwall and hangingwall of the ZSZ. The bounding upper fault to the GHS may also be heterogeneously distributed across multiple fault strands (Chapter 2).

A number of endmember tectonic models have been proposed to account for the exhumation of the HMC (e.g., Beaumont *et al.*, 2001; Godin *et al.*, 2006; Yin, 2006; Webb *et al.*, 2007; Kohn, 2008; Carosi *et al.*, 2010; Webb *et al.*, 2011; Montomoli *et al.*, 2013; He *et al.*, 2015; Carosi *et al.*, 2018). It has recently been recognised that many of the processes implied in the endmember models (e.g., "channel flow" and "critical taper"; Beaumont *et al.*, 2001; Godin *et al.*, 2006; Kohn, 2008) are not mutually exclusive and it might be more reasonable to consider a transition or an alternation between endmember processes over time and/or that the implied processes may operate simultaneously or in progression

at different structural levels within the orogen (e.g., Cottle *et al.*, 2015; Jamieson & Beaumont, 2013; Parsons *et al.*, 2016c; Chambers *et al.*, 2011; Larson *et al.*, 2010; Mukherjee, 2013; Waters, 2019). In such a view, the transition between the channel flow and critical taper endmembers generally occur both temporally and/or spatially as deformation progresses from upper to lower structural levels in the orogen (e.g., Cottle *et al.*, 2015). As channel flow, the Miocene SW-directed flow of a middle crustal layers bounded by the MCT below and STDS above, is generally ascribed as the dominant exhumation mechanism for the upper GHS (e.g., Cottle *et al.*, 2015), it will be the focus of the rest of this discussion.

The channel flow model assumes that heat and mass are advected by the protracted flow of a weak, low-viscosity, fluid-filled channel between rigid yet deformable bounding domains. The channel is envisioned to have flowed laterally southwards (relative to bounding upper and lower crustal units) due to lithostatic loading from beneath the Tibetan plateau, underthrusting of the Indian lower crust, and focused erosion at the orogenic front. Flow is greatest where the rocks are weakest (i.e. at the base of the channel) (Beaumont *et al.*, 2001; Godin *et al.*, 2006). The channel flow model is largely based on geological and geophysical constraints from the Everest, Sikkim and Bhutan regions where the model does provide a robust explanation for the kinematic, dynamic, and temporal evolution of the HMC (Beaumont *et al.*, 2001; Searle & Godin, 2003; Unsworth *et al.*, 2005; Searle *et al.*, 2006; Streule *et al.*, 2010). However, the characteristic features of the Suru Valley region as documented in this study and listed above are not easily accounted for by a channel flow endmember.

The relative preservation of an extensive and consistent passive margin stratigraphy suggests that deformation was dominated by layer-parallel shortening (Law *et al.*, 2013; Long *et al.*, 2016; Parsons *et al.*, 2016b), rather than layer-parallel stretching, which would have significantly disrupted the present distribution of protolith lithostratigraphic units (Dyck *et al.*, 2019). Additionally, the exhumation of an active channel requires the rheological weakening provided by syn-tectonic partial melting (e.g., Grujic, 2006), for which there is little evidence in the Suru Valley region. The dominant phase of tectonometamorphic mineral growth is demonstrably post-D_2 deformation and associated with a major phase of early crustal thickening. Although the partial melting that is observed in the Suru Valley region is concurrent with D_3 deformation, it remains a modally minor component compared with the enormous rock volume of Barrovian mineral assemblages produced by compression and crustal thickening. This would suggest that

D_3 and the ZSZ did not produce the observed tectonometamorphic architecture and instead only slightly modified this earlier developed framework.

Cottle *et al.* (2015) suggest that the structural thickness of the HMC may be a function of the style of orogenic deformation and consequently that tectonic exhumation by channel flow might have occurred where the HMC was hotter and more viscous. In such instances these authors suggest that the extruded mid-crustal material may have progressed from extending flow (vertical thinning/horizontal stretching) characteristic of hinterland-style deformation, to compressing flow (vertical thickening/horizontal compression). However, in contrast, the Suru Valley region is underlain by a notably thick section of upper GHS, yet upper structural levels are characterized by a high viscosity rock units and a preserved protolith stratigraphy that implies minimal horizontal stretching during deformation.

Long-term normal movement along the upper boundary of the channel (STDS) are required to allow for forward flow of the channel (Beaumont *et al.*, 2001; Jamieson *et al.*, 2004), with rheological weakening of the mid-crust (upper GHS), causing the upper (THS) and middle (upper GHS) crust to mechanically decouple (Jamieson & Beaumont, 2013). In contrast to these model requirements, in the Zanskar region a narrow temporal window of normal movement is constrained by Finch *et al.* (2014), to initiate and terminate between a maximum range of *ca.* 26–20 Ma. The combination of both limited throw (implied by minor metamorphic grade variation) in the Suru Valley region and the short temporal window for potential normal movement suggest extrusion of the HMC as a channel could have only been brief and for which evidence may not be lacking at the present erosion surface in the Suru Valley region.

Although the viability of channel flow hinges on a significant decrease in crustal viscosity, the boundaries of the extruding channel might not specifically coincide with the distribution of *in-situ* melting. This is because material softened by strain could also become entrained into the channel, even at temperatures below 700 °C (Beaumont *et al.*, 2004). The relatively high viscosity nature of the HMC, evident in the Suru Valley region, could be viewed as a "carapace" to an exhuming channel at depth (e.g., Searle *et al.*, 2006), or as a result of the decoupled crustal layers (owing to viscosity contrast) having been recoupled to form a mechanically rigid "channel plug" during the later stages of exhumation (e.g., Beaumont *et al.*, 2004; Parsons *et al.*, 2016b). Such explanations might allow the preservation of features such as consistent internal stratigraphy and

require deformation be focused/distributed to the bounding fault (Jamieson *et al.*, 2006) and/or within the more mechanically rigid block through thickening of the crust (Beaumont *et al.*, 2004). The reduction in apparent displacement moving NW-wards along the ZSZ as documented by a widening of metamorphic mineral zones, combined with the lack of later internal crustal thickening suggest that the applicability of such explanations to this region may be limited. It is important to emphasize that although certain regions may support criteria for one model and be at odds with criteria for another it does not mean that one model only is necessarily valid (or invalid) along the full length of the Himalaya. Over the years, Himalayan research has increasingly documented orogen-parallel variation in the lithologic, structural, and tectonometamorphic framework (e.g., Yin, 2006; Long & Mcquarrie, 2010; Gibson *et al.*, 2016; Parsons *et al.*, 2016c; Mottram *et al.*, 2019). Although any model is necessarily simplified from natural systems, they must be tenable within these orogen scale variations that reflect the inherent complexity of continental tectonics. Therefore, predictive criteria of models must be repeatedly tested against the constraints provided by detailed field observations, mapping, and quantitative *P-T-t* results over large length scales and a range of stuctural levels. Such data provides the irrefutable evidence against which the validity of such any derivative model must be assessed.

6.3 Future work

Although significant work has been undertaken in this study to provide a comprehensive documentation of the tectonometamorphic evolution of the Zanskar Himalaya, several questions specific to both the region and the Himalayan orogen remain. In addition, further questions about the tectonometamorphic processes that pertain to the broader evolution of orogenic systems and approaches to effectively record and model them should be considered.

Tectonometamorphic architecture

1. What is the relative sense of movement on the inferred Warwan fault that is located W of the Suru Valley loosely delimiting the boundary between the GHS and THS. Is there any metamorphic variation between the immediate footwall and hanging wall? Does the structure relate to the ZSZ?

2. In what environment did volcanism occur in the Lamayuru Complex, and how did it differ from the temporal and geochemical record of the voluminous

Panjal Trap volcanics? Does this volcanism provide any information on the geometry of the Indian plate during closure of Tethys?

3. What is the orogen-parallel variation between maximum detrital age and minimum igneous age constraints for the volcano-sedimentary sequences of the GHS. What information may this impart about relative timing of sedimentation, igneous activity and tectonic setting on the Indian margin following the assembly of Gondwana?

4. Do superposed orogenic cycles exert significant control over the rheology and metamorphic evolution of mountain belts? Within the Himalaya belt is there a relationship between the volume of pre-Himalayan granitoid bodies (and associated redistribution of radiogenic heating producing elements) and subsequent melting. If so, how does this impact the thermodynamic evolution and ability to model such terrains.

5. How does the rate of movement and amount of displacement across the STD vary along strike in the Himalaya. Is the variation consistent with the relative distribution and volume of partial melt? How can thermodynamic models account for regions where the STD is absent as a discrete structure or where it preserves limited throw? If there is limited or no throw, this may significantly impact the *P-T-t* predictions for each model.

6. What is the relative relationship of sillimanite growth to S_3 fabric development in the Suru Valley region?

P-T modelling and mineral chemistry

1. How can we, as metamorphic petrologists, better integrate statistics in *P-T* modelling and account for and propagate cumulative error in a significant/useable way?

2. How does the considered equilibrium volume impact phase compositions, modes, and assemblage boundaries?

3. What are the most robust compositional parameters that should be used with the current thermodynamic datasets based on comparisons between natural and modelled compositional information?

4. Are other areas of the Himalaya with lower melt volumes attributable to devolatilisation reactions under reduced $a\mathrm{H_2O}$ conditions? Combined

with changes in the distribution and abundance of contrasting lithological units, do these account for the applicability of different tectonic models of exhumation along the length of the orogen?

5. What apparent differences can be documented by metabasic and pelitic assemblages across other *P-T* regimes and sequences? How well are these differences predicted in phase equilibrium modelling? Are there consistent variations/differences between the two rock types and in what parts of the metamorphic cycle? How can we integrate this information to better constrain metamorphic field gradients for thermal modelling?

Geochronology

1. Can bulk compositional variation account for quantitative differences in the initiation of monazite growth? Or is bulk composition principally relevant for the initiation of other REE-rich phases that control the available REE-budget and thereby possible pulses of monazite growth?

2. When did the movement on the ZSZ start in the Suru Valley region? How does this relate to initiation of decompression from peak-pressures at different structural levels? Secondly, when did movement on the ZSZ end? U-Pb calcite dating of brittle calcite veins cutting through the upper portion of the ZSZ could inform the relative timing of the ductile-brittle transition at the highest structural level.

3. What are the implications of *ca.* 1.9 Ga age determinations within igneous zoned zircons in the group B metavolcanic rocks? What does this imply about sedimentation and volcanic activity in the Indus Suture Zone?

4. How can the contrasting metamorphic record of the leucogranite-rich and melt-rich SE Zanskar regions (Gianbul, Gumburanjum) and the melt-poor NW Zanskar regions (Suru Valley) be explained? Does the variation in the metamorphic age record in both regions represent SW- directed crustal thickening? Detailed studies similar to the one undertaken for this project, for the SE-region and intervening regions would be key to resolve this apparent temporal variation/discrepancy.

References

Ackermand, D. & Karl, F. (1972). Experimental studies on the formation of inclusions in plagioclases from metatonalites, Hohe Tauern, Austria (lower temperature stability limit of the paragenesis anorthite plus potash feldspar). *Contributions to Mineralogy and Petrology*, 35(1), 11–21.

Ahmad, T., Mukherjee, P. K., & Trivedi, J. R. (1999). Geochemistry of Precambrian mafic magmatic rocks of the Western Himalaya, India: Petrogenetic and tectonic implications. *Chemical Geology*, 160(1), 103–119.

Aikman, A. B., Harrison, T. M., & Lin, D. (2008). Evidence for Early (> 44 Ma) Himalayan Crustal Thickening, Tethyan Himalaya, southeastern Tibet. *Earth and Planetary Science Letters*, 274(1), 14–23.

Albee, A. L. (1968). Metamorphic Zones in Northern Vermont. In E.-a. Zen, W. S. White, J. J. Hadley, & J. B. Jr. Thompson (Eds.), *Studies of Appalachian Geology - Northern and Maritime* (pp. 329–341). New York: Interscience Publisher.

Aleinikoff, J. N., Schenck, W. S., Plank, M. O., Srogi, L., Fanning, C. M., Kamo, S. L., & Bosbyshell, H. (2006). Deciphering igneous and metamorphic events in high-grade rocks of the Wilmington Complex, Delaware: Morphology, cathodoluminescence and backscattered electron zoning, and SHRIMP U-Pb geochronology of zircon and monazite. *GSA Bulletin*, 118(1-2), 39–64.

Ambrose, T., Larson, K., Guilmette, C., Cottle, J., Buckingham, H., & Rai, S. (2015). Lateral extrusion, underplating, and out-of-sequence thrusting within the Himalayan metamorphic core, Kanchenjunga, Nepal. *Lithosphere*, 7(4), 441–464.

An, W., Hu, X., Garzanti, E., Wang, J.-G., & Liu, Q. (2021). New Precise Dating of the India-Asia Collision in the Tibetan Himalaya at 61 Ma. *Geophysical Research Letters*, 48(3), e2020GL090641.

Anczkiewicz, R., Oberli, F., Burg, J. P., Villa, I. M., Günther, D., & Meier, M. (2001). Timing of normal faulting along the Indus Suture in Pakistan Himalaya and a case of major 231Pa/235U initial disequilibrium in zircon. *Earth and Planetary Science Letters*, 191(1), 101–114.

Anderson, J. L. & Smith, D. R. (1995). The effects of temperature and fO2 on the Al-in-hornblende barometer. *American Mineralogist*, 80, 549–559.

Arai, T., Omori, S., Komiya, T., & Maruyama, S. (2015). Intermediate P/T-type regional metamorphism of the Isua Supracrustal Belt, southern west Greenland: The oldest Pacific-type orogenic belt? *Tectonophysics*, 662, 22–39.

Aranovich, L. Ya. & Newton, R. C. (1998). Reversed determination of the reaction; phlogopite+quartz = enstatite+potassium feldspar+H 2 O in the ranges 750-875 degrees C and 2-12 kbar at low H 2 O activity with concentrated KCl solutions. *American Mineralogist*, 83(3-4), 193–204.

Argles, T. W., Prince, C. I., Foster, G. L., & Vance, D. (1999). New garnets for old? Cautionary tales from young mountain belts. *Earth and Planetary Science Letters*, 172(3), 301–309.

Auzanneau, E., Schmidt, M. W., Vielzeuf, D., & D Connolly, J. A. (2010). Titanium in phengite: A geobarometer for high temperature eclogites. *Contributions to Mineralogy and Petrology*, 159(1), 1–24.

Avigad, D., Kolodner, K., McWilliams, M., Persing, H., & Weissbrod, T. (2003). Origin of northern Gondwana Cambrian sandstone revealed by detrital zircon SHRIMP dating. *Geology*, 31, 227–230.

Axelsson, E., Pape, J., Berndt, J., Corfu, F., Mezger, K., & Raith, M. M. (2018). Rutile R632 – A New Natural Reference Material for U-Pb and Zr Determination. *Geostandards and Geoanalytical Research*, 42(3), 319–338.

Ayres, M. & Harris, N. (1997). REE fractionation and Nd-isotope disequilibrium during crustal anatexis: Constraints from Himalayan leucogranites. *Chemical Geology*, 139(1), 249–269.

Banno, S. & Sakai, C. (1989). Geology and metamorphic evolution of the Sanbagawa metamorphic belt, Japan. *Geological Society, London, Special Publications*, 43, 519–532.

Barker, A. J. (1998). *Introduction to Metamorphic Textures and Microstructures*. Boston, MA: Springer US.

Baud, A., Gaetani, M., Garzanti, E., Fois, E., Nicora, A., & Tintori, A. (1984). Geological observations in southeastern Zanskar and adjacent Lahul area (northwestern Himalaya). *Eclogae Geologicae Helvetiae*, 77(1), 161–197.

Beaumont, C., Jamieson, R. A., Nguyen, M. H., & Lee, B. (2001). Himalayan tectonics explained by extrusion of a low-viscosity crustal channel coupled to focused surface denudation. *Nature*, 414, 738–742.

Beaumont, C., Jamieson, R. A., Nguyen, M. H., & Medvedev, S. (2004). Crustal channel flows: 1. Numerical models with applications to the tectonics of the Himalayan-Tibetan orogen. *Journal of Geophysical Research: Solid Earth*, 109(B6).

Bégin, N. J. (1992). Contrasting mineral isograd sequences in metabasites of the Cape Smith Belt, northern Québec, Canada: Three new bathograds for mafic rocks. *Journal of Metamorphic Geology*, 10(5), 685–704.

Bell, T. & Welch, P. (2002). Prolonged Acadian orogenesis: Revelations from foliation intersection axis (FIA) controlled monazite dating of foliations in porphyroblasts and matrix. *American Journal of Science*, 302, 549–581.

Berman, R. G. (1991). Thermobarometry using multi-equilibrium calculations; a new technique, with petrological applications. *The Canadian Mineralogist*, 29, 833–855.

Bhargava, O. N., Thoni, M., & Miller, C. (2016). Isotopic evidence of Early Palaeozoic metamorphism in the Lesser Himalaya (Jutogh Group), Himachal Pradesh, India: Its implication. *Himalayan Geology*, 37(2), 73–84.

Bhat, I. M., Ahmad, T., & Rao, D. V. S. (2019a). Petrology and Geochemistry of Mafic Intrusive Rocks from the Sapi-Shergol Ophiolitic Mélange, Indus Suture Zone, Western Ladakh: Constraints on Petrogenesis and Tectonic Setting. *The Journal of Geology*, 127(5), 543–566.

Bhat, I. M., Ahmad, T., & Subba Rao, D. V. (2019b). The tectonic evolution of the Dras arc complex along the Indus Suture Zone, western Himalaya: Implications for the Neo-Tethys Ocean geodynamics. *Journal of Geodynamics*, 124, 52–66.

Bhat, I. M., Chauhan, H., Ahmad, T., & Dar, R. A. (2023). Geochemistry and petrogenesis of ophiolitic rocks from the Indus Suture Zone (ISZ), Ladakh Himalaya: Insights for depleted mantle beneath an intra-oceanic island arc complex. *International Geology Review*.

Bhat, M. I., Claesson, S., Dubey, A. K., & Pande, K. (1998). Sm–Nd age of the Garhwal–Bhowali volcanics, western Himalayas: Vestiges of the Late Archaean Rampur flood basalt Province of the northern Indian Craton. *Precambrian Research*, 87(3), 217–231.

Bhat, M. I., Le Fort, P., & Ahmad, T. (1994). Bafliaz volcanics, NW Himalaya: Origin of a bimodal, tholeiite and alkali basalt suite. *Chemical Geology*, 114(3), 217–234.

Bingham, C. (1974). An Antipodally Symmetric Distribution on the Sphere. *The Annals of Statistics*, 2(6), 1201–1225.

Black, L. P., Kamo, S. L., Allen, C. M., Davis, D. W., Aleinikoff, J. N., Valley, J. W., Mundil, R., Campbell, I. H., Korsch, R. J., Williams, I. S., & Foudoulis, C. (2004). Improved 206Pb/238U microprobe geochronology by the monitoring of a trace-element-related matrix effect; SHRIMP, ID–TIMS, ELA–ICP–MS and oxygen isotope documentation for a series of zircon standards. *Chemical Geology*, 205(1), 115–140.

Boullier, A.-M., France-Lanord, C., Dubessy, J., Adamy, J., & Champenois, M. (1991). Linked fluid and tectonic evolution in the High Himalaya mountains (Nepal). *Contributions to Mineralogy and Petrology*, 107(3), 358–372.

Bousquet, R. (2008). Metamorphic heterogeneities within a single HP unit: Overprint effect or metamorphic mix? *Lithos*, 103(1), 46–69.

Boyle, A. P. (1986). Metamorphism of basic and pelitic rocks at Sulitjelma, Norway. *Lithos*, 19(2), 113–128.

Bracciali, L., Parrish, R. R., Horstwood, M. S. A., Condon, D. J., & Najman, Y. (2013). UPb LA-(MC)-ICP-MS dating of rutile: New reference materials and applications to sedimentary provenance. *Chemical Geology*, 347, 82–101.

Braden, Z., Godin, L., & Cottle, J. M. (2017). Segmentation and rejuvenation of the Greater Himalayan sequence in western Nepal revealed by in situ U–Th/Pb monazite petrochronology. *Lithos*, 284–285, 751–765.

Brodie, K. H. & Rutter, E. H. (1985). On the Relationship between Deformation and Metamorphism, with Special Reference to the Behavior of Basic Rocks. In A. B. Thompson & D. C. Rubie (Eds.), *Metamorphic Reactions: Kinetics, Textures, and Deformation*, Advances in Physical Geochemistry (pp. 138–179). New York, NY: Springer.

Brookfield, M. E. & Reynolds, P. H. (1981). Late Cretaceous emplacement of the Indus suture zone ophiolitic mélanges and an Eocene-Oligocene are on the northern edge of the Indian plate. *Earth and Planetary Science Letters*, 55, 157–162.

Brown, M. (2009). Metamorphic patterns in orogenic systems and the geological record | - https://www.lyellcollection.org/doi/full/10.1144/SP318.2. *Geological Society, London, Special Publications*, 318, 37–74.

Budzyń, B., Harlov, D. E., Williams, M. L., & Jercinovic, M. J. (2011). Experimental determination of stability relations between monazite, fluorapatite, allanite, and REE-epidote as a function of pressure, temperature, and fluid composition. *American Mineralogist*, 96(10), 1547–1567.

Burchfiel, B. C. & Royden, L. H. (1985). North-south extension within the convergent Himalayan region. *Geology*, 13(10), 679–682.

Burchfiel, B. C., Zhiliang, C., Hodges, K. V., Yuping, L., Royden, L. H., Changrong, D., & Jiene, X. (1992). The South Tibetan Detachment System, Himalayan Orogen: Extension Contemporaneous With and Parallel to Shortening in a Collisional Mountain Belt. *The South Tibetan Detachment System, Himalayan Orogen: Extension Contemporaneous With and Parallel to Shortening in a Collisional Mountain Belt*, 269, 41.

Burg, J. P., Brunel, M., Gapais, D., Chen, G. M., & Liu, G. H. (1984). Deformation of leucogranites of the crystalline Main Central Sheet in southern Tibet (China). *Journal of Structural Geology*, 6(5), 535–542.

Burton, J. (1995). *Petrogenesis of Garnet Migmatites and Garnet Granitoids with Reference to Namaqualand, South Africa and the Western Himalaya*. PhD thesis, University of Oxford.

Butler, R. W. (2017). Basement-cover tectonics, structural inheritance, and deformation migration in the outer parts of orogenic belts: A view from the western Alps. In R. D. Law, J. R. Thigpen, A. J. Merschat, & H. H. Stowell (Eds.), *Linkages and Feedbacks in Orogenic Systems*, volume 213 (pp.0̃). Geological Society of America.

Carmichael, D. M. (1969). On the mechanism of prograde metamorphic reactions in quartz-bearing pelitic rocks. *Contributions to Mineralogy and Petrology*, 20(3), 244–267.

Carosi, R., Montomoli, C., & Iaccarino, S. (2018). 20 years of geological mapping of the metamorphic core across Central and Eastern Himalayas. *Earth-Science Reviews*, 177, 124–138.

Carosi, R., Montomoli, C., Iaccarino, S., & Visonà, D. (2019). Structural evolution, metamorphism and melting in the Greater Himalayan Sequence in central-western Nepal. *Geological Society, London, Special Publications*, 483(1), 305–323.

Carosi, R., Montomoli, C., Rubatto, D., & Visonà, D. (2010). Late Oligocene high-temperature shear zones in the core of the Higher Himalayan Crystallines (Lower Dolpo, western Nepal). *Tectonics*, 29(4).

Carosi, R., Montomoli, C., & Visonà, D. (2007). A structural transect in the Lower Dolpo: Insights on the tectonic evolution of Western Nepal. *Journal of Asian Earth Sciences*, 29(2), 407–423.

Catlos, E. J., Gilley, L. D., & Harrison, T. M. (2002a). Interpretation of monazite ages obtained via in situ analysis. *Chemical Geology*, 188(3), 193–215.

Catlos, E. J., Harrison, T. M., Manning, C. E., Grove, M., Rai, S. M., Hubbard, M. S., & Upreti, B. N. (2002b). Records of the evolution of the Himalayan orogen from in situ Th–Pb ion microprobe dating of monazite: Eastern Nepal and western Garhwal. *Journal of Asian Earth Sciences*, 20(5), 459–479.

Catlos, E. J., Sorensen, S. S., & Harrison, T. M. (2000). Th-Pb ion-microprobe dating of allanite. *American Mineralogist*, 85(5-6), 633–648.

Cawood, P., Hawkesworth, C., & Dhuime, B. (2012). Detrital zircon record and tectonic setting. *Geology*, 40(10), 875–878.

Cawood, P. A., Johnson, M. R., & Nemchin, A. A. (2007). Early Palaeozoic orogenesis along the Indian margin of Gondwana: Tectonic response to Gondwana assembly. *Earth and Planetary Science Letters*, 255(1-2), 70–84.

Cawood, P. A., Martin, E. L., Murphy, J. B., & Pisarevsky, S. A. (2021). Gondwana's interlinked peripheral orogens. *Earth and Planetary Science Letters*, 568, 117057.

Cesare, B., Parisatto, M., Mancini, L., Peruzzo, L., Franceschi, M., Tacchetto, T., Reddy, S., Spiess, R., Nestola, F., & Marone, F. (2021). Mineral inclusions are not immutable: Evidence of post-entrapment thermally-induced shape change of quartz in garnet. *Earth and Planetary Science Letters*, 555, 116708.

Chakraborty, S., Anczkiewicz, R., Gaidies, F., Rubatto, D., Sorcar, N., Faak, K., Mukhopadhyay, D., & Dasgupta, S. (2016). A review of thermal history and timescales of tectonometamorphic processes in Sikkim Himalaya (NE India) and implications for rates of metamorphic processes. *Journal of Metamorphic Geology*, 34(8), 785–803.

Chambers, J., Caddick, M., Argles, T., Horstwood, M., Sherlock, S., Harris, N., Parrish, R., & Ahmad, T. (2009). Empirical constraints on extrusion mechanisms from the upper margin of an exhumed high-grade orogenic core, Sutlej valley, NW India. *Tectonophysics*, 477(1-2), 77–92.

Chambers, J., Parrish, R., Argles, T., Harris, N., & Horstwood, M. (2011). A short-duration pulse of ductile normal shear on the outer South Tibetan detachment in Bhutan: Alternating channel flow and critical taper mechanics of the eastern Himalaya. *Tectonics*, 30(2).

Chambers, J. A. & Kohn, M. J. (2012). Titanium in muscovite, biotite, and hornblende: Modeling, thermometry, and rutile activities of metapelites and amphibolites. *American Mineralogist*, 97(4), 543–555.

Chemenda, A. I., Burg, J.-P., & Mattauer, M. (2000). Evolutionary model of the Himalaya-Tibet system: Geopoem based on new modelling, geological and geophysical data. *Earth and Planetary Science Letters*, 174, 397–409.

Chemenda, A. I., Mattauer, M., Malavieille, J., & Bokun, A. N. (1995). A mechanism for syn-collisional rock exhumation and associated normal faulting: Results from physical modelling. *Earth and Planetary Science Letters*, 132(1-4), 225–232.

Chen, W.-Y., Shellnutt, J. G., Bhat, G. M., Tejada, M. L. G., Suzuki, K., & Denyszyn, S. W. (2023). Geochronology and geochemistry of the Panjal Traps from the southern Pir Panjal Range, Kashmir, India. *Lithos*, 436–437, 106967.

Chen, Y.-X. & Zheng, Y.-F. (2015). Extreme Nb/Ta fractionation in metamorphic titanite from ultrahigh-pressure metagranite. *Geochimica et Cosmochimica Acta*, 150, 53–73.

Cherniak, D. J. (1993). Lead diffusion in titanite and preliminary results on the effects of radiation damage on Pb transport. *Chemical Geology*, 110(1), 177–194.

Cherniak, D. J. (2000). Pb diffusion in rutile. *Contributions to Mineralogy and Petrology*, 139(2), 198–207.

Cherniak, D. J. (2015). Nb and Ta diffusion in titanite. *Chemical Geology*, 413, 44–50.

Cherniak, D. J., Watson, E. B., Grove, M., & Harrison, T. M. (2004). Pb diffusion in monazite: A combined RBS/SIMS study1 1Associate editor: Y. Amelin. *Geochimica et Cosmochimica Acta*, 68(4), 829–840.

Chew, D. M., Petrus, J. A., & Kamber, B. S. (2014). U–Pb LA–ICPMS dating using accessory mineral standards with variable common Pb. *Chemical Geology*, 363, 185–199.

Chew, D. M. & Spikings, R. A. (2015). Geochronology and Thermochronology Using Apatite: Time and Temperature, Lower Crust to Surface. *Elements*, 11(3), 189–194.

Chinner, G. A. (1961). The Origin of Sillimanite in Glen Clova, Angus. *Journal of Petrology*, 2(3), 312–323.

Clift, P. D., Carter, A., Krol, M., & Kirby, E. (2002). Constraints on India-Eurasia collision in the Arabian Sea region taken from the Indus Group, Ladakh Himalaya, India. *Geological Society, London, Special Publications*, 195, 97–116.

Clift, P. D., Degnan, P. J., Hannigan, R., & Blusztajn, J. (2000). Sedimentary and geochemical evolution of the Dras forearc basin, Indus suture, Ladakh Himalaya, India. *GSA Bulletin*, 112(3), 450–466.

Coggon, R. & Holland, T. J. B. (2002). Mixing properties of phengitic micas and revised garnet-phengite thermobarometers. *Journal of Metamorphic Geology*, 20(7), 683–696.

Connolly, J. (1990). Multivariable phase diagrams: An algorithm based on generalized thermodynamics. *American Journal of Science*, 290, 666–718.

Connolly, J. (2005). Computation of phase equilibria by linear programming: A tool for geodynamic modeling and its application to subduction zone decarbonation. *Earth and Planetary Science Letters*, 236(1-2), 524–541.

Cooper, A. F. (1972). Progressive Metamorphism of Metabasic Rocks from the Haast Schist Group of Southern New Zealand. *Journal of Petrology*, 13(3), 457–492.

Copley, A. & Weller, O. (2022). The controls on the thermal evolution of continental mountain ranges. *Journal of Metamorphic Geology*, 40(7), 1235–1270.

Copley, A. & Weller, O. M. (2024). Modern-style continental tectonics since the early Archean. *Precambrian Research*, 403, 107324.

Corfield, R. I. & Searle, M. P. (2000). Crustal shortening estimates across the north Indian continental margin, Ladakh, NW India. *Geological Society, London, Special Publications*, 170(1), 395–410.

Corrie, S. L. & Kohn, M. J. (2008). Trace-element distributions in silicates during prograde metamorphic reactions: Implications for monazite formation. *Journal of Metamorphic Geology*, 26(4), 451–464.

Cottle, J. M., Jessup, M. J., Newell, D. L., Horstwood, M. S. A., Noble, S. R., Parrish, R. R., Waters, D. J., & Searle, M. P. (2009a). Geochronology of granulitized eclogite from the Ama Drime Massif: Implications for the tectonic evolution of the South Tibetan Himalaya. *Tectonics*, 28(1).

Cottle, J. M., Jessup, M. J., Newell, D. L., Searle, M. P., Law, R. D., & Horstwood, M. S. A. (2007). Structural insights into the early stages of exhumation along an orogen-scale detachment : The South Tibetan Detachment System , Dzakaa Chu section , Eastern Himalaya. *Journal of Structural Geology*, 29(11), 1781–1797.

Cottle, J. M., Larson, K. P., & Kellett, D. A. (2015). How does the mid-crust accommodate deformation in large, hot collisional orogens? A review of recent research in the Himalayan orogen. *Journal of Structural Geology*, 78, 119–133.

Cottle, J. M., Searle, M. P., Horstwood, M. S. A., & Waters, D. J. (2009b). Timing of Midcrustal Metamorphism, Melting, and Deformation in the Mount Everest Region of Southern Tibet Revealed by U(-Th)-Pb Geochronology. *The Journal of Geology*, 117(6), 643–664.

Cottle, J. M., Waters, D. J., Riley, D., Beyssac, O., & Jessup, M. J. (2011). Metamorphic history of the South Tibetan Detachment System, Mt. Everest region, revealed by RSCM thermometry and phase equilibria modelling. *Journal of Metamorphic Geology*, 29(5), 561–582.

Craw, D. (1990). Fluid evolution during uplift of the Annapurna Himal, central Nepal. *Lithos*, 24(2), 137–150.

Cruz-Uribe, A. M., Feineman, M. D., Zack, T., & Barth, M. (2014). Metamorphic reaction rates at ∼650–800°C from diffusion of niobium in rutile. *Geochimica et Cosmochimica Acta*, 130, 63–77.

Cruz-Uribe, A. M., Feineman, M. D., Zack, T., & Jacob, D. E. (2018). Assessing trace element (dis)equilibrium and the application of single element thermometers in metamorphic rocks. *Lithos*, 314–315, 1–15.

Cunningham, D. (2013). Mountain building processes in intracontinental oblique deformation belts: Lessons from the Gobi Corridor, Central Asia. *Journal of Structural Geology*, 46, 255–282.

Dahlen, F. (1990). Critical Taper Model Of Fold-And-Thrust Belts And Accretionary Wedges. *Annual Review of Earth and Planetary Sciences*, 18(1), 55–99.

Dale, J., Holland, T., & Powell, R. (2000). Hornblende–garnet–plagioclase thermobarometry: A natural assemblage calibration of the thermodynamics of hornblende. *Contributions to Mineralogy and Petrology*, 140(3), 353–362.

Dale, J., Powell, R., White, R. W., Elmer, F. L., & Holland, T. J. B. (2005). A thermodynamic model for Ca–Na clinoamphiboles in Na2O–CaO–FeO–MgO–Al2O3–SiO2–H2O–O for petrological calculations. *Journal of Metamorphic Geology*, 23(8), 771–791.

Dalmayrac, B. & Molnar, P. (1981). Parallel thrust and normal faulting in Peru and constraints on the state of stress Peter Molnar. *Earth and Planetary Science Letters*, 55, 473–481.

Daniel, C. G., Hollister, L. S., Parrish, R. R., & Grujic, D. (2003). Exhumation of the Main Central Thrust from Lower Crustal Depths, Eastern Bhutan Himalaya. *Journal of Metamorphic Geology*, 21(4), 317–334.

de Capitani, C. & Brown, T. H. (1987). The computation of chemical equilibrium in complex systems containing non-ideal solutions. *Geochimica et Cosmochimica Acta*, 51(10), 2639–2652.

de Capitani, C. & Petrakakis, K. (2010). The computation of equilibrium assemblage diagrams with Theriak/Domino software. *American Mineralogist*, 95(7), 1006–1016.

DeCelles, P. G., Gehrels, G. E., Quade, J., LaReau, B., & Spurlin, M. (2000). Tectonic implications of U-Pb zircon ages of the himalayan orogenic belt in nepal. *Science (New York, N.Y.)*, 288(5465), 497–499.

DeCelles, P. G., Kapp, P., Gehrels, G. E., & Ding, L. (2014). Paleocene-Eocene foreland basin evolution in the Himalaya of southern Tibet and Nepal: Implications for the age of initial India-Asia collision. *Tectonics*, 33(5), 824–849.

DeCelles, P. G., Robinson, D. M., & Zandt, G. (2002). Implications of shortening in the Himalayan fold-thrust belt for uplift of the Tibetan Plateau. *Tectonics*, 21(6), 12–1–12–25.

Deer, W. A., Howie, R. A., & Zussman, J. (2013). *An Introduction to the Rock-Forming Minerals*. Mineralogical Society of Great Britain and Ireland.

Dewey, J. F., Holdsworth, R. E., & Strachan, R. A. (1998). Transpression and transtension zones. *Geological Society, London, Special Publications*, 135(1), 1–14.

Dèzes, P. J., Vannay, J. C., Steck, A., Bussy, F., & Cosca, M. (1999). Synorogenic extension: Quantitative constraints on the age and displacement of the Zanskar shear zone (northwest Himalaya). *GSA Bulletin*, 111(3), 364–374.

Diener, J. F. A. & Powell, R. (2010). Influence of ferric iron on the stability of mineral assemblages. *Journal of Metamorphic Geology*, 28(6), 599–613.

Diener, J. F. A. & Powell, R. (2012). Revised activity–composition models for clinopyroxene and amphibole. *Journal of Metamorphic Geology*, 30(2), 131–142.

Diener, J. F. A., Powell, R., White, R. W., & Holland, T. J. B. (2007). A new thermodynamic model for clino- and orthoamphiboles in the system Na2O–CaO–FeO–MgO–Al2O3–SiO2–H2O–O. *Journal of Metamorphic Geology*, 25(6), 631–656.

Dietrich, V. J., Frank, W., & Honegger, K. (1983). A Jurassic-Cretaceous island arc in the Ladakh-Himalayas. *Journal of Volcanology and Geothermal Research*, 18(1), 405–433.

Dodson, M. H. (1973). Closure temperature in cooling geochronological and petrological systems. *Contributions to Mineralogy and Petrology*, 40, 259–273.

Doukkari, S. A., Diener, J. F., Ouzegane, K., & Kienast, J.-R. (2018). Mineral equilibrium modelling and calculated chemical potential relations of reaction textures in the ultrahigh-temperature In Ouzzal terrane (In Hihaou area, Western Hoggar, Algeria). *Journal of Metamorphic Geology*, 36(9), 1175–1198.

Dransfield, M. (1994). *Extensional Exhumation of High-Grade Metamorphic Rocks in Western Norway and the Zanskar Himalaya*. PhD thesis, University of Oxford.

Dumond, G., Goncalves, P., Williams, M. L., & Jercinovic, M. J. (2015). Monazite as a monitor of melting, garnet growth and feldspar recrystallization in continental lower crust. *Journal of Metamorphic Geology*, 33(7), 735–762.

Dyck, B., St-Onge, M., Searle, M. P., Rayner, N., Waters, D., & Weller, O. M. (2019). Protolith lithostratigraphy of the greater Himalayan series in Langtang, Nepal: Implications for the architecture of the Northern Indian margin. *Geological Society Special Publication*, 483(1), 281–304.

Dyck, B., Waters, D. J., St-Onge, M. R., & Searle, M. P. (2020). Muscovite dehydration melting: Reaction mechanisms, microstructures, and implications for anatexis. *Journal of Metamorphic Geology*, 38(1), 29–52.

Dymek, R. F. (1983). Titanium, aluminum and interlayer cation substitutions in biotite from high-grade gneisses, West Greenland. *American Mineralogist*, 68, 880–899.

Egufluz, L. & Abalos, B. (1992). Tectonic setting of Cadomian low-pressure metamorphism in the central Ossa-Morena zone (Iberian massif, SW spain). *Precambrian Research*, 56(1), 113–137.

Enami, M., Nishiyama, T., & Mouri, T. (2007). Laser Raman microspectrometry of memtamorphic quartz: A simple method for comparison of metaorphic pressures. *American Mineralogist*, 92, 1303–1315.

Engi, M. (2017). Petrochronology Based on REE-Minerals: Monazite, Allanite, Xenotime, Apatite. *Reviews in Mineralogy and Geochemistry*, 83(1), 365–418.

England, P. & Jackson, J. (1989). Active Deformation of the Continents. *Annual Review of Earth and Planetary Sciences*, 17(Volume 17, 1989), 197–226.

England, P. C. & Thompson, A. B. (1984). Pressure–Temperature–Time Paths of Regional Metamorphism I. Heat Transfer during the Evolution of Regions of Thickened Continental Crust. *Journal of Petrology*, 25(4), 894–928.

Epard, J.-L. & Steck, A. (2004). The Eastern prolongation of the Zanskar Shear Zone (Western Himalaya). *Eclogae Geologicae Helvetiae*, 97, 193–212.

Epard, J.-L., Steck, A., Vannay, J.-C., & Hunziker, J. (1995). Tertiary Himalayan structures and metamorphism in the Kulu Valley (Mandi-Khoksar transect of the Western Himalaya)-Shikar Beh Nappe and Crystalline Nappe. *Schweizerische Mineralogische und Petrographische Mitteilungen*, 75, 59–84.

Essene, E. J. (1989). The current status of thermobarometry in metamorphic rocks. *Geological Society, London, Special Publications*, 43(1), 1–44.

Faak, K., Chakraborty, S., & Dasgupta, S. (2012). Petrology and tectonic significance of metabasite slivers in the Lesser and Higher Himalayan domains of Sikkim, India. *Journal of Metamorphic Geology*, 30(6), 599–622.

Ferry, J. M. (2000). Patterns of mineral occurrence in metamorphic rocks. *American Mineralogist*, 85(11-12), 1573–1588.

Ferry, J. M. & Spear, F. S. (1978). Experimental calibration of the partitioning of Fe and Mg between biotite and garnet. *Contributions to Mineralogy and Petrology*, 66(2), 113–117.

Ferry, J. M. & Watson, E. B. (2007). New thermodynamic models and revised calibrations for the Ti-in-zircon and Zr-in-rutile thermometers. *Contributions to Mineralogy and Petrology*, 154(4), 429–437.

Finch, M., Hasalová, P., Weinberg, R. F., & Fanning, C. M. (2014). Switch from thrusting to normal shearing in the Zanskar shear zone, NW Himalaya: Implications for channel flow. *GSA Bulletin*, 126(7-8), 892–924.

Fitzsimons, I. C. W. & Harley, S. L. (1994). The Influence of Retrograde Cation Exchange on Granulite P-T Estimates and a Convergence Technique for the Recovery of Peak Metamorphic Conditions. *Journal of Petrology*, 35(2), 543–576.

Fitzsimons, I. C. W., Kinny, P. D., Wetherley, S., & Hollingsworth, D. A. (2005). Bulk chemical control on metamorphic monazite growth in pelitic schists and implications for U–Pb age data. *Journal of Metamorphic Geology*, 23(4), 261–277.

Forshaw, J. B. & Pattison, D. R. M. (2021). Ferrous/ferric (Fe2+/Fe3+) partitioning among silicates in metapelites. *Contributions to Mineralogy and Petrology*, 176(9), 63.

Forshaw, J. B., Waters, D. J., Pattison, D. R. M., Palin, R. M., & Gopon, P. (2019). A comparison of observed and thermodynamically predicted phase equilibria and mineral compositions in mafic granulites. *Journal of Metamorphic Geology*, 37(2), 153–179.

Foster, G., Gibson, H. D., Parrish, R., Horstwood, M., Fraser, J., & Tindle, A. (2002). Textural, chemical and isotopic insights into the nature and behaviour of metamorphic monazite. *Chemical Geology*, 191(1), 183–207.

Foster, G., Kinny, P., Vance, D., Prince, C., & Harris, N. (2000). The significance of monazite U–Th–Pb age data in metamorphic assemblages; a combined study of monazite and garnet chronometry. *Earth and Planetary Science Letters*, 181(3), 327–340.

Frank, W., Baud, A., Honegger, K., & Trommsdorf, V. (1987). Comparative studies on profiles across the Northwest Himalaya. In J. P. Schaer & J. Rogers (Eds.), *The Anatomy of Mountain Ranges* (pp. 261–275). Princeton, NJ: Princeton University Press.

Fuchs, G. (1982). The geology of Western Zanskar. *Jahrbuch der Geologischen Bundesanstalt*, 125(1-2), 1–50.

Fuchs, G. (1987). The Geology of Southern Zanskar (Ladakh) - Evidence for the Autochthony of the Tethys Zone of the Himalaya. *Jahrbuch der Geologischen Bundesanstalt*, 130(4), 465–491.

Fuchs, G. & Linner, M. (1995). Geological Traverse Across the Western Himalaya – a Contribution to the Geology of Eastern Ladakh, Lahul, and Chamba. *Jahrbuch Der Geologischen Bundesanstalt*, 138(4), 655–685.

Gaetani, M., Casnedi, R., Fois, E., Garzanti, E., Jadoul, F., Nicora, A., & Tintori, A. (1986). Stratigraphy of the Tethys Himalaya in Zanskar, Ladakh. *Rivista Italiana di Paleontologia e Stratigrafia*, 91(4), 443–478.

Gaetani, M. & Garzanti, E. (1991). Multicyclic History of the Northern India Continental Margin (Northwestern Himalaya). *The American Association of Petroleum Geologists Bulletin*, 75(9), 1427–1446.

Gaidies, F., Krenn, E., De Capitani, C., & Abart, R. (2008). Coupling forward modelling of garnet growth with monazite geochronology: An application to the Rappold Complex (Austroalpine crystalline basement). *Journal of Metamorphic Geology*, 26(7), 775–793.

Gansser, A. (1964). *Geology of the Himalayas*. Interscience Publishers.

Gapais, D., Gilbert, E., & Pecher, A. (1984). Structures et trajectoires de déformation dans la zone de suture de l'Indus-Tsangpo en Himalaya du Ladakh, région de la Suru. *Comptes Rendus de l'Académie des Sciences*, 299(4), 179–182.

Gapais, D., Pêcher, A., Gilbert, E., & Ballèvre, M. (1992). Synconvergence spreading of the Higher Himalaya Crystaline in Ladakh. *Tectonics*, 11(5), 1045–1056.

Garzanti, E., Baud, A., & Mascle, G. (1987). Sedimentary record of the northward flight of india and its collision with eurasia (ladakh himalaya, India). *Geodinamica Acta*, 1(4-5), 297–312.

Garzanti, E. & Van Haver, T. (1988). The indus clastics: Forearc basin sedimentation in the Ladakh Himalaya (India). *Sedimentary Geology*, 59(3), 237–249.

Gehrels, G., DeCelles, P., Ojha, T., & Upreti, B. (2006). Geologic and U-Th-Pb geochronologic evidence for early Paleozoic tectonism in the Kathmandu thrust sheet, central Nepal Himalaya. *GSA Bulletin*, 118(1-2), 185–198.

Gehrels, G., Kapp, P., DeCelles, P., Pullen, A., Blakey, R., Weislogel, A., Ding, L., Guynn, J., Martin, A., McQuarrie, N., & Yin, A. (2011). Detrital zircon geochronology of pre-Tertiary strata in the Tibetan-Himalayan orogen. *Tectonics*, 30(5).

Gehrels, G. E., DeCelles, P. G., Martin, A., Ojha, T., Pinhassi, G., & Upreti, B. N. (2003). Initiation of the Himalayan Orogen as an Early Paleozoic Thin-skinned Thrust Belt. *GSA Today*, 13(9), 4–9.

George, F. R. & Gaidies, F. (2017). Characterisation of a garnet population from the Sikkim Himalaya: Insights into the rates and mechanisms of porphyroblast crystallisation. *Contributions to Mineralogy and Petrology*, 172(7), 57.

Gervais, F. & Trapy, P.-H. (2021). Testing solution models for phase equilibrium (forward) modeling of partial melting experiments. *Contributions to Mineralogy and Petrology*, 176(1), 4.

Ghent, E. D. (1976). Plagioclase-garnet-Al2SiO5-quartz: A potential geobarometer-geothermometer. *American Mineralogist*, 61, 710–714.

Gibson, R. (1993). When is a hornfels not a hornfels? Metapelitic rocks from the lower Witwatersrand Supergroup, Vredefort Dome, South Africa. *South African Journal of Geology*.

Gibson, R., Godin, L., Kellett, D. A., Cottle, J. M., & Archibald, D. (2016). Diachronous deformation along the base of the Himalayan metamorphic core, west-central Nepal. *GSA Bulletin*, 128(5-6), 860–878.

Gilbert, E. (1986). *Évolution Structurale d'une Chaine de Collision : Structures et Déformation Dans Le Nord de La Plaque Indienne En Himalaya Du Ladakh (Cristallin Du Haut Himalaya et Séries Téthysiennes)*. These de doctorat, Poitiers.

Godin, L., Grujic, D., Law, R. D., & Searle, M. P. (2006). Channel flow, ductile extrusion and exhumation in continental collision zones: An introduction. In R. D. Law, M. P. Searle, & L. Godin (Eds.), *Channel Flow, Ductile Extrusion and Exhumation in Continental Collision Zones*, volume 268 (pp. 1–23). Geological Society, London, Special Publications.

Gonçalves, G. O., Lana, C., Scholz, R., Buick, I. S., Gerdes, A., Kamo, S. L., Corfu, F., Marinho, M. M., Chaves, A. O., Valeriano, C., & Nalini, H. A. (2016). An assessment of monazite from the Itambé pegmatite district for use as U–Pb isotope reference material for microanalysis and implications for the origin of the "Moacyr" monazite. *Chemical Geology*, 424, 30–50.

Gordon, S. M., Kirkland, C. L., Reddy, S. M., Blatchford, H. J., Whitney, D. L., Teyssier, C., Evans, N. J., & McDonald, B. J. (2021). Deformation-enhanced recrystallization of titanite drives decoupling between U-Pb and trace elements. *Earth and Planetary Science Letters*, 560, 116810.

Goscombe, B., Gray, D., & Foster, D. A. (2018). Metamorphic response to collision in the Central Himalayan Orogen. *Gondwana Research*, 57, 191–265.

Goscombe, B., Gray, D., & Hand, M. (2006). Crustal architecture of the Himalayan metamorphic front in eastern Nepal. *Gondwana Research*, 10(3-4), 232–255.

Goswami, S., Bhowmik, S. K., & Dasgupta, S. (2009). Petrology of a non-classical Barrovian inverted metamorphic sequence from the western Arunachal Himalaya, India. *Journal of Asian Earth Sciences*, 36(4-5), 390–406.

Goswami-Banerjee, S. & Robyr, M. (2015). Pressure and temperature conditions for crystallization of metamorphic allanite and monazite in metapelites: A case study from the Miyar Valley (high Himalayan Crystalline of Zanskar, NW India). *Journal of Metamorphic Geology*, 33(5), 535–556.

Grasemann, B., Fritz, H., & Vannay, J. C. (1999). Quantitative kinematic flow analysis from the Main Central Thrust Zone (NW-Himalaya, India): Implications for a decelerating strain path and the extrusion of orogenic wedges. *Journal of Structural Geology*, 21(7), 837–853.

Green, E., Holland, T., & Powell, R. (2007). An order-disorder model for omphacitic pyroxenes in the system jadeite-diopside-hedenbergite-acmite, with applications to eclogitic rocks | American Mineralogist | GeoScienceWorld. *American Mineralogist*, 92, 1181–1189.

Green, E. C. R., White, R. W., Diener, J. F. A., Powell, R., Holland, T. J. B., & Palin, R. M. (2016). Activity–composition relations for the calculation of partial melting equilibria in metabasic rocks. *Journal of Metamorphic Geology*, 34(9), 845–869.

Green, N. L. & Usdansky, S. I. (1986). Ternary-feldspar mixing relations and thermobarometry. *American Mineralogist*, 71(9-10), 1100–1108.

Green, O. R., Searle, M. P., Corfield, R. I., & Corfield, R. M. (2008). Cretaceous-Tertiary Carbonate Platform Evolution and the Age of the India-Asia Collision along the Ladakh Himalaya (Northwest India). *The Journal of Geology*, 116(4), 331–353.

Gregory, C. J., Rubatto, D., Allen, C. M., Williams, I. S., Hermann, J., & Ireland, T. (2007). Allanite micro-geochronology: A LA-ICP-MS and SHRIMP U–Th–Pb study. *Chemical Geology*, 245(3), 162–182.

Grohmann, C. H. & Campanha, G. A. C. (2010). OpenStereo: Open Source, Cross-Platform Software for Structural Geology Analysis. In *AGU Fall Meeting* (pp. IN31C–06). San Francisco, CA.

Groppo, C., Rolfo, F., Castelli, D., & Mosca, P. (2017). Metamorphic CO2 Production in Collisional Orogens: Petrological Constraints from Phase Diagram Modeling of Himalayan, Scapolite-bearing, Calc-silicate Rocks in the NKC(F)MAS(T)-HC system. *Journal of Petrology*, 58(1), 53–83.

Groppo, C., Rolfo, F., & Indares, A. (2012). Partial Melting in the Higher Himalayan Crystallines of Eastern Nepal: The Effect of Decompression and Implications for the 'Channel Flow' Model. *Journal of Petrology*, 53(5), 1057–1088.

Groppo, C., Rolfo, F., & Mosca, P. (2013). The cordierite-bearing anatectic rocks of the higher Himalayan crystallines (eastern Nepal): Low-pressure anatexis, melt productivity, melt loss and the preservation of cordierite. *Journal of Metamorphic Geology*, 31(2), 187–204.

Groppo, C., Rubatto, D., Rolfo, F., & Lombardo, B. (2010). Early Oligocene partial melting in the Main Central Thrust Zone (Arun valley, eastern Nepal Himalaya). *Lithos*, 118(3), 287–301.

Gross, A. O. M. S., Droop, G. T. R., Porcher, C. C., & Fernandes, L. A. D. (2009). Petrology and thermobarometry of mafic granulites and migmatites from the Chafalote Metamorphic Suite: New insights into the Neoproterozoic P-T evolution of the Uruguayan—Sul-Rio-Grandense shield. *Precambrian Research*, 170(3), 157–174.

Grujic, D. (2006). Channel flow and continental collision tectonics: An overview. In R. D. Law, M. P. Searle, & L. Godin (Eds.), *Channel Flow, Ductile Extrusion and Exhumation in Continental Collision Zones*, volume 268 (pp. 25–37). Geological Society, London, Special Publications.

Grujic, D., Casey, M., Davidson, C., Hollister, L. S., Kündig, R., Pavlis, T., & Schmid, S. (1996). Ductile extrusion of the Higher Himalayan Crystalline in Bhutan: Evidence from quartz microfabrics. *Tectonophysics*, 260, 21–43.

Grujic, D., Coutand, I., Doon, M., & Kellett, D. A. (2017). Northern provenance of the Gondwana Formation in the Lesser Himalayan Sequence: Constraints from 40Ar/39Ar dating of detrital muscovite in Darjeeling-Sikkim Himalaya. *Italian Journal of Geosciences*, 136(1), 15–27.

Guevara, V. E. & Caddick, M. J. (2016). Shooting at a moving target: Phase equilibria modelling of high-temperature metamorphism. *Journal of Metamorphic Geology*, 34(3), 209–235.

Guidotti, C. V. (1974). Transition from Staurolite to Sillimanite Zone, Rangeley Quadrangle, Maine. *Geological Society of America Bulletin*, 85(3), 475.

Guidotti, C. V. (1984). Micas in metamorphic rocks. In S. Bailey (Ed.), *Micas*, volume 13 of *Reviews in Mineralogy & Geochemistry* (pp. 357–468). De Gruyter.

Guidotti, C. V., Cheney, J. T., & Guggenheim, S. (1977). Distribution of titanium between coexisting muscovite and biotite in pelitic schists from northwestern Maine. *American Mineralogist*, 62, 438–448.

Guiraud, M., Powell, R., & Rebay, G. (2001). H2O in metamorphism and unexpected behaviour in the preservation of metamorphic mineral assemblages. *Journal of Metamorphic Geology*, 19(4), 445–454.

Guntli, P. (1993). *Geologie Und Tektonik Des Higher Und Lesser Himalaya Im Gebiet von Kishtwar, SE Kashmir (NW Indien)*. Doctoral Thesis, ETH Zurich.

Harlov, D., Tropper, P., Seifert, W., Nijland, T., & Förster, H.-J. (2006). Formation of Al-rich titanite (CaTiSiO4O–CaAlSiO4OH) reaction rims on ilmenite in metamorphic rocks as a function of fH2O and fO2. *Lithos*, 88(1), 72–84.

Harte, B. & Dempster, T. J. (1987). Regional metamorphic zones: Tectonic controls. *Philosophical Transactions of the Royal Society of London. Series A, Mathematical and Physical Sciences*, 321(1557), 105–127.

Harte, B. & Johnson, M. R. W. (1969). Metamorphic history of Dalradian rocks in Glens Clova, Esk and Lethnot, Angus, Scotland. *Scottish Journal of Geology*, 5(1), 54–80.

Hawthorne, F., Oberti, R., Harlow, G., Maresch, W., Martin, R., Schumacher, J., & Welch, M. (2012). Nomenclature of the amphibole supergroup. *American Mineralogist*, 97, 2031–2048.

Hayashi, M., Komiya, T., Nakamura, Y., & Maruyama, S. (2000). Archean Regional Metamorphism of the Isua Supracrustal Belt, Southern West Greenland: Implications for a Driving Force for Archean Plate Tectonics. *International Geology Review*, 42(12), 1055–1115.

Hayden, L. A. & Watson, E. B. (2007). Rutile saturation in hydrous siliceous melts and its bearing on Ti-thermometry of quartz and zircon. *Earth and Planetary Science Letters*, 258(3-4), 561–568.

Hayden, L. A., Watson, E. B., & Wark, D. A. (2008). A thermobarometer for sphene (titanite). *Contributions to Mineralogy and Petrology*, 155, 529–540.

He, D., Webb, A. A. G., Larson, K. P., Martin, A. J., & Schmitt, A. K. (2015). Extrusion vs. duplexing models of Himalayan mountain building 3: Duplexing dominates from the Oligocene to Present. *International Geology Review*, 57(1), 1–27.

Heim, A. & Gansser, A. (1939). *Central Himalaya: Geological Observations of the Swiss Expedition 1936*, volume LXXIII. Denkschriften der Schweizerischen Naturforschenden Gesellschaft.

Heiss, J., Condon, D. J., McLean, N., & Noble, S. R. (2012). 238U/235U Systematics in Terrestrial Uranium-Bearing Minerals - https://www.science.org/doi/epdf/10.1126/science.1215507. *Science Magazine*, 335, 1610–1614.

Henry, D. J. & Guidotti, C. V. (2002). Titanium in biotite from metapelitic rocks: Temperature effects, crystal-chemical controls, and petrologic applications. *American Mineralogist*, 87(4), 375–382.

Henry, D. J., Guidotti, C. V., & Thomson, J. A. (2005). The Ti-saturation surface for low-to-medium pressure metapelitic biotites : Implications for geothermometry and Ti-substitution mechanisms. *American Mineralogist*, 90, 316–328.

Herren, E. (1987). Zanskar shear zone : Northeast-southwest extension within the Higher Himalayas (Ladakh, India). *Geology*, 15, 409–413.

Hey, M. H. (1954). A new review of the chlorites. *Mineralogical Magazine and Journal of the Mineralogical Society*, 30(224), 277–292.

Hiroi, Y. (1983). Progressive metamorphism of the Unazuki pelitic schists in the Hida terrane, central Japan. *Contributions to Mineralogy and Petrology*, 82(4), 334–350.

Hirth, G. & Tullis, J. (1992). Dislocation creep regimes in quartz aggregates. *Journal of Structural Geology*, 14(2), 145–159.

Hodges, K. V. (2000). Tectonics of the Himalaya and Southern Tibet from two perspectives. *GSA Bulletin*, 112(3), 324–350.

Hodges, K. V. & McKenna, L. W. (1987). Realistic propagation of uncertainties in geologic thermobarometry. *American Mineralogist*, 72(7-8), 671–680.

Hodges, K. V., Parrish, R. R., Housh, T. B., Lux, D. R., Burchfiel, B. C., Royden, L. H., & Chen, Z. (1992). Simultaneous Miocene Extension and Shortening in the Himalayan Orogen. *Science*, 258, 1466–1470.

Hodges, K. V. & Spear, F. (1982). Geothermometry, geobarometry and the Al2SiO5 triple point at Mt. Moosilauke, New Hampshire. *American Mineralogist*, 67, 1118–1134.

Holdaway, M. (2001). Recalibration of the GASP geobarometer in light of recent garnet and plagioclase activity models and versions of the garnet-biotite geothermometer. *American Mineralogist*, 86(10), 1117–1129.

Holder, R. M. & Hacker, B. R. (2019). Fluid-driven resetting of titanite following ultrahigh-temperature metamorphism in southern Madagascar. *Chemical Geology*, 504, 38–52.

Holder, R. M., Hacker, B. R., Kylander-Clark, A. R. C., & Cottle, J. M. (2015). Monazite trace-element and isotopic signatures of (ultra)high-pressure metamorphism: Examples from the Western Gneiss Region, Norway. *Chemical Geology*, 409, 99–111.

Holder, R. M., Hacker, B. R., Seward, G. G. E., & Kylander-Clark, A. R. C. (2019). Interpreting titanite U–Pb dates and Zr thermobarometry in high-grade rocks: Empirical constraints on elemental diffusivities of Pb, Al, Fe, Zr, Nb, and Ce. *Contributions to Mineralogy and Petrology*, 174(5), 42.

Holder, R. M., Yakymchuk, C., & Viete, D. R. (2020). Accessory Mineral Eu Anomalies in Suprasolidus Rocks: Beyond Feldspar. *Geochemistry, Geophysics, Geosystems*, 21(8), e2020GC009052.

Holland, T. & Blundy, J. (1994). Non-ideal interactions in calcic amphiboles and their bearing on amphibole-plagioclase thermometry. *Contributions to Mineralogy and Petrology*, 116(4), 433–447.

Holland, T. J. B., Green, E. C. R., & Powell, R. (2022). A thermodynamic model for feldspars in KAlSi3O8-NaAlSi3O8-CaAl2Si2O8 for mineral equilibrium calculations. *Journal of Metamorphic Geology*, 40(4), 587–600.

Holland, T. J. B. & Powell, R. (1985). An internally consistent thermodynamic dataset with uncertainties and correlations: 2. Data and results. *Journal of Metamorphic Geology*, 3(4), 343–370.

Holland, T. J. B. & Powell, R. (1990). An enlarged and updated internally consistent thermodynamic dataset with uncertainties and correlations: The system K2O–Na2O–CaO–MgO–MnO–FeO–Fe2O3–Al2O3–TiO2–SiO2–C–H2–O2. *Journal of Metamorphic Geology*, 8(1), 89–124.

Holland, T. J. B. & Powell, R. (1998). An internally consistent thermodynamic data set for phases of petrological interest. *Journal of Metamorphic Geology*, 16(3), 309–343.

Holland, T. J. B. & Powell, R. (2011). An improved and extended internally consistent thermodynamic dataset for phases of petrological interest, involving a new equation of state for solids. *Journal of Metamorphic Geology*, 29(3), 333–383.

Holness, M. B. & Sawyer, E. W. (2008). On the Pseudomorphing of Melt-filled Pores During the Crystallization of Migmatites. *Journal of Petrology*, 49(7), 1343–1363.

Honegger, K. (1983). *Struktur Und Metamorphose Des Zaskar/Kristallins, Suru Ladakh*. PhD thesis, E.T.H., Zurich.

Honegger, K., Dietrich, V., Frank, W., Gansser, A., Thöni, M., & Trommsdorff, V. (1982). Magmatism and metamorphism in the Ladakh Himalayas (the Indus-Tsangpo suture zone). *Earth and Planetary Science Letters*, 60(2), 253–292.

Honegger, K., Le Fort, P., Mascle, G., & Zimmermann, J. L. (1989). The blueschists along the Indus Suture Zone in Ladakh, NW Himalaya. *Journal of Metamorphic Geology*, 7(1), 57–72.

Horstwood, M. S. A., Foster, G. L., Parrish, R. R., Noble, S. R., & Nowell, G. M. (2003). Common-Pb corrected in situ U–Pb accessory mineral geochronology by LA-MC-ICP-MS. *Journal of Analytical Atomic Spectrometry*, 18(8), 837–846.

Horstwood, M. S. A., Košler, J., Gehrels, G., Jackson, S. E., McLean, N. M., Paton, C., Pearson, N. J., Sircombe, K., Sylvester, P., Vermeesch, P., Bowring, J. F., Condon, D. J., & Schoene, B. (2016). Community-Derived Standards for LA-ICP-MS U-(Th-)Pb Geochronology – Uncertainty Propagation, Age Interpretation and Data Reporting. *Geostandards and Geoanalytical Research*, 40(3), 311–332.

Horton, F., Lee, J., Hacker, B., Bowman-Kamaha'o, M., & Cosca, M. (2015). Himalayan gneiss dome formation in the middle crust and exhumation by normal faulting: New geochronology of Gianbul dome, northwestern India. *Bulletin of the Geological Society of America*, 127(1-2), 162–180.

Horton, F. & Leech, M. L. (2013). Age and origin of granites in the Karakoram shear zone and Greater Himalaya Sequence, NW India. *Lithosphere*, 5(3), 300–320.

Hu, X., Garzanti, E., Moore, T., & Raffi, I. (2015). Direct stratigraphic dating of India-Asia collision onset at the Selandian (middle Paleocene, 59 ± 1 Ma). *Geology*, 43, 859–862.

Huang, G.-C. D., Wu, F. T., Roecker, S. W., & Sheehan, A. F. (2009). Lithospheric structure of the central Himalaya from 3-D tomographic imaging. *Tectonophysics*, 475(3), 524–543.

Hughes, N. C., Myrow, P. M., Peng, S., & Banerjee, D. M. (2018). The Parahio Formation of the Tethyan Himalaya: The type section, thickness, lithostratigraphy and biostratigraphy of the best characterised Cambrian succession in the

Indian subcontinent. *Journal of the Palaeontological Society of India*, 63(1), 1–18.

Hughes, N. C., Myrow, P. M., Peng, S., & Banerjee, D. M. (2019). The Parahio Formation of the Tethyan Himalaya: Further consideration of a case history in lithostratigraphy. *Journal of the Palaeontological Society of India*, 64(2), 275–282.

Iaccarino, S., Montomoli, C., Carosi, R., Massonne, H.-J., Langone, A., & Visonà, D. (2015). Pressure–temperature–time–deformation path of kyanite-bearing migmatitic paragneiss in the Kali Gandaki valley (Central Nepal): Investigation of Late Eocene–Early Oligocene melting processes. *Lithos*, 231, 103–121.

Iaccarino, S., Montomoli, C., Carosi, R., Massonne, H. J., & Visonà, D. (2017a). Geology and tectono-metamorphic evolution of the Himalayan metamorphic core: Insights from the Mugu Karnali transect, Western Nepal (Central Himalaya). *Journal of Metamorphic Geology*, 35(3), 301–325.

Iaccarino, S., Montomoli, C., Carosi, R., Montemagni, C., Massonne, H. J., Langone, A., Jain, A. K., & Visonà, D. (2017b). Pressure-Temperature-Deformation-Time Constraints on the South Tibetan Detachment System in the Garhwal Himalaya (NW India). *Tectonics*, 36(11), 2281–2304.

Imayama, T., Takeshita, T., & Arita, K. (2010). Metamorphic P–T profile and P–T path discontinuity across the far-eastern Nepal Himalaya: Investigation of channel flow models. *Journal of Metamorphic Geology*, 28(5), 527–549.

Inger, S. (1998). Timing of an extensional detachment during convergent orogeny: New Rb-Sr geochronological data from the Zanskar shear zone, northwestern Himalaya. *Geology*, 26(3), 223–226.

Jackson, S. E., Pearson, N. J., Griffin, W. L., & Belousova, E. A. (2004). The application of laser ablation-inductively coupled plasma-mass spectrometry to in situ U–Pb zircon geochronology. *Chemical Geology*, 211(1), 47–69.

Jain, A., Manickavasagam, R., & Singh, S. (1999). Collision tectonics in the NW Himalaya: deformation, metamorphism, emplacement of leucogranite along Beas-Parbati Valleys, Himachal Pradesh. *Gondwana Research Group Memoir*, 6, 3–37.

Jain, A. K. & Manickavasagam, R. M. (1993). Inverted metamorphism in the intracontinental ductile shear zone during Himalayan collision tectonics. *Geology*, 21(5), 407–410.

Jamieson, R. A. & Beaumont, C. (2013). On the origin of orogens. *GSA Bulletin*, 125(11-12), 1671–1702.

Jamieson, R. A., Beaumont, C., Medvedev, S., & Nguyen, M. H. (2004). Crustal channel flows: 2. Numerical models with implications for metamorphism in the Himalayan-Tibetan orogen. *Journal of Geophysical Research: Solid Earth*, 109(B6), 6407.

Jamieson, R. A., Beaumont, C., Nguyen, M. H., & Grujic, D. (2006). Provenance of the Greater Himalayan Sequence and associated rocks: Predictions of channel flow models. *Geological Society, London, Special Publications*, 268(1), 165–182.

Janots, E., Engi, M., Berger, A., Allaz, J., Schwarz, J.-O., & Spandler, C. (2008). Prograde metamorphic sequence of REE minerals in pelitic rocks of the Central Alps: Implications for allanite–monazite–xenotime phase relations from 250 to 610 °C. *Journal of Metamorphic Geology*, 26(5), 509–526.

Jessup, M. J., Cottle, J. M., Searle, M. P., Law, R. D., Newell, D. L., Tracy, R. J., & Waters, D. J. (2008). P-T-t-D paths of Everest Series schist, Nepal. *Journal of Metamorphic Geology*, 26(7), 717–739.

Johnson, M. R. W. (2003). Insight into the nature of Indian crust underthrusting the Himalaya. *Terra Nova*, 15(1), 46–51.

Johnson, T. A., Cottle, J. M., & Larson, K. P. (2021). Delineation of multiple metamorphic events in the Himalayan Kathmandu Complex, central Nepal. *Journal of Metamorphic Geology*, 39(4), 443–472.

Juteau, T. & Reibel, G. (1981). Indus suture: Petrographic description of the pillow-lavas of the Dras formation, and of the ophiolites of the Spongtang-Photaksar nappe. In *1st Meeting EUG* (pp.19). Strasbourg: Terra Cognita Special Issue.

Kadarusman, A., Maruyama, S., Kaneko, Y., Ota, T., Ishikawa, A., Sopaheluwakan, J., & Omori, S. (2010). World's youngest blueschist belt from Leti Island in the non-volcanic Banda outer arc of Eastern Indonesia. *Gondwana Research*, 18(1), 189–204.

Kalita, P., Phukon, P., Goswami, T. K., Imayama, T., & Srivastava, H. B. (2022). Chemical mass transport during deformation and metamorphism: Insights from the Main Central Thrust and its footwall of Western Arunachal Himalaya, NE India. *Lithos*, 416–417, 106641.

Katagas, C. G. (1980). Metamorphic zones and physical conditions of metamorphism in Leros Island, Greece. *Contributions to Mineralogy and Petrology*, 73(4), 389–402.

Kavanagh-Lepage, C., Gervais, F., Larson, K., Graziani, R., & Moukhsil, A. (2023). Deformation induced decoupling between U-Pb and trace elements in titanite revealed through petrochronology and study of localized deformation. *Geoscience Frontiers*, 14(2), 101496.

Kellett, D. A., Cottle, J. M., & Larson, K. P. (2019). The South Tibetan detachment system: History, advances, definition and future directions. *Geological Society Special Publication*, 483(1), 377–400.

Kellett, D. A., Cottle, J. M., & Smit, M. (2014). Eocene deep crust at Ama Drime, Tibet: Early evolution of the Himalayan orogen. *Lithosphere*, 6(4), 220–229.

Kellett, D. A. & Grujic, D. (2012). New insight into the South Tibetan detachment system: Not a single progressive deformation. *Tectonics*, 31(2).

Kellett, D. A., Grujic, D., Coutand, I., Cottle, J., & Mukul, M. (2013). The South Tibetan detachment system facilitates ultra rapid cooling of granulite-facies rocks in Sikkim Himalaya. *Tectonics*, 32(2), 252–270.

Kelly, E. D., Carlson, W. D., & Connelly, J. N. (2011). Implications of garnet resorption for the Lu–Hf garnet geochronometer: An example from the contact aureole of the Makhavinekh Lake Pluton, Labrador. *Journal of Metamorphic Geology*, 29(8), 901–916.

Khan, A., Jan, M., Windley, B., Tarney, J., & Thirlwall, M. (1989). The Chilas Mafic-Ultramafic Igneous Complex; The root of the Kohistan Island Arc in the Himalaya of northern Pakistan. *Geological Society of America Special Paper*, 232.

Khanal, G. P., Wang, J. M., Larson, K. P., Wu, F. Y., Rai, S. M., Wang, J. G., & Yang, L. (2021). Eocene Metamorphism and Anatexis in the Kathmandu Klippe, Central Nepal: Implications for Early Crustal Thickening and Initial Rise of the Himalaya. *Tectonics*, 40(4), e2020TC006532.

Kirkland, C. L., Spaggiari, C. V., Johnson, T. E., Smithies, R. H., Danišík, M., Evans, N., Wingate, M. T. D., Clark, C., Spencer, C., Mikucki, E., & McDonald, B. J. (2016). Grain size matters: Implications for element and isotopic mobility in titanite. *Precambrian Research*, 278, 283–302.

Kohn, M. J. (2008). P-T-t data from central Nepal support critical taper and repudiate large-scale channel flow of the Greater Himalayan Sequence. *GSA Bulletin*, 120(3-4), 259–273.

Kohn, M. J. (2014a). Himalayan Metamorphism and Its Tectonic Implications. *Annual Review of Earth and Planetary Sciences*, 42(1), 381–419.

Kohn, M. J. (2014b). "Thermoba-Raman-try": Calibration of spectroscopic barometers and thermometers for mineral inclusions. *Earth and Planetary Science Letters*, 388, 187–196.

Kohn, M. J. (2017). Titanite Petrochronology. *Reviews in Mineralogy and Geochemistry*, 83, 419–441.

Kohn, M. J. (2020). A refined zirconium-in-rutile thermometer. *American Mineralogist*, 105(June), 963–971.

Kohn, M. J. & Corrie, S. L. (2011). Preserved Zr-temperatures and U–Pb ages in high-grade metamorphic titanite: Evidence for a static hot channel in the Himalayan orogen. *Earth and Planetary Science Letters*, 311(1), 136–143.

Kohn, M. J. & Malloy, M. A. (2004). Formation of monazite via prograde metamorphic reactions among common silicates: Implications for age determinations. *Geochimica et Cosmochimica Acta*, 68(1), 101–113.

Kohn, M. J., Mazzucchelli, M. L., & Alvaro, M. (2023). Elastic Thermobarometry. *Annual Review of Earth and Planetary Sciences*, 51(1), 331–366.

Kohn, M. J., Paul, S., & Corrie, S. L. (2010). The lower Lesser Himalayan sequence: A Paleoproterozoic arc on the northern margin of the Indian plate. *GSA Bulletin*, 122, 323–335.

Kohn, M. J., Penniston-Dorland, S. C., & Ferreira, J. C. S. (2016). Implications of near-rim compositional zoning in rutile for geothermometry, geospeedometry, and trace element equilibration. *Contributions to Mineralogy and Petrology*, 171(10), 78.

Kohn, M. J. & Spear, F. (2000). Retrograde net transfer reaction insurance for pressure-temperature estimates. *Geology*, 28(12), 1127–1130.

Kohn, M. J. & Spear, F. S. (1991a). Error propagation for barometers: 1. Accuracy and precision of experimentally located end member reactions. *American Mineralogist*, 76, 128–137.

Kohn, M. J. & Spear, F. S. (1991b). Error propagation for barometers: 2. Application to rocks. *American Mineralogist*, 76, 138–147.

Kohn, M. J., Wieland, M. S., Parkinson, C. D., & Upreti, B. N. (2004). Miocene faulting at plate tectonic velocity in the Himalaya of central Nepal. *Earth and Planetary Science Letters*, 228(3), 299–310.

Kohn, M. J., Wieland, M. S., Parkinson, C. D., & Upreti, B. N. (2005). Five generations of monazite in Langtang gneisses: Implications for chronology of the Himalayan metamorphic core. *Journal of Metamorphic Geology*, 23(5), 399–406.

Komiya, T. (2002). Intermediate-P/T type Archean metamorphism of the Isua supracrustal belt: Implications for secular change of geothermal gradients at subduction zones and for Archean plate tectonics. *American Journal of Science*, 302(9), 806–826.

Kooijman, E., Mezger, K., & Berndt, J. (2010). Constraints on the U–Pb systematics of metamorphic rutile from in situ LA-ICP-MS analysis. *Earth and Planetary Science Letters*, 293(3), 321–330.

Kowallis, B., Christiansen, E., Dorais, M., Winkel, A., Henze, P., Franzen, L., & Mosher, H. (2022). Variation of Fe, Al, and F Substitution in Titanite (Sphene). *Geosciences*, 12, 229.

Kumar, A., Lal, N., Jain, A. K., & Sorkhabi, R. B. (1995). Late Cenozoic - Quaternary Thermo-Tectonic History of Higher Himalayan Crystalline (HHC) in Kishtwar- Padar-Zanskar region, NW Himalaya: Evidence from Fission Track Ages. *Geological Society of India*, 45(4), 375–391.

Kundig, R. (1989). Domal structures and high-grade metamorphism in the Higher Himalayan Crystalline, Zanskar Region, north-west Himalaya, India. *Journal of Metamorphic Geology*, 7, 43–55.

Kunz, B. E. & White, R. W. (2019). Phase equilibrium modelling of the amphibolite to granulite facies transition in metabasic rocks (Ivrea Zone, NW Italy). *Journal of Metamorphic Geology*, 37(7), 935–950.

Kylander-Clark, A. R. C., Hacker, B. R., & Cottle, J. M. (2013). Laser-ablation split-stream ICP petrochronology. *Chemical Geology*, 345, 99–112.

Labotka, T. C. (1980). Petrology of a medium-pressure regional metamorphic terrane, Funeral Mountains, California. *American Mineralogist*, 65, 670–689.

Labotka, T. C. (1987). The Garnet+Hornblende Isograd in Calcic Schists from an Andalusite-Type Regional Metamorphic Terrain, Panamint Mountains, California. *Journal of Petrology*, 28(2), 323–354.

Lanari, P. & Engi, M. (2017). Local Bulk Composition Effects on Metamorphic Mineral Assemblages. *Reviews in Mineralogy and Geochemistry*, 83(1), 55–102.

Lanari, P., Ferrero, S., Goncalves, P., & Grosch, E. G. (2019). Metamorphic geology: Progress and perspectives. *Geological Society, London, Special Publications*, 478(1), 1–12.

Lang, H. M. & Rice, J. M. (1985). Geothermometry, Geobarometry and T-X(Fe-Mg) Relations in Metapelites, Snow Peak, Northern Idaho. *Journal of Petrology*, 26(4), 889–924.

Larson, K. P. & Cottle, J. M. (2015). Initiation of crustal shortening in the Himalaya. *Terra Nova*, 27(3), 169–174.

Larson, K. P. & Godin, L. (2009). Kinematics of the Greater Himalayan sequence, Dhaulagiri Himal: Implications for the structural framework of central Nepal. *Journal of the Geological Society, London*, 166, 25–43.

Larson, K. P., Godin, L., & Price, R. A. (2010). Relationships between displacement and distortion in orogens: Linking the Himalayan foreland and hinterland in central Nepal. *GSA Bulletin*, 122(7-8), 1116–1134.

Law, R. D., Stahr, D. W., Francsis, M. K., Ashley, K. T., Grasemann, B., & Ahmad, T. (2013). Deformation temperatures and flow vorticities near the base of the greater himalayan series, sutlej valley and shimla klippe, NW india. *Journal of Structural Geology*, 54, 21–53.

Le Fort, P. (1975). Himalayas: The collided range. Present knowledge of the continental arc. *American Journal of Science*, 275(1), 1–44.

Leake, B. E. (1978). Nomenclature of amphiboles. *The Canadian Mineralogist*, 16, 453–467.

Leger, R. M., Webb, A. A. G., Henry, D. J., Craig, J. A., & Dubey, P. (2013). Metamorphic field gradients across the Himachal Himalaya, northwest India: Implications for the emplacement of the Himalayan crystalline core. *Tectonics*, 32(3), 540–557.

Li, X., Zhang, B., Cheng, F., Zhang, J., Wang, Y., Chen, S., Liu, S., Zhang, L., & Huang, B. (2022). Fluid circulation in the South Tibetan Detachment System: Evidence from fluid inclusions and oxygen isotope data of quartz veins in the Ramba Dome, North Himalayan Gneiss Domes. *Geological Journal*, 57(1), 340–357.

Liao, Y., Wei, C., & Rehman, H. U. (2021). Titanium in calcium amphibole: Behavior and thermometry. *American Mineralogist*, 106(2), 180–191.

Lihter, I., Larson, K. P., Smit, M. A., Cottle, J. M., Ashley, K. T., & Shrestha, S. (2022). Decrypting the polymetamorphic record of the Himalaya. *Geology*, 50(5), 588–592.

Long, S. & Mcquarrie, N. (2010). Placing limits on channel flow : Insights from the Bhutan Himalaya. *Earth and Planetary Science Letters*, 290(3-4), 375–390.

Long, S. P., Gordon, S. M., & Soignard, E. (2017). Distributed north-vergent shear and flattening through Greater and Tethyan Himalayan rocks: Insights from metamorphic and strain data from the Dang Chu region, central Bhutan. *Lithosphere*, 9(5), 774–795.

Long, S. P., Gordon, S. M., Young, J. P., & Soignard, E. (2016). Temperature and strain gradients through Lesser Himalayan rocks and across the Main Central thrust, south central Bhutan: Implications for transport-parallel stretching and inverted metamorphism. *Tectonics*, 35(8), 1863–1891.

Lucas, S. B. (1989). Structural evolution of the Cape Smith Thrust Belt and the role of out-of-sequence faulting in the thickening of mountain belts. *Tectonics*, 8(4), 655–676.

Lucas, S. B. & Byrne, T. (1992). Footwall involvement during arc-continent collision, Ungava orogen, northern Canada. *Journal of the Geological Society*, 149(2), 237–248.

Lucassen, F., Dulski, P., Abart, R., Franz, G., Rhede, D., & Romer, R. L. (2010). Redistribution of HFSE elements during rutile replacement by titanite. *Contributions to Mineralogy and Petrology*, 160(2), 279–295.

Lucassen, F., Franz, G., Dulski, P., Romer, R. L., & Rhede, D. (2011). Element and Sr isotope signatures of titanite as indicator of variable fluid composition in hydrated eclogite. *Lithos*, 121(1), 12–24.

Ludwig, K. R. (1998). On the Treatment of Concordant Uranium-Lead Ages. *Geochimica et Cosmochimica Acta*, 62(4), 665–676.

Luvizotto, G. L., Zack, T., Meyer, H. P., Ludwig, T., Triebold, S., Kronz, A., Münker, C., Stockli, D. F., Prowatke, S., Klemme, S., Jacob, D. E., & von Eynatten, H. (2009). Rutile crystals as potential trace element and isotope mineral standards for microanalysis. *Chemical Geology*, 261(3), 346–369.

Lydekker, R. (1883). The geology of the Kashmir and Chamba territories and the British district of Khagan. *Mem. Geol. Surv. India*, 22, 31–34.

Mahar, E. M., Baker, J. M., Powell, R., Holland, T. J. B., & Howell, N. (1997). The effect of Mn on mineral stability in metapelites. *Journal of Metamorphic Geology*, 15(2), 223–238.

Malavieille, J. (1993). Late orogenic extension in mountain belts: Insight from the Basin and Range and the late Paleozoic Variscan belt. *Tectonics*, 12(5), 1115–1130.

Manickavasagam, R., Jain, A., Singh, S., & Asokan, A. (1999). Metamorphic evolution of the northwest Himalaya, India: Pressure-temperature data, inverted metamorphism, and exhumation in the Kashmir, Himachal, and Garhwal Himalayas. *Special Paper of the Geological Society of America*, 328, 179–198.

Marquer, D., Chawla, H., & Challandes, N. (2000). Pre-Alpine High grade metamorphism in High Himalaya Crystalline Sequences: Evidences from Lower Palaeozoic Kinnar Kailas granite and surrounding rocks in the Sutlej Valley (Himachal pradesch, India). *Eclogae Geologicae Helvetiae*, 93.

Martin, A. J. (2016). A review of definitions of the Himalayan Main Central Thrust. *International Journal of Earth Sciences*.

Martin, A. J. (2017). A review of Himalayan stratigraphy, magmatism, and structure. *Gondwana Research*, 49, 42–80.

Maruyama, S., Suzuki, K., & Liou, J. G. (1983). Greenschist–Amphibolite Transition Equilibria at Low Pressures. *Journal of Petrology*, 24(4), 583–604.

Mattinson, J. M. & Echeverria, L. M. (1980). Ortigalita Peak gabbro, Franciscan complex: U-Pb dates of intrusion and high-pressure–low-temperature metamorphism. *Geology*, 8(12), 589–593.

Mazoz, A., Gonçalves, G. O., Lana, C., Buick, I. S., Corfu, F., Kamo, S. L., Wang, H., Yang, Y.-H., Scholz, R., Queiroga, G., Fu, B., Martins, L., Schannor, M., de Abreu, A. T., Babinski, M., Peixoto, E., & Ventura Santos, R. (2022). Khan River and Bear Lake: Two Natural Titanite Reference Materials for High-Spatial Resolution U-Pb Microanalysis. *Geostandards and Geoanalytical Research*, 46(4), 701–733.

McDonough, W. F. & s. Sun, S. (1995). The composition of the Earth. *Chemical Geology*, 120(3), 223–253.

McFarlane, C. R. M. & McCulloch, M. T. (2007). Coupling of in-situ Sm–Nd systematics and U–Pb dating of monazite and allanite with applications to crustal evolution studies. *Chemical Geology*, 245(1), 45–60.

McQuarrie, N., Robinson, D., Long, S., Tobgay, T., Grujic, D., Gehrels, G., & Ducea, M. (2008). Preliminary stratigraphic and structural architecture of Bhutan: Implications for the along strike architecture of the Himalayan system. *Earth and Planetary Science Letters*, 272(1), 105–117.

Metcalf, K. & Kapp, P. (2017). The Yarlung suture mélange, Lopu Range, southern Tibet: Provenance of sandstone blocks and transition from oceanic subduction to continental collision. *Gondwana Research*, 48, 15–33.

Miller, C., Klötzli, U., Frank, W., Thöni, M., & Grasemann, B. (2000). Proterozoic crustal evolution in the NW Himalaya (India) as recorded by circa 1.80 Ga mafic and 1.84 Ga granitic magmatism. *Precambrian Research*, 103(3), 191–206.

Mitra, S., Sharma, S., Wanchoo, S. K., & Priestley, K. (2023). 3D Crustal Structure of the Jammu and Kashmir Himalaya: Signatures of Mid-Crustal Ramp and Lesser Himalayan Duplex. *Journal of Geophysical Research: Solid Earth*, 128(11), e2023JB027350.

Mohan, S. P., Williams, I. S., & Singh, S. (2022). Direct zircon U–Pb evidence for pre-Himalayan HT metamorphism in the Higher Himalayan Crystallines, eastern Garhwal Himalaya, India. *Geological Journal*, 57(1), 133–149.

Molina, J. F., Cambeses, A., Moreno, J. A., Morales, I., Montero, P., & Bea, F. (2021). A reassessment of the amphibole-plagioclase NaSi-CaAl exchange thermometer with applications to igneous and high-grade metamorphic rocks. *American Mineralogist*, 106, 782–800.

Montel, Kornprobst, & Vielzeuf (2000). Preservation of old U–Th–Pb ages in shielded monazite: Example from the Beni Bousera Hercynian kinzigites (Morocco). *Journal of Metamorphic Geology*, 18(3), 335–342.

Montemagni, C., Fulignati, P., Iaccarino, S., Marianell, P., Montomoli, C., & Sbrana, A. (2016). Deformation and fluid flow in the Munsiari Thrust (NW India): A preliminary fluid inclusion study. *ATTI DELLA SOCIETÀ TOSCANA DI SCIENZE NATURALI RESIDENTE IN PISA. MEMORIE. SERIE A*, 123, 67–77.

Montemagni, C., Montomoli, C., Iaccarino, S., Carosi, R., Jain, A. K., Massonne, H. J., & Villa, I. M. (2019). Dating protracted fault activities: Microstructures, microchemistry and geochronology of the Vaikrita Thrust, Main Central Thrust zone, Garhwal Himalaya, NW India. *Geological Society, London, Special Publications*, 481(1), 127–146.

Montomoli, C., Carosi, R., & Iaccarino, S. (2015). Tectonometamorphic discontinuities in the Greater Himalayan Sequence: A local or a regional feature? In S. Mukherjee, R. Carosi, P. A. Van Der Beek, B. K. Mukherjee, & D. M. Robinson (Eds.), *Tectonics of the Himalaya*, volume 412 (pp. 25–41). Geological Society, London, Special Publications.

Montomoli, C., Iaccarino, S., Carosi, R., Langone, A., & Visonà, D. (2013). Tectonometamorphic discontinuities within the Greater Himalayan Sequence in Western Nepal (Central Himalaya): Insights on the exhumation of crystalline rocks. *Tectonophysics*, 608, 1349–1370.

Mottram, C. M., Argles, T. W., Harris, N. B. W., Parrish, R. R., Horstwood, M. S. A., Warren, C. J., & Gupta, S. (2014a). Tectonic interleaving along the Main Central Thrust, Sikkim Himalaya. *Journal of the Geological Society, London*, 171, 255–268.

Mottram, C. M., Cottle, J. M., & Kylander-Clark, A. R. (2019). Campaign-style U-Pb titanite petrochronology: Along-strike variations in timing of metamorphism in the Himalayan metamorphic core. *Geoscience Frontiers*, 10(3), 827–847.

Mottram, C. M., Warren, C. J., Regis, D., Roberts, N. M., Harris, N. B., Argles, T. W., & Parrish, R. R. (2014b). Developing an inverted Barrovian sequence; insights from monazite petrochronology. *Earth and Planetary Science Letters*, 403, 418–431.

Moynihan, D. P. & Pattison, D. R. M. (2013). An automated method for the calculation of P–T paths from garnet zoning, with application to metapelitic schist from the Kootenay Arc, British Columbia, Canada. *Journal of Metamorphic Geology*, 31(5), 525–548.

Mukherjee, S. (2013). Higher Himalaya in the Bhagirathi section (NW Himalaya, India): Its structures, backthrusts and extrusion mechanism by both channel flow and critical taper mechanisms. *International Journal of Earth Sciences*, 102(7), 1851–1870.

Myers, J. S. (2001). Protoliths of the 3.8-3.7 Ga Isua greenstone belt, West Greenland. *Precambrian Research*, 105, 129–141.

Myrow, P. M., Hughes, N. C., Goodge, J. W., Fanning, C. M., Williams, I. S., Peng, S., Bhargava, O. N., Parcha, S. K., & Pogue, K. R. (2010). Extraordinary transport and mixing of sediment across Himalayan central Gondwana during the Cambrian–Ordovician. *GSA Bulletin*, 122(9-10), 1660–1670.

Myrow, P. M., Hughes, N. C., McKenzie, N. R., Pelgay, P., Thomson, T. J., Haddad, E. E., & Fanning, C. M. (2016). Cambrian–Ordovician orogenesis in Himalayan equatorial Gondwana. *GSA Bulletin*, 128(11-12), 1679–1695.

Myrow, P. M., Hughes, N. C., Searle, M. P., Fanning, C., Peng, S.-C., & Parcha, S. (2009). Stratigraphic correlation of Cambrian–Ordovician deposits along the Himalaya: Implications for the age and nature of rocks in the Mount Everest region. *GSA Bulletin*, 121(3-4), 323–332.

Myrow, P. M., Snell, K., Hughes, N., Paulsen, T., Heim, N., & Parcha, S. (2006). Cambrian Depositional History of the Zanskar Valley Region of the Indian Himalaya: Tectonic Implications. *Journal of Sedimentary Research*, 76, 364–381.

Nanda, M. M. & Singh, M. P. (1976). Stratigraphy and sedimentation of the Zanskar area, Ladakh and adjoining parts of the Lahaul region of Himachal Pradesh. *Himalayan Geol.*, 6, 365–388.

Noble, S. R. & Searle, M. P. (1995). Age of crustal melting and leucogranite formation from U-Pb zircon and monazite dating in the western Himalaya, Zanskar, India. *Geology*, 23(12), 1135–1138.

Noble, S. R., Searle, M. P., & Walker, C. B. (2001). Age and Tectonic Significance of Permian Granites in Western Zanskar, High Himalaya. *The Journal of Geology*, 109(1), 127–135.

Norton, M. G. (1986). Late Caledonide extension in western Norway: A response to extreme crustal thickening. *Tectonics*, 5(2), 195–204.

Ohmoto, H. & Kerrick, D. M. (1977). Devolatilization equilibria in graphitic systems. *American Journal of Science*, 277(8), 1013–1044.

Olierook, H. K., Taylor, R. J., Erickson, T. M., Clark, C., Reddy, S. M., Kirkland, C. L., Jahn, I., & Barham, M. (2019). Unravelling complex geologic histories using U–Pb and trace element systematics of titanite. *Chemical Geology*, 504, 105–122.

Palin, R. M., Treloar, P. J., Searle, M. P., Wald, T., White, R. W., & Mertz-Kraus, R. (2018). U-Pb monazite ages from the Pakistan Himalaya record pre-Himalayan Ordovician orogeny and Permian continental breakup. *Bulletin of the Geological Society of America*, 130(11-12), 2047–2061.

Palin, R. M., Weller, O. M., Waters, D. J., & Dyck, B. (2016). Quantifying geological uncertainty in metamorphic phase equilibria modelling; a Monte Carlo assessment and implications for tectonic interpretations. *Geoscience Frontiers*, 7(4), 591–607.

Pandey, A., Virdi, N., & V.K.Gairola (2003). Evolution of structural fabrics and deformation events in the Kulu-Rampur and Larji Window zones, NW Himalaya, India. *Himalayan Geology*, 24, 1–21.

Pandey, A. K., Sachan, H. K., & Virdi, N. S. (2004). Exhumation history of a shear zone constrained by microstructural and fluid inclusion techniques: An example from the Satluj valley, NW Himalaya, India. *Journal of Asian Earth Sciences*, 23(3), 391–406.

Pareek, H. S. (1976). On studies of the agglomeratic slate and Panjal Trap in the Jhelum, Liddar and Sind Valleys, Kashmir. *Rec. Geol. Surv. India*, 107/2, 12–37.

Parrish, R. R. (1990). U–Pb dating of monazite and its application to geological problems. *Canadian Journal of Earth Sciences*, 27(11), 1431–1450.

Parsons, A. J., Ferré, E. C., Law, R. D., Lloyd, G. E., Phillips, R. J., & Searle, M. P. (2016a). Orogen-parallel deformation of the Himalayan midcrust: Insights from structural and magnetic fabric analyses of the Greater Himalayan Sequence, Annapurna-Dhaulagiri Himalaya, central Nepal. *Tectonics*, 35(11), 2515–2537.

Parsons, A. J., Hosseini, K., Palin, R., & Sigloch, K. (2020). Geological, geophysical and plate kinematic constraints for models of the India-Asia collision and the post-Triassic central Tethys oceans. *Earth-Science Reviews*, 202(January), 103084.

Parsons, A. J., Law, R. D., Lloyd, G. E., Phillips, R. J., & Searle, M. P. (2016b). Thermo-kinematic evolution of the Annapurna-Dhaulagiri Himalaya, central Nepal: The Composite Orogenic System. *Geochemistry, Geophysics, Geosystems*, 17(4), 1511–1539.

Parsons, A. J., Phillips, R. J., Lloyd, G. E., Law, R. D., Searle, M. P., & Walshaw, R. D. (2016c). Mid-crustal deformation of the Annapurna-Dhaulagiri Himalaya, central Nepal: An atypical example of channel flow during the Himalayan orogeny. *Geosphere*, 12(3), 985–1015.

Patel, R. C., Singh, S., Asokan, A., Manickavasagam, R. M., & Jain, A. K. (1993). Extensional tectonics in the Himalayan orogen, Zanskar, NW India. *Himalayan Tectonics*, 74, 445–459.

Paton, C., Hellstrom, J., Paul, B., Woodhead, J., & Hergt, J. (2011). Iolite: Freeware for the visualisation and processing of mass spectrometric data. *Journal of Analytical Atomic Spectrometry*, 26(12), 2508.

Patrick, B. E. & Lieberman, J. E. (1988). Thermal overprint on blueschists of the Seward Peninsula: The Lepontine in Alaska. *Geology*, 16(12), 1100.

Pattison, D. R. M., De Capitani, C., & Gaidies, F. (2011). Petrological consequences of variations in metamorphic reaction affinity. *Journal of Metamorphic Geology*, 29(9), 953–977.

Pattison, D. R. M. & DeBuhr, C. L. (2015). Petrology of metapelites in the Bugaboo aureole, British Columbia, Canada. *Journal of Metamorphic Geology*, 33(5), 437–462.

Pattison, D. R. M. & Goldsmith, S. A. (2022). Metamorphism of the Buchan type-area, NE Scotland and its relation to the adjacent Barrovian domain. *Journal of the Geological Society*, 179, jgs2021–040.

Pattison, D. R. M. & Spear, F. S. (2018). Kinetic control of staurolite–Al2SiO5 mineral assemblages: Implications for Barrovian and Buchan metamorphism. *Journal of Metamorphic Geology*, 36(6), 667–690.

Pattison, D. R. M. & Tinkham, D. K. (2009). Interplay between equilibrium and kinetics in prograde metamorphism of pelites: An example from the Nelson aureole, British Columbia. *Journal of Metamorphic Geology*, 27(4), 249–279.

Paul, A. N., Spikings, R. A., & Gaynor, S. P. (2021). U-Pb ID-TIMS reference ages and initial Pb isotope compositions for Durango and Wilberforce apatites. *Chemical Geology*, 586, 120604.

Pêcher, A. (1979). Les inclusions fluides des quartz d'exsudation de la zone du M. C. T. himalayen au Népal central : données sur la phase fluide dans une grande zone de cisaillement crustal. *Bulletin de Minéralogie*, 102(5), 537–554.

Penniston-Dorland, S. C., Kohn, M. J., & Piccoli, P. M. (2018). A mélange of subduction temperatures: Evidence from Zr-in-rutile thermometry for strengthening of the subduction interface. *Earth and Planetary Science Letters*, 482, 525–535.

Phukon, P., Sen, K., Singh, P. C., Sen, A., Srivastava, H. B., & Singhal, S. (2019). Characterizing anatexis in the Greater Himalayan Sequence (Kumaun, NW India) in terms of pressure, temperature, time and deformation. *Lithos*, 344–345, 22–50.

Pidgeon, R. T., Bosch, D., & Bruguier, O. (1996). Inherited zircon and titanite U-Pb systems in an Archaean syenite from southwestern Australia: Implications for U-Pb stability of titanite. *Earth and Planetary Science Letters*, 141(1), 187–198.

Pognante, U. (1992). Migmatites and Leucogranites of tertiary age from the high Himalayan Crystallines of Zanskar (NW India): A case history of anatexis of Palaeozoic orthogneisses. *Mineralogy and Petrology*, 46(4), 291–313.

Pognante, U., Benna, P., & Fort, P. L. (1993). High-pressure metamorphism in the High Himalayan Crystallines of the Stak valley, northeastern Nanga Parbat-Haramosh syntaxis, Pakistan Himalaya. *Geological Society Special Publication*, 74, 161–172.

Pognante, U., Castelli, D., Benna, P., Genovese, G., Oberli, F., Meier, M., & Tonarini, S. (1990). The crystalline units of the High Himalayas in the Lahul-Zanskar region (northwest India): Metamorphic-tectonic history and geochronology of the collided and imbricated Indian plate. *Geological Magazine*, 127(2), 101–116.

Pognante, U. & Lombardo, B. (1989). Metamorphic evolution of the High Himalayan Crystallines in SE Zanskar, India. *Journal of Metamorphic Geology*, 7(1), 9–17.

Powell, R. & Holland, T. (1988). An internally consistent dataset with uncertainties and correlations: 3. Applications to geobarometry, worked examples and a computer program. *Journal of Metamorphic Geology*, 6(2), 173–204.

Powell, R. & Holland, T. (1994). Optimal geothermometry and geobarometry. *American Mineralogist*, 79, 120–133.

Powell, R. & Holland, T. (2010). Using Equilibrium Thermodynamics to Understand Metamorphism and Metamorphic Rocks. *Elements*, 6(5), 309–314.

Powell, R. & Holland, T. J. B. (2008). On thermobarometry. *Journal of Metamorphic Geology*, 26(2), 155–179.

Powell, W. G., Carmichael, D. M., & Hodgson, C. J. (1995). Conditions and timing of metamorphism in the southern Abitibi greenstone belt, Quebec. *Canadian Journal of Earth Sciences*, 32(6), 787–805.

Prowatke, S. & Klemme, S. (2005). Effect of melt composition on the partitioning of trace elements between titanite and silicate melt. *Geochimica et Cosmochimica Acta*, 69(3), 695–709.

Pyle, J. M. & Spear, F. S. (1999). Yttrium zoning in garnet: Coupling of major and accessory phases during metamorphic reactions.

Pyle, J. M., Spear, F. S., Rudnick, R. L., & McDonough, W. F. (2001). Monazite–Xenotime–Garnet Equilibrium in Metapelites and a New Monazite–Garnet Thermometer. *Journal of Petrology*, 42(11), 2083–2107.

Raase, P., Raith, M., Ackermand, D., & Lal, R. K. (1986). Progressive Metamorphism of Mafic Rocks from Greenschist to Granulite Facies in the Dharwar Craton of South India. *The Journal of Geology*.

Raimondo, T., Hand, M., & Collins, W. J. (2014). Compressional intracontinental orogens: Ancient and modern perspectives. *Earth-Science Reviews*, 130, 128–153.

Ramsay, J. G. (1962). The Geometry and Mechanics of Formation of "Similar" Type Folds. *The Journal of Geology*, 70(3), 309–327.

Ramsay, John. G. (1967). *Folding and Fracturing of Rocks*. New York: McGraw-Hill.

Rapa, G., Groppo, C., Rolfo, F., Petrelli, M., Mosca, P., & Perugini, D. (2017). Titanite-bearing calc-silicate rocks constrain timing, duration and magnitude of metamorphic CO2 degassing in the Himalayan belt. *Lithos*, 292–293, 364–378.

Rasmussen, B., Fletcher, I. R., & Muhling, J. R. (2013). Dating deposition and low-grade metamorphism by in situ UPb geochronology of titanite in the Paleoproterozoic Timeball Hill Formation, southern Africa. *Chemical Geology*, 351, 29–39.

Rasmussen, B., Muhling, J. R., Fletcher, I. R., & Wingate, M. T. D. (2006). In situ SHRIMP U–Pb dating of monazite integrated with petrology and textures: Does bulk composition control whether monazite forms in low-Ca pelitic rocks during amphibolite facies metamorphism? *Geochimica et Cosmochimica Acta*, 70(12), 3040–3058.

Ratschbacher, L., Frisch, W., Neubauer, F., Schmid, S. M., & Neugebauer, J. (1989). Extension in compressional orogenic belts: The eastern Alps. *Geology*, 17, 404–407.

Raz, U. & Honegger, K. (1989). *Magmatic and Tectonic Evolution of the Ladakh Block from Field Studies*. Technical report.

Redler, C., Johnson, T. E., White, R. W., & Kunz, B. E. (2012). Phase equilibrium constraints on a deep crustal metamorphic field gradient: Metapelitic rocks from the Ivrea Zone (NW Italy). *Journal of Metamorphic Geology*, 30(3), 235–254.

Regis, D., Warren, C. J., Mottram, C. M., & Roberts, N. M. (2016). Using monazite and zircon petrochronology to constrain the P–T–t evolution of the middle crust in the Bhutan Himalaya. *Journal of Metamorphic Geology*, 34(6), 617–639.

Reuber, I., Montigny, R., & Thuizat, R. (1989). K-Ar ages of ophiolites and arc volcanics of the Indus suture zone : Clues on the early evolution of the Neo-Tethys.

Ríos, C., García, C., & Takasu, A. (2003). Tectono-metamorphic evolution of the Silgará Formation metamorphic rocks in the southwestern Santander Massif, Colombian Andes. *Journal of South American Earth Sciences*, 16(2), 133–154.

Roberts, N. M. W., Rasbury, E. T., Parrish, R. R., Smith, C. J., Horstwood, M. S. A., & Condon, D. J. (2017). A calcite reference material for LA-ICP-MS U-Pb geochronology. *Geochemistry, Geophysics, Geosystems*, 18(7), 2807–2814.

Robertson, A. (1998). Rift-related sedimentation and volcanism of the north-Indian margin inferred from a Permian-Triassic exotic block at Lamayuru, Indus suture zone (Ladakh Himalaya) and regional comparisons. *Journal of Asian Earth Sciences*, 16, 159–172.

Robertson, A. & Degnan, P. (1994). The Dras arc Complex: Lithofacies and reconstruction of a Late Cretaceous oceanic volcanic arc in the Indus Suture Zone, Ladakh Himalaya. *Sedimentary Geology*, 92, 117–145.

Robertson, A. & Sharp, I. (1998). Mesozoic deep-water slope/rise sedimentation and volcanism along the North-Indian passive margin: Evidence from the Karamba Complex, Indus suture zone (Western Ladakh Himalaya). *Journal of Asian Earth Sciences*, 16, 195–215.

Robertson, A. H. & Degnan, P. J. (1993). Sedimentology and tectonic implications of the Lamayuru Complex: Deep-water facies of the Indian passive margin, Indus Suture Zone, Ladakh Himalaya. *Geological Society Special Publication*, 74, 299–321.

Robertson, A. H. F. (2000). Formation of melanges in the Indus Suture Zone, Ladakh Himalaya by successive subduction-related, collisional and post-collisional processes during Late Mesozoic-Late Tertiary time. *Tectonics of the Nanga Parbat Syntaxis and the Western Himalaya*, 170, 333–374.

Robin, P.-Y. F. & Jowett, E. C. (1986). Computerized density contouring and statistical evaluation of orientation data using counting circles and continuous weighting functions. *Tectonophysics*, 121(2), 207–223.

Robyr, M. (2002). *Thrusting, Extension and Doming in the High Himalaya of Lahul Zanskar Area (NW India): Structural and Pressure-Temperature Constraints*, volume 40. Section des Sciences de la Terre, Université de Lausanne.

Robyr, M. (2023). Evidence for a pre-Himalayan metamorphism in the High Himalayan Crystalline of the Miyar Valley (NW India). *Swiss Journal of Geosciences*, 116(1), 17.

Robyr, M., Banerjee, S., & El Korh, A. (2012). Timing of prograde metamorphism in the High Himalaya of NW Lahul (NW India). *Journal of Nepal Geological Society*, 45, 101–102.

Robyr, M., Epard, J. L., & El Korh, A. (2014). Structural, metamorphic and geochronological relations between the Zanskar Shear Zone and the Miyar Shear Zone (NW Indian Himalaya): Evidence for two distinct tectonic structures and implications for the evolution of the High Himalayan Crystalline of Zans. *Journal of Asian Earth Sciences*, 79(PA), 1–15.

Robyr, M., Hacker, B. R., & Mattinson, J. M. (2006). Doming in compressional orogenic settings: New geochronological constraints from the NW Himalaya. *Tectonics*, 25(2), 1–19.

Robyr, M. & Lanari, P. (2020). Kinematic, Metamorphic, and Age Constraints on the Miyar Thrust Zone: Implications for the Eohimalayan History of the High Himalayan Crystalline of NW India. *Tectonics*, 39(11), 1–24.

Rosenberg, C. L. & Handy, M. R. (2005). Experimental deformation of partially melted granite revisited: Implications for the continental crust. *Journal of Metamorphic Geology*, 23(1), 19–28.

Rubatto, D., Chakraborty, S., & Dasgupta, S. (2013). Timescales of crustal melting in the Higher Himalayan Crystallines (Sikkim, Eastern Himalaya) inferred from trace element-constrained monazite and zircon chronology. *Contributions to Mineralogy and Petrology*, 165(2), 349–372.

Rubie, D. C. (1998). Disequilibrium during metamorphism: The role of nucleation kinetics. *Geological Society, London, Special Publications*, 138(1), 199–214.

Rutherford, E. & Soddy, F. (1902). The Cause and Nature of Radioactivity. Part I. *Philosophical Magazine*, 4, 370–396.

Sachan, H. K., Saxena, A., Verma, P., Rai, S. K., & Kharya, A. (2013). Fluid inclusion study of the Higher Himalayan quartzitic pelites, Garhwal Himalaya, India: Implications for recrystallization history of metasediments. *Journal of the Geological Society of India*, 82(5), 509–518.

Sachan, H. K., Sharma, R., Sahai, A., & Gururajan, N. S. (2001). Fluid events and exhumation history of the main central thrust zone Garhwal Himalaya (India). *Journal of Asian Earth Sciences*, 19(1), 207–221.

Sakai, H., Iwano, H., Danhara, T., Takigami, Y., Rai, S. M., Upreti, B. N., & Hirata, T. (2013). Rift-related origin of the Paleoproterozoic Kuncha Formation, and cooling history of the Kuncha nappe and Taplejung granites, eastern Nepal Lesser Himalaya: A multichronological approach. *Island Arc*, 22(3), 338–360.

Santos, M. M., Lana, C., Scholz, R., Buick, I., Schmitz, M. D., Kamo, S. L., Gerdes, A., Corfu, F., Tapster, S., Lancaster, P., Storey, C. D., Basei, M. A., Tohver, E., Alkmim, A., Nalini, H., Krambrock, K., Fantini, C., & Wiedenbeck, M. (2017). A New Appraisal of Sri Lankan BB Zircon as a Reference Material

for LA-ICP-MS U-Pb Geochronology and Lu-Hf Isotope Tracing. *Geostandards and Geoanalytical Research*, 41(3), 335–358.

Sauniac, S. & Touret, J. (1983). Petrology and fluid inclusions of a quartz-kyanite segregation in the main thrust zone of the Himalayas. *Lithos*, 16(1), 35–45.

Sawyer, E. W. (2008). *Atlas of Migmatites*. Canadian Science Publishing.

Schmitz, M. D. & Bowring, S. A. (2001). U-Pb zircon and titanite systematics of the Fish Canyon Tuff: An assessment of high-precision U-Pb geochronology and its application to young volcanic rocks. *Geochimica et Cosmochimica Acta*, 65(15), 2571–2587.

Schoene, B. & Bowring, S. A. (2006). U–Pb systematics of the McClure Mountain syenite: Thermochronological constraints on the age of the 40Ar/39Ar standard MMhb | Contributions to Mineralogy and Petrology. *Contributions to Mineralogy and Petrology*, 151, 615–630.

Schorn, S. & Diener, J. F. (2019). Seemingly disparate temperatures recorded in coexisting granulite facies lithologies. *Journal of Metamorphic Geology*, 37(8), 1049–1078.

Scibiorski, E., Kirkland, C. L., Kemp, A. I. S., Tohver, E., & Evans, N. J. (2019). Trace elements in titanite: A potential tool to constrain polygenetic growth processes and timing. *Chemical Geology*, 509, 1–19.

Scibiorski, E. A. & Cawood, P. A. (2022). Titanite as a petrogenetic indicator. *Terra Nova*, 34(3), 177–183.

Scott, D. J. & St-Onge, M. R. (1995). Constraints on Pb closure temperature in titanite based on rocks from the Ungava orogen, Canada: Implications for U-Pb geochronology and P-T-t path determinations. *Geology*, 23(12), 1123–1126.

Searle, M. P. (1983). Stratigraphy, structure and evolution of the Tibetan–Tethys zone in Zanskar and the Indus suture zone in the Ladakh Himalaya. *Transactions of the Royal Society of Edinburgh: Earth Sciences*, 73, 205–219.

Searle, M. P. (1986). Structural evolution and sequence of thrusting in the High Himalayan, Tibetan-Tethys and Indus suture zones of Zanskar and Ladakh, Western Himalaya. *Journal of Structural Geology*, 8(8), 923–936.

Searle, M. P. (2015). Mountain Building, Tectonic Evolution, Rheology, and Crustal Flow in the Himalaya, Karakoram, and Tibet. In *Treatise on Geophysics* (pp. 469–511). Oxford: Elsevier B.V.

Searle, M. P., Cooper, D. J. W., & Rex, A. J. (1988). Collision tectonics of the Ladakh-Zanskar Himalaya. *Philosophical Transactions of the Royal Society A: Mathematical, Physical & Engineering Sciences*, 326, 117–150.

Searle, M. P. & Fryer, B. J. (1986). Garnet, tourmaline and muscovite-bearing leucogranites, gneisses and migmatites of the Higher Himalayas from Zanskar, Kulu, Lahoul and Kashmir. *Geological Society, London, Special Publications*, 19(1), 185–201.

Searle, M. P. & Godin, L. (2003). The South Tibetan Detachment and the Manaslu Leucogranite: A Structural Reinterpretation and Restoration of the Annapurna-Manaslu Himalaya, Nepal. *The Journal of Geology*, 111(5), 505–523.

Searle, M. P. & Lamont, T. N. (2019). Compressional metamorphic core complexes, low-angle normal faults and extensional fabrics in compressional tectonic settings. *Geological Magazine*, 157(1), 101–118.

Searle, M. P., Law, R. D., Godin, L., Larson, K. P., Streule, M. J., Cottle, J. M., & Jessup, M. J. (2008). Defining the Himalayan Main Central Thrust in Nepal. *Journal of the Geological Society*, 165(2), 523–534.

Searle, M. P., Law, R. D., & Jessup, M. J. (2006). Crustal structure, restoration and evolution of the Greater Himalaya in Nepal-South Tibet: Implications for channel flow and ductile extrusion of the middle crust. In R. D. Law, M. P. Searle, & L. Godin (Eds.), *Channel Flow, Ductile Extrusion and Exhumation in Continental Collision Zones*, volume 268 (pp. 355–378). Geological Society, London, Special Publications.

Searle, M. P., Noble, S. R., Hurford, A. J., & Rex, D. C. (1999a). Age of crustal melting, emplacement and exhumation history of the Shivling leucogranite, Garhwal Himalaya. *Geological Magazine*, 136(5), 513–525.

Searle, M. P., Pickering, K. T., & Cooper, D. J. W. (1990). Restoration and evolution of the intermontane Indus molasse basin, Ladakh Himalaya, India. *Tectonophysics*, 174, 301–314.

Searle, M. P. & Rex, A. J. (1989). Thermal model for the Zanskar Himalaya. *Journal of Metamorphic Geology*, 7(1), 127–134.

Searle, M. P., Simpson, R. L., Law, R. D., Parrish, R. R., & Waters, D. J. (2003). The structural geometry, metamorphic and magmatic evolution of the Everest massif, High Himalaya of Nepal–South Tibet. *Journal of the Geological Society*, 160, 345–366.

Searle, M. P., Stephenson, B., Walker, J., & Walker, C. (2007). Restoration of the Western Himalaya: Implications for Metamorphic Protoliths, Thrust and Normal Faulting, and Channel Flow Models. *Episodes*, 30(4), 242–257.

Searle, M. P., Waters, D. J., Dransfield, M. W., Stephenson, B. J., Walker, C. B., Walker, J. D., & Rex, D. C. (1999b). Thermal and mechanical models for the structural and metamorphic evolution of the Zanskar High Himalaya. *Geological Society, London, Special Publications*, 164(1), 139–156.

Searle, M. P., Waters, D. J., Rex, D. C., & Wilson, R. N. (1992). Pressure, temperature and time constraints on Himalayan metamorphism from eastern Kashmir and western Zanskar. *Journal - Geological Society (London)*, 149(5), 753–773.

Seydoux-Guillaume, A.-M., Paquette, J.-L., Wiedenbeck, M., Montel, J.-M., & Heinrich, W. (2002). Experimental resetting of the U–Th–Pb systems in monazite. *Chemical Geology*, 191(1), 165–181.

Shaw, D. M. (1956). Geochemistry of pelitic rocks. Part III: Major elements and general geochemistry. *GSA Bulletin*, 67, 919–934.

Shellnutt, J. G. (2018). The Panjal Traps. *Geological Society, London, Special Publications*, 463, 59–86.

Shellnutt, J. G., Bhat, G. M., Brookfield, M. E., & Jahn, B.-M. (2011). No link between the Panjal Traps (Kashmir) and the Late Permian mass extinctions. *Geophysical Research Letters*, 38(19).

Sinclair, H. D. & Jaffey, . N. (2001). *Sedimentology of the Indus Group, Ladakh, Northern India: Implications for the Timing of Initiation of the Palaeo-Indus River*. Technical report.

Singh, K. (2012). Opposite vergent synclines on the flanks of a large-scale box fold in the Chamba–Lahaul region, northwest Himalaya, India. *International Journal of Earth Sciences*, 101(4), 997–1008.

Singh, R., Jamwal, J. S., & Singh, K. (2000). Geology of Part of Warwan Valley, Doda District, Kashmir Himalaya. *Journal Geological Society of India*, 56, 651–659.

Sinha, A. K. & Upadhyay, R. (1993). Mesozoic neo-tethyan pre-orogenic deep marine sediments along the Indus–Yarlung Suture, Himalaya. *Terra Nova*, 5(3), 271–281.

Smit, M. A., Hacker, B. R., & Lee, J. (2014). Tibetan garnet records early Eocene initiation of thickening in the Himalaya. *Geology*, 42(7), 591–594.

Smith, D. (1981). The pressure and temperature dependence of Al-solubility in sphene in the system Ti-Al-Ca-Si-O-F. *Progress in Experimental Petrology*, 18, 193–197.

Smye, A. J., Greenwood, L. V., & Holland, T. J. B. (2010). Garnet–chloritoid–kyanite assemblages: Eclogite facies indicators of subduction constraints in orogenic belts. *Journal of Metamorphic Geology*, 28(7), 753–768.

Smye, A. J., Marsh, J. H., Vermeesch, P., Garber, J. M., & Stockli, D. F. (2018). Applications and limitations of U-Pb thermochronology to middle and lower crustal thermal histories. *Chemical Geology*, 494, 1–18.

Smye, A. J., Roberts, N. M. W., Condon, D. J., Horstwood, M. S. A., & Parrish, R. R. (2014). Characterising the U–Th–Pb systematics of allanite by ID and LA-ICPMS: Implications for geochronology. *Geochimica et Cosmochimica Acta*, 135, 1–28.

Soucy La Roche, R., Godin, L., Cottle, J. M., & Kellett, D. A. (2019). Tectonometamorphic evolution of the tip of the Himalayan metamorphic core in the Jajarkot klippe, west Nepal. *Journal of Metamorphic Geology*, 37(2), 239–269.

Soucy La Roche, R., Godin, L., & Crowley, J. L. (2018). Reappraisal of emplacement models for Himalayan external crystalline nappes: The Jajarkot klippe, western Nepal. *GSA Bulletin*, 130(5-6), 1041–1056.

Spear, F. & Pyle, J. M. (2002). Apatite, monazite, and xenotime in metamorphic rocks. In M. J. Kohn, J. Rakovan, & J. M. Hughes (Eds.), *Phosphates: Geochemical, Geobiological, and Materials Importance*, volume 48 of *Reviews in Mineralogy and Geochemistry* (pp. 293–335). Washington, D. C: Mineralogical Society of America.

Spear, F. S. (1993). *Metamorphic Phase Equilibria And Presure-Temperature-Time-Paths*. Monograph Series. Washington, D.C.: Mineralogical Society of America.

Spear, F. S. (2010). Monazite–allanite phase relations in metapelites. *Chemical Geology*, 279(1), 55–62.

Spear, F. S. & Cheney, J. T. (1989). A petrogenetic grid for pelitic schists in the system SiO2-Al2O3-FeO-MgO-K2O-H2O. *Contributions to Mineralogy and Petrology*, 101(2), 149–164.

Spear, F. S., Kohn, M. J., & Cheney, J. T. (1999). P-T paths from anatectic pelites. *Contributions to Mineralogy and Petrology*, 134(1), 17–32.

Spear, F. S., Pattison, D. R., & Cheney, J. T. (2016). The metamorphosis of metamorphic petrology. In M. Bickford (Ed.), *The Web of Geological Sciences: Advances, Impacts, and Interactions II: Geological Society of America Special Paper 523*. The Geological Society of America.

Spear, F. S., Thomas, J. B., & Hallett, B. W. (2014). Overstepping the garnet isograd: A comparison of QuiG barometry and thermodynamic modeling. *Contributions to Mineralogy and Petrology*, 168(3), 1059.

Spencer, C. J., Dyck, B., Mottram, C. M., Roberts, N. M., Yao, W. H., & Martin, E. L. (2019). Deconvolving the pre-Himalayan Indian margin – Tales of crustal growth and destruction. *Geoscience Frontiers*, 10(3), 863–872.

Spencer, C. J., Harris, R. A., & Dorais, M. J. (2012). Depositional provenance of the Himalayan metamorphic core of Garhwal region, India: Constrained by U–Pb and Hf isotopes in zircons. *Gondwana Research*, 22(1), 26–35.

Spencer, C. J., Hawkesworth, C., Cawood, P. A., & Dhuime, B. (2013a). Not all supercontinents are created equal: Gondwana-Rodinia case study. *Geology*, 41(7), 795–798.

Spencer, K. J., Hacker, B. R., Kylander-Clark, A. R. C., Andersen, T. B., Cottle, J. M., Stearns, M. A., Poletti, J. E., & Seward, G. G. E. (2013b). Campaign-style titanite U–Pb dating by laser-ablation ICP: Implications for crustal flow, phase transformations and titanite closure. *Chemical Geology*, 341, 84–101.

Spring, L., Bussy, F., Vannay, J., Huon, S., & Cosca, M. A. (1993). Early Permian granitic dykes of alkaline affinity in the Indian High Himalaya of Upper Lahul and SE Zanskar: Geochemical characterization and geotectonic implications. *Geological Society, London, Special Publications*, 74, 251–264.

Spry, A. (1963). The chronological analysis of crystallization and deformation of some Tasmanian Precambrian rocks. *Journal of the Geological Society of Australia*, 10(1), 193–208.

St-Onge, M. R., Rayner, N., & Searle, M. P. (2010). Zircon age determinations for the Ladakh batholith at Chumathang (Northwest India): Implications for the age of the India-Asia collision in the Ladakh Himalaya. *Tectonophysics*, 495(3-4), 171–183.

Stacey, J. S. & Kramers, J. D. (1975). Approximation of terrestrial lead isotope evolution by a two-stage model. *Earth and Planetary Science Letters*, 26(2), 207–221.

Starr, P. G. & Pattison, D. R. M. (2019). Equilibrium and disequilibrium processes across the greenschist–amphibolite transition zone in metabasites. *Contributions to Mineralogy and Petrology*, 174(2), 18.

Starr, P. G., Pattison, D. R. M., & Ames, D. E. (2020). Mineral assemblages and phase equilibria of metabasites from the prehnite–pumpellyite to amphibolite facies, with the Flin Flon Greenstone Belt (Manitoba) as a type example. *Journal of Metamorphic Geology*, 38(1), 71–102.

Stäubli, A. (1989). Polyphase metamorphism and the development of the Main Central Thrust. *Journal of Metamorphic Geology*, 7, 73–93.

Stäubli, A. R. (1988). *Metamorphose und Deformation im Bereich der zentralen Hauptüberschiebung (M.C.T.) (Kishtwar Fenster, NW-Himalaya)*. PhD thesis, ETH Zurich.

Stearns, M. A., Cottle, J. M., Hacker, B. R., & Kylander-Clark, A. R. C. (2016). Extracting thermal histories from the near-rim zoning in titanite using coupled U-Pb and trace-element depth profiles by single-shot laser-ablation split stream (SS-LASS) ICP-MS. *Chemical Geology*, 422, 13–24.

Steck, A. (2003). Geology of the NW Indian Himalaya. *Eclogae Geologicae Helvetiae*, 96, 147–196.

Steck, A. & Hunziker, J. (1994). The Tertiary structural and thermal evolution of the Central Alps-compressional and extensional structures in an erogenic belt. *Tectonophysics*, 238, 229–254.

Steltenpohl, M. G. & Bartley, J. M. (1987). Thermobarometric profile through the Caledonian nappe stack of Western Ofoten, North Norway. *Contributions to Mineralogy and Petrology*, 96(1), 93–103.

Stephenson, B. J. (1997). *The Tectonic and Metamorphic Evolution of the Main Central Thrust Zone and High Himalaya around the Kishtwar and Kulu Windows, Northwest India*. PhD thesis, University of Oxford.

Stephenson, B. J., Searle, M. P., Waters, D. J., & Rex, D. C. (2001). Structure of the Main Central Thrust zone and extrusion of the High Himalayan deep crustal wedge, Kishtwar–Zanskar Himalaya. *Journal of the Geological Society*, 158(4), 637–652.

Stephenson, B. J., Waters, D. J., & Searle, M. P. (2000). Inverted metamorphism and the Main Central Thrust: Field relations and thermobarometric constraints from the Kishtwar Window, NW Indian Himalaya. *Journal of Metamorphic Geology*, 18(5), 571–590.

Štípská, P., Hacker, B. R., Racek, M., Holder, R., Kylander-Clark, A. R. C., Schulmann, K., & Hasalová, P. (2015). Monazite Dating of Prograde and Retrograde P–T–d paths in the Barrovian terrane of the Thaya window, Bohemian Massif. *Journal of Petrology*, 56(5), 1007–1035.

Štípská, P., Závada, P., Collett, S., Kylander-Clark, A. R., Hacker, B. R., Tabaud, A. S., & Racek, M. (2020). Eocene migmatite formation and diachronous burial revealed by petrochronology in NW Himalaya, Zanskar. *Journal of Metamorphic Geology*, 38(6), 655–691.

Streule, M. J., Searle, M. P., Waters, D. J., & Horstwood, M. S. A. (2010). Metamorphism, melting, and channel flow in the Greater Himalayan Sequence and Makalu leucogranite: Constraints from thermobarometry, metamorphic modeling, and U-Pb geochronology. *Tectonics*, 29(5).

Stübner, K., Grujic, D., Parrish, R. R., Roberts, N. M., Kronz, A., Wooden, J., & Ahmad, T. (2014). Monazite geochronology unravels the timing of crustal thickening in NW Himalaya. *Lithos*, 210–211, 111–128.

Stüwe, K. (1997). Effective bulk composition changes due to cooling: A model predicting complexities in retrograde reaction textures. *Contributions to Mineralogy and Petrology*, 129(1), 43–52.

Stüwe, K. (2007). *Geodynamics of the Lithosphere*. Berlin, Heidelberg: Springer, 2nd edition.

Sutre, E. (1990). *Les formations de la marge néotethysienne et les mélanges ophiolitiques de la zone de suture de l'Indus en Himalaya du Ladakh - Inde. - Stratigraphie, tectonique, évolution géodynamique*. PhD thesis, Université de Poitiers.

Tajčmanová, L., Connolly, J. a. D., & Cesare, B. (2009). A thermodynamic model for titanium and ferric iron solution in biotite. *Journal of Metamorphic Geology*, 27(2), 153–165.

Taylor, R. J. M., Kirkland, C. L., & Clark, C. (2016). Accessories after the facts: Constraining the timing, duration and conditions of high-temperature metamorphic processes. *Lithos*, 264, 239–257.

Thakur, S. S. (2014). Retrograde corona texture in pre-Himalayan metamorphic mafic xenoliths, Sutlej valley, NW Himalaya: Implication on rare occurrence of high-grade rocks in the Himalaya. *Journal of Asian Earth Sciences*, 88, 41–49.

Thakur, S. S., Patel, c. S. C., & Singh, c. A. K. (2015). A P-T pseudosection modelling approach to understand metamorphic evolution of the Main Central Thrust Zone in the Alaknanda valley, NW Himalaya. *Contributions to Mineralogy and Petrology*, 170(2).

Thakur, S. S. & Patel, S. C. (2012). Mafic and pelitic xenoliths in the Kinnaur Kailash Granite, Baspa river valley, NW Himalaya: Evidence of pre-Himalayan granulite metamorphism followed by cooling event. *Journal of Asian Earth Sciences*, 56, 105–117.

Thakur, S. S. & Tripathi, K. (2008). Regional metamorphism in the Haimanta Group of rocks, Sutlej river valley, NW Himalaya, India. *Current Science*, 95(1), 104–109.

Thakur, V. C. (1981). Regional framework and geodynamic evolution of the Indus-Tsangpo suture zone in the Ladakh Himalayas. *Earth and Environmental Science Transactions of The Royal Society of Edinburgh*, 72(2), 89–97.

Thakur, V. C. (1998). Structure of the Chamba nappe and position of the Main Central Thrust in Kashmir Himalaya. *Journal of Asian Earth Sciences*, 16(2-3), 269–282.

Thomas, J. B., Bruce Watson, E., Spear, F. S., Shemella, P. T., Nayak, S. K., & Lanzirotti, A. (2010). TitaniQ under pressure: The effect of pressure and temperature on the solubility of Ti in quartz. *Contributions to Mineralogy and Petrology*, 160(5), 743–759.

Thomas, J. B. & Spear, F. S. (2018). Experimental study of quartz inclusions in garnet at pressures up to 3.0 GPa: Evaluating validity of the quartz-in-garnet inclusion elastic thermobarometer. *Contributions to Mineralogy and Petrology*, 173(5), 42.

Thomas, J. B., Watson, E. B., Spear, F. S., & Wark, D. A. (2015). TitaniQ recrystallized: Experimental confirmation of the original Ti-in-quartz calibrations. *Contributions to Mineralogy and Petrology*, 169(3), 27.

Thöni, M., Miller, C., Hager, C., Grasemann, B., & Horschinegg, M. (2012). New geochronological constraints on the thermal and exhumation history of the Lesser and Higher Himalayan Crystalline Units in the Kullu-Kinnaur area of Himachal Pradesh (India). *Journal of Asian Earth Sciences*, 52, 98–116.

Tiepolo, M., Oberti, R., & Vannucci, R. (2002). Trace-element incorporation in titanite: Constraints from experimentally determined solid/liquid partition coefficients. *Chemical Geology*, 191(1), 105–119.

Tinkham, D. K., Zuluaga, C. A., & Stowell, H. H. (2001). Metapelite phase equilibria modeling in MnNCKFMASH: The effect of variable Al2O3 and MgO/(MgO + FeO) on mineral stability. *Geological Materials Research*, 3(1), 1–42.

Tobgay, T., McQuarrie, N., Long, S., Kohn, M. J., & Corrie, S. L. (2012). The age and rate of displacement along the Main Central Thrust in the western Bhutan Himalaya. *Earth and Planetary Science Letters*, 319–320, 146–158.

Tomkins, H. S., Powell, R., & Ellis, D. J. (2007). The pressure dependence of the zirconium-in-rutile thermometer. *Journal of Metamorphic Geology*, 25(6), 703–713.

Tracy, R. J. (1982). Compositional Zoning and Inclusions in Metamorphic Minerals. *Reviews in Mineralogy*, 10, 355–397.

Ugwuonah, E. N., Tsunogae, T., & Obiora, S. C. (2017). Metamorphic P–T evolution of garnet-staurolite-biotite pelitic schist and amphibolite from Keffi, north-central Nigeria: Geothermobarometry, mineral equilibrium modeling and P-T path. *Journal of African Earth Sciences*, 129, 1–16.

Unsworth, M. J., Jones, A. G., Wei, W., Marquis, G., Gokarn, S. G., & Spratt, J. E. (2005). Crustal rheology of the Himalaya and Southern Tibet inferred from magnetotelluric data. *Nature*, 438(7064), 78–81.

Upreti, B. N. (1999). An overview of the stratigraphy and tectonics of the Nepal Himalaya. *Journal of Asian Earth Sciences*, 17(5), 577–606.

Valli, F., Guillot, S., & Hattori, K. H. (2004). Source and tectono-metamorphic evolution of mafic and pelitic metasedimentary rocks from the central Quetico metasedimentary belt, Archean Superior Province of Canada. *Precambrian Research*, 132(1), 155–177.

Vance, D., Ayres, M., Kelley, S., & Harris, N. (1998). The thermal response of a metamorphic belt to extension: Constraints from laser Ar data on metamorphic micas. *Earth and Planetary Science Letters*, 162(1), 153–164.

Vance, D. & Harris, N. (1999). Timing of prograde metamorphism in the Zanskar Himalaya. *Geology*, 27(5), 395–398.

Vance, D. & Mahar, E. (1998). Pressure-temperature paths from P-T pseudosections and zoned garnets: Potential, limitations and examples from the Zanskar Himalaya, NW India. *Contributions to Mineralogy and Petrology*, 132, 225–245.

Vannay, J.-C. & Grasemann, B. (1998). Inverted metamorphism in the High Himalaya of Himachal (NW India) : Phase equilibria versus thermobarometry. *Schweizerische Mineralogische und Petrographische Mitteilungen*, 78(1), 107–132.

Vannay, J.-c. & Grasemann, B. (2001). Himalayan inverted metamorphism and syn-convergence extension as a consequence of a general shear extrusion. *Geological Magazine*, 138(3), 253–276.

Vannay, J.-C., Grasemann, B., Rahn, M., Frank, W., Carter, A., Baudraz, V., & Cosca, M. (2004). Miocene to Holocene exhumation of metamorphic crustal wedges in the NW Himalaya: Evidence for tectonic extrusion coupled to fluvial erosion. *Tectonics*, 23(1).

Vannay, J.-C., Sharp, Z. D., & Grasemann, B. (1999). Himalayan inverted metamorphism constrained by oxygen isotope thermometry. *Contributions to Mineralogy and Petrology*, 137(1-2), 90–101.

Vannay, J.-C. C. & Steck, A. (1995). Tectonic evolution of the High Himalaya in Upper Lahul (NW Himalaya, India). *Tectonics*, 14(2), 253–263.

Vermeesch, P. (2018). IsoplotR: A free and open toolbox for geochronology. *Geoscience Frontiers*, 9(5), 1479–1493.

Vermeesch, P. (2020). Unifying the U–Pb and Th–Pb methods: Joint isochron regression and common Pb correction. *Geochronology*, 2(1), 119–131.

Verts, L. A., Chamberlain, K. R., & Frost, C. D. (1996). U-Pb sphene dating of metamorphism: The importance of sphene growth in the contact aureole of the Red Mountain pluton, Laramie Mountains, Wyoming. *Contributions to Mineralogy and Petrology*, 125(2), 186–199.

von Blackenburg, F. (1992). Combined high-precision chronometry and geochemical tracing using accessory minerals: Applied to the Central-Alpine Bergell intrusion (central Europe). *Chemical Geology*, 100(1), 19–40.

Vuorinen, J. H. & Hålenius, U. (2005). Nb-, Zr- and LREE-rich titanite from the ALnö alkaline complex: Crystal chemistry and its importance as a petrogenetic indicator. *Lithos*, 83(1-2), 128–142.

Wadia, D. N. (1961). *Geology of India*. London: Macmillan.

Walker, C. B. (1999). *The Tectonothermal Evolution of the High Himalaya in the Suru Valley, NW Zanskar with Constraints from Metamorphic Modelling*. PhD thesis, University of Oxford.

Walker, C. B., Searle, M. P., & Waters, D. J. (2001). An integrated tectonothermal model for the evolution of the high Himalaya in Western Zanskar with constraints from thermobarometry and metamorphic modeling. *Tectonics*, 20(6), 810–833.

Walker, J. D. (1998). *The Structural and Metamorphic Evolution of the High Himalayan Slab in SE Zanskar and NW Lahaul*. PhD thesis, University of Oxford.

Walker, J. D., Martin, M. W., Bowring, S. A., Searle, M. P., Waters, D. J., & Hodges, K. V. (1999). Metamorphism, Melting, and Extension: Age Constraints from the High Himalayan Slab of Southeast Zanskar and Northwest Lahaul. *The Journal of Geology*, 107(4), 473–495.

Walsh, J., Buckman, S., & Nutman, A. P. (2019). Age and Provenance of the Nindam Formation, Ladakh, NW Himalaya: Evolution of the Intraoceanic Dras Arc Before Collision With India. *Tectonics*, 38, 1–27.

Walsh, J. M. J., Buckman, S., Nutman, A. P., & Zhou, R. (2021). The significance of Upper Jurassic felsic volcanic rocks within the incipient, intraoceanic Dras Arc, Ladakh, NW Himalaya. *Gondwana Research*, 90, 199–219.

Walters, J. B., Cruz-Uribe, A. M., Song, W. J., Gerbi, C., & Biela, K. (2022). Strengths and limitations of in situ U–Pb titanite petrochronology in polymetamorphic rocks: An example from western Maine, USA. *Journal of Metamorphic Geology*, 40(6), 1043–1066.

Walters, J. B. & Kohn, M. J. (2017). Protracted thrusting followed by late rapid cooling of the Greater Himalayan Sequence, Annapurna Himalaya, Central Nepal: Insights from titanite petrochronology. *Journal of Metamorphic Geology*, 35(8), 897–917.

Walther, J. V. & Orville, P. M. (1982). Volatile production and transport in regional metamorphism. *Contributions to Mineralogy and Petrology*, 79, 252–257.

Wang, J.-M., Zhang, J.-J., Liu, K., Zhang, B., Wang, X.-X., Rai, S., & Scheltens, M. (2016). Spatial and temporal evolution of tectonometamorphic discontinuities in the central Himalaya: Constraints from P–T paths and geochronology. *Tectonophysics*, 679, 41–60.

Wang, Y.-H., Zhang, L.-F., Li, S.-Z., & Somerville, I. (2017). Zircon U–Pb dating and phase equilibria modelling of gneisses from Dinggye area, Ama Drime Massif, central Himalaya. *Geological Journal*, 52(S1), 476–494.

Wark, D. A. & Watson, E. B. (2006). TitaniQ: A titanium-in-quartz geothermometer. *Contributions to Mineralogy and Petrology*, 152(6), 743–754.

Warren, C. J., Greenwood, L. V., Argles, T. W., Roberts, N. M. W., Parrish, R. R., & Harris, N. B. W. (2019). Garnet–monazite rare earth element relationships in sub-solidus metapelites: A case study from Bhutan. *Geological Society, London, Special Publications*, 478(1), 145–166.

Waters, D. J. (2001). The significance of prograde and retrograde quartz-bearing intergrowth microstructures in partially melted granulite-facies rocks. *Lithos*, 56(1), 97–110.

Waters, D. J. (2019). Metamorphic constraints on the tectonic evolution of the High Himalaya in Nepal: The art of the possible. *Geological Society London, Special Publication*, 483.

Waters, D. J. & Charnley, N. R. (2002). Local equilibrium in polymetamorphic gneiss and the titanium substitution in biotite. *American Mineralogist*, 87(4), 383–396.

Waters, D. J. & Lovegrove, D. P. (2002). Assessing the extent of disequilibrium and overstepping of prograde metamorphic reactions in metapelites from the Bushveld Complex aureole, South Africa. *Journal of Metamorphic Geology*, 20(1), 135–149.

Watson, E. B., Wark, D. A., & Thomas, J. B. (2006). Crystallization thermometers for zircon and rutile. *Contributions to Mineralogy and Petrology*, 151(4), 413–433.

Webb, A. A. G., Yin, A., Harrison, T. M., Célérier, J., & Burgess, W. P. (2007). The leading edge of the Greater Himalayan Crystalline complex revealed in the NW Indian Himalaya: Implications for the evolution of the Himalayan orogen. *Geology*, 35(10), 955–958.

Webb, A. A. G., Yin, A., Harrison, T. M., Célérier, J., Gehrels, G. E., Manning, C. E., & Grove, M. (2011). Cenozoic tectonic history of the Himachal Himalaya (northwestern India) and its constraints on the formation mechanism of the Himalayan orogen. *Geosphere*, 7(4), 1013–1061.

Weller, O. M., Jackson, S., Miller, W. G. R., St-Onge, M. R., & Rayner, N. (2020). Quantitative elemental mapping of granulite-facies monazite: Textural insights and implications for petrochronology. *Journal of Metamorphic Geology*, 38(8), 853–880.

Weller, O. M., Mottram, C. M., St-Onge, M. R., Möller, C., Strachan, R., Rivers, T., & Copley, A. (2021). The metamorphic and magmatic record of collisional orogens. *Nature Reviews Earth & Environment*, 2(11), 781–789.

Weller, O. M., St-Onge, M. R., Waters, D. J., Rayner, N., Searle, M. P., Chung, S.-L., Palin, R. M., Lee, Y.-H., & Xu, X. (2013). Quantifying Barrovian metamorphism in the Danba Structural Culmination of eastern Tibet. *Journal of Metamorphic Geology*, 31(9), 909–935.

Wheller, C. J. & Powell, R. (2014). A new thermodynamic model for sapphirine: Calculated phase equilibria in K2O–FeO–MgO–Al2O3–SiO2–H2O–TiO2–Fe2O3. *Journal of Metamorphic Geology*, 32(3), 287–299.

White, Powell, Holland, & Worley (2000). The effect of TiO2 and Fe2O3 on metapelitic assemblages at greenschist and amphibolite facies conditions: Mineral equilibria calculations in the system K2O–FeO–MgO–Al2O3–SiO2–H2O–TiO2–Fe2O3. *Journal of Metamorphic Geology*, 18(5), 497–511.

White, R. W., Powell, R., & Holland, T. J. B. (2001). Calculation of partial melting equilibria in the system Na2O–CaO–K2O–FeO–MgO–Al2O3–SiO2–H2O (NCKFMASH). *Journal of Metamorphic Geology*, 19(2), 139–153.

White, R. W., Powell, R., & Holland, T. J. B. (2007). Progress relating to calculation of partial melting equilibria for metapelites. *Journal of Metamorphic Geology*, 25(5), 511–527.

White, R. W., Powell, R., Holland, T. J. B., Johnson, T. E., & Green, E. C. R. (2014a). New mineral activity–composition relations for thermodynamic calculations in metapelitic systems. *Journal of Metamorphic Geology*, 32(3), 261–286.

White, R. W., Powell, R., & Johnson, T. E. (2014b). The effect of Mn on mineral stability in metapelites revisited: New a–x relations for manganese-bearing minerals. *Journal of Metamorphic Geology*, 32(8), 809–828.

Whitney, D. L. & Evans, B. W. (2010). Abbreviations for names of rock-forming minerals. *American Mineralogist*, 95(1), 185–187.

Whitney, D. L., Teyssier, C., & Fayon, A. K. (2004). Isothermal decompression, partial melting and exhumation of deep continental crust. *Geological Society, London, Special Publications*, 227(1), 313–326.

Wiesmayr, G. & Grasemann, B. (2002). Eohimalayan fold and thrust belt: Implications for the geodynamic evolution of the NW-Himalaya (India). *Tectonics*, 21(6), 8–1–8–18.

Wilks, W. J. & Cuthbert, S. J. (1994). The evolution of the Hornelen Basin detachment system, western Norway: Implications for the style of late orogenic extension in the southern Scandinavian Caledonides. *Tectonophysics*, 238(1-4), 1–30.

Williams, M. L., Jercinovic, M. J., & Hetherington, C. J. (2007). Microprobe Monazite Geochronology: Understanding Geologic Processes by Integrating Composition and Chronology. *Annual Review of Earth and Planetary Sciences*, 35(1), 137–175.

Wing, B. A., Ferry, J. M., & Harrison, T. M. (2003). Prograde destruction and formation of monazite and allanite during contact and regional metamorphism of pelites: Petrology and geochronology. *Contributions to Mineralogy and Petrology*, 145(2), 228–250.

Wolfe, O. M., Spear, F. S., & Harrison, T. M. (2021). Pronounced and rapid exhumation of the Connecticut Valley Trough revealed through quartz in garnet Raman barometry and diffusion modelling of garnet dissolution–reprecipitation reactions. *Journal of Metamorphic Geology*, 39(8), 1045–1069.

Woodsworth, G. J. (1977). Homogenization of zoned garnets from pelitic schists. *The Canadian Mineralogist*, 15, 230–242.

Worley & Powell (2000). High-precision relative thermobarometry: Theory and a worked example. *Journal of Metamorphic Geology*, 18(1), 91–101.

Wu, C.-M. & Chen, H.-X. (2015). Revised Ti-in-biotite geothermometer for ilmenite- or rutile-bearing crustal metapelites. *Science Bulletin*, 60(1), 116–121.

Wu, F. Y., Clift, P. D., & Yang, J. H. (2007). Zircon Hf isotopic constraints on the sources of the Indus Molasse, Ladakh Himalaya, India. *Tectonics*, 26(2).

Wyss, M. (2000). Metamorphic evolution of the northern Himachal Himalaya: Phase equilibria constraints and thermobarometry. *Schweizerische mineralogische und petrographische Mitteilungen*, 80, 317–350.

Wyss, M., Hermann, J., & Steck, A. L. (1999). Structural and metamorphic evolution of the northern Himachal Himalaya, NW India (Spiti-eastern Lahul-Parvati valley traverse). *Eclogae Geologicae Helvetiae*, 92, 3–44.

Yakymchuk, C. & Brown, M. (2014). Behaviour of zircon and monazite during crustal melting. *Journal of the Geological Society*, 171, 465–479.

Yakymchuk, C. & Godin, L. (2012). Coupled role of deformation and metamorphism in the construction of inverted metamorphic sequences: An example from far-northwest Nepal. *Journal of Metamorphic Geology*, 30(5), 513–535.

Yakymchuk, C., Kirkland, C. L., & Clark, C. (2018). Th/U ratios in metamorphic zircon. *Journal of Metamorphic Geology*, 36(6), 715–737.

Yardley, B. W. D. (1977). The nature and significance of the mechanism of sillimanite growth in the Connemara schists, Ireland. *Contributions to Mineralogy and Petrology*, 65(1), 53–58.

Yin, A. (2006). Cenozoic tectonic evolution of the Himalayan orogen as constrained by along-strike variation of structural geometry, exhumation history, and foreland sedimentation. *Earth-Science Reviews*, 76(1-2), 1–131.

Zack, T., Moraes, R., & Kronz, A. (2004). Temperature dependence of Zr in rutile: Empirical calibration of a rutile thermometer. *Contributions to Mineralogy and Petrology*, 148(4), 471–488.

Zack, T., Stockli, D. F., Luvizotto, G. L., Barth, M. G., Belousova, E., Wolfe, M. R., & Hinton, R. W. (2011). In situ U–Pb rutile dating by LA-ICP-MS: 208Pb correction and prospects for geological applications. *Contributions to Mineralogy and Petrology*, 162(3), 515–530.

Zhang, L., Ye, Y., & Qin, S. (2018). Water in the Thickened Lower Crust of the Eastern Himalayan Orogen. *Journal of Earth Sci-ence*, 29(5), 1040.

Zhao, L., Zeng, L., Gao, L., Hu, M., Sun, D., & Zhang, L. (2023). Rutile to Titanite Transformation in Eclogites and its Geochemical Consequences: An Example from the Sumdo Eclogite, Tibet. *Acta Geologica Sinica - English Edition*, 97(1), 122–133.

Zhong, X., Moulas, E., & Tajčmanová, L. (2020). Post-entrapment modification of residual inclusion pressure and its implications for Raman elastic thermobarometry. *Solid Earth*, 11(1), 223–240.

Zhu, D.-C., Wang, Q., Chung, S.-L., Cawood, P. A., & Zhao, Z.-D. (2019). Gangdese magmatism in southern Tibet and India–Asia convergence since 120 Ma. *Geological Society, London, Special Publications*, 483(1), 583–604.

Zhu, D.-C., Wang, Q., Zhao, Z.-D., Chung, S.-L., Cawood, P. A., Niu, Y., Liu, S.-A., Wu, F.-Y., & Mo, X.-X. (2015). Magmatic record of India-Asia collision. *Scientific Reports*, 5(1), 14289.

Zuluaga, C. A., Stowell, H. H., & Tinkham, D. K. (2005). The effect of zoned garnet on metapelite pseudosection topology and calculated metamorphic P-T paths. *American Mineralogist*, 90, 1619–1628.

Appendix A

Structure

Owing to the large dataset used in this study digital files are primarily used. The appendices are structured as follows:

A.1 includes separate 1:50,000 geological map and vertical cross-sections, sample locations, structural data, descriptions of fabric-defining mineral assemblages, and supplementary field photos. A kmz file for use with Google Earth is also included and contains the georeferenced geological and simplified maps.

A.2 XRF bulk rock compositions, EPMA mineral analyses, BSE and X-ray maps for all analysed phases, spot location screenshots for all analyses, and spectrometer parameters

A.3 includes RM pooled ages and long-term reproducibility plots, RM collated table, and U-(Th)-Pb compiled data file for all analysed phases.

Table A.1 Structure of digital appendices and location and contents of all files

Parent	Content	File/folder name	File type
A.1	Google Earth georeferenced geological map + all line-form maps	suru_valled_all_maps	.kmz
A.1	1:50,000 geological map of the Suru Valley region	suru_valley_map	.pdf
A.1	1:50,000 cross-sections of the Suru Valley region	suru_valley_cross-sections	.pdf
A.1	Descriptions of fabric defining mineral assemblages and additional field photos	fabric_assemblages_field_photos	.pdf
A.1	Sample locations and metamorphic indicator minerals	ICSV_sample_locations	.xlsx
A.1	D_1–D_3 planar and linear structural data	ICSV_structural_data	.xlsx
A.2	XRF bulk rock compositions	ICSV_bulk_comp	.xlsx
A.2	EPMA mineral analyses (pelite)	ICSV_pelite_mineral_chemistry	.xlsx
A.2	EPMA mineral analyses (metabasite)	ICSV_metabasite_mineral_chemistry	.xlsx
A.2	EPMA rutile Zr analysis	ICSV_Zr-in-Rt	.xlsx
A.2	BSE and CL imagery	BSE_CL_images	folder
A.2	X-ray maps	X-ray_maps	folder
A.2	Spectrometer parameters	EPMA_setup	.pdf
A.3	Analytical conditions for all U-(Th)-Pb analyses	U-Th-Pb_analytical_conditions	.xlsx
A.3	Reference material pooled ages and long term reproducibility plots	RM_ages	.pdf
A.3	U-(Th)-Pb compiled data file for standards and unknowns	ICSV_U-Th-Pb_compiled_tables	.xlsx
A.3	Spot locations screenshots for analysed phases	Spot_locations	folder